

AD-A281 446



DOCUMENTATION PAGE

Form Approved
OMB No 0704-0188

①

Information is estimated to average 1 hour per response, including the time for reviewing instructions, searching existing data sources, gathering and maintaining the data needed, completing and reviewing the collection of information, Send comments regarding this burden estimate or any other aspect of this collection of information, including suggestions for reducing this burden, to Washington Headquarters Services, Directorate for Information Operations and Reports, 1215 Jefferson Davis Highway, Suite 1204, Arlington, VA 22202-4302, and to the Office of Management and Budget, Paperwork Project (0704-0188), Washington, DC 20503.

k) 2. REPORT DATE
June 1994

3. REPORT TYPE AND DATES COVERED
Final 5 Mar 93-4 Mar 94

4. TITLE AND SUBTITLE Organization of the 1993 Optical Remote Sensing Topical Meeting		5. FUNDING NUMBERS DAAH04-93-G-0041	
6. AUTHOR(S) Jarus W. Quinn (principal investigator)			
7. PERFORMING ORGANIZATION NAME(S) AND ADDRESS(ES) Optical Society of America Washington, DC 20036		8. PERFORMING ORGANIZATION REPORT NUMBER	
9. SPONSORING / MONITORING AGENCY NAME(S) AND ADDRESS(ES) U.S. Army Research Office P.O. Box 12211 Research Triangle Park, NC 27709-2211		10. SPONSORING / MONITORING AGENCY REPORT NUMBER ARO 31110.1-GS-CF	
11. SUPPLEMENTARY NOTES The views, opinions and/or findings contained in this report are those of the author(s) and should not be construed as an official Department of the Army position, policy, or decision, unless so designated by other documentation.			
12a. DISTRIBUTION / AVAILABILITY STATEMENT Approved for public release; distribution unlimited.		12b. DISTRIBUTION CODE	
13. ABSTRACT (Maximum 200 words) The conference was held as scheduled. Summaries of papers presented at the meeting appear in the 1993 Technical Digest Series Volume 5 Postconference Edition of the Optical Society of America.			
14. SUBJECT TERMS Remote Sensing, Optical Remote Sensing, Conference, Atmosphere		15. NUMBER OF PAGES 521	
		16. PRICE CODE	
17. SECURITY CLASSIFICATION OF REPORT UNCLASSIFIED	18. SECURITY CLASSIFICATION OF THIS PAGE UNCLASSIFIED	19. SECURITY CLASSIFICATION OF ABSTRACT UNCLASSIFIED	20. LIMITATION OF ABSTRACT UL

POSTCONFERENCE EDITION

94-21206



Sponsored by
Optical Society of America

In Cooperation with
American Meteorological Society

1993 OSA Technical Digests

- Vol 1 High Resolution Spectroscopy** Salt Lake City, UT (January 18-21)
Postconference edition: ISBN 1-55752-273-1 [U.S. List Price: \$66 / OSA Member Price: \$43]
- Vol 2 Compact Blue-Green Lasers** New Orleans, LA (February 2-4)
Postconference edition: ISBN 1-55752-278-2 [U.S. List Price: \$75 / OSA Member Price: \$48]
- Vol 3 Ophthalmic and Visual Optics AND Noninvasive Assessment of the Visual System**
Monterey, CA (February 19-23)
Postconference edition: ISBN 1-55752-280-4 [U.S. List Price: \$92 / OSA Member Price: \$60]
- Vol 4 Optical Fiber Communication Conference & International Conference on Integrated Optics and Optical Fiber Communication** San Jose, CA (February 21-26)
Postconference edition: ISBN 1-55752-282-0 [U.S. List Price: \$92 / OSA Member Price: \$60]
- Vol 5 Optical Remote Sensing of the Atmosphere** Salt Lake City, UT (March 8-12)
Postconference edition: ISBN 1-55752-284-7 [U.S. List Price: \$92 / OSA Member Price: \$60]
- Vol 6 Spatial Light Modulators and Applications** Palm Springs, CA (March 15-17)
Postconference edition: ISBN 1-55752-288-1 [U.S. List Price: \$75 / OSA Member Price: \$48]
- Vol 7 Optical Computing** Palm Springs, CA (March 16-19)
Postconference edition: ISBN 1-55752-290-1 [U.S. List Price: \$75 / OSA Member Price: \$48]
- Vol 8 Quantum Optoelectronics** Palm Springs, CA (March 17-19)
Postconference edition: ISBN 1-55752-292-8 [U.S. List Price: \$75 / OSA Member Price: \$48]
- Vol 9 Optical Design for Photonics** Palm Springs, CA (March 22-24)
Postconference edition: ISBN 1-55752-294-4 [U.S. List Price: \$75 / OSA Member Price: \$48]
- Vol 10 Integrated Photonics Research** Palm Springs, CA (March 22-25)
Postconference edition: ISBN 1-55752-296-0 [U.S. List Price: \$92 / OSA Member Price: \$60]
- Vol 11 Conference on Lasers and Electro-Optics** Baltimore, MD (May 2-7)
Postconference edition: ISBN 1-55752-300-2 [U.S. List Price: \$92 / OSA Member Price: \$60]
- Vol 12 Quantum Electronics and Laser Science** Baltimore, MD (May 2-7)
Postconference edition: ISBN 1-55752-301-0 [U.S. List Price: \$92 / OSA Member Price: \$60]
- Vol 13 Light and Color in the Open Air** University Park, PA (June 16-18)
Postconference edition: ISBN 1-55752-305-3 [U.S. List Price: \$66 / OSA Member Price: \$43]
- Vol 14 Optical Amplifiers and Their Applications** Yokohama, Japan (July 4-6)
Postconference edition: ISBN 1-55752-310-X [U.S. List Price: \$75 / OSA Member Price: \$48]
- Vol 15 Nonlinear Guided Wave Phenomena** Southampton, UK (September 19-22)
Postconference edition: ISBN 1-55752-312-6 [U.S. List Price: \$75 / OSA Member Price: \$48]
- Vol 16 OSA Annual Meeting** Toronto, Canada (October 3-8)
Postconference edition: ISBN 1-55752-314-2 [U.S. List Price: \$75 / OSA Member Price: \$48]
- Vol 17 Organic Thin Films for Photonic Applications** Toronto, Canada (October 6-8)
Postconference edition: ISBN 1-55752-316-9 [U.S. List Price: \$75 / OSA Member Price: \$48]

(All Technical digests and Postconference editions are paperback.)

Order by phone, fax, or mail. To charge by phone, call (202) 416-1907.
(We accept VISA, MasterCard, Diner's Club, and AMEX.) Fax your order and charge information to (202) 416-6120. Mail your order to: OSA Publications Dept.,
ATTN: Susan Bornt, 2010 Massachusetts Ave., NW, Washington, DC 20036-1023.
Orders are accepted up to six months in advance of the meeting.





Optical Remote Sensing of the Atmosphere

*Summaries of papers presented at the
Optical Remote Sensing of the Atmosphere
Topical Meeting*

March 8–12, 1993
Salt Lake City, Utah

1993 Technical Digest Series
Volume 5

POSTCONFERENCE EDITION

Sponsored by
Optical Society of America

In Cooperation with
American Meteorological Society

Partially Supported by
Army Research Office

Optical Society of America
2010 Massachusetts Avenue, NW
Washington, DC 200361023

Articles in this publication may be cited in other publications. In order to facilitate access to the original publication source, the following form for the citation is suggested:

Name of Author(s), "Title of Paper," in Optical Remote Sensing of the Atmosphere
Technical Digest, 1993 (Optical Society of America, Washington, D.C., 1993), Vol. 5,
pp. xx-xx.

ISBN Number

Conference Edition	1-55752-283-9
Postconference Edition	1-55752-284-7
(Note: Postconference Edition includes postdeadline papers.)	
1993 Technical Digest Series	1-55752-317-7

Library of Congress Catalog Card Number

Conference Edition	92-62850
Postconference Edition	92-62849

Copyright © 1993, Optical Society of America

Individual readers of this digest and libraries acting for them are permitted to make fair use of the material in it, such as to copy an article for use in teaching or research, without payment of fee, provided that such copies are not sold. Copying for sale is subject to payment of copying fees. The code 1-55752-317-7/93/\$2.00 gives the per-article copying fee for each copy of the article made beyond the free copying permitted under Sections 107 and 108 of the U.S. Copyright Law. The fee should be paid through the Copyright Clearance Center, Inc., 21 Congress Street, Salem, MA 01970.

Permission is granted to quote excerpts from articles in this digest in scientific works with the customary acknowledgment of the source, including the author's name and the name of the digest, page, year, and name of the Society. Reproduction of figures and tables is likewise permitted in other articles and books provided that the same information is printed with them and notification is given to the Optical Society of America. Republication or systematic or multiple reproduction of any material in this digest is permitted only under license from the Optical Society of America; in addition, the Optical Society may require that permission also be obtained from one of the authors. Address inquiries and notices to Director of Publications, Optical Society of America, 2010 Massachusetts Avenue, NW, Washington, DC 20036-1023. In the case of articles whose authors are employees of the United States Government or its contractors or grantees, the Optical Society of America recognizes the right of the United States Government to retain a nonexclusive, royalty-free license to use the author's copyrighted article for United States Government purposes.

The views, opinions, and/or findings contained in this report are those of the author(s) and should not be construed as an official Department of the Army position, policy, or decision, unless so designated by other documentation.

Printed in U.S.A.

CONTENTS

Agenda of Sessions.....	v
MA Keynote Session	1
MB Water Vapor	9
MC Space & Ground Based Remote Sensing 1	31
MD Space & Ground Based Remote Sensing 2	43
TuA Space & Ground Based Remote Sensing 3	63
TuB Constituents.....	87
TuC Clouds and ECLIPS	105
TuD Poster Session 1	135
WA Winds 1	223
WB Winds 2	235
WC Ozone 1	255
WD Ozone 2	267
ThA Aerosols 1	281
ThB Aerosols 2	297
ThC Spectroscopy 1	321
ThD Spectroscopy 2	337
ThE Poster Session 2	351
FA New Developments 1	431
FB New Developments 2	453
Key to Authors and Presiders	466

Accession For	
NTIS GRA&I	<input checked="" type="checkbox"/>
DTIC TAB	<input type="checkbox"/>
Unannounced	<input type="checkbox"/>
Justification	
By	
Distribution/	
Availability Codes	
Dist	Avail and/or Special
A-1	

TECHNICAL PROGRAM COMMITTEE

Allan Carswell, *General Cochair*
York University, Canada

William Mankin, *General Cochair*
National Center for Atmospheric Research

Stuart McDermid, *Program Cochair*
Jet Propulsion Laboratory

William Smith, *Program Cochair*
University of Wisconsin, Madison

Alain Chedin
Ecole Polytechnique, France

Shepard A. Clough
Atmospheric Environmental Research, Inc.

Herbert Fisher
Meteorological Institut Munchen, Germany

Raymond M. Hoff
Atmospheric Environment Service, Canada

Horst Jager
Fraunhofer Institute, Germany

Thomas J. McGee
NASA Goddard Space Flight Center

John Meriwether
Phillips Laboratory

Clive Rodgers
Oxford University, England

Yasuhiro Sasano
National Institute for Environmental Studies, Japan

D. P. J. Swart
RIVM, Holland (The Netherlands)

Ed Westwater
NOAA/Environmental Research Laboratories

MONDAY, MARCH 8, 1993

SALON D

7:55 am-8:00 am

OPENING REMARKS

William Mankin, General Co-chair

SALON D

8:15 am-9:45 am

MA, KEYNOTE SESSION

William Mankin, National Center for Atmospheric Research, President

8:15 am

MA1 Remote sensing of atmospheric trace constituents using mid-ir Fourier transform spectrometry, H. Fischer, Univ. Karlsruhe, Germany. This paper profiles Michelson interferometer for passive atmospheric sounding experiments. (p. 2)

8:30 am (Invited)

MA2 Giant lidars for middle and upper atmosphere studies: observational capabilities of the new advanced electro-optic system (AEOS) at Haleakala, Hawaii, Chester S. Gardner, Univ. Ill.-Urbana-Champaign. AEOS includes a fully steerable 4-m class telescope and powerful Rayleigh/Raman and Na Doppler/Temperature lidars. We discuss the observational capabilities of the proposed facility with particular emphasis on measurements of temperature, winds, water vapor, and ozone. (p. 5)

9:00 am (Invited)

MA3 EASOE campaign and lidar observation, Gerard J. Megie. Abstract not available at press time. (p. 6)

9:30 am (Invited)

MA4 Results from the flight of the atmospheric trace molecule spectroscopy on the ATLAS-1 Space Shuttle mission, M. R. Gunson, M. C. Abrams, C. B. Farmer, L. L. Lowes, Jet Propulsion Laboratory; C. P. Rinsland, NASA Langley Research Center; R. Zander, Univ. Liège, Belgium. Measurements of atmospheric composition by the atmospheric trace molecule spectroscopy (ATMOS) experiment flown on the ATLAS-1 Space Shuttle mission of March 24-April 2, 1992, are presented. (p. 7)

SALON C

10:00 am-10:20 am COFFEE BREAK

MONDAY, MARCH 8, 1993—Continued

SALON D

10:20 am-12:30 pm

MB, WATER VAPOR

Allan I. Carswell, York Univ., President

10:20 am (Invited)

MB1 Temporal scales of water vapor measured with a Raman lidar during SPECTRE, S. Harvey Melfi. Abstract not available at press time. (p. 10)

10:50 am

MB2 Coincident measurements of atmospheric aerosol properties and water vapor by a scanning Raman lidar, R. A. Ferrare, K. D. Evans, Hughes STX Corp.; S. H. Melfi, D. N. Whiteman, NASA Goddard Space Flight Center. We discuss coincident measurements of aerosol extinction, backscatter; e.g. extinction/backscatter ratio, water vapor mixing ratio, and relative humidity made by a scanning Raman lidar. (p. 11)

11:10 am

MB3 Evaluation of Raman lidar profiling of atmospheric water vapor: simultaneous measurements with two advanced systems, J. E. M. Goldsmith, Scott E. Bisson, Sandia National Laboratories; David N. Whiteman, S. H. Melfi, NASA Goddard Space Flight Center; Richard A. Ferrare, Keith D. Evans, Hughes STX Corp. We describe intercomparisons of two advanced Raman lidar systems for profiling atmospheric water vapor. Nighttime, daytime, and simultaneous aerosol measurements are discussed. (p. 15)

11:30 am

MB4 Daytime tropospheric water vapor profile measurements with a Raman lidar, Scott E. Bisson, J. E. M. Goldsmith, Sandia National Laboratories. A narrowband, dual field-of-view Raman lidar system for daytime tropospheric water vapor profile measurements is described. Daytime results are presented. (p. 19)

11:50 am

MB5 Atmospheric water vapor column determination: from polar orbiting operational satellites, radiosondes and analyses, N. Husson, N. A. Scott, A. Chedin, J. P. Chaboureaud, C. Claud, Ecole Polytechnique, France. Accuracy of atmospheric water vapor contents, as retrieved from radiometric measurements from NOAA-TOVS and DMSP-SSM/I, has been assessed against radiosondes and ECMWF analyses. (p. 23)

12:10 pm

MB6 Stratospheric Aerosol and Gas Experiment II water vapor profiling: an inversion study, J. C. Larsen, S. N. Tiwari, Old Dominion Univ.; W. P. Chu, NASA Langley Research Center. In this paper we apply two inversion methods to the SAGE II limb absorption solar occultation measurements of water vapor at 940 nm and compare the results to the operational method based on the standard onion peel method. (p. 27)

12:30 pm-2:00 pm LUNCH

MONDAY, MARCH 8, 1993—Continued

SALON D

2:00 pm–3:40 pm

MC, SPACE & GROUND BASED REMOTE SENSING 1

William L. Smith, *Univ. Wisconsin-Madison, Presider*

2:00 pm (Invited)

MC1 Advances in retrieval methodology for the analysis of present and future generations vertical sounders, A. Chedin, N. A. Scott, F. Cheruy, J. Escobar, H. Rjeu, *Ecole Polytechnique, France*. The methodology developed in the past for processing NOAA/TOVS data and relying on pattern recognition has been extended to the processing of high-spectral-resolution vertical sounding data. A new methodology, based on neural networks, has been successfully applied to those kinds of data. (p. 32)

2:30 pm (Invited)

MC2 Recent results in combined ground-based and satellite remote sensing, E. R. Westwater, B.B. Stankov, *NOAA*. In this paper we discuss recent results in combining ground-based and satellite data for sounding of temperature, water vapor, and clouds. (p. 33)

3:00 pm

MC3 Removal of the 3.7- μ m solar contamination in AVHRR data, N. X. Rao, S. C. Ou, *Liou and Associates*; K. N. Liou, *Univ. Utah*. A numerical scheme for the removal of the 3.7- μ m solar contamination in AVHRR data has been developed to retrieve daytime cirrus cloud parameters. (p. 36)

3:20 pm

MC4 Remote sensing of cirrus cloud parameters using AVHRR 3.7- and 10.9- μ m channel data, S. C. Ou, W. Gooch, N. Rao, *Liou and Associates*; K. N. Liou, Y. Takano, *Univ. Utah*. Results are presented of the cirrus cloud temperature, optical depth, and mean effective ice crystal size determined from a retrieval scheme using AVHRR 3.7- and 10.9- μ m data over the United States on October 28, 1986. (p. 40)

SALON C

3:40 pm–4:10 pm COFFEE BREAK

SALON D

4:10 pm–6:00 pm

MD, SPACE & GROUND BASED REMOTE SENSING 2

Ed Westwater, *NOAA, Presider*

4:10 pm (Invited)

MD1 Atmospheric remote sensing studies at the National Institute for Environmental Studies (NIES), Yasuhiro Sasano, Hideaki Nakane, Nobuo Sugimoto, *The National Institute for Environmental Studies, Japan*. Studies on active and passive remote sensing of atmospheric constituents conducted at NIES will be summarized. They include lidars, and earth-satellite-earth long path laser absorption experiments and a satellite-borne spectrometer for solar occultation measurements aboard ADEOS. (p. 44)

MONDAY, MARCH 8, 1993—Continued

4:40 pm

MD2 Radiation energy budget studies using collocated AVHRR and ERBE observations, Steven A. Ackerman, *Univ. Wisconsin*; Toshiro Inoue, *Meteorology Research Institute, Japan*. Radiative properties of clouds and clear sky atmospheres are specified using collocated AVHRR and ERBE observations. Cloud forcing is quantified according to cloud type. (p. 48)

5:00 pm

MD3 Spatial and spectral information densities from satellite sounding instruments, Hung-Lung Huang, R. J. Purser, William L. Smith, *Univ. Wisconsin-Madison*. Spatial and spectral information densities are presented for simulated measurements of a high-resolution infrared sounder. (p. 51)

5:20 pm

MD4 Initial data from a new high spectral resolution lidar, E. W. Eloranta, A. K. Piironen, *Univ. Wisconsin-Madison*. The University of Wisconsin High Spectral Resolution Lidar has been redesigned for field operations with polarization and multiple scatter measurement capabilities. Initial results are presented. (p. 53)

5:40 pm

MD5 Boundary layer height measurements with an eyesafe lidar system, E. M. Patterson, G. G. Gimmetstad, D. W. Roberts, S. C. Gimmetstad, *Georgia Institute of Technology*. An eyesafe lidar system has been developed for measurements of the vertical distribution of boundary layer aerosols. This lidar was used to determine boundary layer height on a semiautomated basis during a major air chemistry study. (p. 57)

6:00 pm–8:00 pm CONFERENCE RECEPTION

TUESDAY, MARCH 9, 1993

SALON D

8:00 am–10:20 am

TuA, SPACE & GROUND-BASED REMOTE SENSING 3

Alain Chedin, *Ecole Polytechnique, Presider*

8:00 am (Invited)

TuA1 Retrieval of atmospheric state parameters from high-resolution spectral radiance data, Shepard A. Clough, *Atmospheric and Environmental Research, Inc.* The retrieval of atmospheric profiles of atmospheric state parameters (e.g., ozone) from spectral radiance data is generally an overdetermined poorly posed problem. Methods of approaching this problem are discussed. (p. 64)

8:30 am (Invited)

TuA2 Continuous measurement of boundary layer temperature and moisture structure using ground-based FTIR, W. L. Smith, R. O. Knuteson, H. E. Revercomb, H. B. Howell, *Univ. Wisconsin-Madison*. A ground-based high-resolution interferometer sounding (GB-HIS) system has been developed for continuous monitoring of the atmosphere's low level temperature and moisture structure. The system, retrieval method, and results from field trials are presented. (p. 68)

9:00 am

TuA3 Polar ozone and aerosol measurement experiment (POAM-II), F. J. Lehmann, R. M. Bevilacqua, W. J. Glaccum, J. S. Hornstein, E. P. Shettle, *U.S. Naval Research Laboratory*; S. S. Krigman, J. D. Lumpe, *Computational Physics Inc.* The U.S. Naval Research Laboratory will launch POAM II in September 1993 to measure polar stratospheric O_3 , H_2O , NO_2 , and aerosol extinction. The satellite system description is presented. (p. 72)

9:20 am

TuA4 Retrieval of tropospheric and stratospheric distribution of HCl from ground-based FTIR spectra, G. P. Adrian, M. Baumann, E. Frank, H. Oelhaf, *Kernforschungszentrum Karlsruhe GmbH*. Synthetic and measured ground-based FTIR spectra of moderate spectral resolution are used to demonstrate the feasibility to distinguish between tropospheric and stratospheric HCl burden and to quantify that in terms of an error analysis. (p. 74)

9:40 am

TuA5 Retrieval of tropospheric profiles from IR emission spectra: investigations with the double beam interferometer sounder (DBIS), J.-M. Thériault, *Defence Research Establishment Valcartier, Canada*; Y. Qu, *Univ. Wisconsin-Madison*; G. P. Anderson, J. H. Chetwynd, E. Murphy, V. Turner, M. Cloutier, A. Smith, *Phillips Laboratory/U.S. Air Force*. Atmospheric emission spectra recorded from the ground in clear and cloudy sky conditions are compared to model calculations. The approach adopted for the retrieval of tropospheric profiles from DBIS spectra is presented. (p. 78)

TUESDAY, MARCH 9, 1993—Continued

10:00 am

TuA6 Ground-based system for measuring atmospheric emitted radiance at high spectral resolution, H. E. Revercomb, W. L. Smith, R. O. Knuteson, F. A. Best, R. G. Dedeker, T. P. Dirkx, R. A. Herbsleb, J. F. Short, *Univ. Wisconsin*; H. B. Howell, *NOAA*. The atmospheric emitted radiance interferometer system being deployed at the Oklahoma ARM site provides accurate downwelling radiation spectra for both radiative transfer modeling and remote sensing applications. (p. 82)

SALON C

10:20 am–11:10 am COFFEE BREAK

SALON D

11:00 am–1:00 pm

TuB, CONSTITUENTS

Q. N. Liu, *University of Utah, Presider*

11:10 am (Invited)

TuB1 Combined lidar, long-path extinction and in-situ aerosol experiment in southern Ontario, Raymond M. Hoff, *Atmospheric Environment Service, Canada*. Results of experiments conducted in 1992 using long-path extinction devices, including DOAS for precursor gases, lidar, and in-situ particle sizing (20–21000 nm particle diameters) experiments are presented. (p. 88)

11:40 am

TuB2 Diode-laser-based sensor system for long-path absorption measurements of atmospheric concentration and near-IR molecular spectral parameters, Neil Goldstein, Jamine Lee, Steven M. Adler-Golden, Fritz Bien, *Spectral Sciences Inc.* A field-portable sensor using wavelength modulation, line-locking, and a retroreflector/telescope configuration measures absorption of multiple species over atmospheric path lengths of hundreds of meters. (p. 90)

12:00 pm

TuB3 Doppler detection of the stratospheric hydroxyl column abundance, N. Iwagami, S. Inomata, *Univ. Tokyo, Japan*. The Doppler shift of solar UV spectrum due to the solar rotation is used to discriminate the slight terrestrial absorption in determining the stratospheric column. (p. 94)

12:20 pm

TuB4 Singular value decomposition analysis of ozone profile retrieval from high-resolution interferometer sounder data, R. O. Knuteson, S. C. Lee, H. E. Revercomb, W. L. Smith, *Univ. Wisconsin-Madison*. A singular value decomposition technique is used to obtain an ozone profile retrieval from observed upwelling radiance measured by the high-resolution interferometer sounder (HIS). (p. 97)

TUESDAY, MARCH 9, 1993—Continued

12:40 pm

TuB5 Chlorine nitrate and nitric acid profiles in the arctic vortex derived from limb emission measurements with MIPAS-B, H. Oelhaf, T. v. Clarmann, H. Fischer, F. Friedl-Vallon, Ch. Fritzsche, A. Linden, Ch. Piesch, M. Seefeldner, *Kernforschungszentrum/Univ. Karlsruhe, Germany*; W. Volker, *Univ. Munchen, Germany*. Limb emission spectra obtained in January and March 1992 have been analyzed to infer vertical profiles of several trace gases. Results for ClONO₂ and HNO₃ are presented. (p. 101)

1:00 pm–2:30 pm LUNCH

SALON D

2:30 pm–5:40 pm

TuC, CLOUDS AND ECLIPS

Allan I. Carswell, *York Univ.*, *President*

2:30 pm

TuC1 Dual-wavelength CO₂ lidar method for distinguishing ice, water, or mixed-phase clouds, Wynn L. Eberhard, *NOAA*. A dual-wavelength CO₂ lidar backscatter method for revealing cloud phase is introduced. In some respects it promises better performance than the shortwave depolarization method. (p. 106)

2:50 pm

TuC2 Application of optical remote sensing to the study of surface fluxes related to cloud formation, W. M. Porph, *Los Alamos National Laboratory*; W. Shaw, *Pacific Northwest Laboratory*. Optical scintillation instrumentation has been applied to studies of cloud effects on surface fluxes. Spatial averaging of optical-turbulence-based estimates of fluxes can be made much faster than conventional tower techniques. (p. 110)

3:10 pm

TuC3 Lidar and radiometer observations of midlevel clouds, C. M. R. Platt, S. A. Young, G. R. Patterson, P. J. Manson, *CSIRO, Australia*. The lidar/radiometer technique in the ECLIPS experiment has been used to obtain new information on the optical properties of midlevel clouds. (p. 114)

3:30 pm

TuC4 Summary of the experimental cloud lidar pilot study (ECLIPS) at ISTS/York Lidar Observatory, S. R. Pal, A. Y. Fong, A. I. Carswell, *York Univ. Canada*. A summary of the results from ECLIPS I and II is presented. Cloud physical and optical properties are discussed in relation to meteorological parameters. (p. 118)

SALON C

3:50 pm–4:20 pm COFFEE BREAK

TUESDAY, MARCH 9, 1993—Continued

SALON D

4:20 pm

TuC5 ECLIPS Phase 2 at LMD, R. Valentin, S. Elouraghi, P. H. Flamant, L. Menenger, *Ecole Polytechnique, France*; J. Pelon, *Univ. Paris*. Ground-based lidar and radiometers are deployed to retrieve cloud base height and radiative properties. Simultaneous measurements with airborne lidar are conducted on two days. (p. 122)

4:40 pm

TuC6 Cloud measurements with a polarization Raman elastic-backscatter lidar, Ulla Wandinger, Claus Weitkamp, *GKSS-Forschungszentrum Geesthacht GmbH, Germany*. Cloud optical properties determined with a polarization-sensitive combined Raman elastic-backscatter lidar are shown to contribute valuable information to the ECLIPS program. (p. 126)

5:00 pm

TuC7 The results of laser measurements of cloud parameters under the ECLIPS program, S. S. Khmelevtsov, We report on the cloud condition measurements carried out in the period from 29 May, 1991 up to 29 June, 1991 at Obninsk lidar station. (p. 129)

5:20 pm

TuC8 Lidar cloud observation: in part of ECLIPS Phase 2 in the region of Sofia, I. Kolev, O. Parvanov, B. Kaprielov, Y. Tomova, *Institute of Electronics, Bulgaria*. Method of study and fair-weather clouds generation caused by the humidity upward motion during the formation of a convective planetary boundary layer over the region of Sofia City is studied. (p. 130)

SALON A

8:00 pm–10:00 pm

TuD, POSTER SESSION

TuD1 Neural nets for temperature retrievals, Howard E. Mottelet, J. Anthony Gualtieri, *NASA Goddard Space Flight Center*; L. Larrabee Strow, James Lo, *Univ. Maryland, Baltimore County*; Larry McMillin, *NOAA/NESDIS*. Neural networks allow us to make effective use of the large AIRS channel set, giving good performance with noisy input. We briefly describe the sort of networks we are using, describe our datasets, and present a number of representative results. (p. 136)

TuD2 Satellite-derived products from TOVS as a database for climate and global change studies, Leah W. Casey, Tim J. Gardner, *Hughes STX Corp.*; Michael W. Chalfant, *NOAA*. Upgraded products include TOVS total ozone, cloud top temperature and pressure, and cloud amount; the new sulfur dioxide (SO₂) concentration is the latest climate product, and radiation flux parameters are expected to become operational products in the near future. (p. 140)

TuD3 Tomographic inversion of stellar occultation measurements, Johanna Tamminen, Erkki Kyrola, Liisa Oikarinen, Elina Sihvola, *Finnish Meteorological Institute, Finland*; Heikki Haario, *Univ. Helsinki, Finland*. Tomographic studies of stellar occultation measurements are discussed and different methods compared. The specific application is the global ozone monitoring by occultation of stars (GOMOS) instrument. (p. 141)

TuD4 Assessment of the effects of diffraction on ir measurements from geosynchronous orbit, Harry E. Montgomery, William E. Shenk, *NASA Goddard Space Flight Center*. The effects of diffraction were calculated for selected current and future geosynchronous satellite infrared profiling and imaging channels. The future geosynchronous satellite calculations were made for the GOES I-M instruments. For comparison, some calculations were also made for similar measurements in low earth orbit. (p. 145)

TuD5 HALOE data processing techniques, Larry L. Gordley, Robert E. Thompson, Jr., *G & A Technical Software, Inc.*; James M. Russell III, *NASA Langley Research Center*. The operational use of high-density forward models and line-by-line calculations for processing the HALOE data are described. (p. 146)

TuD6 The satellite project GOME: potential precision of trace gas retrieval under ozone hole conditions, D. Diebel, J. P. Burrows, R. J. D. Spurr, *Univ. Bremen, Germany*; V. V. Rozanov, *Univ. St. Petersburg, Russia*. The precision of trace gas retrieval under ozone hole conditions is discussed for GOME satellite measurements performed in the ultraviolet and visible wavelength range. (p. 149)

TuD7 Probing the martian atmosphere in the uv, Bernhard Lee Lindner, *Atmospheric and Environmental Research, Inc.*. The efficacy of the uv spectroscopy technique used by Mariner 9 to remotely measure ozone at Mars is discussed, as are alternative techniques for future measurements. (p. 153)

TuD8 Temperature profile measurements using oxygen DIAL, C. Laurence Korb, Geary K. Schwemmer, Coorg Prasad, *Science and Engineering Services, Inc.*; Chi Y. Weng, *Science Systems and Applications, Inc.*; Joseph Famiglietti, Cyrille N. Flamant, *Univ. Maryland*. This paper describes measurements of the atmospheric temperature profile with 1-K accuracy and 300 m vertical resolution for a 90-sec integration time using a two-wavelength differential absorption lidar technique. (p. 157)

TuD9 Laser sounding of stratospheric ozone in Obninsk, S. S. Khmelevtsov, E. D. Svetogorov. In the paper it is shown that knowing vertical profiles of air density and having a background value of ozone, the measurement accuracy of vertical profiles of ozone concentration is adequate. (p. 161)

TuD10 Multi-wavelength sequential seeding method for water vapor DIAL measurements, Glen Sachse, Syed Ismail, Edward Browell, *NASA Langley Research Center*; Liang-guo Wang, *College of William and Mary*. A water vapor DIAL concept is presented which uses diode laser seeding at three wavelengths (line center, absorption line side, and off line). (p. 162)

TuD11 Solar blind Raman scattering measurements of water vapor using a KrF excimer laser, D. N. Whiteman, S. H. Melfi, *NASA Goddard Space Flight Center*; R. A. Ferrare, K. D. Evans, *Hughes STX Corp.*. A daytime measurement of water vapor mixing ratio to 2.5–3.0 km is presented using a correlative electrochemical cell measurement of ozone for differential transmission correction. (p. 165)

TuD12 Tropospheric temperature measurements using a Raman lidar, K. D. Evans, R. A. Ferrare, *Hughes STX Corp.*; S. H. Melfi, D. N. Whiteman, *NASA Goddard Space Flight Center*. Density and temperature in the troposphere were calculated using the Raman nitrogen data from a 351-nm XeF excimer laser. (p. 169)

TuD13 Atmospheric Environmental Service DIAL system for monitoring of tropospheric ozone, J. F. Hahn, A. Sheppard, R. M. Hoff, *Atmospheric Environment Service, Canada*. We are building a DIAL system for climatological monitoring of tropospheric ozone. Details of the experimental set-up and preliminary results are presented. (p. 173)

TuD14 Airborne ozone measurements with the USEPA UV-DIAL, H. Moosmüller, *Univ. Nevada*; R. J. Alvarez II, *NOAA*; C. M. Edmonds, D. H. Bundy, J. L. McElroy, *U.S. Environmental Protection Agency*; R. M. Turner, *Harry Reid Center for Environmental Studies*. The initial airborne operation of the USEPA UV-DIAL has been fully successful. The measured ozone distributions are in good agreement with in-situ measurements. (p. 176)

TuD15 Arecibo observatory daytime lidar: preliminary results, Kalpak A. Dighe, *Clemson Univ.*; Craig A. Tepley, *Raul Garcia, Jonathan Friedman, NAIC Arecibo Observatory*. We present results from the newly developed, and as yet experimental, daytime lidar system at the Arecibo Observatory. (p. 180)

TuD16 Real-time simultaneous monitoring of atmospheric methane and carbon dioxide by using diode lasers, Hideo Tai, Ryoichi Toriumi, *Tokyo Gas Co., Ltd., Japan*; Kiyoji Uehara, *Keio Univ., Japan*. Real-time high-sensitivity simultaneous measurement of the atmospheric methane and carbon dioxide concentrations by using two single-mode diode lasers and a multipass cell has been demonstrated. (p. 184)

TuD17 Solid-state laser technology as a quantitative solution in ambient air pollution monitoring, Craig A. Smith, *Schwartz Electro-Optics*. The on-going development of a pulsed Ti:Sapphire DIAL system capable of transmitting wavelengths from 210 nm all the way out to 2.6 μ m will be discussed. (p. 188)

TuD18 Arecibo Observatory lidar upgrade: possibilities for new science, Jonathan S. Friedman, Craig A. Tepley, *NAIC Arecibo Observatory, Puerto Rico*; Paul A. Castleberg, Michael C. Kelley, *Cornell Univ.*; Kalpak A. Dighe, *Clemson Univ.*. The Arecibo Observatory Doppler lidar system is being upgraded to include a large telescope, tunable laser, and daytime capabilities. We present new science possibilities. (p. 189)

TuD19 NORMALS—noise reduction method using multivariate analysis technique for lidar echo signal, Hiroshi Okumura, Tadashi Sugita, Hironori Matsumoto, Nobuo Takeuchi, *Chiba Univ., Japan*. A new noise reduction method based on the canonical correlation analysis, which results in negligible wave-form distortion, was proposed and validated using a lidar data. (p. 193)

TuD20 Clear air turbulence detection with a 2- μ m lidar employing velocity width processing, Robert J. Martinsen, Andrew J. Jankevics, Charles P. Plum, *Lightwave Atmospheric, Inc.*; John H. Flint, *Schwartz Electro-Optics*. An airborne lidar system exploits the decorrelation of the heterodyne signal to detect turbulence over 3 km in clear air, and over 20 km in subvisual cirrus. (p. 197)

TuD21 Laser long-path absorption measurements with the retroreflector in space for the ADEOS satellite, N. Sugimoto, A. Minato, Y. Sasano, *National Institute for Environmental Studies, Japan*; T. Itabe, N. Hiromoto, M. Takabe, *Communications Research Laboratory, Japan*. This paper describes a plan for experiments on laser long-path absorption measurements of atmospheric trace species with the retroreflector-in-space for the ADEOS satellite which is scheduled for launch in early 1996. (p. 201)

TuD22 Comparative studies of single- and dual-beam CO₂ laser analyzer for remote sensing of air pollutants, Mohammad A. Rob, *Univ. Houston—Clear Lake*. Air pollution detection system using a cw CO₂ laser and a room-temperature HgCdTe detector has been studied. The instrument has the capability of detecting 2.2 ppm-m of ethylene. Comparative results of a dual-beam CO₂ laser analyzer are presented. (p. 204)

TuD23 Observation of sea fog incursion with a diode-pumped YAG portable lidar, Nobuo Takeuchi, Hiroshi Okumura, Tadashi Sugita, Hironori Matsumoto, *Chiba Univ., Japan*; Shigesumi Kuwashima, *OKK, Inc., Japan*; Satoshi Yamaguchi, *Nippon Steel Corp., Japan*. An all-solid portable high-repetitive lidar system using a diode-pumped Q-switched YAG laser and an avalanche-photodiode was constructed and was used for the observation of sea-fog intrusion. (p. 208)

TuD24 Simultaneous inference of multiple atmospheric parameters using multiple channels of information, Benjamin T. Marshall, Larry L. Gordley, *G&A Technical Software*. A technique of general utility is developed for simultaneous retrieval of multiple emitters from multiple channels of information. Implementation and examples of results are presented. (p. 212)

TuD25 Tunable mid-infrared source for remote sensing, Norman P. Barnes, Keith E. Murray, *NASA Langley Research Center*; Mahendra G. Jani, *STC Corp.* An optical parametric oscillator and amplifier system, pumped by a 2.0- μ m solid-state laser, can provide a source for DIAL applications which is tunable throughout the mid-infrared. Performance of the laser and the oscillator and amplifier is reported. (p. 215)

TuD26 Remote sensing techniques for stratospheric and tropospheric gas monitoring, P. T. Woods, B. W. Jolliffe, M. J. T. Milton, N. R. Swann, W. Bell, N. A. Martin, T. D. Gardiner, *National Physical Laboratory, U.K.*; P. F. Fogal, D. G. Murcray, *Univ. Denver*. Different remote sensing techniques have been developed and utilized for a range of atmospheric monitoring applications. These include laser heterodyne and Fourier-transform spectrometers for stratospheric measurements, and an infrared DIAL system for industrial and urban pollution monitoring. (p. 217)

SALON D

8:00 am–9:20 am

WA, WINDS 1

John W. Meriwether, *Clemson Univ., President*

8:00 am (Invited)

WA1 Development and application of compact Doppler lidar systems for atmospheric probing, R. Michael Hardsy, *NOAA*. Doppler lidar systems operating at 2.02 and 9.1–11.2 μ m are being developed to provide high radial wind velocity accuracy and good temporal and spatial resolution. The systems are aimed at observing fine-scale motions in the boundary layer and in the vicinity of cloud boundaries. (p. 224)

8:30 am (Invited)

WA2 Observations of winds of the stratosphere and mesosphere at Arecibo, Puerto Rico using a Doppler Rayleigh lidar, Craig A. Tepley, *Cornell Univ.* We present lidar wind observations of the tropical middle atmosphere made over a two-year period. Both seasonal patterns and daily variability are discussed. (p. 227)

9:00 am

WA3 Doppler lidar observations of a frontal passage in the vicinity of steep topography, Madison J. Post, F. Martin Ralph, Paul N. Neiman, Lisa D. Olivier, *NOAA*. We present meteorological analyses of Doppler lidar data showing orographic generation of gravity waves and downward transport of stratospheric debris into the troposphere. (p. 231)

SALON C

9:20 am–9:50 am COFFEE BREAK

SALON D

9:50 am–11:40 am

WB, WINDS 2

Thomas J. McGee, *NASA, President*

9:50 am (Invited)

WB1 Lidar and radar studies of dynamics in the lower atmosphere, John W. Meriwether, *Clemson Univ.* Lidar and radar instrumentation at the Arecibo Observatory have detected long period wave structure between 12 and 26 km exhibiting a vertical phase velocity of 1 to 2 cm/sec. Two possible theories of explanation are orographic activity and inertio-gravity waves. (p. 236)

10:20 am

WB2 Wind profiling with the volume imaging lidar: a comparison with aircraft and balloon based measurements, A. K. Piironen, E. W. Eloranta, *Univ. Wisconsin—Madison*. Vertical profiles of the horizontal wind measured with the University of Wisconsin Volume Imaging Lidar are compared to winds measured with aircraft and meteorological balloons. (p. 240)

WEDNESDAY, MARCH 10, 1993—Continued

10:40 am

WB3 Optically based air data using Doppler-shifted, high spectral resolution lidar, W. R. Lempert, J. Forkey, N. Finkelstein, R. Miles, *Princeton Univ.* We present a concept for airborne optical air data, based on spectrally filtered Rayleigh backscatter. System components and wind tunnel proof-of-concept measurements are described. (p. 244)

11:00 am

WB4 Multicenter airborne coherent atmospheric wind sensor, J. Rothermel, *NASA Marshall Space Flight Center*; R. M. Hardesty, *NOAA Wave Propagation Laboratory*; R. T. Menzies, *Jet Propulsion Laboratory*. A joule-class scanning airborne CO₂ Doppler lidar system is being developed to address issues of atmospheric dynamic processes and performance of satellite-borne lidar-based wind sensors. (p. 247)

11:20 am

WB5 Simulation of space-based Doppler lidar wind measurements using ground-based single-shot observations, G. D. Emmitt, J. Dieudonné, S. A. Wood, L. Wood, *Simpson Weather Associates, Inc.* Single-shot and poly-pulse pair processing of ground-based Doppler lidar wind sounder data is used to simulate the expected performance of a proposed space-based system (p. 250)

11:40 am–1:00 pm LUNCH

SALON D

1:00 pm–2:30 pm

WC, OZONE 1

Iain S. McDermid, *Jet Propulsion Laboratory, Presider*

1:00 pm (Invited)

WC1 Lidar developments for tropospheric ozone research in Europe, Jens Bösenberg, *Max-Planck-Institut für Meteorologie, Germany*. The TESLAS subproject of the joint European environmental program EUROTRAC has started an initiative to develop accurate, reliable, and easy to operate lidar systems for measurements of the ozone vertical distribution in the troposphere. The progress is reported. (p. 256)

1:30 pm (Invited)

WC2 DIAL lidar measurements of stratospheric ozone in the presence of volcanic aerosols, Thomas J. McGee, *NASA Goddard Space Flight Center*. Differential absorption measurements of stratospheric ozone have been made difficult or impossible because of the presence of large concentrations of aerosols from the eruption of Mt. Pinatubo. Raman scattering has been used to minimize the effects of the aerosol and has also yielded data to improve aerosol corrections to the data. (p. 258)

WEDNESDAY, MARCH 10, 1993—Continued

2:00 pm (Invited)

WC3 RIVMs tropospheric and stratospheric ozone lidars for European and global monitoring networks, Daan P. J. Swart, Arnoud Apituley, Jan Spakman, Eric P. Vissers, Hans B. Bergwerff, *National Institute of Public Health and Environmental Protection, The Netherlands*. High-quality routine observation of the ozone profile in both troposphere and stratosphere is of prime importance in the study of trends and their underlying mechanisms. RIVM activities on the development of ozone lidars and their implementation in international networks are described. (p. 261)

SALON C

2:30 pm–3:00 pm COFFEE BREAK

SALON D

3:00 pm–4:30 pm

WD, OZONE 2

Yasuhiro Sasano, *National Institute for Environmental Studies, Presider*

3:00 pm (Invited)

WD1 NDSC and lidar observations at OHP, Sophie Godin. Abstract not available at press time. (p. 268)

3:30 pm

WD2 Errors introduced in differential absorption lidar measurements of stratospheric ozone by Pinatubo aerosols, W. Steinbrecht, A. I. Carswell, *York Univ., Canada*. Enhanced aerosol backscattering and extinction can lead to errors in measured ozone concentrations. The errors are characterized, examples are given, and possible corrections are discussed. (p. 269)

3:50 pm

WD3 New lidar for the network for the detection of stratospheric change—Mauna Loa Observatory: system description, T. Daniel Walsh, L. Oscar Linquist, Mary L. White, Apostolis Deslis, I. Stuart McDermid, *Jet Propulsion Laboratory*. A system that utilizes DIAL, Rayleigh, and Raman lidar techniques to measure stratospheric ozone, temperature and aerosol profiles simultaneously has been designed, constructed, and tested. (p. 273)

4:10 pm

WD4 New lidar for the network for the detection of stratospheric change—Mauna Loa Observatory: initial results, I. Stuart McDermid, T. Daniel Walsh, *Jet Propulsion Laboratory*. Initial measurements of ozone, temperature, and aerosol profiles with the new lidar and comparison of the results with other lidars at JPL-TMF are presented. (p. 276)

THURSDAY, MARCH 11, 1993

SALON D

8:00 am–9:40 am

ThA, AEROSOLS 1

Horst Jäger, *Fraunhofer Institute, Presider*

8:00 am (Invited)

ThA1 Lidar measurements of stratospheric aerosols at Mauna Loa Observatory: 1974 to present, T. E. DeFoor, S. Ryan, D. J. Hofmann, E. G. Dutton, *NOAA*. The 18-year Mauna Loa lidar data record shows that the stratosphere over Hawaii was perturbed by two major volcanic eruptions: El Chichón (Mexico, 1982) and Mt. Pinatubo (Philippines, 1991). Details of this and a comparison with Mauna Loa atmospheric transmission and aerosol optical depth measurements were discussed. (p. 282)

8:30 am (Invited)

ThA2 The Pinatubo eruption in relation to the El Chichon event and the stratospheric background load, H. Jäger, *Fraunhofer Institute for Atmospheric Environmental Research, IFU, Germany*. Midlatitude lidar observations are focused on the stratospheric dispersion patterns of the perturbations following the eruptions of both El Chichón and Pinatubo and on anthropogenic activities affecting the stratosphere. (p. 284)

9:00 am

ThA3 Evolution of Pinatubo and Cerro Hudson aerosol over the Antarctic during the 1991 Austral spring, Michael C. Pitts, *Science Applications International Corp.*; Larry W. Thomason, William P. Chu, *NASA Langley Research Center*. Satellite measurements of aerosol extinction are utilized to identify and track the movement of Pinatubo and Cerro Hudson aerosol over the Antarctic during the spring. (p. 288)

9:20 am

ThA4 Airborne lidar measurements of aerosols, William B. Grant, Edward V. Browell, Bruce E. Anderson, Syed Ismail, *NASA Langley Research Center*. The UV-DIAL system has collected aerosol data over the past decade. Progress in analyzing and interpreting the data for global climate changes is discussed. (p. 292)

9:40 am–10:10 am COFFEE BREAK

SALON D

10:10 am–12:10 pm

ThB, AEROSOLS 2

Raymond M. Hoff, *Atmospheric Environment Ser., Presider*

10:10 am

ThB1 Time-dependent behavior of Mount Pinatubo aerosol, Joseph Michalsky, *State Univ. New York-Albany*; Nels Larson, *Pacific Northwest Laboratory*. Ground-based solar radiometry from three northern mid-latitude sites is used to follow the time-dependent behavior of the Mount Pinatubo aerosol cloud. (p. 298)

THURSDAY, MARCH 11, 1993—Continued

10:30 am

ThB2 Observations of Mount Pinatubo aerosol with a Raman elastic-backscatter lidar over northern Germany at 53.5° N, Ulla Wandinger, Claus Weitkamp, *GKSS Forschungszentrum Geesthacht GmbH, Germany*; Albert Ansmann, *Institut für Troposphärenforschung, Germany*. The long-time behavior of the geometrical (base, top, backscatter-weighted mean height) and optical (extinction, backscattering) properties of Pinatubo stratospheric aerosol is presented. (p. 302)

10:50 am

ThB3 Lidar measurements of the stratospheric aerosol layer over Toronto, D. P. Donovan, W. Steinbrecht, A. I. Carswell, *York Univ., Canada*. Lidar measurements of the Pinatubo aerosol made with an ozone DIAL system and a Nd:YAG polarization sensitive lidar are presented. Derived physical and optical properties at 532 nm and 353 nm are discussed. (p. 305)

11:10 am

ThB4 Particle size characterization by means of depolarization measurements, C. Flesia, L. de Schoulepnikoff, *Observatoire Cantonal de Neuchâtel, Switzerland*. A new inversion method has been used to characterize the size and the shape of Pinatubo aerosol by means of depolarization measurements. (p. 309)

11:30 am

ThB5 Lidar observations of Mt. Pinatubo aerosols: effects on the global radiation budget, T. D. Stevens, S. Maruvada, T. J. Kane, C. R. Philbrick, *The Pennsylvania State Univ.* Lidar observations of the latitudinal distribution of aerosols arising from Mt. Pinatubo's eruption yield insight into the effects of these particles on global solar radiance. (p. 313)

11:50 am

ThB6 Implications of aerosol phenomenology on sensor and algorithm design, Steve Westerman, *Lockheed Missiles & Space Co.* Paper discusses results from a study connecting visibility to measured visible radiance. Study analyzes the potential of determining visibility passively over a broad meteorological range. (p. 317)

12:10 pm–1:30 pm LUNCH

SALON D

1:30 pm–3:00 pm

ThC, SPECTROSCOPY 1

Shepard A. Clough, *Atoms. & Environ. Res. Inc., Presider*

1:30 pm (Invited)

ThC1 HITRAN molecular database: enhancements for remote sensing, Laurence S. Rothman, *Hanscom AFB*. This presentation will summarize some of the major updates, improvements, modifications, and future directions to the spectroscopic molecular database, HITRAN, that enhance its application for remote sensing. (p. 322)

2:00 pm

ThC2 Molecular absorption parameter measurements for remote sensing applications, Zhiping, Chu, Li Chen, Peter K. Cheo, *Univ. Connecticut*. High-resolution measurements of molecular absorption parameters, including line frequency, frequency shift, line strength, and Lorentz linewidth of NH_3 and C_2H_4 in the mid-infrared are presented. (p. 326)

2:20 pm

ThC3 Infrared spectroscopic data needed for atmospheric remote sensing, P. Varanasi, U. Shin, A. Gopalan, *State Univ. New York—Stony Brook*. High resolution measurements of line intensities, N_2 , O_2 , and airbroadened half-widths, and pressure-induced shifts in the infrared bands of several atmospheric molecules are reported. (p. 330)

2:40 pm

ThC4 Network for detection of stratospheric change (NDSC) infrared observations at Mauna Loa, Hawaii, F. J. Murcray, D. G. Murcray, S. J. David, R. D. Blatherwick, J. J. Kusters, F. H. Murcray, A. Goldman, *Univ. Denver*; C. P. Rinsland, *NASA Langley Research Center*. High-resolution (0.004 cm^{-1}) infrared observations at the Mauna Loa site of the NDSC and related activities are described. (p. 334)

SALON C

3:00 pm–3:20 pm COFFEE BREAK

SALON D

3:20 pm–4:00 pm

ThD, SPECTROSCOPY 2

Herbert Fischer, *Institute for Meteorology, President*

3:20 pm

ThD1 Atmospheric constituents from high-resolution infrared atmospheric and laboratory spectra, A. Goldman, F. J. Murcray, R. D. Blatherwick, F. H. Murcray, J. J. Kusters, F. S. Bonomo, S. J. David, D. G. Murcray, *Univ. Denver*; C. P. Rinsland, *NASA Langley Research Center*. Recent studies of atmospheric trace gases from high-resolution ($0.002\text{--}0.006\text{ cm}^{-1}$) infrared balloon-borne, ground-based and laboratory spectra are presented. (p. 338)

3:40 pm

ThD2 Comparison of ozone columns between FTIR and CLAES over Mauna Loa, Hawaii, Shelle David, Sheryl Beaton, Aaron Goldman, Frank J. Murcray, *Univ. Denver*; Aiden Roche, Jack Kumer, *Palo Alto Research Laboratory*. Infrared solar spectra from Mauna Loa, Hawaii, have been analyzed for ozone column amount. These are compared with results from the CLAES instrument on UARS. (p. 340)

4:00 pm

ThD3 HALOE observations of ozone, halogen, nitrogen, and hydrogen compounds made from the UARS platform, James M. Russell III, Jae H. Park, *NASA Langley Research Center*; Larry L. Gordley, *G&A Technical Software*; S. Roland Drayson, *Univ. Michigan*. The HALOE experiment launched September 12, 1991, on the UARS has operated successfully since turn on, October 11, 1991. It has provided global data on O_3 , HCl , HF , NO , NO_2 , CH_4 , H_2O , and temperature. (p. 342)

4:20 pm

ThD4 An analysis of the MVS physical retrieval method using several approaches based on a satellite radiance temperature classification, Hal J. Bloom, *Hughes STX Corp.*; Anthony L. Reale, Larry M. McMillin, *NOAA*. Results are based on a benchmark data set of collocated radiosonde and NOAA-10 satellite observations and include comparisons to the current operational method. Discussions concerning these results and future research are planned. (p. 346)

4:40 pm

ThD5 Atmospheric trace molecule spectroscopy (ATMOS) data analysis method, M. C. Abrams, M. R. Gunson, L. L. Lowes, *Jet Propulsion Laboratory*; R. Zander, *Univ. Liege*; C. P. Rinsland, *NASA Langley Research Center*. The ATMOS experiment makes use of a Fourier transform spectrometer to measure solar spectra from the Space Shuttle payload bay. The data analysis strategy and method used during the ATLAS-1 mission are described. (p. 348)

SALON A

8:00 pm–10:00 pm

ThE, POSTER SESSION

ThE1 Monitor of ejections of industrial pollutants in the atmosphere using a TV camera, V. A. Banakh, I. N. Smalikho, I. A. Sutorikhin, *Institute of Atmospheric Optics, Russia*; V. L. Mironov, V. V. Morskii, *Altai State Univ., Russia*. This paper is concerned with a theoretical analysis of the possibilities of determining pollution ejection power and average concentration of smoke plume particles according to brightness of their respective optical images. (p. 352)

ThE2 Determination of ejection power of pollutants according to optical radiation backscattering, V. A. Banakh, I. N. Smalikho, *Institute of Atmospheric Optics, Russia*. The paper presents a method for remote determination of ejection power of a local source of pollution from the measurements of backscattering intensity when sounding the smoke plumes using a directed cw optical beam. (p. 353)

ThE3 Paper withdrawn.

ThE4 Demonstration of a new GFCR method with CH₄ measurements at 2.3 μ m, Liang-guo Wang, *College of William and Mary*; Glen Sachse, Peter LeBel, Andrew Wallio, Stephanie Vay, *NASA Langley Research Center*. The feasibility of a nonmechanical gas filter correlation radiometer (GFCR) concept using a photoelastic polarization modulator was demonstrated with measurements of methane at 2.3 microns. (p. 354)

ThE5 HNO₃ profiles obtained during EASOE, F. J. Murray, J. R. Starkey, W. J. Williams, *Univ. Denver*; W. A. Matthews, *NIWAR, New Zealand*; U. Schmidt, *KFA Julich, Germany*; P. Aumedieu, *Service D'Aeronomie du CNRS, France*; C. Camy-Peyret, *Laboratory Physics Molecular et Atmospherique, France*. Five HNO₃ height profiles measured during EASOE are presented. Profiles were derived from atmospheric emission spectra measured with a small, balloon-borne, cryogenically cooled spectral radiometer. (p. 358)

ThE6 Determining the carbon budget (CO and CO₂) of the lower thermosphere from nonequilibrium ir limb radiance, Jeremy R. Winick, Richard H. Picard, *Phillips Laboratory*; P. P. Wintersteiner, A. J. Paboojian, R. A. Joseph, *ARCON Corp.* CIRRIS 1A high resolution spectra in the 4–5 μ m region are analyzed to understand the nonequilibrium emission and investigate the carbon budget of the lower thermosphere. (p. 361)

ThE7 Flight results for the balloon-borne ozone profiler with variable footprint, William S. Heaps, *NASA Goddard Space Flight Center*. Engineering test flight results of the variable footprint ozone profiler described at the Optical Remote Sensing meeting at Incline Village in 1990 are presented. (p. 364)

ThE8 Remote sensing of tropospheric gases by thermal emission spectroscopy, W. F. J. Evans, E. Puckrin, *Trent Univ., Canada*. Measurements of tropospheric gases using FTIR thermal emission spectroscopy are compared with laboratory thermal emission spectra of chlorofluorocarbons, hydrocarbons, and NO₂/HNO₃/N₂O₅. (p. 367)

ThE9 Signal-processing approach for the retrieval of global tropospheric CO using the atmospheric infrared sounder (AIRS), L. Larrabee Strow, *Univ. Maryland-Baltimore County*. The capability of the atmospheric infrared sounder (AIRS) to measure the global CO column content is explored. (p. 370)

ThE10 Analyses of the potential of tropospheric trace gas observations from satellites, R. de Winter-Sorkina, H. van der Woerd, *National Institute of Public Health and Environmental Protection, The Netherlands*; M. Roemer, *TNO Institute of Environmental Sciences, The Netherlands*. Analyses of the potential of the observations of tropospheric ozone, NO₂, SO₂ and formaldehyde by the GOME spectrometer, which will be launched on ERS-2 satellite in 1994, was carried out. (p. 374)

ThE11 Derivation of CLAES filter shapes, J. L. Mergenthaler, J. F. Potter, J. B. Kumer, T. C. James, A. E. Roche, *Lockheed Palo Alto Research Laboratory*. The derivation of system spectral transmission functions for the Cryogenic Etalon Array Spectrometer (CLAES) on UARS is described. Simulated and measured atmospheric earthlimb spectral radiance are compared. (p. 378)

ThE12 Novel collector for high-altitude aircraft observations of solar uv flux, J. Burris, *NASA Goddard Space Flight Center*. An inexpensive technique to quickly and reliably collect the integrated solar flux over a hemisphere is described. (p. 382)

ThE13 From onion peeling to cutting onion cubes, Thomas v. Clarmann, *Kernforschungszentrum Karlsruhe GmbH, Germany*. A data evaluation concept is described and discussed which is based on classical one-dimensional onion peeling approach, but avoids the assumption of spherical homogeneity. (p. 384)

ThE14 Forward model comparisons with the high-resolution interferometer sounder (HIS), R. O. Knuteson, H. E. Revercomb, W. L. Smith, *Univ. Wisconsin-Madison*. FASCOD3P/HITRAN92 forward model radiances are compared with observations of the HIS to illustrate outstanding spectroscopic issues. (p. 388)

ThE15 CO₂ non-LTE excitation and emission at 4.3- μ m from a line-by-line radiative transfer model, Henry Nebel, R. H. Picard, R. D. Sharma, J. R. Winick, *Phillips Laboratory*; P. P. Wintersteiner, *ARCON Corp.* Radiative transfer in the 4.3- μ m bands of CO₂ is calculated using a line-by-line model. The resulting limb radiance is compared with an atmospheric dataset. (p. 391)

ThE16 Daytime measurements of the atmospheric boundary layer using an alexandrite lidar, Cyrille N. Flamant, Thomas D. Wilkerson, *Univ. Maryland*; Coorg Prasad, *Science and Engineering Service Inc.*; Joseph Famiglietti, *NASA Goddard Space Flight Center*. A backscatter lidar is used in conjunction with tropospheric pollutant measurements to retrieve pollution cycle correlations with boundary layer height over Prince George's County, Maryland. (p. 395)

ThE17 SAGE II measurements of volcanic aerosols, Robert E. Veiga, *Science Applications International Corp.* Satellite measurements of global stratospheric aerosols for the period 1984–1992 show periodic variations superposed with volcanic intrusions. The dispersion of Pinatubo aerosols is shown. (p. 399)

ThE18 Comparison of remotely measured multispectral scattering parameters for tropospheric aerosols, D. R. Cutten, *Univ. Alabama in Huntsville*; E. W. McCaul, Jr., *Universities Space Research Assoc.*; J. D. Spinhirne, *NASA Goddard Space Flight Center*; R. T. Menzies, *Jet Propulsion Laboratory*; R. Pueschel, *NASA Ames Research Center*; A. D. Clarke, *Univ. Hawaii*; D. A. Bowdle, *Univ. Alabama in Huntsville*. Tropospheric aerosol backscatter data from the GLOBE program are analyzed at several wavelengths to isolate, identify, and characterize aerosol types and examine their properties. (p. 403)

ThE19 Relationships between lidar backscatter and meteorological fields, Eugene W. McCaul, Jr., *Universities Space Research Association*; David A. Bowdle, Dean R. Cutten, Robert T. Menzies, James D. Spinhirne, *NASA Goddard Space Flight Center*. Lidar measurements of aerosol backscatter are compared with meteorological fields obtained from other sources. Vertical variations of backscatter often correlate well with those of moisture. (p. 407)

ThE20 Practical model for the calculation of multiply scattered lidar returns, Edwin W. Eloranta, *Univ. Wisconsin-Madison*. An approximate equation predicting lidar returns due to n^{th} order multiple scattering is presented. Excellent agreement is shown in comparisons with exact second order computations. (p. 411)

ThE21 Application of a new iterative technique for determining particulate extinction profiles from airborne lidar data obtained in clear tropospheric conditions, Vladimir A. Kovalev, *U.S. Environmental Protection Agency*; Ramesh Viswanathan, *Center of Environmental Studies, Univ. Nevada*. A new iterative technique for determining the particulate extinction profiles is used to invert airborne lidar data obtained in clear tropospheric conditions. (p. 415)

ThE22 Stratospheric aerosol measuring from Obninsk lidar station following the volcano Pinatubo eruption, S. S. Khmelevtsov, Yu. G. Kaufman. The paper chronicles the measurements of stratospheric aerosol from July 1991 through February 1992. (p. 418)

ThE23 Evolution of the Pinatubo volcanic cloud over Hampton, Virginia, Mary T. Osborn, Robert J. DeCoursey, *Science Applications International Corp.*; David M. Winker, David C. Woods, *NASA Langley Research Center*. Ground-based lidar measurements show the formation, spread, and decay of Pinatubo aerosols over Hampton, Virginia. Comparisons are made with similar measurements obtained after El Chichón. (p. 419)

ThE24 Wavelength dependence of the total extinction coefficient under volcanic conditions, Rene Rodriguez, Scott D. Johnson, *Idaho State Univ.*; John Burris, Thomas McGee, *NASA Goddard Space Flight Center*. The calculated wavelength dependence of the extinction coefficient is dependent on the particle distribution's refractive index, modal size, and shape, which vary under volcanic conditions. (p. 423)

ThE25 Lidar observations of Mt. Pinatubo aerosols at Table Mountain (34° N), David A. Haner, Eric W. Sirko, I. Stuart McDermid, *Jet Propulsion Laboratory*. A temporal record of the stratospheric aerosol backscatter ratios at 532 and 1064 nm, and a parametric description of the loading are presented. (p. 427)

FRIDAY, MARCH 12, 1993

SALON D

8:00 am–9:50 am

FA, NEW DEVELOPMENTS 1

Dennis Karl Killinger, *Univ. South Florida, Presider*

8:00 am (Invited)

FA1 Development of laser altimeter sensors for Earth and planetary observations, Jack L. Bufton, David J. Harding, J. Bryan Blair, James B. Garvin, *NASA Goddard Space Flight Center*. Laser altimeter sensors are now operating from aircraft and spacecraft for topographic measurement of Earth and planetary surfaces. They incorporate diode-pumped laser transmitters and high-speed digitization technology and will employ multiple-beam techniques for lidar imaging of the surface. (p. 432)

8:30 am

FA2 Performance calculations and test of Sciamachy detector modules, A. P. H. Goede, R. W. M. Hoogeveen, *SRON-Utrecht, The Netherlands*; R. J. van der A, J. de Vries, *SRON-Leiden, The Netherlands*. Sciamachy is an uv-vis-nir spectrometer for atmospheric research on ENVISAT-1 (1998) and comprises 8 detector modules of which performance calculations and breadboard results are presented. (p. 436)

8:50 am

FA3 Laser diode characterization for optical remote sensing applications, Thomas H. Chyba, G. Sachse, L. Mayo, Alene W. Heuser, *NASA Langley Research Center*; L.-G. Wang, *College of William and Mary*. A computer-controlled laboratory apparatus that characterizes laser diodes is described. Results are presented for diodes being evaluated for use in a differential absorption lidar instrument. (p. 440)

9:10 am

FA4 Charge-coupled-device detection for a Doppler-Rayleigh lidar, Jonathan S. Friedman, Craig A. Tepley, *NAIC Arecibo Observatory, Puerto Rico*; Mark W. Robison, *Univ. Minnesota*; Paul A. Castleberg, Francisco J. Garcia, *Cornell Univ.* We record Fabry-Perot fringes in a Doppler-Rayleigh lidar using a charge-coupled device. We compare wind measurements with those obtained with a photomultiplier detector. (p. 444)

9:30 am

FA5 Automated rotating shadowband spectroradiometer, Lee Harrison, Mostafa A. Beik, Joseph J. Michalsky, *State University of New York-Albany*. The rotating shadowband spectroradiometer provides high-accuracy measurements of spectrally resolved direct normal, total horizontal, and diffuse horizontal irradiances between 360- and 1060-nm region. (p. 448)

SALON C

9:50 am–10:20 am **COFFEE BREAK**

FRIDAY, MARCH 12, 1993—Continued

SALON D

10:20 am–11:50 am

FB, NEW DEVELOPMENTS 2

D. P. Swart, *RIVM, Holland, Presider*

10:20 am (Invited)

FB1 New laser sources and detectors for industrial emission and open path air monitoring, Dennis Killinger, *Univ. South Florida*. This paper covers recent work in the development of new, tunable laser sources and their potential utility for remote sensing of atmospheric emissions and gases. In addition, the use of several new detectors or optical (fiber) routing applications will be covered. (p. 454)

10:50 am

FB2 DIAL in the 3.1–3.7- μ m spectral region using two simultaneously pumped optical parametric oscillators, Scott Taylor, *Phillips Petroleum Co.* A mobile differential absorption lidar system tunable in the 3.1–3.7- μ m region is introduced with preliminary topographic detection data of propane presented. (p. 455)

11:10 am

FB3 NASA Lidar Atmospheric Sensing Experiment's titanium-doped sapphire tunable laser system, James Barnes, William Edwards, *NASA Langley Research Center*; Larry Petway, *Science Applications International Corp.*; Liang-Guo Wang, *College of William and Mary*. A tunable titanium-doped sapphire lidar laser transmitter, which will be integrated into NASA's Lidar Atmospheric Sensing Experiment, will be described. Discussion of the laser design and its performance capabilities with respect to the experiment requirements will be discussed. (p. 459)

11:30 am

FB4 Diode laser injection seeded, Raman shifted alexandrite laser tunable narrowband lidar source, St. Schmitz, U. von Zahn, *Univ. Bonn, Germany*; T. Wilkerson, *Univ. Maryland*; D. F. Heller, J. C. Walling, *Light Age, Inc.* Diode laser injection seeded alexandrite lasers have been developed and their fundamental and Raman shifted output characterized. Application to water vapor, sodium, and other lidars is described. (p. 462)

11:50 am–12:00m

CLOSING REMARKS

Alan Carswell

Monday, March 8, 1993

Keynote Session

MA 8:00am–10:00am
Salon F

William Mankin, *Presider*
National Center for Atmospheric Research

Remote Sensing of Atmospheric Trace Constituents Using Mid-IR Fourier Transform Spectrometry

H. Fischer

Institut für Meteorologie und Klimaforschung
Kernforschungszentrum/Universität Karlsruhe
P.O. Box 3640, 7500 Karlsruhe 1, Tel. 7247-823643

Introduction

The impact of industrial and agricultural human activities on the environment has now reached such proportions that even global scale effects are clearly observed. These activities lead to a steady growth in the atmospheric abundance of several radiatively and chemically active trace gases which influence the greenhouse effect and the tropospheric and stratospheric ozone.

The profound investigation of these anthropogenic changes requires simultaneous, global and time-independent observations of atmospheric trace species. The derived vertical profiles of trace species should have a reasonable vertical resolution.

Appropriate instrumentation

Many atmospheric trace species exhibit rovibrational absorption bands in the infrared (IR). In order to measure a large number of these trace gases simultaneously with redundant information, the required instrument has to detect a wide spectral range with high spectral resolution.

Obviously, Fourier Transform Spectrometers (FTS) are especially appropriate for this measurement task. Due to technical reasons the spectral range has to be limited to a certain degree, e.g. to the mid-infrared. Time-independent measurements can be performed with a cooled FTIR operating in the emission mode. Reasonable vertical resolution is to be reached by applying the limb sounding technique. Last not least, global measurements can be performed if the instrument is flown aboard a polar orbiting satellite.

Previous experiments

During the last ten years FTIR experiments for measuring trace species have already been performed by different scientific groups (overview see Fischer 1992). There is a considerable number of uncooled mid-IR experiments which yielded very interesting

scientific results in the past but can not meet all the requirements as specified above. With one exception all investigators have applied the limb sounding geometry (Revercomb et al. 1988). The best known FTIR experiment is the ATMOS (Atmospheric Trace Molecule Spectroscopy, Farmer et al. 1987) Project. Twenty occultations were recorded during the Spacelab 3 flight which result in concentration profiles for about 30 trace gases in both the Northern and Southern hemisphere.

Cooled Michelson-type interferometers have already been operated aboard stratospheric balloon gondolas by different groups and aboard a Transall aircraft (see Fischer 1992 and below). The recorded emission spectra are of high quality and allow the determination of vertical profiles of many trace species, e.g. the main reactive and reservoir nitrogen compounds. These contributions to atmospheric research were essential even if no cooled interferometer for time-independent emission measurements has been flown in space so far.

MIPAS (Michelson Interferometer for Passive Atmospheric Sounding) Experiments

MIPAS has been designed to meet the requirements for measurement of atmospheric trace gases as defined above. The central part of MIPAS is a rapid scanning Fourier Transform Spectrometer operating in the 3 to 15 μm region and recording one interferogram within a few seconds. The objective to fly a cooled FTIR in space leads to a novel optical design, the so-called double pendulum interferometer (DPI, Burkert et al. 1983).

In these days, MIPAS is not a single instrument but a measurement programme. An uncooled version of this interferometer has been developed during the first half of the 1980ies. This MIPAS-LM (Laboratory Model) is being used as a ground-based device for measuring column amounts of trace gases at polar stations by detecting the attenuated solar radiation. During the CHEOPS III campaign (1990) and during EASOE (European Arctic Stratospheric Ozone Experiment), time series of zenith column amounts of several trace gases have been derived from the recorded interferograms and analysed with respect to dynamical and chemical processes in the arctic stratosphere (Adrian et al. 1991).

A cooled version of MIPAS has been constructed to observe the composition and structure of the stratosphere as well as their diurnal variations with good vertical resolution from balloon-borne platforms. Field experiments have been performed during balloon flights in France in May 1989 and May 1990 as well as in Kiruna/Northern Sweden in January and March 1992. Limb emission spectra were

measured within the altitude range between 5 and 40 km. A considerable number of atmospheric trace species are identified in the spectra, namely CO_2 , O_3 , H_2O , CH_4 , N_2O , CCl_4 , CF_2Cl_2 , CFCl_3 , CHF_2Cl , ClONO_2 , HNO_3 , N_2O_5 and C_2H_6 . The capability of MIPAS-B (Balloon) has been proven by retrieving vertical concentration profiles of different trace species and, in particular, by discovering the high amount of ClONO_2 in the lower arctic stratosphere in springtime 1992 (Oelhaf et al. 1993).

Besides the MIPAS ground based and the balloon experiment, our new cooled MIPAS aircraft experiment was also operated during the EASOE campaign in winter 1991/92. First results from these measurements show an interesting correlation between stratospheric column amounts of O_3 and HNO_3 (Blom et al. 1993).

The cooled MIPAS space experiment is in development for the core payload of the 1. European Polar Platform (ENVISAT) which will be launched in 1998.

References

Adrian G.P. , T. Blumenstock, H. Fischer et al. 1991, Column amounts of trace gases derived from ground-based measurements with MIPAS during CHEOPS III, *Geophys. Res. Lett.* 18, 783

Blom C., H. Fischer et al. 1993, Airborne measurements during the arctic stratospheric experiment 4. Column amounts of HNO_3 and O_3 derived from FTIR emission sounding, submitted to GRL in Nov. 1992

Burkert P., F. Fergg and H. Fischer 1991, A compact high resolution Michelson Interferometer for passive atmospheric sounding (MIPAS), *IEEE Trans. Geosci. Rem. Sens.* GE-21, 345

Farmer C.B. et al. 1987, Final Report on the first flight of the ATMOS instrument during the Spacelab 3 mission, April 29 through May 6, 1985, JPL-Publication 87-32

Fischer H. 1992, Remote sensing of atmospheric trace constituents using Fourier Transform spectrometry, *Ber. Bunsenges. Phys. Chem.*, 96, 306-314

Oelhaf H. T.v. Clarmann, H. Fischer et al 1993, Stratospheric ClONO_2 , HNO_3 and O_3 profiles inside the arctic vortex from MIPAS-B limb emission spectra obtained during EASOE 1992, submitted to GRL in Nov. 1992

Revercomb H.F. et al. 1988, Radiometric calibration of IR Fourier Transform spectrometers: Solution to a problem with the High-resolution Interferometer Sounder (HIS), *Appl. Optics*, 27, 3210-3218

Giant Lidars for Middle and Upper Atmosphere Studies:
Observational Capabilities of the New Advanced
Electro-Optic System (AEOS) at Haleakala, Hawaii

By

Chester S. Gardner
Office of the Vice Chancellor for Research
601 East John Street, 420 Swanlund Building
Champaign, Illinois 61820

The development and refinement of sophisticated remote sensing techniques during the past three decades have contributed enormously to our knowledge of the atmosphere. Lidar technologies have progressed especially rapidly since the invention of the laser in 1961. Today, sophisticated systems are used to probe composition and structure throughout the atmosphere from the troposphere into the lower thermosphere and are making important contributions to several global change studies. While the recent advances in lidar technology have been impressive, the accuracy, resolution and sensitivity of many systems are still limited by signal levels.

Opportunities to test the capabilities of very large lidars may be available within the next several years at the Advanced Electro-Optic System (AEOS) being constructed by the Air Force Phillips Laboratory at Haleakala, Maui. AEOS includes a fully steerable 4m class telescope and powerful Rayleigh/Raman and Na Doppler/Temperature lidars. We discuss the observational capabilities of the proposed facility with particular emphasis on measurements of temperature, winds, water vapor, and ozone.

EASOE Campaign and Lidar Observation

Gerard J. Megie
University Pierre & Marie Curie
B102, 4 Jussieu Pl., Paris, France

Summary not available at press time.

**Results from the flight of the Atmospheric Trace Molecule Spectroscopy
on the ATLAS-1 Space Shuttle Mission**

M. R. Gunson, M. C. Abrams, C. B. Farmer, L. L. Lowes

Jet Propulsion Laboratory
California Institute of Technology
Pasadena, California

C. P. Rinsland

NASA Langley Research Center
Hampton, Virginia
R. Zander

Institut d'Astrophysique
Université de Liège
Liège-Contee, Belgium

During the ATLAS-1 space shuttle mission, the ATMOS experiment, a Fourier transform infrared spectrometer operating in solar occultation mode from on-orbit (*Farmer, 1987*), collected data through more than 90 orbital sunrises and sunsets at latitudes between 30°N and 55°S. The resulting high-resolution infrared solar absorption spectra from these observations have so far been analyzed for the vertical profiles of several species (O_3 , HNO_3 , ClNO_3 , HCl , HF , N_2O , CH_4 , and H_2O) of immediate importance as correlative measurements for other satellite instruments, such as those carried on the Upper Atmospheric Research Satellite. Results for these gases together with those of other species measured by ATMOS, such as the more abundant man-made chlorofluorocarbons (CFC-11, CFC-12, HCFC-22) are compared with similar measurements made by this instrument from data acquired during its first flight in April, 1985. In the period between these two flights, the halogenated gases are expected to have increased measurably in concentration due to the continued release of the halogenated source gases. These ATMOS data provide a simultaneous measurement of the increase in the tropospheric source gases as well as the halogen sink species, HCl and HF .

The residual stratospheric aerosol layer created by the 1991 Mt. Pinatubo volcanic eruption resulted in a loss of instrument suntracking capability at heights below 28 km in a large number of occultations. By comparison to spectra obtained in the first flight of the instrument on board the shuttle in 1985, several broad spectral features can be assigned in the 600 to 4800 cm^{-1} interval as arising from this stratospheric aerosol. These are observed in spectra with tangent

heights as high as 35 km. The vertical profiles of HCl, ClNO_3 , and HNO_3 have been obtained through the lower stratosphere, and can be used as a test of the chemical effect due to the presence of this aerosol.

References

C. B. Farmer, "High resolution infrared spectroscopy of the sun and the earth's atmosphere from space," *Mikrochim. Acta (Wien)*, III, 189-214, 1987.

Monday, March 8, 1993

Water Vapor

MB 10:20am–12:30pm
Salon F

Allan I. Carswell, *Presider*
York University, Canada

Temporal scales of water vapor measured
with a Raman lidar during SPECTRE

S. Harvey Melfi
NASA Goddard Space Flight Center
Code 617, Greenbelt, MD 20771

Summary not available at press time.

Coincident Measurements of Atmospheric Aerosol Properties and Water Vapor by a Scanning Raman Lidar

R. A. Ferrare
Hughes STX Corporation
Code 917
NASA/Goddard Space Flight Center
Greenbelt, MD 20771
301-286-2327

S.H. Melfi
NASA/Goddard Space Flight Center
Code 917
Greenbelt, MD 20771
301-286-6348

D. N. Whiteman
NASA/Goddard Space Flight Center
Code 924
Greenbelt, MD 20771
301-286-3115

K.D. Evans
Hughes STX Corporation
Code 917
NASA/Goddard Space Flight Center
Greenbelt, MD 20771
301-286-9113

Knowledge of the physical and optical properties of atmospheric aerosols is required to determine the impact aerosols will have on radiative transfer, heterogeneous chemistry, and cloud dynamics. Since the composition and size of atmospheric aerosols are functions of the atmospheric water vapor, aerosols must be studied in their natural state in order to fully understand how they are affected by various meteorological conditions and how they in turn will affect the processes listed above. By measuring high resolution profiles of aerosol extinction and backscattering as well as simultaneous profiles of atmospheric water vapor, Raman lidar can provide information regarding aerosol microphysical characteristics [Ansmann, et al., 1992; Ferrare et al., 1992]. In addition, the aerosol extinction/backscatter ratio measured directly by Raman lidar can be used in the estimation of aerosol extinction and optical thickness in the inversion procedures used by simpler backscatter lidars. In this presentation, we discuss measurements of aerosol extinction, backscattering, extinction/backscatter ratio, water vapor mixing ratio, and relative humidity made by a scanning Raman lidar over Wallops Island, Virginia (37.95 N, 75.47 W) during August, 1992.

The GSFC Raman lidar is a trailer-based system which uses an XeF excimer laser to transmit light at 351 nm. System details are discussed by Whiteman et al. [1992b] and Ferrare et al. [1992]. A steerable elliptical flat provides full 180 degree horizon to horizon scan capability within a single scan plane. Light backscattered by molecules and aerosols at the laser wavelength is detected as well as Raman scattered light from water vapor, nitrogen, and oxygen molecules. Data were acquired only at night to avoid interference from background skylight.

Profiles of the aerosol scattering ratio R , aerosol volume backscatter and extinction cross sections β_a and α_a , aerosol extinction/backscatter ratio S , water vapor mixing ratio w , and relative humidity RH were computed as functions of range and zenith angle following procedures discussed by Ferrare et al. [1992] and Whiteman et al. [1992a]. R was derived from the Raman nitrogen return signal and the signal detected at the laser wavelength; β_a was then computed from R and from the molecular volume backscatter cross section β_m obtained from a molecular number

density profile computed using coincident radiosonde pressure and temperature data. The derivative of the Raman nitrogen return signal with respect to range was used to compute α_a . Ratios of the Raman water vapor and nitrogen signals were used to derive w which was used along with radiosonde temperature profiles to calculate RH. During the lidar measurements, NASA/GSFC/ Wallops Flight Facility personnel launched several radiosonde packages from a coastal site approximately 3 km downrange from the lidar; the lidar scan was oriented to acquire data over both this radiosonde launch site and the land-ocean interface.

Lidar data acquired on the nights of August 2, 3, and 4 have been analyzed. Figures 1 and 2 show aerosol extinction ($\lambda=351$ nm) and relative humidity measured during one scan on August 3. These figures were constructed using 54 fifty second (20,000 shots) profiles acquired between 05:01-05:48 UT. Range resolution for α_a increases from 300 meters at a range of 3 km to 600 meters at a range of 6 km; range resolution for RH is 75 meters. Since atmospheric attenuation increases with decreasing scan elevation angle, longer averaging times were used at low elevation angles to achieve comparable precision for a given range. Random errors for figures 1 and 2 are: $\Delta\alpha_a < 0.011 \text{ km}^{-1}$ and $\Delta\text{RH} < 10\%$. The approximate extinction due to a cloud at an altitude between 3.6-4.5 km is also shown in figure 1. Note that aerosol extinction is greatest for altitudes between 1.0-3.3 km rather than at the location of maximum relative humidity just below cloud base as might be expected. Obviously, total aerosol concentration and aerosol dry particle composition affect aerosol extinction as well as the growth of the aerosol particles due to increases in the relative humidity.

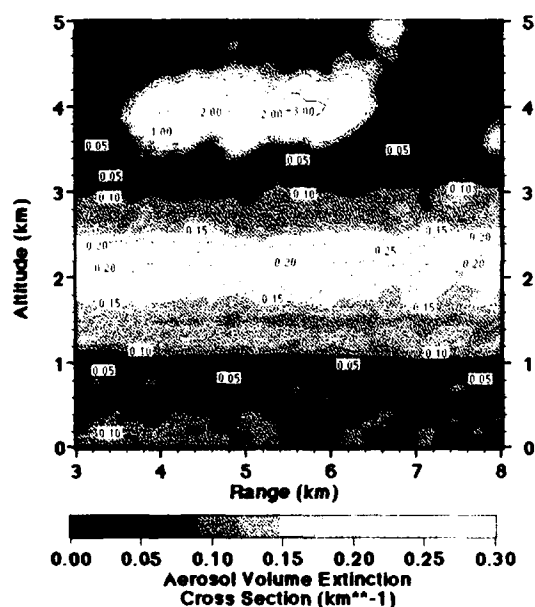


Figure 1. Aerosol volume extinction cross section α_a (km^{-1}) at 351 nm derived from the lidar scan data between 05:01-05:48 UT on August 3.

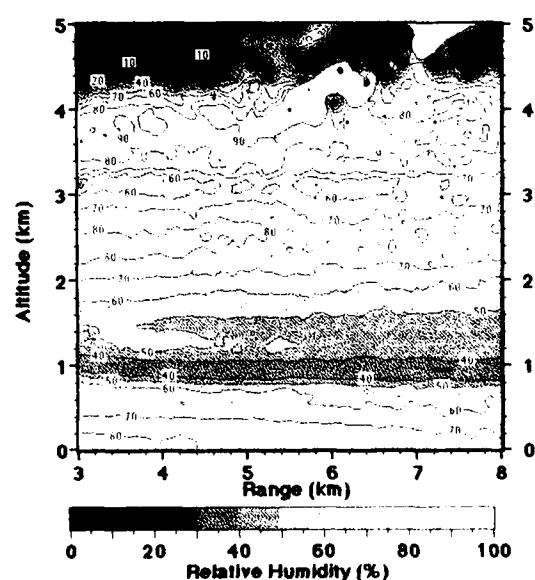


Figure 2. Same as figure 1 except for relative humidity (%).

In an attempt to separate aerosols according to various air masses, the lidar data were segregated into layers using the water vapor mixing ratio, since w is conserved except for condensation and evaporation and can, therefore, act as a tracer of air motion. The averages and standard deviations of α_a , β_a , S , RH , and w for these altitude layers are listed in Table 1. Also listed are the least squares best fit parameters A and B for the relation $\beta_a = B\alpha_a^A$ which is traditionally used to relate aerosol backscattering to extinction [Klett, 1985]. Note that the S values appear to be more consistent with the "rural" aerosol values of $S \approx 40$ -50 sr rather than the "maritime" value of $S \approx 20$ -25 sr [Shettle and Fenn, 1979], even though much of the scan data were located above the ocean.

Table 1. Average α_a , β_a , S , RH , and w derived from the lidar data for selected altitudes. Standard deviations are shown in parentheses. Aerosol parameters correspond to $\lambda = 351$ nm. Also shown are best fit parameters A and B for the relation $\beta_a = B\alpha_a^A$.

Date	Altitude (km)	α_a (km^{-1})	β_a (km-sr^{-1})	S (sr)	RH (%)	w (g/kg)	B	A
August 2	0.3-1.75	0.0489 (0.023)	0.00103 (0.00048)	47.9 (9.1)	51.6 (13.8)	6.22 (2.00)	0.015	0.89
August 3	0.0-1.0	0.096 (0.027)	0.0025 (0.00047)	39.4 (9.8)	61.2 (14.5)	9.16 (2.23)	0.0052	0.32
August 3	1.0-2.5	0.177 (0.046)	0.0035 (0.00078)	49.8 (6.2)	62.2 (14.9)	7.39 (0.85)	0.012	0.70
August 3	2.5-3.3	0.103 (0.0573)	0.0025 (0.00086)	38.7 (8.6)	64.4 (16.7)	5.54 (1.56)	0.010	0.60
August 3	3.3-4.5	0.0462 (0.0135)	0.0013 (0.00028)	35.3 (6.7)	77.3 (19.0)	5.33 (1.06)	0.0082	0.60
August 4	1.0-3.0	0.350 (0.0801)	0.0056 (0.00011)	62.8 (5.5)	80.9 (9.8)	9.29 (1.51)	0.013	0.80
August 4	3.0-5.0	0.1517 (0.120)	0.0024 (0.0016)	54.4 (14.5)	78.5 (15.1)	5.94 (1.41)	0.011	0.79

Figure 3 shows the correlation between aerosol extinction and relative humidity for data acquired on August 3. With the exception of data acquired above 3.3 km, aerosol extinction increases with relative humidity; however, as shown in figure 4, this increase is much faster than that expected from aerosol models. This difference may be attributed to the lidar observing increases in particle number concentration as well as increases in particle size; since the model results are for a constant aerosol number density, one must use caution when comparing these data. In general, there was little or no correlation found between aerosol extinction/backscatter ratio and relative humidity.

Additional aerosol/water vapor data will be presented. Mie theory computations of possible aerosol size distributions and compositions consistent with the lidar observations will also be discussed.

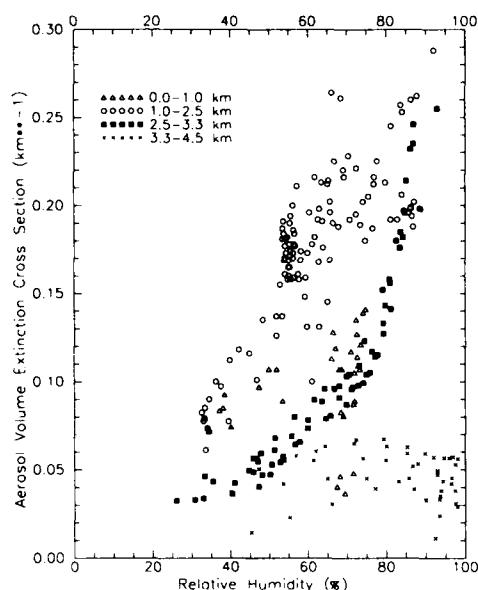


Figure 3. Aerosol volume extinction cross section α_a (km^{-1}) at 351 nm as a function of relative humidity derived from the lidar scan data between 05:01-05:48 UT on August 3, 1992.

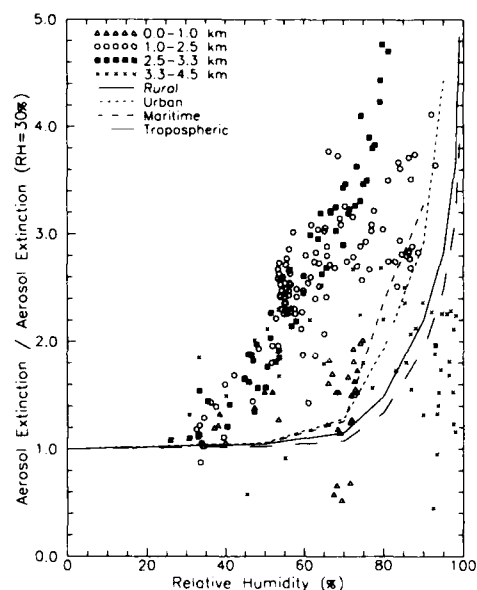


Figure 4. Ratio $\alpha_a(\text{RH})/\alpha_a(\text{RH}=30\%)$ as a function of relative humidity for data shown in figure 3. Aerosol model data from Shettle and Fenn [1979] have been normalized to constant total particle number concentration.

Ansmann, A., M. Riebesell, U. Wandinger, C. Weitkamp, E. Voss, W. Lahmann, and W. Michaelis, 1992: Combined Raman Elastic-Backscatter LIDAR for vertical profiling of moisture, aerosol extinction, backscatter, and LIDAR ratio., *Appl. Phys. B*, **55**, 18-28.

Ferrare, R.A., S.H. Melfi, D.N. Whiteman, and K.D. Evans, 1992: Raman lidar measurements of Pinatubo aerosols over southeastern Kansas during November-December 1991, *Geophys. Res. Letters*, **19**, No. 15, 1599-1602.

Klett, J.D., 1985: Lidar inversion with variable backscatter/extinction ratios, *Appl. Opt.*, **24**, No. 11, 1638-1643.

Shettle, E.P., and R.W. Fenn, 1979: Models for the aerosols of the lower atmosphere and the effects of humidity variations on their optical properties. AFGL-TR-79-0214, Air Force Geophysics Lab., Hanscom AFB, MA.

Whiteman, D.N., S.H. Melfi, and R.A. Ferrare, 1992a: Raman lidar system for the measurement of water vapor and aerosols in the earth's atmosphere, *Appl. Opt.*, **31**, No. 16, 3068-3082.

Whiteman, D.N., S.H. Melfi, R.A. Ferrare, K.D. Evans, L. Ramos-Izquierdo, O.G. Staley, R. W. DiSilvestre, I. Gorin, K.R. Kirks, W.A. Mamakos, L.S. Wan, N.W. Walsh, J.M. Marsh, and R.A. Aldridge, 1992b: Advanced Raman water vapor lidar, Sixteenth International Laser Radar Conference, NASA Conference Publication 3158, Cambridge, MA.

Evaluation of Raman Lidar Profiling of Atmospheric Water Vapor: Simultaneous Measurements with Two Advanced Systems

J. E. M. Goldsmith and Scott E. Bisson
Sandia National Laboratories
Livermore, CA 94551-0969
510-294-2432 (JEMG)

David N. Whiteman and S. H. Melfi
NASA Goddard Space Flight Center
Greenbelt, MD 20771

Richard A. Ferrare and Keith D. Evans
NASA Goddard Space Flight Center
Hughes STX Corporation
Greenbelt, MD 20771

Introduction

The Raman lidar technique has proven to be a powerful method for profiling atmospheric water vapor, one of the most important variables that characterizes the atmosphere. Detailed evaluation of the performance of Raman lidar systems (or lidar systems in general) is complicated by the lack of an appropriate instrument that can provide accurate measurements for intercomparison purposes. In this paper, we describe a detailed intercomparison program performed using two advanced Raman lidar systems. The paper treats in detail only a nighttime intercomparison of water vapor profiles, but the intercomparison program itself will feature daytime and nighttime measurements of both water vapor and aerosol scattering ratios.

Description of Lidar Systems

The Raman lidar systems used in this intercomparison were developed at the NASA Goddard Space Flight Center and at Sandia National Laboratories (referred to henceforth simply as the Goddard and Sandia lidars). The Goddard lidar is the latest in a series of instruments developed over the past 12 years; the current version was first fielded at the SPECTRE/FIRE campaign in the fall of 1991, and its performance has been evaluated very carefully since it came on line. The Sandia lidar was constructed during the past year, and the full system became operational in October, 1992, just before the intercomparison described here.

The Goddard and Sandia lidars share many common characteristics. The systems are housed in two mobile semitrailers each, one trailer serving as a mobile laboratory and the other as a support vehicle providing a data acquisition/analysis area. Both systems employ high-average-power, high-repetition-rate excimer lasers as light sources, and have identical telescopes as the primary element of the receiver subsystems. The major

differences are in the design of the optical elements located after the receiving telescope. The Goddard lidar operates with a single adjustable field-of-view (fov), and has two complete sets of optics, one configured for 351-nm laser excitation and one for 248-nm laser excitation. Each set has high- and low-sensitivity channels (to provide extended dynamic range) at four detection wavelengths, with photon counting used in all channels. The Sandia lidar operates in a dual field-of-view configuration (for enhanced daytime capabilities) designed for 308-nm laser excitation. Enhanced dynamic range, for daytime operation in particular, is provided by using photon counting in the narrow field-of-view channel, and analog to digital conversion in the wide field-of-view channel. The characteristics of the systems are summarized in Table 1.

Table 1. Lidar Characteristics (showing nighttime configuration of the Goddard system)

Subsystem	Characteristic	Sandia	Goddard
Transmitter	Laser	XeCl Excimer	XeF Excimer
	Wavelength	308 nm (XeCl)	351 nm (XeF)
	Energy/pulse	90 mJ	45 mJ
	Repetition rate	200 Hz	400 Hz
	Bandwidth	3 pm	Three lines*
	Divergence	~0.2 mr	~0.5 mr
Receiver	Configuration	Cassegrain	Cassegrain
	Diameter	0.76 m	0.76 m
	f number	4.5	4.5
	Scanning	Zenith, horizontal only	180° scan, vertical plane
	Channel bandpass	0.4 nm	6-9 nm
	Field of view	Dual (0.4 mr, 4 mr)	Adjustable (0.5-3.0 mr)
	Ranges	2 (narrow, wide fov)	2 (low, high sensitivity)
	Channels	3	4
	Species	Rayleigh/aerosol (308 nm) Water vapor (347 nm) Nitrogen (332 nm)	Rayleigh/aerosol (351 nm) Water vapor (403 nm) Nitrogen (383 nm) Oxygen (372 nm)
Electronics	Short range	Analog to Digital Conv.	Photon counting
	Long range	Photon counting	Photon counting
	Range resolution	75 m (0.5 μ sec)	75 m (0.5 μ sec)

*Output contains three lines at 349, 351, and 353 nm

Initial Intercomparison Results

The Raman lidar intercomparisons were carried out in November, 1992, at the NASA Goddard Space Flight Center, with sonde support provided at the lidar site by personnel from the NASA Wallops Flight Facility. The lidar systems were operated simultaneously for extended periods during three nights, with two sondes launched during two of the nights. These sondes were used to calibrate the Sandia lidar, and to confirm the calibration of the Goddard lidar (extensive lidar-sonde comparisons performed using the latter over the past year have yielded a calibration consistent on the order of $\pm 5\%$, limited at least in part by the reliability of the sonde measurements).

Figure 1 displays a gray-scale time-height representation of the water-vapor mixing ratio obtained using the two systems. Each vertical "stripe" in the images corresponds to a single profile recorded as a one-minute average with 75-m vertical resolution; thus each image represents 428 independent measurements. The speckled regions that appear periodically at altitudes greater than 4 km are caused by attenuation of the laser beams by clouds. The quantitative agreement between this pair (and other similar pairs) of original images is striking, especially when viewed as false-color images, although this agreement may not be evident in the reproduction of the images here.

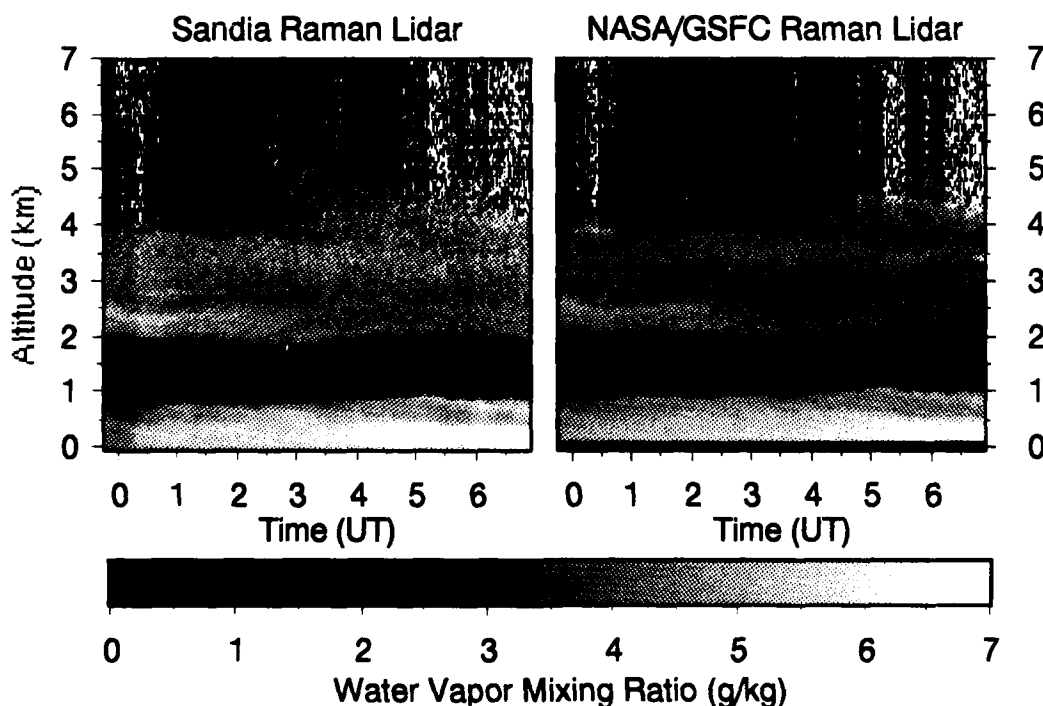


Figure 1. Gray-scale time-height representation of the water-vapor mixing ratio obtained using the two lidar systems during the night of November 10-11, 1992, recorded from 6:47 pm - 1:54 am local time (23:47 - 6:54 UT).

Figure 2 displays lidar and sonde profiles obtained at the indicated time during the same period as the image shown in Fig. 1. The lidar profiles represent ten-minute averages started at the time that the sondes were launched. The quantitative agreement between the two lidars is more evident in this figure, as is their agreement with the sonde. Details of the behavior of the two systems for profiling atmospheric water vapor, as well as their capabilities for measuring aerosol characteristics, will be presented at the meeting.

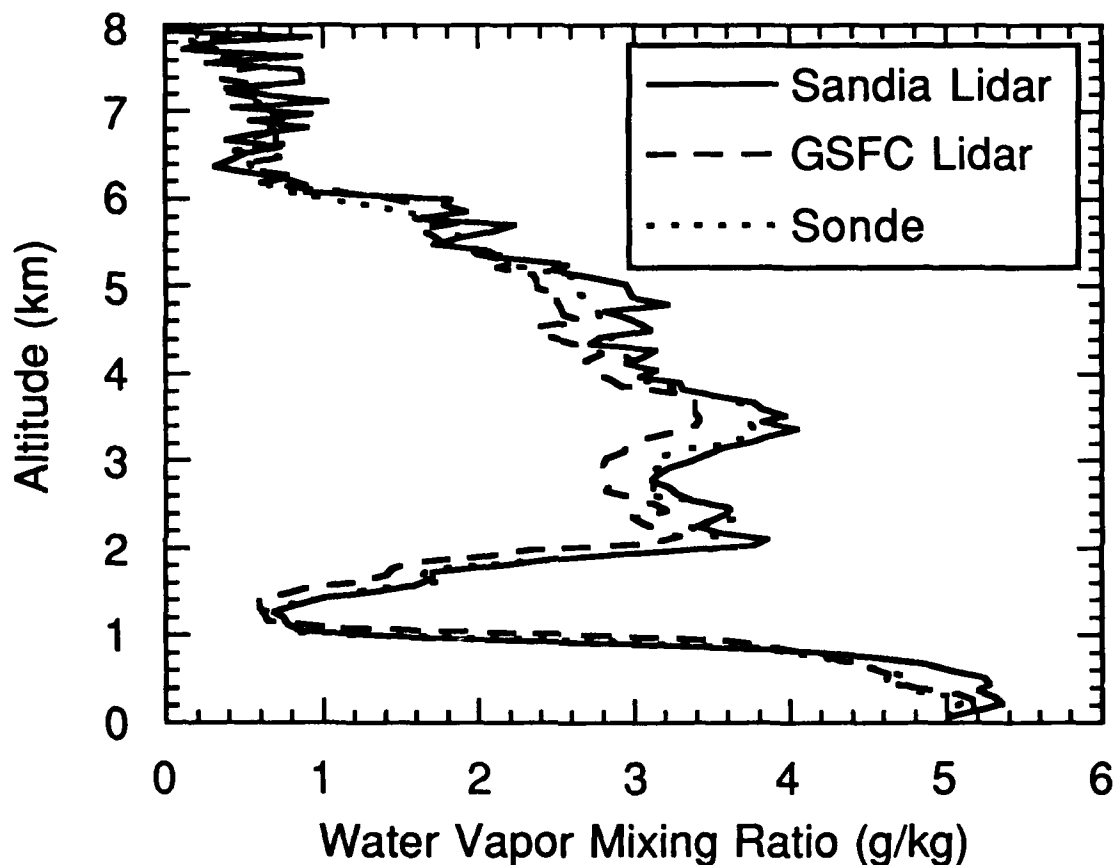


Figure 2. Water-vapor profiles obtained at 9:58 pm local time on November 10, 1992 (2:58 UT on November 11) at the Goddard Space Flight Center.

Acknowledgments

We wish to thank Marshall Lapp and John Vitko for many helpful discussions, and Mark Mitchell and Glenn Staley for their expert technical assistance. The Sandia authors also wish to thank the Goddard authors for the expertise they provided throughout the development of the Sandia lidar. This work is supported by the U. S. Department of Energy, Atmospheric Radiation Measurement (ARM) Program, and by the NASA Atmospheric Dynamics and Radiation Program.

Daytime Tropospheric Water Vapor Profile Measurements with a Raman Lidar

Scott. E. Bisson, J. E. M. Goldsmith
Sandia National Laboratories
Livermore, CA 94551-0969
(510) 294-2467

1. Introduction

Water vapor is one of the most important quantities needed to define the state of the atmosphere. Water vapor plays an important role in determining the earth's radiation budget, both directly as an absorber of infrared radiation and through its role in cloud formation. Because convection effectively short-circuits greenhouse absorption at altitudes below about 6 km, surface temperatures depend strongly on the vertical distribution of water vapor. The vertical distribution of water vapor also determines convective stability, and hence storm development. Water vapor is highly variable, both spatially and temporally, and is one of the most uncertain parameters in GCMs (General Circulation Models). Therefore, knowledge of the vertical and temporal variations of water vapor are essential for understanding atmospheric processes.

Raman lidar has proven to be a powerful tool for measuring nighttime water vapor profiles.^{1,2} Whiteman et al.² have developed a Raman lidar system to measure sustained nighttime water vapor profiles with high accuracy (>90%) at altitudes up to 9 km with a vertical resolution of 75 m in one-minute integration periods. The influence of solar radiative forcing and the need for continuous data records provides strong motivation for the development of similar daytime capabilities. Daytime measurements are limited, however, by the difficulty of detecting the relatively weak backscattered Raman signal against the large solar background. We have developed a high performance, dual field-of-view (fov), narrowband Raman lidar system capable of both daytime and nighttime operation. The key features of this system are its dual fov capability and narrowband, high transmission UV interference filter system. Initial measurements with this system indicate that daytime measurements of several kilometers with 75 m range resolution and a few minutes integration time may be possible.

2. Daytime Concepts

The central problem in the development of a daytime capable Raman lidar is the detection of the relatively weak backscattered Raman signal against the large solar background. One approach to overcoming this problem is to operate in the solar blind region of the spectrum.³ This approach effectively reduces the solar background, but attenuation of the laser beam and the backscattered Raman radiation (primarily due to tropospheric ozone) greatly reduces the signal also. Alternatively, the background skylight reaching the detector can be reduced by using a narrow fov receiver and narrowband detection. Ansmann et al.⁴ have used this approach and have obtained daytime water vapor profiles up to 2.5 km with 180 m range resolution using

integration times of approximately 15 min. Reducing the fov of the receiver reduces the number of detected background sky photons, but unfortunately increases the altitude at which the receiver fov and laser beam overlap, providing poorer short-range performance. One solution to this problem is to use a dual fov detection system to provide enhanced range coverage and increased dynamic range. The weak high-altitude signals are detected by a narrow fov channel, and the low-altitude signals are detected by a wide fov channel, in which the stronger signal levels compensate for the higher background level. The number of detected background sky photons can be reduced further by using narrow bandwidth detection. Optimum efficiency requires a laser with a bandwidth substantially narrower than the water vapor Raman linewidth, and with a divergence smaller than the narrow receiver fov.

3. Instrument

Figure 1 shows a schematic of the Sandia lidar system. The transmitter is a Lambda Physik LPX 150 T injection-locked, tunable XeCl laser. The receiver employs a 0.76 m diameter, f 4.5 Cassegrain telescope. A mirror with a small hole drilled through its center is placed at the focal point of the telescope; the hole provides the field stop for the narrow fov channels (light passing through the hole), and the light reflected by the mirror is directed to the wide fov channels. The narrow and wide fov channels both have three detectors for monitoring Rayleigh/aerosol scattering in addition to H₂O and N₂ Raman scattering.

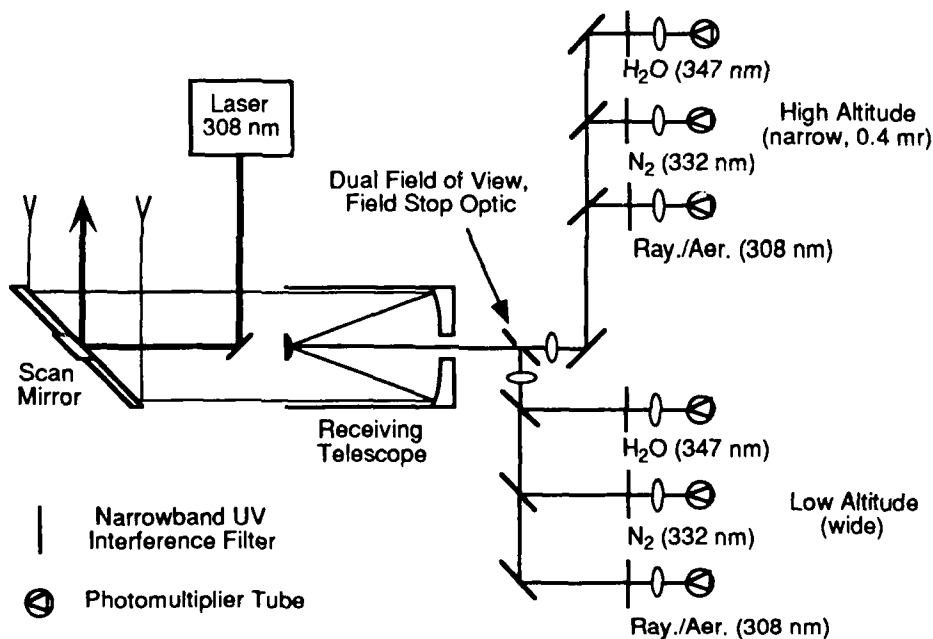


Figure 1. Schematic of the narrowband, dual field-of-view Raman lidar system.

We use photon counting in the high-altitude channels, where the signal and background count rates are manageable, but use analog-to-digital conversion in the low-altitude channels, where the count rates are much higher. Dichroic mirrors and high transmission (35%), high background rejection, narrowband (0.35 nm) UV interference filters are used to detect the different spectral components. Filters with these characteristics, which have only recently become commercially available, provide narrow bandwidth approaching that provided by polychromators, but in a much simpler system and with substantially better peak transmission. Table 1 summarizes the instrument characteristics.

Table 1.

Transmitter		Receiver	
Laser	XeCl Excimer	Telescope	Cassegrain (Dall-Kirkham)
Wavelength	308 nm (XeCl)	Diameter	0.76 m
Energy/pulse	90 mJ	f number	4.5
Repetition rate	200 Hz	Channel bandpass	0.4 nm
Bandwidth	3 pm	Field of view	Dual (0.4 mr, 4 mr)
Divergence	~0.2 mr	Range resolution	75 m (0.5 μ sec)
		Species	Rayleigh/aerosol (308 nm) Water vapor (347 nm) Nitrogen (332 nm)

4. Results

Figure 2 shows one of our first daytime water vapor profiles, obtained with an integration time of 56 minutes and 75 m range resolution and operating at reduced laser energy (75 mJ/pulse). Because of noise problems in our initial measurements with the low-altitude analog-to-digital system, the profile only displays the photon-counting data. For comparison, a profile taken approximately 4 hours later at night and under stable atmospheric conditions is also shown in Fig. 2. The integration time for the nighttime data was 10 minutes, although a 1 minute integration time also gives excellent results. The large discrepancy between the profiles below 0.5 km is most likely caused by difficulties in using the narrow fov channel at short range; the addition of the wide fov capability should provide much better short-range measurements. The rapid falloff in the water vapor mixing ratio above 2 km makes it difficult to assess the daytime range capability of the system, but it is possible that with system improvements (in particular, operation of the laser at higher output power), the maximum achievable range will be 3-4 km, consistent with our model calculations.⁵

5. Acknowledgements

We gratefully acknowledge helpful discussions with Marshall Lapp and John Vitko, the technical assistance of Mark Mitchell, and the expertise obtained in our collaborations with Harvey Melfi, Rich Ferrare, Dave Whiteman, and Keith Evans. This work was supported by the U. S. Department of Energy, Atmospheric Radiation Measurement (ARM) Program.

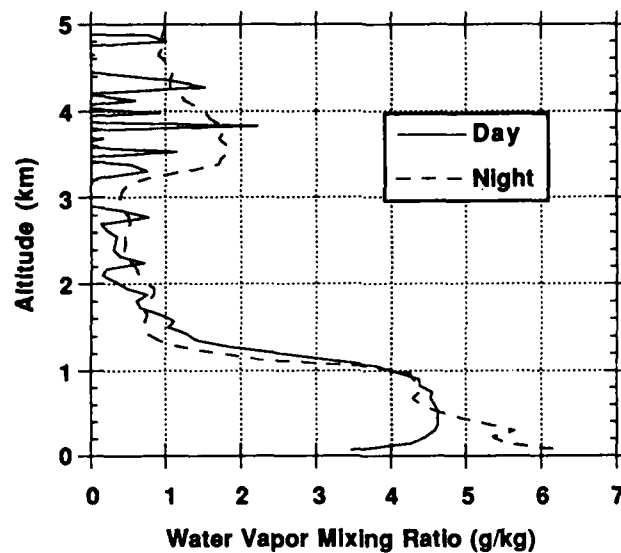


Figure 2. Comparison of daytime and nighttime measurements. The daytime profile represents signals integrated from 3:07-4:03 pm, and the nighttime profile represents signals integrated from 7:55-8:55 pm.

1. S. H. Melfi and D. Whiteman, "Observation of Lower-Atmospheric Moisture Structure and its Evolution using a Raman Lidar," *Bull. Am. Meteor. Soc.* **66**, 1288-1292 (1985).
2. D. N. Whiteman, S. H. Melfi, and R. A. Ferrare, "Raman Lidar System for the Measurement of Water Vapor and Aerosols in the Earth's Atmosphere," *Appl. Opt.* **31**, 3068-3082 (1992).
3. D. Renaut and R. Capitini, "Boundary-Layer Water Vapor Probing with a Solar Blind Raman Lidar: Validations, Meteorological Observations and Prospects," *J. Atm. and Oceanic Technol.*, **5**, 585-601 (1988).
4. A. Ansmann, M. Riebesell, U. Wandinger, C. Weitkamp, E. Voss, W. Lahmann, and W. Michaelis, "Combined Raman Elastic-Backscatter Lidar for Vertical Profiling of Moisture, Aerosol Extinction, Backscatter, and Lidar Ratio," *Appl. Phys. B* **42**, 1-11 (1992).
5. J. E. M. Goldsmith and Richard A. Ferrare, "Performance Modeling of Daytime Raman Lidar Systems for Profiling Atmospheric Water Vapor," *5th International Laser Radar Conference* (NASA Conference Publication 3158, Part 2, 1992), 667-670.

ATMOSPHERIC WATER VAPOR COLUMN DETERMINATION: COMPARISONS BETWEEN RETRIEVALS FROM POLAR ORBITING OPERATIONAL SATELLITES (NOAA AND DMSP SERIES), RADIOSONDES AND ANALYSES.

N. HUSSON, N.A. SCOTT, A. CHEDIN, J.P. CHABOUREAU, C. CLAUD
ARA / Laboratoire de Météorologie Dynamique du CNRS
Ecole Polytechnique, 91128 Palaiseau Cedex, France

Phone : (33) 1 69 33 48 02

I. INTRODUCTION

Accurate determination of the distribution of atmospheric water vapor is of major importance for improving our understanding of its role and variability in global meteorological and climatological processes as well as in space altimetry studies – e.g. TOPEX-POSEIDON programme –. An assessment of the accuracy of atmospheric water vapor retrieved from satellites, through comparisons with radiosonde measurements and ECMWF (European Center for Medium Range Weather Forecasts) analyses, has been performed. Two different types of satellite observations have been investigated :

- observations from the TIROS-N Vertical Operational Sounder (TOVS) aboard the NOAA satellites ;
- observations from the SSM/I (Special Sensor Microwave/Imager) instrument aboard the DMSP satellites.

II. ALGORITHMS FOR NOAA-TOVS AND DMSP-SSM/I WATER VAPOR RETRIEVALS

II.1 The "3I" retrieval algorithm for NOAA-TOVS observations

The "3I" (Improved Initialization Inversion) algorithm (Chedin & Scott, 1985 ; Chedin et al., 1985 ; Chedin, 1988) has been designed with the purpose of retrieving geophysical parameters from space radiometric measurements and orientated towards the processing of the NOAA series observations made by the TOVS instrument.

Retrievals of water vapor quantities (dew point temperatures, relative humidities, integrated precipitable water vapor) are made for 3 layers delimited by the levels 1000, 800, 500 and 300 hPa (Wahiche, 1984). Following the temperature profile inversion, the brightness temperatures associated with the initial guess are corrected for the deviations between the initial temperature profile and the final solution giving rise to the initial guess for water vapor and surface temperature retrievals. The method used is based upon a simultaneous physical inversion of the water vapor amounts and of surface temperature.

This method has been refined first in 1991 – use of dew-point temperatures instead of relative humidities as variable – (Tahani, 1991) and, second, very recently, - more accurate representation of the dew point depression within a given layer - giving rise to a new version of the water vapor algorithm. Qualities of the revised versions have been assessed and will be discussed.

II.2 Algorithms for water vapor retrievals from SSM/I observations

For deriving atmospheric total water vapor content from SSM/I brightness temperatures, several different published algorithms have been selected for the present evaluation : Petty & Katsaros, 1990 and 1992 ; Alishouse et al., 1990 ; Schlüssel & Emery, 1990,.... These algorithms are statistical or physico-statistical.

III. SELECTED DATA SET FOR PRESENT STUDY

In the frame of two studies sponsored by ESA (European Space Agency), large NOAA/TOVS and SSM/I data sets have been acquired, as well as radiosonde measurements and meteorological analyses from ECMWF.

Two geographic areas have been selected for the study presented here :

- an area over Northern Europe concentrated on two time periods in 1988 :
 - 1) from June 7, at 00:00Z, to June 10, at 00:00Z,
 - 2) from June 16, at 17:00Z, to June 20, at 06:00Z ;
- an area over the Gulf of Mexico of maximum extent 10°N, 50°N, 140°W, 60°W, concentrated on a one time period in 1989, from February 4 to February 20.

With the purpose of evaluating the accuracy of retrieved total atmospheric water vapor content from TOVS and SSM/I and to study the complementarity between both instruments, a selection has been made among the available data, as follows :

a) TOVS/NOAA-10 and co-located SSM/I orbits

A total of 13 NOAA/TOVS and 21 SSM/I sets of data have been selected :

- 8 TOVS situations over Europe, co-located with 13 SSM/I orbits,
- 5 TOVS situations over Gulf of Mexico, co-located with 8 SSM/I orbits.

b) Radiosonde measurements data set

- *Europe area*

Radiosondes come from six sites in Sweden, Norway and Denmark. Radiosondes from these stations are available for each considered day at 00:00 and 12:00Z.

- Gulf of Mexico area

Radiosonde data have been extracted at ECMWF for the 15 days period 6 to 20 February 1989. Measurements from all the stations within the area 10°N, 50°N, 140°W, 60°W, are provided at 00:00Z and 12:00Z.

c) Meteorological analysis

- Europe area

Meteorological analysis fields at 00:00, 06:00, 12:00 and 18:00Z, for each day concerned in this study, have been obtained from ECMWF. These data overlay a geographical area limited by latitudes 25° and 75° North and longitudes 45° West and 45° East.

- Gulf of Mexico area

Similar data have been obtained for the geographical area 10°N, 50°N, 140°W, 60°W.

IV. RESULTS OF VALIDATION OF TOVS AND SSM/I ATMOSPHERIC WATER VAPOR RETRIEVAL ALGORITHMS AGAINST CONVENTIONAL DATA

Statistics of differences between TOVS ("3I") or SSM/I atmospheric water vapor retrieval algorithm, on one hand, and radiosonde measurements or ECMWF analyses, on the other hand, have been performed for the data sets described above. The quality of the "3I" retrievals is discussed.

The most interesting conclusion, coming out from these computations, is the fact the two satellite based approaches are in excellent agreement (almost no bias and RMS errors between 15 and 20 %). This result has to be compared with the 25% accuracy found between radiosoundings and the satellite based approaches (TOVS as well as SSM/I). Another interesting finding is the fact that the overall global accuracy is independent of the quantity of water vapor (RMS about 18 % of the total atmospheric water vapor content, whatever this content is).

REFERENCES

Alishouse J.C., S. Snyder, R.R. Ferraro, 1990. Determination of oceanic total precipitable water from the SSM/I. IEEE Trans. Geo. Remote Sensing, vol. 26, nb. 5, p.811-816.

Chedin A., N.A. Scott, 1985. Initialization of the radiative transfer equation inversion problem from a pattern recognition type approach : application to the satellites of the TIROS-N series. In "Advances in Remote Sensing Retrieval Methods", A. Deepak Pub., pp.495-512.

Chedin A., N.A. Scott, C. Wahiche, P. Moulinier, 1985. The Improved Initialization Inversion method : a high resolution physical method for temperature retrievals from satellites of the TIROS-N series. J. Clim. Appl. Meteor., 24,128-143.

Chedin A., 1988. The "3I" retrieval method : recent local and global applications. Seminar Proceedings ECMWF "Data Assimilation and the Use of Satellite Data", 5-9 September 1988, ECMWF, Reading, UK, vol. II, pp. 181-184.

Petty G.W., K.B. Katsaros, 1990. New geophysical algorithms for the Spatial Sensor Microwave/Imager. Proceedings of the 5th Conference on Satellite Meteorology and Oceanography, September 3-7, 1990, London (UK), p.247-251.

Schlüssel P., W.J. Emery, 1990. Atmospheric water vapor over oceans from SSM/I measurements. Int. J. Remote Sensing, vol. 11, nb. 5, p.753-766.

Tahani Y., 1991. Restitution de la vapeur d'eau atmosphérique à partir des observations de satellites météorologiques. Intérêt pour l'altimétrie spatiale. PhD. dissertation (in French), Univ. P.et M. Curie, 132 pp. Avail. Lab. de Météorologie Dynamique, Ecole Polytechnique, 91128 Palaiseau Cedex, France.

Wahiche C., 1984. Contribution au problème de la détermination de paramètres météorologiques et climatologiques à partir de données fournies par les résultats de la série TIROS-N. Impact de la couverture nuageuse. Thèse de Doctorat d'Ingénieur, Paris University.

SAGE II WATER VAPOR PROFILING; AN INVERSION STUDY

J.C. Larsen[†], W.P. Chu[‡], and S.N. Tiwari[†]

[†]Old Dominion University, Norfolk, Va 23529

[‡] NASA Langley Research Center, Hampton, Va 23665

INTRODUCTION

The utility of the onion peel method to invert remotely sensed occultation data is well proven for satellite and balloon borne instruments at a variety of spectral resolutions. The advantages of the onion peel technique include stability in the presence of noise, insensitivity to first guess values, computational speed and relatively simple software coding. A major concern with the onion peel inversion method is the potential for the downward propagation of error into successively lower tangent levels that can be accentuated at the highest tangent levels by low signal to noise ratios. A number of inversion techniques have been formulated, tested and successfully applied to atmospheric data that are less susceptible to error propagation. In the Mill and Drayson(1977) method the inversion starts at the lowest tangent level where the highest signals are typically found and proceeds upwards. The profile at and above the tangent level is adjusted with a constant factor derived from the difference between the measured and calculated signal. Measurement errors are dispersed over the full slant path rather than just the tangent level as is the case for the standard onion peel. The method of Carlotti(1988) takes a global-fit approach to limb inversion. At each update step the profile is fit in a least squares sense to the set of limb measurements. Both techniques appear to offer an improvement over the standard onion peel method.

In this paper we apply both methods to the Stratospheric Aerosol and Gas Experiment II (SAGE II) limb absorption solar occultation measurements of water vapor at 940. nm and compare the results to the operational method based on the standard onion peel method as described in Chu et al.(1992). Modeling studies will also be presented.

SAGE II

SAGE II is a multiwavelength spectrometer which infers the vertical distribution of aerosols, ozone, nitrogen dioxide, and water vapor. Global observations from cloud top into the stratosphere have been routinely obtained since launch aboard the Earth Radiation Budget Satellite in October 1984. The water vapor channel is approximately 20. nm wide and centered at 935.5 nm. A complete description of the instrument may be found in McMaster(1986) and Mauldin et al.(1985). The solar occultation technique used by SAGE II produces 15 sunrise and 15 sunset measurements each day. Horizontal resolution, along the instrument line of sight, is approximately 200 km. The instantaneous field of view gives a 0.5 km vertical resolution that is later smoothed to 1 km in processing. Vertical coverage ranges from approximately 45 km, when the water vapor signal emerges from the noise, down to the earths surface unless clouds are encountered. Typically, the upper troposphere is sampled 50.% of the time and the middle troposphere is sampled 25.% of the time relative to the number of stratospheric measurements.

INVERSION METHODOLOGY

Calculation of the water vapor slant path optical depth and estimated errors is described in Chu et al. (1992). First, the solar radiances at 1020 nm and 940 nm are converted to slant path

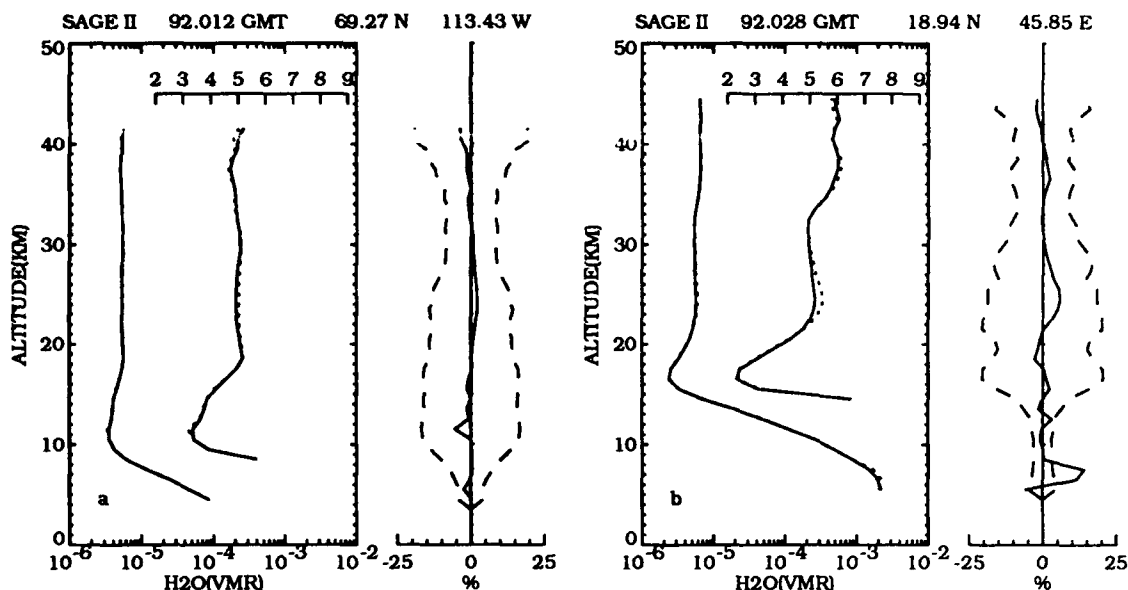


Figure 1: Two examples of SAGE II water vapor inverted with the operational method described in Chu et al.,1992 (solid line) and the Mill-Drayson method (dotted line). The stratospheric portion of each profile is replotted on the inset scale (in ppmv). On the right is shown the percent difference between the two methods (solid line) and the estimated measurement uncertainty expressed as a percentage (dashed line). a) April 2,1987, northern high latitude. b) April 2,1987, tropics.

transmittances and then ratioed to produce a differential transmission profile containing residual ozone absorption, aerosol and Rayleigh extinction. Next, Rayleigh extinction is calculated with a coincident temperature profile provided by the National Weather Service. The ozone and aerosol components are then removed using the results from these inversions. The resulting water vapor optical depth profile is inverted in a two step procedure. The first step in the operational procedure is to apply the standard onion peel inversion using Chahine's(1972) updating procedure. The resulting water vapor profile is next smoothed above 18.5 km. The two step procedure repeats until the residuals between the measured and calculated values are less than the estimated errors. To test the Mill-Drayson method we replaced the standard downward inversion with their upward approach and retained Chahine's updating procedure. Both methods start with identical first guess profiles for each measurement event. The first guess profile is 4.0 ppmv in the stratosphere with an exponentially increasing value in the troposphere that is adjusted for latitude.

PRELIMINARY RESULTS

Figure 1 compares water vapor profiles inverted with the standard onion peeling method and the Mill-Drayson method. The two examples shown here are typical of those in the northern hemisphere high latitudes and tropics. Small differences are found between the two methods in the high latitudes. In the troposphere the methods track each other closely. In the region of the hygropause, where the greatest vertical variation occurs, the agreement is also quite good. However, from 23. km to about 28. km the Mill-Drayson values are consistently higher by $\approx 2-3\%$. Above this the methods are again indistinguishable. Larger Mill-Drayson values from 23 to 28 km appear to be a consistent feature not only at the high latitudes but also in the tropics where the difference increases to $\approx 5\%$. While not insignificant, the profile differences at all levels fall within the estimated measurement uncertainty (including systematic and random error components) as shown by the dashed line, for the most part.

To see if other biases might exist between the two methods we calculated monthly zonal means for April 1987. Figure 2 displays the results for 20.°N and 50.°N. The higher Mill-Drayson values appear again between 23. and 30. km in both zonal means. In addition, values between the hygropause and 23. km fall slightly below the standard onion peel method. This under-shoot/overshoot phenomena appears in many of the other zonal means. The systematic biases shown here are greater than the accuracy of the radiative transfer code and somewhat less than the uncertainty in the water vapor band strength. Clearly, the choice of inversion method can effect accuracy to a degree equivalent to many of the other experimental uncertainties.

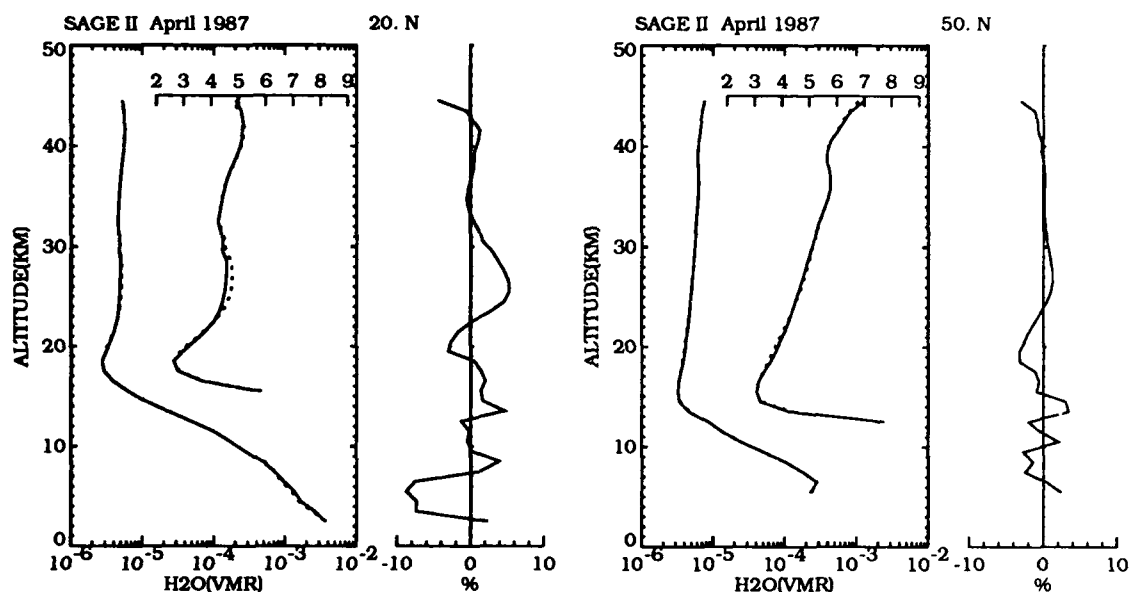


Figure 2: SAGE II zonal mean water vapor for April 1987 at 20.°N and 50.°N inverted with the operational method described in Chu et al., 1992 (solid line) and the Mill-Drayson method (dotted line). The stratospheric portion of each profile is replotted on the inset scale (in ppmv). On the right is shown the percent difference between the two methods.

REFERENCES

- Carlotti, M., Global-Fit Approach to the Analysis of Limb-scanning Atmospheric Measurements, *Applied Optics*, 27, 3250-3254, 1988.
- Chahine, M.T., A General Relaxation method for Inverse Solution of the Full Radiative Transfer Equation, *J. Atm. Sci.*, 29, 741-747, 1972.
- Chu, W. P., E. W. Chiou, J. C. Larsen, D. Rind, J. J. Buglia, M. P. McCormick, and L. R. McMaster, 1992: Inversion of the SAGE II Water Vapor Data, *J. Geophys. Res.*, accepted.
- Mauldin, L. E., M. P. McCormick, L. R. McMaster, and W. R. Vaughan, The Stratospheric Aerosol and Gas Experiment II (SAGE II) design and in-orbit performance, *SPIE 2nd Intl. Tech. Sympos. on Optical and Electro-Optical Appl. Sci. and Eng.*, Cannes, France, Paper No. 589018, 1985.
- McMaster, L. R., Stratospheric Aerosol and Gas Experiment (SAGE II), *Sixth Conference on Atmospheric Radiation*, Williamsburg, Va., May 13-16, 1986.
- Mill, J.D. and S.R. Drayson, A Nonlinear Technique for inverting limb absorption profiles, *Remote Sensing of the Atmosphere: Inversion Methods and Applications*, A.L. Fymat and V.E. Zuev, Eds., Elsevier, 123-135, 1977.

Monday, March 8, 1993

Space & Ground Based Remote Sensing 1

MC 2:00pm–3:40pm
Salon F

William L. Smith, *Presider*
University of Wisconsin–Madison

ADVANCES IN RETRIEVAL METHODOLOGY FOR THE ANALYSIS OF PRESENT AND FUTURE GENERATIONS VERTICAL SOUNDERS

A. CHEDIN, N.A. SCOTT, F. CHERUY, J. ESCOBAR, H. RIEU
ARA / Laboratoire de Météorologie Dynamique du CNRS
Ecole Polytechnique, 91128 Palaiseau Cedex, France

Phone : (33) 1 69 33 45 33

SUMMARY

The ARA (Atmospheric Radiation Analysis) group at LMD has developed a good experience in the retrieval of atmospheric temperature and moisture profiles with the "3I" (Improved Initialization Inversion) algorithm using TOVS observations. However, for operational numerical weather prediction or climate researches, the weaknesses of this kind of observations are now well recognized : too limited vertical resolution and accuracy ($\approx 2\text{K rms}$ in temperature and 20-30 % in water vapor profiles). The high spectral resolution infrared sounders like AIRS (Atmospheric Infrared Sounder) or IASI (Improved Atmospheric Sounding in the Infrared) will provide a great improvement in the retrieval of atmospheric and surface properties. Such an increase in spectral resolution in the observations will be successful only if the processing tools are adequate. Among them are : a fast and accurate radiative transfer model, a carefully selected set of channels throughout the infrared spectrum, a well elaborated retrieval/assimilation procedure. This paper presents an overview of these developments, a special emphasis being given to the latter one. Results recently obtained within the frame of the activities of the AIRS scientific team in cooperation with GLA (Goddard Laboratory for Atmosphere) will be discussed.

At the same time, a new methodology is being developed and improved for the processing of either TOVS or high spectral resolution observations, based on neural networks. The learning process is carried out using the so-called TIGR (Thermodynamic Initial Guess Retrieval) data set which archive about 1800 atmospheric situations and associated brightness temperatures for either TOVS or AIRS/IASI channels. Application to noisy simulated data show spectacular improvements over "classical" approaches. Application to real data (DMSP/SSM-T) confirm this result. A new forward model also based on neural networks will be presented.

Recent Results in Combined Ground-based and Satellite Remote Sensing

E. R. Westwater and B. B. Stankov
NOAA/ERL/Wave Propagation Laboratory
Boulder, Colorado 80302

I. INTRODUCTION

The implementation of the Wind Profiler Demonstration Network [1] is an indication of the increased reliance of the operational community on remote sensors. The Wind Profilers themselves can measure winds to about 16 km with a spatial resolution of 300-900 m on an hourly basis; their horizontal spacings vary from about 200 to 300 km. If the same spatial and temporal coverage of temperature, water vapor and clouds could be achieved many of the needs of forecasters and researchers could be met. However, even if the ambitious goal of measuring both dynamic and thermodynamic variables from a network of surface-based stations could be met, station deployment on a 25 to 50 km grid would be prohibitively expensive. Observations from both polar-orbiting and geostationary satellites, when combined with data from a limited grid of surface-based remote sensors, may provide the necessary horizontal coverage as well as improve upper altitude accuracy. In this paper, we present new results and discuss several possibilities of combining surface-based and satellite data.

II. TEMPERATURE SOUNDING

During the last three years, rapid advances have occurred in ground-based remote sensing of temperature [2, 3]. Temperature sensing with the Radio Acoustic Sounding System (RASS) may be possible on Wind Profiler radars. In addition, infrared Fourier Transform interferometers [3] may be able to provide accurate soundings in the first 1-2 km above the surface. Microwave radiometers [3] also produce accurate low-altitude profiles. However, measurements above 500 mb may be very difficult to achieve with such surface-based sensors. Combination of surface-based data with those from satellites can extend the range of accurate vertical soundings [4]. We will present the combination of temperature soundings from the TIROS N Operational Vertical Sounder, RASS, and commercial aircraft ACARS data. The Wave Propagation Laboratory (WPL) and the Forecast Systems Laboratory (FSL) of NOAA are currently developing a real time combination of these data.

III. WATER VAPOR SOUNDING

During the last three years, rapid advances have also occurred in ground-based remote sensing of water vapor. Both data from a Raman lidar [5] and from a Fourier Transform infrared interferometer [3] may be combined with microwave radiometer data to provide soundings in both clear and cloudy conditions. Several types of active and passive soundings may be combined to produce water vapor profiles. The combination of GOES precipitable water vapor soundings with those from ground-based radiometers soundings are also promising to extend the horizontal coverage of surface-based sensors. We will present several examples to illustrate these capabilities of combined sensors.

IV. CLOUD SENSING

Recently millimeter wavelength radars have been used to measure the morphology of both upper- and lower-altitude clouds [6]. In contrast to lidars, which are usually attenuated by dense lower-altitude clouds, these radars can penetrate multi-layer cloud structures. Such data could be used to supplement satellite AVHRR and GOES images with quantitative information on cloud heights. In a similar way, ceilometer measurements of cloud-base height have been combined with infrared and microwave radiometers to provide information on the temperature and liquid structure of low altitude clouds [6]. Again, we will present examples of these data combinations and products.

V. CONCLUDING REMARKS

The data from active and passive sensors can be combined in a surprising variety of ways. For example, thermal information derived from wind profiles could be used to supplement both radiometric and RASS soundings. RASS soundings can be used with cloud boundary measurements to derive humidity profiles within clouds. Developing techniques for blending the information from the new remote sensors will become increasingly important to operational meteorology.

VI. REFERENCES

- [1] Chadwick, R.B., "The Wind Profiler Demonstration Network," Lower Tropospheric Profiling: Needs and Technologies, May 31-June 3, Boulder, CO, Amer. Meteor. Soc., pp. 109-100, 1990.
- [2] May, P.T., R.G. Strauch, K.P. Moran and W.L. Ecklund, "Temperature Sounding by RASS with wind profiler radars: A preliminary study," IEEE Trans. Geosci. Remote Sensing, Vol. GE-28, pp. 19-28, 1990.
- [3] Smith, W.L. et al., "GAPEX: A ground-based atmospheric profiling experiment," Bull. Amer. Meteorol. Soc., Vol. 71, pp. 310-318, 1990.
- [4] Schroeder, J.A., E.R. Westwater, P.T. May and L.M. Mcmillin, "Prospects for temperature sounding with satellite and ground-based RASS measurements," J. Atmos. Oceanic Technol., Vol. 8, pp. 506-513, 1991.
- [5] Melfi, S. H. and D. Whiteman, "Observation of lower-atmospheric moisture structure and its evolution using a Raman lidar," Bull. Amer. Meteor. Soc., Vol. 66, pp. 1288-1292, 1985.
- [6] Kropfli, R.A., B.W. Bartram, and S.Y. Matrosov, "The upgraded WPL dual-polarization radar for microphysical and climate research," Preprints of the Conf. on Cloud Physics, July 23-27, Amer. Meteorol. Soc., San Francisco, CA, 1990.

Removal of the 3.7 μm Solar Contamination in AVHRR DataN.X. Rao¹, S.C. Ou¹, and K.N. Liou²¹. Liou and Associates, 4480 Adonis Dr., Salt Lake City, Utah 84124 (801)537-1554². Department of Meteorology/CARSS, University of Utah, Salt Lake City, Utah 84112 (801)581-3336

1. Introduction

We have developed a numerical scheme for the removal of the solar contamination in the AVHRR 3.7 μm (Ch.3) radiance for the retrieval of cirrus cloud parameters during daytime. The scheme involves an iterative procedure coupled with the clear sky detection technique described by Saunder and Kriebel (1988) and the nighttime retrieval algorithm developed by Ou et al. (1992). In section 2, the removal scheme, based on the correlation between 0.63 and 3.7 μm solar reflectances, is presented. In section 3, we discuss a synthetic study using the midlatitude atmospheric profile and a sensitivity study involving the removal of the 3.7 μm solar component by adding random errors due to surface inhomogeneity and instrument noises. Application of the removal scheme to AVHRR data for inferring cirrus cloud parameters, and comparisons with available observations and retrieval results presented by other investigators are described in section 4. Finally, conclusions are given in section 5.

2. Removal Scheme

To remove the 3.7 μm solar contamination, we use the 0.63 μm (Ch. 1) radiance. First, the correlation between 0.63 and 3.7 μm solar reflectances for a set of mean effective ice crystal sizes is established. This is done by employing the solar radiation transfer program involving cirrus clouds developed by Takano and Liou (1989). Second, the effects of surface albedo on the solar reflectances for Chs. 1 and 3 are taken into account by using the following equations (Liou, 1980):

$$R_{js} = R_j^* + \frac{R_{ajs}\mu_0 F_{0j}}{1 - R_{ajs}\bar{r}_j} \gamma_j(\mu_0)\gamma_j(\mu), \quad j=1,3, \quad (1)$$

where R_{js} is the total reflectance, \bar{r}_j is the global albedo, F_{0j} is the solar flux, $\gamma_j(\mu_0)$ and $\gamma_j(\mu)$ are the total transmittances corresponding to the cosines of the solar zenith angle (μ_0) and satellite zenith angle (μ), respectively, R_{ajs} is the effective surface albedo, and R_j^* is the reflectance of cirrus clouds. The terms R_j^* , \bar{r}_j , $\gamma_j(\mu_0)$, and $\gamma_j(\mu)$ are computed from the adding method for radiative transfer (Takano and Liou, 1989). The Ch. 1 effective surface albedo, which includes the combined effects of the surface albedo and Rayleigh scattering of the atmosphere, is determined from a clear sky detection technique. The Ch. 3 effective surface albedo is estimated from the following expression that includes atmosphere absorption in the form

$$R_{a3s} = (1 - A_3/\mu_0)R_{s3}(1 - A_3/\mu), \quad (2)$$

where A_3 is the atmospheric absorption computed from a radiative transfer program based on the sounding data and R_{s3} is the surface albedo obtained from available laboratory measurements. The total solar reflectances for cirrus clouds involving different mean effective ice crystal sizes are shown in Fig. 1 where each correlation curve approaches an asymptotic value for thick cirrus clouds and converges to the clear sky values for thin clouds.

The 3.7 μm solar component, which is found from a look-up correlation table with the aid of the Ch. 1 reflectance and a guessed mean effective ice

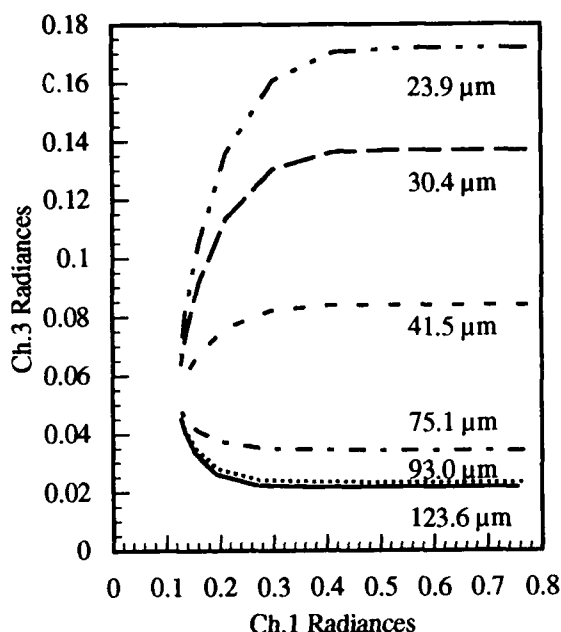


FIG. 1. Correlation between Ch. 1 ($0.63 \mu\text{m}$) and Ch. 3 ($3.7 \mu\text{m}$) solar reflectances.

crystal size, is removed from the Ch. 3 radiance. After this removal, the remaining infrared radiance of Ch. 3 coupled with the Ch. 4 ($10.9 \mu\text{m}$) radiance is used to perform nighttime retrieval to obtain the cirrus cloud temperature, mean effective ice crystal size, and optical depth. If the difference between the retrieved mean effective ice crystal size and the guessed size is within a prescribed value, the removed amount is considered to be correct. Otherwise, the procedures are repeated with a newly guessed ice crystal size which is determined from the under-relaxation technique.

3. Synthetic and Sensitivity Studies

The synthetic study has been carried out using the midlatitude summer atmosphere. With the prescription of surface albedos, synthetic radiances of Chs. 1, 3, and 4 are calculated for the three different cloud temperatures that correspond to the cloud base heights of 7, 9, and 11 km. Performing the removal procedures based on the calculated synthetic radiances, the

removed solar component for Ch. 3 (R_{3s}) and the resulting cloud temperatures are identical to the original values.

For the sensitivity study, random errors due to surface inhomogeneity and instrument noises are added to the computed synthetic radiances. Based on the study of Dudhia (1989), instrument noises added are within 0.4 and 0.12 K for Ch. 3 and Ch. 4, respectively. To test the effect of surface inhomogeneity, Ch. 1 and Ch. 3 surface albedos are randomly varied within the ranges of ± 0.02 and ± 0.05 , respectively. Removal and retrieval processes are carried out using the perturbed Ch. 3 and Ch. 4 radiances and the correlation involving Ch. 1 and Ch. 3 solar reflectances. The root mean square errors for the Ch. 3 solar component are shown in Fig. 2. Large errors are associated with small optical depths and high clouds.

4. Application to AVHRR Data

We have applied the removal scheme to the AVHRR daytime data, collected on October 28, 1986, at 2100 UTC, over the Fort McCoy, Wisconsin area between 42°N and 47°N latitudes and 87°W and 92°W longitudes during the First ISCCP Regional Experiment (FIRE) Intensive Field Observation (IFO). The brightness temperature of Ch. 4 over this area is shown in Fig. 3. The darker areas corresponding to high temperature values are associated with either clear or very thin cirrus cloud cases, while the lighter areas corresponding to low temperature values are associated with cloudy cases.

To alleviate the effect of surface inhomogeneity on the retrieval, the whole area is divided into $25 1^\circ \times 1^\circ$ small areas. Performing the removal of solar contamination and the retrieval of cirrus cloud parameters for each small area, the optical depth, cloud temperature, and mean effective ice crystal size for cirrus clouds are obtained. The retrieved optical depths depicted in Fig. 4 range from 0 to 8. These results agree reasonably well with those presented by Minnis et al.

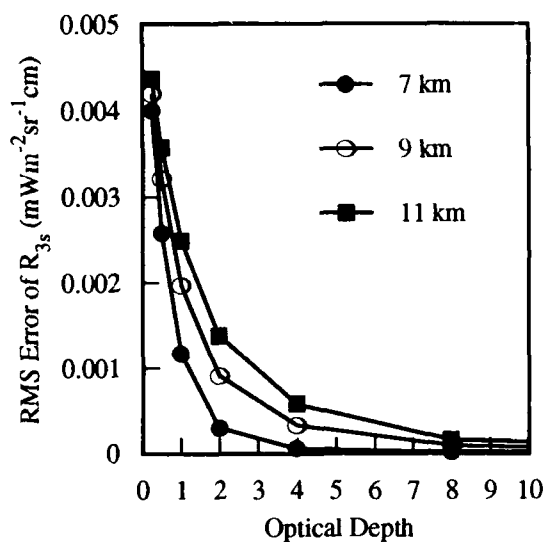


FIG. 2. The root mean square errors in the Ch. 3 solar component (R_{3s}) due to surface inhomogeneity and instrument noises.

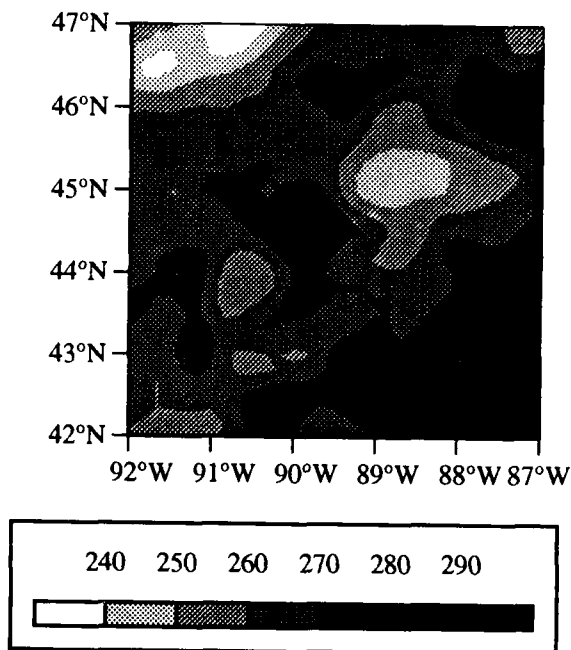


FIG. 3 The Ch. 4 ($10.9 \mu\text{m}$) brightness temperature over the Fort McCoy, Wisconsin area on October 28, 1986.

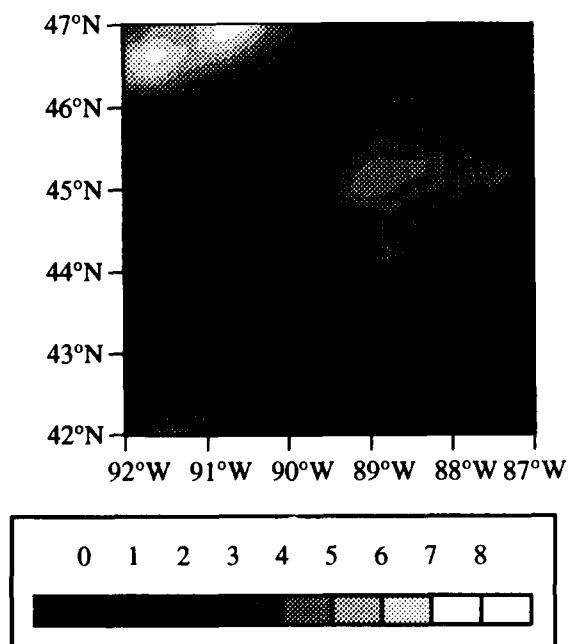


FIG. 4 The retrieved optical depths over the Fort McCoy, Wisconsin area between 42°N and 47°N latitude and 87°W and 92°W longitude, October 28, 1986.

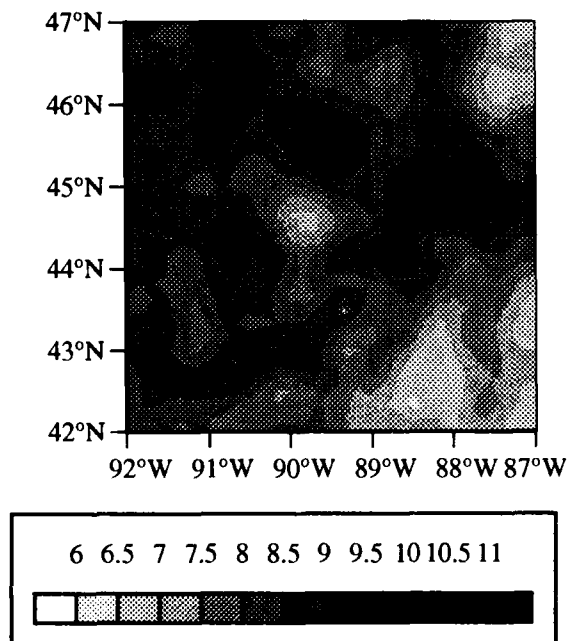


FIG. 5. The retrieved cloud height over the same area represented in Fig. 4.

Table 1. Cirrus cloud temperature, mean effective ice crystal size, cloud height, and optical depth determined from the present retrieval program.

	$T_c(K)$	$D_e(\mu m)$	$z_c(km)$	τ
Wausan (45.0°N, 89.7°W)	226.5	57.1	9.5	1.54
Fort McCoy (45.9°N, 90.8°W)	229.7	61.3	9.1	2.16
Madison (43.1°N, 89.4°W)	225.6	53.9	9.6	1.48

(1990a) who used Ch. 1 to determine the optical depth for the same area and time period. The retrieved cloud temperatures for this area range from 210 to 245 K, while the retrieved mean effective ice crystal sizes range from 40 to 100 μm . The sounding data from Fort McCoy, Wausan, and Madison, Wisconsin (Starr and Wylie, 1990) are used to obtain a lapse rate of about 8.3°C/km. The cirrus cloud heights are determined from this lapse rate, and are presented in Fig. 5. The cloud heights have values between 6 and 11 km, which are comparable to those derived by Minnis et al. (1990a). The retrieved cirrus parameters are averaged over a 1° x 1° area close to the sounding stations. The averaged values listed in Table 1 are also comparable to the lidar-observed data presented in Minnis et al. (1990b).

5. Conclusions

In this paper, we have developed a removal scheme that provides a new way of inferring cirrus cloud parameters from AVHRR data during the daytime. We illustrate from synthetic studies that this scheme successfully removes the solar component in the 3.7 μm radiance. Sensitivity studies show that large errors in the retrieval can occur due to surface inhomogeneity and/or instrument noises when very thin cirrus clouds are present. The retrieved cirrus parameters agree reasonably well with lidar observations and other available analyses.

This research work has been supported by the Geophysics Directorate, Air Force System Command,

through the Phase II Small Business Innovative Research Program under contract F19628-90-C-0123.

REFERENCES

- Dudhia, A., 1989: Noise characteristics of the AVHRR infrared channels. Int. J. Remote Sens., **10**, 637-644.
- Liou, K.N., 1980: An Introduction to Atmospheric Radiation. Academic Press, 392 pp.
- Minnis, P., P.W. Heck, and E.F. Harrison, 1990a: The 27-28 October 1986 FIRE IFO cirrus case study: Cloud parameter fields derived from satellite data. Mon. Wea. Rev., **118**, 2426-2446.
- Minnis, P., D.F. Young, K. Sassen, J.M. Alvarez, and C.J. Grund, 1990b: The 27-28 October 1986 FIRE IFO cirrus case study: Cirrus parameter relationships derived from satellite and lidar data. Mon. Wea. Rev., **118**, 2402-2425.
- Ou, S.C., K.N. Liou, W.M. Gooch, and Y. Takano, 1992: Remote sensing of cirrus cloud parameters using AVHRR 3.7 and 10.9 μm channels. Appl. Opt., **31**, (in press).
- Saunders, R.W., and K.T. Kriebel, 1988: An improved method for detecting clear sky and cloudy radiances from AVHRR data. Int. J. Remote Sens., **9**, 123-150.
- Starr, D.O'C., and D.P. Wylie, 1990: The 27-28 October 1986 FIRE cirrus case study: Meteorology and clouds. Mon. Wea. Rev., **118**, 2259-2287.
- Takano, Y., and K.N. Liou, 1989: Solar radiative transfer in cirrus clouds: II. Theory and computation of multiple scattering in an isotropic medium. J. Atmos. Sci., **46**, 20-36.

Remote Sensing of Cirrus Cloud Parameters Using AVHRR 3.7 and 10.9 μm Channel Data

S.C. Ou¹, K.N. Liou², W. Gooch¹, N. Rao¹, and Y. Takano²

¹. Liou and Associates, 4480 Adonis Dr., Salt Lake City, Utah 84124, 801-537-1554

². Department of Meteorology/CARSS, University of Utah, Salt Lake City, Utah 84112, (801)581-3336

1. Introduction

Cirrus clouds are global in nature and occupy primarily the upper troposphere and lower stratosphere. Information on cirrus cloud parameters is critically important to the development of cirrus cloud forecast models, the upgrading of real-time global cloud analysis, and the investigation of cloud-radiation feedback to the temperature perturbations in global climate change.

In recent years, data from multi-channel imagery sources, particularly the Advanced Very High Resolution Radiometer (AVHRR) onboard NOAA operational satellites, have been made available for the retrieval of cloud parameters. Verification of the retrieved results has also been possible because of the availability of concurrent and collocated measurements by instruments onboard aircraft, ground-based lidar, and rawinsonde that were carried out during the First ISCCP Regional Experiment (FIRE) Intensive Field Observation (IFO) period, October - November 1986.

In this paper, we present a physical retrieval scheme based on the theory of radiative transfer to infer cirrus cloud parameters, using the AVHRR 3.7 and 10.9 μm channels. We illustrate that the brightness temperature difference (BTD) between these two channels can be used to detect the presence of cirrus clouds. The effects of nonspherical ice crystals are also accounted for in the development of radiative transfer parameterizations for remote sensing applications. We apply the retrieval

scheme to the AVHRR data collected around 0900 UTC, October 28, 1986, over the entire United States. Section 2 describes the retrieval algorithm. Section 3 presents the results of application to satellite data. Finally, conclusions are given in section 4.

2. Description of the Retrieval Scheme and Verification

We have developed a retrieval scheme to simultaneously determine the cirrus cloud temperature and emissivity using the AVHRR 3.7 μm (Ch. 3) and 10.9 μm (Ch. 4) data. The methodology follows the principles of the dual IR channel technique presented in Liou et al. (1990). The retrieval of cirrus cloud parameters is based on the numerical solution of the following set of nonlinear algebraic equations derived from the theory of radiative transfer (Ou, et al., 1992):

$$R_{3,4} = R_{a3,4}(1 - \epsilon_{3,4}) + \epsilon_{3,4}B_{3,4}(T_c), \quad (1)$$

$$B_3(T_c) = \sum_{n=0}^3 a_n [B_4(T_c)]^n, \quad (2)$$

$$\epsilon_{3,4} = 1 - \exp(-k_{3,4}\tau), \quad (3)$$

where $R_{3,4}$ are the upwelling radiances at the top of the atmosphere for Ch. 3 and Ch. 4 for cirrus cloudy atmospheres, $R_{a3,4}$ are the corresponding radiances reaching the cloud base for the two channels, $\epsilon_{3,4}$ are the cloud emissivities, T_c is the mean cirrus temperature, $B_{3,4}(T_c)$ are the Planck intensities at T_c , $k_{3,4}$ are the adjustment factors to account for scattering referred to as the effective extinction coefficients, and τ is the visible optical depth.

The solution involves the effective extinction ratio for the two channels, k_4/k_3 , which is dependent on ice crystal size distribution represented by the mean effective size defined by

$$D_e = \int D \cdot LD \cdot n(L) dL / \int LD \cdot n(L) dL, (4)$$

where D and L denote the width and length of an ice crystal and $n(L)$ is the size distribution in terms of L . We have analyzed 12 measured ice crystal size distributions to obtain a set of D_e 's. We then use the light scattering and radiative transfer programs developed by Takano and Liou (1989) to compute k_4/k_3 as a function of D_e . The k_4/k_3 ratio decreases with increasing D_e and can be parameterized in terms of a second-order polynomial in D_e^{-1} with relatively high accuracy. Based on radiative transfer calculations, the ice crystal size distribution and the nonsphericity of ice crystals are both important in the development of the retrieval of cirrus cloud parameters.

The cloud optical depth can be determined from cloud emissivity on the basis of radiative transfer parameterizations. Furthermore, the ice crystal size distribution and hence, the mean effective size, can be evaluated from cloud temperature based on observed data. In the retrieval, cirrus clouds are first detected using the technique involving the BTD between the 3.7 and 10.9 μm channels. We find that the presence of nonblack cirrus clouds is always associated with BTDs that exceed about 2 K.

We use the AVHRR GAC (Global Area Coverage) data over the United States corresponding to 0900 UTC (local nighttime), October 28, 1986, to test the retrieval scheme. A $1^\circ \times 1^\circ$ area ($43.5^\circ - 44.5^\circ\text{N}$; $91^\circ - 92^\circ\text{W}$) west of Fort McCoy, Wisconsin, has been selected for an in-depth study of the performance of the retrieval scheme. A distinct band of cirrus clouds associated with $\text{BTD} > 2 \text{ K}$ was present in the area. Retrieved results indicate clouds are colder and ice

crystal sizes are smaller in the center of the cloudy region than near the cloud edge. This may be explained by the mechanism of the formation of cirrus uncinus suggested by Heymsfield (1975). The colder temperatures with smaller sizes may correspond to the head region where ice crystals grow, while the warmer temperatures with larger particles may be associated with the stable precipitating region. The retrieved optical depth is between 0 and 2 for most of the cirrus region. The distribution of optical depth does not necessarily match that of cloud temperature or mean effective size, because optical depth is virtually independent of cloud temperature.

Since the collocated ground and in-situ aircraft measurements for cloud parameters are not available, a direct verification of the retrieved results can not be made. However, we have carried out an indirect comparison using the available surface and aircraft data collected near the sounding areas. The Langley Research Center lidar systems located at Fort McCoy were continuously collecting data from 0800 to 2400 UTC, October 28, 1986. Significant responses due to the presence of cirrus were detected only after 1100 UTC. The data shows cirrus cloud heights are mostly between 6 and 8 km. The retrieved cirrus heights are within the observed range. In addition, we have analyzed the microphysical data collected by the NCAR King Air turboprop near Madison between 1525 and 1729 UTC. The average ice crystal size distributions for the samples collected during the last 15 minutes of the flight period have a mean D_e of $\sim 107 \mu\text{m}$. From the retrieval program a mean D_e of $\sim 104 \mu\text{m}$ is derived.

3. Applications to Large-Scale Cloud Retrievals

We have performed the retrieval of cirrus clouds covering the entire United States for the time period 0900 UTC, October 28, 1986. Figures 1(a) and 1(b) show the display of Ch. 4

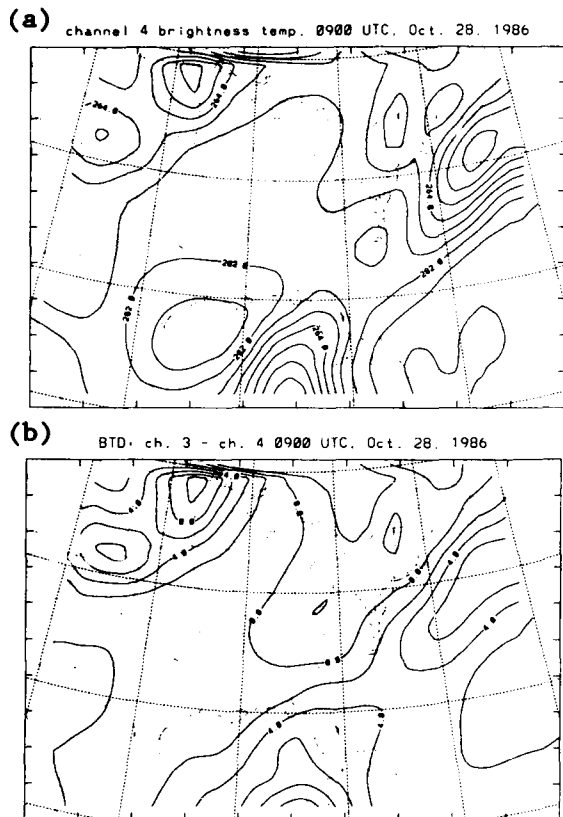


FIG. 1. Display of (a) the Ch. 4 brightness temperature and (b) the brightness temperature difference (BTD) between 3.7 and 10.9 μm channels over the United States and parts of the Atlantic Ocean and Gulf of Mexico.

brightness temperature and BTD over the area, respectively. Cirrus clouds (associated with $\text{BTD} > 2 \text{ K}$) are present over the western Atlantic Ocean and the Gulf of Mexico. It is also noted that a band of continental cirrus clouds extends from the northern Plain States to southern Wyoming. The rest of the United States is relatively clear. Over the northeastern United States, there is a region of negative BTDs, possibly produced by the combined effects of the nighttime near-surface temperature inversion and the presence of air pollution. For comparison, Fig. 2 shows the GOES-6 IR satellite imagery over the United States at 1200 UTC, 28 October 1986 (Starr and Wylie, 1990). A band of cirrus clouds is evident over the continental United States.

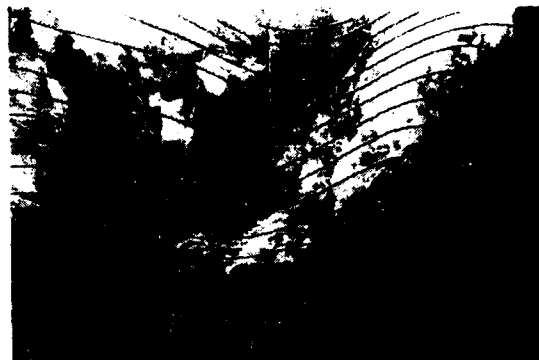


FIG. 2. The GOES-6 IR satellite imagery over the United States at 1200 UTC, 28 October, 1986 (after Starr and Wylie, 1990).

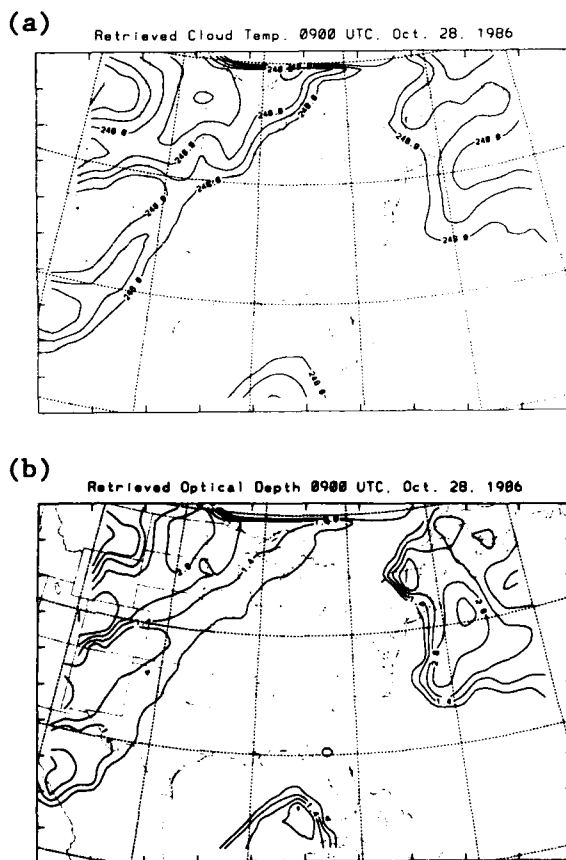


FIG. 3. The contour maps for the retrieved (a) cloud temperature and (b) optical depth over the area shown in Fig. 1.

The data domain is divided into a number of $3^\circ \times 3^\circ$ boxes. Data points associated with cirrus clouds in each box are identified using the

BTD technique. Moreover, for each box, we determine a pair of mean clear radiances using the two-dimensional statistical scheme developed by Liou et al. (1990). From Figs. 1(a) and (b) we see that the distribution of Ch. 4 brightness temperatures is fairly homogeneous over the clear region. Thus, a single pair of mean clear radiances can be adequately obtained from a $3^\circ \times 3^\circ$ box. The retrieval scheme is applied to each cirrus data point that has been identified from the BTD technique. The mean cirrus parameters for each box are then obtained. Figures 3(a) and (b) show the display of the retrieved cirrus cloud temperature (T_c), and optical depth (τ), respectively. We find that $T_c < 248$ K over the intermountain region, Plain States, New England, western Atlantic Ocean, and Gulf of Mexico. Between the Gulf of Mexico and the western Atlantic Ocean, the BTD is between 2 and 4 K. However, the retrieved cloud temperatures are mostly higher than 250 K and are not counted as cirrus. Figure 4(b) shows that the mean cirrus optical depth is between 0 and 3.5. This figure is based on the mean value for each box so that the resulting contours are smooth and adequately separated. The optical depth value for individual cirrus data points ranges between 0 and 7. The regions for the optical depth greater than 1 roughly correspond to those for the cloud temperature less than 248 K. Optical depths greater than 2.8 are present over the northern Plain States and the western Atlantic Ocean. The present retrieval scheme can be applied to both oceanic and continental areas.

4. Conclusions

We have developed a retrieval scheme which uses radiance data of AVHRR 3.7 and $10.9 \mu\text{m}$ channels to simultaneously determine cirrus temperature, mean effective ice crystal size, and optical depth. This retrieval scheme has been applied to

the satellite data collected over the United States at 0900 UTC, October 28, 1986. For a $1^\circ \times 1^\circ$ area where indirect verifications are available, the retrieved cirrus heights and mean effective ice crystals sizes are in general agreement with lidar observations and in-situ aircraft microphysical measurements, respectively. Finally, we show that the present retrieval scheme can be applied to large-scale regions with varying surface characteristics for the mapping of cirrus cloud parameters.

Research work contained in this paper has been supported by the Geophysics Directorate, Air Force System Command, through the Phase II Small Business Innovative Research Program under contract F19628-90-C-0123.

REFERENCES

- Heymsfield, A., 1975: Cirrus Uncinus Generating Cells and the Evolution of Cirriform Clouds. Part I: Aircraft Observations of the Growth of the Ice Phase. J. Atmos. Sci., **32**, 799-808.
- Liou, K.N., S.C. Ou, Y. Takano, F.P.J. Valero, and T.P. Ackerman, 1990: Remote Sounding of the Tropical Cirrus Cloud Temperature and Optical Depth Using 6.5 and $10.5 \mu\text{m}$ Radiometers during STEP. J. Appl. Meteor., **29**, 716-726.
- Ou, S.C., K.N. Liou, W.M. Gooch, and Y. Takano, 1992: Remote Sensing of Cirrus Cloud Parameters using AVHRR 3.7 and $10.9 \mu\text{m}$ Channels. Appl. Opt., **31**, (in press).
- Starr, D.O'C., and D.P. Wylie, 1990: The 27-28 October 1986 FIRE Cirrus Case Study: Meteorology and Clouds. Mon. Wea. Rev., **118**, 2259-2287.
- Takano, Y., and K.N. Liou, 1989: Solar Radiative Transfer in Cirrus Clouds. Part II: Theory and Computation of Multiple Scattering in a Anisotropic Medium. J. Atmos. Sci., **46**, 20-36.

Monday, March 8, 1993

Space & Ground Based Remote Sensing 2

MD 4:10pm–6:00pm
Salon F

Ed Westwater, *Presider*
NOAA/Environmental Research Laboratories

Atmospheric Remote Sensing Studies at the National Institute for Environmental Studies (NIES), Japan

Yasuhiro Sasano, Hideaki Nakane and Nobuo Sugimoto

The National Institute for Environmental Studies
Tsukuba, Ibaraki 305 Japan
Tel: 81-298-51-6111 Fax: 81-298-51-4732

1. Introduction

In the middle of 1970's, we began lidar studies at NIES with constructing a mobile Mie lidar for application to lower atmospheric structure studies in relation to air pollution phenomena. A large-scale lidar was built in 1979 for the purpose of developing measurement techniques for aerosol distribution over a wide-area. The large lidar was also used for studies on atmospheric structures such as mixed layer and sea-breeze front.

Since the El Chichon eruption in 1982, the large lidar has been used for monitoring the stratospheric aerosol layers, which is still in operation. In 1988, an ozone DIAL system was built and stratospheric ozone measurements have been carried out since then.

We have embarked on a new field since 1990 to be involved in remote sensing studies using satellites. One of them is laser long path absorption measurements of trace gases between the earth and a satellite, which is called Retroreflector In-Space (RIS) project. In the RIS project, a large retroreflector will be installed on the ADEOS (Advanced Earth Observing Satellite) and a laser transmitting and receiving facility will be developed in collaboration with Communications Research Laboratory (CRL) which will develop a satellite tracking technique. The ADEOS is scheduled to be launched in early 1996 by National Space Development Agency (NASDA) of Japan.

Another project we have been engaged in for atmospheric sensing from space is called the Improved Limb Atmospheric Spectrometer (ILAS) project. The ILAS instrument, which will also be aboard ADEOS, consists of an infrared and a visible spectrometer, which measure atmospheric absorption spectrum in a solar occultation mode. The purpose of the ILAS project is to get stratospheric ozone and ozone-related species profiles as well as temperature and aerosol profiles.

This paper describes briefly the present status of our studies in active and passive atmospheric remote sensing, putting a special emphasis on the recent results of lidar measurements of aerosol and ozone, and the RIS/ILAS projects.

2. Stratospheric aerosol monitoring

Stratospheric aerosols have been monitored since the fall of 1982 using the NIES large lidar (Shimizu et al., 1985; Hayashida-Amano et al., 1991; Hayashida and Sasano, 1992). After the eruption of Mt. Pinatubo in Philippines in June, 1991, a three-wavelength Mie lidar, which was originally developed for aerosol profiling in the lower atmosphere, was modified to be equipped with photon counting capabilities and has been employed for stratospheric aerosol measurements.

Figure 1 shows a temporal changes in integrated backscattering coefficient between 15 km and 30 km obtained with the large lidar. The lidar signal was solved using the Fernald solution (Fernald, 1984) with the scattering parameter $S_1=50$ and the matching method was applied to give a boundary condition. Details of data reduction procedures are found in Hayashida-Amano et al.(1991).

Tropospheric aerosol profiles have also been measured for these three years. The measurement is carried out with the large lidar in the RHI mode to get profiles down

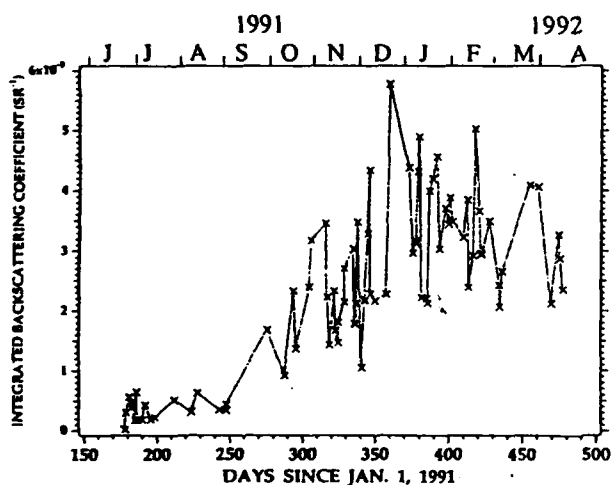


Figure 1 Stratospheric aerosol changes due to Mt. Pinatubo eruption. Integrated backscattering coefficients for 532 nm is shown as a function of day number after Jan. 1, 1991.

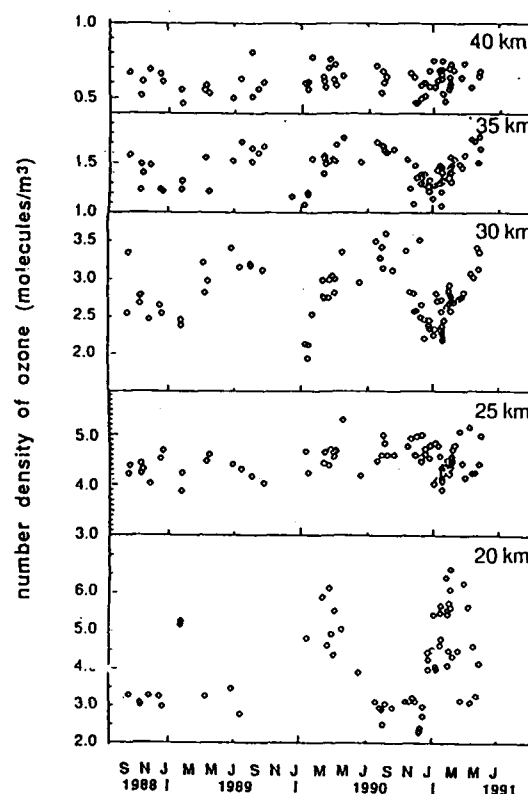


Figure 2 Stratospheric ozone changes at 20, 25, 30, 35 and 40 km in altitude.

to the ground level. The data are now being accumulated to generate aerosol profile models as a function of air mass condition.

Along with the lidar measurements, direct solar radiation and angular distirradiation are measured with a sunphotometer and an aureolemeter (scanning spectral radiometer). From these measurements, columnar aerosol size distribution and the scattering parameter are derived (Hayashida et al., 1992).

3. Stratospheric ozone measurements by DIAL

An excimer laser-based ozone DIAL system was constructed in 1988. After some preliminary investigations and modifications, routine measurement has been carried out since 1989. Figure 2 depicts ozone changes from the start of the measurement until before the Mt. Pinatubo eruption in June 1991. Data obtained at 20, 25, 30, 35 and 40 km over Tsukuba, Japan are shown. A clear indication of seasonal variation can be found at 30 and 35 km.

Due to the presence of dense aerosol layers originating Mt. Pinatubo eruption, DIAL measurements have been in trouble since the summer of 1991. Figure 3a shows ozone profiles derived from different combinations of laser wavelength. The derived ozone profiles are very much dependent on the wavelength separation between on- and off-lines, especially in the region of dense aerosol layer shown in Figure 3c (Nakane et al., 1992). In Figure 3b, an ozone profile corrected for aerosol scattering and extinction is depicted. The correction was based on the Fernald solution using the optical parameters inferred from the multi-wavelength lidar measurements. The deviations were greatly reduced but still exist a little.

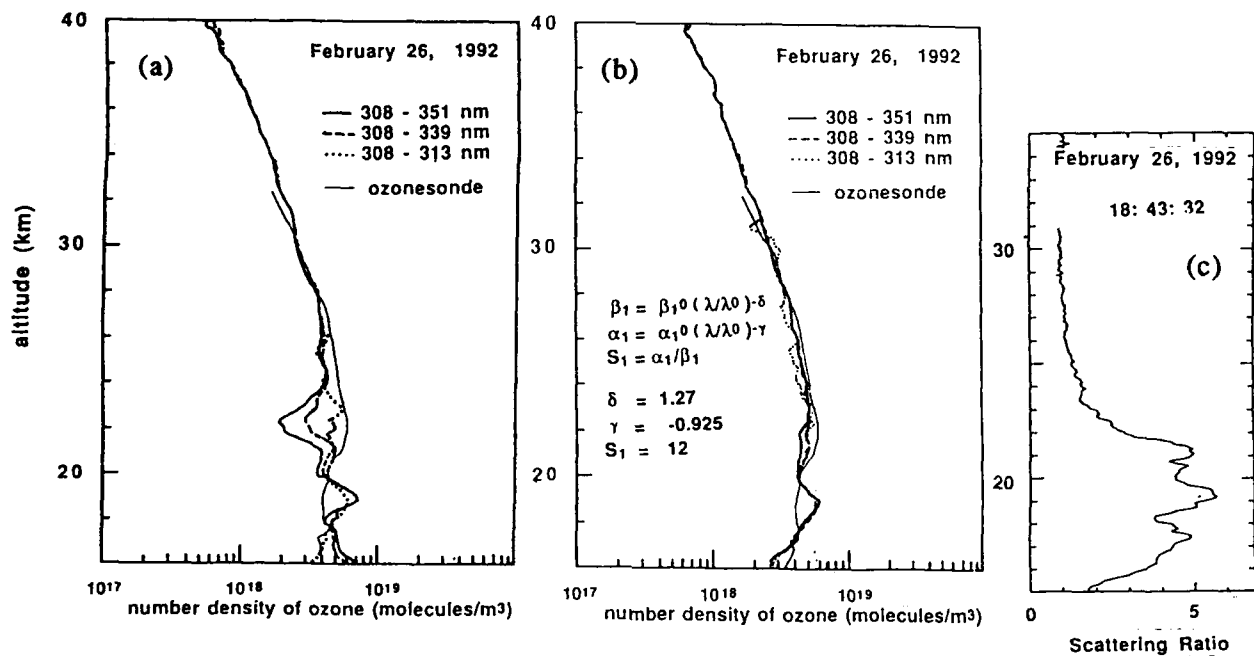


Figure 3 (a) Ozone profiles obtained with the DIAL and an ozone sonde. (b) Ozone profiles corrected for aerosol effects. (c) Aerosol scattering ratio profile.

4. Retroreflector In-Space project

A very challenging experiment using a satellite-borne large retroreflector (RIS: Retroreflector In-Space) was proposed for earth-satellite-earth laser long path absorption measurements as schematically shown in Figure 4. The RIS measurement utilizes the Doppler effect in the return laser signal to get spectral information (absorption line shape) of molecules in the atmosphere (Sugimoto et al., 1992).

NASDA is going to launch the earth observing satellite ADEOS in early 1996 into a sun-synchronous polar orbit with an inclination angle of 98.6 degree and with the descending equatorial crossing time of 10:30AM. The ADEOS will carry eight earth sensing instruments, one of which is the RIS described here.

To realize the RIS measurement, a precise satellite tracking capability is required as well as a laser transmitter and receiver for absorption measurement. The satellite tracking will be implemented by Dr. Itabe's group at CRL (Communications Research Laboratory, Koganei, Tokyo, Japan). They are developing an active tracking technique using a laser to illuminate the satellite for better detection.

NIES are responsible for developing a laser transmitter and receiver system, which will be integrated into the tracking system. We are also in charge of software development for data processing.

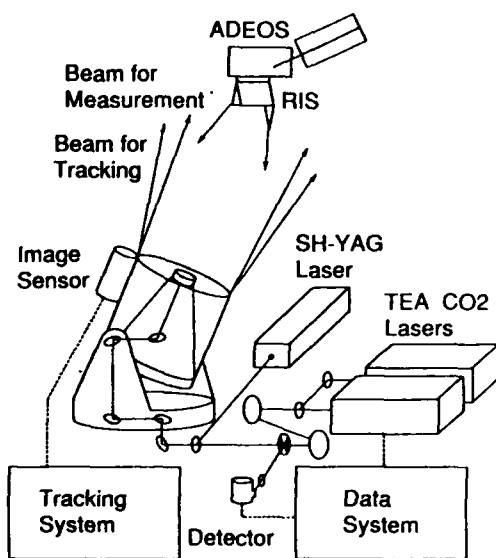


Figure 4 Configuration diagram of RIS experiments

5. ILAS project

The ADEOS will carry another atmospheric sensor ILAS (Improved Limb Atmospheric Spectrometer) sponsored by Japan Environmental Agency. The ILAS measures the atmospheric absorption spectrum using the solar occultation method.

The ILAS has 44 infrared channels covering from 850 cm^{-1} to 1610 cm^{-1} in wavenumber and 1024 visible channels covering from 753 nm to 784 nm in wavelength. The latter channels are used for deriving temperature, air density and aerosol information. In the infrared region, there are several species which has absorption. Targets of ILAS measurements are O_3 , HNO_3 , NO_2 , N_2O , H_2O , CH_4 , CFC11 , temperature, aerosol, and air density in the stratosphere over the high latitude regions.

We are responsible for scientific aspects of the ILAS project. The ILAS Science Team was established to carry out the related researches and supervise the software development and the instrument manufacturing and testing. The science team is also responsible for validation experiments.

6. Concluding remarks

Research activities on lidar and satellite remote sensing at NIES are summarized. The atmospheric remote sensing research group at NIES has their basis on optical sensing technologies as well as atmospheric sciences. Therefore, while development of new technologies are always targets of our research, applications to atmospheric sciences is another important field we should be involved in. The long-term monitoring of the atmospheric environment is one of those applications. Ozone monitoring using the DIAL has been implemented for three years, which could be expanded further as one of the NDSC-type monitoring.

Atmospheric sensing from space is one of the fields which the research community in Japan has failed to promote so far. From the proposals responding to the AO (Announcement of Opportunity) for the ADEOS instruments, the ILAS and the RIS by Japan Environmental Agency have been selected along with IMG (Interferometric Monitor for Greenhouse gases) by MITI (Ministry of International Trade and Industry). To support those projects (ILAS, RIS and IMG), a science (mission) team has been established for each project and many Japanese scientists have started to be involved in them, which is a bright sign of future development in this field in Japan.

References

- Fernald, F. G. (1984): *Appl. Opt.*, 23, 652-653.
- Hayashida-Amano, S. et al. (1991): *J. Geophys. Res.*, 96, 15469-15478.
- Hayashida, S. and Y. Sasano (1992): *GRL* (in press)
- Hayashida, S. et al. (1992): *Proceedings of Quadrennial Ozone Symposium*, 1992.
- Nakane, H. et al. (1992): *Proceedings of Quadrennial Ozone Symposium*, 1992 .
- Shimizu, H. et al. (1985): *Appl. Opt.*, 24, 617-626.
- Sugimoto, N. et al. (1992): *Abstracts for 16th ILRC, NASA Conf. Publication 3158*, Part 1, 659-662.

Radiation Energy Budget Studies using Collocated AVHRR and ERBE Observations by

Steven A. Ackerman
Cooperative Institute of Meteorological Satellite Studies
Department of Atmospheric and Oceanic Sciences
University of Wisconsin
Madison WI 53706
608-263-3647 (stevea@ssecmail.ssec.wisc.edu)

Toshiro Inoue
Meteorology Research Institute
Tsukuba, Ibaraki Japan

Introduction

The radiative modulation of the planet by clouds depends on the cloud optical properties and the temperature difference between the surface and the cloud. These properties can, to first order, be estimated based on the cloud classification (e.g., stratus, cumulonimbus, altocumulus). This study investigates cloud radiative forcing as a function of cloud classification. In addition, for clear sky conditions, the greenhouse parameter is determined. This is accomplished by collocated AVHRR (Advanced Very High Resolution Radiometer) observations within the ERBE (Earth Radiation Budget Experiment) scanner footprints. This collocation in time and space, allows one to take full advantage of the capabilities of each instrument.

Data Analysis

This study makes use of AVHRR and ERBE observations made from the NOAA-9 polar orbiting satellite, over the eastern Pacific for the year 1986. The NOAA-9 nominal equator crossing times are 0900 UTC and 2100 UTC.

The AVHRR data used in this study is the Global Area Coverage (GAC) data which has a nominal resolution at nadir of 4 km. The AVHRR has 5 spectral bandpasses: Channel 1 (0.56-0.68 μm); Channel 2 (.725-1.1 μm); Channel 3 (3.55-3.93 μm); Channel

4 (10.3-11.3 μm); and Channel 5 (11.5-12.5 μm). These 5 channels are located in spectral regions where atmospheric gases are characterized by weak absorption. The AVHRR data are therefore good for studying surface properties, such as sea surface temperature and vegetation properties, and cloud top properties. Inoue (1987) developed a cloud type classification based on the equivalent brightness temperature in Channel 4 (11 μm) and the temperature difference between Channel 4 and 5 (11 - 12 μm). This technique has been referred to as the split window method. On the basis of the two-dimensional histogram, cirrus, dense cirrus, cumulonimbus and cumulus/stratus clouds can be classified over the ocean. This classification scheme is adopted in the present study.

ERBE observations are used to specify the broadband energy budget at the top of the atmosphere. At nadir the ERBE footprint is approximate 35 km. The ERBE scanning instrument has been discussed by Kopia (1986). The method of inverting the instantaneous scanner observations to the top of the atmosphere fluxes is discussed in Barkstrom et al (1989), and Smith et al (1986).

Collocation of the AVHRR pixels with the ERBE footprint is accomplished based on the method developed by Aoki

(1980). The method is based on the scanning geometry of both instruments.

Clear Sky Results

The effect of water vapor on planetary energy budget as recently by described by Raval and Ramanathan, Ramanathan and d Collins, 1991, Stephens and Greenwald, and Ackerman et al (1991). The greenhouse effect of water vapor is quantified based on the greenhouse parameter:

$$G = \frac{T_s^4}{T_e^4}$$

Where T_s is the sea surface temperature and T_e is the effective clear sky planetary temperature determined from the ERBE measured outgoing longwave radiation. While ERBE has scene identification algorithm, the present study determines clear sky scenes based on the split window technique developed by Inoue (1987). Specifically, if the 11 μ m brightness temperature (BT_{11}) is greater than 290°C, the BT difference between 11 and 12 μ m (ΔBT_{11-12}) is $0 \leq \Delta BT_{11-12} \leq 3$, and the standard deviation of the BT_{11} within the ERBE footprint is less than 0.1°C. This latter condition is referred to as the scene uniformity and is calculated using the radiance observations. Under clear sky conditions, the sea surface temperatures are derived from the AVHRR observations using the NOAA operational method described by McClain (1989).

The previous studies have all demonstrated a coupling between the greenhouse parameter and sea surface temperature and precipitable water. The relationship between sea surface temperature and precipitable water has been discussed by Stephens (1990). The ΔBT_{11-12} is an indication of the atmospheric water vapor structure in the lower atmosphere, which makes a large contribution to the total precipitable water. The relationship derived in the present study is shown in figure 2. This relationship is in agreement with the

previous studies. The variability about the linear relationship is likely due to variations in the upper tropospheric water vapor. The good correlation between ΔBT_{11-12} and the greenhouse parameter indicates that the variability of the greenhouse parameter can be studied at a higher spatial scale than previously done.

Cloudy Sky Results

The radiative properties of clouds are described in terms of the cloud longwave (LW) forcing defined as the difference between the observed flux and the clear sky flux. Ramanathan et al (1989), Harrison et al (1990) derived the global distribution of cloud forcing based on ERBE observations on a spatial scale of 2.5×2.5 degrees and monthly averages. Ackerman et al (1991) combined ERBE, AVHRR and HIRS/2 observations to describe cloud forcing as a function of cloud amount and altitude. Due to the fields of view, Ackerman et al (1990) described these relations on a spatial scale on the order of 3×3 ERBE footprints. The advantage of this study, is the higher spatial resolution, individual ERBE footprints, and a classification of cloud type. An example of the radiative properties of cloud type is shown in figure 3 that depicts the ERBE observed LW versus SW observations for the months March, April and May 1986. The four classifications are clear, stratus, cirrus and cumulo-nimbus. The cumulonimbi display the largest albedo and coldest OLR. Notice that stratus clouds and thin cirrus clouds can have the same effect on modifying the clear sky OLR; however, the stratus has a larger effect on the shortwave because of the greater water contents. These types of relationships can not be directly derived with ERBE observations alone. SW and LW cloud forcing will be presented at the conference.

References

- Ackerman, S. A., R. A. Frey and W. L. Smith, 1992: Radiation budget studies using collocated observations from AVHRR, HIRS/2 and ERBE instruments. *J. Geo. Res.*, 97, 11513-11525.
- Barkstrom, B. R., E. F., Harrison, G. Smith, R. Green, J. Kebler, R. Cess and the ERBE Science Team, 1989: Earth Radiation Budget Experiment (ERBE) Archival and April 1985 results. *Bull Am. Meteorol. Soc.*, 70, 1254-1262.
- Harrison, E. F., P. Minnis, B. R. Barkstrom, V. Ramanathan, R. D. Cess and G. G. Gibson, 1990: Seasonal variation of cloud radiative forcing derived from the Earth radiation budget experiment. *J. Geophys. Res.*, 95, 18687-18703.
- Kopia, L. P., 1986: Earth radiation budget experiment scanner instruments, *J. Geophys. Res.*, 24, 400-406.
- McClain, E. P., 1989: Global sea surface temperatures and cloud clearing for aerosol optical depth estimates, *Int. J. Remote Sensing*, 10, 763-769.
- Ramanathan, V. and W. Collins, 1991: Thermodynamic regulation of ocean warming by cirrus clouds deduced from observations of the 1987 El Nino, *Nature*, 351, 27-32.
- Ramanathan, V., R. D. Cess, E. F. Harrison, P. Minnis, B. R. Barkstrom, E. Ahmad, and D. Hartmann, 1989: Cloud-radiative forcing and climate: Results from the Earth radiation budget experiment, *Science*, 243, 57-63.
- Raval, A., and V. Ramanathan, 1989: Observation determination of the greenhouse effect. *Nature*, 342, 758-761.
- Smith, G. L., R. N. Green, E. Raschke, L. B. Avis, J. T. Suttles, B. A. Wielicki and R. Davies, 1986: Inversion methods for satellite studies of the Earth's radiation budget: Development of algorithms for the ERBE mission, *Rev. Geophys.*, 24, 407-421.
- Stephens, G. L., 1990: On the relations between water vapor over the

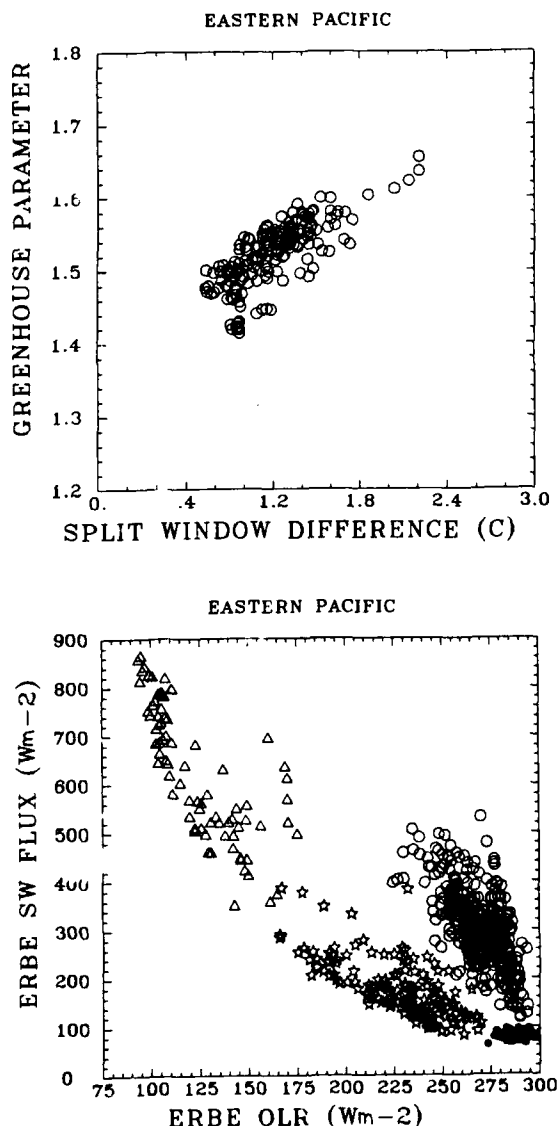
oceans and sea surface temperature, *J. Clim.*, 3, 634-645.

Stephens, G. L. and T. J. Greenwald, 1991: The Earth's radiation budget and its relation to atmospheric hydrology, Part I: Observations of the clear sky greenhouse effect, *J. Geophys. Res.* 86, 15311-15324.

List of Figures

Figure 1. AVHRR split window difference versus the greenhouse parameter.

Figure 2. The longwave and shortwave fluxes for different cloud classifications: filled circles - clear sky, open circles - stratus; stars - cirrus; triangles - cumulonimbus.



SPATIAL AND SPECTRAL INFORMATION DENSITIES FROM SATELLITE SOUNDING INSTRUMENTS

by
Hung-Lung Huang, R. J. Purser* and William L. Smith

Cooperative Institute for Meteorological Satellite Studies
University of Wisconsin-Madison
1225 West Dayton Street
Madison, WI 53706
(608)263-5283

*UCAR Visiting Scientist,
National Meteorological Center,
Washington, DC

Recently objective measures of the information densities in both the spatial and spectral domains have been developed in the context of satellite retrievals of temperature and moisture profiles of the atmosphere (Purser and Huang, 1993; Huang and Purser, 1993). Densities of two measures of "information" are formulated. The first measure, "degrees of freedom for signal" (DFS) corresponds approximately to the effective dimensionality of the constraints imposed upon each retrieval by the set of measurements (Wahba, 1985). The second measure is the decrease in "entropy" in the sense defined by Shannon (1984) in the theory of communication. The matrix algebra of optimal linear retrieval suggests very natural definitions of both of these quantities, not only as distributions in height but, with equal validity, as densities distributed in the infrared spectrum itself.

The spatial densities of DFS and entropy-reduction provide quantitative insight into the way in which the sounding system improves the knowledge of the thermal and moisture structure of the atmosphere at each elevation. For example, the results of simulations show that there is a relatively large contribution of information at mid-troposphere (300 - 700 mb) and low contributions at the tropopause (around 250 mb) and at upper regions of the stratosphere (5 - 25 mb).

Likewise, the spectral domain densities of information delineate precisely those regions of the optical spectrum (or, if preferred, the instrument channels) which are responsible for providing the greatest contributions of information to the sounding. Inspecting the information density in this domain therefore provides an objective way to understand which portions of the optical spectrum are liable to yield the most valuable contributions in planned and future instrument designs.

Application of the analysis of the information content in the form of densities in the context of a future high-resolution infrared sounder (Smith et al., 1991) will be discussed in the conference. The technique of analysis, involving the method of singular value decomposition, will be described and the merits of our technique will be discussed.

References

- Huang, H.-L. and R. J. Purser, 1993: An objective evaluation of the information content of satellite infrared instruments. Preprint, Eighth Symposium on Meteorological Observations and Instrumentation, Anaheim CA. AMS, Boston.
- Purser, R. J., and H.-L. Huang, 1993: Objective definitions of spectrum-domain information densities for satellite infrared instruments. Preprints, Eighth Symposium on Meteorological Observations and Instrumentation, Anaheim CA. AMS, Boston.
- Shannon, C., 1948: A mathematical theory of communication. Bell System Tech. J., 27, 379-423 and 523-656.
- Smith, W. L., H. M. Woolf, and H. E. Revercomb, 1991: Linear simultaneous solution for temperature and absorbing constituent profiles from radiance spectra. Appl. Optics, 30, 1117-1123.
- Wahba, G., 1985: Design criteria and eigensequence plots for satellite-computed tomography. J. Atmos. Ocean Tech., 2, 125-132.

Initial Data from a New High Spectral Resolution Lidar

E.W. Eloranta and P.K. Piironen
University of Wisconsin
1225 W. Dayton
Madison, Wisconsin 53706

Introduction

The University of Wisconsin High Spectral Resolution Lidar (HSRL) has been recently redesigned for operation in an electronics semi-trailer van (ref 1). The HSRL can now be deployed in support of field experiments. This paper presents initial observations with the new configuration along with an analysis of measurement accuracy.

New measurement capabilities have been added; these include: observation of the signal variation with angular field of view, and observation of depolarization in all data channels. Depolarization measurements have been implemented by transmitting orthogonal linear polarizations on alternate laser pulses. Pulses are transmitted at 250 μ s intervals such that the lidar observes the same ensemble of particles for both polarizations. Orthogonal polarizations are measured with a single detector per channel (see figure 2). Since the optical components and detector gains are identical for the two polarizations the measured depolarization ratios are independent of these factors and the system delivers very precise depolarizations. A new data channel with a computer controlled aperture allows measurements of multiple scattering as a function of receiver field of view. Since the field of view variation is dependent on the size of the scattering particles it is expected that this will allow remote measurements of cloud particle size. Other technical improvements in the new system include active control of spectrometer temperatures, greatly increased mechanical stability, an increased receiver aperture, injection of calibration signals into the signal profiles to allow continuous monitoring of system calibration drifts, and extensive computer control of system operations.

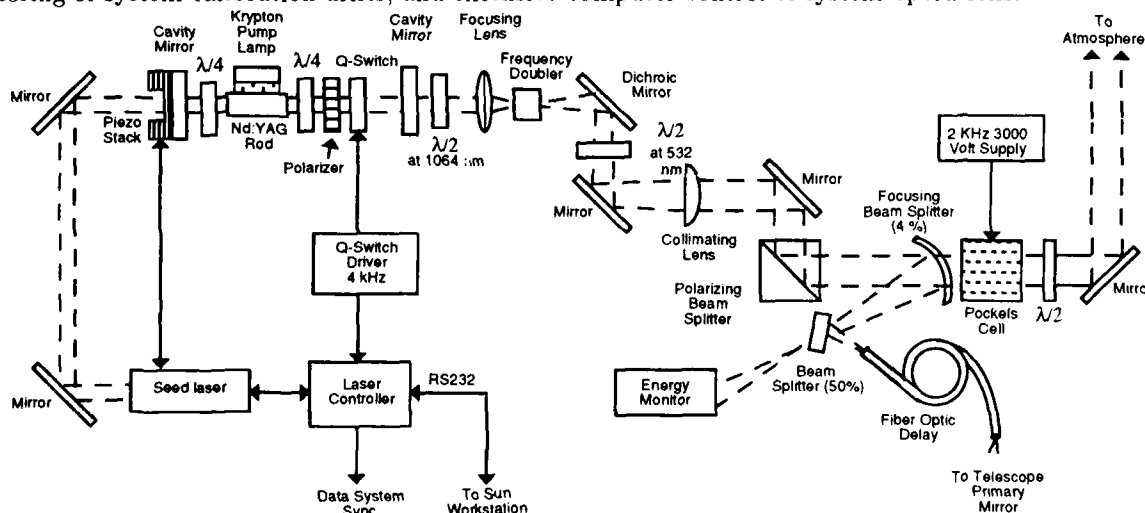


Figure 1: HSRL transmitter schematic. The transmitted polarization is rotated by 90° between successive laser pulses by a Pockels cell. A sample of each transmitted laser pulse is extracted by a beam splitter, delayed in an optical fiber and then injected into the receiver to monitor system calibration.

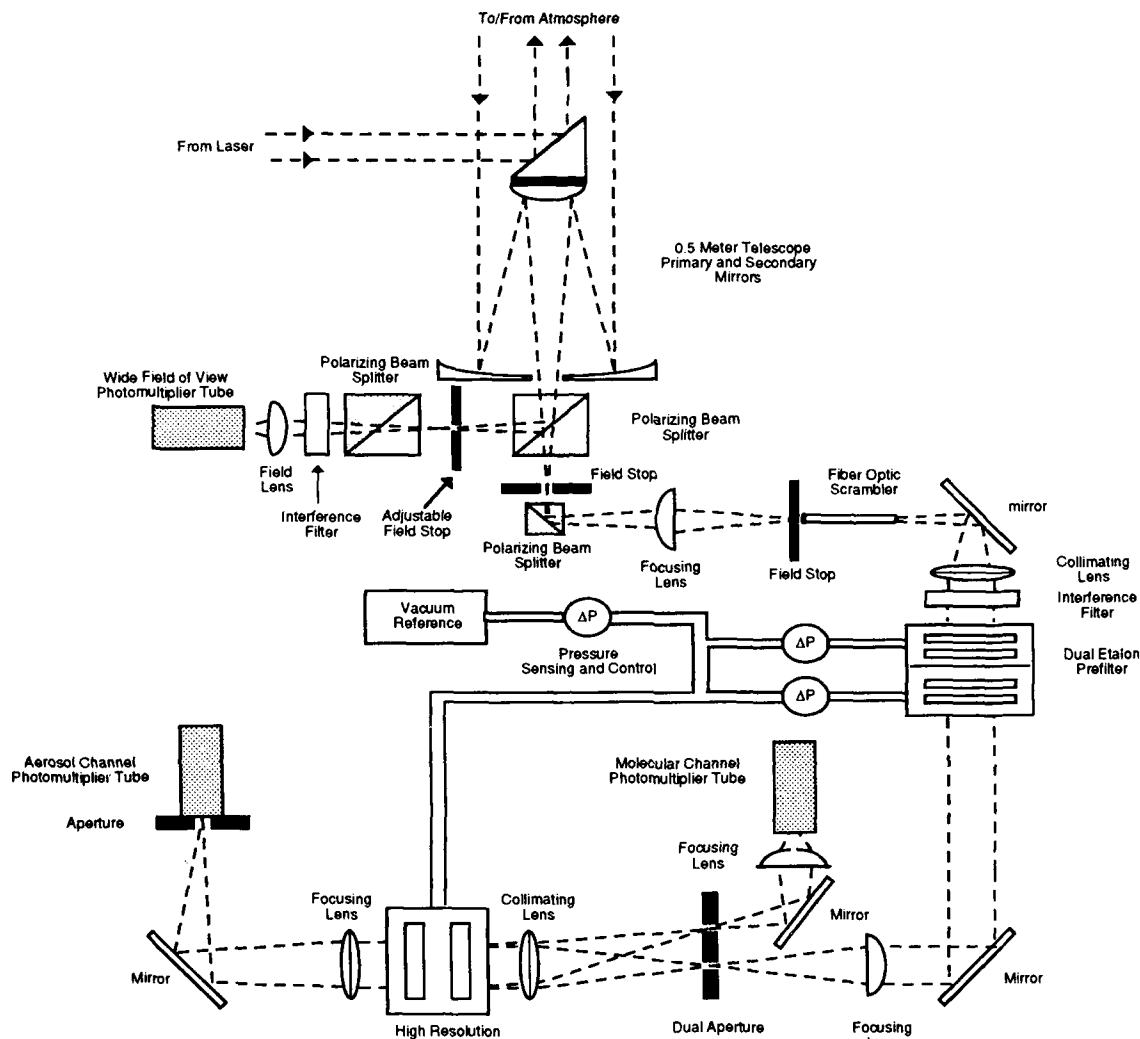


Figure 2: HSRL receiver schematic. A polarizing prism at the output of the receiving telescope separates orthogonal linear polarizations between the wide field of view channel and the spectrometer channels of the HSRL. Since the polarization of the transmitted pulse alternates between successive laser pulses each channel alternately receives parallel and perpendicular polarization components.

Backscatter Cross Section Measurements

The HSRL divides the lidar return into separate molecular and aerosol returns. The Doppler broadening of the molecular return caused by the thermal motion is used to distinguish molecular scattering from aerosol scattering. Computing the ratio of aerosol scattering to molecular scattering and computing the molecular scattering from an independently measured density profile provides calibrated aerosol backscatter cross section measurements. These differ from estimations of backscatter cross sections made with conventional single channel lidars: they do not require an assumed relationship between backscatter and extinction and they do not require an initial value of the scattering cross section. Furthermore the inversion is not subject to the numerical instabilities encountered in single channel lidar inversions.

Figure 3 shows separate aerosol and molecular lidar returns observed on Sept 30, 1992 along with calibrated backscatter cross sections derived for that case.

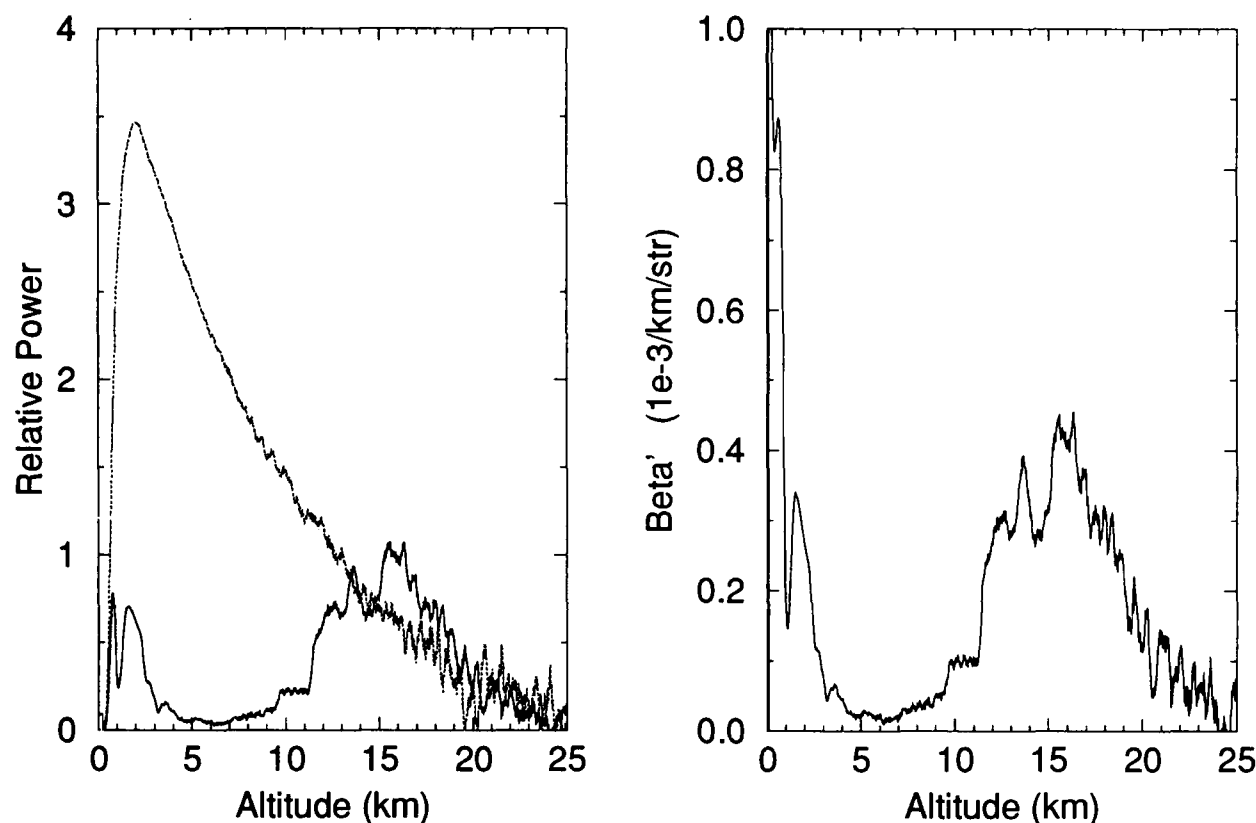


Figure 3: Separated aerosol (solid line) and molecular (dashed line) returns measured on Sept 30, 1992 are shown in the left panel. Calibrated backscatter cross sections derived from this data are shown in the right panel. Notice the strong stratospheric aerosol layer remaining from the Mt. Pinatubo eruption.

Polarization Measurements

Separate depolarization measurements can be made in both the "molecular" and "aerosol" channels of the HSRL while simultaneously observing the depolarization in the wide field of view channel. Calibrations show that the system contributes a depolarization of less than 0.1%. The molecular and aerosol channel signals can be inverted to separate aerosol and molecular depolarizations. This serves to demonstrate the accuracy of the HSRL depolarization measurements and to clearly show the depolarization due to aerosol particles.

Figure 4 shows inverted molecular depolarizations for the data presented in figure 3 along with a separate case showing ice and water cloud depolarization measurements. The right panel of figure 4 shows HSRL returns from a super-cooled water cloud (at an altitude of 5 km) and from ice crystal precipitation falling from this cloud (between altitudes of 3.3 and 4.8 km). The received signals polarized parallel and perpendicular to the transmitted polarization are shown along with the depolarization ratio. Notice that the depolarization observed in the clear air below the cloud is approximately 1% and thus very near the depolarization expected for molecular depolarization of the Cabannes line. Depolarization in the ice crystal virga is $\sim 32\%$. Also note that the water cloud depolarization is approximately 2% indicating that for this cloud the 200 microradian field-of-view of the HSRL effectively suppresses depolarization caused by multiple scattering.

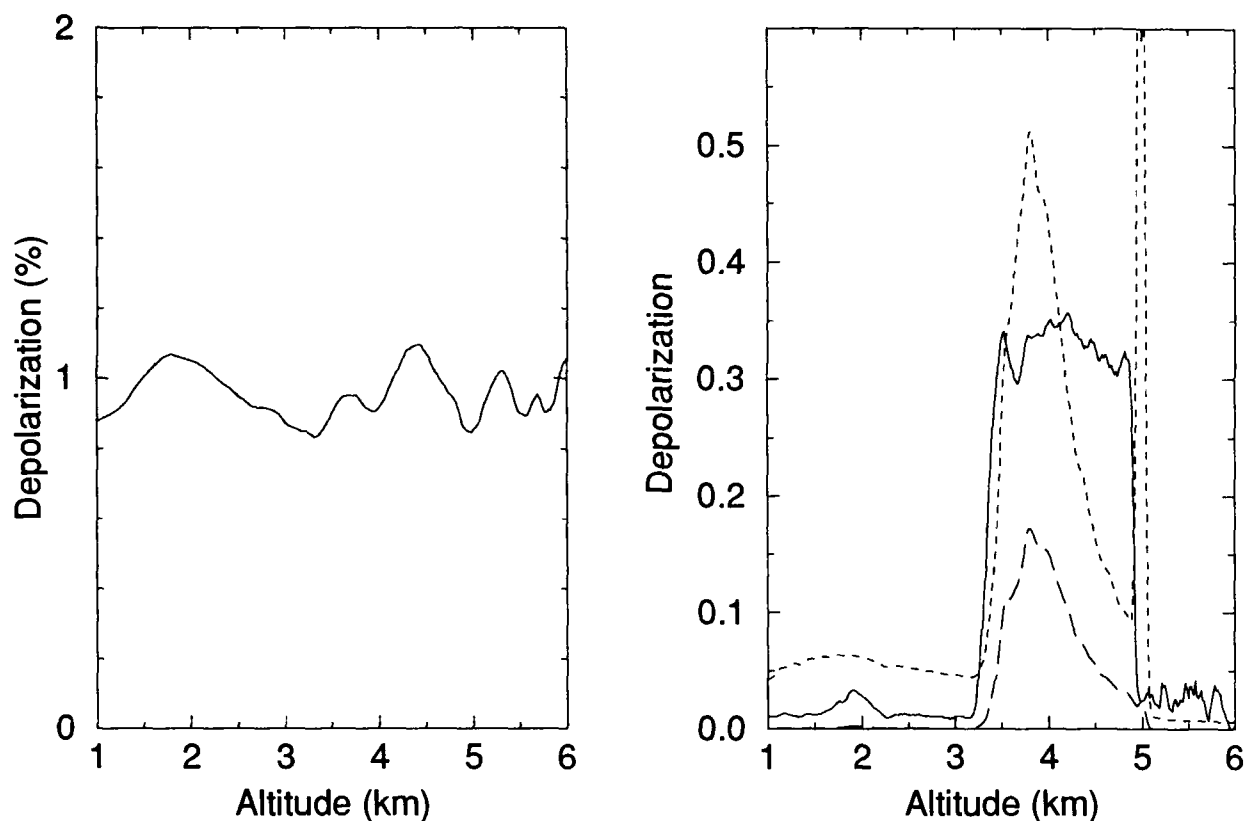


Figure 4: Depolarization measurements. The left panel shows inverted molecular depolarizations for the lidar returns presented in figure 3. Notice the small values of the depolarization; these are consistent with the depolarization expected for the Cabannes line of molecular scattering and support HSRL calibrations showing system depolarizations of less than 0.1%. The right panel shows cloud depolarizations. The un-inverted molecular returns with polarization parallel and perpendicular to the transmitted polarization are shown as short dashed and long dashed lines respectively. The depolarization is shown as a solid line.

Acknowledgements

Support for this work has been provided by Department of Energy grant DE-FG02-90ER61058 and Office of Naval Research grant N00014-91-J-1558. Support to P.K. Piironen was provided by the Foundation of Maj and Tor Nessling, and the University of Joensuu, Finland.

References:

- Grund, C.J. and E.W. Eloranta, 1991: The University of Wisconsin High Spectral Resolution Lidar, *Optical Engineering* 30, 6-12.

Boundary Layer Height Measurements with an Eyesafe Lidar System

E. M. Patterson, G. G. Gimmestad, D. W. Roberts, and S. C. Gimmestad

Electro Optics and Physical Sciences Laboratory
Georgia Tech Research Institute
Georgia Institute of Technology
Atlanta, Georgia 30332

Introduction

Air chemistry studies require measurements of the depth of the mixed layer in which many of the chemical reactions take place. Lidar measurements provide an attractive option for providing high temporal resolution mixed layer depths in support of these studies. We have developed an eyesafe lidar system for measurements of the vertical distribution of boundary layer aerosols in support of an intensive series of air chemistry measurements conducted as part of the Southern Oxidants Research Program in Atlanta, Ga, during the summer of 1992. This lidar system was used in a semi-automated mode to monitor diurnal variations in vertical distributions of aerosols from which the depths of the boundary layer were inferred.

Lidar System Description

The lidar system has a Raman-shifted Nd:YAG source laser at 1.54 microns wavelength with a pulse energy of 50 mJ operating at a 4 Hz pulse repetition frequency. This source laser system is similar to that reported by Patterson et al, (1989); but with several technical improvements to improve beam quality and system operations. These changes included a longer Raman-shift cell with a less tightly focused pump beam (100 cm focal length vs 50 cm focal length) and the addition of helium to the methane in the cell to provide a better thermal transfer in the cell.

These changes solved the two major problems associated with our previous system, a difficulty in limiting the divergence of the output beam and a breakdown of the methane inside of the cell, with the decomposition products depositing on the windows. No methane breakdown was observed, and there was no window contamination. Divergence of the outgoing beam was approximately 0.4 mr.

The system was designed with two receivers to cover an expected range in boundary layer thickness from 50 m to 4 km, one with a 4.6 cm aperture and 105 mm focal length and another with a 150 mm aperture and 300 mm focal length. Both channels use InGaAs PIN diode detectors. Because of operational difficulties with the detector on the larger aperture channel, only the small aperture channel was used in the summer 1992 measurements; sensitivity, however, was still sufficient to make the desired measurements. The alignment of the lidar

system proved to be very stable, with no significant changes in alignment during the period of operation.

The return signal was digitized with 12 bit resolution at a rate of 10 Msamples/sec, which corresponds to a range resolution of 15 m. The transient digitizer output is recorded using an IBM PC-AT computer which also provided system control. The system was operated in a semi-automated mode in which the computer controlled system operation and data collection after an initial start up procedure.

Data and Analysis

The return signal was analyzed by calculating a normalized return. This analysis included a subtraction of the background from the signal and a multiplication of the resulting values by the range squared according to the formula

$$A_i = (S_i - B)R_i^2$$

with A_i the normalized return for a range R_i , S_i the return signal for the given range, and B the background. The value A is proportional to the aerosol return. This formula is used to normalize the returns rather than the more commonly used scattering ratio because the return due to molecular Rayleigh scattering is so much less than the aerosol return at the 1.54 micron wavelength that the return is effectively due to the aerosol backscatter only.

A_i is proportional to the aerosol return. With appropriate calibration, the A_i terms could be converted to quantitative backscatter values. A complete calibration was not done as part of this effort because of our interest in relative concentrations only.

Two examples of the relative aerosol profiles are shown in Figures 1 and 2. Both of these profiles represent data taken with the 5 cm aperture telescope on August 31, 1992; the times are GMT, which is 4 hours ahead of EDT. Figure 1, the 14:38 data, shows an aerosol profile with relatively high aerosol levels extending up to approximately 1200 meters. There is a good deal of structure in the profile; a comparison of the 14:38 data with earlier data shows that there is variation in the aerosol below 500 m that is indicative of a boundary layer extending to approximately 500 m. The aerosol between 500 and 1200 m is not boundary layer aerosol, but is likely due to aerosol mixed up to the level from previous days or transported from a distance. Figure 2, the 18:06 data, shows a quite different profile in which the structure in the profile has been replaced by a smooth variation up to 1200 m. This profile is interpreted as being due to a mixed layer extending to 1200 m.

An examination of these two data sets, as well as the other data from this study, indicates that the determination of the mixing depth from the aerosol data is not always a straightforward matter. In order to determine mixing layer depths, aerosol data that are closely spaced in time with high spatial resolution are needed. Improvement in the estimation of mixed layer depth from the data is an ongoing effort.

Discussion

The lidar system performed well during this study. The system provided the resolution, sensitivity, and reliability needed to measure the vertical distributions of boundary layer and other aerosols. This program has demonstrated that a simple, relatively inexpensive eyesafe lidar system suitable for autonomous operation can provide the atmospheric aerosol profile data needed to support atmospheric chemistry studies.

References

Patterson, E. M., D. W. Roberts, and G. G. Gimmestad, Initial measurements using a 1.54 μm eyesafe Raman shifted lidar. Appl. Opt., 28, 4978-4981, 1989.

This work was supported by the US EPA under Contract No CR- 817732-01.

Normalized Return vs Altitude

8/31/92 at 14:38

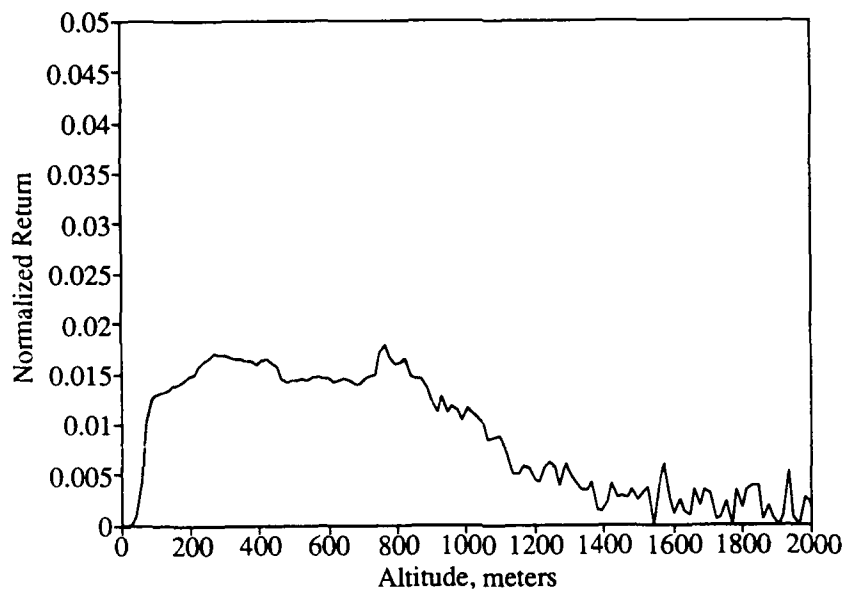


Figure 1. Relative aerosol profile data for 14:38 on August 31, 1992

Normalized Return vs Altitude

8/31/92 at 18:06

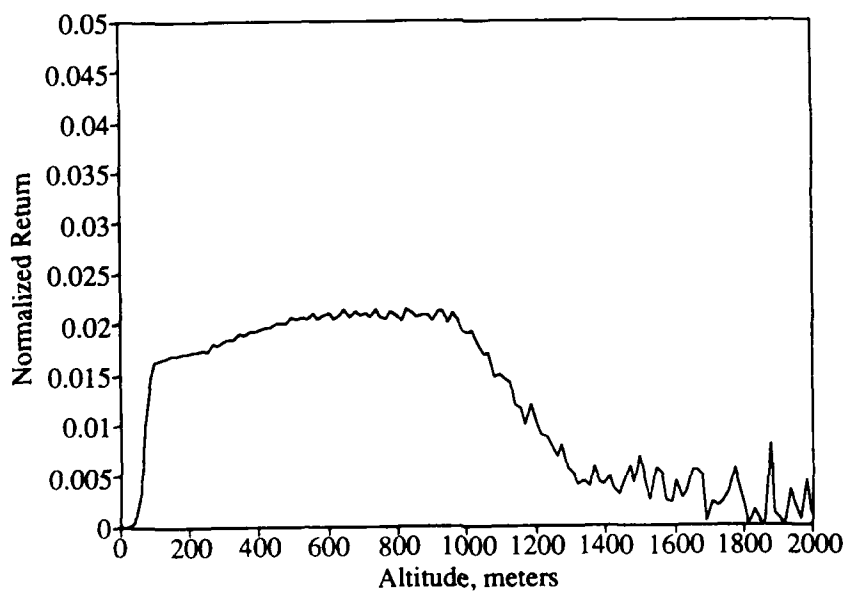


Figure 2. Relative aerosol profile data for 14:38 on August 31, 1992

Tuesday, March 9, 1993

Space & Ground Based Remote Sensing 3

TuA 8:00am–10:20am
Salon F

Alain Chedin, *Presider*
Ecole Polytechnique, France

Retrieval of Atmospheric State Parameters from High Resolution Spectral Radiance Data

Shepard A. Clough
Atmospheric and Environmental Research, Inc.
840 Memorial Drive
Cambridge, MA 02139

The retrieval of temperature and molecular trace gas profiles from spectral radiance data is an important but complex problem in optimization. In this presentation we are concerned with profile retrievals along the radiating path, examples of which include zenith remote sensing from the surface and nadir remote sensing from space. The latter application is of particular interest in the context of obtaining global maps of trace molecular species using high resolution spectral radiance data from spectrometers orbiting in space. The retrieval method to be explored is the method of non-linear least squares in which the state parameters are optimized to obtain the minimum variance of the spectral residuals, Rodgers (1976) and Clough et al. (1990, 1991). The residuals are defined as the spectral differences between the measurement and the calculated result from an appropriate forward radiative transfer model. In the present case we are concerned with high resolution so that the objective of the retrieval process is to obtain for a given spatial resolution, the most probable profile values for the state parameter of interest.

There are a number of methods for solving minimization problems including single value decomposition, conjugate gradient methods, the method of steepest descent, the secant method and interior point methods. The method on which we focus here is the classical Newton method including the closely related Gauss-Newton method, Dennis (1983) and Gill et al. (1981). There are two different but related aspects to the solution of the optimization problem with this method: the solution of a quasi-linear problem in the spirit of a Taylor series expansion and the iteration of the quasi-linear problem, the goal of which is to obtain the global minimum of

the variance for the full non-linear problem. In this approach an understanding of the role of the penalty function is essential. There are two important roles served by the penalty function. In the solution of the non-linear problem the penalty function serves to control the size and direction of step at each iteration commencing with the starting point, the first guess, and terminating at the solution. In our case the computational cost of the forward model, the calculation of line-by-line radiative transfer, is extremely high so that achieving accelerated convergence to the solution is of paramount concern. The second role served by the penalty function is more physical in nature and is concerned with addressing what is in general a very poorly posed inverse problem.

In the most direct approach to the optimization problem it is required to retrieve the atmospheric state parameters at the vertical spatial resolution of the radiative transfer calculation. Presumably the atmospheric layering has been defined such that finer vertical resolution produces changes in the calculated spectral radiance negligibly small with respect to the noise variance of the measurement. There are in general two principal causes for the ill posedness of the problem contributing to the near singularity of the solution set: (1) the strong inter-level correlations at the vertical resolution at which the radiative transfer is calculated and (2) atmospheric state parameters that are in null space or near null space. A properly chosen penalty function serves to address these two problems. Two approaches for the definition of the penalty function are considered: the maximum likelihood method for which the penalty function is given as the inverse of the error covariance matrix of the atmospheric state parameters and more direct methods which themselves can be based on a priori information about the atmospheric state. Among the latter approaches to be explored is the method of second derivative damping. Related methods have been discussed by Twomey (1977). An important advantage of the present approach is the availability of an error analysis in the solution domain, Rodgers (1990). This error analysis assumes linearity which in our experience has proven satisfactory at the level the error values are required.

It is common in these types of parameter retrieval problems to reduce the ill posedness by decreasing the vertical resolution, generally by retrieving

parameters for combined layers. It is important to recognize that with this procedure, the profile of the first guess is inherent in the combined layers. The application of a judiciously chosen penalty function can mitigate this difficulty. The present method allows the analysis of the trade off between vertical resolution and retrieved profile accuracy for different assumptions about the nature of the penalty function.

For this method of approaching the retrieval problem, a heavy computational burden is placed on the forward model. Currently we are using LBLRTM (Line-By-Line Radiative Transfer Model), a vectorized version of FASCODE, as the forward model. The Jacobian and the Hessian, required for our approach, are obtained by perturbing the designated state parameter and obtaining an approximation to the derivatives from finite differences. A strategy for achieving accelerated performance and obtaining analytic derivatives for certain state parameters will be suggested.

The particular problem to be considered in some detail is the retrieval of ozone mixing ratio profiles from ground based and spaced spectral radiance measurements using the 1043 cm^{-1} band of ozone. The instrument considered is the fourier transform interferometer although the approach is applicable to other high resolution spectral radiometric instruments. The weight matrix for the observations is the inverse of the error covariance matrix of the spectrum. For an unapodized spectrum sampled at the Nyquist sampling interval, the error covariance matrix is diagonal resulting in a diagonal weight matrix with the elements given as the reciprocal of the square of the spectral measurement error. For certain purposes such as localizing and/or excluding effects of interfering spectral features, it may be desirable to use apodized spectra in which case the weight matrix is in general non-diagonal and must be obtained in detail. For the case of ozone profile retrievals, the sensitivity of retrieval accuracy as a function of spectral resolution will be considered. The effect of spectral resolution has been studied for fixed observation time and the results demonstrate the value of the error analysis inherent in the present method.

References

- Clough, S.A., R.G. Isaacs, R.D. Worsham and J.-L. Moncet, 1990: Application of the Optimal Probability Method to the Retrieval of Temperature, Water Vapor and Ozone Profiles, Proc. of the Meeting on Optical Remote Sensing of the Atmosphere, Incline Village NE.
- Clough, S.A., C.P. Rinsland, C.D. Rodgers and A Goldman, 1991: Retrieval of Tropospheric Ozone from Simulations of Spectral Radiances as Observed from Space, Proc. of the Meeting on Optical Remote Sensing of the Atmosphere, Williamsburg ,VA.
- Dennis, J.E., Jr. and R.B. Schnabel, 1983: Numerical Methods for Unconstrained Optimization and Nonlinear Equations. Prentice-Hall, Inc., Englewood Cliffs, NY.
- Eyre, J., 1987: On systematic errors in satellite sounding products and their climatological mean values. *Quat. J. Roy. Meteorol. Soc.*, 113, 279-292.
- Eyre, J., 1989: Inversion of cloudy satellite radiances by non-linear optimal estimation. Theory and simulation for TOVS. *Quat. J. Roy. Meteorol. Soc.*, 115, 1001-1037.
- Gill, E.G., W. Murray and M.H. Wright, 1981: Practical Optimization. Academic Press, Inc., New York.
- Rodgers, C.D., 1976: Retrieval of atmospheric temperature and composition from remote measurements of thermal radiation, *Rev. Geophys. Space Phys.*, 14, 609-624, 1976.
- Rodgers, C.D., 1990: Characterization and Error Analysis of Profiles Retrieved from Remote Sounding Measurements, *J. Geophys. Res.*, 95, 5587-5595.
- Twomey, S., 1977: Introduction to the Mathematics of Inversion in Remote Sensing and Indirect Measurements. In **Developments in Geomathematics 3**, Elsevier Scientific Publishing Company, New York.

Continuous Measurement of Boundary Layer Temperature and Moisture Structure Using Ground-Based FTIR

W. L. Smith, R. O. Knuteson, H. E. Revercomb, and H. B. Howell

University of Wisconsin - Madison
Cooperative Institute for Meteorological Satellite Studies
1225 W. Dayton St., Madison, WI 53706
(608-263-7974)

1. INTRODUCTION

During the past decade a number of remote sensing devices to provide continuous atmospheric profile observations from the ground have been examined (Dabbert 1990). Several of these, including the doppler radar wind "Profiler" and the Radar Acoustic temperature Sounding System (RASS), are close to routine operational implementation. A RAMAN Lidar, developed for water vapor profiling, has proven to be an excellent research tool with some hope for operational implementation when the cost and complexity of the technology is reduced during the coming years.

Using a sophisticated High resolution Interferometer Sounder (HIS) designed for airborne use, the potential application of a groundbased upward viewing interferometer for sounding the lower troposphere was demonstrated in a 1988 field experiment (Smith et al., 1990). Since that time, low cost Fourier Transform Infrared (FTIR) Spectrometers, i.e. Michelson interferometers, have become commercially available to provide an instrument basis for a PBL sounding system. At the University of Wisconsin, we have explored the development of such a system using BOMEM (of Quebec, Canada) Michelson-series instruments.

The development of systems at the University of Wisconsin began with a single detector (6 - 20 μm) BOMEM M-120 interferometer with a scene imaging scan mirror and a three point calibration system. The M-120 based sounding system has been named the "Baby HIS" since it was an outgrowth of the UW aircraft HIS science program. A personal computer based data subsystem enables both calibrated radiance spectra and atmospheric temperature and humidity profiles to be displayed in realtime. During 1991, data with the "Baby HIS" was obtained during two field campaigns; one in February/March at Platteville, CO and another aboard the NFS research vessel Pt Sur off the California coast during May.

More recently, with financial support of the Department of Energy's Atmospheric Radiance Measurement (ARM) program, a system based on a two detector (3 - 20 μm) BOMEM MB100 interferometer was developed. This system has been named the Atmospheric Emitted Radiance Interferometer (AERI). Both the AERI and the Baby HIS were operated during the Spectral Radiation Experiment (SPECTRE) held in Coffeyville Kansas during November and December 1991. Since then the AERI was operated continuously for six weeks during February - March, 1992 at Seneca, Kansas as part of the STORMFEST Boundary Layer Subprogram.

The "Baby HIS" and the AERI systems are two implementations of a design philosophy which grew out of the HIS development program. The system design developed for groundbased application is generically referred to as the Ground-Based High resolution Interferometer Sounder or GB-HIS. In this paper we describe the GB-HIS system from the point of view of using it to profile the Planetary Boundary Layer. Results achieved from data collected during the SPECTRE and STORMFEST experiments are presented to demonstrate this important new meteorological sounding capability.

2. INSTRUMENT CHARACTERISTICS

The GB-HIS system obtains an uncalibrated spectrum every two seconds. The data is co-added (i.e., averaged) over a few minutes time interval to reduce the data volume as well as the radiometric noise prior to sounding retrieval. A ten minute calibration cycle has been chosen in which the atmospheric spectra are averaged over a three minute time period with the remaining time spent viewing blackbody references. Figure 1 shows comparisons of observed spectra with spectra calculated using a fast model for the period 13-22 November, 1991, of the SPECTRE experiment at Coffeyville Kansas. The coefficients of the fast model are obtained by empirical fits to FASCODE calculations with the HITRAN 1991 database using a diverse statistical sample of radiosonde data. Excellent agreement between the mean observation and mean fast model calculation is portrayed except in regions where the calculations are known to be deficient (i.e., 820 - 935 cm^{-1} where CFC's influence the observed spectra, and are not modeled for the calculations).

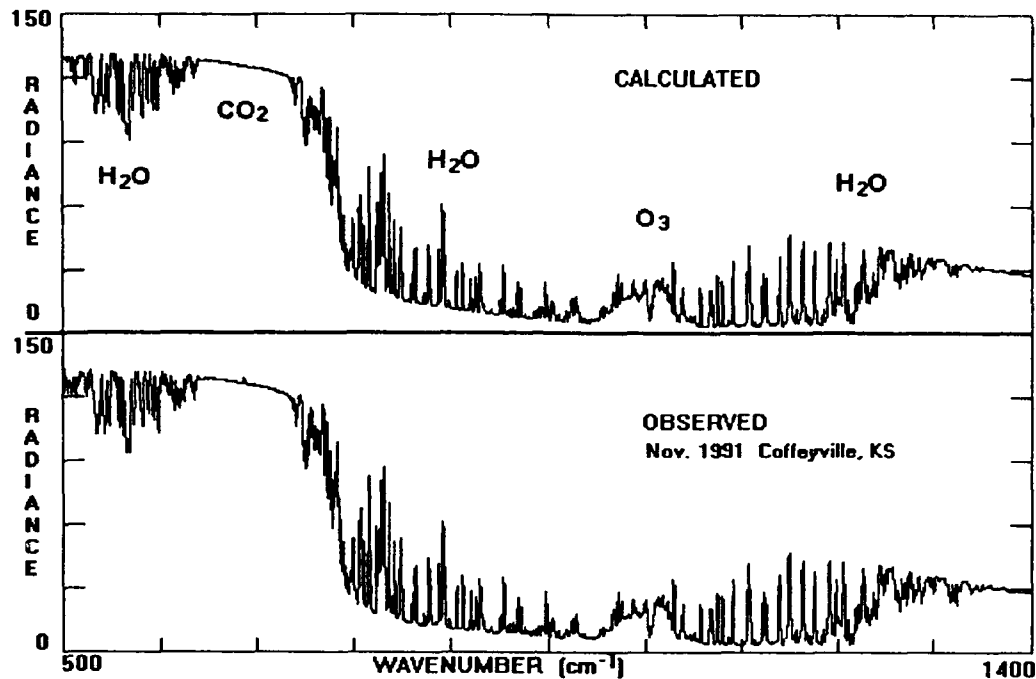


Figure 1. Mean observed and calculated downwelling atmospheric radiances used for retrieval of temperature and water vapor (13-22 November, 1991 at Coffeyville, Kansas). These results are based on longwave channel observations of the AERI instrument and calculations using a fast transmittance model based on coincident temperature and water vapor radiosonde measurements.

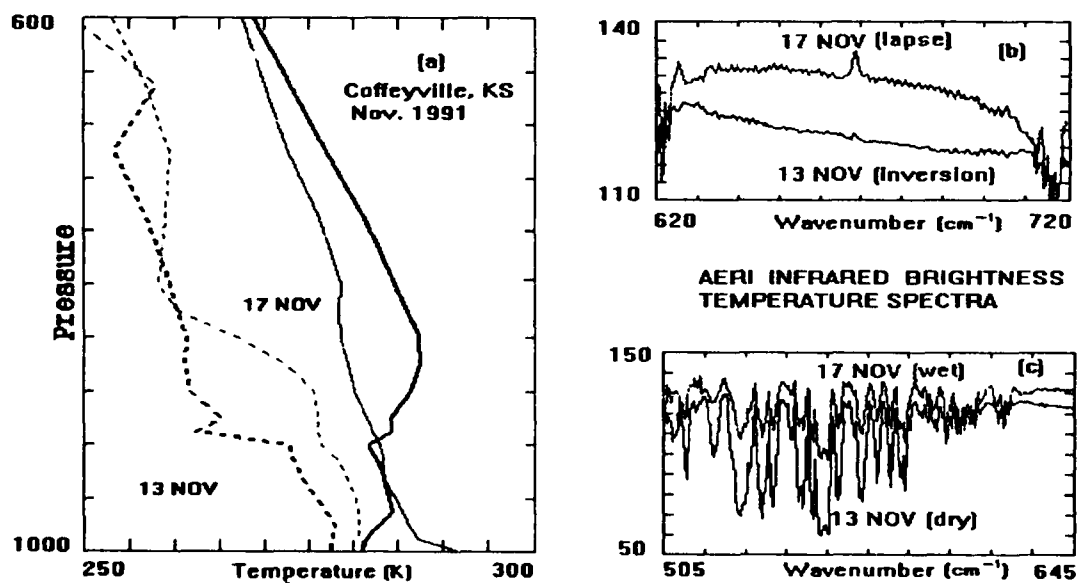


Figure 2. Two lower tropospheric temperature and moisture situations observed during the SPECTRE experiment. (a) The temperature (solid) and dewpoint temperature (dashed) for 17 November and 13 November, relatively wet and dry cases, respectively. (b) The signature of the low level temperature inversion in the 15 micron CO₂ band. (c) The signature of water vapor concentration differences in the two cases.

3. MEASUREMENT CHARACTERISTICS

The sensitivity to atmospheric structure can best be conveyed by comparing spectral radiance features for different sounding situations. Shown in Figure 2 are portions of two brightness temperature spectra observed with the GB-HIS and simultaneous radiosonde measurements achieved with the "CLASS" system. One of the soundings (17 November) is for a low tropospheric temperature lapse situation whereas the other is for a low level temperature inversion case (13 November). In the case of the temperature lapse situation, the radiance tends to decrease away from the opaque center of the $15\text{ }\mu\text{m}$ CO_2 absorption band. Figure 3 shows the signature of the inversion in the $4.3\text{ }\mu\text{m}$ CO_2 absorption band (i.e., $2200\text{--}2400\text{ cm}^{-1}$). As with the $15\text{ }\mu\text{m}$ band in the inversion case, the radiance tends to first increase with somewhat weaker absorption away from band center and then abruptly decreases corresponding to the decrease in temperature above the inversion level and the sensing through the atmosphere into cold space. It is evident from figures 2 and 3 that the lapse rate of temperature within the boundary layer can be subjectively diagnosed from the raw brightness temperature measurement spectrum.

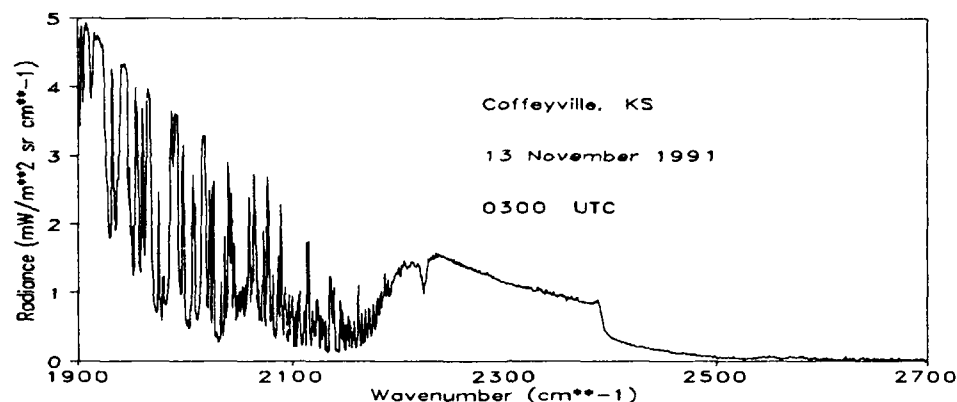


Figure 3. AERI shortwave channel.

The water vapor concentration in the lower atmosphere is similarly evident from the amplitude of the water vapor line features within the $17\text{--}19\text{ }\mu\text{m}$ region. For a given atmospheric temperature structure, the smaller the concentration of water vapor, the greater the amplitude of the H_2O emission lies. This feature is due to the change in radiance emitted from in between absorption line centers.

4. METEOROLOGICAL RESULTS

Radiance emission spectra are transformed into vertical temperature and moisture profiles using a recursive solution of the radiative transfer equation (Smith et al., 1992). In this solution the temperature and water vapor mixing ratio are solved simultaneously using a set of two equations formed by convolution of the radiance residual spectrum with the weighting functions of temperature and mixing ratio, respectively, for each sounding level. The recursive procedure starts with the solution for temperature and mixing ratio at ground level, where the weighting functions peak, and progresses upward. The solution for temperature and mixing ratio at each level is retrieved from the residual radiance spectrum obtained by removing the radiance contribution from below the solution level from the observed downwelling radiance spectrum. The procedure requires a first guess which is initially taken as a radiosonde observation and subsequently in time taken as the prior retrieval.

Figure 4 shows a time sequence of GB-HIS soundings obtained every 10 minutes as a time cross-section over a 24 hour period.

5. CONCLUSIONS

The GB-HIS can provide continuous measurements of the Planetary Boundary Layer (PBL). Results obtained during several field experiments indicate that the radiance measurement sensitivity and retrieval accuracy are sufficient to provide extremely valuable and unique observations of PBL morphology. The GB-HIS observations compliment observations from other groundbased remote sensors and satellite sounding data through its extreme sensitivity to thermodynamic structure in the lowest few kilometers of the atmosphere.

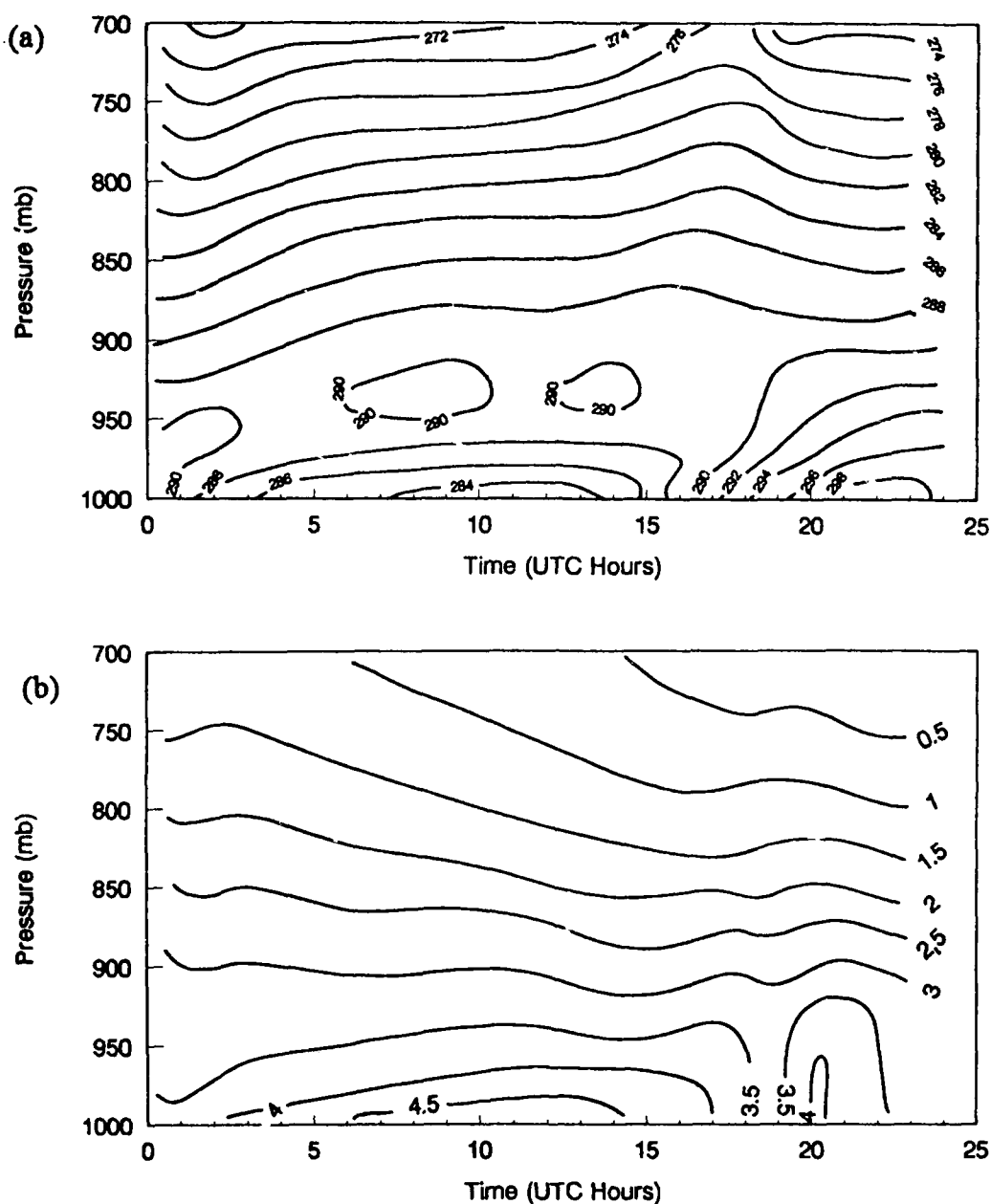


Figure 4. Time sequence of GB-HIS system boundary layer temperature (a) and mixing ratio (b) soundings for a 24 hour period (1 March 1992) during the STORMFEST experiment at Seneca, KS. Note the development and decay of the nocturnal inversion.

6. REFERENCES

- Dabberdt, W. F. et al, 1990 Summary of the Symposium on Lower Tropospheric Profiling: Needs and Technologies. BAMS, 71, 665.
- Smith, W. L. et al., 1990 GAPEX: A Ground-Based Atmospheric Profiling Experiment. BAMS, 71, 310.
- Smith, W. L. et al, 1992 Remote Sensing of the Planetary Boundary Layer with a High resolution Interferometer Sounder, to be submitted to BAMS.

Polar Ozone and Aerosol Measurement Experiment (POAM-II)

F. J. Lehmann
Naval Research Laboratory
Code 7227
4555 Overlook Avenue SW
Washington, D.C. 20375-5320
(202)404-7871

R. M. Bevilacqua
Naval Research Laboratory
4555 Overlook Avenue SW
Washington, D.C. 20375-5320

W. J. Glaccum
Naval Research Laboratory
4555 Overlook Avenue SW
Washington, D.C. 20375-5320

J. S. Hornstein
Naval Research Laboratory
4555 Overlook Avenue SW
Washington, D.C. 20375-5320

S. S. Krigman
Computational Physics Inc.
2750 Prosperity Avenue
Fairfax, VA 22031

J. D. Lumpe
Computational Physics Inc.
2750 Prosperity Avenue
Fairfax, VA 22031

E. P. Shettle
Naval Research Laboratory
4555 Overlook Avenue SW
Washington, D.C. 20375-5320

NRL will launch POAM II in September 1993, to measure polar stratospheric O_3 , H_2O , NO_2 , and aerosol extinction. The satellite system description is presented.

In September, 1993 the Naval Research Laboratory (NRL) will launch its Polar Ozone and Aerosol Measurement II (POAM-II) experiment aboard the French SPOT 3 satellite. POAM-II is a satellite-based multi-filter photometer which employs solar extinction (occultation) techniques to measure stratospheric aerosol and gas profiles. The instrument, built by the ThermoTrex Corp., San Diego, CA, consists of a sun sensor/servo system for solar tracking, and nine coaligned optical sensors, each containing a lens arrangement, an interference filter (to isolate a particular spectral region), and a photodiode detector. POAM-II will directly measure the stratospheric abundances of O_3 , H_2O , NO_2 , and aerosol extinction at five wavelengths with a vertical resolution of 1 km. Atmospheric temperature will be inferred indirectly from measurements of solar extinction by O_2 absorption. SPOT-3 will be placed in a 833 km nearly polar orbit, with an equatorial crossing time of about 1100. Therefore, POAM-II solar occultations will occur at high latitudes in both hemispheres, making POAM-II ideally suited for investigating the polar stratosphere and, in particular, the high latitude ozone depletion phenomenon. POAM-II is sponsored by the innovative Science and Technology Office of the Strategic Defense Initiative Organization (SDIO/IST), and the DoD Space Test Program (STP).

We present here a satellite description and the techniques for the data retrieval. Collaborations from within the general scientific community for POAM-II data analysis and interpretation are welcomed.

Retrieval of tropospheric and stratospheric distribution of HCl from ground-based FTIR spectra

G.P. Adrian, M. Baumann, E. Frank, H. Oelhaf

Institut für Meteorologie und Klimaforschung
Kernforschungszentrum Karlsruhe GmbH / Universität Karlsruhe
P.O. Box 3640, W-7500 Karlsruhe 1, Germany, tel: + 49-7247-82-5945

Introduction

FTIR spectrometers are often employed from the ground to detect the column amount of trace gases. For most applications it is sufficient to derive the total column amount without retrieving any information on the vertical distribution of the trace gases. However, some knowledge on the vertical distribution would be helpful in any case for the interpretation of the received trace gas contents. Of still greater importance is the fact that the uncertainty of the total column amount may be high due to an incorrectly assumed *a priori* profile. There is a chance to reduce that by taking into account the full information content of spectral line shapes. This is in particular the case for gases which contribute both by tropospheric and stratospheric contents to the total column amount, e.g. HCl or NO₂.

Problem definition

In general, only column amounts integrated along the optical path are obtained from atmospheric attenuation spectra in the middle infrared with the observation geometry looking upward. A particular shape of the vertical profile of each trace gas has to be assumed as *a priori* information, which is scaled as a whole in the fitting procedure.

In the case of HCl, both tropospheric and stratospheric burdens contribute to the total amount, and the tropospheric burden may be highly variable. Therefore it becomes necessary to fit the tropospheric and the stratospheric burdens separately. With a spectroscopic resolution being high enough (higher than the pressure broadened half-widths of the spectral lines under study), and an instrumental line shape being well-known and precisely modelled in the evaluation procedure, the measured spectral line shape can be used to retrieve some low resolved information on the vertical distribution of HCl.

Up to about 25 km, the line shape in the infrared is dominated by the pressure broadened Lorentzian shape. Above, the shape is mainly given by Doppler broadening being independent from pressure. No more information on the vertical distribution can be derived there. The method presented here considers the weighting function being different at different positions of the spectral line. Near to the line centre, the weighting function has its maximum in the lower stratosphere, whereas in the line wings it is in the troposphere. This study has been undertaken for measurements performed during field campaigns in the Arctic winter with a spectral resolution of 0.028 cm⁻¹ after apodization (for a description, see e.g. Adrian et al., 1991). For this spectral resolution, the stratospheric vertical distribution cannot be resolved.

Two series of test retrievals with synthetic spectra were performed. In both cases, the effect of the deviation of the tropospheric profile from the reference profile on the retrieval of the stratospheric burden of HCl is investigated. The first set of test calculations studies the retrievability of stratospheric HCl concentrations for the case that the total column amount, but not the distribution into troposphere and stratosphere is correctly assumed in the first guess profiles. The second set starts from first guess profiles with only the stratospheric column amount being correct. Finally, a similar study was performed for measured HCl spectra where all information on the tropospheric and stratospheric content had to be retrieved from the spectra themselves. All calculations were performed with the RAT (Retrieval of Atmospheric Trace gases) algorithm based on v. Clarmann (1990).

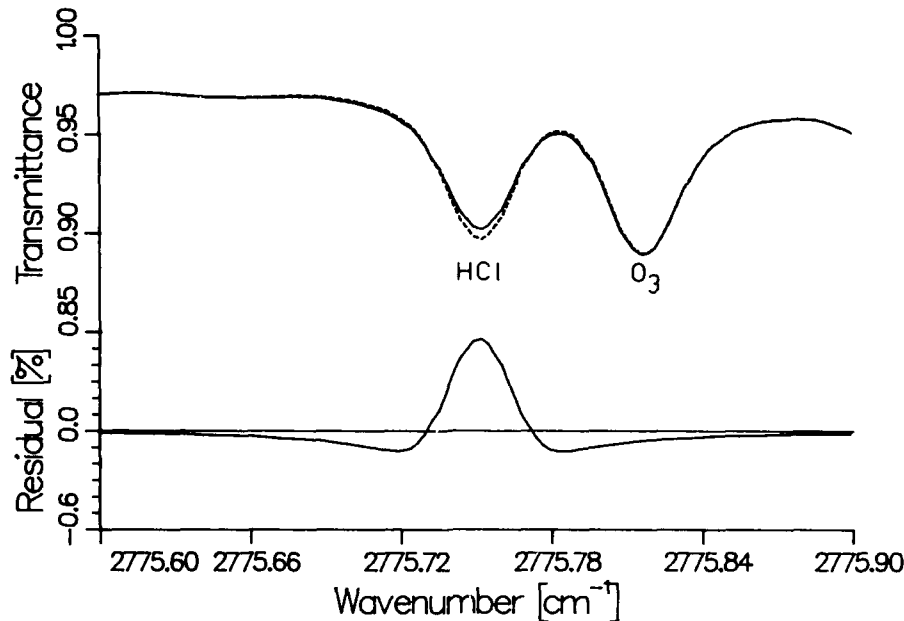


Figure 1. Comparison of two spectral HCl lines, belonging to the same zenith column amount. (Solid line = spectrum calculated from the reference profile; dashed line = spectrum calculated by increasing the stratospheric content by 17% and reducing the tropospheric one by 12.5%). The spectra are shown without noise.

Test retrievals

For the test retrievals, the best fit of a measured spectrum taken in Kiruna at March 12, 1992 under an observation angle of 12.3° was used as reference spectrum (Adrian et al., 1993). The spectra was taken at an observer altitude of 470 m above sea level. The apodized spectral resolution was 0.028 cm^{-1} using 'strong' apodisation following Norton and Beer (1976). Synthetic noise derived from the measurement corresponding to a SNR (related to the baseline signal between the lines) of 1200 ($\text{rms} = 7.9 \times 10^{-4}$) was added to the calculated spectrum. No other sources of errors (e.g. uncertainty of temperature or observation angle) or artefacts modifying the spectral line shape (e.g. phase errors) were considered.

For the first series of test retrievals, a set of first guess profiles were built as follows: the tropospheric profiles of HCl were scaled in a range of + to - 50 % and the resulting zenith column amounts (ZCA) were calculated. In a second step, the whole profile was scaled so that it corresponds to the ZCA of the reference profile. The HCl lines calculated from these vmr profile differ significantly in their spectral line shapes (see Fig.1). The residuals become comparable to those caused by noise when reducing the stratospheric deviations to 8 % and the tropospheric ones to 10 %.

Starting with the first guess vmr profiles, the stratospheric ZCA of HCl was retrieved by fitting the reference spectrum via scaling of only the stratospheric part of the vmr profile. Fits were accepted if the residuals all over the HCl line were less than 3 times the residuals produced by the noise. This describes the procedure which is followed when evaluating measured data. For practical reason it is necessary to reduce the effort, but proceeding such, it is borne in mind that not the whole information content of the spectra is exhausted. The results are summarized in Fig. 2. The highest deviation in the tropospheric ZCA is 30 % leading to a fit which is still acceptable in the sense of the given criterion. For this case, the error in the stratospheric ZCA is derived to be 20%, and the total ZCA calculated from this fit is wrong by 8%.

The second set of test retrievals starts from guess profiles with the stratospheric column amount being correctly assumed. By fitting the spectral line shape only via scaling the stratospheric part of the vmr profile, the stratospheric column amount is falsified by

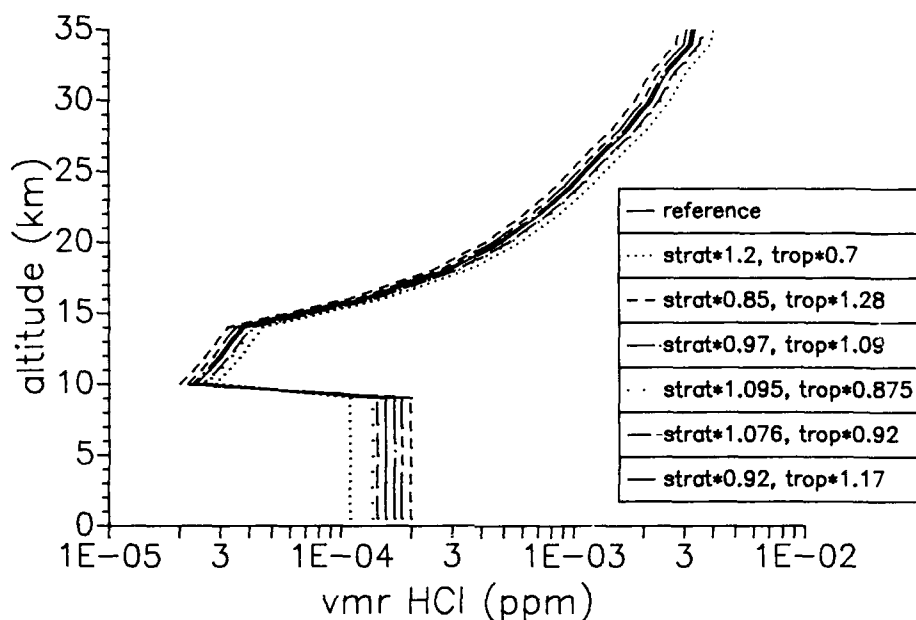


Figure 2. Results of the first set of test retrievals. Starting from first guess profiles with the same zenith column amount, but differing in tropospheric and stratospheric contribution, fits of a synthetic spectrum calculated from the reference profile (SNR = 1200, observation angle = 12.3°) (solid line) were performed. The best fit profiles with residuals less than 3 times the residuals produced by noise are shown.

20% for the highest tropospheric deviation being acceptable (= 30%) following the residual criterion. For this worst case, the total column amount is wrong by 9%. If the whole vmr profile is fitted, the highest deviation in the stratospheric ZCA is 16%, whereas the tropospheric deviation is reduced to 19% and the deviation of the total ZCA to 4 %.

Investigation of measured spectra

In order to investigate further errors or artefacts, the tropospheric and stratospheric HCl amounts were retrieved from a measured spectrum starting with a similar set of first guess profiles. The measured spectrum was chosen to be typical for the MIPAS-LM experiment during the EASOE campaign (Adrian et al., 1993). In a first step, first guess profiles were built which varied in their tropospheric part, whereas the stratospheric profiles were fixed to the best fit profile taken from the evaluation of the spectrum. The tropospheric profiles differed in absolute concentration (for profiles having a constant vmr within the troposphere) and in the shape of the tropospheric part. With this set of profiles, the spectral line shapes of the HCl lines at 2775.8 and 2925.9 cm⁻¹ were tried to fit. From the same acceptance criterion set up as for the test retrievals, the residuals had to be better than 0.5 % of the measured signal. The profiles were scaled as a whole by a multiplicative factor. For the profiles which fitted the line wings sufficiently well, a second step was added in which only the stratospheric concentration was fitted starting from the result of the first step. This was done by scaling the profile only above the tropopause. After this, the centre of the spectral line was described sufficiently well.

We found that the range for the stratospheric profiles to produce a proper fit was much narrower than that of the tropospheric profiles. The stratospheric column amounts varied within $\pm 9\%$ around the best fit one, whereas the tropospheric column amounts could vary by $\pm 26\%$ without making the fit much worse. In the same understanding, the total column amount can be derived to an accuracy of $\pm 4\%$. The profiles producing an acceptable fit are summarized in Fig. 3. For the accurate retrieval of the tropospheric content, the determination of the spectral baseline is of major importance. When narrowing the spectral interval which is evaluated and fitting the baseline simultaneously, the variabil-

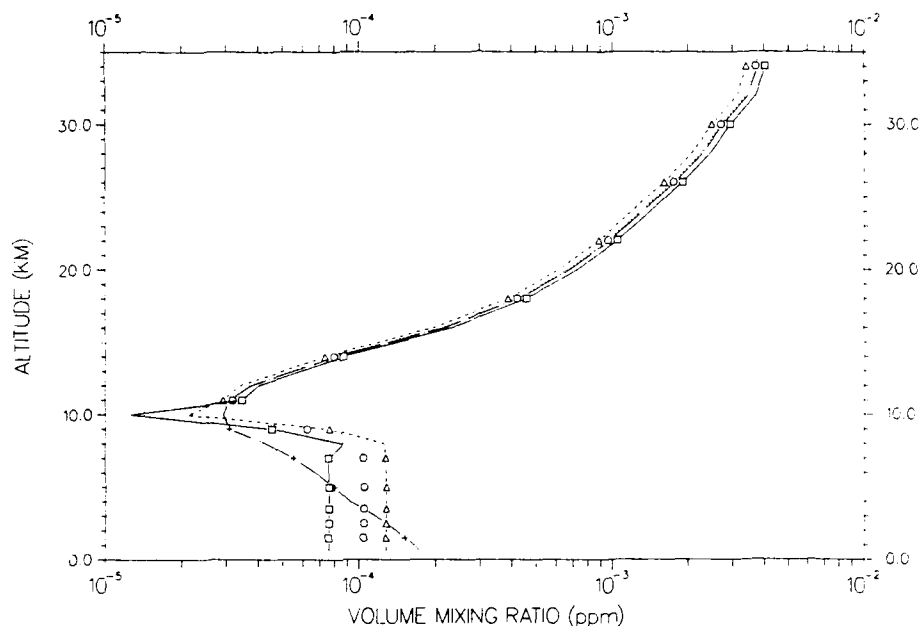


Figure 3. Results of the investigation of a typical measured spectrum

ity of the tropospheric zenith column amount producing a proper fit becomes more than 50 % without reducing the stratospheric accuracy.

Conclusions

This study shows that it is possible to distinguish between tropospheric and stratospheric HCl burdens in the case of only moderately resolved ground-based infrared spectra. Even with an apodized spectral resolution of 0.028 cm^{-1} , the integrated tropospheric and stratospheric content can be derived separately from the spectral line shape. An accuracy of 30 % for the tropospheric content and of better than 20 % for the stratosphere is obtained for spectra not influenced by other errors and artefacts than noise. When retrieving HCl column amounts from measured spectra, similar accuracy, even better for higher SNR, can be reached. A major difficulty is the correct description of the HCl line wings and the baseline, particularly in the presence of artefacts e.g. due to channeling or residual phase error effects. They reduce the accuracy of determining the tropospheric burden to about 50 %. The accuracy of the retrieval of the stratospheric burden remains nearly unaffected in this case. A study on the influence of the tropopause height on the accuracy of the retrieved zenith column amounts is in progress, as well as a similar study concerning the profile shapes of N_2O , HF, ClONO_2 , and HNO_3 .

References

- Adrian, G.P. T. Blumenstock, H. Fischer, L. Gerhardt, T. Gulde, H. Oelhaf, P. Thomas, and O. Trieschmann, Column Amounts of Trace Gases Derived from Ground-based Measurements with MIPAS During CHEOPS III, *Geophys. Res. Lett.*, 18, 783, 1991
- Adrian, G.P., M. Baumann, T. Blumenstock, H. Fischer, A. Friedle, L. Gerhardt, G. Maucher, H. Oelhaf, W. Scheuerpflug, P. Thomas, O. Trieschmann, and A. Wegner, First Results of Ground-based FTIR Measurements of Atmospheric Trace Gases in North Sweden and Greenland During EASOE, submitted to *Geophys. Res. Lett.*, 1993
- v. Clarmann, T., Die Bestimmung von Mischungsverhältnissen stratosphärischer Spurengase aus Emissionsspektren im infraroten Spektralbereich, *KfK report*, 4698, Kernforschungszentrum Karlsruhe, Germany, 1990
- Norton, R.H., and R. Beer, New Apodizing Functions for Fourier Spectroscopy, *J. Opt. Soc. Am.*, 66, 259 (1976)

RETRIEVAL OF TROPOSPHERIC PROFILES FROM IR EMISSION SPECTRA: INVESTIGATIONS WITH THE DOUBLE BEAM INTERFEROMETER SOUNDER (DBIS):

J.-M. Thériault*, G. P. Anderson, J. H. Chetwynd, Y. Qu⁺, E. Murphy,
V. Turner, M. Cloutier, and A. Smith
Geophysics Directorate, Phillips Laboratory / GPOA
Hanscom Air Force Base, MA 01731, USA

* DREV-Defence Research Establishment Valcartier
P.O. Box 8800, Courcelette, Québec, Canada, G0A 1R0

+ University of Wisconsin-Madison,
1225 West Dayton Street, Madison WI 53706 USA.

1. INTRODUCTION

In order to develop a method for the retrieval of temperature and water vapor profiles from IR emission spectra, the Defence Research Establishment Valcartier (DREV) has recently acquired a new device referred to as the Double input Beam Interferometer Sounder (DBIS). This sounder has been conceived to match the needs encountered in many remote sensing scenarios. It is a portable device composed of a Fourier spectrometer and one or optionally two telescopes that measures the atmospheric emission in the IR region from 3 to 20 μm at a spectral resolution of 1 cm^{-1} and at any prescribed viewing angles. In the summer 1992, the DBIS has been deployed successfully in a series of field experiments, producing spectral data of good quality for a variety of sky conditions. These spectral data are now being utilized as a guide for the development of an optimized inversion algorithm

2. EXPERIMENTAL CONSIDERATIONS

Essentially, the DBIS consists of one or optionally two 10-in. diameter Cassegrain telescopes, optically coupled to a double-input port Fourier transform spectrometer-interferometer and two detection units (InSb detector: 2-5 μm and MCT detector: 5-20 μm). The pointing capability of the instrument allows slant path measurements at any zenith angles from 0 to 360 degrees with a tilt adjustment of ± 10 degrees in azimuth and an accuracy of 0.1 degree. The spectrometer is a standard BOMEM MB100 field interferometer that uses corner reflectors rather than flat plate mirrors in the usual Michelson configuration. With such an interferometer (ideal case), two beams coming from different scenes can be optically combined and spectrally subtracted in real time. Basically, this arises from the fact that the modulated components of the two interferograms associated to each input port are out of phase. The development of a differential observation technique based on spectral subtraction with the DBIS is a major goal of our project. In this initial study, only preliminary tests of the dual beam technique have been undertaken. Instead, the field measurements performed so far have been done with the single beam configuration. In this case, the second telescope module has been replaced by a stable cold blackbody (liquid nitrogen). The methodology for the radiometric calibration of DBIS spectra is fully consistent with the solution given by Revercomb et al. (1988). In usual conditions of operation, the accuracy of the DBIS has been evaluated to be better than 0.4 K in terms of brightness temperature with an RMS noise component below 0.1 K almost everywhere in the usable portion of the 3-20 μm region.

From May to July 1992, in a series of field experiments organized by the Phillips Laboratory (Hanscom, AFB) at Ft. Devens annex in Sudbury MA, the DBIS has been run successfully in a wide variety of clear and cloudy sky conditions. One major objective of the experiment was the acquisition of coincident radiosonde and spectral data to be used as a support for the development and the validation of inversion algorithms. A typical example of atmospheric emission spectra (1 cm^{-1} res. apodized) recorded with the sounder in hot-dry conditions for zero zenith angles is shown in Fig. 1. Several atmospheric emission spectra recorded with the sounder have been compared to calculations with FASCODE (Clough et al., 1981; and Anderson et al., 1989) and MODTRAN (Berk et al., 1989) models. In both cases, the agreement is remarkably good. To a certain extent, these comparisons validate the experimental methodology developed for the sounder.

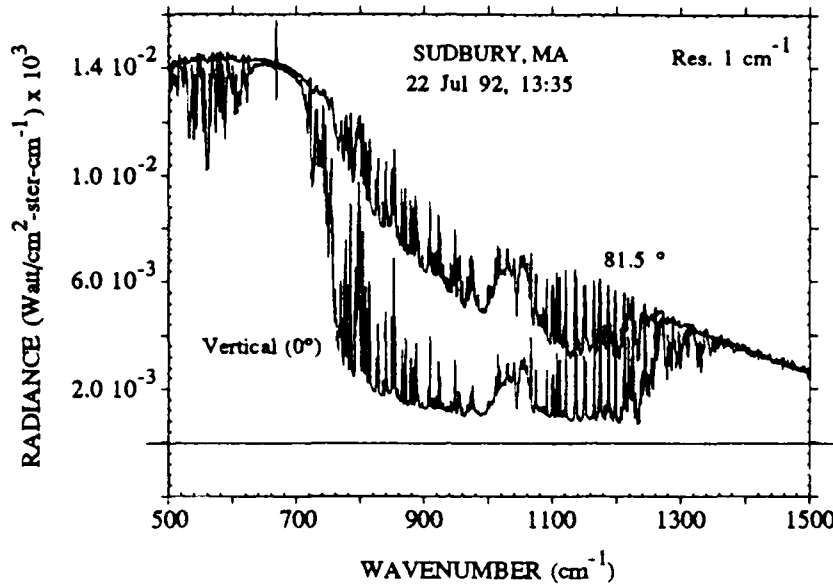


Figure 1. Atmospheric slant path IR emission measurements performed with the Double input Beam Interferometer Sounder (DBIS) in hot-dry conditions for two zenith angles.

3. GENERAL RETRIEVAL APPROACH

The optimized algorithm for the retrieval of temperature and water vapor profiles from DBIS spectra is not finalized yet. However, a definitive retrieval approach has been adopted and is now being developed. Essentially, the approach is based on a formulation often referred to as the minimum information method (see, for example, Fleming and Smith, 1972). The two main advantages of this formulation are: first, no a priori information on the statistics of atmospheric profiles is required and second, it allows the simultaneous retrieval of temperature and constituents profiles (Smith et al., 1991; and Isaccs 1988). The theory of this method can be formulated as follows. First, the problem is linearized by considering that the measured radiance $R(\nu)$ is a first order perturbation of the radiance $R^0(\nu)$ computed with first guess profiles of temperature $T^0(z)$ and absolute humidity $\rho^0(z)$ i.e.

$$R(\nu) = R^0(\nu) + \delta R(\nu) \quad (1)$$

A multi-variable Taylor expansion of eq. 1 in terms of the first guess profiles, evaluated at L predefined discrete levels leads to

$$\begin{aligned} \delta R(\nu) = & \left(\frac{\partial R^0}{\partial T_1} \right) \delta T_1 + \left(\frac{\partial R^0}{\partial T_2} \right) \delta T_2 + \dots \left(\frac{\partial R^0}{\partial T_L} \right) \delta T_L \\ & + \left(\frac{\partial R^0}{\partial \rho_1} \right) \delta \rho_1 + \left(\frac{\partial R^0}{\partial \rho_2} \right) \delta \rho_2 + \dots \left(\frac{\partial R^0}{\partial \rho_L} \right) \delta \rho_L \end{aligned} \quad (2)$$

where $\delta T_1, \delta T_2, \dots, \delta T_L$ and $\delta \rho_1, \delta \rho_2, \dots, \delta \rho_L$ represent the unknown profiles ($T_1 = T_1^0 + \delta T_1 \dots$) to be evaluated, R^0 and the related partial derivatives are computed using a radiative transfer model. Equation 2 may be written in a matrix form

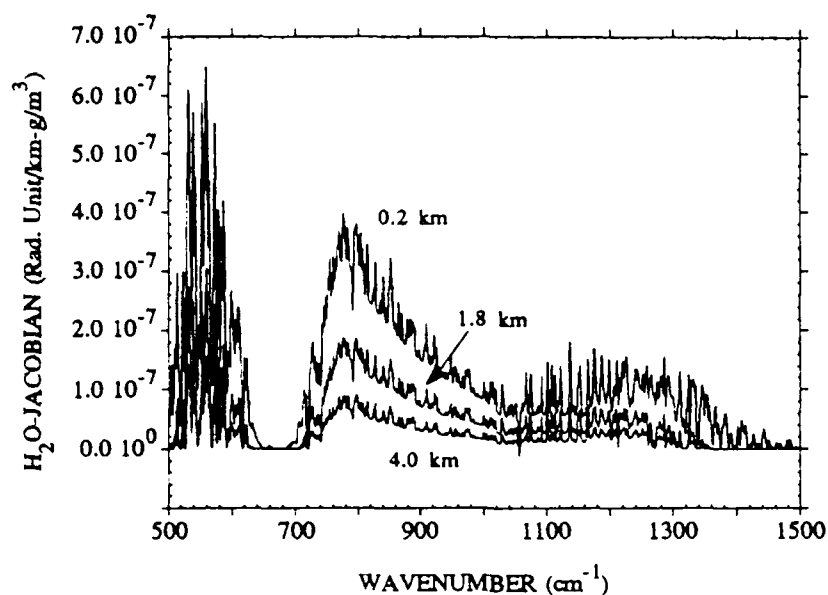


Figure 2. Water vapor Jacobian (normalized) computed with the MODTRAN2 model for three different levels for typical summer condition.

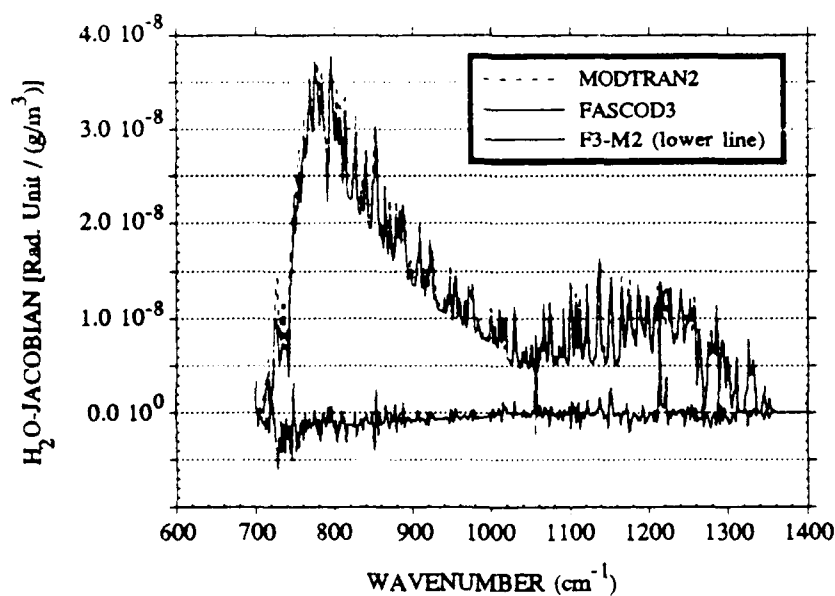


Figure 3. Typical comparison of the Jacobians (no normalization, 2 cm^{-1} res.) computed with FASCOD3 and MODTRAN2 models for the water vapor case: altitude 1.8 km.

$$r = K x \quad (3)$$

where r is the vector of spectral measurements, x is the vector of the unknown profiles (temperature and humidity merged) and K is the matrix of partial derivatives often referred to as the Jacobian. The solution of this overdetermined system of equations (~ 2000 spectral elements for ~ 80 unknowns) is given by the minimum information method as

$$x = [K^t S_e^{-1} K + S_b^{-1}]^{-1} K^t S_e^{-1} r \quad (4)$$

where S_e is a diagonal matrix having for elements the noise standard deviation associated with spectral measurements and S_b is a diagonal matrix composed of damping parameters adjusted for each level and each constituent. These damping parameters are introduced to stabilize the solution which oscillates when improperly adjusted. Because of the linearization constraint in the problem, eq. 4 provides only an approximate solution of the actual profiles. The final solution may be obtained by iterations on eq. 4 for which the K matrix is updated with the previous profile estimate.

There are two main difficulties encountered in the practical implementation of this method. First, there is no systematic procedure to optimize the matrix of damping parameters (S_b). Second, the method requires the evaluation of the Jacobian (partial derivatives) for each level and each parameter (temperature and humidity) at each step of the iterative procedure. In our approach, the Jacobian is evaluated numerically by computing the spectral radiance of an atmosphere that contains a small perturbation (2 K for temperature or 0.1 g/m³ for humidity) at a given level, subtracting it from the radiance computed without perturbation and dividing the result by the corresponding normalization factor. This operation involves a large number of radiance computations and consequently represents the main limiting factor of the method in terms of speed or efficiency. Figure 2 shows examples of Jacobian elements computed with the MODTRAN model for water vapor perturbations at three different levels. Overall, for sounding from the ground sensitivity peaks at the earth surface and decreases exponentially (approximately) with increasing altitude.

4. CONCLUDING REMARKS

Preliminary tests of the minimum information method using a prototype algorithm based on the FASCOD model have shown promising results. The benefit of using FASCOD as a forward model to compute the radiance and the K matrix is its accuracy. However, this approach is very inefficient in terms of computing time: a single retrieval can require days, even with a fast minicomputer. To avoid this limitation, we are now developing a fast retrieval algorithm that uses FASCOD for the radiance calculations and MODTRAN for updating the K matrix. This would reduce the computing time by several orders of magnitude. Figure 3 represents a typical comparison of the Jacobians computed with FASCOD3 and MODTRAN2 for the water vapor case at an altitude of 1.8 km. The very good agreement between the two models support the choice of MODTRAN for K matrix computations. The final step in the optimization of the method is the adjustment of the damping parameters required in the solution (eq. 4), which will be readily accomplished by a series of simulations performed with the fast retrieval algorithm.

REFERENCES

- Anderson, G. P. et al., 1989: FASCOD3 Update. Proceeding, 12th Annual Review Conference on Atmospheric Transmission Models, Geophysics Laboratory, Hanscom AFB, MA: 163-187.
- Berk, A., Bernstein, L. S., and Robertson, D. C., 1989: MODTRAN: A Moderate Resolution Model for LOWTRAN7. GL-TR-89-0122, Geophysics Laboratory, Hanscom AFB, MA 01732.
- Clough, S. A., Kneizys, F. X., Rothman, L. S. and Gallery, W. O., 1981: Atmospheric Transmittance and Radiance: FASCOD1B. Proc. Soc. Photo-Opt. Instrum. Eng., 277 : 152-166.
- Fleming, H. E. and Smith W. L., 1972: Inversion Techniques for Remote Sensing of Atmospheric Temperature Profiles. Harmon H. Plumb Ed. (Temperature: Its Measurements and Control in science and Industry), Pittsburgh, 4 : 2239-2250.
- Isacacs, R. G., 1988: Retrieval Technics for Atmospheric Path Characterization. Proc. Soc. Photo-Opt. Instrum. Eng., 928 : 136-164.
- Revercomb, H. E., et al. 1988: Radiometric Calibration of IR Fourier Transform Spectrometers: Solution to a Problem with the High-Resolution Interferometer Sounder. Appl. Opt., 27 : 3210-3218.
- Smith, W. L., Woolf, H. M. and Revercomb, H. E., 1991: Linear Simultaneous Solution for the Retrieval of Temperature and Absorbing Constituents from Radiance Spectra. Appl. Opt., 30 : 1117-1123.

A GROUND-BASED SYSTEM FOR MEASURING ATMOSPHERIC EMITTED RADIANCE AT HIGH SPECTRAL RESOLUTION

H.E. Revercomb, W.L. Smith, R.O. Knuteson, F.A. Best, R.G. Dedecker,
T.P. Dirkx, R.A. Herbsleb, J.F. Short, and H.B. Howell*

University of Wisconsin SSEC, and NOAA SDAB*
1225 W. Dayton Street, Madison, Wisconsin
(608) 263-6758

Downwelling spectral radiances will be observed routinely for the Atmospheric Radiation Measurement (ARM) program by a new complement of instruments. Accurate and spectrally detailed observations of the thermal emission from radiatively important atmospheric gases, aerosols, and clouds are crucial for realizing the overall objectives of the ARM program to improve the treatment of radiation and clouds in climate models. The importance of broadband infrared radiation to modeling climatic processes stems, of course, from its basic role in the energy balance of the atmosphere. Observations of the spectrum of infrared radiation also contain a great deal of remote sensing information on the instantaneous state of the atmosphere and on fundamental molecular spectroscopy.

The observed spectra will be used for many diverse applications, including identification and elimination of absolute errors in calculated clear sky spectra for known atmospheric states; evaluation and improvement of cloud radiation calculations; characterization of the distribution and evolution of effective cloud radiative properties; and studies of the state parameter changes associated with cloud formation, evolution, and dissipation. Analyses will involve both the direct use of measured radiances for comparison with accurate radiative transfer model calculations and the use of remote sensing techniques to derive atmospheric state parameters and effective cloud radiative and geometric properties. To capture the temporal and spatial properties of atmospheric weather systems and to sample climatological diversity, several high spectral resolution instruments will be deployed at each of the geographically distributed ARM Cloud and Radiation Testbed (CART) sites.

1. Background

The ARM Instrument Development Program (IDP) has supported the development of three high spectral resolution instruments with spectral coverage in the range from 4 to 20 microns, through a joint project between the University of Wisconsin (UW) and the University of Denver (UD). These instruments consist of the Atmospheric Emitted Radiance Interferometer (AERI), its extra-high resolution cousin the AERI-X, and the ultra-high resolution Solar Radiance Transmission Interferometer (SORTI). They are each named for the quantities they measure and for the technique employed, interferometry. All are built around commercially available Michelson interferometers.

This paper will focus on the first of these instruments to be operational at the CART site in Oklahoma, the AERI, which will make frequent spectral observations continuously, day and night. The higher spectral resolution instruments, which will follow shortly, are very important for diagnosing the spectroscopic origin of discrepancies between observed and calculated clear spectra identified with AERI and for identifying changes in trace constituents which are not strong enough to play significant roles in the greenhouse effect, but which can be important to changes in atmospheric chemistry. They are the prime responsibility of the UD. The AERI is an outgrowth of the High-resolution Interferometer Sounder (HIS) program at the UW.

2. Measurement capabilities

The spectral measurement characteristics of the AERI are illustrated in Figure 1 by the sample spectrum collected during the DOE Spectral Radiance Experiment (SPECTRE) conducted in Coffeyville, Kansas in the Fall of 1991. A spectrum of this type will be collected by each AERI every 10 minutes, 24 hours a day. The spectral coverage is essentially continuous from 3 to 18 microns, although regions with little spectral interest such as the strongest, and opaque, portions of the 6.3 micron water band are not shown. The spectral resolution is about 1 cm^{-1} , and is high enough to separately identify features caused by broad continua or cloud reflectance from those of absorption lines.

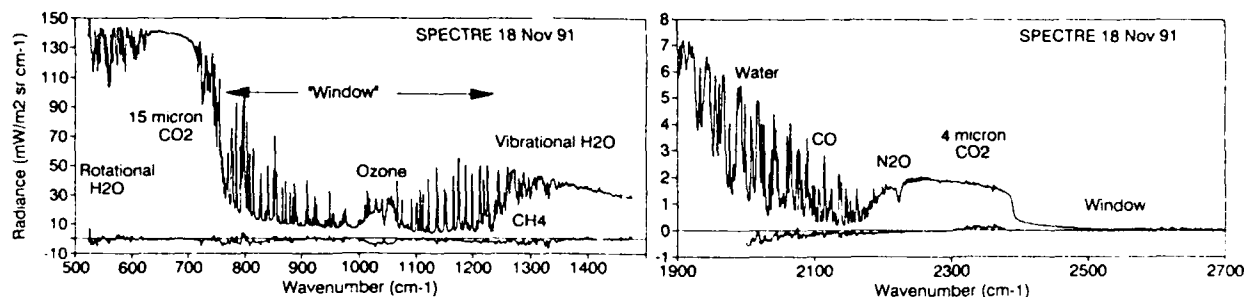


Figure 1. Sample spectra from the AERI longwave and shortwave bands. The difference of the measurements from spectra calculated with the Air Force Philips Lab line-by-line program (FASCOD3) is also shown.

To satisfy the requirements for verifying radiative transfer models and for remote sensing, the AERI will incorporate state-of-the-art radiometric performance. The absolute calibration accuracy is better than 1% of local peak radiances, and the calibration reproducibility and noise levels is less than a few 0.1%. Figure 1 demonstrates that this high level of performance is necessary to clearly identify differences between observed and calculated spectra (differences from FASCOD3 line-by-line calculations using balloon sonde temperature and water vapor concentrations are on the order of several percent of peak radiances).

3. The AERI Instrument

The AERI is an advanced version of the "Baby HIS", a prototype designed and fabricated at UW in 1989. AERI employs a commercially available interferometer (Michelson Series MB100 from Bomem, Inc. of Quebec, Canada), with corner-cube Michelson mirrors mounted on a common rocking arm supported by flex pivots. It has proven to be very rugged and dependable. The interferometer data is digitized, transferred to an IBM personal computer where it is Fourier transformed and stored, and then linked to another more powerful IBM personal computer for data analysis and ARM network transfers.

A pair of detectors in a "sandwich" configuration are used to give the broad spectral coverage desired, without the need for two cooling systems. The detectors are photoconductive HgCdTe for the longwave and InSb for the shortwave regions, operated at liquid nitrogen (LN₂) temperatures. The shortwave detector is placed in front of the longwave detector and absorbs the shortwave radiation, while transmitting about 50% of the longwave radiation. Initially the detectors are to be cooled using dewars, equipped with an LN₂ auto-fill system. Soon we expect that mechanical Sterling coolers will become cost effective for eliminating the need for routine LN₂ use.

The AERI radiometric calibration subsystem consists of up to three reference blackbodies, one hotter than ambient by 30-40 °C, one at ambient temperature, and one at liquid nitrogen

temperature. We will use the hot and the ambient reference sources for routine calibration to avoid the problems associated with operating cold references in humid environments. The LN_2 source will be used for occasional checks on the long term stability of the hot/ambient calibration. Periodic cycling through approximately two-minute views of the reference blackbodies and four-minute nadir sky views will yield a calibrated sky spectrum approximately every 10 minutes. All of the reference sources are high emissivity cavities built at the UW. The cavity temperature observations are referenced to NIST standards using a Guildline digital Platinum Resistance Thermometer. The AERI will be linked to the CART data system and operated remotely without the attendance of expert operators.

4. Field Campaigns and Results

The first AERI has seen extensive use in the field, since its completion late in 1991. It operated very successfully in three campaigns, including SPECTRE at Coffeyville Kansas conducted by DOE in conjunction with the NASA FIRE cirrus cloud study (11 Nov. - 7 Dec. 1991), the joint agency STORM-FEST program boundary layer site at Seneca Kansas (1 Feb. - 15 Mar. 1992), and aboard the ship Point Sur off Monterey California for Navy sponsored atmospheric refractivity observations (8-11 May 1992). We present a small sampling of results to illustrate applications for identifying deficiencies of radiative transfer models and for remote sensing.

An example of cloudy brightness temperature spectra from SPECTRE are shown in Figure 2. As found with HIS aircraft observations, clouds often do not behave as pure "blackbodies" for which the brightness temperature would be constant in the regions between absorption lines in the atmospheric window between 8 and 13 microns ($770\text{-}1250\text{ cm}^{-1}$). The low cloud spectrum in the figure is close to that of a pure blackbody cloud, but the middle cloud shows major deviations from that simple behavior. The deviations from blackbody behavior can be used to derive effective cloud particle properties.

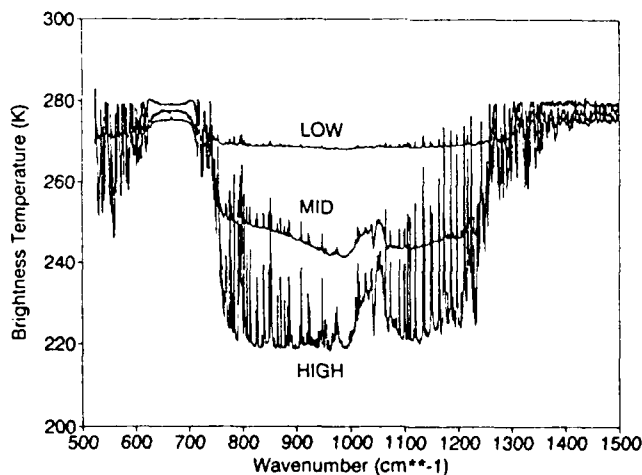


Figure 2. AERI measurements of the downwelling spectra of clouds showing deviations from pure blackbody emission.

Examples of differences between observed and calculated spectra are shown for selected water vapor features in Figure 3. The two STORM-FEST spectra on the left of figure 3 are in excellent agreement with calculations for the weak lines from $1100\text{ to }1225\text{ cm}^{-1}$, a region which consistently showed large differences before the recent update of the HITRAN line parameter data base. The right-hand side of Figure 3 illustrates substantial, consistent differences in a region where the water vapor continuum from foreign broadening needs substantial improvement. These are both regions where verification for the long paths and variable temperatures of the actual atmosphere is important.

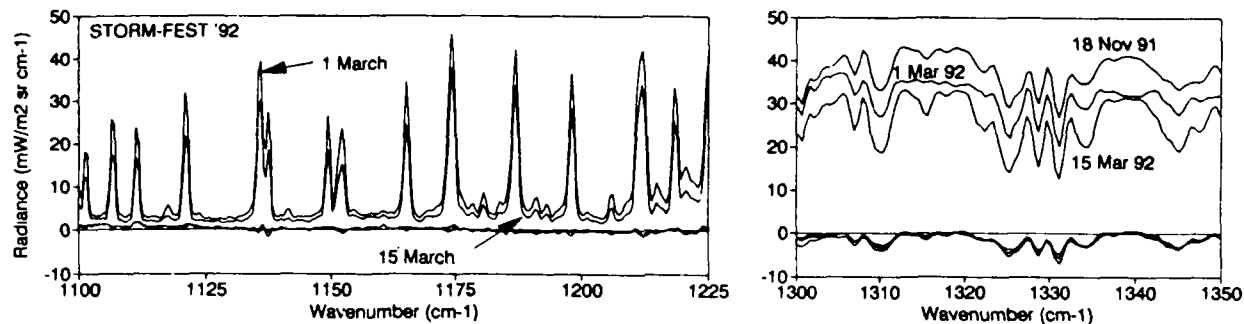


Figure 3. Examples from STORM-FEST of water vapor spectroscopy for which recent improvements have been made (left) and for which improvements are still needed (right).

The influence of atmospheric temperature structure on the downwelling radiance spectrum is illustrated in Figure 4, which shows a close-up of the 15 micron carbon dioxide band. The positive curvature of the general radiance trend between 625 and 710 cm^{-1} is indicative of a temperature inversion in the atmospheric boundary layer, as was present on March 1 during this observation. The negative curvature of the same region for the 15 March spectrum shows that the temperature decreased with altitude in the boundary layer. The excellent correspondence of the detailed features of the calculated and observed spectra also shows that the individual CO_2 lines contribute toward characterizing the vertical temperature structure.

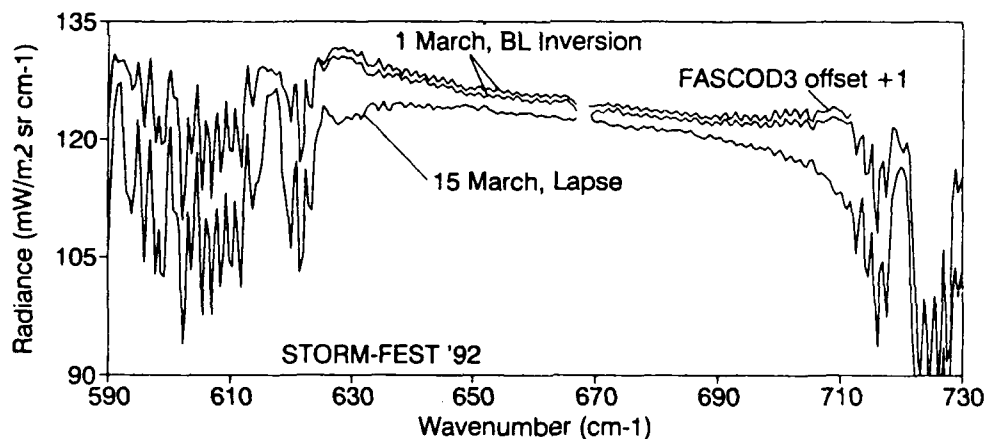


Figure 4. Spectra illustrating the strong sensitivity of high resolution downwelling radiances to the temperature lapse rate.

Finally, temperature and water vapor retrievals have been obtained from the 6 weeks of AERI STORM-FEST data and will be described in a separate paper by W.L. Smith.

5. AERI Implementation Plans

Implementation of the first AERI instrument to provide continuous high resolution spectra from the Oklahoma CART central facility is scheduled for late 1992. We expect that additional AERI's will be fabricated for the four boundary sites as soon as possible.

Tuesday, March 9, 1993

Constituents

TuB 11:10am-1:00pm
Salon F

Q. N. Liu, *Presider*
University of Utah

A Combined Lidar, Long-path Extinction and In-situ
Aerosol Experiment in Southern Ontario

Raymond M. Hoff

Center for Atmospheric Research Experiments
Atmospheric Environment Service

R. R. #1, Egbert, Ontario L0L 1N0 CANADA

Tel: (705)458-1141; FAX: (705)458-1143; E-mail: arqtgen@cid.aes.doe.ca

During August, 1992, a number of colocated optical and chemical experiments were performed at the Center for Atmospheric Research Experiments at Egbert (north of Toronto), Ontario, Canada. These experiments were symbiotic in that they were designed to address a number of atmospheric research problems of interest to Canada, including the need to determine: (1) the deposition velocity of polynuclear aromatic hydrocarbons and trace metals, (2) the size distribution and hygroscopic behaviour of particles affecting eastern Canadian visibility, (3) the evolution of nitrogen chemistry at nighttime, (4) the formation of particulate nitrate from gaseous precursors, and (5) the need to understand the photochemical particle production processes in early morning sunrise events. This work involved AES scientists as well as scientists from Germany visiting Canada under a bilateral exchange program. This paper will present the initial results from these experiments.

Under Annex 15 of the Great Lakes Water Quality Agreement, Canada is tasked with determining the loading of several trace elemental and organic species from air to the Great Lakes and the basin around the lakes. The deposition velocity of many of these species are not known and thus the calculation of the atmospheric input of lead, cadmium, selenium, arsenic, polynuclear aromatic hydrocarbons, for example, is not yet possible. The deposition of particles in general, however, is relatively well known and the problem reduces to one of determining the particle size spectrum of the aerosol particles and the fractionation of the chemical species on those particles -- a much less difficult problem to understand and measure than the flux of the particles themselves.

During this experiment, Active Scattering Aerosol Spectrometer Probes (PMS ASA30) were operated to obtain particle sizes of aerosols in the range 0.1 to 8 μm . Four different impactors (Berner and Andersen types) were run to sample particle mass, inorganic ions (sulphates, nitrates, etc.), trace element and polynuclear aromatic hydrocarbon as a function of particle size from 0.4 - 21 μm . A differential mobility analyser was operated to give the condensation mode aerosol growth in the range 20 - 180 nm. In addition, an in-situ photoemissive polynuclear hydrocarbon analyser was also run to give a high resolution time series of the concentration of these combustion produced organic.

At the same time, the recent Canada/U.S. on Air Quality has also required Canada to put in place by 1995 a program to protect visibility in the U.S. and Canada from transboundary aerosol flows. In the west of the U. S. such movement of aerosol may be from Canada to more pristine areas in the U.S. and in the east, the flows of aerosols (containing sulphates, for example) may occur the south to north direction. The particle sizing experiments required in the first project above are very relevant to the apportionment

of extinction required to assess the visibility issue. It was obvious that these two experiments would support each other. During the August project, measurements of extinction using long-path transmissometry (Optec LPV), scattering using an ambient air integrating nephelometer (Optec NGN-2), and scattering and extinction using a 1.064 nm lidar were made simultaneously with the particle sizing experiments. Figure 1 shows an example of a lidar time-height diagram from August 18. The explosive growth of the boundary layer at 1500Z (1000 AM EDT) is followed by cumulus cloud formation at the top of the boundary layer.

The period of rapid increase in the light scattering coefficient during the early morning was also seen the growth of condensation mode aerosols in the 20 - 180 nm region. This indicates that rapid photochemical production of particles was occurring at this time. In addition, the increase in the lidar backscatter coefficient shows that these particles also rapidly grew into the accumulation mode and became effective light scatterers. The particle growth phenomenon is also apparent in the larger particles (0.1 - 8 μm diameters) seen with ASAP probes.

The in-situ analysis of the polynuclear aromatic hydrocarbons and total elemental carbon on filters can be used to close the loop on the amount of scattering, absorption and extinction of these aerosols. At the time of the writing of this abstract, work is progressing on the analysis of the in-situ aerosol data and more current results will be presented at this meeting.

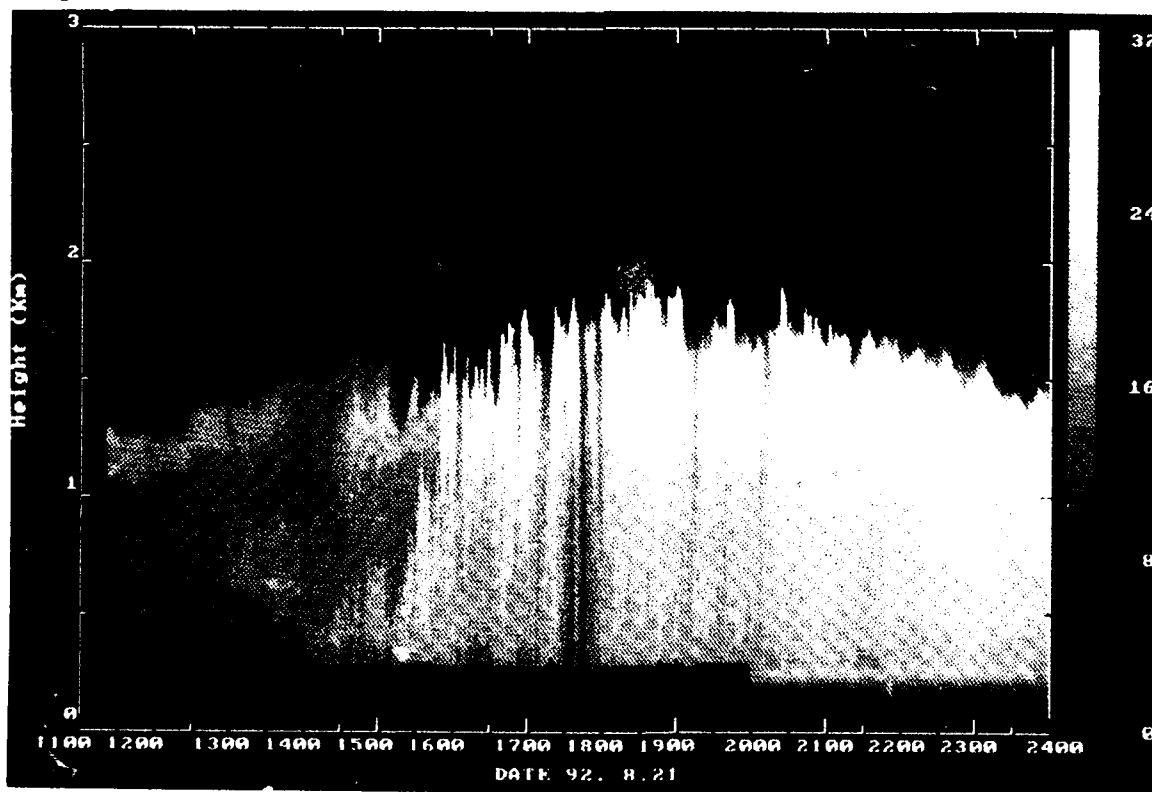


Fig. 1: Time-height crosssection of lidar backscatter, R, showing the height of the boundary layer at about 1.5-1.8 km and the rapid growth of scattering at 1500 Z.

Diode Laser-based Sensor System for Long-Path Absorption Measurements of Atmospheric Concentration and Near-IR Molecular Spectral Parameters.

Neil Goldstein, Jamine Lee, Steven M. Adler-Golden, and Fritz Bien
Spectral Sciences Inc.
99 South Bedford Street
Burlington, MA 01803-5169
(617)273-4770

Line-locked near-IR diode lasers and a simple retroreflector/telescope system were used for remote sensing of atmospheric constituents over long atmospheric paths. Figure 1 shows the experimental configuration used in preliminary measurements of atmospheric water vapor and oxygen with AlGaAs diode lasers. A prototype field sensor system currently under development shares the same basic configuration but incorporates interchangeable AlGaAs and InGaAsP diode-laser modules for monitoring a variety of atmospheric gases.

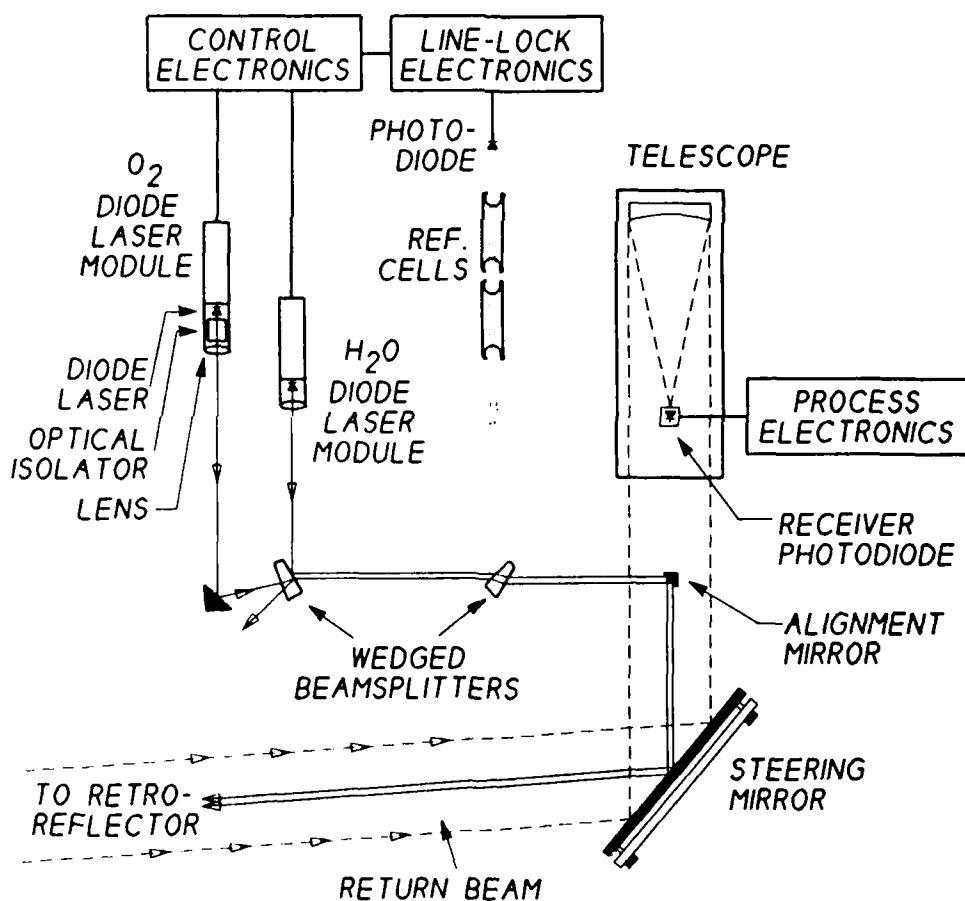


Fig.1

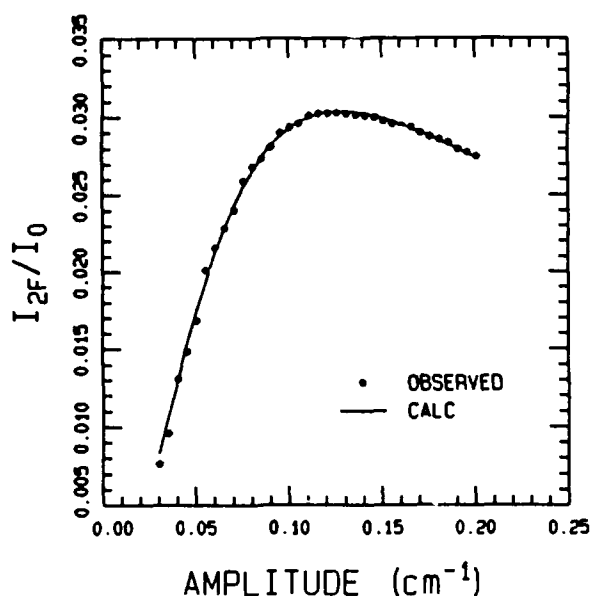


Fig.2

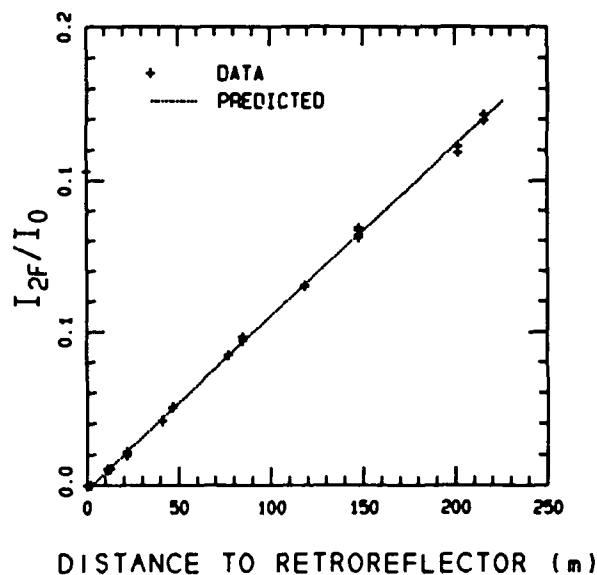


Fig.3

Absorption is detected via wavelength modulation and second harmonic detection. Figure 2 illustrates the variation of the second harmonic signal with the amplitude of modulation of the laser frequency about the line center. The data are for an atmospheric $^{16}\text{O}_2$ line at 13118.0 cm^{-1} . Theoretical fits of such spectra yield the line strength and pressure broadening parameters required to quantify the molecular absorption.

Figure 3 illustrates the quantification of $^{16}\text{O}^{18}\text{O}$ column density over distances ranging from 12 to 220 meters. Each data point corresponds to a measurement over a distinct atmospheric path defined by the stationary transceiver system and a movable retroreflector. Absorption of the P_9Q_8 line at 13097.3 cm^{-1} was quantified by the ratio of the second and first harmonic signals I_{2f} / I_{1f} at a fixed modulation amplitude. The I_{1f} signal at the line center is directly proportional to the transmitted intensity and independent of molecular absorption. The I_{2f} signal had a constant offset due to curvature in the diode-laser current-intensity relationship, and a component proportional to the absorption. Figure 3 shows the predicted dependence of the signal on path length based on literature values for spectral parameters and independent measurements of the temperature, laser modulation amplitude, and laser harmonic signals.

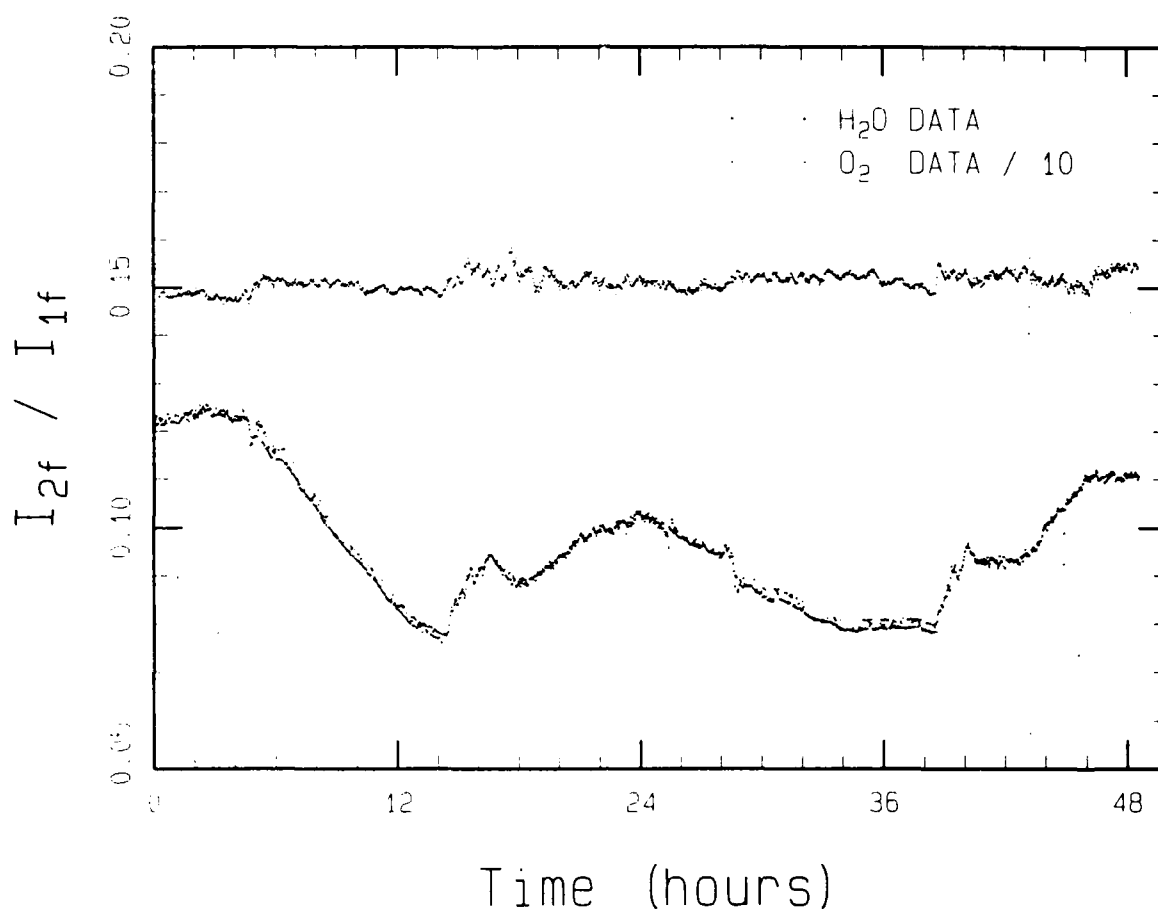


Fig. 4

Figure 4 shows simultaneous measurements of $^{16}\text{O}_2$ and H_2O over a common indoor path using two diode lasers. The absorbances at the line center were 0.6 and 0.08 respectively. Both species show diurnal and short-term variations in concentration. The range of oxygen absorption signals is consistent with the number densities associated with the $15^\circ\text{--}23^\circ$ temperature range observed during the two day test. The gross trends in the water column density were confirmed by periodic wet/dry bulb hygrometer readings.

Figure 5 shows 24 hour column density measurements of the weak $^{16}\text{O}^{18}\text{O}$ P_9Q_8 line absorption over short path lengths of 1.7 and 11.9 m. The absorbance at the line center was 1.2×10^{-4} for the lower trace and 9×10^{-4} for the upper trace. Data points were collected at 5 minute intervals with a 1 second time constant. The long term drift visible in the lower trace was due to electronics baseline drift and had a standard deviation equivalent to an absorption of 1×10^{-5} . The standard deviation on a 10 minute time scale was a factor

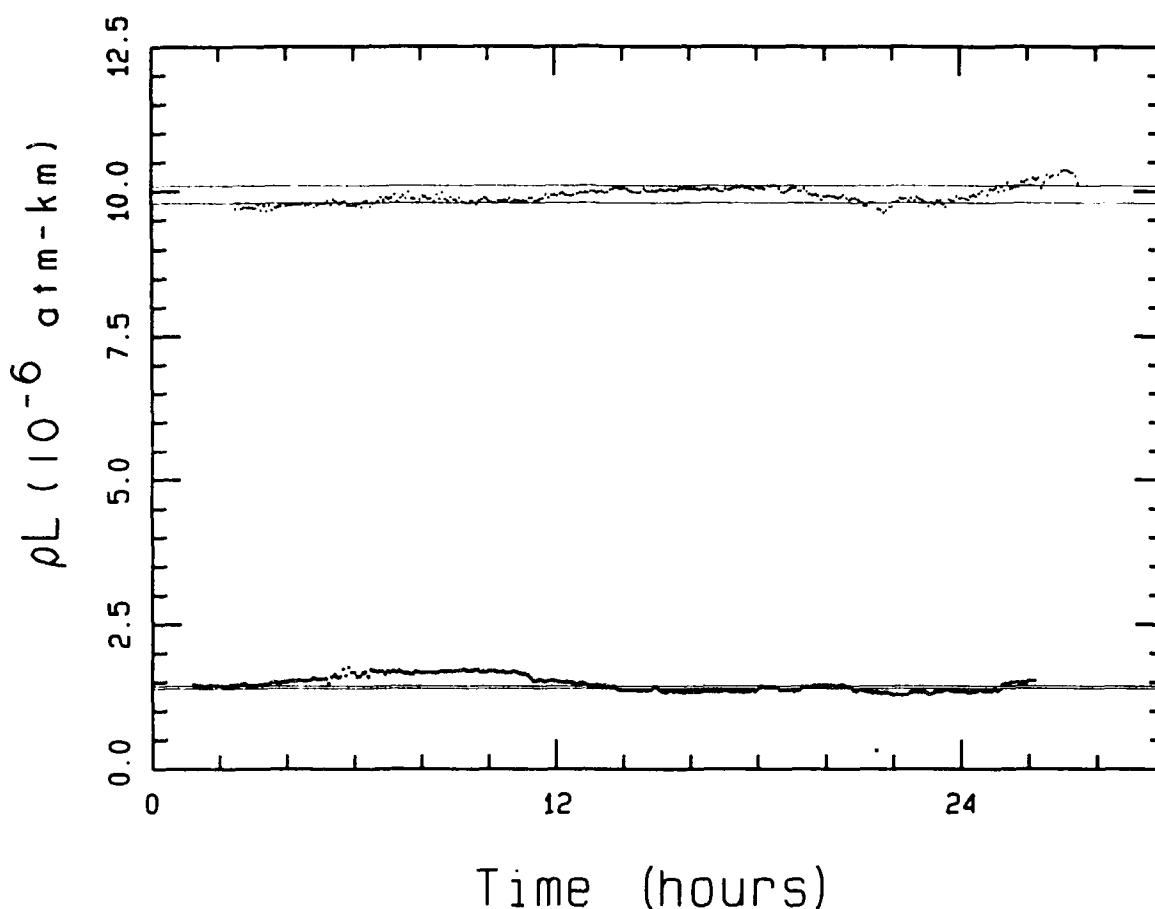


Fig. 5

of ten lower. The upper trace shows additional variation due to changes in oxygen density with temperature. The solid lines represent the range of column densities associated with the measured temperature variation over the 24 hour period.

In conclusion, these measurements of water and oxygen lines demonstrate accurate and sensitive remote monitoring of concentrations and spectral properties of atmospheric constituents. This technique can be applied to a large number of atmospheric trace species absorbing in the near-IR. Spectral Sciences is currently developing a prototype instrument for automated, unattended operation in field studies of atmospheric composition. Progress toward that end and the application of the technique with InGaAsP diode lasers will also be discussed.

N. Goldstein, S. Adler-Golden, J. Lee, and F. Bien, "Measurements of Molecular Concentrations and Line Parameters using Line-locked Second Harmonic Spectroscopy with AlGaAs Diode Lasers," *Appl. Opt.*, **31**, 3409 (1992)

DOPPLAR DETECTION OF THE STRATOSPHERIC HYDROXYL COLUMN ABUNDANCE

IWAGAMI, N. and INOMATA, S.

Dep. of Earth and Planetary Phys., University of Tokyo
Bunkyo-ku, Tokyo 113, JAPAN; phone: 3-3815-8020

Stratospheric OH column is measured with ground-based UV spectroscopy using the sun as a light source. The distinctive feature of our method is to utilize the Doppler shift of solar spectrum due to the solar rotation to discriminate the slight terrestrial OH absorption from prominent solar features. The method is schematically outlined in Fig.1. By comparing spectra measured on the east and west edges of the solar disk, it is possible to cancel out most of solar structures to make the terrestrial features evident.

The measuring apparatus consists of a 1.5 m double-path grating monochromator and a linear diode array detector with a

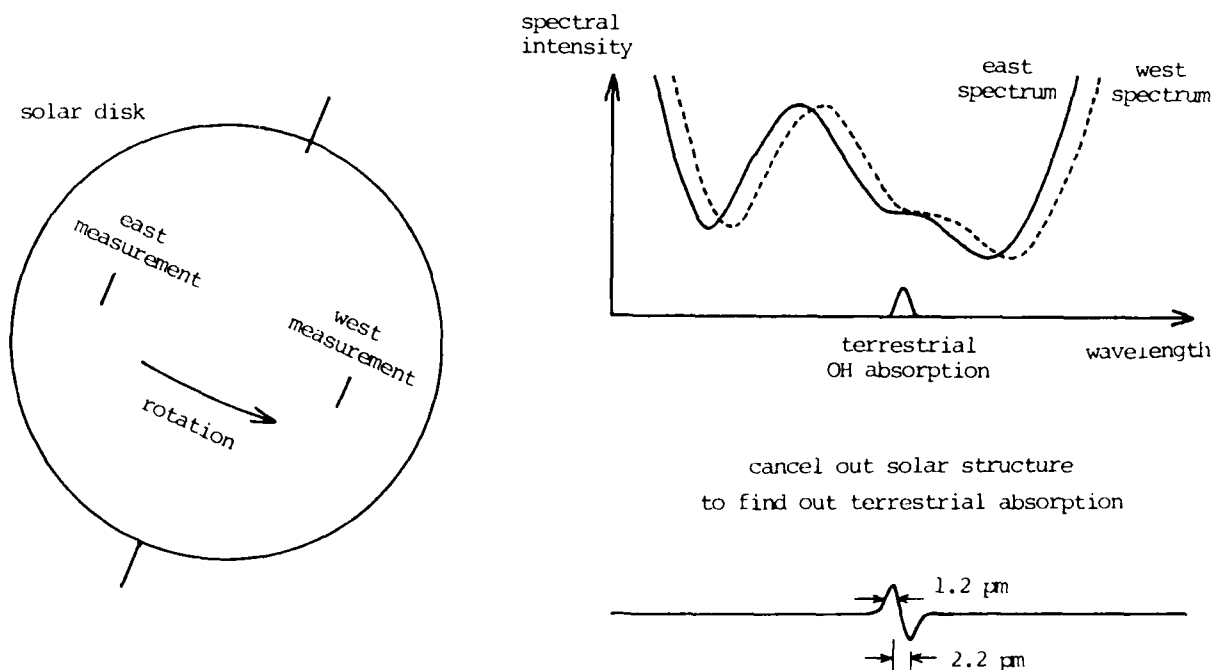


Fig.1 Method to detect terrestrial absorption using Dopplar shift

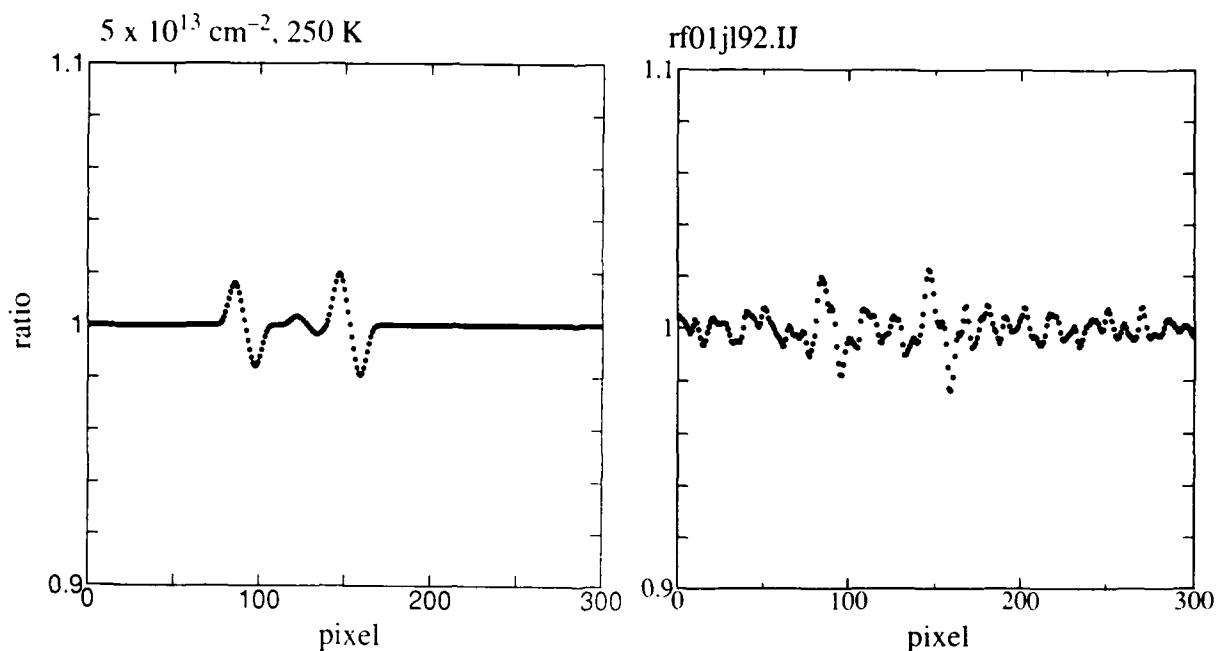


Fig.2 Calculated (left) and measured (right) east to west ratio spectra, 300 pixels for 55 pm in wavelength

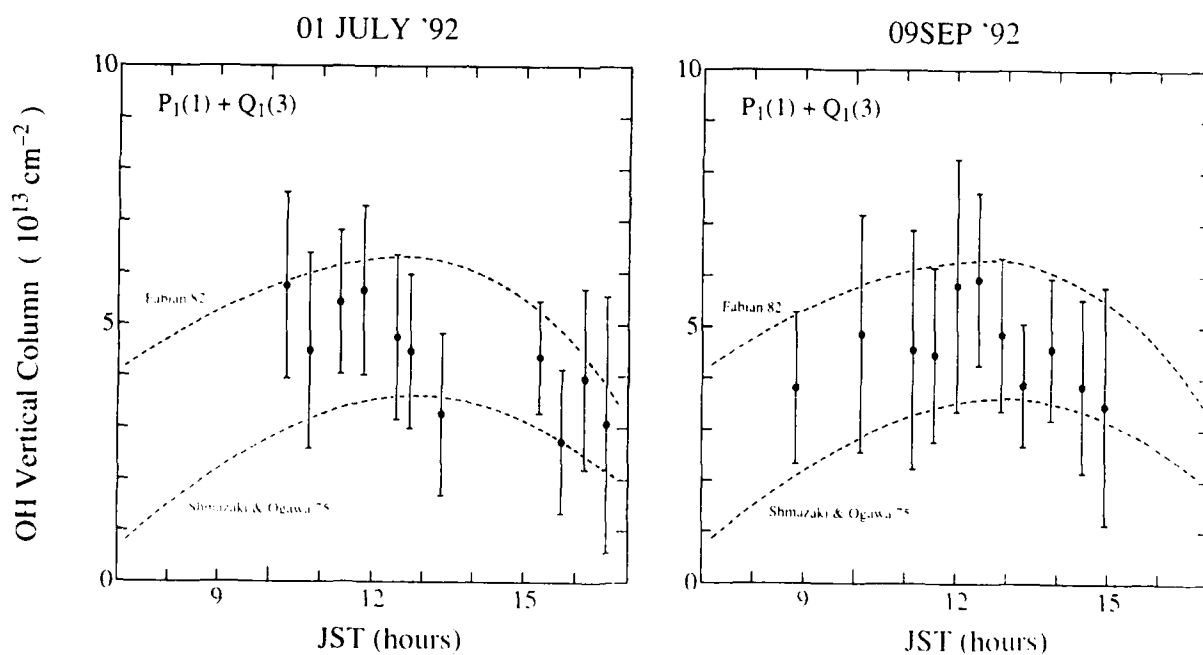


Fig.3 Comparison of measured and calculated diurnal variations of the vertical column

one-stage MCP. The OH column abundance is quantified by measuring absorptions due to $1P_1$ and $3Q_1$ lines of the $X^2\Pi - A^2\Sigma^+$ (0,0) band at 308 nm. Comparison of calculated and measured east to west ratio spectrum is shown in Fig.2. The wavelength difference between the east and west solar spectra is 2.2 pm, and the instrumental FWHM is 1.2 pm. The signatures due to the terrestrial absorptions are evident; those due to $3Q_1$ and $1P_1$ appear at around 90 and 150 pixel, respectively.

In Fig.3 diurnal variations of measured vertical column abundances are compared to model calculations of Fabian (1982) and of Shimazaki and Ogawa (1975). Those models predicted general tendencies seen in the measured diurnal variations; a broad mid-day maximum of about $5 \times 10^{13} \text{ cm}^{-2}$ and a gradual decrease in the afternoon. Those two models are for middle latitudes equinox conditions; columns in summer should be larger by 20-30%. Our understanding about the stratospheric OH chemistry appears to be not far from the truth. Ground-based measurements by Burnett (1989) show larger columns than the present report by 30-50%. The cause of the difference is not known at present.

references

- Fabian, P., Pyle, J.A. and Wells, R.J., Diurnal variation of minor constituents in the stratosphere modeled as a function of latitudes and season, *J. Geophys. Res.*, **87**, 4981-5000, 1982
- Shimazaki, T. and Ogawa, T., A theoretical model of minor constituents distributions in the stratosphere including diurnal variations, *J. Geophys. Res.*, **79**, 3411-3422, 1975.
- Burnett, E.B., Burnett, C.R. and Minschwaner, K.R., Periodic behavior in the vertical column abundances of atmospheric hydroxyl, *Geophys. Res. Lett.*, **16**, 1285-1288, 1989

Singular Value Decomposition Analysis of Ozone Profile Retrieval from High-resolution Interferometer Sounder Data

R.O. Knuteson, S.C. Lee, H.E. Revercomb, W.L. Smith

University of Wisconsin-Madison CIMSS
1225 W. Dayton St., Madison, WI 53706
(608) 263-7974

Introduction

In recent years the High-resolution Interferometer Sounder (HIS) program at the University of Wisconsin has made substantial contributions to the remote sensing of temperature and moisture vertical profiles from high spectral resolution infrared data.[Smith 1990] With the support of a NASA grant, the HIS program has been extended to include the development and validation of algorithms for the retrieval of trace constituents from HIS data. This paper is a summary of the analysis applied for the retrieval of ozone profiles (and column densities) from observed upwelling radiance obtained from NASA high altitude aircraft at about 20 km altitude. The analysis used makes use of the theory of singular value decomposition (SVD) in the solution of the under-determined nonlinear least squares problem posed by the data. Use of SVD is a powerful method for handling the ill conditioned inverse involved. The relevant theory and measurements are summarized and the result of application to observed data is provided below.

Theory

Infrared atmospheric radiation of the type measured by the HIS are reasonably well modeled by terrestrial atmospheric line-by-line transmittance models as functions of atmospheric temperature and constituent concentrations. The complete radiative transfer equation, of which these models are an approximation, is the appropriate starting point for the inversion of the unknown constituent profiles from the observed upwelling radiances. If a guess concentration profile

for the gas of interest is chosen and the temperature and all other concentrations are considered known, the correct linearized form of the radiance change, dR , induced by a fractional change in concentration, dQ/Q , is given by

$$dR = \int W_v(P) \frac{dQ}{Q}(P) d\ln P \quad (1)$$

where

$$W_v = \frac{Q}{g} P k_v \left[\int_{P_s}^P \frac{dT}{d\ln P'} \tau_v \frac{dB}{dT} d\ln P' + \tau_v \frac{dB_s}{dT} \Delta T_s \right]$$

and P is the pressure, Q is the concentration and k_v is the absorption cross-section of the gas, $dT/d\ln P$ is the temperature lapse rate, τ_v is the combined transmittance of all constituents, $B=B_v(T)$ is the Planck radiation function and "s" refers to the skin surface/air temperature difference. This equation has been shown to provide the exact radiance perturbation for sufficiently small deviations dQ/Q . [Lee, 1992]

Equation (1) can be written in the form $Ax=b$, where $A = W d\ln P$, $x = dQ/Q$, and $b = dR$. The least squares problem posed thereby is to obtain the solution x which minimizes the norm of the residual $\|Ax-b\|$. Since the solution is under-determined it is useful to enforce the additional constraint that the norm of the solution vector $\|x\|$ also be minimized. In the context of concentration profile retrieval, this means that the desired solution will be the smoothest solution which minimizes the norm of the residuals.

The determination of the solution vector will follow the singular value decom-

position procedure as outlined in Lawson and Hanson [Lawson and Hanson, 1974]. There exist orthogonal matrices U and V such that $A = USV^T$, where S is a diagonal matrix whose diagonal elements, s_i , are the singular values of A . The solution which minimizes both $\|Ax-b\|$ and $\|x\|$ is the pseudo-inverse solution given by

$$x = A^+ b = VS^+U^Tb$$

where $S^+ = 1/s_i$ for $i=1,\dots,k$, $S^+=0$ for $i>k$, and k is the rank of A . The value of k is determined by the relative size of the singular values and the noise level of the data.

Measurement

The HIS instrument has flown over 60 successful missions on NASA U2/ER-2 aircraft since 1986. The particular data used for this case study was selected from the Dec. 5, 1991 flight near Coffeyville, KS as part of the NASA FIRE II experiment. An average of just four clear sky spectra (less than 1 minute of data) was used in the analysis. Ground truth is represented by an ozone sonde launched from the Coffeyville airport on this day as part of the Spectral Radiation Experiment (SPECTRE). The in-situ ozone profile is shown in Figure 1 along with the midlatitude winter climatological ozone profile. The observed radiance is

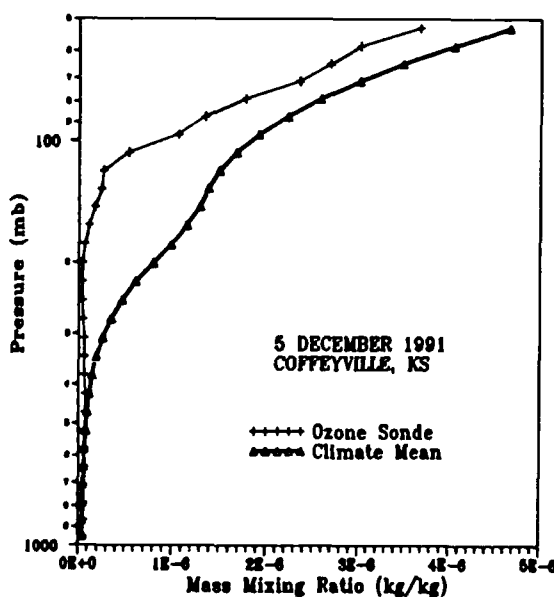


Figure 1. Ozone mixing ratio profiles.

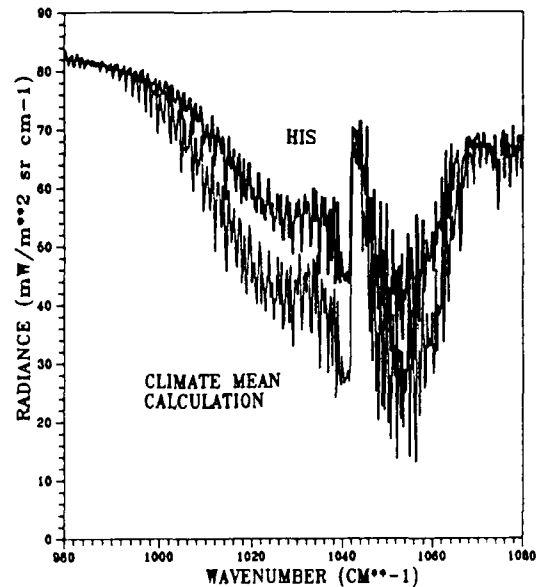


Figure 2. Upwelling infrared radiance measured by the HIS at 20 km altitude.

shown in Figure 2 along with the calculated spectrum obtained from the climatological profile. The observed radiation spectrum is at a spectral resolution of 0.3 cm^{-1} .

Results

To apply equation (1) to this case, the weighting function matrix W was constructed using FASCOD3P and the HITRAN92 database to compute the absorption cross-section, k_v , and the transmittance, τ , as a function of pressure at high resolution [Anderson, Rothman]. The Dec. 5th temperature and water vapor radiosonde profile was used as a first guess along with the climatological ozone profile. The weights W were then spectrally reduced to match the resolution of the interferometric measurements. A layering uniform in $\ln P$ was used with 30 layer boundaries between 50 and 1000 mb. Then a SVD algorithm was used to obtain U , V , and the singular values. Figure 3 shows the first three columns of V and the corresponding rows of U which represent the eigenvectors of the matrix $A^T A$ and $A A^T$, respectively. The solution $x = VS^+U^Tb$ was constructed for each potential solution k and the norms inspected.

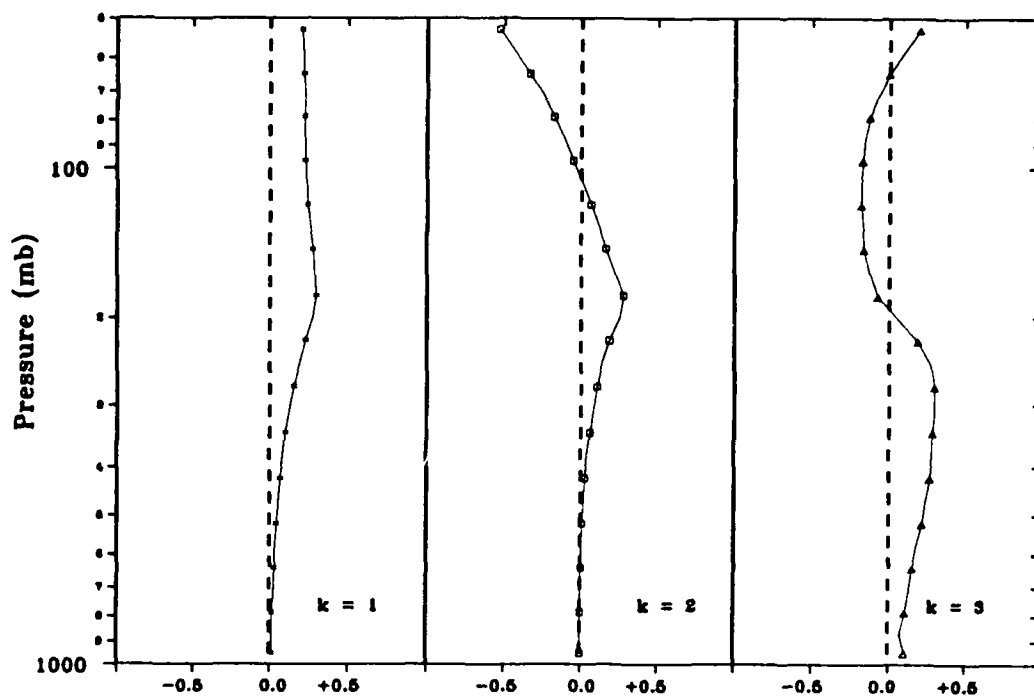


Figure 2a. The first three eigenvectors $V(k)$ of the singular value decomposition $A=USV^T$. All solutions dQ/Q are composed of linear combinations of these eigenvectors. Higher order eigenvalues have an increasing number of zero crossings.

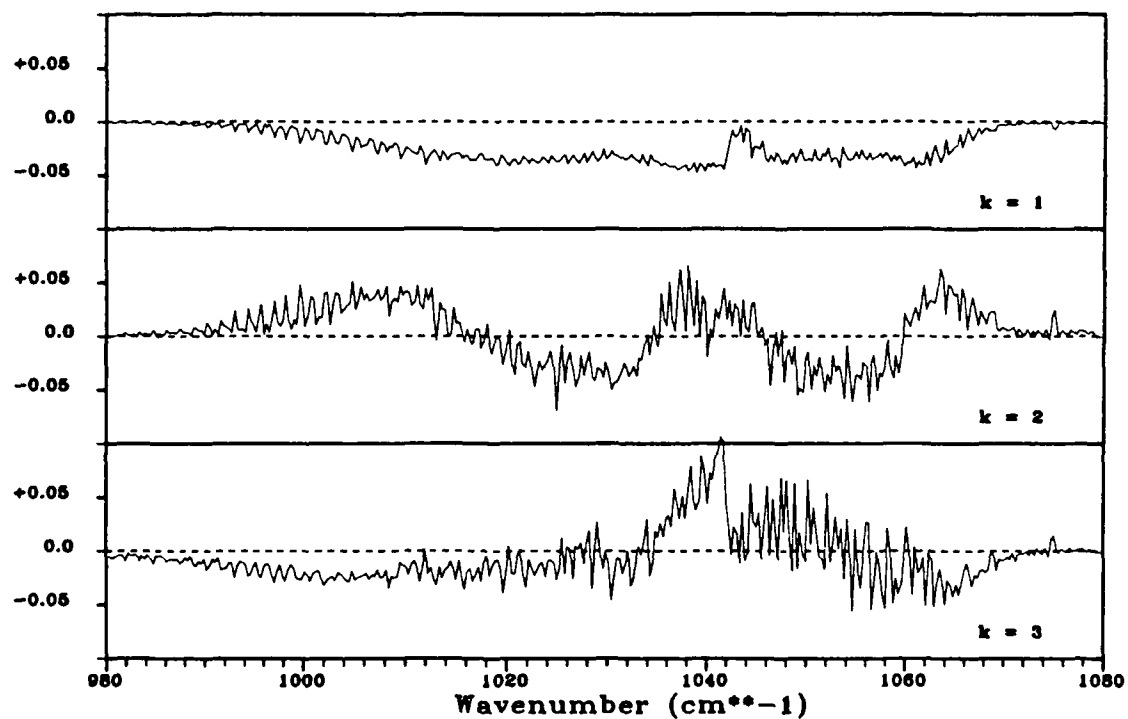


Figure 2b. The first three eigenvectors $U(k)$ of the singular value decomposition $A=USV^T$. These represent the dR spectral shapes which will be selected, via $U^T b$, to weight the eigenvectors $V(k)$ of the solution shown in part (a).

Note that the $k=1$ solution can be thought of as a multiplicative scaling, $f \cdot dQ/Q$, of the first guess by a constant, while higher order k values provide the profile shape details. Also note that the lower k values are less sensitive to random noise in the data.

The retrieval shown in Figure 4 was accomplished in two steps. The first step was to use the $V(k=1)$ eigenvector to scale the climatological guess until the radiance dR was reasonably small. Then the weights

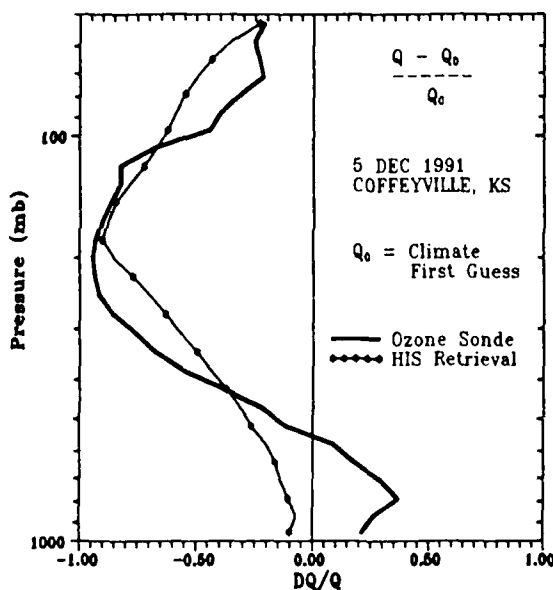


Figure 4. HIS dQ/Q retrieval.

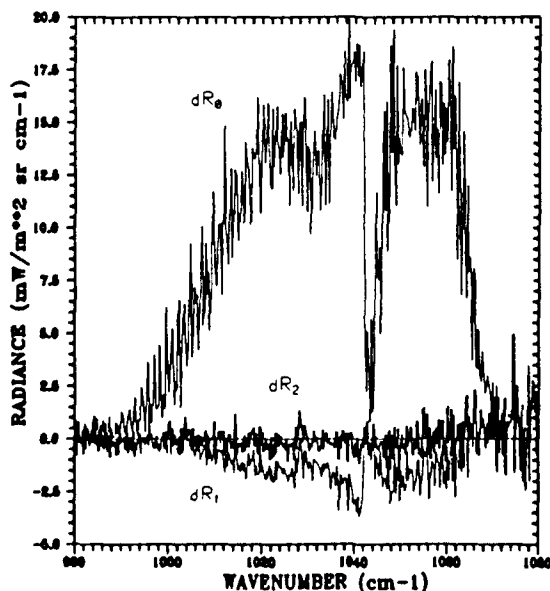


Figure 5. Initial and residual radiances.

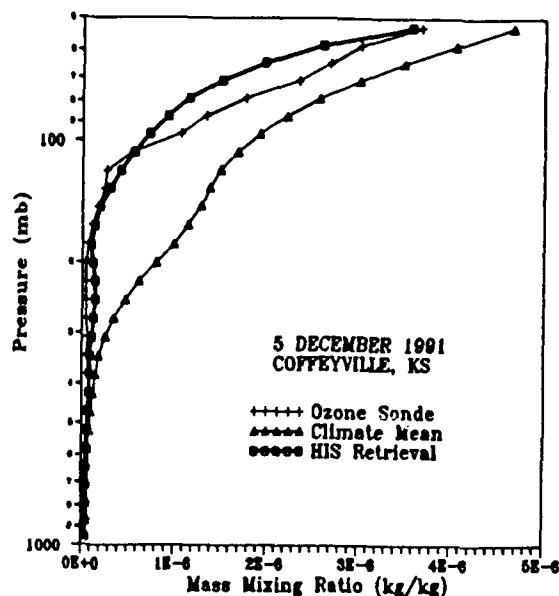


Figure 6. HIS ozone mixing ratio retrieval.

were recomputed and the $k = 3$ solution chosen using data in the range $980-1060 \text{ cm}^{-1}$. The residual, dR_2 , shown in Figure 5 is at the noise level, indicating the retrieval is satisfactory. The retrieval result is also compared as a mixing ratio profile in Figure 6 to both the initial guess and the in-situ ozone sonde profiles. The ozone total column density of the retrieval differs by less than 10% from the raob. This is compared to the 115% of the climatological guess.

References

Smith, W.L., et al. 1990. *GHIS - The GOES High Resolution Interferometer Sounder*. JAM, Vol 29 No. 12, Dec 1990.

Lee, S.C. 1992. *Simulated Retrieval of Atmospheric Ozone from Aircraft Interferometer Observations*. Masters thesis. University of Wisconsin-Madison.

Lawson, C.L. and R.J. Hanson, 1974. *Solving Least Squares Problems*, Englewood Cliffs, N.J.: Prentice Hall.

Anderson, G., et al. *FASCOD3P March 1992*, Phillips Lab, Hanscom AFB, Mass.

Rothman, L., et al. *HITRAN 1992*. Phillips Lab, Hanscom AFB, Mass.

Chlorine Nitrate and Nitric Acid Profiles in the Arctic Vortex Derived from Limb Emission Measurements with MIPAS-B

H. Oelhaf, T. v. Clarmann, H. Fischer, F. Friedl-Vallon, Ch. Fritzsche,
A. Linden, Ch. Piesch and M. Seefeldner
Institut für Meteorologie und Klimaforschung
Kernforschungszentrum/Universität Karlsruhe
Postfach 36 40
7500 Karlsruhe, Germany
Tel.: + +49-7247-82 59 48

W. Völker
Meteorologisches Institut,
Universität München

INTRODUCTION

Investigation of chemical and physical processes driving the composition of the polar stratosphere and being responsible for the formation of the ozone hole over the Antarctic continent each spring is a major topic of stratospheric research. In particular in the Arctic region knowledge of the distribution of primary reservoir and reactive species is rather poor. While several publications appeared on column amount measurements from ground and from aircrafts, no vertical distributions have been reported till now on some key reservoir molecules like ClONO_2 , HCl and N_2O_5 . Imbedded in the European Arctic Stratospheric Ozone Experiment (EASOE) the balloon-borne version of MIPAS (Michelson Interferometer for Passive Atmospheric Sounding) had two flights near the northern polar circle in January and March 1992. This report gives an overview on the large amount of information recorded and focusses on the analysis of vertical profiles of ClONO_2 and HNO_3 .

SYSTEM CONFIGURATION AND MEASUREMENT PROGRAMME

The MIPAS-B instrument was a novel cryogenic Fourier Transform Spectrometer which was especially designed to measure limb emission spectra of atmospheric trace gases during night or polar winter conditions from balloon-borne platforms. One of the most important requirements was to achieve sufficiently high sensitivity and spectral resolution to detect the weak emissions of atmospheric gases with an adequate signal-to-noise ratio. A second important requirement, resulting from the geometry of limb sounding, was a precise and commandable azimuth and elevation pointing device. The FTS was a rapid scanning interferometer using a modified Michelson arrangement which allowed a spectral resolution of 0.04 cm^{-1} (unapodized) to be achieved. The spectral regions covered were 770 to 970 cm^{-1} and 1170 to 1400 cm^{-1} . Solid carbon-dioxide cooling of the spectrometer and liquid-helium cooling of the detectors provided adequate sensitivity. The pointing system was designed to stabilize the line of sight in terms of azimuth and elevation. A three-mirror off-axis telescope provided good vertical resolution and straylight rejection. Calibration is based on high elevation and internal blackbody measurements. A more detailed technical description can be found elsewhere [1].

Previous successful flights with the MIPAS-B instrument were performed in 1989 and 1990 from mid-latitudes (Aire-sur-l'Adour, France, 44° N). Some results of

those flights are described elsewhere [2], [3]. Experience with the previous flights gave us confidence to operate the partly modified instrument also under the often unfavorable polar environmental conditions. The two flights of which part of the analysis is reported here were performed within the framework of EASOE on January 13 and on March 14/15, 1992 from Esrange, Sweden, at about 68° N latitude. Balloon operations were carried out by the Centre National d'Etudes Spatiales (CNES) balloon team together with the Swedish Space Corporation.

Both EASOE flights were performed when the stratosphere above northern Scandinavia was well inside the polar vortex. During the January flight the lower stratosphere was principally cold enough to enable NAT formation. From an average floating altitude of 31 km limb emission spectra were recorded at nominal elevation angles between -4.7 and $+3^\circ$ corresponding to tangent altitudes down to 9 km. The second flight in the night from 14th to 15th March 1992 brought a wealth of spectra from about 33 km floating altitude for two different azimuth directions. For one limb sequence the instrument was looking towards the centre of the vortex for the other towards its edge. Again tangent heights between the upper troposphere and nearly floating altitude were covered. Stratospheric temperatures in the aged vortex were above 200 K during this period.

ANALYSIS AND RESULTS

The housekeeping data were analyzed to evaluate the status of the instrument during the flight and to get elevation and azimuth pointing information. The onboard sensors for temperature and pressure as well as radiosoundings from adjacent stations were used to construct a multilevel atmospheric model. The interferograms were quality-controlled and phase-corrected using a short, two-sided interferogram. Deep space and blackbody measurements provided the offset and the gain required to calibrate the raw atmospheric spectra.

The calibrated spectra were analyzed by least squares fitting of simulated spectra to the measured ones. For this, the RAT (Retrieval of Atmospheric Trace Gas Profiles) algorithm [4] has been used. The first steps were to check the spectra for spectral resolution, pointing information, frequency shifts, and baseline offset. Whenever necessary, these parameters have been corrected by utilizing the information contained in the spectra as derived from the fitting results. The simulated spectra were calculated using most recent spectroscopic data [5] and a modified version of FASCOD2 [6] which permits also the calculation of CFCs and ClONO_2 from absorption cross-sections (G. Adrian and G. Wetzel, private communication). Trace gas profiles have been retrieved from a sequence of atmospheric spectra using the well-known onion peeling method.

For retrievals of HNO_3 profiles the ν_5 P branch regions was used because this spectral region offers rather reliable spectroscopic data and is only very slightly blended by lines of other molecules. ClONO_2 profiles have been retrieved by using the ν_4 Q branch after a preceding fit of the O_3 lines to account for their interference on the ClONO_2 feature.

The retrieval and error analysis strategies are described in detail by Clarmann et al., [7].

One of our most interesting results is the large amount of ClONO_2 in the lower stratosphere during our flight in March. This is already evident by visual inspection of the measured spectra (Fig. 1) and comparing them with previously performed measurements in mid-latitudes by other limb emission spectrometers (see e.g. [8]). Table 1 presents retrieved mixing ratios of ClONO_2 and HNO_3 from the

March data. The bulk of the exceptionally high ClONO_2 values between 16 and 21 km represents most of the total available chlorine (ClO_y) at these levels. While no other ClONO_2 profile measurements in polar regions have been reported up to now, the ClONO_2 column amount calculated from the vertical profile is consistent within the error bars with ground-based infrared measurements performed during the same period from Esrange [9].

REFERENCES

- [1] Friedl-Vallon, F., H. Fischer, T. v. Clarmann, C. Fritzsche, H. Oelhaf, C. Piesch, M. Seefeldner, D. Rabus and W. Völker: Limb Emission Spectroscopy with the Balloon-Borne Michelson Interferometer for Passive Atmospheric Sounding (MIPAS), submitted to Proc. International Symposium on Environmental Sensing, Berlin, Germany, 22-26 June 1992 (SPIE).
- [2] Oelhaf, H., T. v. Clarmann, F. Fergg, H. Fischer, F. Friedl-Vallon, C. Fritzsche, C. Piesch, D. Rabus, M. Seefeldner, W. Völker: Remote Sensing of Trace Gases with a Balloon-Borne Version of the Michelson Interferometer for Passive Atmospheric Sounding (MIPAS), ESA-Publ. SP-317, pp. 207-213 (November 1991).
- [3] Clarmann, T. v.: Retrieval of atmospheric O_3 , HNO_3 , CFC-11 and CFC-12 profiles from MIPAS-B-89 limb emission spectra, submitted to Applied Optics, Sept. 1992.
- [4] Clarmann, T. v.: Die Bestimmung von Mischungsverhältnissen atmosphärischer Spurengase aus Emissionsspektren im infraroten Spektralbereich, KfK-Report No. 4698, Kernforschungszentrum Karlsruhe GmbH, D-W-7500 Karlsruhe 1, P.O. Box 36 40 (1990).
- [5] Rothman, L. et al.: The HITRAN 92 database, accepted for publication by J. Quant. Spect. Radiat. Transfer, Vol. 48, (1992).
- [6] Clough, S.A., F.X. Kneizys, E.P. Shettle, G.P. Anderson: Atmospheric radiance and transmittance: FASCOD2, in Proceedings of the Sixth Conference on Atmospheric Radiation, May 1986, Williamsburg, Va. (American Meteorological Society, Boston, Mass., 1986) p. 141.
- [7] Clarmann, T. v., et al.: Retrieval strategy and error analysis for Arctic stratospheric profiles of O_3 , HNO_3 and ClONO_2 from the 1992 MIPAS-B limb emission spectroscopy experiment, in preparation.
- [8] Maguire, W.C., V.G. Kunde and L.W. Herath: Atlas of high resolution stratospheric limb infrared emission spectra, NASA, GSFC, Greenbelt, Maryland 20771, 1988.
- [9] Adrian, G.P., M. Baumann, T. Blumenstock, H. Fischer, A. Friedle, L. Gerhardt, G. Maucher, H. Oelhaf, W. Scheuerrpflug, P. Thomas, O. Trieschmann, A. Wegner: First results of ground-based FTIR measurements of atmospheric trace gases in north Sweden and Greenland during EASOE, submitted to Geophys. Re. Lett., Nov. 1992.

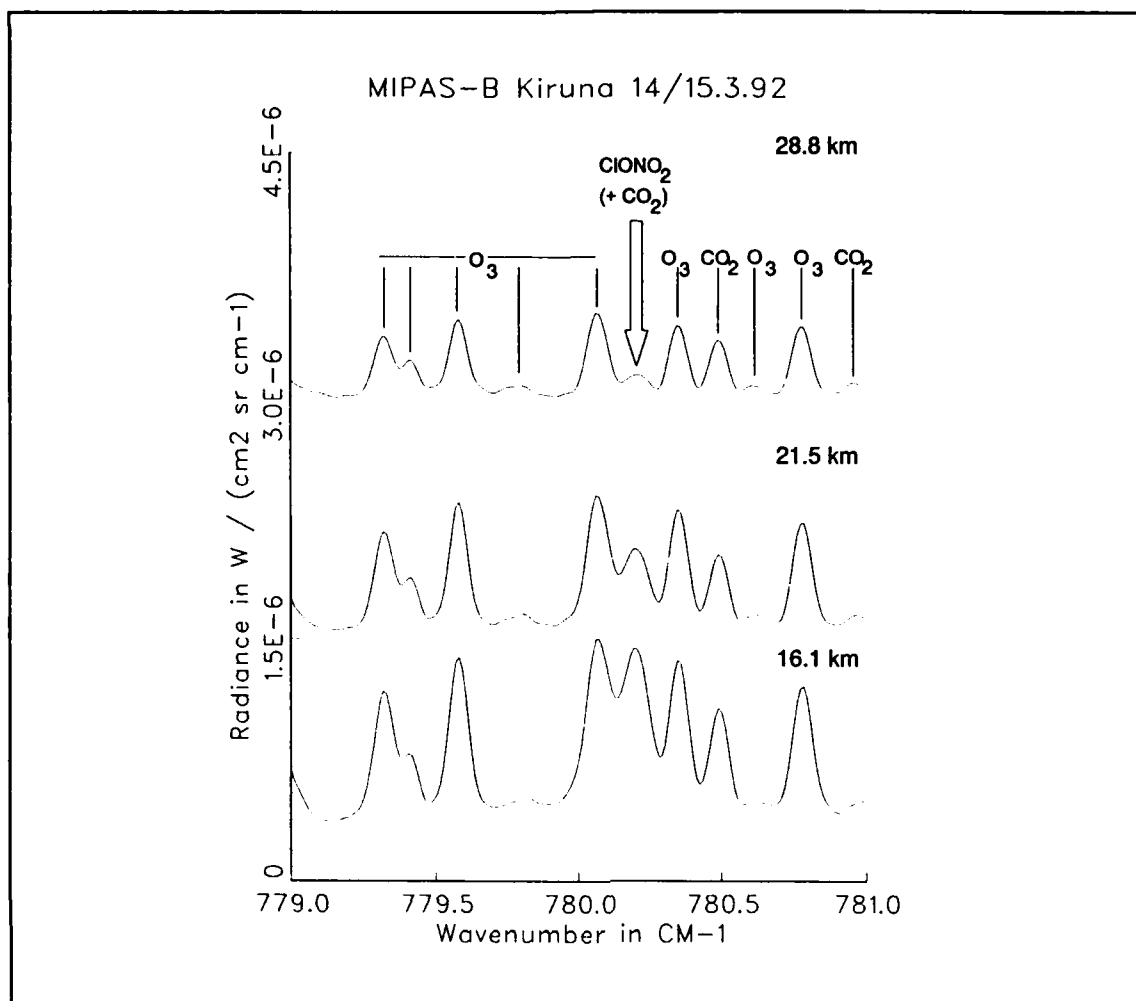


Fig. 1 Samples of a measured limb sequence of a narrow spectral interval recorded during the flight on March 14. The huge amount of ClONO_2 in the lower stratosphere is evident. Tangent heights are given in km.

Table 1 Retrieved mixing ratios of HNO_3 and ClONO_2 for the flight on March 14/15, 1992 at about 70°N latitude. The ClONO_2 values are at present still preliminary.

Altitude [km]	HNO_3 [ppbv]	ClONO_2 [ppbv]
31.7	0.9	0.4
28.8	2.1	1.2
25.1	4.1	1.6
21.5	6.1	2.2
18.9	8.8	2.6
16.1	5.1	2.6
14.5	6.4	1.5
11.3	2.7	0.05

Tuesday, March 9, 1993

Clouds and ECLIPS

TuC 2:30pm–5:40pm
Salon F

Allan I. Carswell, *Presider*
York University, Canada

Dual-wavelength CO₂ Lidar Method for Distinguishing Ice, Water, or Mixed-phase Clouds

Wynn L. Eberhard

NOAA Wave Propagation Laboratory
325 Broadway
Boulder, Colorado 80303
(303) 497-6560

I. Introduction

A dual-wavelength CO₂ lidar technique is proposed that shows excellent promise for discriminating between ice and water within clouds. It could potentially provide more quantitative measurements of mixed-phase clouds than the depolarization technique of shortwave lidars.

A technique useful in atmospheric studies uses shortwave lidar to observe depolarization of backscatter to identify the ice or water phase of clouds¹. (For this purpose, shortwave lidars are defined as those operating in or near the visible part of the spectrum where absorption within ice is small.) The depolarization from water drops, which are almost exactly spherical, is small (<3%). For ice, the refraction and internal reflection of rays at non-normal incidence cause depolarization ratios in backscatter of typically 50%. There are two complicating situations in this method. One is that multiple scatter in water clouds can introduce considerable depolarization. Another is that oriented plate crystals cause little depolarization if the lidar is aimed within a few degrees of vertical. A large number of researchers have used the depolarization method with shortwave lidar in cloud studies¹.

A CO₂ lidar operates at a selected laser line between 9 and 11.5 μm in the infrared. Ice particles absorb very strongly at these wavelengths, so reflection (with diffraction) from the surface facing the lidar dominates the backscatter. Depolarization ratios from ice clouds at these wavelengths remain small ($\sim 1\%$), so CO₂ lidars cannot use depolarization to identify water or ice phase in clouds². The proposed dual-wavelength method would enable a CO₂ lidar to discriminate between ice, water, or mixed phase clouds.

II. Method

The index of refraction of ice changes with wavelength in a manner quite different from water over much of the wavelength range of CO₂ lasers. This causes the backscatter

cross section β_i for ice clouds to increase substantially between 10.5 and 11.5 μm wavelength, whereas β_w for water drops decreases slightly. One attractive wavelength pair for this technique is 10.74 and 11.19 μm generated by a lidar operating with a $^{13}\text{C}^{16}\text{O}_2$ isotope. Simultaneous transmission and detection would be preferable, but rapidly alternating wavelengths between pulses with enough averaging to smooth variations from fluctuations in cloud density should also suffice.

The ratio of backscatter for water drops $B_w = \beta_w(11.19)/\beta_w(10.74)$ is shown in Fig. 1. The assumed drop size distribution for the Mie scattering calculations was a modified gamma distribution with mean radius r_m and non-dimensional width v varying over the range of values common in nature. B_w depends slightly on r_m and, to an even lesser degree, on v , but is limited to 0.87 ± 0.10 for this set of size distributions.

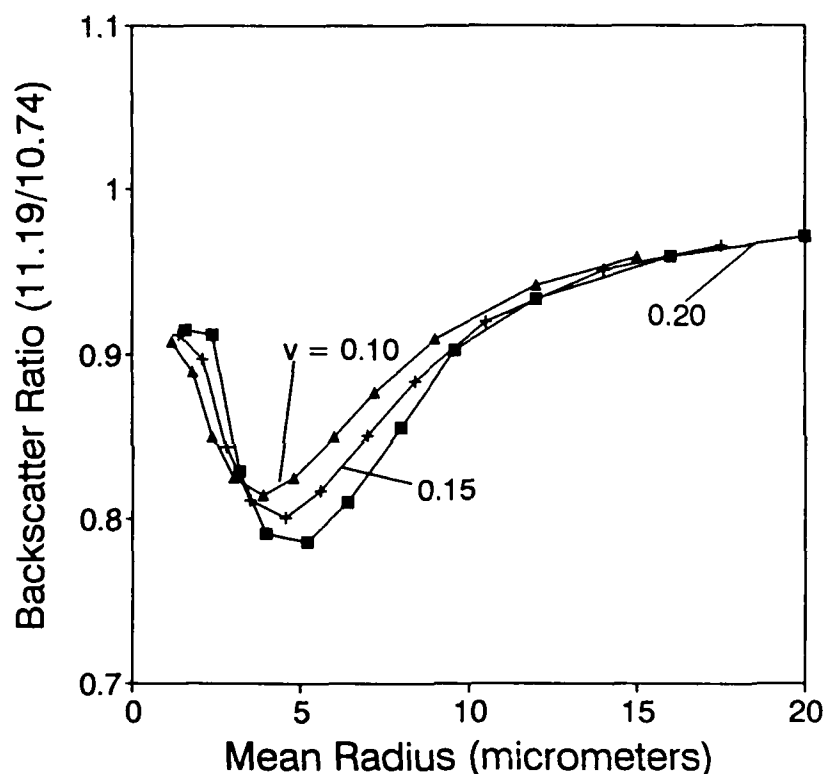


Fig. 1. Calculated ratio of backscatter cross section β_w at a wavelength of 11.19 μm to that at 10.74 μm for typical water cloud drop size distributions as a function of mean radius and non-dimensional width v .

The corresponding values of B_i , assuming larger particles typical of size distributions in cirrus clouds, appear in Fig. 2. B_i equals 2.83 except for a slight dependence on r_m and v for very small size distributions. Spherical particles were assumed in these calculations, which can be a poor approximation in many applications. However, the spherical assumption is adequate for determining the ratio of backscatter at two infrared wavelengths. Because backscatter at these wavelengths is dominated by reflection from the front surface, the refractive index of ice and not the shape of the particles primarily controls the ratio B_i .

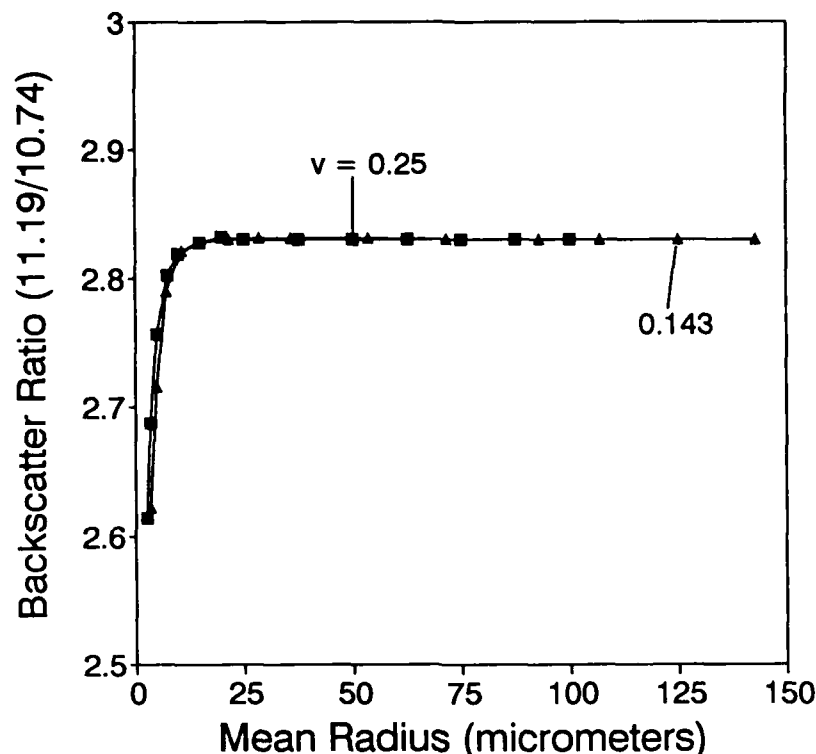


Fig. 2. As in Fig. 1, except for ice particles assuming spherical shapes.

One example for a nonspherical shape is backscatter from infinitely long cylinders with incident radiation normal to the cylinder axis. The calculated results for this geometry are similar to Fig. 2, reaching exactly the same limit of $B_i = 2.83$ for large cylinder radius. Further research is needed to confirm the predicted value of B_i for nonspherical particles.

A measurement of $B = \beta(11.19)/\beta(10.74)$ by a dual-wavelength lidar and comparison with the anticipated values for ice or water phase would show whether a cloud layer is composed of water or ice particles.

III. Discussion

The difference of a factor of three between B_i and B_w should be quite easy to observe. With reasonable care in calibration, a good measure of the fractions of ice and water particles (weighted by their backscatter cross sections) is also anticipated.

The wavelength dependence of extinction presents one potential source of error. Differences in molecular absorption (principally by water vapor and CO_2) can be calculated to good accuracy based on radiosonde data or climatological profiles. Wavelength differences in cloud extinction cross sections may become problematic for observations at large optical depths. Scattering calculations show similarities in the extinction cross sections at the two wavelengths, but the differences can't be neglected and do depend on particle sizes and phase. Current research is evaluating schemes to minimize the effect of these uncertainties, so measurement of B even at large optical depths can dependably reveal

whether ice or water particles dominate.

The effect of multiple scatter on the dual-wavelength technique is anticipated to be negligible. Multiple scatter contributes very little to the signal of a coherent CO₂ lidar, which has narrow receiver field of view, much wider forward diffraction peak from cloud particles than shortwave lidars, and strong absorption by cloud particles. Even if a CO₂ lidar uses direct detection with a large field of view, multiple scatter will be almost identical at the two wavelengths.

A dual-wavelength CO₂ lidar admittedly may be more complex than a polarization-sensitive shortwave lidar. However, CO₂ lidars have the practical advantage of complete eye safety, even when powerful enough to detect thin cirrus with good sensitivity.

The results of error analysis, including those arising from wavelength differences in extinction, will be presented at the conference. The performance of a few candidate wavelength pairs will be compared.

IV. References

1. K. Sassen, "The polarization lidar technique for cloud research: A review and current assessment," *Bull. Amer. Meteorol. Soc.* **72**, 1848-1866 (1991).
2. W.L. Eberhard, "Ice cloud depolarization of backscatter for CO₂ and other infrared lidars," *Appl. Opt.* **31**, 6485-6490 (1992).

APPLICATION OF OPTICAL REMOTE SENSING TO THE STUDY OF SURFACE FLUXES RELATED TO CLOUD FORMATION

W.M. Porch
Los Alamos National Lab.
Los Alamos, NM 87545
505-667-0971

W. Shaw
Pacific Northwest Lab.
Richland, WA 99352

1. INTRODUCTION

One of the largest uncertainties in climate change prediction is associated with cloud formation. A change in cloudiness small enough to be undetectable by satellites can have a large impact on global climate. It is therefore very important to accurately measure the meteorological parameters associated with cloud formation. These parameters include water vapor, cloud condensation nuclei (CCN), and vertical lofting of air to colder altitudes. For boundary layer clouds, the vertical velocities associated with lofting need only be a few centimeters per second. The vertical velocity can be induced by topographical features and/or surface heat flux. We will describe an experiment that used optical techniques to quantify surface heat flux changes related to boundary layer cloud formation and cloud shadowing effects and relate these changes to convergence associated with vertical velocities over a dry prairie grassland. The major result of this experiment showed that optical turbulence at different scales provides heat and momentum flux changes associated with cloud effects on a time scale fast enough to resolve cloud formation and movement. Standard tower measurements, because they are not spatially averaged, require tens of minutes for valid comparable estimates.

2. EXPERIMENT

An experiment was conducted in June 1992 over a region of prairie grassland (Boardman, OR Bombing Range) adjacent to an area of irrigated agricultural land. The experiment was part of the Department of Energy's Atmospheric Radiation Measurement (DOE/ARM) program to study regional fluxes and their importance to climate (Doran et al., 1993). Our role was to explore the use of optical techniques to provide spatially-averaged flux and wind convergence measurements and relate these to cloud variability (Porch et al., 1993).

Figure 1 shows the design of the experiment. Two triangles were constructed of optical cross-wind sensors. These systems use the optical turbulence moving across a light beam to estimate the cross-path wind speed (Ochs et al., 1976). One triangle consisted of three HeNe laser space-averaging systems spaced 200 m apart. The second triangle consisted of 3 cross-wind sensors with larger optics spaced 400 m apart. These larger optics systems avoid optical turbulence saturation effects at the larger distances. This system configuration allows the determination of convergence (the net wind flow into the triangle multiplied by the peripheral length divided by the area) on two scales. Conventional weather station towers were placed at each corner of the two triangles. This allowed the average wind components from each end of the triangle to be used to determine convergence for comparison to the optical cross-wind sensor values. Also, hemispheric pyranometers and net radiometers provided data at each weather station. These data were used to isolate the effects of clouds and cloud movement across the triangles. Information on cloud properties were also obtained continuously with an all-sky camera and a lidar-ceilometer.

Two scintillometer systems were set up parallel to the south path of the convergence triangles. These systems use optical turbulence at different scales to determine both the heat flux and turbulent energy dissipation. One system developed by Hill et al. (1992) uses two receiving apertures and both a HeNe laser and an infrared light emitting diode to provide turbulence at two scales. The second system developed by Thiermann (1992) uses parallel diode laser beams discriminated by polarization to provide data at two scales. The Hill system (NOAA/WPL in Fig. 1) was operated over a 100 m path with an average height of 1.53 m. The Thiermann system (Scintec in Fig. 1) was operated over a 100 m path with an average height of 1.16 m. The data collected with both the optical flux systems and the convergence systems were recorded digitally as 1 minute averages.

3. RESULTS

Since the June, 1992 experiment is only recently completed, the results presented here are preliminary. We will concentrate on the data taken on 14 June. This was one of the few days with well defined cloud shadows (most days were either clear or dominated by uniform cirrus). Also, winds were relatively light. Stronger winds from the southwest appear to interact with local topography to generate a net divergence (downward wind velocities). This day showed relatively little net convergence and good agreement between convergence measured at 200 and 400 m scales. This implies that the larger values of convergence were generated by structures larger than 200 m. There was also a strong correspondence between convergence and vertical velocities determined with a high frequency Doppler acoustic sounder (Coulter et al., 1992) at heights of 17, 35, and 120 m (Fig. 2).

The effects of cloud shadows were evident in the pyranometer and net radiometer data. These showed that at times clouds shadowed the triangles and at other times only over one or two corners of the triangles. When all three corners were affected the north corner was shadowed first. This is consistent with flow from the north measured at the surface and low level puffy clouds observed during the day. The major shadowing events occurred at about 11:00 and 13:40 PDT. It is important to point out that even though the clouds shadowed the triangles they did not necessarily pass directly over the triangles. This allows the separation of shadowing effects and dynamical effects associated with the clouds.

Figure 3 shows the heat flux determined from the two optical turbulence systems and 30 minute values determined from the tower measurements. Both optical systems show the 11:00 and 13:40 PDT cloud shadowing events in detail that is not possible from the tower measurements. Though the heat flux values from the systems compare closely for values below about 150 W/m^2 , above this value the two systems differ consistently by about 10%. The higher values are derived from the NOAA/WPL system (solid line). The two systems differ in the Monin-Obukov similarity parameters they assume, and this difference may be the result. Comparisons have not been conducted over enough of the data set to show a clear distinction between the two systems. Figure 4 shows the turbulent energy dissipation rates (m^2/s^3) determined by the two optical systems (Scintec system dashed line) and at the tower. Unfortunately, during this period the winds were relatively light and from a direction (East) that may have contaminated the turbulence measurements on the tower with the wake of the tower itself. This, however, points out another advantage of the optical systems.

4. REFERENCES

- Coulter, R.L., W. Gao, T.J. Martin, J.D. Shannon, J.C. Doran, J.M. Hubbe and W.M. Shaw, 1992: Evolution of the Lower Planetary Boundary Layer Over Strongly Contrasting Surfaces, *Third Symposium on Global Change Studies*, American Meteorological Society, Atlanta, GA, Jan. 5-10, 1992.
- Doran, J.C., F.J. Barnes, R.L. Coulter and T.L. Crawford, 1993: Boundary Layer Structure Over Areas of Heterogeneous Surface Heat Fluxes, *Fourth Symposium on Global Change Studies*, American Meteorological Society, Anaheim, CA, Jan. 18-21, 1993.
- Hill, R.J., G.R. Ochs and J.J. Wilson, 1992: Measuring Surface-Layer Fluxes of Heat and Momentum Using Optical Scintillations, *Boundary Layer Meteorology* 58, 391-408.
- Ochs, G.R., S.F. Clifford and T-I Wang, 1976: Laser Wind Sensing: the Effects of Saturation of Scintillation, *Applied Optics*, 15, 403-408.
- Porch, W.M., F. Barnes, M. Buchwald, J. Stephens, J. Archuleta and K. Kunkel, 1993: Applications of Spatially Averaging Optical Techniques to the Study of Short-Term Flux Changes Associated With Clouds, *Fourth Symposium on Global Change Studies*, American Meteorological Society, Anaheim, CA, Jan. 18-21, 1993.
- Thiermann, V., 1992: A Displaced-Beam Scintillometer for Line-Averaged Measurements of Surface Layer Turbulence, *Tenth Symposium on Turbulence and Diffusion*, American Meteorological Society, Portland, Or, Sept. 29- Oct. 2, 1992.

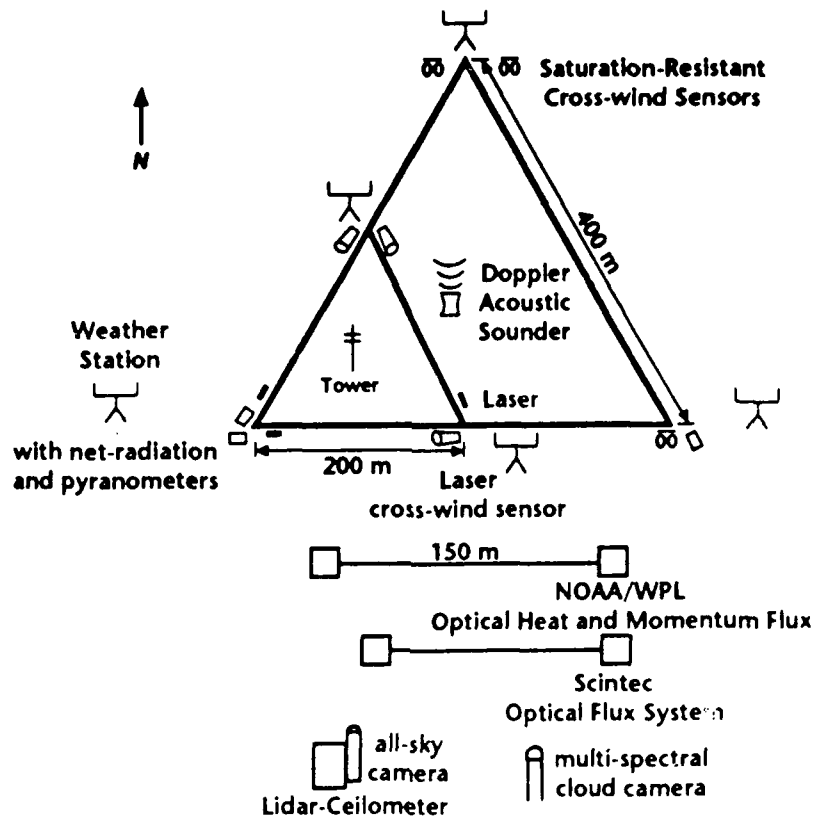


Figure 1. Measurement design for ARM surface flux experiment in Boardman, Oregon 1992.

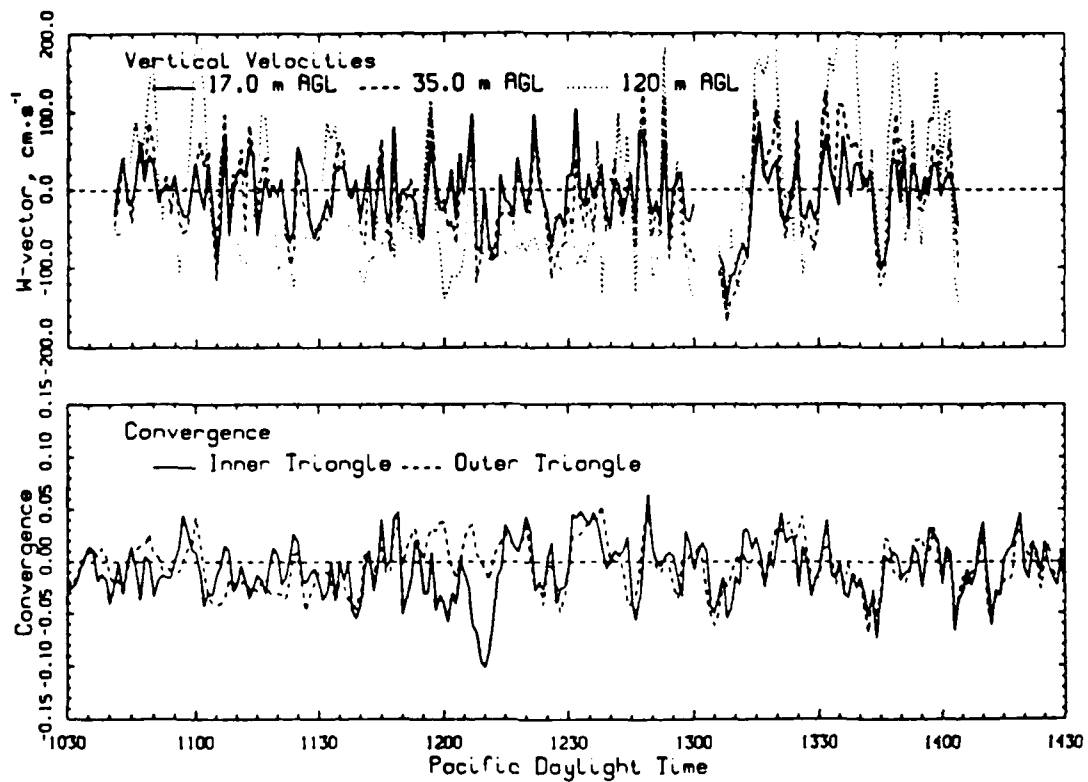


Figure 2. Comparison of the wind convergence (units 1/second) into the two triangles with vertical velocities determined with a high frequency Doppler acoustic sounder at three heights above ground level.

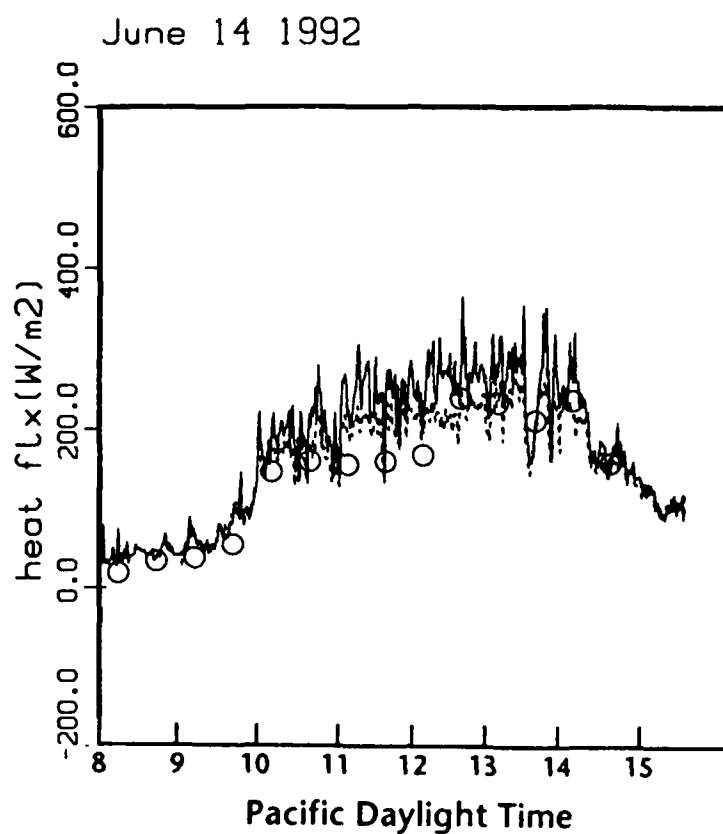


Figure 3. Heat fluxes determined by two different optical scintillometers (NOAA/WPL solid line, Scintec dashed). The circles are heat flux from the meteorological tower.

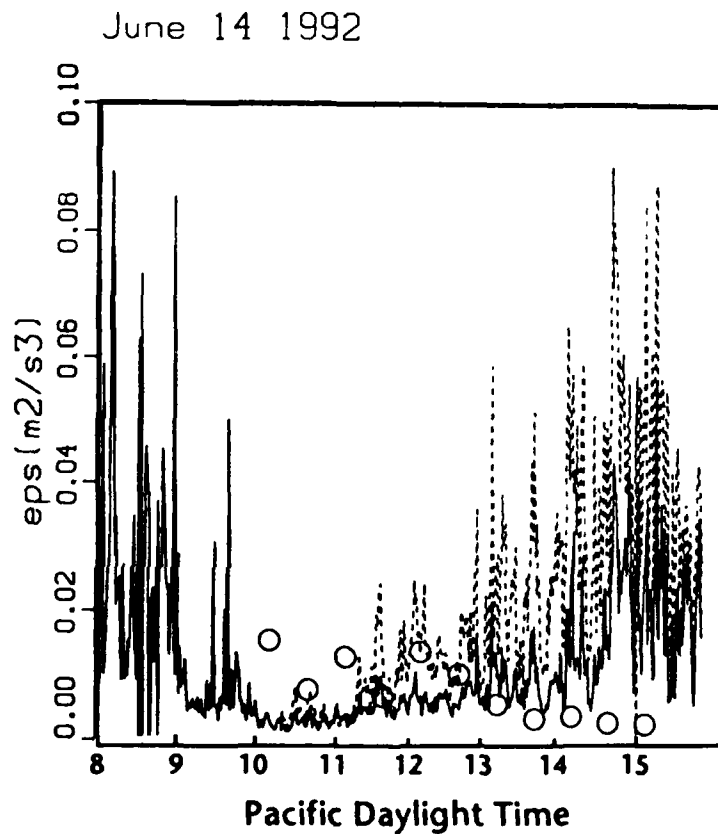


Figure 4. Energy dissipation rates determined from the two scintillometers and the tower.

Lidar and Radiometer Observations of Midlevel Clouds
by
C.M.R. Platt, S.A. Young, G.R. Patterson and P.J. Manson

CSIRO, Division of Atmospheric Research
Private Mail Bag No.1, Station Street,
Aspendale Victoria 3195 Australia
Telephone (03) 586 7666
Fax (03) 586 7600

Midlevel clouds occur in the region of the troposphere, lying between high cirrus ice clouds and low boundary layer stratus, stratocumulus and cumulus clouds. Midlevel clouds are associated with moisture advected to the middle part of the troposphere between about 2km and 6km, or temperatures between about 0°C and -20°C. However, there is no sharp gradation between cirrus and altus clouds, rather, a blending of one into the other. Again, deep frontal clouds, which include midlevel cloud, can extend from cirrus level to the boundary layer. Both the depths and the compositions of midlevel clouds are thus very variable. The clouds can often exist as supercooled water drops, which sometimes glaciate rapidly; as the saturation vapour pressure over ice is lower than over water, and the deficit is maximum at about -15°C in the mid-troposphere, any tendency for ice crystals to form can cause rapid growth of the crystals at the expense of the water drops. Optical remote sensing of these clouds has been confined in the past to a few observations (e.g. Platt and Gambling, 1971, Platt and Bartusek, 1974, Platt, 1977, Sassen, 1984, Uchino et al., 1988). However, recently, a few more observations were made in the first FIRE experiment (e.g. Heymsfield et al., 1991) although observations tended to concentrate on cirrus.

This paper reports on recent observations on midlevel clouds done as part of the CSIRO, DAR's contribution to the ECLIPS (Experimental Cloud Lidar Pilot Study) project.

The ECLIPS project at Aspendale, Australia was done in two phases in November/December 1989 and June/July 1991. The instrument complement was as shown in Table 1.

During both periods, midlevel clouds occurred quite frequently, particularly in the second period. The weather during June 1991 was more disturbed than usual, and the passage of fronts was a common occurrence.

The ECLIPS observations were made generally at Aspendale for 90 minutes each side of an afternoon AVHRR overpass. This allowed exploitation of the surface data for comparison with retrievals of optical properties from satellite data.

Other cloud properties retrieved in the ECLIPS project were cloud base and top (where possible), visible extinction coefficient at the lidar wavelength, lidar depolarization ratio, surface shortwave and longwave fluxes, and the infrared emittance at 10-12 μm .

The ECLIPS data are being archived at NASA Langley Research Centre, Hampton, Virginia for the use of the atmospheric science community.

TABLE 1.
INSTRUMENTS USED AT ASPENDALE IN THE ECLIPS EXPERIMENT

INSTRUMENT	PHASE 1	PHASE 2
<u>Lidar</u>	Ruby 0.694 μm	Nd:Yag DOUBLED 0.532 μm Nd:Yag 1.064 μm
<u>Radiometer</u>	Beam IR (10-12 μm) (Vertical)	Ditto
	Infrared Flux Pygeometer	"
	Solar Flux Pyranometer	"
	All-sky Camera	"
	All-sky video	"
<u>Satellite</u>	AVHRR Channels 1-5. Local reception	"
<u>Radiosonde</u>	Morning and evening temperature, humidity. (Station 40km distant)	"
<u>Rawin</u>	Wind profiles at three-hourly intervals.	"

The work reported here concerns only the analysis of the lidar and narrow-beam radiometer data - the LIRAD method. This involves calculating the infrared emittance from the radiometer data at the times of the lidar firings. The lidar backscatter profile is taken as a guide to the variation of infrared absorption coefficient with altitude. The lidar integrated attenuated backscatter is then plotted against the infrared emittance, as shown in Figure 1. Equation 1 shows the relation between the integrated attenuated isotropic backscatter γ' and the emittance ϵ :

$$\gamma' = \frac{k}{2\eta} \{ 1 - \exp [-2\eta \alpha \log (\frac{1}{1-\epsilon})] \} \quad (1)$$

When $\epsilon \rightarrow 1$, $\gamma \rightarrow k/2\eta$, where k is the isotropic backscatter to extinction ratio and η is a multiple scattering factor. The value of $k/2\eta$ so obtained can be used to correct the backscatter curve for attenuation, after which values of ϵ can be recalculated. The ratio α of the visible extinction coefficient to the infrared absorption coefficient gives additional information. LIRAD is described in detail in Platt and Dilley, (1981.)

The emittance of the cloud in Figure 1 was quite variable, as shown. However, in many of the other cases, the emittances approached unity, the clouds being optically thick. This was verified by lidar profiles which exhibited complete attenuation, and in these cases retrieval of the visible extinction coefficient indicated values varying from 5 to up to 70 km^{-1} . The latter was from an

altostratus cloud which exhibited a very variable cloud base but cloud penetration of only tens of metres.

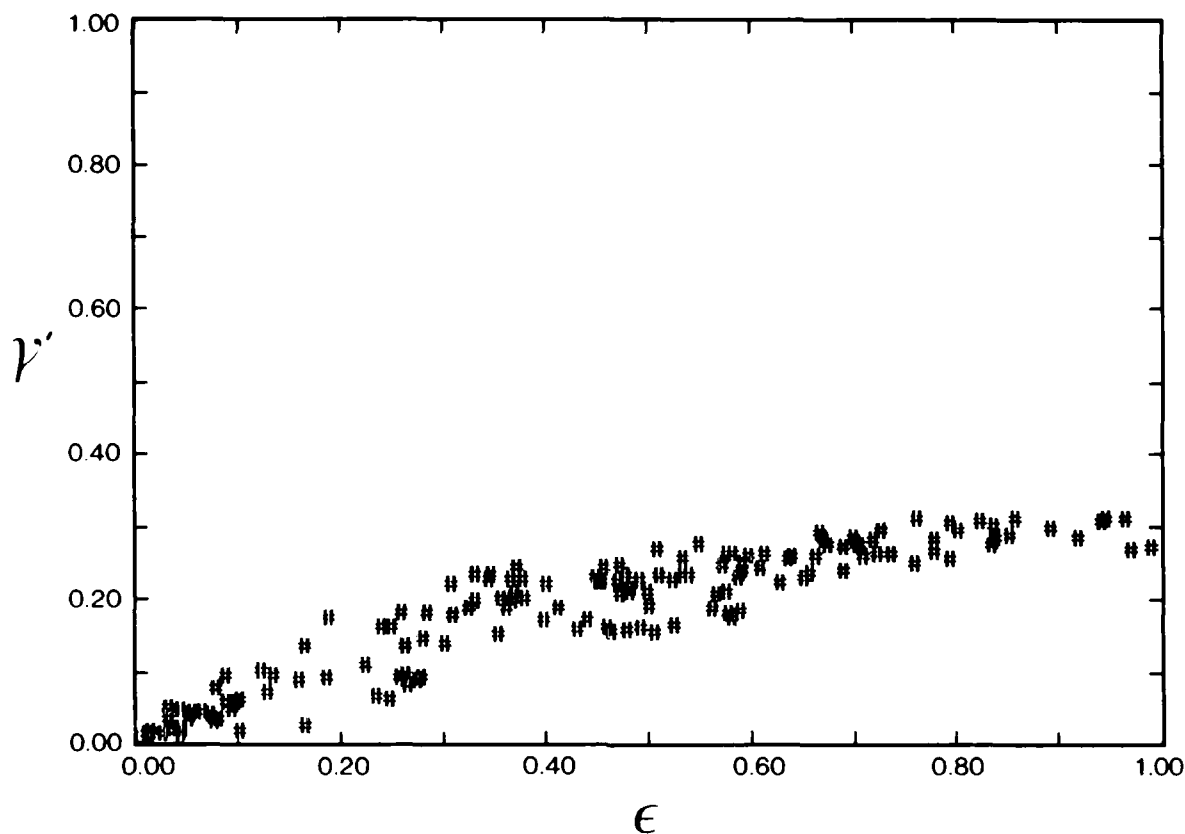


Figure 1. Integrated backscatter γ' plotted against ϵ for one cloud system.

In yet another case, the cloud appeared to be mainly in the ice phase (from lidar depolarization diversity) and over 1km deep. However, the infrared radiance was rather constant and the LIRAD calculation again showed a cloud of emittance approaching unity.

One feature of this cloud was the presence of a shallow water layer with low depolarization ratio which seemed to persist throughout the observations. The glaciated portion of the cloud appeared to be falling through the water layer and subsequently evaporating.

Full results from the ECLIPS midlevel cloud data sets will be published elsewhere.

References

- Heymsfield, A.J., L.M. Miloshevich, A. Slingo, K. Sassen and D. O'C. Starr, 1991: An observational and theoretical study of highly supercooled altocumulus. *Jour. Atmos. Sci.*, 48, 923-945.
- Platt, C.M.R., and D.J. Gambling 1971: Emissivity of high layer clouds by combined lidar and radiometric techniques. *Quart. Jour. Roy. Met. Soc.*, 97, 322-325.

- Platt, C.M.R., and K. Bartusek, 1974: Structure and optical properties of some middle-level clouds. *J. Atmos. Sci.*, 31, 1079-1088.
- Platt, C.M.R., 1977: Lidar observation of a mixed - phase altostratus cloud. *J. Appl. Meteor.*, 16, 339-345.
- Platt, C.M.R., and A.C. Dilley, 1981: Remote sounding of high clouds. IV: Observed temperature variations in cirrus optical properties. *J. Atmos. Sci.*, 38, 1069-1082.
- Sassen, K., 1984: Deep orographic cloud structure and composition derived from comprehensive remote sensing observations. *J. Clim. App. Meteor.*, 23, 568-583.
- Uchino, O., I. Tabata, K. Kai and Y. Okada, 1988: Polarization properties of middle and high level clouds observed by lidar. *Jour. Met. Soc. Japan.*, 66, 607-616.

Summary of the Experimental Cloud Lidar Pilot Study (ECLIPS) at ISTS/York Lidar Observatory

S. R. Pal, A. Y. Fong and A. I. Carswell

Institute for Space and Terrestrial Science
and Department of Physics and Astronomy , York University
4700 Keele St., North York, Ontario, Canada, M3J 1P3
Tel: 416-736-2100 Fax: 416-736-5516

Clouds play an important but complex role in modifying the solar radiative transfer in the atmosphere. To gain better insight into cloud physical and optical properties, which form the basis for cloud parameterization in general circulation models, the ECLIPS [1] was initiated in which about a dozen lidar groups have participated. The ECLIPS program has provided an opportunity to conduct lidar measurements of cloud systems simultaneously observed by a satellite (NOAA-10 or 11). A lidar measurement time series, typically of 3 hours encompasses a satellite overpass. Two ECLIPS phases (Sep-Nov 1989, Jun-Jul 1991) have provided consistent cloud lidar measurement time series on a variety of cloud formations. Our achievements in developing analytical methodologies to utilize large amounts of lidar data and to extract information on cloud physical and optical parameters are summarized in this paper. The behaviour of lidar derived cloud parameters in relation to important meteorological parameters will also be discussed.

The ECLIPS measurements at the ISTS/York Lidar Observatory were carried out with a Nd:YAG lidar system transmitting two wavelengths (532 and 1064 nm) at 20 Hz, with a 0.5 m diameter 4-channel polarization receiver [2].

Cloud Physical Parameters

A cloud base algorithm [3] developed during the ECLIPS phase I provides retrieval of initial cloud physical parameters, altitude of cloud base, and top (r_b , r_t) for each lidar return in a given time series. These, along with horizontal cloud extent obtained using simultaneously determined cloud wind vectors, provide the basic set for studying the statistical behaviour of cloud physical parameters. Cloud height r_b and thickness ($r_t - r_b$) play an important role in radiative transfer. Frequency of occurrence of these parameters in a locale is expected to have a seasonal dependence. Lidar data can provide typical statistical information on these parameters which can be useful for GCM parameterization. Figure 1a and 1b show the statistical behaviour of cloud base height and thickness in the two ECLIPS phases. Low clouds occurred more frequently in both phases, however the ECLIPS II exhibited a higher occurrence of mid level and high clouds with a distinct peak at 12 km for cirrus clouds. The cloud thickness shows an approximate exponential decrease from the most frequently observed value of about 500m.

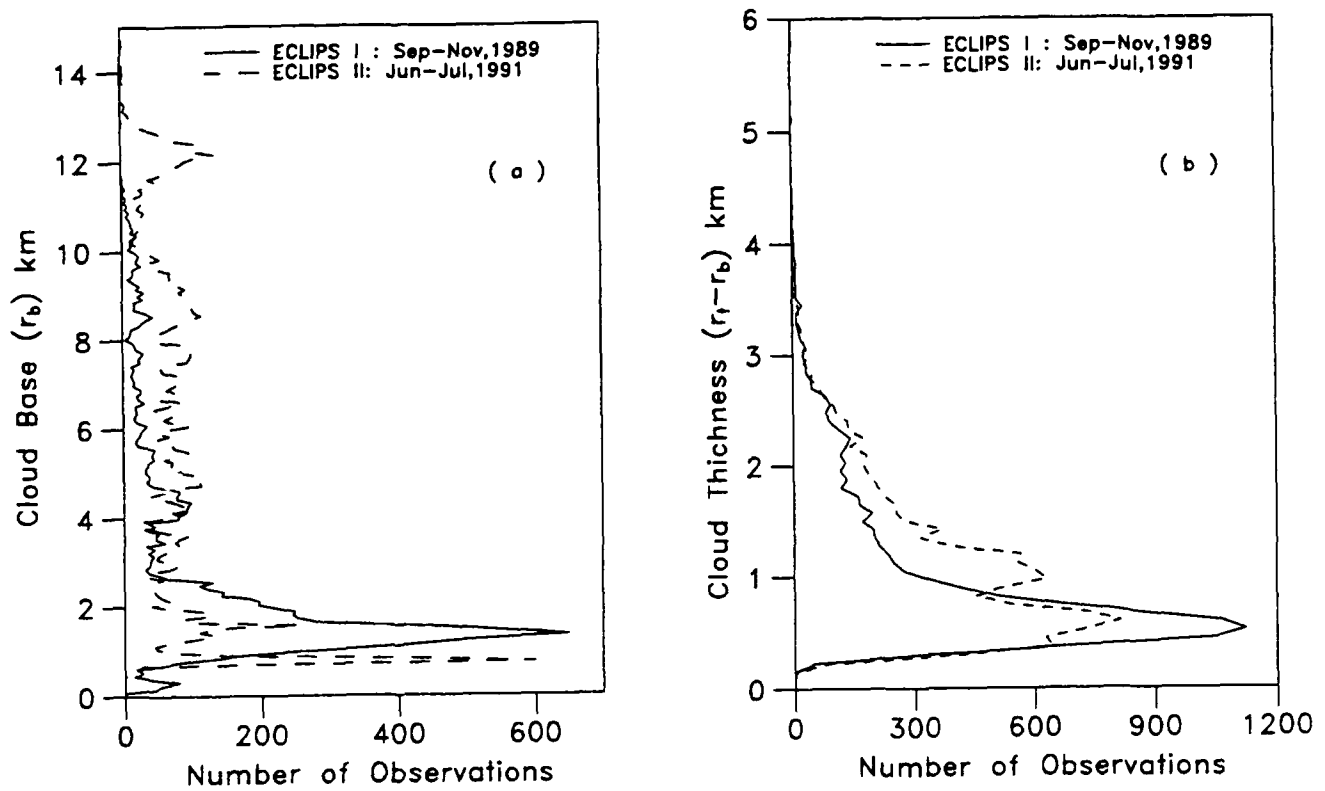


Figure 1(a,b). Frequency histogram of cloud base height (Fig.1a) and cloud thickness (Fig.1b) for ECLIPS I and II. Height resolution is 75 m.

Cloud Optical Parameters

The ECLIPS committee has assigned to our group at York the task of preparing a summary of methodologies used by all ECLIPS participants for retrieving the cloud extinction coefficient (σ). A discussion on these methodologies will be presented in this paper. We have utilized Klett's [4] far-end inversion in conjunction with a radiosonde-derived boundary condition to determine cloud σ profiles and the related optical depths, τ . Figure 2 presents a sample time series of average extinction, σ_{av} , and the corresponding optical depth, τ . The distance axis shown at the top provides the extent of cloud studied in this time series. The time axis is translated into distance using lidar determined r_b and cloud feature displacement from simultaneous time lapse videography. This spatial information permits ready comparison of the lidar data with satellite imagery. The high variability of σ with time clearly demonstrates the typical optical inhomogeneity of cloud systems.

The comparison of the σ_{av} and τ plots shows a general correspondence as might be expected. However there are marked differences in many regions caused by the variability in cloud physical thickness as well as the extinction coefficient. In a given cloud system, σ values were often found to vary by several orders of magnitude.

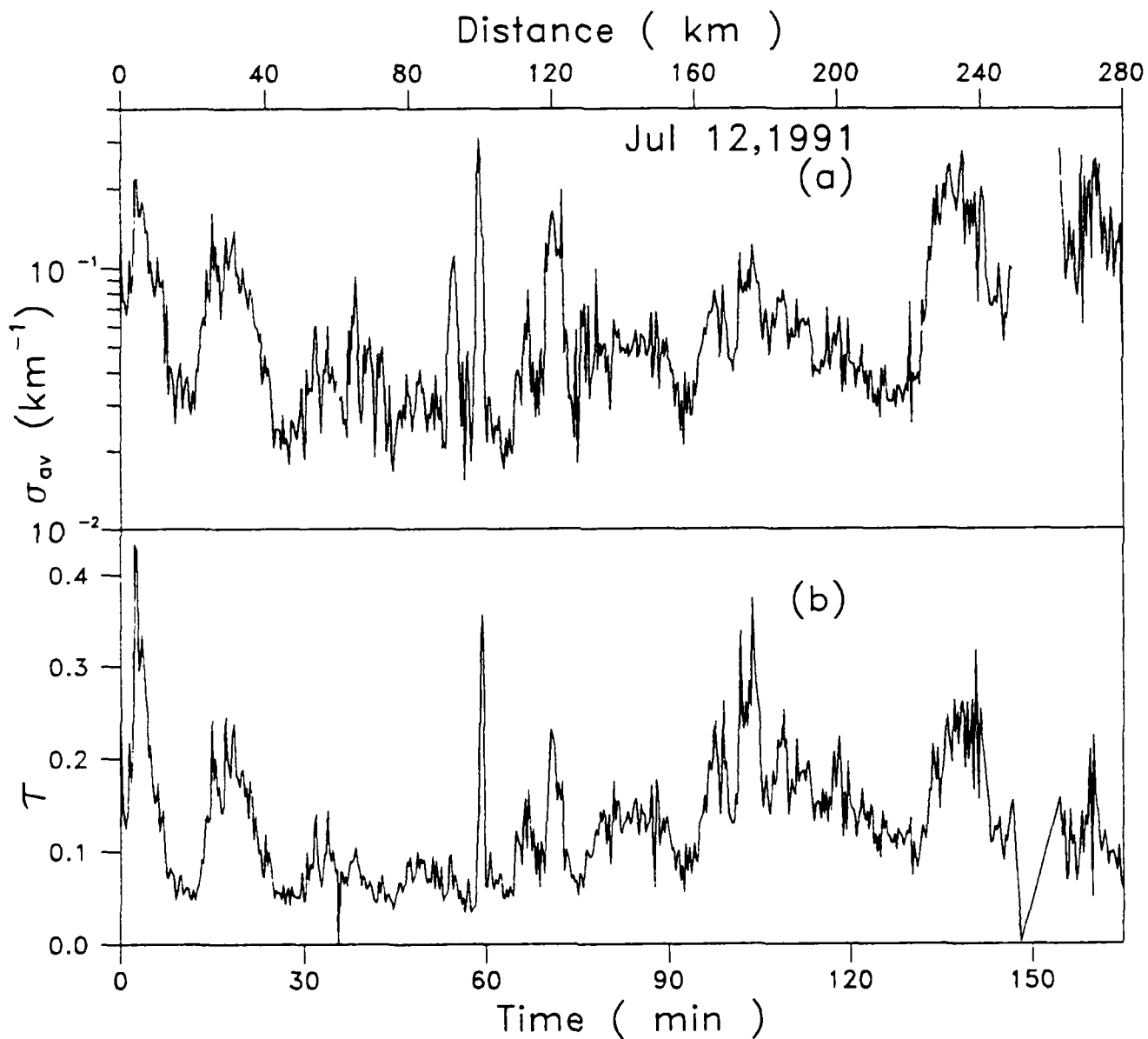


Figure 2. A sample time series of average cloud extinction σ_{av} (a) and corresponding optical depth τ (b)

Figure 3 shows a summary histogram of the optical depth measurements made on high clouds ($\tau_b > 4\text{km}$) at 532 nm for both ECLIPS phases. For these clouds, predominantly constituted of ice particles, the most common optical depth was less than 0.25.

In this paper we present an overview of the lidar-derived cloud properties and discuss the correlation of these data with the simultaneous meteorological and satellite observations.

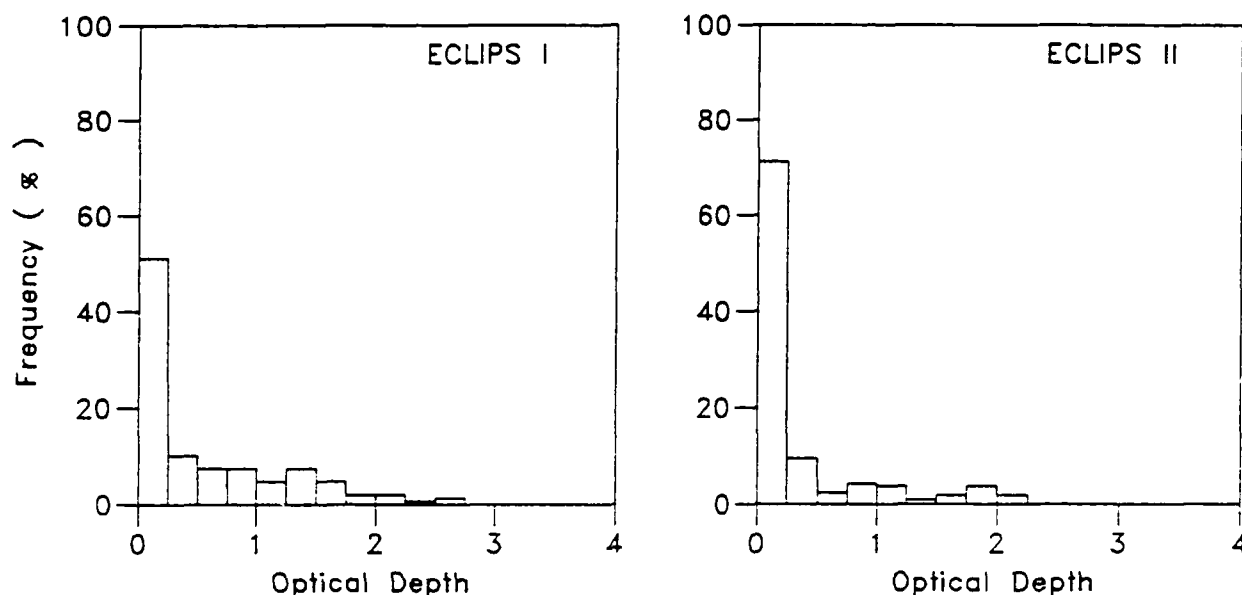


Figure 3. Frequency histograms of optical depth for clouds $\tau_b > 4\text{km}$ for ECLIPS I and II data.

References

- [1] "Experimental Cloud Lidar Pilot Study (ECLIPS)," Report of the WCRP/ CSIRO, Cloud Base Measurement Workshop, CSIRO, Division of Atmospheric Research, Mordialloc, Victoria, Australia, (Feb. 29 - Mar. 3, 1988).
- [2] A.I. Carswell, S.R. Pal, W. Steinbrecht, J.A. Whiteway, A. Ulitsky and T-Y Wang, "Lidar measurements of the Middle Atmosphere", Can. J. Phys., Vol. 69, 1076-1086, 1991.
- [3] S.R. Pal, W. Steinbrecht and A.I. Carswell, "Automated Method for Lidar Determination of Cloud Base Height and Vertical Extent", Appl. Opt., Vol. 31, 1488-1494, 1992.
- [4] J. D. Klett, "Stable Analytical Inversion Solution for processing Lidar Returns", Appl. Opt., Vol. 20, 211-220, 1981.

ECLIPS Phase 2 at LMD

*R. Valentin, S. Elouragini, P.H. Flamant, L. Menenger, **J. Pelon

*Laboratoire de Météorologie Dynamique, Ecole Polytechnique, 91128 Palaiseau

** Service d'Aéronomie, Université Paris 6, 4 place Jussieu, 75252 Paris Cedex

The LMD ground-based backscatter lidar station (48°4 N, 02°0E) near Paris was operated daily (Monday through Friday) during ECLIPS phase 2 from May 22 to June 19, 1991, with a simultaneous recording of the downward short wavelength (SW) flux and long wavelength (LW) flux. A day-by-day summary of the field measurements is displayed as a function of universal time (UT) on figure 1. There are only two days of missing data (05/31 and 06/06) in our record due to bad weather conditions. The nearby meteorological station (10 km away) provides with rawindsondings twice a day (00UT and 12UT). We have also collected the meteorological observations and synoptic weather charts. In addition, in two occasions (05/22 and 05/27) LEANDRE the french airborne backscatter lidar was flown over the ground-based station to make simultaneous lidar measurements looking from above and below. The two lidars were operated at 532 nm ; the on-board and ground-based radiometric equipments were identical. The ground-based operations were synchronized with AVHRR overpasses as required by ECLIPS. We also indicate the Meteosat data. We analysed on a day-by-day basis the ground-based lidar and radiometer data to derive a temporal evolution of cloud base height, cloud depth and optical parameters, and also histograms of cloud base and cloud (apparent) top. A summary of cloud base height (X) for all clouds, and cloud top height (Δ) for semi transparent layers or apparent top (O) for dense clouds is plotted on figure 2, as retrieved using the ground-based lidar. Cloud base heights for low clouds range from 1 km to 1.5 km, with two exceptions (0.5 and 1.8 km respectively). An example of lidar, pyrgeometer and pyranometer data is displayed on figure 3. A single stratus layer is present on June 3. The cloud base as recorded by the ground-based lidar (upper curve) varies between 1.4 and 2 km. Holes occur at various time, which are well correlated with pyranometer measurement (lower curve). Holes are identified by sharp peaks larger than 600 W m^{-2} in downward visible flux in the absence of one or more overlaying clouds. On the contrary when the cloud layer is thick and solid the SW flux ranges from 200 to 400 W m^{-2} . On June 5, an altostratus at about 5 km overlayed a stratus layer at 2 km, and the SW recording showed a smooth variation. Taking advantage of up and down lidar measurements on May 27 we compare histograms of cloud base and apparent top heights as retrieved by the ground-based lidar versus histograms of cloud top and apparent base as obtained from LEANDRE (Fig. 4). A discrepancy in shape can be due to different temporal resolution or sampling. Cloud base and apparent top (or vice versa) are separated by about 200 m which is the maximum lidar penetration (apparent base is not plotted for LEANDRE). This comparison was done on a compact cumulus layer (with a large fractional cloudiness). We also looked at the probability density function for cloud top and boundary layer heights (Fig. 5) which address a representativeness error associated to a scale integration problem. They are derived from histogram as displayed on figure 4. The skewness of opposite sign can be associated to a larger scale boundary layer circulation. The results of ECLIPS phase 2 at LMD will be presented in depth at the conference.

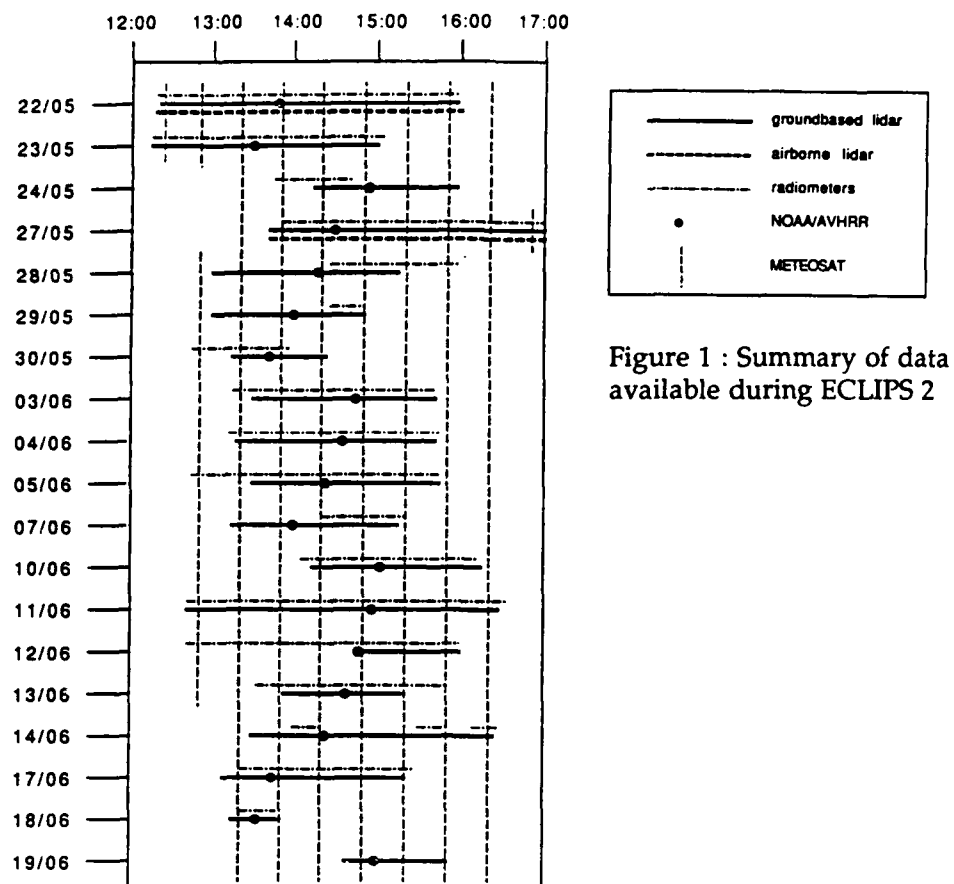


Figure 1 : Summary of data available during ECLIPS 2

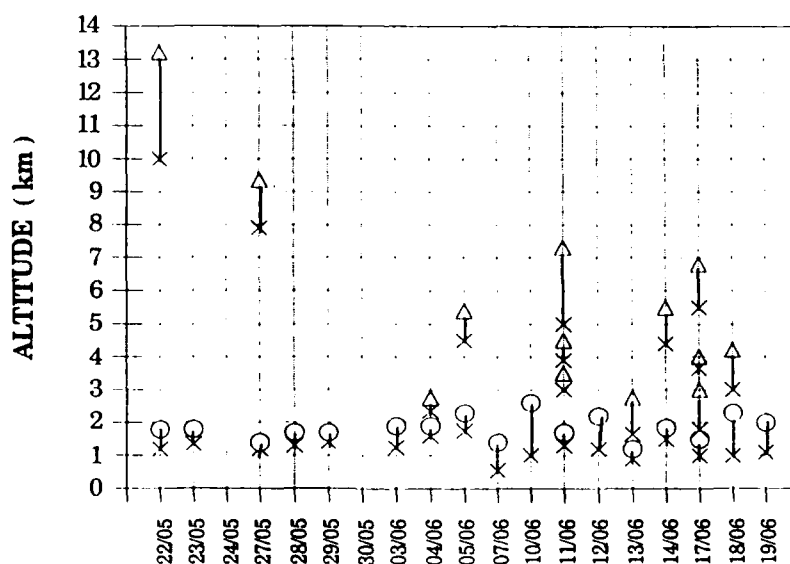


Figure 2 : Summary of cloud base & top heights retrieved from ground-based lidar

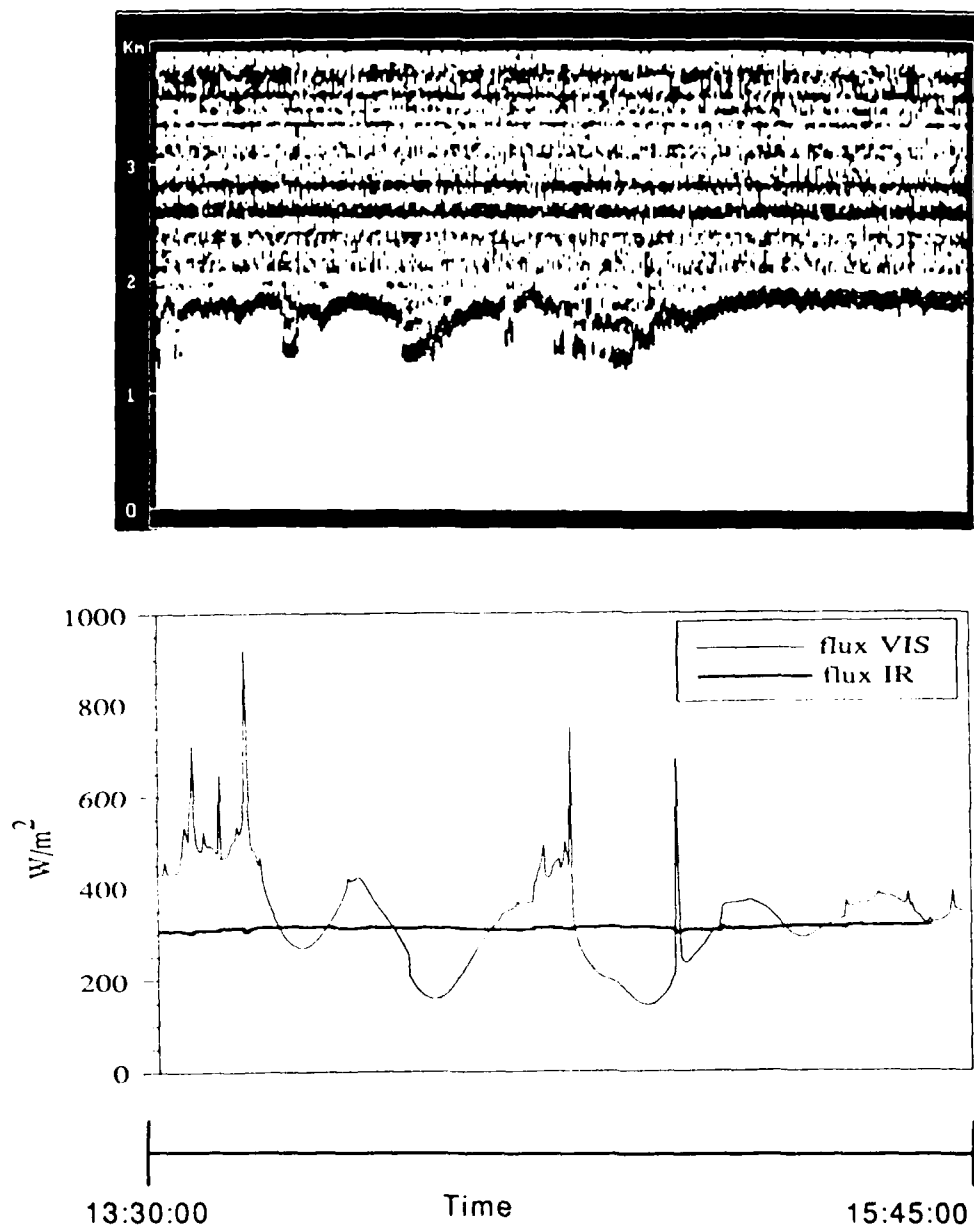


Figure 3 : Cloud base height by lidar as a function of time (upper curve), SW & LW fluxes as a function of time (lower) retrieved from ground.

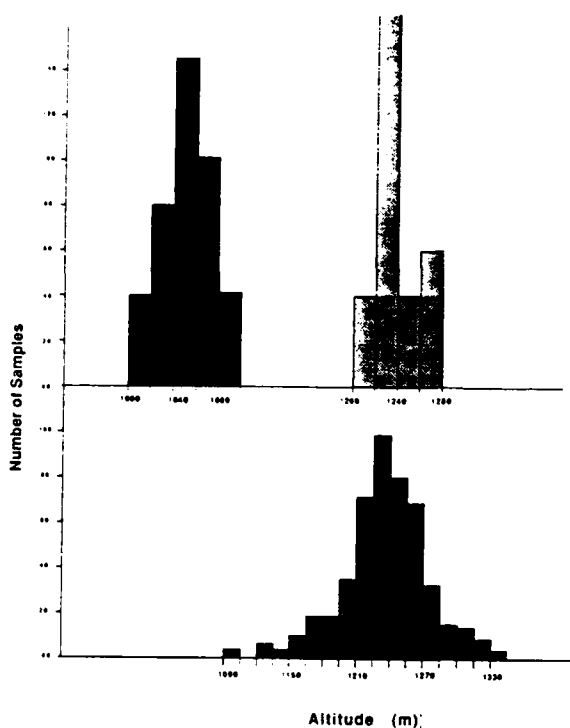


Figure 4 : Comparison of cloud & apparent top heights by ground-based lidar (upper curve) versus cloud top height by LEANDRE (lower curve)

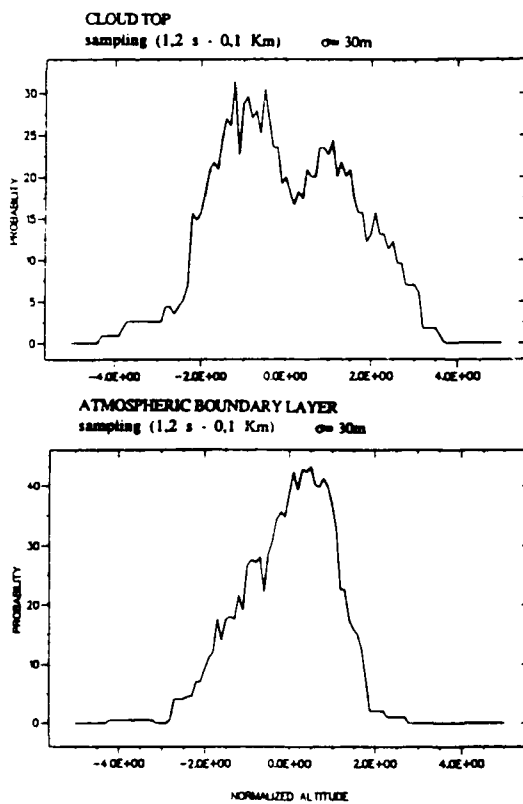


Figure 5 : Probability density function for cloud top & PBL heights retrieved by LEANDRE

CLOUD MEASUREMENTS WITH A POLARIZATION RAMAN ELASTIC-BACKSCATTER LIDAR

Ulla Wandinger and Claus Weitkamp
GKSS-Forschungszentrum Geesthacht GmbH,
Postfach 1160, W-2054 Geesthacht, Germany
(Tel. ++49 4152 871854)

The GKSS Raman elastic-backscatter lidar is part of the worldwide lidar network established for the ECLIPS (Experimental Cloud Lidar Pilot Study) project. A detailed review of the aims and philosophy of this international program is given in Ref. 1. During the first ECLIPS observational phase in autumn 1989 the GKSS lidar was also part of the ICE (International Cirrus Experiment) lidar network in the German Bight of the North Sea (Ref. 2). Measurements were taken on the island of Norderney (53.7° N, 7.2° E) between 18 September and 24 October 1989. In this campaign predominantly cirrus clouds were studied. The measurements of the second ECLIPS field phase were made at Geesthacht (53.5° N, 13.5° E) between 29 May and 27 June 1991. Each day two or three two-hour sessions centered around the overpass times of the satellites NOAA 10 and NOAA 11 were carried out.

At daytime the GKSS lidar is used as a conventional polarization-sensitive elastic-backscatter lidar. A XeCl excimer laser serves as the source, a dielectrically coated polarizer allows to emit linearly polarized light. The backscattered light at 308 nm is measured in two polarization directions. At nighttime three additional receiver channels are used, two for the Raman nitrogen signals at 332 nm in two polarization planes and one for the Raman water vapor signal at 347 nm. A description of the system is given, e.g., in Refs. 3 and 4.

As was shown previously (see, e.g., Ref. 5), a combined Raman elastic-backscatter lidar allows the independent measurement of extinction and backscatter coefficients and thus the determination of the lidar ratio, which is an important input parameter for the Klett inversion method. A polarization Raman elastic-backscatter lidar gives, in addition, the independent information on multiple-scattering depolarization and depolarization due to single scattering from nonspherical particles (Ref. 6). As most of the lidars of the ECLIPS network are conventional backscatter lidars, some with depolarization detection capability, the polarization Raman elastic-backscatter lidar can be used to provide data necessary for the data retrieval procedure of the former, and thus help improve the accuracy of the results of the network. In particular, the range of typical lidar ratios for different cloud types is measured; comparisons of extinction coefficients derived from the Klett and from the Raman method give an idea of the usefulness of extinction retrieval from elastic backscatter signals; the influence of multiple scattering effects in ice clouds on the data evaluation can be studied; etc.

In order to demonstrate the capabilities of a polarization Raman elastic-backscatter lidar, the measurement of a mixed-phase cloud is discussed here. The profiles of the backscatter and extinction coefficients, the optical depth, the lidar ratio, and the depolarization ratios of the elastically and Raman backscattered light determined from four measured

signals — the nitrogen Raman signals in parallel and perpendicular polarization with respect to the polarization plane of the emitted laser light, and the elastic backscatter signals also in the two polarization directions — are shown in Fig. 1 (for equations see Refs. 3 and 5).

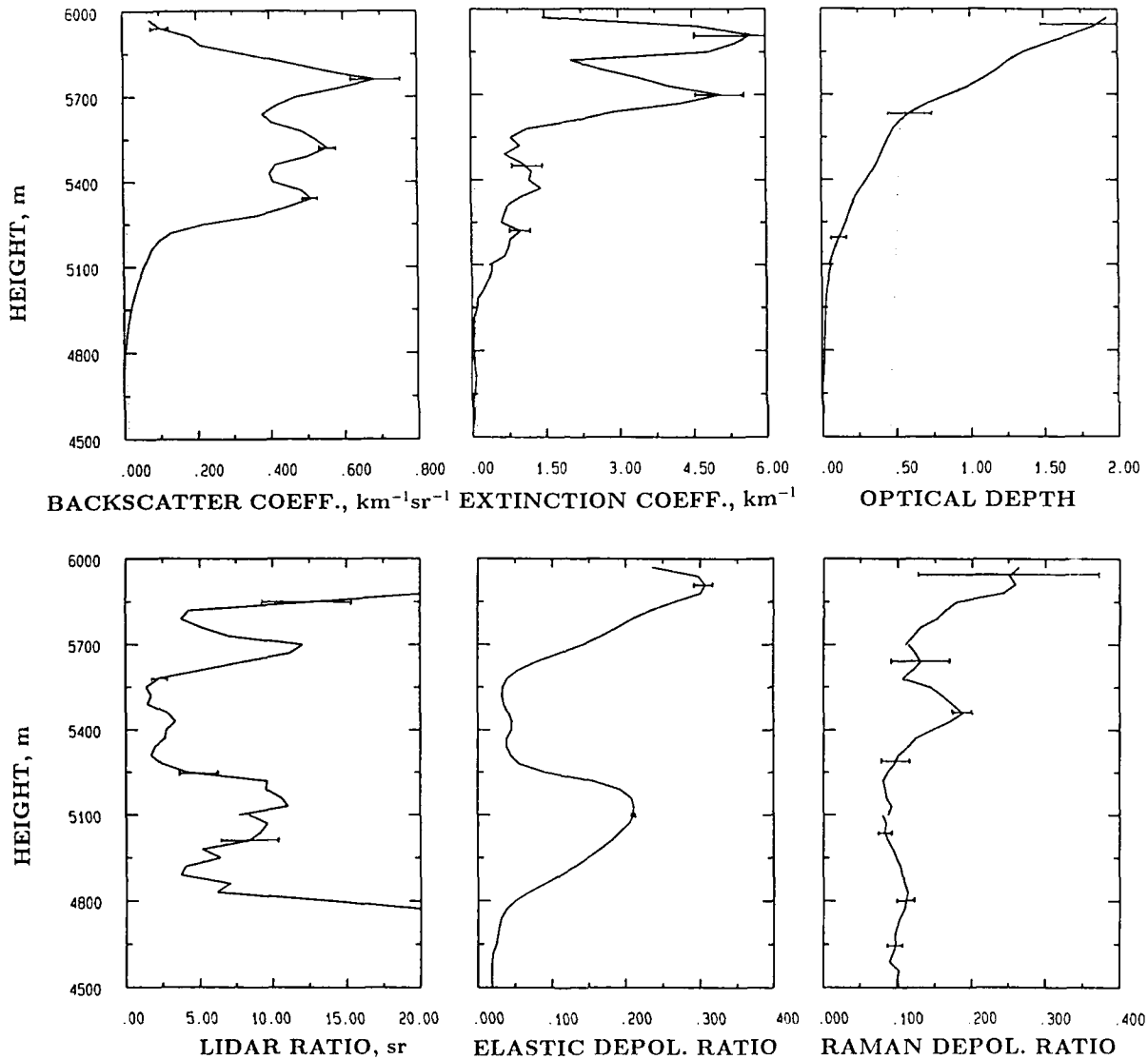


Fig. 1: Backscatter coefficient, extinction coefficient, optical depth, lidar ratio, elastic depolarization ratio, and Raman depolarization ratio measured in a mixed-phase cloud. Dotted lines indicate Rayleigh scattering. Measurement time is 10 min, 120,000 laser shots are averaged. Signals are smoothed with a gliding average window length of 240 m below and 120 m above 5100 m.

The measured cloud represents the remains of thunderstorm clouds that had formed in a warm and moist air mass. The mixed-phase character could be observed by eye in the late-evening light. The cloud base is found at about 4800 m, the cloud top at

6000m. Below the cloud the depolarization ratios of pure Rayleigh (0.016) and pure Raman scattering (0.096) are found. Between 4600 and 4800m the somewhat enhanced extinction and elastic depolarization ratio indicate the presence of precipitating particles. The cloud layer between 4800 and 5250m is characterized by moderate extinction and backscattering, a lidar ratio between 5 and 10sr and elastic depolarization ratios up to 0.2. These values are typical for randomly oriented ice crystals. No significant changes in the Raman depolarization are found, hence multiple scattering does not play a role in this cloud region. In the layer between 5250 and 5600m very low values of the lidar ratio (1.5 to 3.5sr) and of the elastic depolarization ratio (0.03 to 0.05) are measured. This observation is commonly made when horizontally oriented ice crystals are present. The increasing Raman depolarization ratio shows that at least part of the Raman photons undergo additional elastic scattering processes, i.e., that multiple scattering occurs in this region. Above 5600m the optical thickness of the cloud increases rapidly. Extinction coefficients up to 6 km^{-1} are measured. It appears that water droplets dominate the scattering processes in this layer. The increasing Raman depolarization ratio indicates again the influence of multiple scattering. Further quantitative evaluation of the measured depolarization ratios must show if the increasing elastic depolarization ratio above 5600m is due to multiple scattering only or if ice crystals are present in this layer. A technique to correct the elastic depolarization for multiple scattering effects by using the Raman depolarization is presently under development.

References

1. C.M. Platt et al., "The Experimental Cloud Lidar Pilot Study (ECLIPS) for Cloud-Radiation Applications", submitted to Bulletin of the American Meteorological Society
2. A. Ansmann et al., "Lidar network observations of cirrus morphological and scattering properties during the International Cirrus Experiment 1989: The 18 October 1989 case study and statistical analysis", submitted to Journal of Applied Meteorology
3. A. Ansmann et al., "Combined Raman elastic-backscatter lidar for vertical profiling of moisture, aerosol extinction, backscatter, and lidar ratio", Appl. Phys. B **55**, 18-28, 1992.
4. C. Schulze et al., "Verification measurement of a polarization Raman elastic-backscatter lidar", Proceedings of the *Sixteenth International Laser Radar Conference*, Cambridge, Massachusetts, July 20-24, 1992
5. A. Ansmann et al., "Independent measurement of extinction and backscatter profiles in cirrus clouds by using a combined Raman elastic-backscatter lidar", Appl. Opt. **31**, 1992, in press.
6. U. Wandinger et al., "Measurement of multiple scattering effects with a polarization Raman elastic-backscatter lidar", Proceedings of the *Sixteenth International Laser Radar Conference*, Cambridge, Massachusetts, July 20-24, 1992

The Results of Laser Measurements of Cloud Parameters under the ECLIPS Program

S. S. Khmelevtsov

**Institute for Experimental Meteorology, Lenin 82, Moscow, Russia
249020**

Cloud condition measurements were carried out in the period from 29 May 1991 to 29 June 1991 at Obninsk lidar station. The lidar, operating daily at the wavelength of 532 nm over 24 days from 2.5 to 4.5 h., when NOAA satellites overpassed Obninsk, where the measurements of outgoing infrared irradiance flows were carried out. The overall duration of the measurements is 55 h. According to laser sounding results computations were carried out at the height of the cloud bases, the top of clouds, and the optical thickness of clouds (in those cases when it was possible to do).

Simultaneously with laser sounding of clouds, the measurements of irradiance flow, directed vertically downward, have been carried out using a narrow band infrared radiometer and pyranometer. Besides, using aerological sounding and ground meteorological devices, the atmospheric parameters were measured.

LIDAR CLOUD OBSERVATION: IN PART OF ECLIPS PHASE II IN THE REGION OF SOFIA

I.Kolev, O.Parvanov, B.Kaprielov, Y.Tomova
Institute of Electronics, Bulgarian Academy of Sciences
72 blvd. Trakia, Sofia 1784, Bulgaria
Institute of Meteorology and Hydrology, Bulg. Acad. Sci.

INTRODUCTION

The ECLIPS project in which our lidar group also takes part is well described [1]. In general, the main purpose is a ground-based lidar observation of the clouds simultaneously with the NOAA 10 and NOAA 11 meteorological satellites overpassing the same areas to be performed. Essential data are the recorded profiles of the lidar returns from which certain information about the clouds height, optical depth and vertical extinction can be derived.

Besides the participation in the ECLIPS project, the investigation of the clouds is essential for us in three aspects connected with the applied meteorology, namely, the clouds physics, aviation meteorology and the ecological problems of the industrial centers (which city of Sofia, situated in a valley near the Vitosha mountain, represents).

METHODS AND APPARATUS

The presented experiments were conducted using triple-beam aerosol meteorological lidar, well described previously [2] (TBAML in Fig. 1), developed at the Institute of Electronics of Bulgarian Academy of Sciences. In Fig. 1 the scheme of the performed soundings is also shown.

A standard commercial Q-switched doubled-frequency ND-YAG laser of about 10-20 mJ (wavelength $\lambda = 532$ nm) at a repetition rate up to 50 Hz is used as transmitters.

The receiving antennae and electronics are based on three 150 mm in dia. Cassegrain type telescopes (eq. FL=2250 mm) aligned with model FEU 84 (made in USSR) photomultipliers. The interference filters at the working wavelength with bandwidths of 1 nm and a transmission of about 50 per cent are incorporated in order the day-time optical background to be rejected.

The data acquisition and processing system is constituted basically by a 10 bits 50 ns Waveform Recorder model HP 5180 A and a PC Pravetz 16 (fully 8 MHz IBM PC-XT compatible).

The listed main characteristics of the lidar determine adjustable time and spatial solutions as high as 0.02 seconds and 7.5 meters respectively.

The clouds are the first investigation objects for the most of the lidar groups through the strong backscattered signal. Due to the reliable lidar return we used three different algorithms to determine the clouds base height, namely, the signal maximum, the slope change of the derivative and based on the statistical characteristics of the time series 5 recorded at close volumes (strokes) along the sounding paths. The first two algorithms are well known. The third one is based on the mode structure of the lidar returns' amplitude distributions at each distance (stroke).

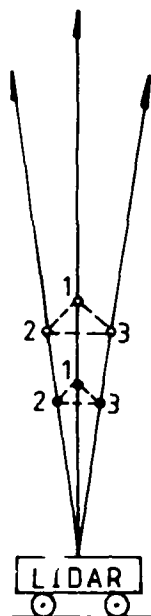


FIG 1

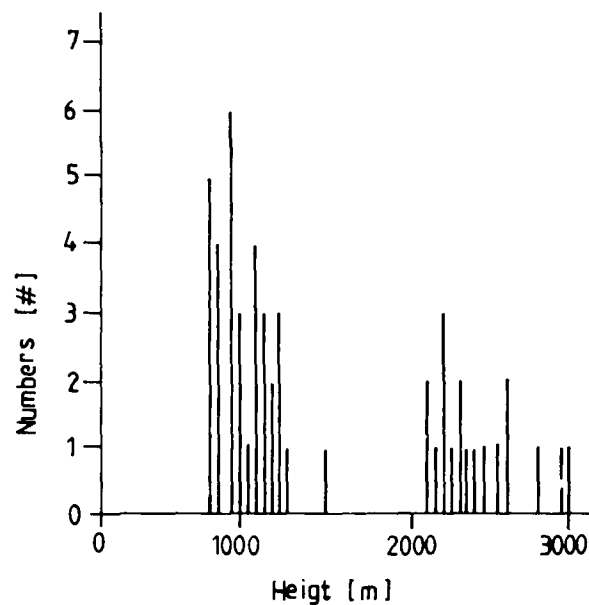


FIG 3

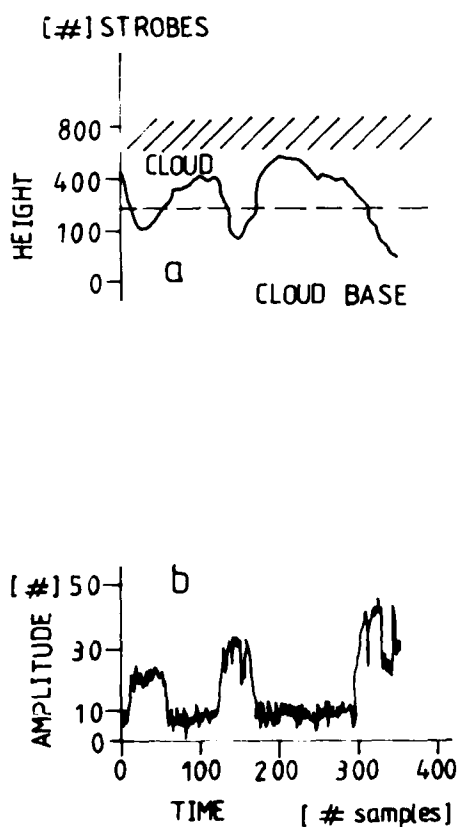


FIG 2

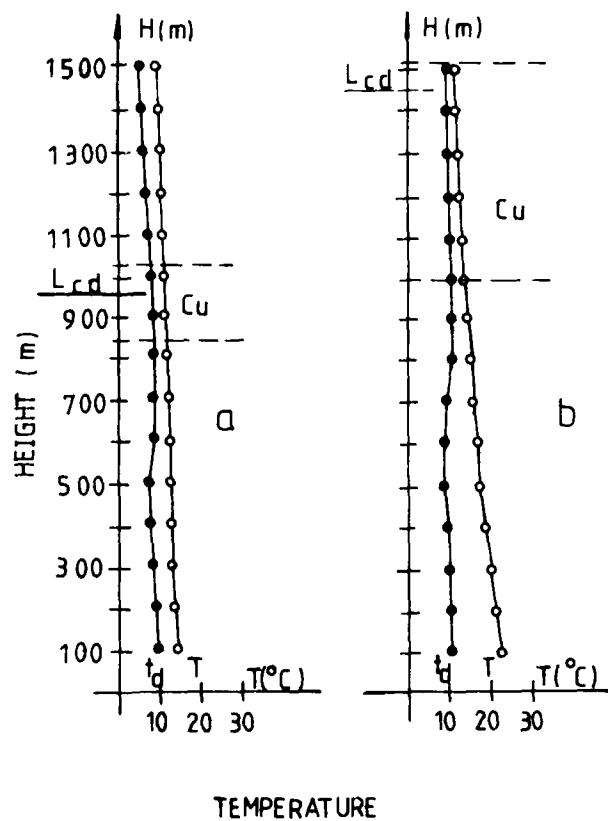


FIG 4

The amplitude level of the signal from a cloud (if presents) for a certain strobe can be determined on the basis of the typical mode distributions from a "clear atmosphere" (normal) and from a cloud (log-normal). Further obtaining such values for each strobe, the time change of the cloud base height is rendered. We shall not go in more details, but every algorithm can be used in dependence of the specific condition [5]. It should be noted that we are interested basically in low clouds St and Sc on account of already mentioned three aspects. So a part of these studies are directed to serve forecasting purposes [7]. From the lidar data the height of the mixing layer and the depth of the interaction layer can be determined as well [4]. The lidar is in close vicinity to the Institute of Hydrology and Meteorology and we used their surface measurements data about the temperature, wind velocity, pressure and humidity as well as those from the standard radiosoundings routinely carried out at 08 a.m., 02 and 08 p.m. SLT. Soon a satellite photographs receiving system will be put into operation.

EXPERIMENTAL RESULTS

The measurements described in the present work were performed within the ECLIPS Phase II. A near-vertical sounding along three paths was conducted and the clouds' development during NOAA 10 and NOAA 11 overpasses as well as the twenty-four-hours changes of the aerosol stratification in the whole planetary boundary layer (PBL) were observed.

For more proper study of the observed processes two types of data have been acquired during the campaign:

1. Time series (12,5 minutes) of 2058 points with a discretization of $\Delta t = 0.3$ s along the three paths from 8 heights.
2. The profiles of lidar returns containing from 200 to 500 points with a spatial resolution of 7.5 meters and a time averaging of out 32 seconds.

The experimental data required for the ECLIPS Phase II measurements were recorded during the period from 21 May to 09 July 1991 at 30 observations by 3 hours each i.e. 1 hour before and 1 hour after the NOAA 10 and NOAA 11 satellites overpasses. The lidar data were completed with the mentioned above meteorological information obtained by the conventional means.

On Fig. 3 the cloud base height distribution obtained from 54 measurements during the ECLIPS session is summarized. Two cloud groups are mainly observed: one at 700-1200 m and another at 2000-2600 m. The great bulk is concentrated at the lower height.

Shown on Fig. 4a are typically observed during that season the temperature (T) and the dew point (td) height profiles obtained from the sounding at 09:03 a.m. An approaching of the curves reveals an approaching to an air saturation with water vapours, while a moving of the two curves at a distance indicates a moving apart from the saturation condition i.e. a decreasing of the humidity at the certain height [2]. So the possibility of clouds appearance at certain heights can be determined C_u . The lidar measured clouds base height L_{cb} is also marked.

Fig. 2 illustrates: (a) - the shape and the base height time behaviour of a cloud, (b) - the corresponding time series recorded from one of the strobes.

DISCUSSION

The typical aerosol stratification over the region caused by a multilayer temperature inversion was observed. Systematic lidar investigation of the PBL over the region of Sofia city confirm a presence of aerosol layers at heights of 50-70 m, 200-400 m and 600-800 m which stratification remains several hours after the sunrise. After the beginning of the CBL formation, at these heights a periodically increasing of the lidar return is observed owing to an increasing of the humidity. The vertical speed determined from our data is in the limits of 0.3 to 1.5 m/s similar to that obtained in [6].

The formation of the CBL completes about 02 p.m. local time. Fair-weather clouds are observed above 1200 m, usually in the limits of 1400-2000 meters.

The clouds at 700-1200 m also form in the aerosol layers zone but not at the height of the first elevated inversion (as in case of the winter observation), they form at one of the higher located inversions i.e. where proper conditions exist. In Fig. 4b the temperature (T) and the dew point (td) height profiles obtained from the sounding at 02:30 p.m. are shown. The zone of the cloud formation possibility (1000-1500 m) with a depth of about ≈ 500 m is marked. On the same graph the determined from the lidar data clouds base height L_{cb} at $H=1440$ m is also marked.

On the grounds of a field experiment conducted during the ECLIPS'91 (Sofia) it is concluded that the cloud base heights reported by the operational weather services based on the lifting condensation levels (LCL) are inaccurate for the fair-weather cumulus clouds. LCLs also vary with a diurnal cycle, starting low in the morning and reaching a peak at about three hours before the local sunset.

CONCLUSION

In summer due to the development of the convective boundary layer a decreasing of the humidity in the ground boundary layer occurs owing to the evaporation processes and the turbulence which transport the humidity to the higher layers bordering upon the free atmosphere. This transportation in proper conditions leads to a fair-weather cloudiness formation.

REFERENCES

1. Report of the WCR/CSIRO Workshop on Cloud Base Measurement, WMO/TD-No 251, September 1988.
2. I.N.Kolev, O.P.Parvanov, B.K.Kaprielov and S.I.Kolev, 1989, Atmospheric Research, Vol. 24, pp. 13-32.
3. S.Peterssen, Weather Analysis and Forecasting, McGraw-Hill Book Company, New York, 1956.
4. E.Donev., D.Ivanov, I.Kolev, B.Kaprielov, O.Parvanov, K.Zeller, 1992, Bulg. J. Meteorology & Hydrology, in press.
5. Kolev I.N., O.Parvanov, B.Kaprielov, V.Naboko, Proceedings of Optika'87, 18-20 May, 1987, Varna, pp. 366-369.
6. T.D.Crum, R.B.Stull, E.W.Eloranta, 1987, Climate Appl. Meteor., Vol. 26, p.p. 774-788.
7. Kolev S.I., Parvanov O., Kostadinov L. and Kolev I., 1988, Proc. 10 Int. Cloud Physics Conf., Bad Homburg, pp. 515-517.

Tuesday, March 9, 1993

Poster Session 1

TuD 8:00pm–10:00pm
Salon E

Neural Nets for Temperature Retrievals

Howard E. Motteler
NASA/GSFC, Code 930
Greenbelt, MD 20771

L. Larrabee Strow
Department of Physics
UMBC, Baltimore, MD 21228

J. Anthony Gualtieri
NASA/GSFC, Code 902.2
Greenbelt, MD 20771

Larry McMillin
NOAA/NESDIS
5200 Auth Road
Camp Springs, MD 20746

James Lo
Department of Mathematics
UMBC, Baltimore, MD 21228

1. Introduction

We use neural networks to perform temperature retrievals [1,2] from simulated clear-air radiances for the Atmospheric Infrared Sounder (AIRS) [3]. Neural networks allow us to make effective use of the large AIRS channel set, giving good performance with noisy input. Using 653 temperature and surface sensitive channels, RMS error on retrievals with 0.2K noise is below 1.2K. We briefly describe the sort of networks we are using, describe our datasets, and present a number of representative results.

2. Neural Networks

We use a three-layer feed-forward neural network, which is trained with a modified back-propagation algorithm [4,5]. This network can be represented as

$$F(x) := F_3(W_3 F_2(W_2 F_1(W_1 x + b_1) + b_2) + b_3),$$

where each F_i maps vectors to vectors by applying a *transfer function* to each vector component. The W_i are *weight matrices* and the b_i are *bias vectors*. The mapping F_i is often referred to as a *layer*, with the weight matrices representing connections between layers. We use the hyperbolic tangent as a transfer function in the first two layers, and a linear function in the third.

Back-propagation training is a variation of gradient descent, in which weight and bias vectors are incrementally adjusted in an attempt to match the network output with a set of training examples. This training set is a set of pairs, where each pair is an input together with the desired output. A single presentation of training data and corresponding weight adjustment is called an *epoch*. Training consists of a sequence of epochs, and typically continues until the sum-squared error is acceptable or some resource limit is encountered. Training is a computationally intensive process for non-trivial networks. Although training is slow, applying a trained net is very fast, with the runtime being dominated by the time for the three matrix-vector multiplies.

The networks we use for temperature retrievals have one input component for each instrument channel, and one output component for each AIRS pressure level. Input is scaled brightness temperature and output is scaled temperature. The first layer has between 90 and 108 transfer functions, the second between 60 and 72 transfer functions, and the output layer has a linear function for each pressure level.

Our general method is to partition a dataset into training and extrapolation sets. The net is trained on the training set, and is then tested with the extrapolation set, both with and without noise; the noise inputs have a normal distribution and 0.2K standard deviation. Large training

runs are done using code we have developed for the 16,000 processor MasPar at the Goddard Space Flight Center.

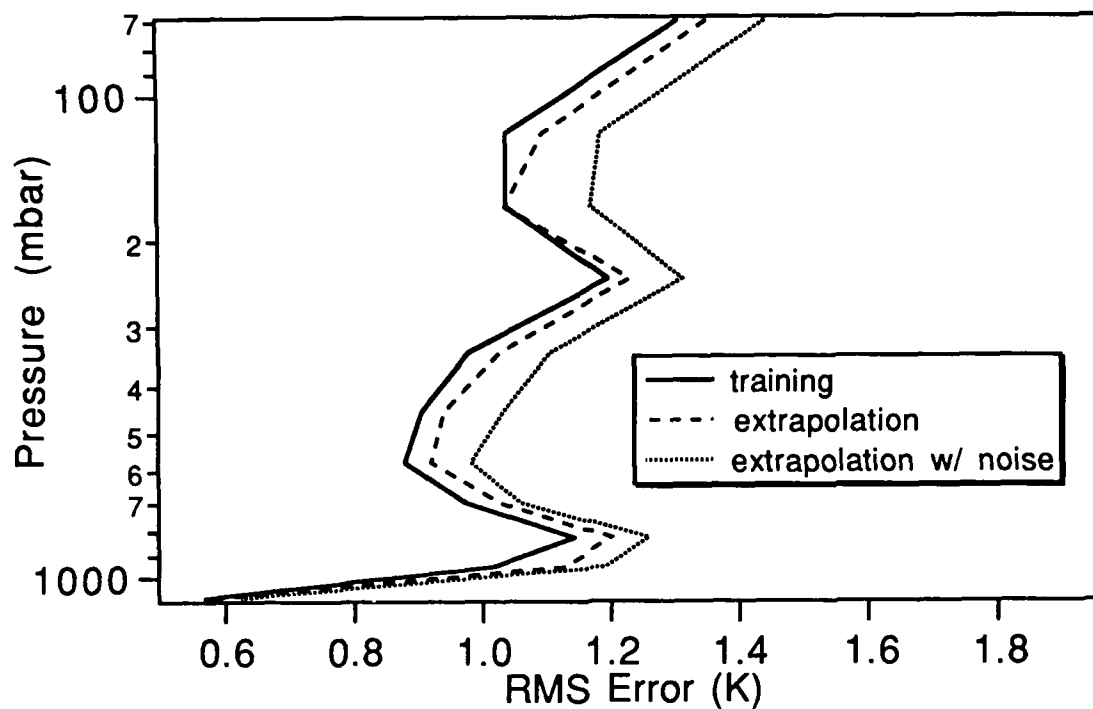


Fig. 1. RMS error with 1737 TIGR Profiles, 653 AIRS channels

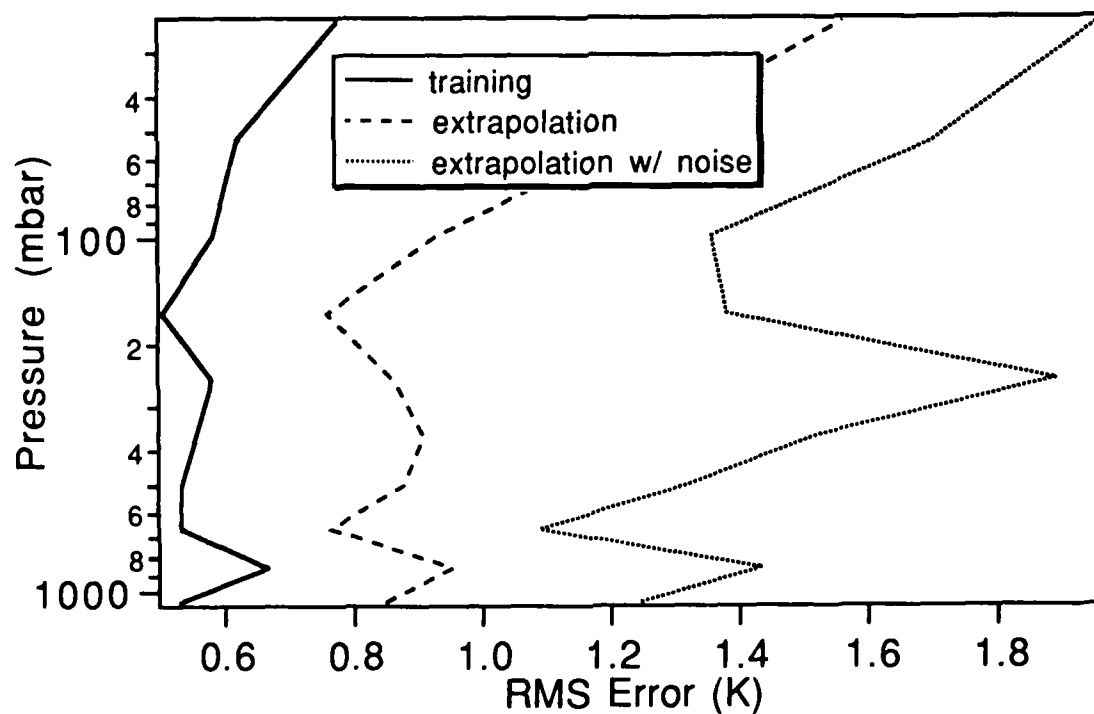


Fig. 2. RMS error with 400 Phillips Profiles, 59 AIRS channels

3. Datasets

We use both the set of 1761 TIGR profiles [6] and the set of 1200 Phillips profiles [7]. The TIGR profiles have been interpolated from the original 40 to 66 TOVS pressure levels, and the Phillips profiles have been interpolated to 100 AIRS pressure levels. In these preliminary studies, we use the first 50/66 pressure levels of the TIGR profiles and the first 80/100 pressure levels of the Phillips profiles. We have used subsets of both the HIRS/MSU and the proposed AIRS channel sets. In both cases we use simulated brightness temperatures [8]. In runs with the TIGR dataset ground temperature is retrieved, and is distinct from the first layer air temperature.

4. Results

In this section we present representative results for several profile and channel sets. In general, training runs were stopped when the RMS training error stopped showing significant improvement; this occurred anywhere between 20,000 and 60,000 epochs. Once network parameters (adaptive learning parameters, sizes of hidden layers, and in particular, initial distributions) are fixed in a useful range, different sets of random initial weights typically effect final RMS error by only a few percent. Switching training and extrapolation subsets from a given dataset also has a small effect.

In run 130, 742 mid-latitude TIGR profiles were used; even numbered profiles were used for training and odd for testing the net. Input to the net is brightness temperature for 653 AIRS channels, selected for surface and air temperature sensitivity. Output is surface temperature and air temperature at 50 distinct pressure levels. The network has 90 hyperbolic tangent transfer functions in the first layer, and 60 hyperbolic tangent transfer functions in the second layer. After $7 \cdot 10^4$ epochs, RMS training error is 0.95K, RMS extrapolation (testing) error is 1.09K, and RMS extrapolation error with 0.2K std noise is 1.22K.

In run 100, 1202 TIGR profiles were used, consisting of the original set of 1761 profiles with $2\text{-}\sigma$ outlier profiles discarded. Run 100 used the same channel set and network size as run 130. After $7 \cdot 10^4$ epochs, RMS training error is 1.03K, RMS extrapolation error is 1.07K, and RMS extrapolation error with 0.2K std noise is 1.16K.

Figure 1 shows the results of run 120. In this run 1737 of the 1761 TIGR profiles are used, with only the 24 $3\text{-}\sigma$ outlier profiles discarded. This profile set contains a large number of representatives from all latitudes. Training was done on even and testing on odd numbered profiles. The same 653 channels were used, with a slightly larger net: 108 transfer functions in the first layer, and 72 in the second. After $7 \cdot 10^4$ epochs, RMS training error is 1.05K, RMS extrapolation error is 1.10K, and RMS extrapolation error with 0.2K std noise is 1.17K.

Figure 2 shows the results of run 40. In this run, 400 mid-latitude Phillips profiles were used, with training on even and testing on odd profiles. A smaller set of 59 AIRS channels were used, together with a net with 60 transfer functions in each of the first two layers. After $5 \cdot 10^4$ epochs, RMS training error is 0.59K, RMS extrapolation error is 0.96K, and RMS extrapolation error with 0.2K std noise is 1.51K. The smaller channel set and restricted latitude group has reduced training error, but performance with noise is worse.

5. Conclusions

The neural network allows us to make effective use of the large AIRS channel set, especially for better noise performance. Restricting the network to a particular latitude group can also reduce error.

As with more traditional methods of interpolation, neural networks can both under- and over-fit. High training error or inability to converge on the training set is a sign of under-fitting, while poor performance on new data is a sign of over-fitting. The close correspondence between training and extrapolation errors on the runs with 653 channels, and appropriate smoothness of retrieved profiles, suggest that the size of our hidden layers is not too large, and that we are not overfitting. It may be possible to use larger hidden layers to improve training and also (though to a lesser degree) extrapolative behavior.

There are a number of directions for further work. Our present results indicate it is likely that a somewhat larger net may have errors below 1K across all latitudes. The retrieval of other atmospheric parameters, such as H_2O , O_3 , etc., are promising areas for further investigation, as are the potential application of neural nets to cloud tests and cloud clearing. It should be possible to extract dependency information from the net. By performing sensitivity analysis on input/output pairs with a trained net, we can grade input channels according to their effect at a given pressure level. In principle, one could take the entire AIRS channel set, train a net for (say) temperature retrievals, perform a sensitivity analysis on the resultant net, get a smaller set of temperature sensitive channels, and use the smaller channel set to train a second net. Computation time for the sensitivity analysis should be much less than the time for training such a net; the difficulty is that training is much slower when a large number of channels do not have 'usable' information.

Acknowledgement: The authors would like to thank Alain Chedin and Milt Halem for helpful discussions of this problem.

6. References

1. C. Rodgers. *Rev. Geophys. Space Phys.*, 14:609-624, 1976.
2. A. Deepak, H.E. Fleming, and J.S. Theon. *RSRM '87: Advances in Remote Sensing Retrieval Methods*. Deepak Publishing, 1988.
3. Atmospheric Infrared Sounder: Science and Measurement Requirements. Technical Report D6665 Rev. 1, Jet Propulsion Laboratory, Pasadena, CA, 1991.
4. Robert Hecht-Nielsen. *Neurocomputing*. Addison-Wesley Publishing Company, New York, NY, 1990.
5. Patrick K. Simpson. *Artificial Neural Systems*. Pergamon Press, Inc., Elmsford, New York, 1990.
6. A. Chedin et al. *Journal of Climate and Applied Meteorology*, Feb., 1985.
7. PDS1200 data set, made available on diskette by L. McMillan (NESDIS) and J. Looper (SMSRC), Nov., 1985.
8. J. Susskind, J. Rosenfield, and D. Reuter. *J. Geophys. Res.*, 88, pp 8550-8586, 1983.

Paper withdrawn.

TOMOGRAPHIC INVERSION OF STELLAR OCCULTATION MEASUREMENTS

Johanna Tamminen, Erkki Kyrölä, Liisa Oikarinen, and Elina Sihvola
Finnish Meteorological Institute
Department of Geophysics
P.O. Box 503, SF-00101 Helsinki, Finland
tel. 358-0-19291

Heikki Haario
University of Helsinki
Department of Mathematics
SF-00101 Helsinki, Finland

1. Introduction

We have studied the possibilities of the stellar occultation method in monitoring the global distribution of stratospheric ozone. In this paper we discuss the tomographic inversion problem of stellar occultations. We present different techniques and compare them using the characteristic properties of GOMOS instrument.

The GOMOS (Global Ozone Monitoring by Occultation of Stars) satellite instrument is a proposal by French Service d'Aéronomie du CNRS and the Finnish Meteorological Institute for the first European Polar Platform, POEM-1, which will be launched in 1998. POEM-1 will orbit the Earth 15 times a day and on every orbit GOMOS will observe 25-40 stellar occultations. During every occultation GOMOS follows a star from a tangential altitude 100 km down to 15 km and measures the stellar spectra about 40-60 times.

The main detectors in the GOMOS instrument are 2-dimensional CCD-cameras which give a good spectral resolution. The wavelength range 250-675 nm is used to measure in addition to ozone also NO_2 , NO_3 , and aerosol concentrations. There are also two spectrometers in the IR-region in order to measure the density of oxygen and water vapor. The wavelength resolution is 0.6 nm in the UVIS-band and 0.12 nm in the IR-bands.

2. Retrieval of the line densities

Atmospheric transmission is obtained as the ratio between the stellar spectra measured above and through the atmosphere. If we consider the cross sections σ_k to be independent

of temperature T we can write the extinction coefficient as

$$\tau(\lambda, l) = \sum_k N^k(l) \sigma_k(\lambda) \quad (1)$$

where the tangential line density of the constituent k along the measurement line l is

$$N^k(l) = \int_l \rho_k(s) ds. \quad (2)$$

The great amount of spectral data from one measurement makes it difficult to invert the vertical distribution directly from the transmission data. Equations (1) and (2) show that we can divide the problem into two subproblems. First we calculate the line densities N of different constituents from a measured transmission. After that we calculate the global density functions ρ of each constituent from the already calculated line densities.

Because real measurements do not exist yet we use simulated measurement data for testing different methods. We have calculated the measurement coordinates, simulated the stellar spectra, transmission of the atmosphere, the scattered solar light, and the instrument. The atmospheric model includes O_3 , NO_2 , NO_3 , aerosols, and neutral density. The number density of these constituents are described as a function of altitude, latitude, and time.

The noise in the data includes three components, photon noise, instrument dark current noise and read-out noise. Due to a relatively large amount of noise the inherently Poissonian noise processes can reasonably be approximated by Gaussian processes which simplifies the problem.

The data for the tomographic inversion (i.e line densities) is the result of a spectral inversion which means that it also includes the error caused by the first inversion method. The retrieval accuracy of the retrieved tangential line density depends on the temperature and the brightness of the star and on the tangent height of the measurement line. A knowledge of the noise level can be used in smoothing the data of the tomographic inversion.

3. Tomographic inversion

In local vertical inversion we use only measurements from one occultation. We consider the atmosphere to be locally spherically symmetric. Let l be the light path from star to satellite and r be the distance of a point at l from the center of the Earth and r_0 the distance of the tangent point of l from the center of the Earth. Now if we ignore the refraction the line density for one constituent can be written as

$$N(r_0) = 2 \int_{r_0}^{\infty} \frac{\rho(r) r dr}{\sqrt{r^2 - r_0^2}}. \quad (3)$$

This is the Abel's integral equation which is exactly invertible:

$$\rho(r) = \frac{-1}{\pi} \int_r^{\infty} \frac{dN(r_0)}{dr_0} \frac{dr_0}{\sqrt{r_0^2 - r^2}}. \quad (4)$$

Because this method uses the derivatives of the line density data it makes the solution unstable and therefore we have studied different smoothing algorithms in order to stabilize the problem.

Another solution is to discretize the problem. We divide the atmosphere to radial cores and determine the density in each core. The line density data spans over several orders of magnitudes depending on the tangential altitude of the measurement. The unbalanced data creates special difficulties to the inversion. To alleviate the effect of unbalanced data we have used the well known *Onion peeling* idea. The Onion peeling-technique is a simple inversion method where the linear equation is solved row by row using the previously solved volume densities.

In the global inversion we use measurements made for example in one day and treat the problem as tomography. The problem is to determine the three-dimensional ozone density function ρ from the line densities N_i :

$$N_i = \int_{l_i} \rho(z(s), \theta(s), \varphi(s)) ds, \quad (5)$$

where $i = 1, \dots, m$ and m is the number of measurements. This integral operator is known as *Radon transform*. The reconstruction problem is now to find the inversion of Radon transform. We have a so called *exterior problem*, where N_i is given only for $|r_i| \geq a$ where a is greater than Earth radius and $\rho(x)$ is to be determined for $|x| > a$ only.

The tomographic inversion is made by discretizing the atmosphere into volume cells and considering the density function to be constant inside each volume element. Now the problem (5) is

$$N_i = \sum_{j=1}^n a_{ij} \rho_j, \quad (6)$$

where j numbers the cells and a_{ij} is the length of the i th ray in the j th volume cell.

The GOMOS instrument will make as many as 25000 measurements in one day with different geographical location and different altitudes. Because of the noise in the line density data we have to keep the problem overdetermined. With a suitable division the number of unknown densities is about 5000-7000. This means that the kernel matrix a_{ij} is strongly overdetermined and very sparse, only less than 2 % of the elements are nonzero.

Because the data is strongly unbalanced the inversion can not be made directly. This leads us to the Onion peeling-technique generalized to three-dimensional problems. Since the subproblems are still overdetermined and sparse we have used different methods to solve them like iterative reconstruction methods (ART) and methods to minimize the sum of least squares.

We have used these methods also without the Onion Peeling-technique, but the direct application is not very successful. One possible solution is the "Onion wrapping"-technique. It means that we invert first the whole equation, and then save only the well determined

densities at the lowest cores. After that we invert the rest of the equation and save again only the well determined densities and continue the same way up to the highest core.

4. Conclusions

The stellar occultation technique seems to be a promising method to monitor the atmospheric ozone content as well as few other trace gases. It's advantages over e.g solar occultation are good vertical resolution (1.7 km) and daily global geographical coverage. The retrieval accuracy in tomographic inversion reaches a reasonably good level in the most critical region between 20-45 km where the ozone layer resides.

References:

- Bertaux, J. L. et al., GOMOS, Proposal in response to ESA EPOP-1. A.O, January 1988.
- Korpela, S., A Study of the Operational Principles of the GOMOS Instrument for Global Ozone Monitoring by the Occultation of Stars, PhD thesis, Geophysical publications 22, Finnish Meteorological Institute, 1991.
- Kyrölä, Tuomi, Sihvola, Tikka, Kotivuori, Tuomi, and Haario, Inverse Theory for Occultation Measurements I: Spectral Inversion, to be published in J. of Geophys. Res.
- Natterer, F., The Mathematics of Computerized Tomography, John Wiley & Sons Ltd and B G Teubner, Stuttgart, 1986.
- Piironen A., Application of Inversion Methods for Satellite-Based Occultation Measurements, Thesis at the University of Joensuu, Department of Physics, Finland, 1991.

**An Assessment of the Effects of Diffraction on Infrared
Measurements from Geosynchronous Orbit**

Harry E. Montgomery, William E. Shenk
NASA Goddard Space Flight Center, Greenbelt, MD 20771

The effects of diffraction were calculated for selected current and future geosynchronous satellite infrared profiling and imaging channels. The future geosynchronous satellite calculations were made for the GOES I-M instruments. For comparison, some calculations were also made for similar measurements in low earth orbit. The results indicate that substantial diffraction effects, as high as 17 K, are and will be present for geosynchronous 15 μm profiling channels and 11 μm profiling and imaging channels when clouds are close to the sensor instantaneous field-of-view and the difference between the equivalent blackbody temperature between the cloud and the clear air scene is ≥ 20 K. Similar diffraction calculations at 4 μm show a reduction of 5-10 K in the diffraction effects which suggests that, wherever possible, 4 μm channels should be used for profiling and imaging whenever quantitative radiometric measurements are made of surface properties (e.g. surface temperature).

HALOE DATA PROCESSING TECHNIQUES

Larry L. Gordley
Robert E. Thompson, Jr.
G & A Technical Software, Inc.
28 Research Drive
Hampton, VA
804-865-7491

James M. Russell III
NASA Langley Research Center
Hampton, VA
804-864-5691

Introduction:

The Halogen Occultation Experiment (HALOE)¹ was launched aboard the UARS satellite in September of 1991 and has performed flawlessly since activated on October 11, 1991. HALOE uses both broadband radiometry and gas correlation radiometry techniques during occultation to obtain measurements for inferring temperature, pressure, and mixing ratios of O₃, H₂O, NO₂, HF, HCl, CH₄, and NO.

The HALOE instrument achieves a vertical resolution on the limb of about 2 km. The solar disk, in combination with accurate tracking and ephemeris information, allows very precise knowledge of viewing geometry. With high signal to noise (>1000 for radiometer channels, >100 for correlation channels) and measurements spaced at roughly .3 km or less in the apparent limb vertical, it is a major processing challenge to achieve optimum information retrieval.

Signal Conditioning

Signals are corrected for electronic filtering and smoothed in regions of low signal to noise. An initial pressure registration is achieved through comparison of CO₂ transmission measurements to calculated transmission using NMC temperature and pressure data.

Exoatmospheric scans across the sun are processed to infer a source function for use in signal modeling. A first order correction for sunspot perturbations is also performed using solar scan data.

Radiometer Channel Retrievals

Retrievals for all channels are performed by iteratively changing the retrieved parameter of a signal model until model matches measurement. The high density measurement spacing in the vertical combined with the ability to do rapid limb path model calculations² allows the use of an interleave signal profile model. Numerically it is equivalent to retrieving 5 to 10 profiles at 1.5 to 3.0 km vertical point spacing measured at the same location, but interlaced to give an equivalent .3 km spacing. Retrieval stability comes from using 1.5 to 3.0 km vertical mesh for individual profiles plus an interlevel covariance constraint³. The interlevel constraint width on each point is confined to 2 km (1 km above or below). At .3 km spacing, 7 points are included in the estimate at each level. This results in a vertical resolution at or slightly better than the natural 2 km FOV width of the instrument. Details and results for O₃, H₂O, and NO₂ will be shown.

Gas Correlation Channels

The HALOE instrument uses a gas correlation technique to measure the transmission of HF, HCl, CH₄, and NO. The method involves splitting the incoming beam into two paths ending on separate detectors. One path contains a gas cell filled with the gas of interest. The signals from the two detectors are balanced exoatmospherically and the difference signal measured at high gain during occultation. It can be shown that the difference signal divided by the vacuum path signal ($\Delta V/V$) is equivalent to the following:

$$\Delta V/V = K (\tau_w - \tau_n) / \tau_w$$

Where:

- ΔV = the difference signal in volts
- V = full vacuum path signal in volts
- K = a constant dependent on the cell fill conditions
- τ_w = the average transmission over the broadband instrument spectral filter
- τ_n = the average transmission over a pseudo high resolution filter defined by the gas cell absorption

Due to spectral dependence on thermal and orbital (relative velocity) conditions, an accurate forward model demands high resolution calculations. Routines developed at LaRC are used to process the 30 occultations per day for each of the

correlation channels. Line-by-Line tangent ray calculations at 3 km spacing from upper troposphere to mid mesosphere for HF, HCl, CH₄ and up to 140 km for NO are used in the retrieval process. Bandpasses average 70 cm⁻¹ wide with several thousand lines each.

Computer speeds currently inhibit the ability to implement techniques used for the radiometer channels but this limitation should end soon. The limiting calculation is the spectral integration which are fully vectorizable, during retrieval (as opposed to cross section calculation) . Expected improvements will be shown and compared to current results.

Aerosol Corrections

Mt. Pinatubo has contributed what was originally believed to be problems for data analysis, but has become instead a scientific gift. The correlation channel measurements ΔV and V are ratioed to give an aerosol insensitive value. This is used to retrieve molecular concentrations which are in turn used in the V model to infer aerosol transmission. The correlation channel inferred aerosol extinction profiles are then used with Mie theory and refractive index data to correct radiometer signals for aerosol effects. These methods have proven very successful, resulting in both good species retrievals in the lower stratosphere along with a comprehensive global aerosol data set, inferred directly in four bandpasses.

An overview of the above techniques will be graphically displayed. A few correlative data comparisons will be shown to demonstrate the quality of results.

References

- (1) Russell, J.M, III, et al (submitted); The Halogen Occultation Experiment. submitted to Journal of Geophysical Research, Special Issue on UARS.
- (2) Gordley, L. L. and J. M. Russell III (1981); Rapid inversion of limb radiance data using an emissivity growth approximation. Appl. Opt., Volume 20, pages 807-813.
- (3) Rodgers, C.D. (1990); Characterization and Error Analysis of Profiles Retrieved From Remote Sounding Measurements. Journal of Geophysical Research., vol. 95, pages 5587-5595.

**The Satellite Project GOME:
Potential Precision of Trace Gas Retrieval under Ozone Hole Conditions**

D. Diebel, J.P. Burrows, R.J.D. Spurr
University of Bremen, Kufsteiner Strasse, 2800 Bremen 33, F.R.G., (049) 421-218-4582
V.V. Rozanov
University of St. Petersburg, Uljanovskaja 1, St. Petersburg-Petrodvorez, Russia

1. Introduction

GOME (Global Ozone Monitoring Experiment) is an ESA satellite project, centered around the development of a new, diode-array based spectrometer [1]. It will measure the radiation back-scattered from the atmosphere and Earth's surface in the ultraviolet and visible range in nadir-viewing direction. This instrument will be launched in late 1994 on board the ERS-II satellite. The medium-high resolution (0.2 to 0.4 nm) and extended wavelength coverage (240 to 790 nm) of the instrument will enable profiles or column densities of different trace gases to be measured such as of O₃, NO₂, NO₃, ClO, OClO, BrO, HCHO, and SO₂. In addition, the distribution of aerosols and surface spectral reflectance properties can be investigated.

The algorithms for the retrieval of these parameters must take into account the special characteristics of the GOME measurements, e.g., the large number of 3584 spectral channels, the overlapping absorption features of many trace gases, and the limitation to the nadir direction. The retrieval precision of any atmospheric parameter of interest is, for a given algorithm, determined by these characteristics in conjunction with any random or systematic errors on the measurements. In the following, a theoretical precision analysis will be presented for the example of an antarctic ozone hole condition with the focus on O₃, NO₂, and the halogen compounds ClO, OClO, and BrO.

2. Mathematical Principles

The propagation of radiation through the atmosphere is mathematically described by the Radiative Transfer Equation. This integro-differential equation can be solved numerically to provide the radiance received at the satellite as a function of the distribution of atmospheric gases and aerosols, i.e. the parameters under investigation. For GOME measurements, a new Radiative Transfer Model, GOMETRAN [2], has been developed assuming a plane-parallel geometry and based on the "finite difference method" [3]. This method combines medium computational speed with high accuracy and is especially suitable for linearization procedures, which allow very time-efficient calculations of the so called "weighting functions".

A weighting function describes the change in measured radiation for a given change in an atmospheric parameter of interest. They have to be calculated for each parameter, at all of the 3584 GOME wavelengths and for a number of discrete atmospheric levels (in case of GOME, typically 50). The weighting functions are fundamental to the retrieval of unknown atmospheric parameters from a measured radiance spectrum. There are a number of different procedures available for this inversion problem in remote sensing, which have been reviewed by Rodgers [4]. The recommended algorithm is a statistical regularization method ("Optimal Estimation") where *a priori* information about the parameters to be retrieved is used to stabilize the inversion of the weighting function matrix.

The assessment of precision of the retrieved parameters requires the quantification of random and systematic error sources. Systematic errors include biases of the Radiative Transfer Model, uncertainties in absorption and scattering cross sections and systematic errors in the measurement. In the following discussion, only random errors will be considered with respect to the

precision of GOME retrieval algorithms. The random error of the measurement is composed of photon shot noise and instrumental noise. Both the random noise and the statistical variance of the *a priori* information to be included have to be described in form of covariance matrices. With the matrices **S** for the measurement noise, **D** for the *a priori* variance, and **A** for the weighting functions, the precision for a parameter at the chosen atmospheric levels is given by the square root of the diagonal elements of the matrix **E** with

$$\mathbf{E} = (\mathbf{A}^T \mathbf{S}^{-1} \mathbf{A} + \mathbf{D}^{-1})^{-1}$$

The precision in case of an atmospheric layer is derived by summation of the appropriate on- and off-diagonal matrix elements.

3. Precision Studies for Ozone Hole Conditions

The understanding and modelling of the chemical mechanisms leading to the production or depletion of O₃ in polar regions requires comprehensive measurements of the atmospheric composition in these regions. In addition to O₃, nitrogen and halogen compounds are of paramount importance. The possibilities of GOME to investigate O₃, NO₂, ClO, OClO, and BrO will be discussed. The absorption bands of these gases strongly overlap, rendering it necessary to examine their cross-correlation in the retrieval process. Furthermore, it is essential to take into account the interference of aerosol and molecular scattering and the influence of surface reflectance properties.

The model ozone hole scenario features an O₃ depletion between 16 and 24 km with a maximum depletion of about 75% at the center height. For the remaining altitude range the values correspond to background levels for October and 85°S as calculated from the MPI two-dimensional chemo-dynamical model [5], which also provides the distribution of NO₂, ClO, OClO, and BrO. The aerosol profile consists of a maritime aerosol type for the first two kilometers and of background tropospheric, stratospheric and mesospheric aerosol types above. The viewing geometry for the calculation of the weighting functions is a sun zenith angle of 80°, a line-of-sight (i.e. scan) angle of 45°, and a relative azimuth angle between sun and satellite of 0°. A surface reflectance of 0.85 (i.e. ice) was used for all wavelengths. A realistic measurement noise spectrum was calculated, resulting in noise levels ranging between 10⁻¹ at 240 nm and 0.3*10⁻⁴ at 790 nm. The correlation radius for the *a priori* covariance matrix is 5 km. All precisions discussed below are for a +/- 1σ standard deviation from a mean value. This covers approximately 67% of the measurements assuming a Gaussian distribution.

The precision of O₃ and NO₂

O₃ and NO₂ are, due to their high concentration levels, major trace gases in the atmosphere. This, in conjunction with their wide-range absorption bands in the ultraviolet and visible, should result in sufficient information in the measured spectra to allow the retrieval of vertical profiles. Precisions are shown in Fig. 1 for a retrieval on an atmospheric grid with a 2 km vertical resolution. For this condition, it would be possible to obtain O₃ with a precision of about 3% in the altitude range around 25 km (maximum O₃ densities) and about 10 to 15% above and below if all extraneous parameters were known precisely. Including *a priori* uncertainties and hence limited retrieval precisions for the other parameters degrades the O₃ precision to 8% in the O₃ maximum and 15 to 20% otherwise.

NO₂ concentrations are several orders of magnitude lower than those of O₃. In addition, under ozone hole conditions NO₂ is depleted ("Noxon cliff"). The consequence is a much smaller impact of NO₂ on the measured spectrum. The information content is lower and the retrieval less precise. Precisions of 12% in the NO₂ maximum could be achieved if all other parameters were known exactly. Outside the altitude regions where NO₂ is high, the precision degrades rapidly

due to the decrease in NO_2 concentration and approaches the limit of the *a priori* uncertainty of 50%. Taking into account the cross correlation to O_3 , aerosols, molecular density, and surface reflectance reduces the precision in the maximum to 18%. A more accurate retrieval of NO_2 requires a lower vertical resolution. For atmospheric layers of 6 km, the precision in the range with the NO_2 maximum was shown to be around 5%.

The precision of BrO, ClO, and OClO

Compared to O_3 and NO_2 concentrations, halogen compounds are minor constituents in the atmosphere, with concentrations being orders of magnitude below the concentration levels of O_3 and NO_2 . As a consequence, the retrieval of profiles is impossible for background levels of these halogen compounds. Under ozone hole conditions, for a variety of reasons [6], enhanced amounts of these gases may occur. To study scenarios with such increased levels, Gaussian profiles were added to the MPI background values, with the center height of 20 km and the halfwidth of 8 km coinciding with the features of the ozone hole. The concentration levels in the maximum follow typical values found in the literature [7,8]. Fig. 2 shows the achievable precision for the retrieval of column densities in 6-km layers. Even for this reduced vertical resolution, an improvement by a factor of 2 or more over the *a priori* uncertainty is limited to a very restricted altitude range.

High precisions can be obtained, even for background levels of BrO, ClO, and OClO, provided only the total column densities are to be derived. Results are given in Table 1 for the total column between 0 and 60 km for two different scenarios: one with background levels for BrO, ClO, and OClO; the other one with increased levels for these gases. The retrieval of ClO is the least accurate because of the masking effect of O_3 whose absorption band fully overlaps with those of ClO. In case of the calculations for OClO, twilight concentrations were used in combinations with a rather high sun elevation given by the used zenith angle of 80° . A more realistic measurement scenario has to use larger values around 90° to model a twilight condition. This is at present not possible due to the plane-parallel nature of the Radiative Transfer Model GOMETRAN, which restricts sun zenith angles to values below 80° . Larger zenith angles would result in lower light levels, hence lower signal-to-noise ratios and therefore degrade the precision for OClO by, presumably, a factor of 2 or 3.

Table 1: Column Retrieval Precision (%)		
	background scenario	increased levels
BrO	3.5	2.3
ClO	40.5	11.2
OClO	1.0	0.9

4. References

- [1] Burrows, J.P., and K.V. Chance, Proc. of the SPIE Symposium on Environmental Sensing, 22-26 June, 1992, Berlin, F.R.G., in press (1992).
- [2] Diebel, D., R.J.D. Spurr, J.P. Burrows, V. Rozanov, and Y. Timofeyev, Proc. of the SPIE Symposium on Environmental Sensing, 22-26 June, 1992, Berlin, F.R.G., in press (1992).
- [3] Lenoble, J. (Ed.), A. Deepak Publishing, Hampton, VA, U.S.A., 300 pp. (1985)
- [4] Rodgers, C.D., Rev. Geophys. Space Phys. 14, 609-624 (1976).
- [5] Crutzen, P.J., and L.T. Gidel, J. Geophys. Res. 88, 6641-6661 (1983).
- [6] WMO, Global Ozone Research and Monitoring Project, Report No. 20, 486 pp. (1989).
- [7] Brune, W.H., J.G. Anderson, and K.R. Chan, J. Geophys. Res. 94D, 16,649-16,663 (1989).
- [8] Solomon, S., G.H. Mount, R.W. Sanders, and A.L. Schmeltekopf, J. Geophys. Res. 92D, 8329-8338 (1987).

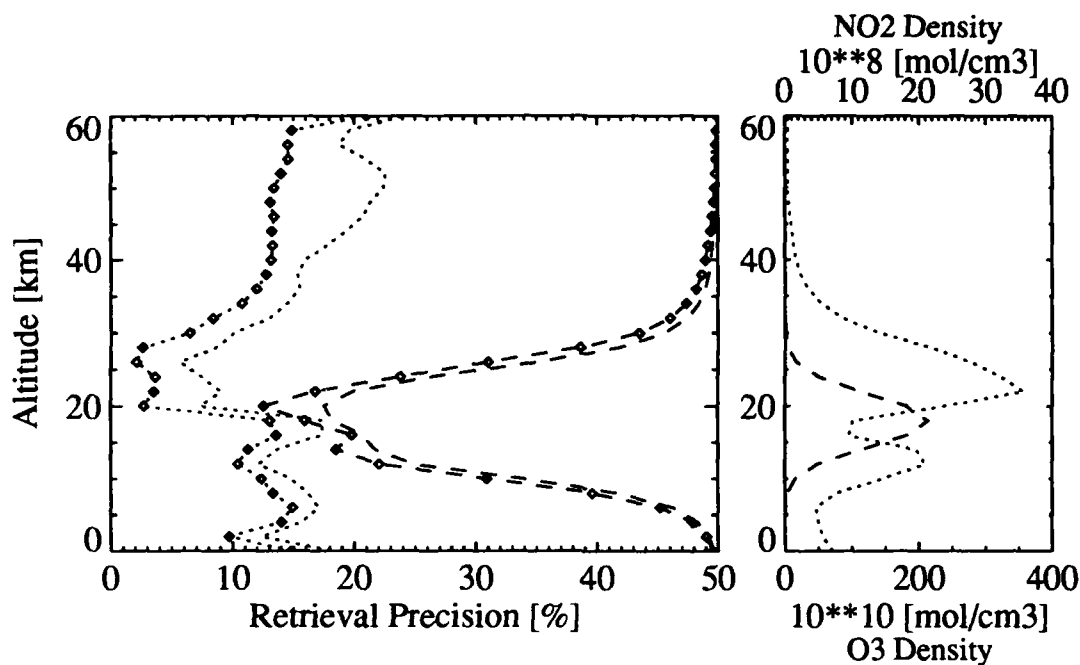


Fig. 1: Left: Retrieval precision for O₃ (dotted lines) and NO₂ (dashed lines) for a vertical resolution of 2 km. The curves without the square symbols are calculated assuming *a priori* uncertainties of 30% for O₃, 50% for NO₂, 100% for aerosol parameters, 30% for the molecular density, and 100% for the surface reflectance. The curves with the symbols correspond to a retrieval under the assumption of an *a priori* error of 30% for O₃ in case of the O₃ retrieval, 50% for NO₂ in case of the NO₂ retrieval, and an accurate knowledge of all other atmospheric parameters.

Right: Profiles used for O₃ and NO₂ densities.

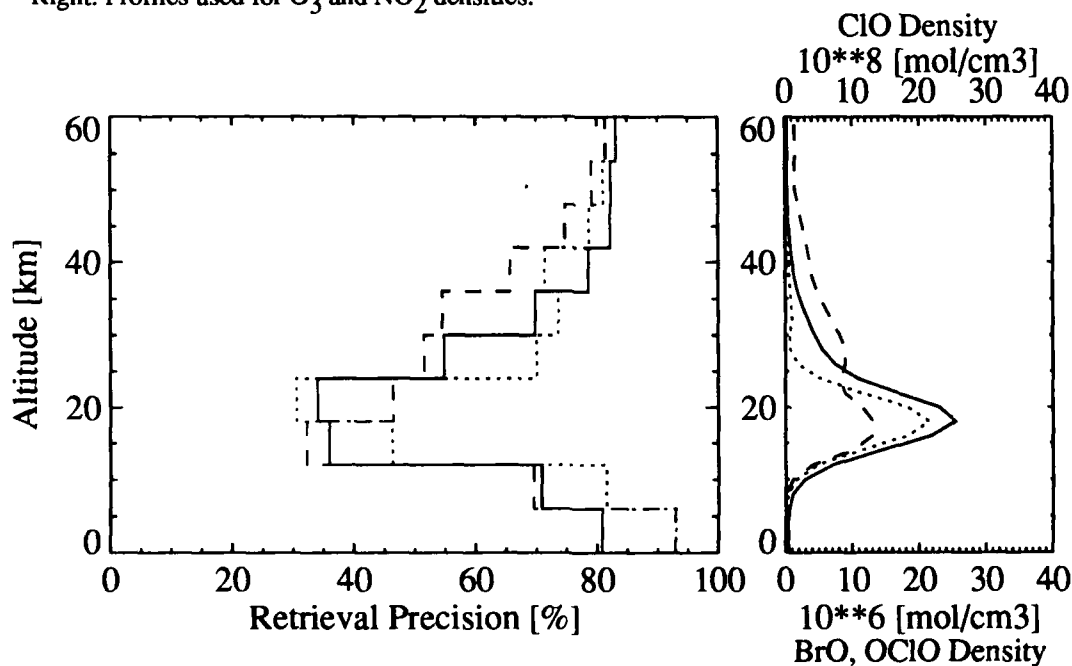


Fig. 2: Left: Retrieval precisions for BrO (solid line), OCIO (dashed line), and ClO (dotted line) for column densities in 6-km layers. *A priori* uncertainties: 30% for O₃, 100% for aerosol parameters, 30% for the molecular density, 100% for the surface reflectance, and 100% each for BrO, ClO, and OCIO (no cross-correlation included between BrO, ClO, and OCIO).

Right: Profiles used for BrO, ClO, and OCIO densities.

PROBING THE MARTIAN ATMOSPHERE IN THE ULTRAVIOLET

Bernhard Lee Lindner

Atmospheric and Environmental Research, Inc.
840 Memorial Drive
Cambridge, Massachusetts 02139
(617)349-2280

Several fundamental differences in atmospheric chemistry exist between Mars and the Earth. The martian atmosphere is primarily CO₂ (95%), with strong vertical mixing, cold temperatures (typically 220K), low pressures (6 mb at the surface), high atmospheric dust and cloud particle content, and no man-made atmospheric constituents. Earlier difficulties in explaining why the atmosphere was not more decomposed into CO and O₂ have been placated with models using updated reaction rates, 'moderate' eddy mixing of order $10^7 \text{ cm}^2 \text{ s}^{-1}$, and the odd hydrogen catalytic cycle (Shimazaki, 1989; Krasnopolsky, 1992). Odd nitrogen and sulfur catalytic cycles are of marginal importance, and other catalytic cycles shown to be important in the terrestrial atmosphere are unimportant on Mars (Yung et al., 1977; Krasnopolsky, 1992). Currently, much work is being undertaken to examine the importance of heterogeneous chemistry (e.g., Atreya and Blamont, 1990; Krasnopolsky, 1992), but uncertainties in particle properties make efficiencies difficult to evaluate. Also, atmospheric chemistry may significantly alter atmospheric composition on climatic timescales, particularly during periods of low obliquity (Lindner and Jakosky, 1985).

Ozone is a key to understanding atmospheric chemistry on Mars. The O₃ abundance has been inferred from UV spectra by several spacecraft, with the most complete coverage provided by Mariner 9 (Lane et al., 1973). The Mariner 9 UV spectrometer scanned from 2100 to 3500 Angstroms in one of its two spectral channels every 3 seconds with a spectral resolution of 15 Angstroms and an effective field-of-view of approximately 300 km². The only atmospheric absorption in the 2000 to 3000 Angstrom region was assumed to come from the Hartley band system of ozone, which has an opacity of order unity. Therefore the amount of ozone was inferred by fitting this absorption feature with laboratory data of ozone absorption, as shown in Fig. 1. Mars O₃ shows strong seasonal and latitudinal variation, with column abundances ranging from

0.2 $\mu\text{m-atm}$ at equatorial latitudes to 60 $\mu\text{m-atm}$ over the northern winter polar latitudes [Lane et al., 1973] (1 $\mu\text{m-atm}$ is a column abundance of 2.689×10^{15} molecules cm^{-2}). However, the O₃ abundance is never great enough to significantly affect atmospheric temperatures (Lindner, 1991) or surface temperatures and frost budgets (Lindner, 1990). Figure 2 shows some of the inferred O₃ abundances.

I use a radiative transfer model based on the discrete ordinate method to calculate synthetic radiance spectra. Assuming a constant mixing ratio for ozone and no chemical or radiative interaction between O₃ and clouds/dust, Fig. 3

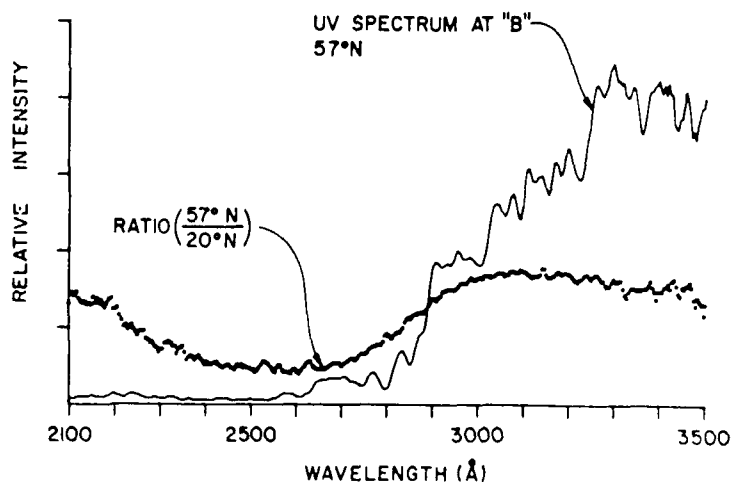


Figure 1. Ultraviolet spectrum measured by Mariner 9 at 57N latitude on orbit 144. To enhance the O₃ absorption feature, this spectrum was divided by one obtained at 20N latitude on orbit 144, where O₃ abundances are minimal (Lane et al., 1973).

shows that when typical amounts of dust and cloud are present that significant underestimation of O_3 occurs. A factor of 3 times as much O_3 is needed to generate the same spectrum as for a clear atmosphere. If the scattering properties of martian clouds and dust were well known, then their appearance would not be a problem, as a model would be capable of retrieving the O_3 abundance. However, these properties are not well known, which raises doubts about the effectiveness of the current UV reflectance spectroscopy technique used to measure O_3 .

Spatial and temporal variability in temperature and water vapor account have been claimed to account for the scatter of the data points in Fig. 2 (Barth and Dick, 1974). A decrease in temperature would result in a decrease in water vapor, if saturated as expected at prevalent temperatures. A decreased water vapor abundance decreases the availability of odd hydrogen, which converts CO and O into CO_2 catalytically, decreasing the abundance of O needed to form O_3 . However, water vapor is a small source of odd hydrogen in the winter polar atmosphere compared to H_2 , and may not account for most of the variability in Fig. 2 (Lindner, 1988). Masking by clouds and dust may also account for some of the observed O_3 variability, because the nature and opacity of the clouds and dust in the polar hood change dramatically in latitude and even on a day-to-day basis. As the maximum O_3 abundance resides near the surface (Lindner, 1988), spacecraft must be able to observe through the entire cloud and dust abundance in order to actually see the total O_3 column abundance. If reflectance spectroscopy is used, as on Mariner 9, then the cloud and the airborne dust must be traversed twice; first by the incoming solar flux down to the surface, and then once again upon reflection from the surface out to the spacecraft. In addition, the large solar zenith angles at winter polar latitudes mean several times the vertical opacity of cloud and dust must be traversed. Indeed, part of the observed latitudinal variation in O_3 in Fig. 2 may be due to the inability of the spacecraft to observe through the increasing effective optical depths as one goes poleward.

By using a photochemical model which included multiple scattering of solar radiation, Lindner (1988) showed that the absorption and scattering of solar radiation by clouds and dust actually increased O_3 abundances at winter polar latitudes. Hence, regions with high dust and cloud abundance could contain high O_3 abundances (heterogeneous chemistry effects have yet to be worked out). It is quite possible that the maximum O_3 column abundance observed by Mariner 9 of $60 \mu\text{m-atm}$ is common. In fact, larger quantities may exist in some of the colder areas with optically thick clouds and dust. As the Viking period often had more atmospheric dust loading than did that of Mariner 9, the reflectance spectroscopy technique may even have been incapable of detecting the entire O_3 column abundance during much of the Mars year that Viking observed, particularly at high latitudes.

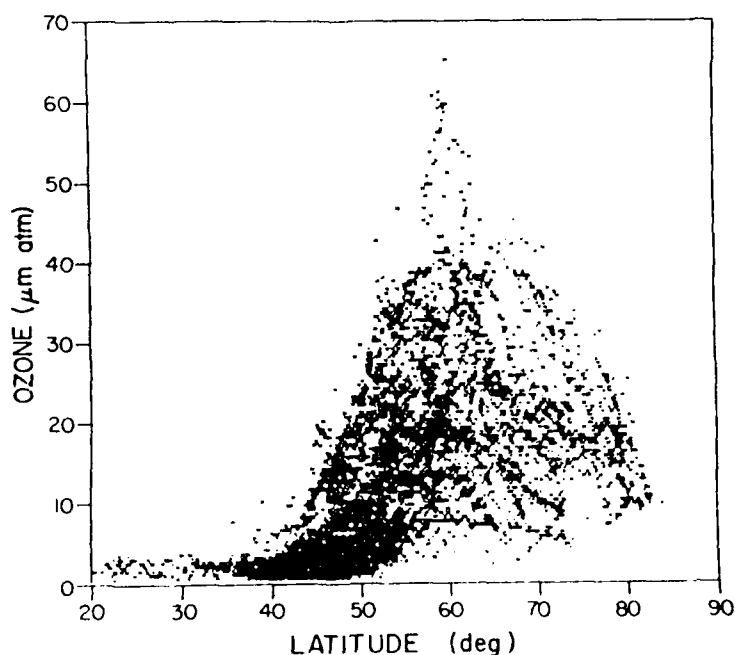


Figure 2. Measurements of the O_3 column abundance inferred from the Mariner 9 UV spectrometer data during the northern winter, $L_s = 330-360$, in the northern hemisphere (Barth, 1985).

However, observing the UV spectrum from the surface would greatly reduce the effects of clouds and dust, and hence significantly increase the accuracy of ozone abundance retrievals. A lander with a simple photometer having only 2 channels, one in the O₃ absorption band at 2500 Angstroms and one out of the band at 3500 Angstroms, would achieve this. Other possibilities for measuring ozone include solar occultation (Blamont et al., 1989), IR observations in the 9.6 μm O₃ band (e.g., Espanak et al., 1990), and observations of the O₂ dayglow at 1.27 μm , produced by photolysis of O₃ (Traub et al., 1979). However, further studies of these other techniques are required, especially as regards the effects of clouds and dust.

Atreya, S.K. and J.E. Blamont, 1990: Stability of the martian atmosphere: Possible role of heterogenous chemistry, *Geophys. Res. Lett.*, **17**, 287-290.

Barth, C.A., 1985: Photochemistry of the atmosphere of Mars, in *The Photochemistry of Atmospheres. Earth, other Planets, and Comets* (Ed. J. Levine). Academic Press, Orlando, Fla.

Barth, C.A. and M.L. Dick, 1974: Ozone and the polar hood of Mars, *Icarus*, **22**, 205-211.

Blamont, J.E., E. Chassefiere, J.P. Goutail, B. Mege, M. Nunes-Pinharanda, G. Souchon, V.A. Krasnopolsky, A.A. Krysko and V.I. Moroz, 1989: Vertical profiles of dust and ozone in the martian atmosphere deduced from solar occultation measurements, *Nature*, **341**, 600-603.

Espanek, F., M.J. Mumma, T. Kostiuik, and D. Zipoy, 1990: Ground based IR measurements of the global distribution of O₃ in the atmosphere of Mars, *Bull. Amer. Astron. Soc.*, **22**, 1077.

Krasnopolsky, V.A., 1992: Photochemistry of the martian atmosphere (mean conditions), *J. Geophys. Res.*, in Press.

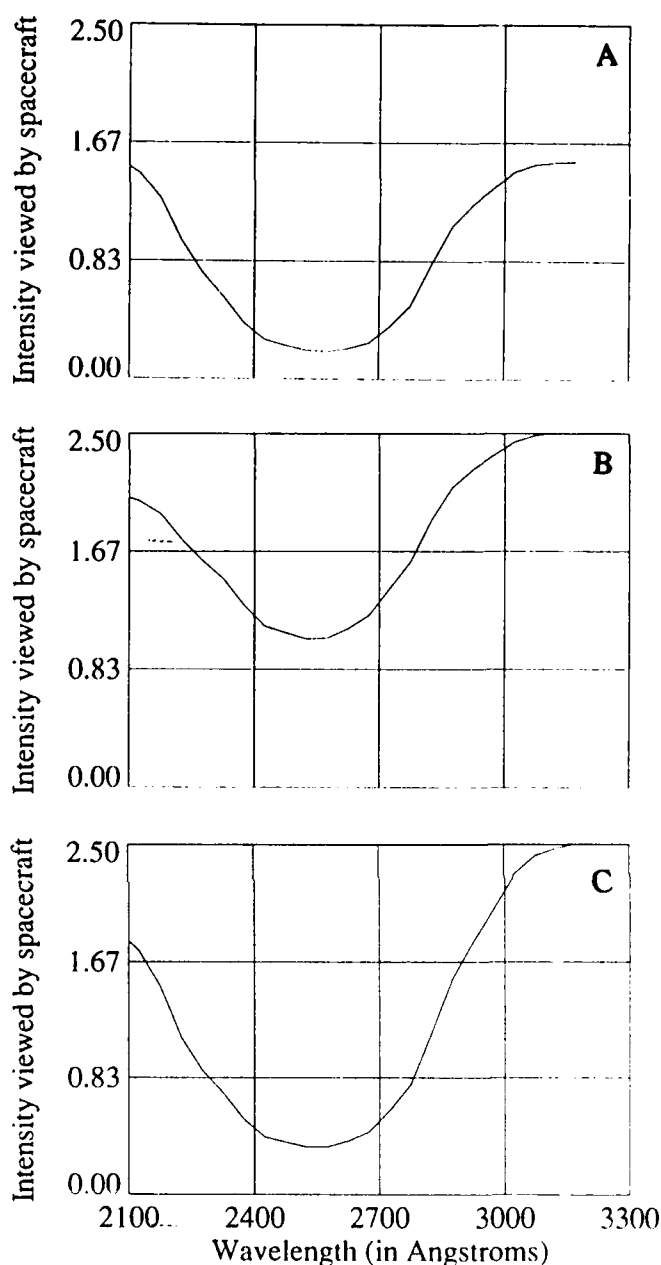


Figure 3. Synthetic spectra as would be observed by spacecraft for atmospheres with (A) no cloud or dust and 30 μm -atm O₃, (B) vertical opacities of dust and cloud of 0.3 and 1.0, respectively, and 30 μm -atm of O₃, and (C) vertical opacities of dust and cloud of 0.3 and 1.0, respectively, and 100 μm -atm of O₃. All cases assume a solar zenith angle of 75 (typical for winter polar observations), and viewing angle of 60, with azimuth angle of 0 (typical for Mariner 9). Polar-cap albedo of 0.8 (new ice).

- Lane, A.L., C. Barth, C. Hord, and A.I. Stewart, 1973: Mariner 9 UV spectro-meter experiment: Obser-vations of ozone on Mars, *Icarus*, **18**, 102-108.
- Lindner, B.L., 1988: Ozone on Mars: The effects of clouds and airborne dust, *Planet. Space Sci.*, **36**, 125-144.
- Lindner, B.L., 1990: The martian polar cap: Radiative effects of ozone, clouds, and airborne dust, *J. Geophys. Res.*, **95**, 1367-1379.
- Lindner, B.L., 1991: Ozone heating in the martian atmosphere, *Icarus*, **93**, 354-361.
- Lindner, B.L. and B.M. Jakosky, 1985: Martian atmospheric photochemistry and composition during periods of low obliquity, *J. Geophys. Res.*, **90**, 3435-3440.
- Shimazaki, T., 1989: Photochemical stability of CO₂ in the martian atmosphere: Reevaluation of the eddy diffusion coefficient and role of water vapor, *J. Geomag. Geoelectr.*, **41**, 273-301.
- Traub, W.A., N.P. Carleton, P. Connes and J.F. Noxon, 1979: The latitudinal variation of O₂ dayglow and O₃ abundance on Mars, *Astrophys. J.*, **229**, 846-850.
- Yung, Y.L., T.Y. Strobel, T.Y. Kong, and M.B. McElroy, 1977: Photochemistry of nitrogen in the martian atmosphere, *Icarus*, **30**, 26-41.

Temperature Profile Measurements Using Oxygen DIAL

C. Laurence Korb, Geary K. Schwemmer, Coorg Prasad¹,
Chi Y. Weng², Joseph Famiglietti and Cyrille N. Flamant³

Laboratory for Atmospheres
NASA/Goddard Space Flight Center
Greenbelt, MD 20771
(301)286-6233

¹Science and Engineering Services, Inc.

²Science Systems and Applications, Inc.

³University of Maryland

We describe differential absorption lidar(DIAL) measurements of the vertical temperature profile in the lower troposphere made in the oxygen A band. A 1 K accuracy, compared with a radiosonde observation made 54 km away, was obtained with a 300 m vertical resolution and a 90 s integration time.

Temperature is one of the fundamental atmospheric state variables. A knowledge of temperature is needed for predicting weather on all time scales and for understanding basic atmospheric processes. The temperature profile can be used along with measurements of atmospheric surface pressure to calculate the vertical atmospheric pressure profile. The derived pressure fields are used to construct the basic maps of surfaces of constant pressure. Furthermore, horizontal gradients of pressure represent the primary physical force leading to all scales of atmospheric circulations in the horizontal dimension, including the large-scale general circulation, extratropical and tropical cyclones and anticyclones, and mesoscale phenomena such as sea/land breezes. Vertical circulations are coupled to the horizontal circulations but are also strongly governed by the vertical gradients of temperature (static stability), especially in the case of precipitation-producing deep convection on the mesoscale.

High vertical resolution temperature profile measurements of 500 m or better are needed to resolve significant structure in the atmosphere such as temperature inversions. Passive instruments which are used for temperature profile measurements from satellites are limited to a 5 to 8 km vertical resolution due to the width of the weighting functions which describe the altitudes of the emissions contributing to each spectral channel. Lidar can provide the high vertical resolution needed.

A two-wavelength differential absorption lidar technique that we have described (Korb and Weng, 1979, 1982) is used for measuring the atmospheric temperature profile. We make a measurement of the absorption at the center of a high J line in the oxygen A band which originates from a quantum state with high ground state energy. The population of the state depends strongly on temperature through the Boltzmann distribution and can be used to obtain a highly sensitive temperature determination. The absorption is found experimentally from the ratio of the on-line backscatter signal spectrally located on the appropriate O₂ line to a reference measurement at a nearby unabsorbed (off-line) frequency.

Our alexandrite lidar system has been described previously by Schwemmer *et al.* (1987). The system includes two narrowband pulsed alexandrite lasers with associated diagnostic instrumentation, a 40 cm diameter telescope, photomultiplier detectors, low noise amplifiers, and a microcomputer controlled data acquisition system. The laser diagnostics include a wavemeter which measures and records the on-line laser spectrum pulse by pulse (Prasad *et al.*, 1988) with an optical resolution of 0.0038 cm^{-1} and a frequency precision of 1 part in 10^8 .

The DIAL temperature measurement requires a laser with better than 0.01 cm^{-1} resolution and better than 0.002 cm^{-1} frequency stability. To achieve this we developed a frequency stabilized diode laser injection seeded alexandrite system (Schwemmer *et al.*, 1991). The on-line laser is injection seeded with the output of a low power, continuous wave, single mode diode laser which is frequency stabilized to the center of the absorption line used for temperature measurements. The diode is attached to a multi-stage thermo-electric cooler for broad wavelength temperature tuning, and housed in a vacuum chamber to prevent condensation from obscuring the beam or shorting the leads. We operate with a diode having a room temperature wavelength of between 773 and 780 nm, and cool it to about -30°C to shift the wavelength to the 768.3 nm oxygen line. The diode laser current is dithered a small amount, causing the wavelength to oscillate. A non-resonant photoacoustic cell, housed inside a gas cell, is used to generate a feedback signal for controlling the laser current to actively stabilize it to the oxygen absorption line.

We made our first high accuracy range resolved measurements of the atmospheric temperature profile on 28 April 1992. The injection-seeded laser was tuned to the P_{27} line of oxygen at 13010.81 cm^{-1} and the off-line laser set at a non-absorbing frequency near 13008 cm^{-1} . The on-line laser energy was 12 mJ per pulse and the off-line energy was set at 6 mJ. The lidar signal returns were measured with a 200 nsec range gate (30 m vertical sampling). The signals were averaged over 900 shots (90 s). In order to analyze the data, the fraction of the signal scattered from aerosols and molecules is determined. The off-line signal is first range squared corrected. For our data, we found a clean, nearly aerosol-free atmospheric return at 9.8 km altitude, just below the tropopause. We used this region to determine the molecular backscatter at this altitude. The molecular return is then found as a function of altitude using the ratio of the atmospheric density at each altitude to that at 9.8 km. This can be accomplished using a climatic estimate for the temperature profile and surface pressure from which the pressure profile and hence the density profile can be determined. In our case, we used radiosonde data taken at the same time 54 km away. The backscatter ratio, 1 + the ratio of the aerosol to molecular backscatter, was then determined as shown in Fig. 1 at a resolution of 30 m. The reference level near 9.8 km which corresponds to a minimum in the backscatter ratio is clearly evident.

The transmission due to the oxygen absorption is found as the ratio of the on-line to off-line signal. The differential absorption over various layers is then calculated from the transmission for layer thicknesses of 300 m. The backscatter ratio is utilized since different scattering processes affect the absorption on the return path from the atmosphere. For the outgoing path, the spectral width of the atmospheric absorption is much broader than the spectrally narrow laser beam. In the case of aerosol scattering, the absorption on the return path is essentially the same as that on the outgoing path since the signal is elastically scattered with no change in the shape of the incident spectrum. In the case of molecular (Rayleigh) scattering, the signal is broadened in the scattering process due to the Doppler effect since the molecules are moving with an ensemble of velocities along the line of sight of the laser beam. Thus, each component of the incoming signal is scattered into a Gaussian spectrum with a width of $2b_d$ where b_d is the Doppler width. The resultant spectrum after scattering is the sum of Gaussian spectra with a width of $2b_d$ for each incoming spectral component. This spectrum is then only partially absorbed on the return path through the atmosphere since it is spectrally broader than the absorption line. In addition, 2.55% of the molecular scattered signal is Raman scattered. In this case, the signal is treated as being absorbed due to resonant absorption only along the outgoing laser path.

The differential absorption for each of the measured layers is calculated using the backscatter ratio to determine the fraction of the signal scattered by aerosol and molecular processes. The temperature profile is then calculated by finding the temperature for each layer such that the calculated differential absorption agrees with that which is measured. A single point calibration procedure using radiosonde data is used to calibrate the molecular absorption line parameters to the measured data. The analysis also included a technique for correcting for laser spectral impurity

which was found to be 6%. The observed transmission is treated as having a spectrally pure component which is absorbed by the atmosphere and a spectrally impure component which is not absorbed. The spectral impurity is found by matching the observed to the calculated transmission at a relatively high altitude, 6.5 km, where the transmission is small, known, and far above the temperature measurement region. As a result, the correction could be made in two iterations in a manner which is relatively independent of the temperature measurement. Non-homogeneous scattering had a significant effect on the measured temperatures, and corrections for this were made.

The resulting temperature profile is shown in Fig. 2 for a vertical resolution of 300 m (on 150 m spacing) and a 900 shot average. The radiosonde profile taken at Dulles airport is also shown for comparison. The average deviation of the lidar and radiosonde data is 0.9 K. The inversion feature just below 2 km altitude matches the shear aerosol layer which is clearly shown in the backscatter ratio.

Korb, C. L. and C. Y. Weng, 1979: A two-wavelength lidar technique for the measurement of atmospheric temperature profiles. Proc., 9th Int. Laser Radar Conf., Munich, *Amer. Meteor. Soc.*, 185-186.

Korb, C. L. and C. Y. Weng, 1982: A theoretical study of a two-wavelength lidar technique for the measurement of atmospheric temperature profiles, *J. Appl. Meteor.*, **21**, 1346-1355.

Prasad, C. R., C. L. Korb, and G. K. Schwemmer, 1988: Laser wavemeter measurement in presence of speckle. 14th International Laser Radar Conf., Abs., Innichen-San Candido, Italy, *Amer. Meteor. Soc.*, 253-256.

Schwemmer, G. K., M. Dombrowski, C. L. Korb, J. Milrod, H. Walden, and R. H. Kagann, 1987: A lidar system for measuring atmospheric pressure and temperature profiles, *Rev. Sci. Instrum.*, **58**, 2226-2237.

Schwemmer, Geary K., H. S. Lee, Coorg Prasad, 1991: Narrowband alexandrite laser injection seeded with frequency dithered diode laser, Earth and Atmospheric Remote Sensing, Robert J. Curran, James A. Smith, Ken Watson, Eds., Proc. SPIE 1492, 52-62.

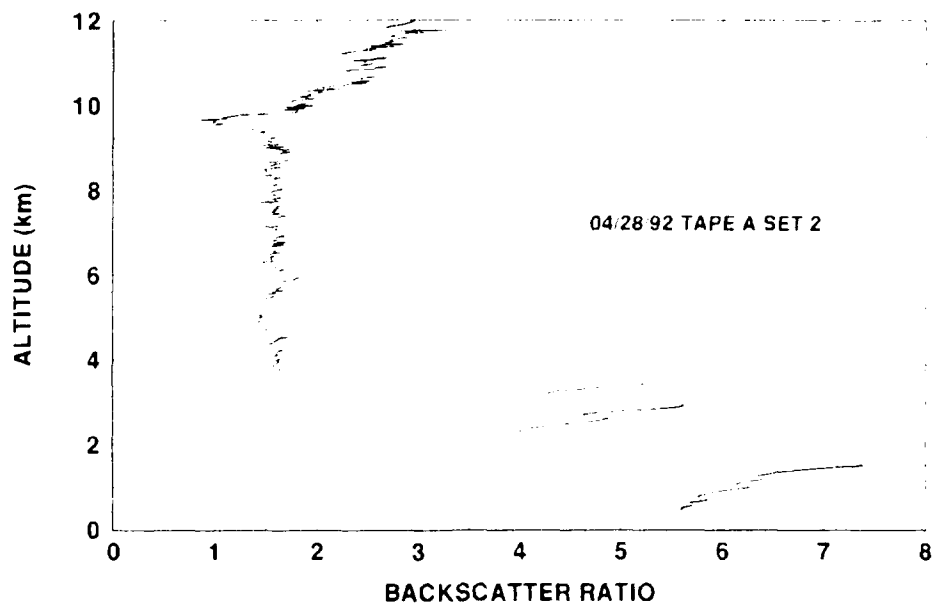


Figure 1 Backscatter ratio, (Mie + Rayleigh)/Rayleigh scattering, as calculated from the off-line signal for 30 m vertical resolution.

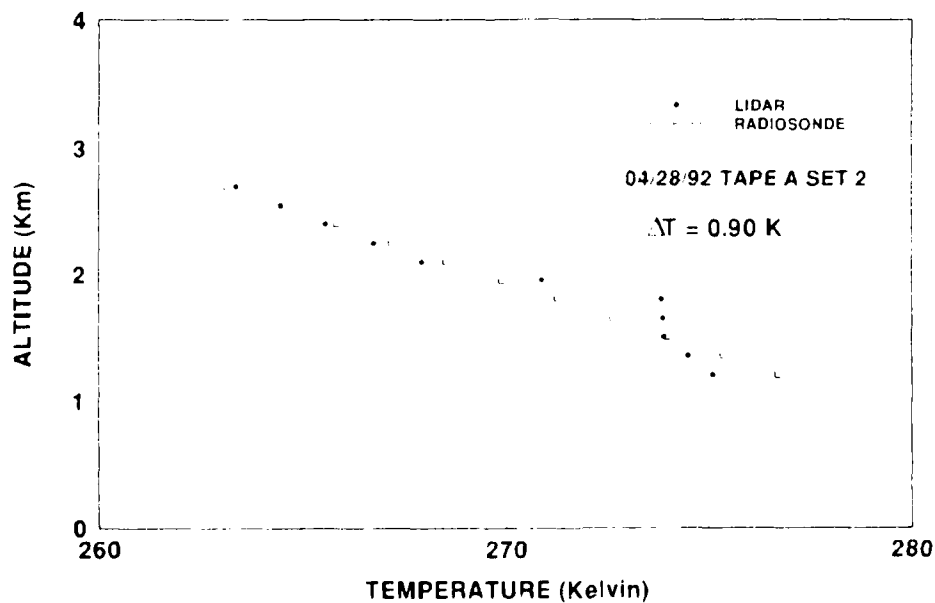


Figure 2. Lidar temperature profile measured at Goddard Space Flight Center with an upward viewing lidar with a 300 m vertical resolution. Radiosonde measurements were made at Dulles Airport.

LASER SOUNDING OF STRATOSPHERIC OZONE IN OBNINSK (RUSSIA)

S.S.Khmelevtsov, E.D. Svetogorov

Measurements of vertical profiles of stratospheric ozone concentrations in one wavelength sounding at the wavelength of 308 nm of eximer laser were started 16 of October, 1990 in Obninsk. Procedure and results of such measurements are given in [1]. In the paper it was shown that knowing vertical profiles of air density and having a background value of ozone the measurement accuracy of vertical profiles of ozone concentration is adequate.

Two frequency measurements by lidar, using diffirential method, were started in Obninsk in March, 1992. During these measurements we have met with some difficulties because of extreme growth of errors of measurements, due to aerosol of the volcano Pinatubo eruption. Similar increase of measurement errors were observed when operating the data laser ozone sounding following volcano El Chichon eruption [2]. To decrease the number of measurement error we have used an averaging sliding window, where the data of 9-10 separate 150 meters intervals have been integrated over the height. The results of data processing by such a technique are given in Fig.2.

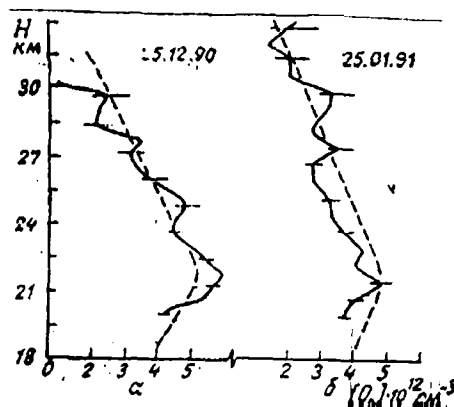


fig.1

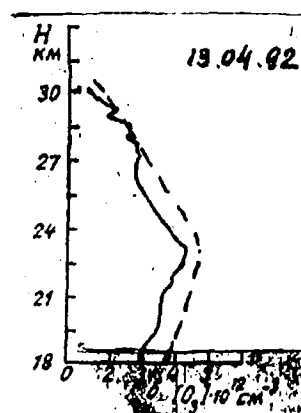


fig.2

1. Kostko O.K., Khmelevtsov S.S., Kaufman Yu.G., Svetogorov E.A., Kalyagina G.A. Measurements of the stratospheric ozone using a single-frequency lidar.- " Optics of atmosphere and ocean ", 5, N 4 (1992).
2. Shibata T., Uchino O. and Maeda M. Eximer lidar measurements of ozone . " Handbook for MAP ", v. 18, 1985.

Multi-Wavelength Sequential Seeding Method for Water Vapor DIAL Measurements

Glen Sachse¹, Liang-guo Wang², Syed Ismail³, Edward Browell³, and
Curtis Banziger⁴

1. NASA Langley Research Center, M/S 472, Hampton, VA 23681, (804)864-1566
2. College of William and Mary, Williamsburg, VA23185, (804)864-1565
3. NASA Langley Research Center, M/S 401A, Hampton, VA 23681, (804)864-2719
4. Science Appl. Int. Corp., 1 Enterprise Parkway, Hampton, VA, 23666 (804)864-8142

Near IR diode lasers have many attractive features for injection seeding solid-state lasers including low cost, relatively high power, single mode operation and wide wavelength tunability. These laser devices are currently being used in the development, at NASA Langley, of an injection-seeded Ti:Al₂O₃-based DIAL instrument to remotely sense water vapor (H₂O(v)) from an ER2 aircraft.

In this instrument a single diode laser provides both the "on" and "off" - line seeding wavelengths (λ_{on} and λ_{off}). The on-line seeding wavelength is maintained by locking the diode laser wavelength to line center of a H₂O(v) transition in the 813-818 nm region using a single-tone FM spectroscopy technique (Wang et al.). The H₂O(v) reference wavelength is provided by diverting a few percent of the diode laser beam through a 4 meter-path White cell containing H₂O(v). Line locking stability of ± 0.12 pm has been demonstrated on strong H₂O(v) lines in this spectral region. The off-line wavelength is achieved by applying a short (~ 400 μ sec) current pulse that momentarily tunes the diode laser wavelength some 20 to 70 pm off line center. With this method the diode laser wavelength is positioned on line center ~ 97 percent of the time.

Due to the strong vertical gradient of H₂O(v) in the atmosphere, it is difficult to achieve, with the above technique, sensitive H₂O(v) measurements simultaneously at high and low altitudes. For example, operation on strong H₂O(v) transitions yields good measurements at high altitudes yet poor results at low altitudes due to strong attenuation of the return signal. Thus high sensitivity measurements at low altitudes necessitate smaller absorption coefficients. Smaller cross-sections may be attained by using weaker transitions or by tuning the diode laser wavelength to an intermediate wavelength, λ_{side} , along the side of a strong transition. Operating a DIAL instrument on the side of an absorption line was previously studied by Brockman et al., for the remote measurement of H₂O(v) using a CO₂ pulsed laser. This paper will analyze various considerations in using a wavelength-agile injection seed source to optimize the remote measurement of H₂O(v) using a

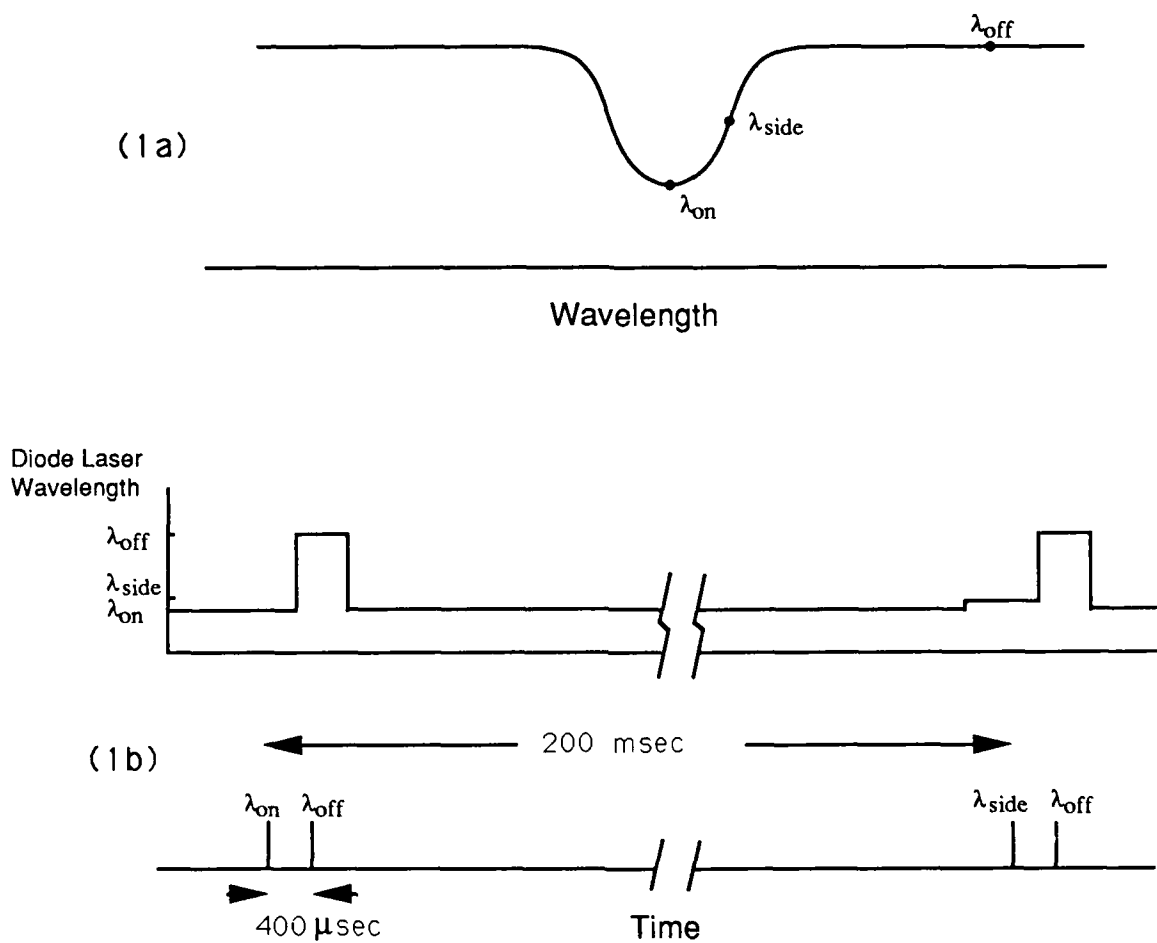
Ti:Al₂O₃-based DIAL system.

The proposed technique involves injection seeding at λ_{on} , λ_{off} and one or more wavelengths on the side of the absorption line. Figure 1 illustrates a three-wavelength (λ_{on} , λ_{side} , λ_{off}) approach. Pulse pair (λ_{on} , λ_{side}) is followed 200 msec later by pulse pair (λ_{side} , λ_{off}). Time separation within a pulse pair is 400 μsec . As before the "home" position of the diode laser is at absorption line center. There are a number of potential advantages of this approach. The obvious benefit being that the entire atmosphere (both high and low altitude regions) is optimally probed with alternate pulse pairs (i.e., λ_{on} , λ_{off} followed by λ_{side} , λ_{off} , respectively). A more subtle benefit is an inherent consistency check that may be utilized to improve the accuracy of the H₂O(v) retrieval. This consistency check is based on the fact that an altitude region exists where sufficient return signals are available from both pulse pair types which permits the retrieval of independent measurements of the H₂O(v) profile. Comparison of these two H₂O(v) profiles averaged over some adequate time period (perhaps minutes or longer) should yield the same result. However, a number of factors will create a systematic offset or divergence between the profiles. Among these systematic error sources are small uncertainties in the λ_{side} value and the pressure broadening coefficient and the presence of spectral impurity in the Ti:Al₂O₃ laser output pulse. Thus by comparing average profiles, retrieval errors due to systematic noise sources will be highlighted. This information may then be used to reduce the effect of these errors.

This paper will present experimental results showing the accuracy and repeatability of diode laser wavelength shifting from λ_{on} to λ_{side} , an analysis of the procedure for selection of λ_{side} , and a calculation of temperature and pressure dependences of the absorption coefficient at λ_{on} and λ_{side} .

References

1. L. -G Wang, J. C Barnes, C. Edwards, R. V. Hess, P. Ponsardin and G. Sachse, "Diode Laser Injection Seeding of A Pulsed Ti:Sapphire Laser for Remote Sensing," OSA 1991 Annual Meeting, San Jose, California, November 3-8, 1991.
2. P. Brockman, R. V. Hess, L. D. Staton, and C. H. Bair, "DIAL With Heterodyne Detection Including Speckle Noise: Aircraft/Shuttle Measurements of O₃, H₂O, and NH₃ With Pulsed Tunable CO₂ Lasers", NASA Technical Paper 1725, August 1980.



1a: The three seed wavelengths in relation to a $\text{H}_2\text{O}(\nu)$ absorption line.

1b: Graphical representations of the diode laser wavelength vs. time and the timing of the DIAL laser pulses.

Figure 1

Solar Blind Raman Scattering Measurements of Water Vapor Using a KrF Excimer Laser

D. N. Whiteman, Code 924, NASA/Goddard Space Flight Center, Greenbelt, MD 20771 (301) 286-3115

R. A. Ferrare, Hughes STX Corp, Code 917, NASA/GSFC, Greenbelt, MD, 20771 (301) 286-2327

S. H. Melfi, Code 917, NASA/GSFC, Greenbelt, MD 20771 (301) 286-7024

K. D. Evans, Hughes STX Corp, Code 917, NASA/GSFC, Greenbelt, MD, 20771 (301) 286-9113

The use of Raman scattering for measurements of water vapor in the atmosphere during the night-time is well established¹⁻⁴. Raman measurements of water vapor during the daytime are considerably more limited. The solar blind technique (SB) for making these measurements has received the most attention to date.

The solar blind technique is so called because stratospheric ozone attenuates essentially all downwelling solar radiation at wavelengths shorter than about 300 nm⁵. The choice of an excitation wavelength which will stimulate Raman-shifted return wavelengths from O₂ (1555 cm⁻¹), N₂ (2329 cm⁻¹) and H₂O (3654 cm⁻¹) which are below the 300 nm solar cutoff allows measurements to be performed with essentially no solar background.

The first SB measurements of water vapor reported were in 1979 by Renaut et al⁶ using a quadrupled Nd:YAG laser (266 nm). Later SB measurements were reported in 1985 Cooney et al⁷ (KrF laser - 248 nm), Renaut et al⁵ again in 1988 (Nd:YAG), and in 1990 by Barnes et al⁸ (KrF). The maximum range reported in any of these accounts is about 1.2 km. We report here a SB Raman measurement of water vapor mixing ratio to a range of 2.5-3.0 km using a KrF laser when coupled with an independent measurement of the ozone profile provided by an ECC (Electrochemical Cell) radiosonde which was used for differential transmission correction of the lidar data.

Our lidar system consists of a Lambda Physik LPX240iCC excimer laser with KrF gas mixture (248.4 nm), .75m Dall-Kirkham telescope aligned colinear with a 1.1mx.8m scanning mirror. The detectors for these measurements were Hamamatsu 2078 and Phillips 2978 PMTs. Dichroic beamsplitters and interference filters select the desired wavelengths. Two PMTs are used per wavelength in a low gain/high gain configuration allowing the exclusive use of photon counting in the data acquisition system. With excitation wavelength of 248.4 nm, the return wavelengths for O₂, N₂, H₂O are 258.4, 263.7, 273.2 nm, respectively.

Figures 1 and 2 represent lidar-derived water vapor mixing ratio measurements made at Greenbelt, MD on October 8, 1992 and October 20, 1992 where differential transmission has been calculated using the appropriate ozone profile presented in figure 3. The lidar profiles are averages over 20 minutes. The radiosonde measurement of mixing ratio and the mixing ratio corresponding to 20% relative humidity are plotted for comparison. The differential transmission of the Raman return signals due to molecular and aerosol scattering and ozone absorption must be calculated prior to deriving the water vapor mixing ratio. We have used model aerosol profiles estimated from the direct backscatter lidar data for the aerosol correction while the ECC ozone measurements have been used to perform the ozone calculation. We feel that afterpulsing in the PMTs is currently limiting our ability to adequately derive the ozone profile directly from the lidar data.

The correspondence between the lidar and the radiosonde measurements is generally good with a few discrepancies. In figure 1, the lidar measurement at about 1.5km is thought to be real as the influence of afterpulsing at this level is negligible, whereas in figure 2 the influence of afterpulsing becomes evident above 2.5km. The limitation of the carbon hygistor radiosonde below relative humidities of about 20% can be seen in the region between 1.5 - 2.2 km in figure 2 where the lidar is able to measure substantially

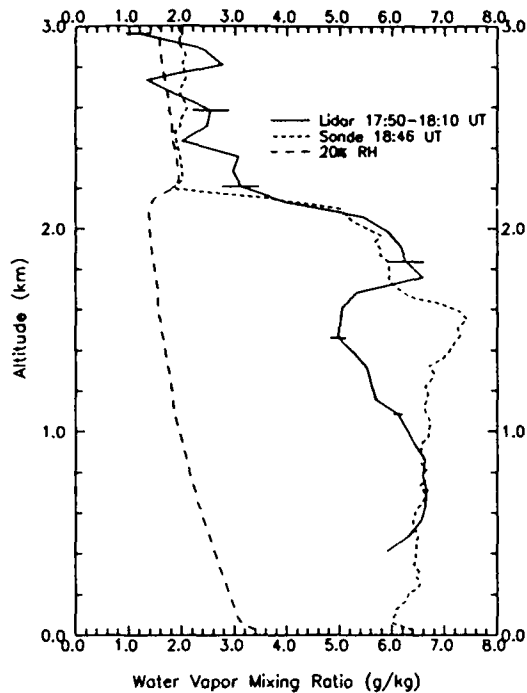


Fig 1. October 8, 1992 Lidar derived water vapor mixing ratio using ECC ozone measurement compared with radiosonde water vapor mixing ratio

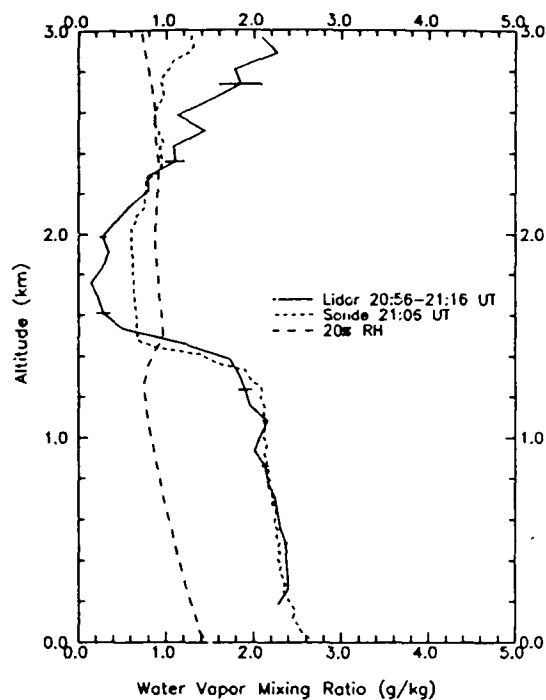


Fig 2. October 20, 1992 Lidar derived water vapor mixing ratio using ECC ozone measurement compared with radiosonde water vapor mixing ratio

lower mixing ratio values.

The difference in the ozone cross section between 258 nm and 263 nm is about 15%⁹. The DIAL

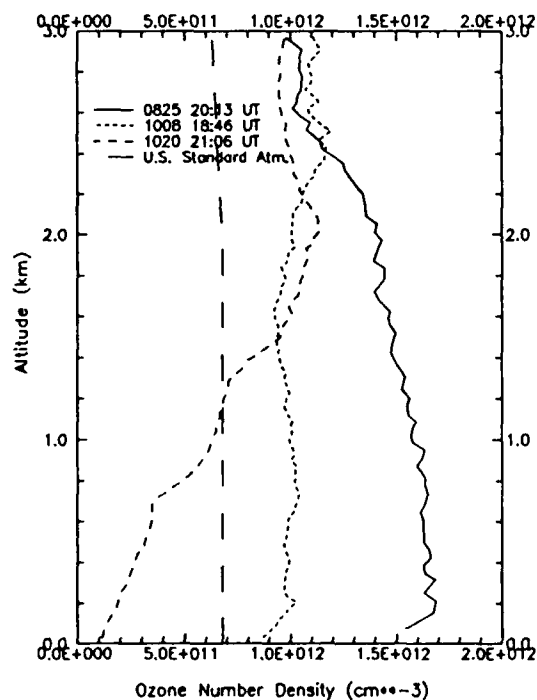


Fig 3. ECC measurements of ozone on Aug. 25, Oct. 8, Oct. 20, 1992 at Greenbelt, MD

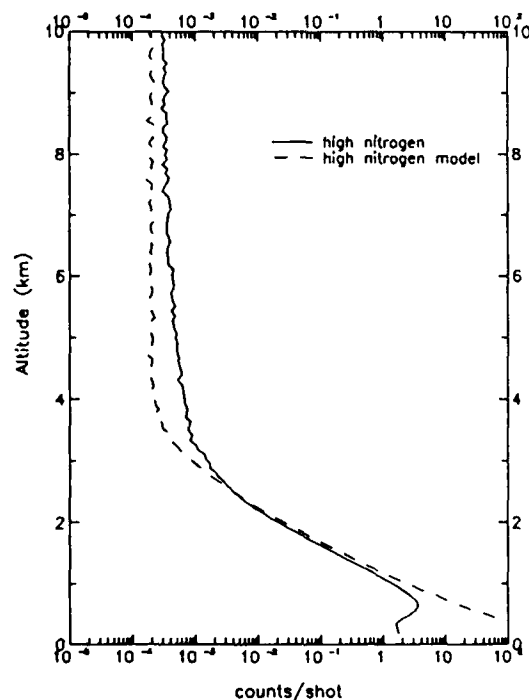


Fig 4. Raman lidar measurement of nitrogen on Oct. 20, 1992 compared with model prediction using measured ozone

calculation of ozone from the lidar data is thus looking at small slope changes between the Raman nitrogen and oxygen signals. Small errors in the determination of the overlap function, application of pulse pileup correction, or afterpulsing in the PMTs are magnified greatly due to the nature of the differential calculation of ozone. With the differential transmission correction calculated using the radiosonde measurement of ozone, the water vapor mixing ratio calculation is simply a ratio of the water vapor and nitrogen signals which is substantially less influenced by the presence of afterpulsing. A detailed error analysis will be presented. Let's now look further at the issue of afterpulsing.

The difference in signal attenuation due to different ozone loadings is quite remarkable. On October 20, 1992 the ratio of the Raman oxygen signal between 200m and 1000m was approximately 130 while on August 25, 1992, a day of much higher ozone concentration, the same ratio was approximately 1000. This represents a factor of 80 or so increased attenuation under the higher ozone loading conditions. Laboratory measurements of afterpulsing in detectors are performed by supplying the detector with an impulse of light and comparing the current generated by the PMT due to the impulse to the current following the impulse¹⁰. The three order of magnitude decrease in the signal intensity over 800m (approximately 5 microseconds) provides a reasonable facsimile of an impulse of light. Small amounts of afterpulsing that might be present in the PMTs can be detected under these conditions.

Figure 4 shows the lidar profile of nitrogen used to generate figure 2 compared with a model prediction which incorporates the ECC ozone profile. Beyond about 3 km, the additional signal due to afterpulsing in the detectors can easily be seen. Work continues on measuring the amount of afterpulsing under controlled conditions as has been reported by other groups¹⁰ and also on reducing afterpulsing to improve the ozone derivation.

Recently, measurements of water vapor mixing ratio have also been performed during the daytime using a narrow-band, narrow field of view technique (NFOV) and excitation wavelengths at wavelengths longer than the SB cutoff. Ansmann et al¹ reported measurements of water vapor mixing ratio to about 1.7 km during the daytime using NFOV, 308 nm excitation, and 20 minute averaging. We have made measurements to 2.5 km using 351 nm excitation with 50 minute averaging. These measurements were made with the current system which has only photon counting data acquisition capability. In order to keep the signal within the photon counting regime, the input signal intensity was reduced by a factor of 200. We are in the process of adding an analog to digital recording capability which will obviate the need to attenuate the signal. Goldsmith¹¹ and colleagues at DOE/Sandia National Laboratory are also using this approach with their new Raman lidar system.

The NFOV technique has the obvious advantage over SB in that ozone is not a factor. However, due to the high solar background, the measurement is being performed under conditions where on a single shot basis the signal to noise ratio is much less than one. The signal must be pulled out of the high background through long term averaging. Also, the solar background is greatly variable depending on solar zenith angle, sky cloudiness, etc. which will result in variable measurement range capability under differing conditions.

Additional daytime water vapor mixing ratio measurements, an error analysis of the ozone and water vapor calculations from the lidar data, and further experimental results on afterpulse characterization will be presented.

References

1. G. Vaughan, D. P. Wareing, L. Thomas, V. Mitev, "Humidity measurements in the free troposphere using Raman backscatter", *Q. J. R. Meteor. Soc.*, **114**, pp. 1471-1484, (1988)
2. S. H. Melfi, D. Whiteman, and R. Ferrare, "Observation of Atmospheric Fronts Using Raman Lidar Moisture Measurements", *J. Appl. Meteor.*, **28**, No. 9 789-806 (1989)

3. A. Ansmann, M. Riebesell, U. Wandinger, C. Weitkamp, E. Voss, W. Lahmann, and W. Michaelis, "Combined Raman Elastic-Backscatter Lidar for Vertical Profiling of Moisture, Aerosol Extinction, Backscatter, and Lidar Ratio", *Appl. Phys. B* 54, pp 18-28, (1992)
4. D. N. Whiteman, S. H. Melfi, R. A. Ferrare, "Raman Lidar System for the Measurement of Water Vapor and Aerosols in the Earth's Atmosphere", *Appl. Opt.*, **31**, 16, 3068-3082 (1992)
5. D. Renaut, R. Capitini, "Boundary-Layer Water Vapor Probing with a Solar-Blind Raman Lidar: Validations, Meteorological Observations and Prospects", *J. Atmos. Oceanic Tech.*, **5**, 5 (1988)
6. D. Renaut, J. C. Pournay, R. Capitini, "Daytime Raman-lidar measurements of water vapor", *Opt. Lett.*, **5**, 6, 232-235 (1980)
7. John Cooney, Kenneth Petri, and Alfred Salik, "Measurements of high resolution atmospheric water-vapor profiles by use of a solar blind Raman lidar", *Appl. Opt.*, **24**, 1, 104-108 (1985)
8. Fairley J. Barnes, Robert J. Karl, Kenneth E. Kunkel, Gregory L. Stone, "Lidar Determination of Horizontal and Vertical Variability in Water Vapor over Cotton", *Remote Sens. Environ.*, **32**, 81-90, (1990)
9. A. M. Bass and R. J. Paur, "Ultraviolet cross-sections of ozone, I. Measurements" in *Atmospheric Ozone, Proc. Quadrennial Ozone Symposium*, C. S. Zerophos and A. Ghanzi, eds., D. Reidel, Hingham, Mass (1985).
10. Christian J. Grund, Edwin W. Eloranta, "University of Wisconsin High Spectral Resolution Lidar", *Opt. Eng.*, **30**, 1, 6 - 12 (1991)
11. J. E. M. Goldsmith, Richard A. Ferrare, "Performance Modeling of Daytime Raman Lidar Systems for Profiling Atmospheric Water Vapor", *NASA Conference Publication 3158*, 16th International Laser Radar Conference, pp. 667-670.

Tropospheric Temperature Measurements Using a Raman Lidar

K. D. Evans, Hughes STX Corporation, NASA/Goddard Spaceflight Center,
Code 917, Greenbelt, MD 20771 (301) 286-9113

S. H. Melfi, NASA/Goddard Spaceflight Center, Code 917,
Greenbelt, MD 20771

R. A. Ferrare, Hughes STX Corporation, NASA/Goddard Spaceflight Center,
Code 917, Greenbelt, MD 20771

D. N. Whiteman, NASA/Goddard Spaceflight Center, Code 924,
Greenbelt, MD 20771

The GSFC Raman lidar measures temperature in the troposphere as well as water vapor and aerosols (Whiteman et al. 1992a). Strauch et al. (1971) demonstrated that atmospheric temperature can be determined using the Raman backscatter from nitrogen and Hauchecorne et al. (1992) used the Raman vibrational scattering from nitrogen to calculate temperature in the lower stratosphere. In this paper, we present density and temperature profiles in the troposphere using the Raman vibrational scattering from nitrogen.

The GSFC Raman lidar is a trailer-based system which uses a XeF excimer laser to transmit light at 351 nm. System details are discussed by Whiteman et al. (1992b) and Ferrare et al. (1992). Data were collected in the form of contiguous one minute profiles at night, to avoid interference from the sun, and then integrated over 2 hours.

The density and temperature algorithms used are based on those described by Hauchecorne et al. (1980), Shibata et al. (1986) and Ferrare et al. (1990) and a brief synopsis is presented here. The lidar data were corrected for molecular attenuation of the outgoing and incoming wavelengths. The aerosol attenuation is assumed to be negligible above the boundary layer (≈ 2 km) and below the Pinatubo aerosols (≈ 15 km). The number density is calculated by normalizing the nitrogen Raman lidar data at the isopycnic level (≈ 8 km) to the U.S. Standard Atmosphere 1976, which has a variability of less than 2%. Starting at the isopycnic level, the density is first calculated downward to the top of the boundary layer, and again from the isopycnic level upward to the desired altitude. Then, assuming hydrostatic equilibrium and the ideal gas law, temperature is calculated using a reference temperature at 15 km and then integrated downward. The reference temperature is obtained from the U.S. Standard Atmosphere 1976. As the calculation proceeds downward, the dependence on the reference temperature decreases. Using model data, the temperature calculation converges to within 2 degrees in 4 km for a reference temperature ± 5 degrees of the model temperature and to within 5 degrees in 5 km for a reference temperature of ± 10 degrees.

The lidar system was operated at the Coffeyville, Kansas airport (37.10 N, 95.57 W) during November and December 1991 as part of the coincident SPECTRE (SPECTral Radiance Experiment) and FIRE-II (First ISCCP Regional Experiment) field missions.

Data from five nights were sufficiently aerosol-free to calculate density and temperature discussed above.

Figure 1 presents the density computed from data collected on December 7, 1991, 0020-0220 hours UT. The slope of the calculated lidar density matches the density from the radiosonde (launched at 0155 hours UT) very well above 3 km. That the calculated density does not exactly match the sonde density could be due to density variability at the isopycnic level. This does not impact the temperature calculation as only the relative number density is needed (Hauchecorne et al. (1980)). Figure 2 shows the calculated lidar temperature for the same time period as the density. The lidar data agrees with the sonde data within 4 degrees at 12 km and within 2 degrees at 7 km.

The errors in calculated density and temperature profiles due to the random error of the lidar data and uncertainties in the reference temperature and density will be discussed during the presentation. Data from other nights will also be presented.

- Chanin, M.L., and A. Hauchecorne, 1981: "Lidar Observation of Gravity and Tidal Waves In The Stratosphere and Mesosphere", *JGR*, **86**, No. C10, p 9715-9721.
- Ferrare, R.A., D. Whiteman, and S.H. Melfi, 1990: "Raman Lidar Measurements of Temperature in the Troposphere and Lower Stratosphere", *Optical Remote Sensing of the Atmosphere Topical Meeting*, Incline Village, NV.
- Ferrare, R.A., S.H. Melfi, D.N. Whiteman, and K.D. Evans, 1992: "Raman lidar measurements of Pinatubo aerosols over southeastern Kansas during November-December 1991", *Geophys. Res. Letters*, **19**, No. 15, p 1599-1602.
- Hauchecorne, A., and M.L. Chanin, 1980: "Density and Temperature Profiles Obtained by Lidar Between 35 and 70 km", *GRL*, **7**, no. 8, p 565-568.
- Hauchecorne, A., M.L. Chanin, P. Keckhut, and D. Nedeljkovic, 1992: "LIDAR Monitoring of the Temperature in the Middle and Lower Atmosphere", *Appl. Phys. B*, No. 55, p 29-34.
- U.S. Standard Atmosphere, 1976, U.S. GPO, Washington, D. C.
- Shibata, T., M. Kobuchi, and M. Maeda, 1986: "Measurements of density and temperature profiles in the middle atmosphere with a XeF lidar", *Appl. Opt.*, **25**, No. 5, p 685-688.
- Strauch, R.G., V.E. Derr, and R.E. Cupp, 1971: "Atmospheric Temperature Measurement Using Raman Backscatter", *Appl. Opt.*, **10**, p 2665-2669.
- Whiteman, D.N., S.H. Melfi, and R.A. Ferrare, 1992a: "Raman lidar system for the measurement of water vapor and aerosols in the earth's atmosphere", *Appl. Opt.*, **31**, No. 16, p 3068-3082.
- Whiteman, D.N., S.H. Melfi, R.A. Ferrare, K.D. Evans, L. Ramos-Izquierdo, O.G. Staley, R.W. DiSilvestre, I. Gorin, K.R. Kirks, W.A. Mamakos, L.S. Wan, N.W. Walsh, J.M. Marsh, and R.A. Aldridge, 1992b: "Advanced Raman water vapor lidar", Sixteenth International Laser Radar Conference, NASA Conference Publication 3158, Cambridge, MA.

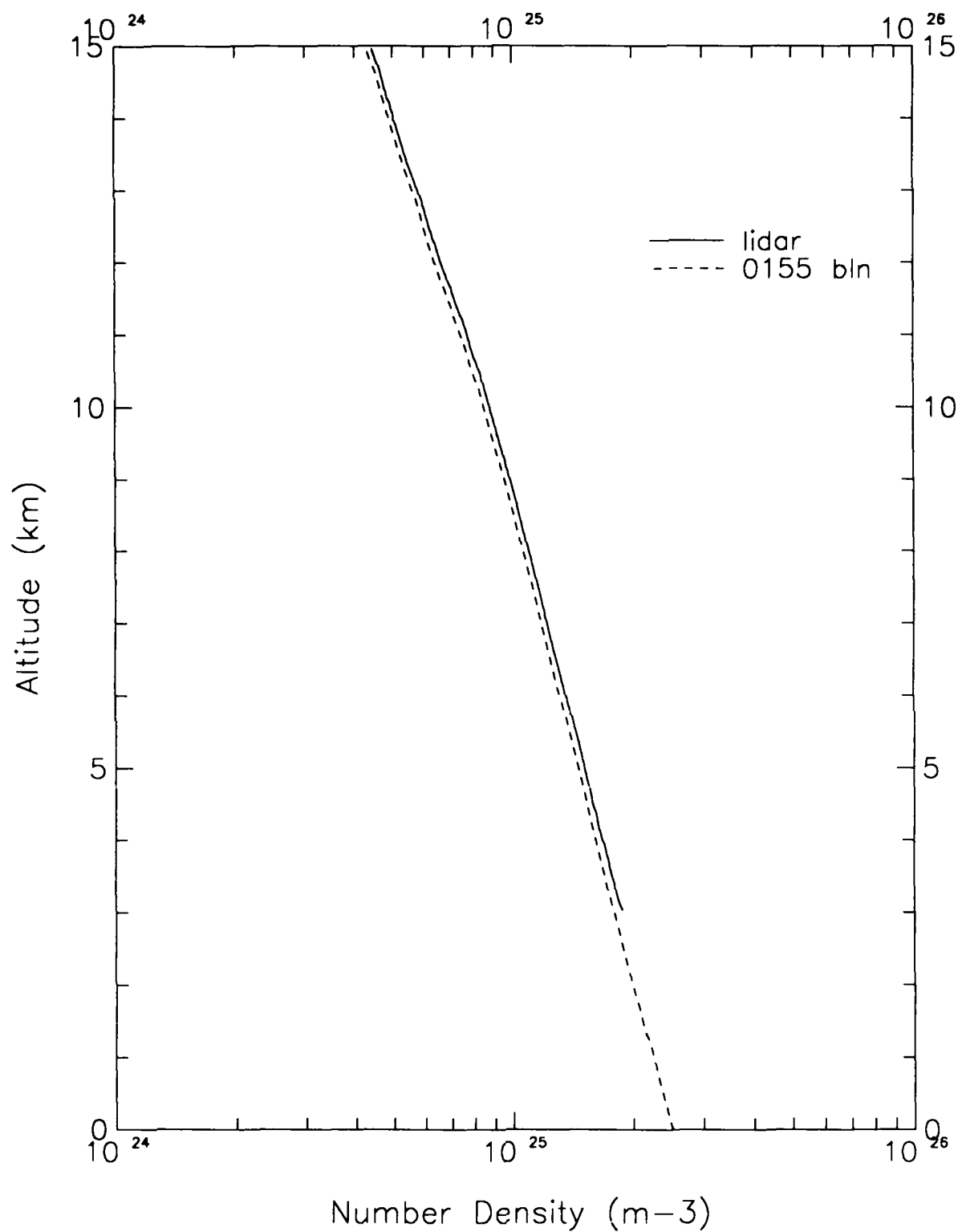


Figure 1. Molecular number density calculated from 2 hour integrated lidar data collected on December 7, 1991, in Coffeyville, Kansas.

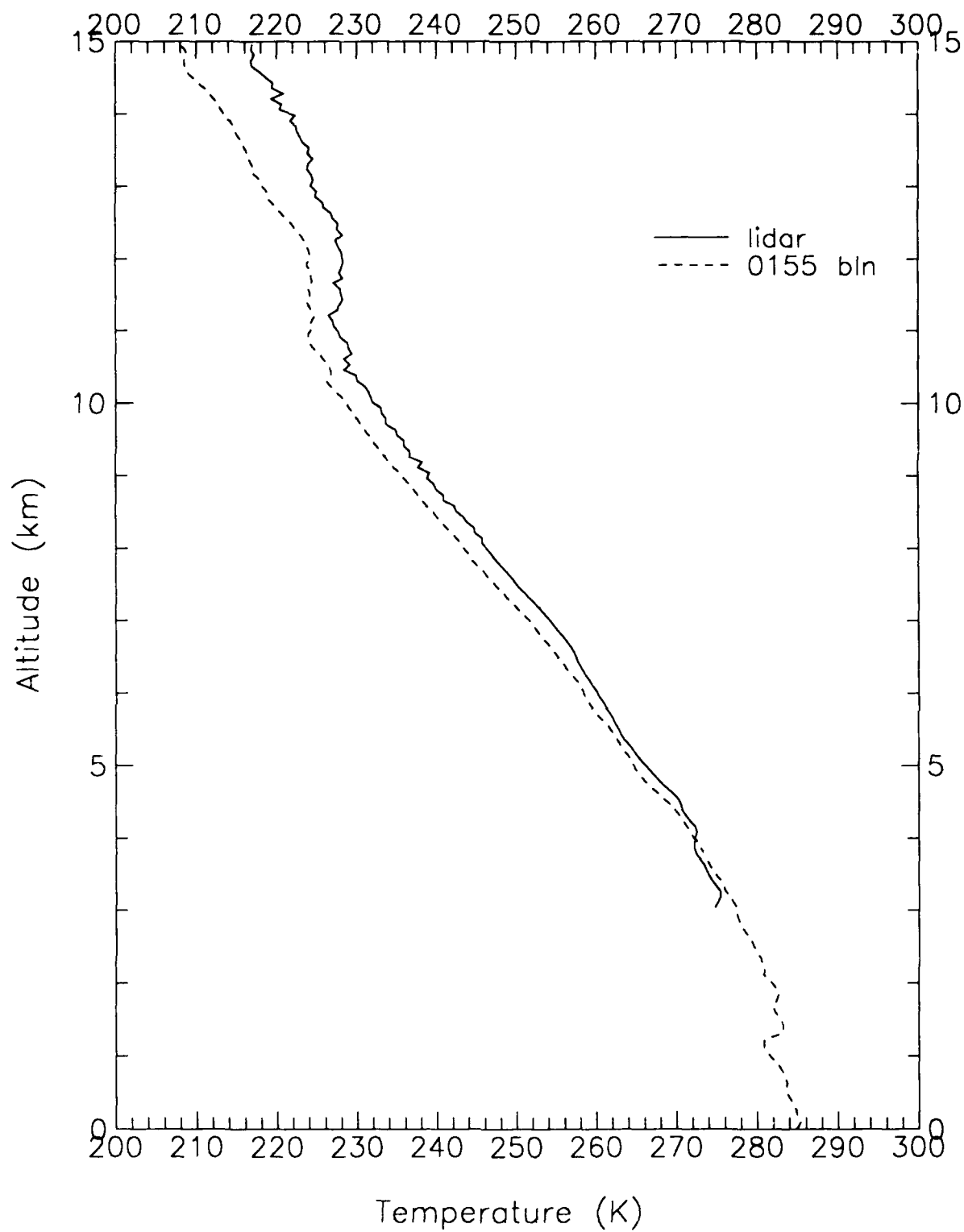


Figure 2. Temperature data calculated from 2 hour integrated data collected on December 7, 1991, in Coffeyville, Kansas.

A.E.S. DIAL System for Monitoring of Tropospheric Ozone.

J. F. Hahn, A. Sheppard and R. M. Hoff
Atmospheric Environment Service, Rural Route 1
Egbert, Ontario L0L 1N0

In order to better understand the mechanisms controlling atmospheric ozone transfer and production in the troposphere, as well as ozone exchange between the troposphere and stratosphere, the Atmospheric Environment Service has undertaken to build a differential absorption lidar (DIAL) system at its Centre for Atmospheric Research Experiments facility in Egbert, Ontario, located approximately 80 kilometres north of metropolitan Toronto. The system under construction will employ Raman shifting of quadrupled Nd:YAG output at 266 nm to 289.9 and 294.2 nm through the use of HD and D₂ respectively (1,2). This is a basic change in approach from the earlier dye laser-based system used by A.E.S. at the Centre for Atmospheric Research Experiments (C.A.R.E.) (3).

The advantages we anticipate in the use of a Raman shifting-based system are ease of maintenance and set-up. The Raman shifters are simply inserted into the beam path and do not require tuning. They do not require attention aside from ensuring that the pressure levels in the cells remain high. HD and D₂ provide Raman shifting sufficiently removed from the peak of ozone absorption to ensure that signal levels are reasonably large, yet the difference in shifted wavelengths is small enough so that aerosol and backscattering error terms in the lidar equation can be ignored (4).

The output from two separate quadrupled Nd:YAG lasers will be passed in turns through the two Raman cells, which permits the on-line/off-line signals to be distinguished from one another temporally. The return signals will be collected with a 16 inch classical Cassegrain telescope and PMTs manufactured by EMI operating in the photon counting mode for UV and visible light and an avalanche photodiode for infrared returns. We are preparing four channels for data collection: the UV channels at 289.9 and 299.4 nm (channels for the on-line and off-line returns respectively) and channels at 1064 and 532 nm for the fundamental and doubled YAG returns respectively. Consequently we will be able to make simultaneous measurements of various aerosol concentrations along with ozone concentration measurements.

It is our aim to monitor ozone concentrations from ground level to an altitude of 12 kilometres. Our work complements work ongoing at the Institute for Space and Terrestrial Science in metropolitan Toronto, where ozone concentrations are monitored between altitudes of eight to 40 kilometres. These two systems together will allow comprehensive monitoring of ozone in the southern Ontario region.

References

- 1) G. Ancellet, A. Papayannis, J. Pelon and G. Megie, "DIAL Tropospheric Ozone Measurement Using a Nd:YAG Laser and the Raman Shifting Technique," J. Atmos. Oceanic Technol. 6 832-839 (1989).
- 2) D. A. Haner and I. S. McDermid, "Stimulated Raman Shifting of the Nd:YAG Fourth Harmonic (266 nm) in H₂, HD and D₂," IEEE J. Quantum Electron. QE-26 1292-1298 (1990).
- 3) R. M. Hoff, R. E. Mickle, F. Fanaki, F. A. Froude, J. Arnold and J. Markes, "Vertical Profiles of Ozone and Meteorology at C.A.R.E., Egbert," Report: ARD-89-009, Atmospheric Environment Service/Environment Canada (1989).
- 4) E. V. Browell, "Differential Absorption Lidar Sensing of Ozone," Proc. IEEE 77 419-432 (1989).

FIG. 1

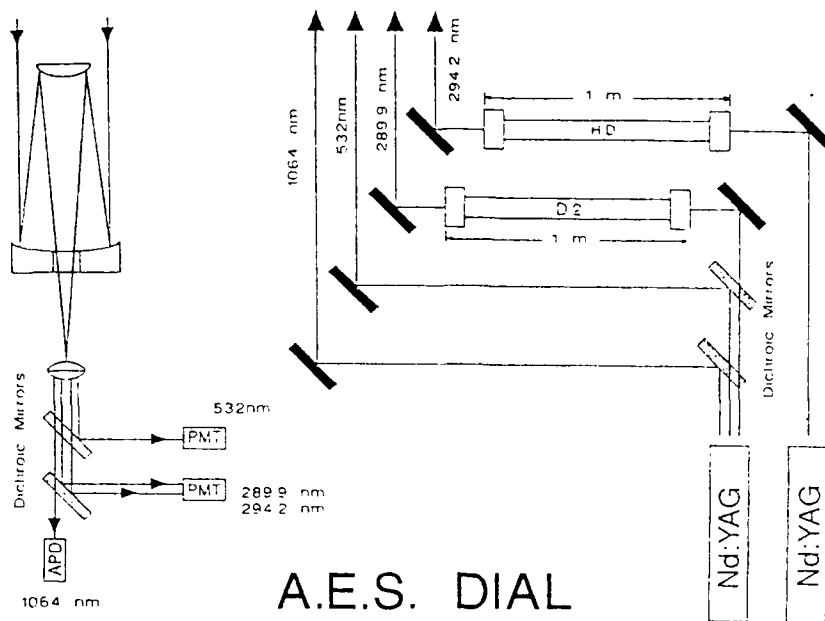
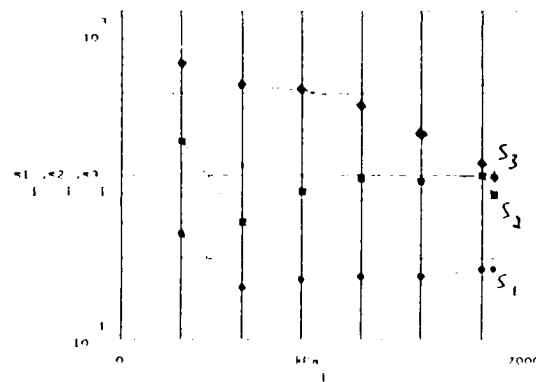
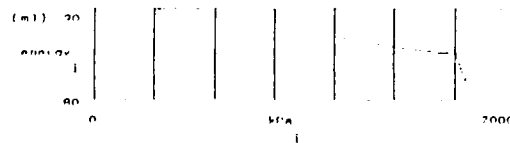


FIG. 2 a & b



Comparative strength of 102 Stokes lines vs pressure from 1 meter Raman cell.

S1: first Stokes line @ 292.1 nm
S2: second Stokes line at 341.5 nm
S3: third Stokes line at 397.2 nm



Pump energy (• 266 nm) in mJ monitored at each pressure tested

Airborne Ozone Measurements with the USEPA UV-DIAL

H. Moosmüller,* R. J. Alvarez II, C. M. Edmonds,[†]
R. M. Turner,[‡] D. H. Bundy,[†] and J. L. McElroy[†]**

** Desert Research Institute, University of Nevada, P.O. Box 19040, Las Vegas, Nevada 89132*

*** National Oceanic and Atmospheric Administration, P.O. Box 93478, Las Vegas, Nevada 89193*

[†] U.S. Environmental Protection Agency, P.O. Box 93478, Las Vegas, Nevada 89193

[‡] Harry Reid Center for Environmental Studies, 4505 Maryland Parkway, Las Vegas, Nevada 89154

A compact airborne down-looking lidar system has been developed at the U. S. Environmental Protection Agency's Environmental Monitoring Systems Laboratory in Las Vegas.^{1,2} This differential absorption lidar (DIAL) is designed to simultaneously measure range-resolved concentrations of ozone (O₃) and sulfur dioxide (SO₂) in the lower troposphere, together with an indication of the aerosol distribution. The five laser wavelengths (i.e., $\lambda_1 = 277$ nm, $\lambda_2 = 292$ nm, $\lambda_3 = 313$ nm, $\lambda_4 = 319$ nm, $\lambda_5 = 359$ nm) are generated via Raman conversion of a focused KrF excimer laser.³

The system has been installed in a mid-sized cargo aircraft (DeHavilland C-7 Caribou) for the initial airborne testing in the Great Lakes area in May 1992. During these test flights the system performance was similar to that during previous ground tests,² and a number of two-dimensional ozone distributions were acquired. For these measurements, the laser was operated at a repetition rate of 20 Hz and data from 300 shots were averaged for each vertical ozone profile. This yields a horizontal resolution of 1.17 km at an average flight speed of 280 km/h. The vertical resolution of about 150 m is determined by a sampling interval of 30 m and the smoothing over 5 data points. Ozone concentrations have been calculated from 90 m above

ground to 150 m below the aircraft flight altitude. A typical two-dimensional ozone distribution measured on May 13, 1992, which extends over nearly 90 km horizontally and up to 2 km vertically is shown in Fig. 1. This distribution begins in the southwestern part of Lake Huron (latitude $43^{\circ} 19' 08''$ N, longitude $82^{\circ} 23' 46''$ W, local time 14:59 h, location in Fig. 1: 0 km), continues over an air quality monitoring station near Port Huron ($42^{\circ} 57' 12''$ N, $82^{\circ} 27' 23''$ W, 15:08 h, 40.5 km) and extends in roughly a southern direction along the western shore of the St. Clair River into Lake St. Clair ($42^{\circ} 34' 04''$ N, $82^{\circ} 41' 18''$ W, 15:18 h, 87 km). No ozone concentrations have been determined in the purely white regions of this graph. Note that the airplane descended a few hundred meters in altitude around kilometer 30. A general downward slope of the ozone layering is clearly visible from just north of the lake/land boundary of Lake Huron (32 km) to just north of the land/lake boundary of Lake St. Clair (82 km). Furthermore,

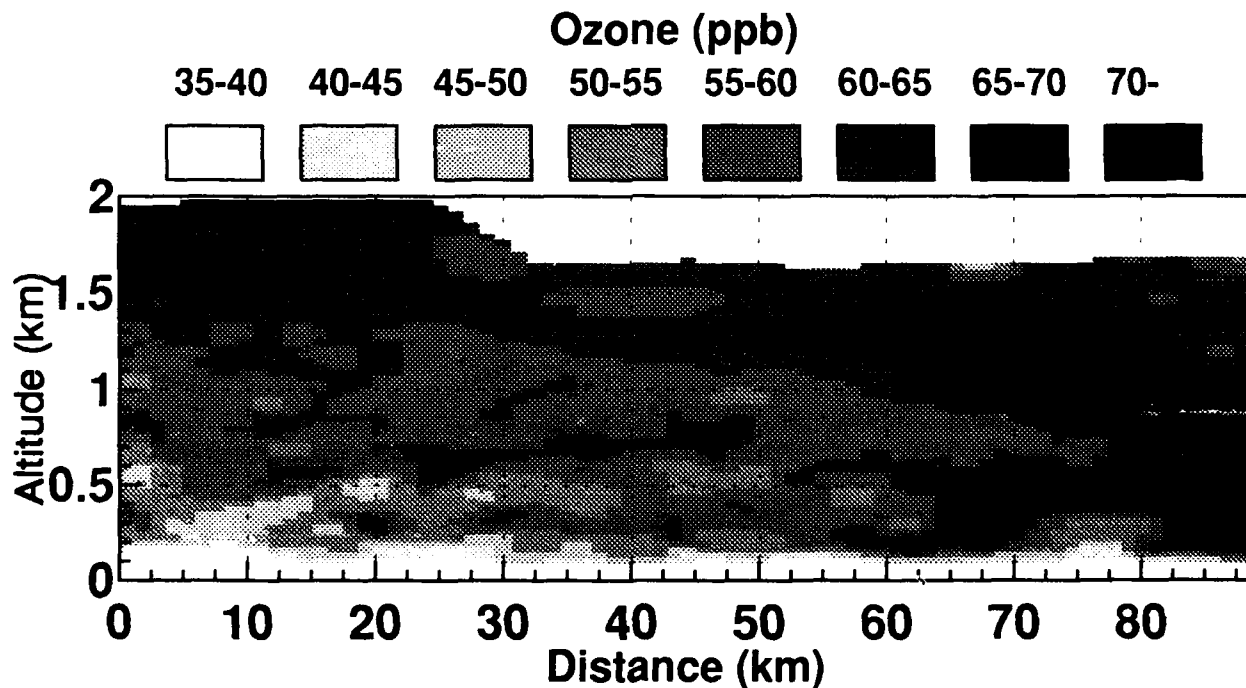


Figure 1: Ozone distribution on May 13, 1992. The lake/land boundaries of Lake Huron and Lake St. Clair are located at 12 km and 82 km, respectively.

the ozone concentrations are generally lower close to the ground. This holds true not only for this particular transect but for all data collected over four days of test flights, corroborating the need for three dimensional ozone profiles rather than only surface observations.

Three additional flights passing at different altitudes over the Port Huron air quality monitoring station yield a comparison of DIAL-derived ozone profiles measured at this location with ground station and onboard *in-situ* measurements (Fig. 2). The DIAL measurements and concurrent onboard *in-situ* measurements were made at time intervals of about 25-30 min. They show rather good agreement (within 10 ppb) with each other. The *in-situ*, hourly-averaged ground measurements agree well with a simple extrapolation of the DIAL profiles and also confirm our previous observation of lower ozone concentrations close to the ground.

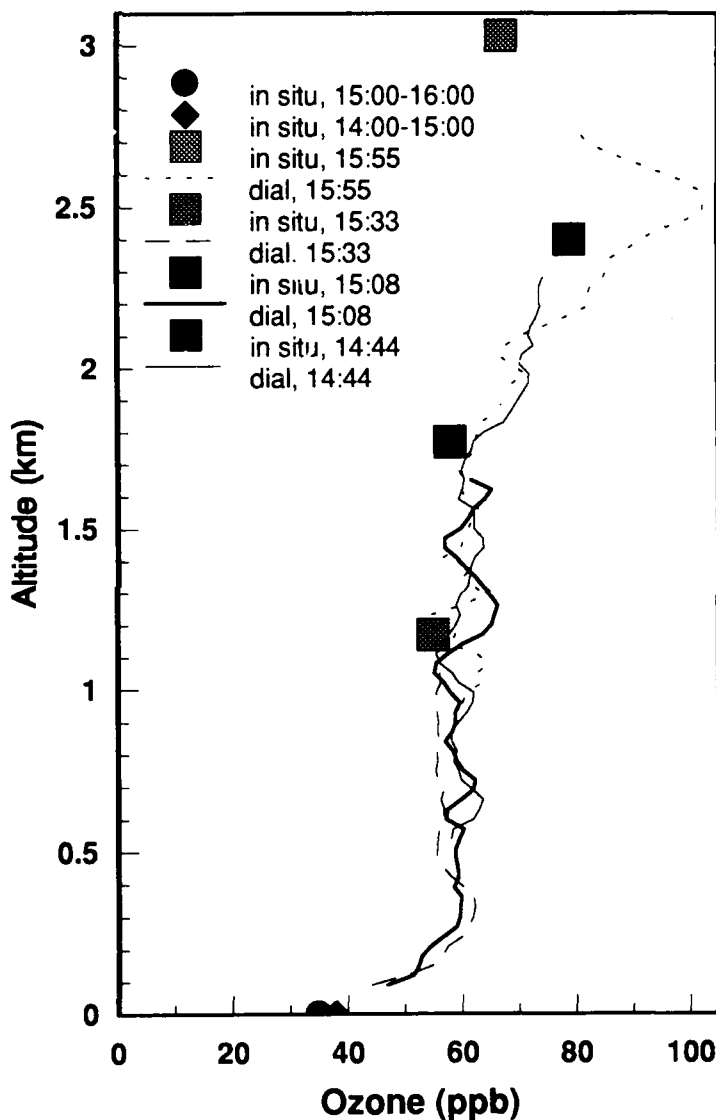


Figure 2: Comparison of four DIAL ozone profiles with airborne and ground *in-situ* measurements at Port Huron on May 13, 1992.

References:

1. H. Moosmüller, D. Diebel, D. H. Bundy, M. P. Bristow, C. M. Edmonds, R. M. Turner, V. A. Kovalev, R. P. Haas, and J. L. McElroy, "The U.S. EPA airborne UV-DIAL system," *Technical Digest on Optical Remote Sensing of the Atmosphere*, volume 18, Optical Society of America (Washington, D.C., 1991), p. 253-255.
2. H. Moosmüller, D. Diebel, D. H. Bundy, M. P. Bristow, R. J. Alvarez II, V. A. Kovalev, C. M. Edmonds, R. M. Turner, and J. L. McElroy, "Ozone Measurements with the U.S. EPA UV-DIAL: Preliminary Results," *Sixteenth International Laser Radar Conference*, edited by M. P. McCormick, NASA Conference Publication 3158, Part 1 (Hampton, VA, 1992), p. 95-98.
3. D. Diebel, M. P. Bristow, and R. Zimmermann, "Stokes shifted laser lines in KrF-pumped hydrogen: reduction of beam divergence by addition of helium," *Appl. Opt.* **30**, 626-628 (1991).

The Arecibo Observatory Daytime Lidar : Preliminary Results

Kalpak A. Dighe, Clemson University, Department of Physics, Kinard Hall,
Clemson, SC 29634-1911. (803)-656-0310.

Craig A. Tepley, NAIC Arecibo Observatory, P.O.Box 995, Arecibo, PR 00613.
(809)-878-2612.

Raul Garcia, NAIC Arecibo Observatory, P.O.Box 995, Arecibo, PR 00613.
(809)-878-2612.

Jonathan Friedman, NAIC Arecibo Observatory, P.O.Box 995, Arecibo, PR
00613. (809)-878-2612.

Scientific Rationale

The vertical propagation of atmospheric tides and acoustic gravity waves and their corresponding travelling ionospheric disturbances play a crucial role in the transportation and balance of momentum and energy in the earth's atmosphere. The unique availability of both radar and lidar instrumentation at Arecibo can provide simultaneous access to the neutral density, temperature and wind perturbations induced by such wave activity at mesospheric and stratospheric altitudes.

The use of lidar for middle atmospheric studies is now a proven science and is an indispensable diagnostic tool for measurements made in the vicinity of the stratopause (45-60 km), an altitude range which is 'blind' to radar.

Previous temporal studies of density and temperature profiles obtained from lidar systems have aided in the study of tides and gravity waves in this altitude region. Measurements of temperature perturbations using a Rayleigh lidar were obtained by Wilson *et al* (1991) in France, and a dominant oscillatory mode was observed in the stratosphere and lower mesosphere. The diurnal tidal effects, caused by solar heating, have been observed to generate both stationary (zero phase speed) and upward propagating waves (phase speeds of 0.1-1.0 m/sec) (Chanin, 1984; Wilson, 1991).

The Doppler Rayleigh lidar system at Arecibo has been operational since 1990 and initial results were reported by Tepley *et al* (1991). Observations of the Doppler spectral components of the Rayleigh backscattered signal from the atmosphere were used to obtain both the neutral winds and temperatures up to mesospheric heights (see for example, Figures 3 and 4 of Tepley *et al*, 1991). Until now there has been no study designed specifically to investigate the vertical propagation of energy and momentum due to atmospheric tides and gravity waves using the Arecibo lidar. A coordinated radar and lidar experiment to compare the measured stratospheric and lower mesospheric winds would certainly reveal the details of the characteristics of propagating waves from the lower to the higher altitudes. Also, such a data set would enable us to determine the possible dissipative effects of turbulence on these propagating waves near the stratopause.

In the mesosphere and lower ionosphere, the incoherent scatter radar is restricted to daytime operations because of the absence of sufficient ionization for backscatter at night. On the other hand, the lidar is currently limited to nighttime use because the background signal present during the day overwhelms the present electronics. Thus, in order to obtain an overlap in the altitude region between the radar and the lidar, it is necessary to reduce the daylight background signal that the lidar sees by a significant amount, since we have no control over the degree of lower mesospheric ionization. It is this necessity, the need for a daytime lidar system, that has motivated our present experiment.

Experimental Setup

The approach taken for achieving daytime lidar observations was to make use of two pressure-scanned Fabry-Perot interferometers (FPI) placed in tandem, preceded by a narrow bandwidth (0.6 Å) DayStar filter centered at the frequency of the laser, which is an injection seeded Nd:YAG laser operating at its second harmonic of 532.05 nm (Fig. 1 a). The transmitted and received beams are made coaxial (Fig. 1 b) to facilitate the use of a single steerable mirror system mounted on the roof. The combination of multiple etalons and a narrow prefilter is essential to achieve daytime capability for the system by significantly reducing the strong solar continuum. The space between the plates of the first FPI is 1 cm and that between the second one is 2.5 cm. This gives a ratio of 2:5 for the Free Spectral Ranges (FSR) of the two etalons. Thus, by using the output of the first FPI as the input to the second, every fifth order of the interference pattern undergoes constructive interference and we have a system that has an effective FSR that is twice that of the low resolution etalon (Fig. 2).

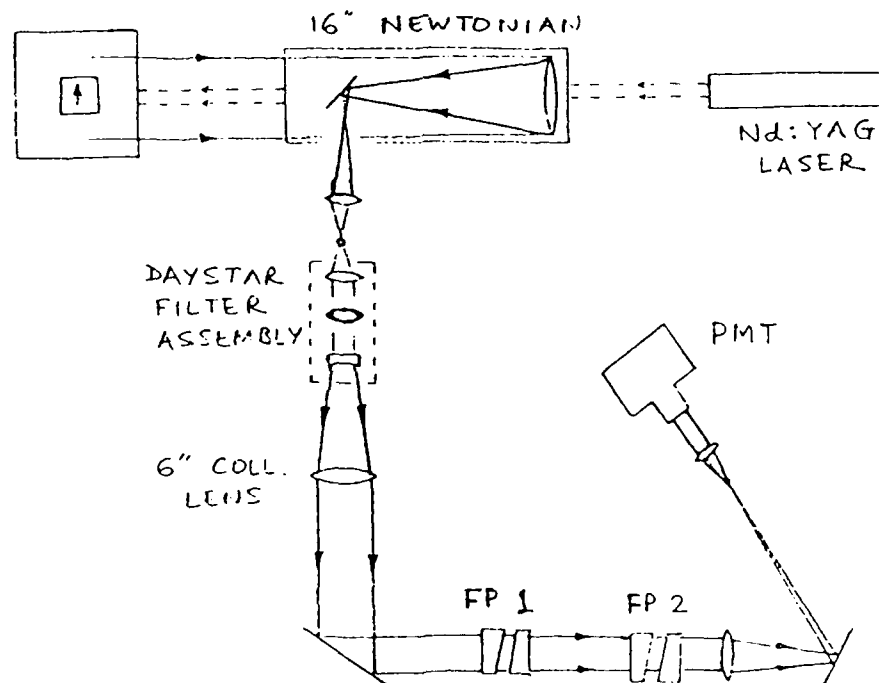


Fig. 1 (a). Configuration of the Arecibo Daytime Lidar system (top view).

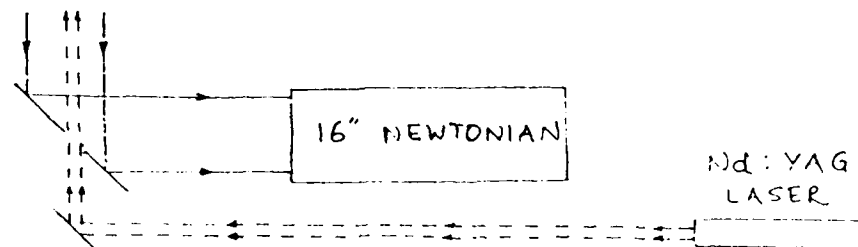


Fig. 1 (b). Side view of the laser (transmitter) and telescope (receiver) signal paths.

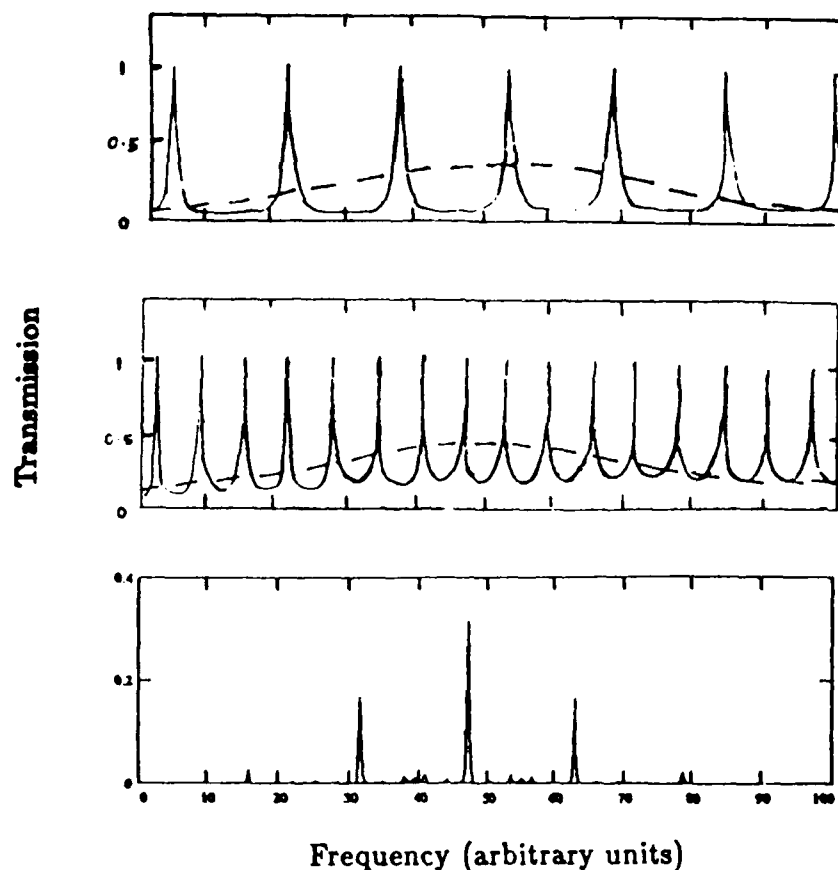


Fig. 2. Transmission curve (bottom) obtained by convolving those of the two FPIs (top : FPI with 1 cm spacers = FSR of 15 GHz; middle : FPI with 2.5 cm spacers = FSR of 6 GHz). The dashed line represents the transmission curve of the DayStar prefilter (30 %).

Results

Test runs of the system using the configuration outlined above were carried out in the first half of November 1992. It is these preliminary results which we present here. Fig. 3 shows power profiles obtained during a typical day. The laser was pulsed at 20 Hz. We have been able to reach an altitude of 30 km only until now. There are a number of factors which we feel are responsible for this current altitude limit, including

- a) a reduction in the average power of the laser from 13 to 10 W due to aging of the flashlamps (soon to be changed) used for the optical pumping,
- b) hazy skies which are responsible for attenuating the transmitted and backscattered signal as well as increasing the background level,
- c) a less than perfect understanding of the polarization of the backscattered signal received from the atmosphere for different azimuth and zenith angles, and
- d) lack of optimization of the orientation of the Daystar prefilter with respect to the polarization effects.

We also plan to optimize the ratio of the spacers in the FPIs to obtain a better signal to noise ratio. We have reason to believe that with continued improvements the altitude range of the system will increase to about 60 km, as we can measure at night.

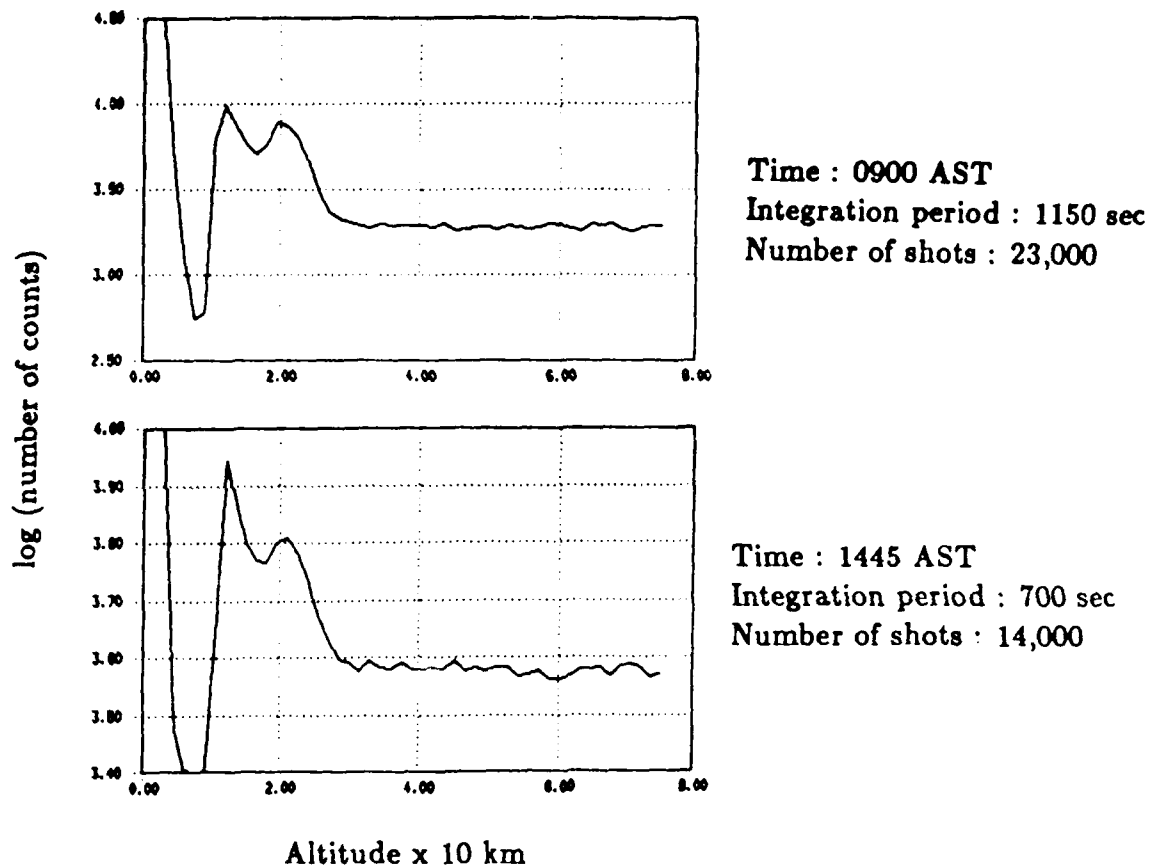


Fig. 3. Power profiles obtained using the daytime lidar at Arecibo.

Future Plans

The Doppler Rayleigh lidar system at Arecibo is designed for measuring winds. We have not implemented the wind measuring capability in the daytime system as yet, since we are still in the optimization stage of the receiver system, but intend to do so in the very near future.

The establishment of a data set of winds from the stratosphere up through the mesosphere, employing both the daytime Doppler Rayleigh lidar and the Arecibo 430 MHz incoherent scatter radar, would greatly enhance our current understanding of the structure and propagation of tides and gravity waves in these regions.

References

- Wilson, R., M. L. Chanin and A. Hauchecorne, Gravity waves in the middle atmosphere observed by Rayleigh lidar, *Jour. Geophys. Res.*, 96, 5153-5167, 1991.
- Chanin, M. L., Review of lidar contributions to the description and understanding of the middle atmosphere, *Jour. Atmos. Terr. Phys.*, 46, 987-993, 1984.
- Tepley, C. A., S. I. Sargoytchev and C. O. Hines, Initial Doppler Rayleigh lidar results from Arecibo, *Geophys. Res. Lett.*, 18, 167-170, 1991.

Real-Time Simultaneous Monitoring of Atmospheric Methane and Carbon Dioxide by using Diode Lasers

Hideo TAI and Ryoichi TORIUMI
Tokyo Gas Co., Ltd.
Information Technology Research Institute
1-16-25 Shibaura, Minato-ku, Tokyo 105, Japan
tel +81-3-5484-4672
and

Kiyoji UEHARA
Keio University
Department of Physics, Faculty of Science and Technology
3-14-1 Hiyoshi, Kohoku-ku, Yokohama, Kanagawa 223, Japan
tel +81-45-563-1141

Precise measurement of the atmospheric trace methane and carbon dioxide concentrations is essential to investigate the spatial and temporal variations of the green-house gases. A measurement system which is capable of monitoring these gases simultaneously in real time will be of great use.

Recently, a real-time methane detection system with a ppb sensitivity using a 1.66- μm InGaAsP distributed feedback (DFB) laser has been developed by some of the authors [1], [2]. This high sensitivity became possible owing partly to the single-mode operation of the DFB diode laser at the wavelength where the methane absorption is appreciably strong, and partly to the frequency modulation-harmonic detection technique. This system was then combined with optical fibers to achieve long-distance detection of methane with a high sensitivity [3], which was approximately three orders of magnitude improved over the earlier fiber-coupled detection systems [4], [5]. This high-sensitivity long-distance detection technique was extended to simultaneous monitoring of methane and acetylene with 1.66- μm and 1.53- μm diode lasers [6].

In the present paper, we demonstrate, as another extension of the real-time high-sensitivity detection technique, simultaneous monitoring of atmospheric methane and carbon dioxide by passing two diode laser emissions through a multipass cell. High sensitivities of 5 ppb and 2 ppm for methane and carbon dioxide, respectively, have been achieved and applied to long-time measurements of up to 24 hours.

Methane and carbon dioxide have very strong absorption bands in the wavelength regions of 3 μm or longer. However, diode lasers which operate at room temperature are available only in the spectral region below 2 μm . The strongest bands of methane and carbon dioxide below 2 μm are located at 1.66 μm (2 ν_1 band) and 1.43 μm (3 ν_1 band), respectively. DFB lasers at these wavelengths have been developed recently [7].

Figure 1 shows the absorption spectrum of the 3 ν_1 band of carbon dioxide observed by temperature tuning of a 1.43- μm DFB laser whose injection current was modulated sinusoidally at a frequency f of 5.35 MHz for frequency modulation. We chose 5.35 MHz because its second harmonic coincides with the intermediate frequency, 10.7 MHz, of FM radio receivers so that the tuned circuits were easily fabricated. Trace (a) shows the transmitted power while traces (b) and (c) show the phase-sensitive detected f (fundamental) and $2f$ (second harmonic) signals, respectively. The three traces were recorded simultaneously as a function of the laser junction voltage that proved to be a good monitor of the oscillation frequency [8], [9]. One problem in carbon dioxide detection is the interference with strong absorption lines of water vapor in air. We have found that the R(14) line is one of a few lines that can be almost free from interference after water vapor is removed by a simple dry column. In the case of methane, the Q(6) line is safe from interference [2]. From Fig. 1(a) and a similar measurement for the methane 2 ν_1 band the peak absorption coefficients of the R(14) line of carbon dioxide

and the Q(6) line of methane at atmospheric pressure are calculated to be $6.4 \times 10^{-6} \text{ cm}^{-1} \cdot \text{torr}^{-1}$ and $2.3 \times 10^{-3} \text{ cm}^{-1} \cdot \text{torr}^{-1}$, respectively. Because the average atmospheric concentrations of carbon dioxide and methane are 330 ppm and 1.7 ppm, respectively, the ratio of the absorption strengths of these gases in the atmosphere is about 1:2.

As shown in Fig. 1(b), the f signal suffers a large offset owing to the fact that the modulation of the injection current results in intensity modulation as well as frequency modulation. On the other hand, the offset in the $2f$ signal is much smaller as shown in Fig. 1(c), indicating that the $2f$ signal is more advantageous for absorption detection. If the frequency of the laser is stabilized at the center of an absorption line, one can measure in real time the amount of gas from the $2f$ signal once the signal intensity is calibrated. The f -signal intensity at the absorption-line center, on the other hand, is directly proportional to the laser power received by the detector. Therefore the $2f$ -signal intensity normalized by the f -signal intensity indicates the amount of gas independently of the received laser power, as investigated in earlier studies [2], [10]. This ratioing technique for quantitative detection of gases is useful when the received laser power may change owing to the turbulence of the flowing gas in the absorption cell, changes in optical alignment, attenuation by dust, etc.

Figure 2 depicts the block diagram of the experimental setup for the simultaneous measurement of atmospheric methane and carbon dioxide by using two diode lasers and a multipass cell (White cell). Each set of the laser transmitter and modulator-controller provides a modulated laser emission whose center frequency is stabilized at the center of the Q(6) line of methane (or R(14) line of carbon dioxide) by the following method. The diode laser is mounted on a thermoelectric element which controls the laser operating temperature to stabilize the oscillation frequency. The laser is modulated by a sinusoidal current of $f = 5.35 \text{ MHz}$ for methane (or $f = 5.34 \text{ MHz}$ for carbon dioxide), which is superposed upon a constant dc injection current. The laser light is emitted from both the front and the back facets of the laser chip. The light of about 1 mW emitted forward is used as the probe beam. The backward light passes through a 2-cm-long reference cell containing 9.6 % methane mixed with nitrogen (or 100 % carbon dioxide) at 1 atm and is received by a photodiode. The output of the photodiode is phase-sensitive detected at f by a lock-in amplifier. The signal from the lock-in amplifier is integrated after appropriate offset compensation and is fed into the current source of the thermoelectric element. The fluctuation of the laser frequency thus stabilized is less than $\pm 10 \text{ MHz}$. The further details of the laser transmitter and the modulator-controller are given elsewhere [2]. The two laser emissions from the laser emitters are combined by a beam splitter and are transmitted into a White cell which is adjusted to hold a 85-m pathlength. The transmitted light is received by a p-i-n photodiode. The output signal of the photodiode is sent to four lock-in amplifiers (EG&G; 5202), which detect the f and $2f$ components of the two

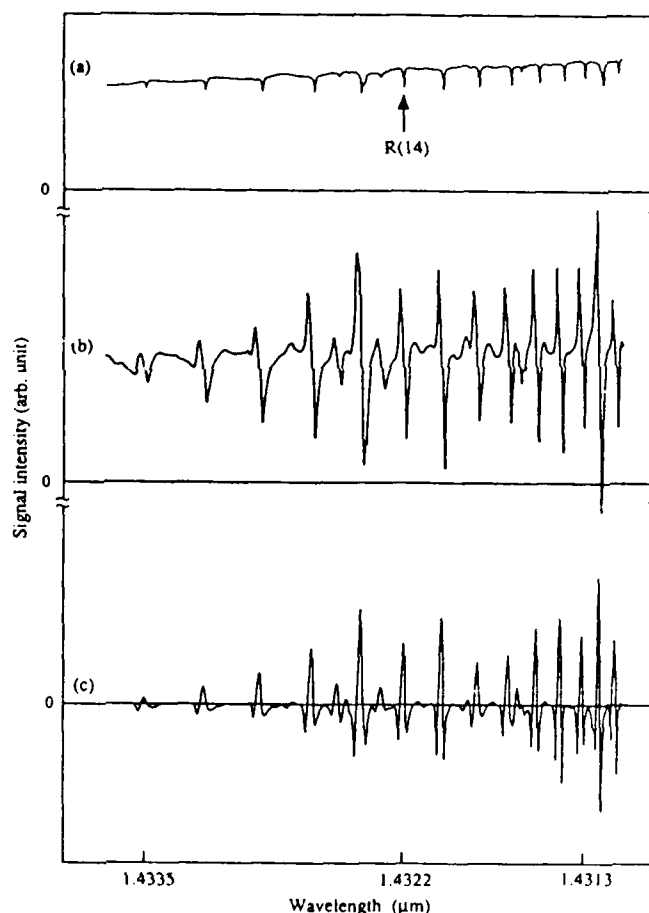


Fig. 1. Absorption spectra of the $3v_3$ band of carbon dioxide observed by a DFB laser. Transmitted power (a) and the fundamental (b) and second-harmonic (c) phase-sensitive-detected signals.

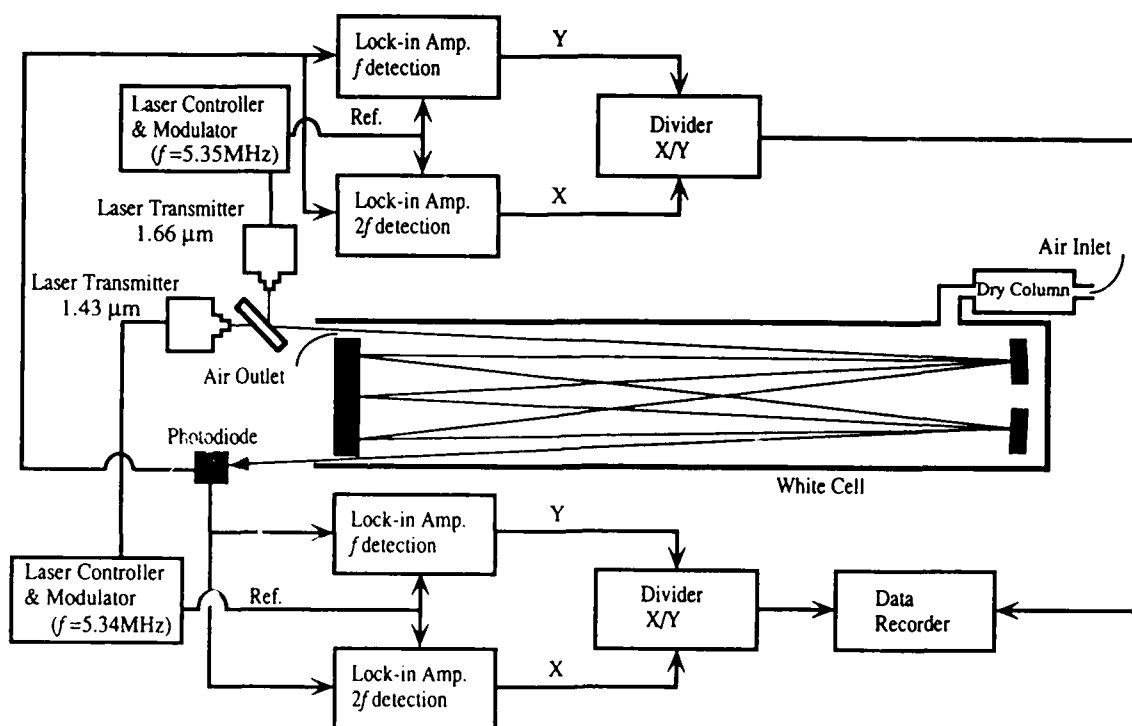


Fig. 2. Experimental setup for simultaneous monitoring of methane and carbon dioxide.

modulation frequencies. Analogue dividers are used to normalize the $2f$ signal by the f signal for both modulation frequencies. The outputs of the dividers were recorded in a data recorder.

The outdoor air flows continuously through the White cell with a small air pump after passing a dry column which removes water vapor. It takes 2 min. to replace 90 % of the whole volume of the White cell by new air. Methane-nitrogen and carbon dioxide-nitrogen mixtures of known concentrations were supplied at intervals for calibration. The measurements were done at the Keio University Yagamidai Campus in Yokohama.

Figure 3 shows the result of a test run of simultaneous measurement of methane and carbon dioxide. Traces (a) and (b) are the normalized signals obtained with reference to 5.35 MHz and 5.34 MHz, respectively, when air, 335-ppm carbon dioxide, and 2.0-ppm methane samples at atmospheric pressure were introduced successively into the White cell. The signal averaging time was 1.3 s. Figure 3 indicates that there is no appreciable interference between the two signals. Since the signal-to-noise ratio (S/N) in Fig. 3 (a) is about 400, the minimum detectable concentration of methane in atmosphere in a 85-m absorption pathlength is calculated to be 5 ppb assuming that $S/N=1$ gives the detection limit. Similarly, from Fig. 3 (b), the minimum detectable concentration of carbon dioxide is about 2 ppm.

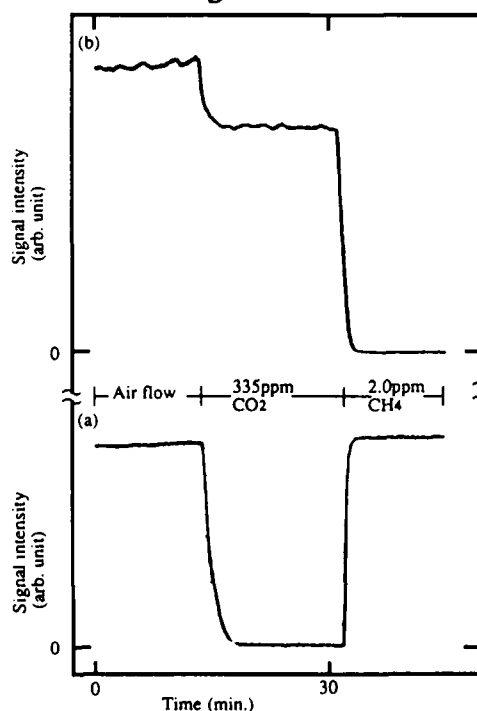


Fig. 3. Result of a test run of simultaneous monitoring of methane and carbon dioxide, indicating the high sensitivities and no interference of the two signals.

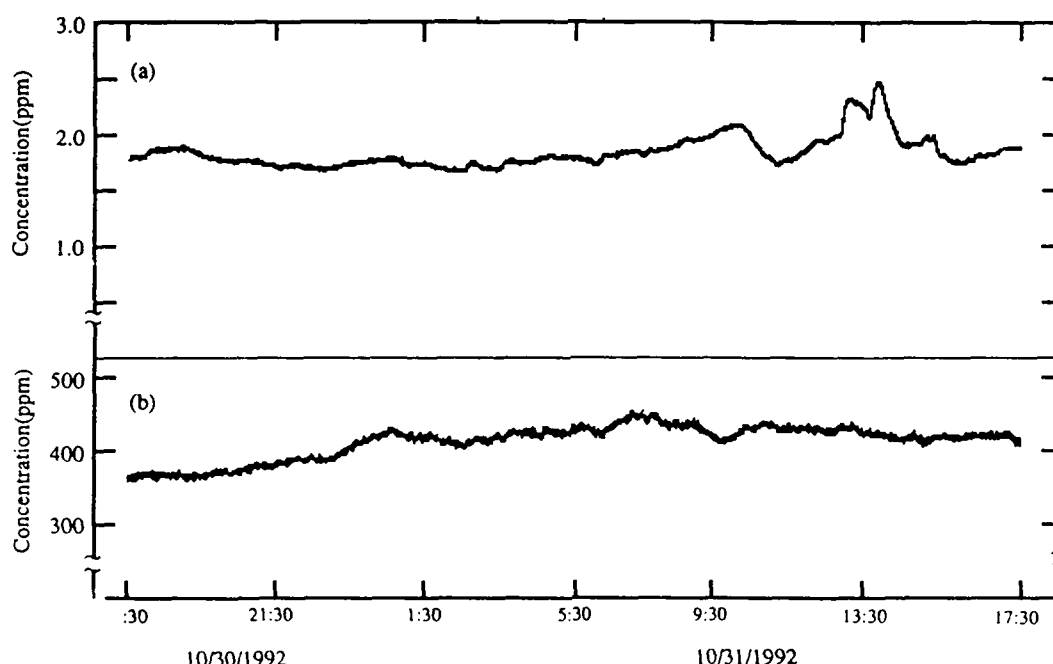


Fig. 4. Result of a 24-hour simultaneous monitoring of atmospheric methane (a) and carbon dioxide (b).

Figure 4 shows the result of a 24-hour continuous monitoring of atmospheric methane and carbon dioxide. The methane concentration changed by 35 % around 2 ppm and the carbon dioxide concentration changed by 20 % around 400 ppm.

For more precise calculation of the concentrations, the dependance of the $2f$ signal (I_{2f}) on pressure and temperature of the monitored air must be taken into account. It can be shown that the pressure dependance is almost eliminated if the frequency modulation amplitude of the laser is set to 2.2 times as large as the half width of the absorption line. The temperature dependence is then given by $I_{2f} \propto \exp(-317/T)/T^2$ for the methane Q(6) line and $I_{2f} \propto \exp(-118/T)/T^{3/2}$ for the carbon dioxide R(14) line, where T is the temperature in K. A 5-K variation around 293 K, for example, requires ~2% corrections in the concentrations.

In conclusion, we have demonstrated a 24-hour high-sensitivity simultaneous monitoring of the two main green-house gases. There is no limit to the possible period of duration of a continuous measurement.

References

- [1] H. Tai, H. Tanaka, and K. Uehara, "Remote detection of methane with a 1.66- μ m diode laser," 1990 OSA Annual Meeting, Technical Digest, p. 93, 1990.
- [2] K. Uehara and H. Tai, "Remote detection of methane with a 1.66- μ m diode laser," *Appl. Opt.*, vol. 31, pp. 809-814, 1992.
- [3] H. Tai, K. Yamamoto, S. Osawa, and K. Uehara, "Remote detection of methane using a 1.66- μ m diode laser in combination with optical fibers," the 7th Optical Fiber Sensors Conference, Proceedings, pp. 51-54, 1990.
- [4] K. Chan, H. Ito, and H. Inaba, "10-km-long fiber-optic remote sensing of CH₄ gas by near infrared absorption," *Appl. Phys. B*, vol. 38, pp. 11-15, 1985.
- [5] A. Mohabati and T. A. King, "Remote detection of gases by diode laser spectroscopy," *J. Mod. Opt.*, vol. 35, pp. 319-324, 1988.
- [6] H. Tai, K. Yamamoto, M. Uchida, S. Osawa, and K. Uehara, "Long-distance simultaneous detection of methane and acetylene by using diode lasers coupled with optical fibers," *IEEE Photon. Technol. Lett.*, vol. 4, pp. 804-807, 1992.
- [7] Y. Shimose and T. Okamoto, private communication.
- [8] K. Uehara, "Signal recording and averaging in diode laser spectroscopy," *Opt. Lett.*, vol. 12, pp. 81-83, 1987.
- [9] K. Uehara and K. Katakura, "New method of frequency stabilization of semiconductor lasers," *Jpn. J. Appl. Phys.*, vol. 27, pp. L244-L246, 1988.
- [10] D. T. Cassidy and J. Reid, "Atmospheric pressure monitoring of trace gases using tunable diode lasers," *Appl. Opt.*, vol. 21, pp. 1185-1190, 1982.

Solid-State Laser Technology as a Quantitative Solution
in Ambient Air Pollution Monitoring

Craig A. Smith
Schwartz Electro-Optics
3404 N. Orange Blossom Trail
Orlando, FL 32804

The on-going development of a pulsed Ti:Sapphire DIAL system capable of transmitting wavelengths from 210 nm all the way out to 2.6 μm will be discussed.

The Arecibo Observatory Lidar Upgrade: Possibilities for New Science.

Jonathan S. Friedman, NAIC Arecibo Observatory, P.O. Box 995, Arecibo, PR 00613-0995, (809)878-2612

Paul A. Castleberg, Cornell University, Department of Electrical Engineering, 351 Engineering and Theory Center, Ithaca, NY 14853, (607)255-8298

Kalpak A. Dighe, Clemson University, Department of Physics, Kinard Hall, Clemson, SC 29634-1911

Craig A. Tepley, NAIC Arecibo Observatory, P.O. Box 995, Arecibo, PR 00613-0995, (809)878-2612

Michael C. Kelley, Cornell University, Department of Electrical Engineering, 316 Engineering and Theory Center, Ithaca, NY 14853, (607)255-7425

1. Introduction:

The Doppler-Rayleigh lidar at the Arecibo Observatory has been in operation since the spring of 1990. Since that time regular measurements have been conducted of the wind structure of the stratosphere and mesosphere above Puerto Rico. At the present time, the lidar is capable of measuring horizontal wind velocities in an altitude range from less than 10 km to nearly 60 km. The main purpose of the upgrade is to extend the upper limit of the Doppler-wind measurements to meet the lower limit of the incoherent scatter radar (ISR). This will be done by the completion of a large telescope and by adding resonance lidar capability. A benefit of the resonance scatter lidar, and one that is certainly not of secondary interest, is to study the density and dynamics of trace species near the mesopause.

With the Arecibo ISR we are able to measure winds in the ionosphere from a low range of 60 km during the day and 100 km at night. This, coupled with the wind-measuring capability of the Doppler lidar, opens the possibility of measuring winds from near ground level up to the upper range of the ISR, which is near half an earth's radius. To achieve this continuous time and altitude coverage of atmospheric winds, two capabilities are necessary for the lidar. The first is to acquire a daytime capability, and the second is to extend the altitude range. A daytime capability is achieved by extremely narrow-bandwidth filtering of background light with interference filters and twin-tandem Fabry-Perot (FP) etalons. The altitude range can be extended in two ways. One is by an increased power \times aperture (PA) product, and the second is by taking advantage of resonance emission from trace metals in the upper atmosphere. Development of both of these capabilities are underway with the construction of a new large telescope, and work on a tunable laser system based on new solid-state tunable laser materials.

The tunable solid-state laser system opens up more than just the ability to extend the Doppler lidar. Resonance scattering is of interest, whether used to monitor upper atmospheric thermodynamics or to study atmospheric chemistry in general. The broad tunability also opens up possibilities for differential absorption lidar (DIAL) measurements. Tropospheric measurements of water and pollutants, and stratospheric measurements of ozone and NO₂ will be possible.

2. Daytime Lidar Capability:

The development of a daytime lidar system is in progress. During the day, the present upper altitude limit of our lidar is close to the lower extremes of the ISR measurements. Thus, once the

daytime lidar is operational, continuous altitude measurements of winds will be possible during the day.

The central component necessary for a daytime lidar system is the ability to filter out as much background light as possible. This is done by successive filtering of the return light. First, a narrow-band (0.6\AA) Daystar filter is used to eliminate all background light except for that surrounding the laser line. A twin-tandem FP follows the Daystar filter. One FP is used to achieve the desired resolution while the other, with a different free spectral range (FSR) from the first, allows only every 5th order of the first FP to be transmitted, thus pushing higher-order modes of the first interferometer outside the transmission curve of the Daystar filter. The resulting transmission curve is shown in figure 1.

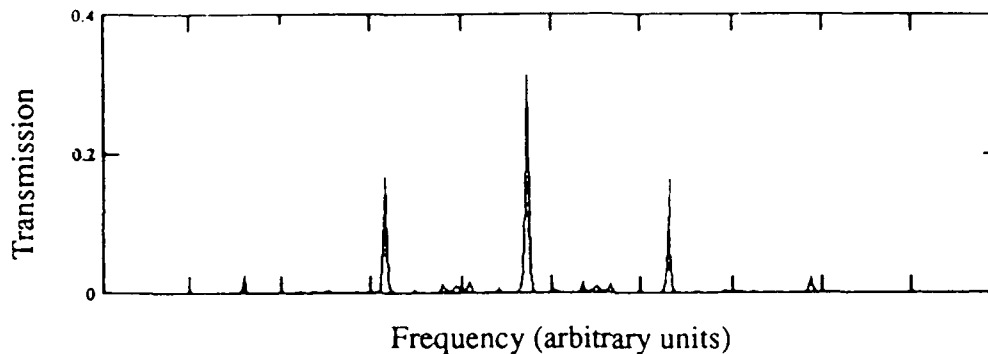


Figure 1. Transmission curve for the daytime lidar light filtering system.

With an ideal system, the signal-to-background transmission ratio cannot be better than 1. In this case, with interferometer spacings of 1 cm and 2.5 cm, the signal-to-background ratio is 0.337. Although these are our initial experimental settings, the spacings can be adjusted so as to optimize this ratio.

3. The New Telescope

For night-time measurements the problem of measuring winds is more difficult. The ionosphere decays, due to the lack of solar radiation, below about 200 km, except for the presence of sporadic ion layers near 100 km altitude. An increase in the PA product of the lidar is necessary to push the Doppler-Rayleigh lidar measurements higher. Development of a new multi-telescope-telescope (MTT) is well underway. It is based on a design by Bagnuolo et al. [1990] that places a number of separate telescopes on the same platform to point at the same object. The collected light is then coupled together via optical fibers. This telescope will consist of 19 individual 30" diameter Cassegrain pairs. A diagram of the MTT is shown in figure 2.

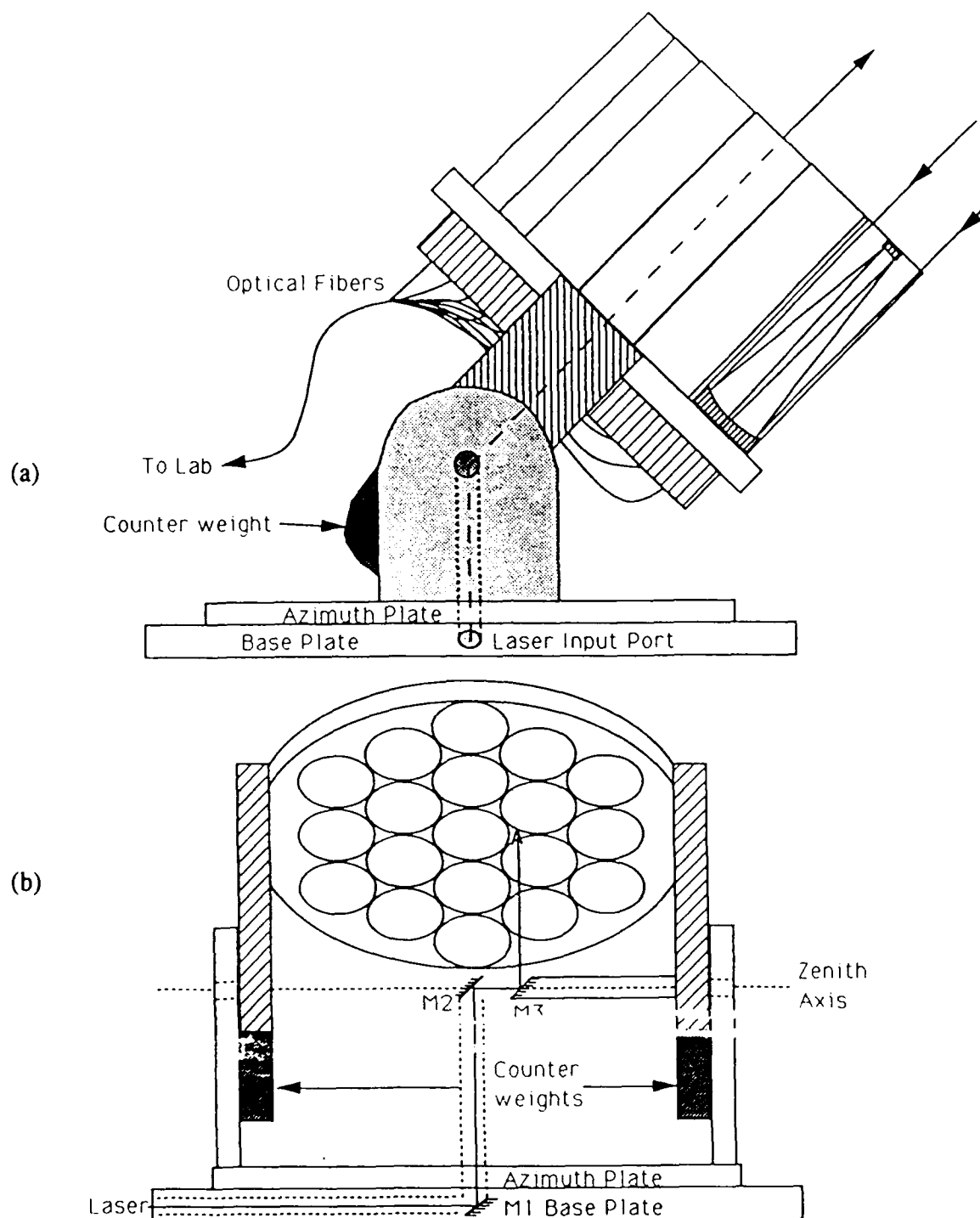


Figure 2. Side (upper) and back (lower) views of the multi-telescope-telescope (MTT). The output laser beam path is shown in both views. In the side view, the return path is shown for one of the 19 telescopes. With whole telescope above the zenith axis the system is completely steerable without any blockage of the transmitter beam.

The upper view is from the side, and the lower is from the back (with telescopes looking away). One of the 19 telescopes is represented on the upper diagram. In that diagram the transmitted laser beam is the dashed line that becomes the solid arrow pointing out from the telescope center. Return light is coupled into optical fibers at the Cassegrain focus of each telescope. Fiber couplers bring the light into a single fiber which transmits the light into the laboratory for spectral analysis. In the lower picture, the individual telescopes and fibers are left out to show more clearly the laser output path. The beam is guided along the azimuth and zenith axes so that there are no positions in azimuth and zenith that are off-limits to the transmitter. The laser can then be steered out either through a gap between three of the telescopes or by using one of the telescopes as a beam expander.

The MTT is replacing a single 16" Newtonian reflector. With its completion we will get an improvement in the PA of a factor of 70. A factor of 10 increase of PA corresponds to a height extension of 2 scale heights. At 60 km, one scale height corresponds to about 7.5 km, thus, the telescope alone will increase the wind-measurement range of our lidar from 60 km to over 85 km. An extended range can be further achieved with an increase in the power of the laser transmitter and size of the altitude sample.

4. Resonance Lidar with Solid-State Laser Sources:

Ti:sapphire ($\text{Ti:Al}_2\text{O}_3$ or Ti:S) is a well established solid-state laser material capable of laser emission in a range from 680 nm to 1100 nm. The second harmonic of the output of a Ti:S laser can be used to study many important minor species deposited in the mesopause by meteor ablation. These include iron, calcium and singly ionized calcium, and aluminum. Another crystal that can be used as a tunable laser gain medium, although it is new and not yet well established, is Cr^{4+} :Forsterite ($\text{Cr:Mg}_2\text{SiO}_4$ or Cr:F). It has a tuning curve that ranges from 1130 nm to 1367 nm [Baryshevski et al., 1988; Carrig and Pollock, 1991; 1992; Petricevic, 1990]. The doubled output from a Cr:F laser can probe sodium at 589 nm. We have begun working on a pulsed Cr:F laser source for this purpose.

References:

Bagnuolo, W.G., Jr., I.K. Furenlid, D.R. Gies, D.J. Barry, W.H. Russell, and J.F. Dorsey, "The Multi-Telescope Telescope: A cost-effective approach to fiber-fed spectroscopy," Pub. A.S.P., **102**, p. 604, (1990).

Baryshevskii, V.G., M.V. Korzhik, A.E. Kimaev, M.G. Livshits, V.B. Pavlenko, M.L. Meil'man, and B.I. Minkov, "Tunable chromium forsterite laser in the near IR region," J. Appl. Spectrosc. (translation of Zh. Prikl. Spektrosk.), **52**, p. 1040, (1988).

Carrig, T.J., and C.R. Pollock, "Tunable, cw operation of a multiwatt forsterite laser," Opt. Lett., **16**, p. 1662, (1991).

Carrig, T.J., and C.R. Pollock, Performance of a continuous-wave forsterite laser with krypton ion, Ti:sapphire, and Nd:YAG pump lasers, in press, IEEE J. Quantum. Elect., (1992).

Petricevic, V., A. Seas, and R.R. Alfano, "Forsterite laser tunes in the near-infrared," Laser Focus World, p. 109, (November 1990).

NORMALS — A Noise Reduction Method

Using Multivariate Analysis Technique for Lidar Echo Signal

Hiroshi OKUMURA, Tadashi SUGITA, Hironori MATSUMOTO and Nobuo TAKEUCHI

Remote Sensing and Image Research Center, Chiba University

1-33, Yayoi-cho, Inage-ku, Chiba, CHIBA 263, JAPAN

Phone: 81-43-251-1111 Fax: 81-43-253-0272

1. INTRODUCTION

Portable lidar system is a powerful tool for monitoring air pollution, stratospheric and boundary layer, plume dispersion, visibility, and studying atmospheric structure and cloud physics. However, the signal-to-noise (S / N) ratio of each echo datum which is acquired with such portable lidar systems is not so high because of its low lasing power in comparison with large scale lidar systems.

Lidar echo data includes not only backscatter signal from scatterer but also various kinds of noise components (*e.g.* shot noise caused by fluctuation of electric current, dark current noise of detector, thermal noise of a resistor in the amplifier *etc.*). The noise reduction methods which are applied for lidar echo data are as follows:

- (a) accumulation of lidar echo data on the assumption of noise randomness;
- (b) moving average method;
- (c) filtering using fast Fourier transform;
- (d) hysteresis smoothing method.

The *METHOD* (a) is generally using for noise reduction. However, this method is not sufficient, because the properties of random noise is not shown in the noise component which is included in the actual lidar echo data in most cases. Although the *METHOD* (b) and (c) are very effective against pulse noise reduction, these methods distorts even the wave form of backscatter signal. In contrast with this, the *METHOD* (d) is not so effective against reduction of strong pulse noises.

We developed a new noise reduction method based on statistical technique, **NORMALS** (a **NO**ise **R**eduction method using **M**ultivariate **A**nalysis technique for **L**idar echo **S**ignals), in order to overcome these problems. Canonical correlation analysis is applied for noise reduction by the **NORMALS**. The **NORMALS** has the advantage of an effective noise reduction without wave form distortion of backscatter signal.

In the following chapters, the details of the **NORMALS** are described and its validity is confirmed by numerical simulation and also by the application to actual lidar echo data.

2. PRINCIPLE

2.1 Canonical Correlation Analysis [1], [2]

Canonical correlation analysis (CCA) is one of multivariate statistical methods. The CCA method converts characteristic variates into uncorrelated integrate variates by the same way as in principal component analysis (PCA). While the PCA is applied to one group of p characteristic variates, the CCA is applied to two characteristic variate groups. The first group (*GROUP-1*) and the second group (*GROUP-2*) consist of s and t ($p = s + t$, $t \geq s$) characteristic variates, respectively.

Suppose that two characteristic variate groups, $x_1 \cdots x_s$ and $x_{s+1} \cdots x_{s+t}$. The mean values of these variates are normalized to 0. Consider following linear compounds;

$$u_i = \sum_{p=1}^s l_{pi} x_p \quad (i = 1, \cdots, s) \quad (1),$$

$$v_j = \sum_{q=1}^t m_{qj} x_{s+q} \quad (j = 1, \dots, t) \quad (2).$$

Coefficients in Eq.1 and Eq.2, l_{pi} and m_{qj} ($i, p=1, \dots, s; j, q=1, \dots, t$), are determined by way of satisfying following conditions;

- ① the mean values and the variance values of u_i and v_j are equal to 0 and 1, respectively,
- ② u_i is uncorrelated with $u_{i'}$ ($i \neq i'$);
- ③ v_j is uncorrelated with $v_{j'}$ ($j \neq j'$);
- ④ u_i is uncorrelated with v_j ($i \neq j$);
- ⑤ correlation coefficients

$$r_1 \geq r_2 \geq \dots \geq r_k \quad (3)$$

exists between u_k and v_k ($k=1, \dots, s$).

Integrated variates u_i and v_j ($i=1, \dots, s; j=1, \dots, t$) are called *canonical variates*, and correlation coefficient r_k is called *k-th canonical correlation*. Fig.1 shows the relation between characteristic variates and canonical variates, schematically.

2.2 Processing algorithm of the NORMALS

In the case where we apply the CCA to noise reduction of lidar echo data, the method for assignment of characteristic variates is important. Here we denote lidar echo signal which is acquired in normal operation by S_I , and assume that S_I can be described as;

$$S_I = S + N_I \quad (4),$$

where S : backscatter signal from scatterer.
 N_I : noise component.

Since it is difficult to estimate N_I , subtraction operation cannot be applied to noise reduction. Then we use lidar echo signal which is acquired in non-lasing operation in place of N_I , and denote this non-lasing signal by S_2 . The S_2 can be described as;

$$S_2 = N_2 \quad (5),$$

where N_2 : noise component.

In the case where S_I and S_2 are assigned to the characteristic variates of *GROUP-1*, the necessary conditions for the assignment of two characteristic variates of *GROUP-2* can be described as follows;

- (1) the outline wave form data of S is required as the characteristic variate S_I' of *GROUP-2* corresponding to S_I of *GROUP-1*;
- (2) the outline wave form data of N_I is required as the characteristic variate S_2' of *GROUP-2* corresponding to S_2 of *GROUP-1*.

In the **NORMALS**, moving averaged S_1 data and S_2 data is assigned to S_1' and S_2' , respectively.

3. EXPERIMENT AND DISCUSSION

Fig.2 shows actual lidar echo data with lasing (S_1) and without lasing (S_2). We used the diode-pumped YAG portable lidar system[3] that we have developed for data acquisition. Fig.3 shows the result by the **NORMALS**. As the result of measurements, amplitude of noise component and mean square error against ground level were reduced by the **NORMALS** 30% and 62%, respectively.

4. SUMMARY

The validity of the proposed method, the **NORMALS**, was confirmed through comparison of the result by moving average method from the view point of the performance of noise reduction and the wave form distortion. As the results of experiments, the **NORMALS** has the advantage of an effective noise reduction without wave form distortion of backscatter signal. Improvement of the performance is a subject for a future study.

ACKNOWLEDGEMENTS : The authors are grateful to Dr. Koji Kajiwara, Institute of Industrial Science, University of Tokyo, JAPAN, and Mr. L. Kithsiri Perera, Remote Sensing & Image Research Center, Chiba University, JAPAN, for their helpful advice, and supports.

REFERENCES

- [1] Rao, C. R. : Linear Statistical Inference and Its Applications (2nd edition), John Wiley & Sons (1973)
- [2] Morrison, D. F. : Multivariate Statistical Methods (3rd edition), McGraw-Hill (1990)
- [3] Takeuchi, N., *et al.* : Observation of sea fog incursion with a diode-pumped YAG portable lidar, in the Digest of Topical Meeting on Optical Remote Sensing of the Atmosphere (1993)

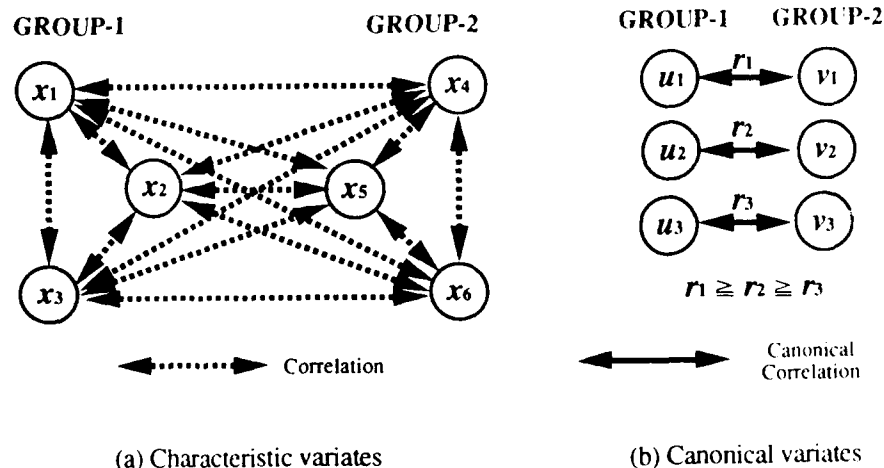


Fig.1 Characteristic variates and canonical variates ($s = t = 3$).

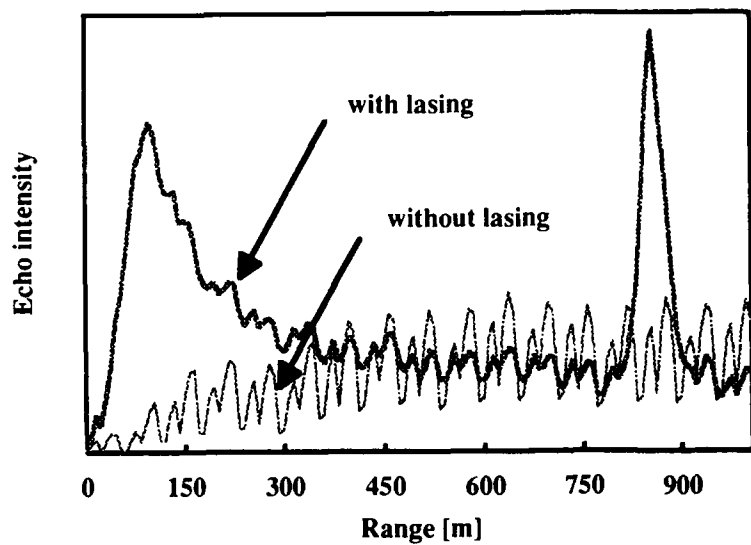


Fig.2 Actual lidar echo data (with lasing and without lasing).

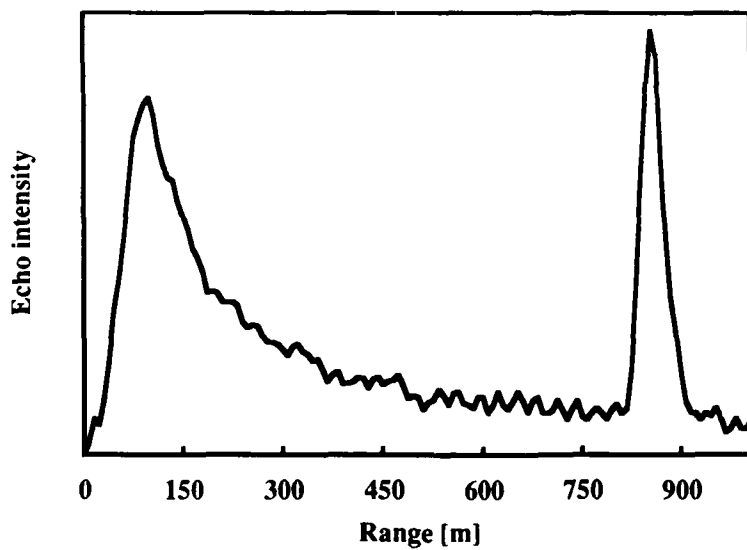


Fig.3 Result of noise reduction by NORMALS.

Clear Air Turbulence Detection with a 2 μm Lidar Employing Velocity Width Processing

Robert J. Martinsen, Andrew J. Jankevics, Charles P. Plum
Lightwave Atmospheric, Inc.
2 Susan Rd. Marblehead, MA 01945

John H. Flint
Schwartz Electro-Optics, Inc.
45 Winthrop St. Concord, MA 01742

Introduction

We describe in this paper results of a system study for an airborne lidar system that makes real-time, range-resolved measurements of clear air turbulence (CAT) to several kilometers forward of an aircraft's projected flight path. Exploiting the width of the IF signal Doppler spectrum (σ_f) is central to the system concept. Since broadening of the Doppler spectrum beyond the transform limit is a function of the mixture of velocities (velocity width, σ_v) in the pulse scattering volume, any combination of shear and/or turbulence in the flight path is immediately revealed by the broadened spectra. Hence, σ_f relates to a property of the velocity field that is particularly important to aircraft and other aerospace vehicles. Explicit spectral width processing is quite powerful for CAT detection lidars because complex atmospheric wind patterns can be characterized in terms of a single observable σ_v for subsequent reckoning against a hazard index.

Doppler Broadened Lidar Signals

Radial velocity $V_r(R)$ profiles of atmospheric winds were generated to (a) study the spectral broadening sensitivity to various incarnations of CAT and (b) to assist in transmitter pulse width selection. Ground-based radar observations and insitu aircraft measurements of CAT reported in the literature served as a basis for $V_r(R)$ synthesis^[1,2]. Wind profiles considered in our analyses included low and high Reynold's number sheared flows for which the shear ranged from .03 - .13 sec^{-1} , and 1 km-long CAT events of different inner scales and spectral densities.

The width of the IF signal power spectrum σ_f was calculated using an untruncated Gaussian temporal pulse profile to evaluate the normalized first and second spectral moments of the radial wind^[3]. The velocity width σ_v contributes to the width of the IF signal spectrum σ_f at range R by the relationship

$$\sigma_f(R) \equiv \sqrt{\left(\frac{2\sigma_v(R)}{\lambda}\right)^2 + \left(\frac{\lambda}{4\pi\tau}\right)^2} \quad [\text{Hz}] \quad (1)$$

where λ is the lidar wavelength, and τ is the pulse duration. The first term in Eq. (1) gives the spectral broadening effect of a distribution of velocities in the pulse scattering volume, and the second term gives the transform-limited [spectral] width due to a finite pulse duration.

Figures (1a) and (1b) show spectral broadening results for two realizations of CAT with different scales of turbulence. The inner scale of turbulence assigned to the radial velocity profile in Fig. (1a) was ≈ 900 meters whereas an inner scale of ≈ 30 meters was assigned to the profile in Fig. (1b). Both events persist for ≈ 1 km and, aside from the brief transient at 1.35 km in Fig. (1b), both undergo a ΔV_r on the order of 4 m/s. Figures (1a) and (1b) are indicative of the early and late stages, respectively, of CAT development such that wave-like undulations from shear instabilities ultimately collapse into small-scale turbulence. In each figure, the top frame shows a simulated radial velocity profile $V_r(R)$ and the bottom frame is a plot of the IF signal frequency width as a function of range for three different pulse widths. Both $V_r(R)$ profiles are based on the familiar $\kappa^{-5/3}$ Kolmogorov power law, although the broadening of the IF signal is rather insensitive to the spectral density statistics assigned to the turbulence.

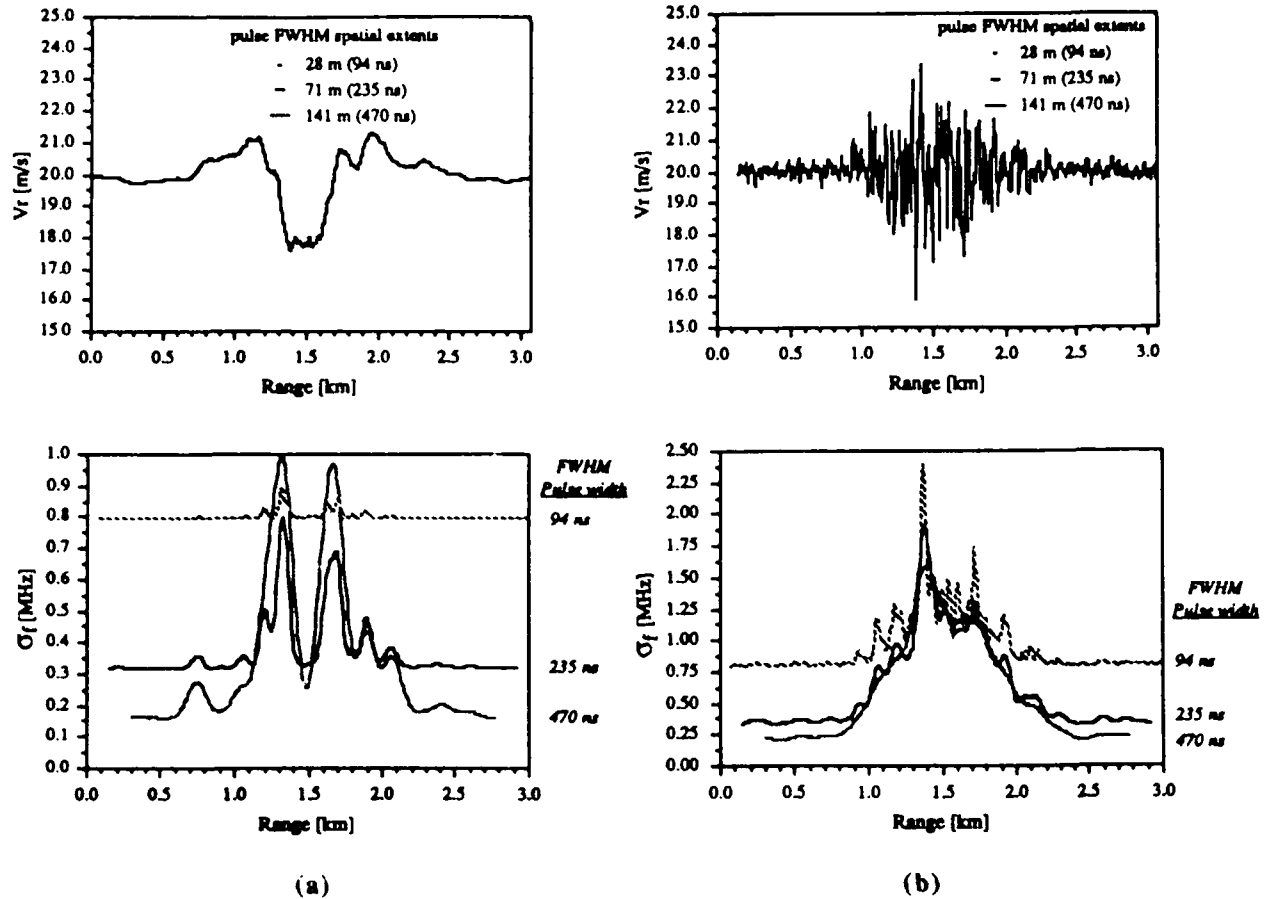


Figure 1. Broadening of the IF signal frequency for three transmitted pulse widths intercepting CAT events having inner scales of (a) 900 meters and (b) 30 meters. Top panels give the synthetic radial velocity profile $V_r(R)$ and bottom panels give the spectral width $\sigma_f(R)$ of the velocity distribution across the spatial extent of each pulse.

It is evident from these two figures that short pulse widths are not well suited for detecting large-scale disturbances that exhibit pure shear over the resolution cell size. The local velocity spread tends to be small except for cases of extreme shear. Longer pulses yield a higher "gain" in their broadening response due to the combined effects of a lower transform limit and a longer window function (i.e. scattering volume) subtending the velocity field. Shear contributes to the velocity width

$$\sigma_{\text{shear}} = \frac{c \tau \Psi}{2\sqrt{12}} \quad [\text{m/s}] \quad (2)$$

where Ψ is the observed shear in the velocity field, $\partial V_r / \partial r$ [sec^{-1}], c is the speed of light [m/s], and τ is the pulse duration. A rational argument can be made for choosing a pulse width that has a spatial extent comparable to the size of the aircraft L or perhaps even $2L$. This would allow the lidar to efficiently detect CAT events that produce high accelerations and filter out low wavenumber disturbances for which the aircraft responds with low accelerations.

Signal Processing Procedure

Autocorrelation processing is an attractive method for directly extracting the second spectral moment of the IF signal in real-time. The basic algorithm has been implemented by Lee^[4] using inexpensive digital circuits and has proven to perform well in low signal-to-noise environments.

When a volume of the atmosphere is convolved with a Gaussian laser pulse profile, the autocorrelation function of the time series signal is well approximated by a Gaussian shape. The width of the Gaussian determines the decorrelation time of the signal which is inversely proportional to the spectral width. Hence, long correlation times are associated with scattering volumes containing a narrow distribution of velocities, and signals that decorrelate rapidly are associated with regions having broad distributions of velocities (e.g. CAT).

The received signal is the sum of amplitude and phase contributions from many individual scatterers over the resolution volume. The received signal at time t after the start of transmission comes from a range interval $\Delta R = c\tau/2$ centered at $R_0(t) = (c/2)(t - \tau/2)$. The signal is passed through a complex demodulator to generate in-phase I and quadrature Q components, which are then digitized. The complex autocorrelation function is calculated

$$\hat{R}(T) = \langle Z(t) \cdot Z^*(t + T) \rangle \quad (3)$$

where $Z(t) = I(t) + iQ(t)$, * denotes conjugation, T is the lag of the autocorrelation dictated by the sampling rate $T = f_s^{-1}$, and the brackets imply ensemble averaging. The autocorrelation function is calculated for multiple pulses P and the values at the respective a^{th} lags are then averaged. Each velocity width estimate for the m^{th} range gate is based on a multi-pulse averaged autocorrelation function:

$$\{\hat{R}_m(aT)\} = \frac{1}{P} \sum_{p=1}^P \hat{R}_m(aT)_p \quad (4)$$

The magnitude of Eq. (4) is submitted for width estimation using a least-squares Gaussian curve-fit. The width of the Gaussian σ_T is a function of the velocity width σ_V by the simple relationship

$$\sigma_T = \frac{\lambda}{4\pi\sigma_V} \quad [\text{sec}] \quad (5)$$

where λ is the laser wavelength [m] and σ_V is in units of velocity [m/s]. By definition, σ_T corresponds to the time it takes for the [normalized] autocorrelation function to fall to a value of 0.61. Another convention describing the decorrelation of the time series is given by

$$T_{1/2} = \frac{0.0937 \lambda}{\sigma_V} \quad [\text{sec}] \quad (6)$$

where $T_{1/2}$ is the time it takes for the autocorrelation function to fade to a value of 1/2. Figure 2 is a plot of the $T_{1/2}$ decorrelation time as a function of velocity width over different regimes of turbulence. The corresponding number of lags of the autocorrelation function are also indicated based on a 70 MHz sampling rate.

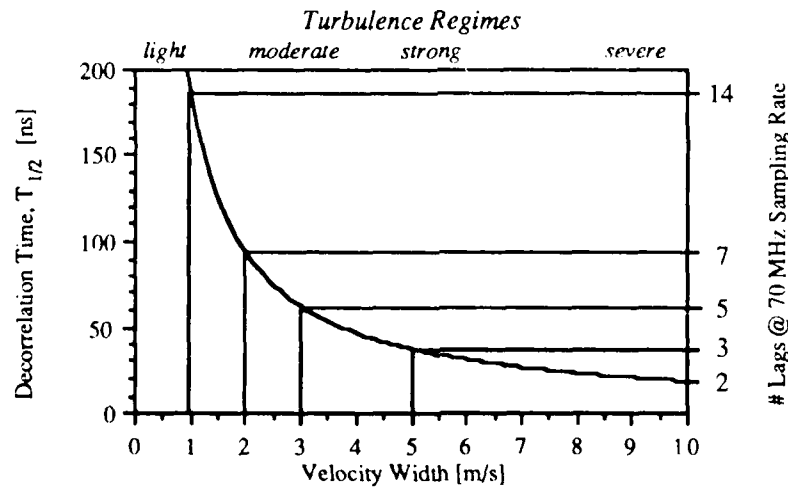


Figure 2. Decorrelation time of the IF signal as a function of velocity width of the radial wind indicating the number of lags required for different regimes of turbulence.

System Performance Evaluation

System trade studies included SNR calculations for horizontal path propagation at the tropopause (~10 km altitude) in clear air, cirrus, and subvisual cirrus environments. The SNR calculated at the tropopause represents the average result for altitudes between 3 - 15 km using the standard model atmosphere for clear air. Subvisual cirrus is an enhanced scattering environment which can extend the measurement range to great distances by increasing the SNR by as much as 30 dB over the standard clear air response at high altitudes. If one accepts the general consensus that *most* CAT is a manifestation of Kelvin-Helmholtz instability (KHI), a compelling argument can then be made which suggests subvisual cirrus are often artifacts of CAT due to the overturning of a stratified shear layer^[5]. Certainly not all CAT episodes are associated with KHI, and therefore, minimum warning time requirements must be satisfied without reliance on subvisual cirrus.

Figure 3 shows the calculated SNR(R) results. The minimum single-pulse SNR for achieving errors less than 1 m/s in the spectral width estimates using 10-pulse averages is -5 dB^[4]. In the clear atmosphere with no subvisual cirrus, a 2 μ m transmitter operating at an average power of only 1 W (10 mJ, 100 Hz) coupled to a 20 cm aperture telescope focused at 3 km, can provide reliable velocity width measurements out to a range of 4 km. If subvisual cirrus are present over the entire propagation path, the maximum measurement range would exceed 20 km, providing over 1.5 minutes of warning for aircraft traveling at 400 knots.

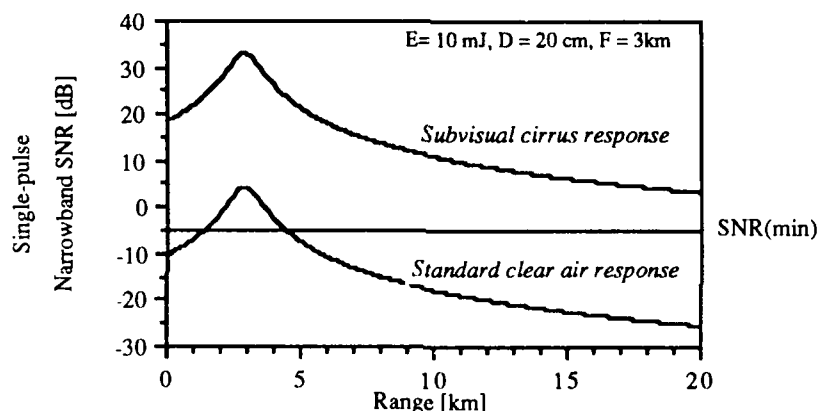


Figure 3. Performance of a 2.01 μ m lidar system transmitting 10 mJ pulses in 470 ns FWHM from an aperture of 20 cm diameter focused at 3 km. The two traces correspond to subvisual cirrus and standard clear air environments at the tropopause.

References

- [1] Browning, K.A., Bryant, G.W., Starr, J.R. and Axford, D.N. "Air motion within Kelvin-Helmholtz billows determined from simultaneous Doppler radar and aircraft measurements", *Quart. J. R. Met. Soc.*, **99**, 1973, pp.608-618.
- [2] Hardy, K.R., Reed, R.J. and Mather, G.K., "Observation of Kelvin-Helmholtz billows and their mesoscale environment by radar, instrumented aircraft, and a dense radiosonde network", *Quart. J. R. Met. Soc.*, **99**, 1973, pp.279-293.
- [3] Targ, R., Kavaya, M.J., Huffaker, R.M. and Bowles, R.L., "Coherent lidar airborne windshear sensor: performance evaluation", *Applied Optics*, **30**, No. 15, 20 May 1991, pp. 2013-2026.
- [4] Personal communications with R. Lee and T. Khan of Lassen Research, Manton, CA, July 1992.
- [5] Lawrence, Jr., J.D., McCormick, M.P., Melfi, S.H. and Woodman, D.P., "Laser backscatter correlation with turbulent regions of the atmosphere", *Clear Air Turbulence and its Detection*, Eds., Y-H- Pao and A. Goldberg, New York, Plenum Press, 1969, pp. 481-495.

Laser Long-Path Absorption Measurements with the Retroreflector In Space for the ADEOS Satellite

N. Sugimoto, A. Minato, and Y. Sasano
National Institute for Environmental Studies
Tsukuba, Ibaraki 305 Japan
T. Itabe, N. Hiromoto, and M. Takabe
Communications Research Laboratory
Koganei, Tokyo 184 Japan

Experiments on earth-satellite-earth laser long-path absorption measurement of atmospheric trace species will be performed with the Retroreflector In Space (RIS) which is to be loaded on the Advanced Earth Observing Satellite (ADEOS). The ADEOS is a Japanese polar-orbit satellite which is scheduled for launch in early 1996. RIS is a single-element cube-corner retroreflector with an effective diameter of 0.5 m. In the RIS experiments, a laser beam is transmitted from a ground station, reflected by RIS, and received at the ground station. The absorption of atmospheric trace species is measured in the round-trip optical path.

The structure of RIS is shown in Fig.1. A slightly curved mirror is used for one of the three mirrors forming the corner cube to overcome the velocity aberration caused by the satellite movement^{1,2)}.

The ground system for the RIS experiment consists of an optical satellite tracking system and a laser transmitter and receiver system for spectroscopic measurements (Fig.2). A satellite tracking system with a telescope with a diameter of 1.5 m will be used. Two single-mode TEA-CO₂ lasers are used in the measurement. One of the lasers is used to measure the absorption of the target molecule, and the other is used to record the reference signal. The Doppler shift of the reflected beam resulting from the satellite movement is utilized to measure absorption spectrum of the target molecule. The magnitude of the Doppler shift is 0 - 0.04 cm⁻¹ at 10 μm, which depends on the satellite position relative to the ground station. High-resolution transmission spectrum of the atmosphere is measured by utilizing the change in the wavelength of the Doppler-shifted return beam. Laser line can be switched over several lines during the measurement to observe the absorption spectrum in wider wavelength region.

Target molecules with isotope TEA-CO₂ lasers (¹²C¹⁶O₂, ¹³C¹⁶O₂) and their second and third harmonics are ozone, methane, CFC12, HNO₃, CO, N₂O, etc. Vertical profile can be obtained for ozone and methane by inversion using absorption line shape. Column contents are obtained for other molecules.

A simulator program and a data reduction program have been developed, and the accuracy of the measurement of each species has been evaluated. Figure 3 shows an example of the simulated return signal in the ozone measurement. Figure 4 shows the retrieved ozone profile from the simulated signal shown in Fig.3.

References

- 1) N.Sugimoto, A.Minato, and Y.Sasano, CLEO'91,450-451 (1991).
- 2) A.Minato, N.Sugimoto, and Y.Sasano, Appl. Opt. in press.

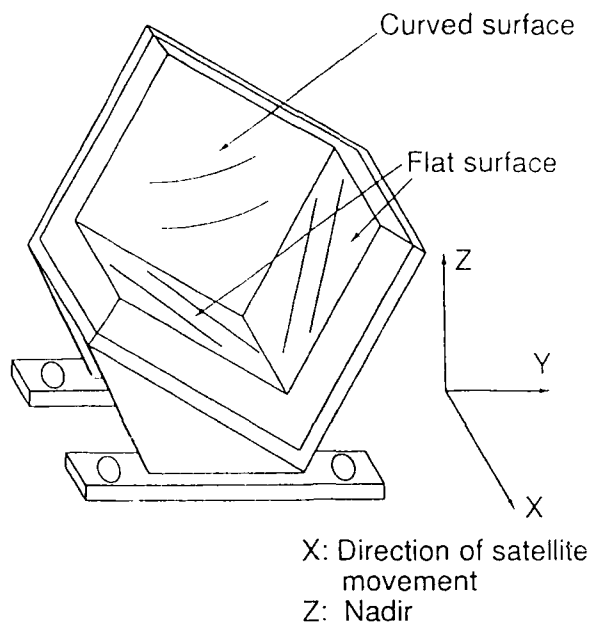


Fig.1 Structure of RIS.

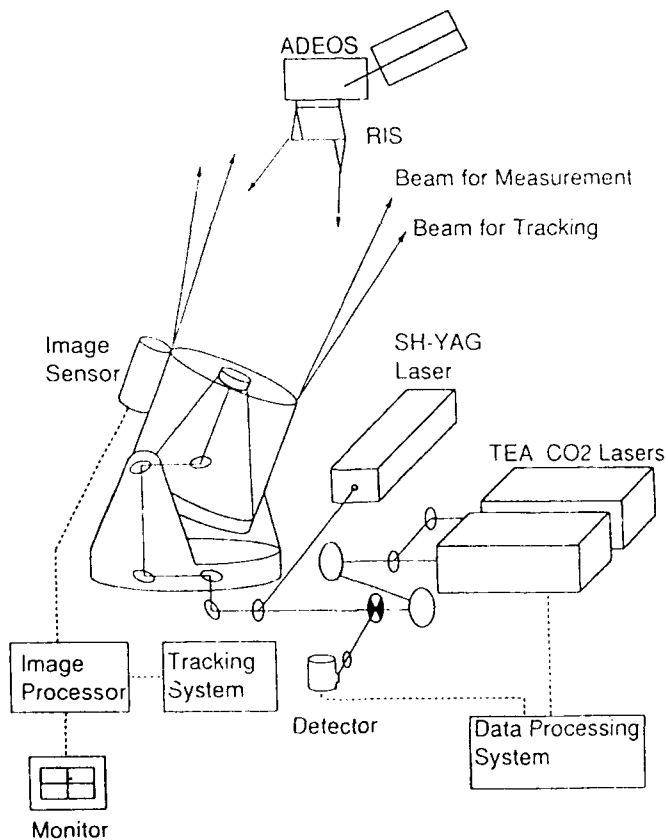


Fig.2 Ground system for the RIS experiment.

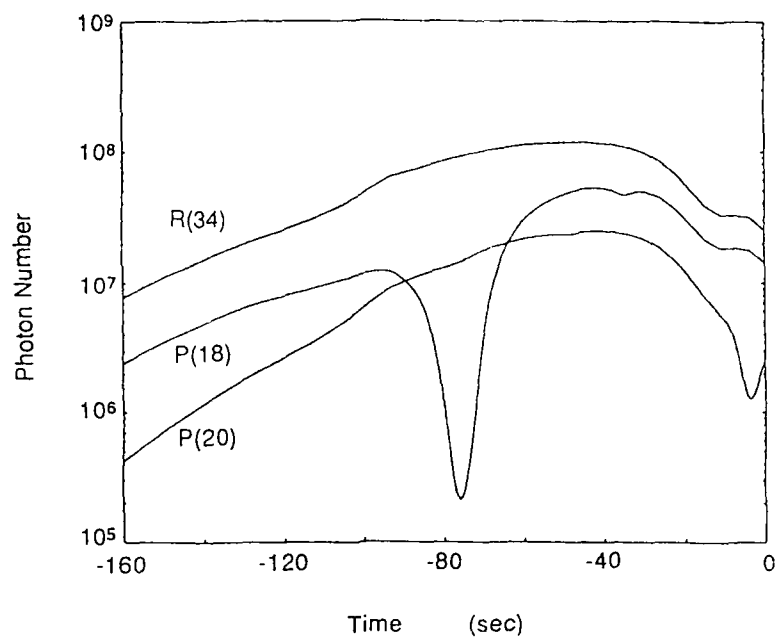


Fig.3 Simulated signal photon number per pulse as a function of time or the satellite position. Laser output energy is 100 mJ/pulse. Output beam divergence is 0.1 mr.

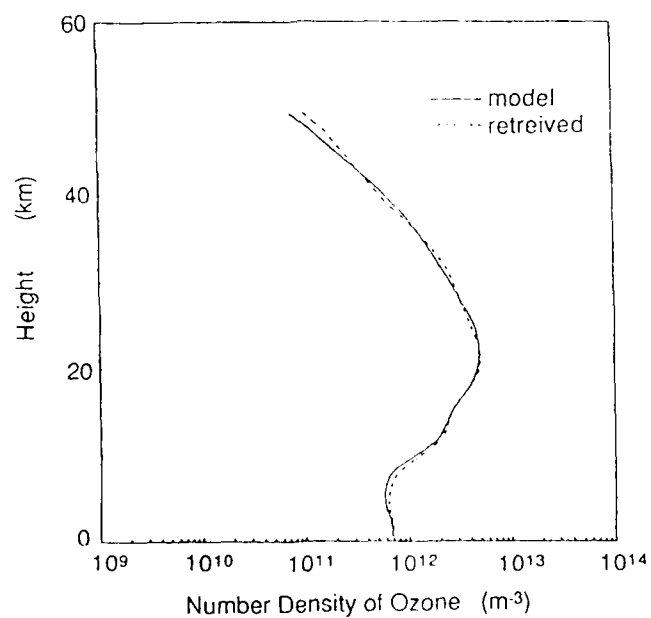


Fig.4 Ozone profile retrieved from the simulated return signal.

Comparative Studies of Single- and Dual-Beam CO₂ Laser Analyzer for Remote Sensing of Air Pollutants

Mohammad A. Rob
Division of Natural and Applied Sciences
University of Houston - Clear Lake
Houston, Texas 77058

Introduction

Laser spectroscopic techniques for detecting minute quantities of atmospheric pollutants have made rapid advances in the last few years.^{1,2} Molecular CO₂ lasers play an important role in atmospheric pollution monitoring. This is because of its high power emission on multiple wavelengths in the 9 - 11 μm range, and which overlap with the absorption spectra of a large number of molecules of environmental concern, such as hydrocarbons (HC), O₃, NH₃, SO₂, NO₂, and others. In addition to using a CO₂ laser for atmospheric pollution detection, one can use it inside a chemical plant to remotely detect leakage of unwanted toxic and hazardous gaseous compounds.² In this article, we present some initial results of an investigation on a simple gas analyzer using a CO₂ laser that can be used as a remote sensor for atmospheric pollution monitoring or for gas leak detection in chemical plants. A dual-beam CO₂ laser analyzer is also under investigation and comparative results will be presented at the conference.

Theoretical

In designing an instrument for air pollution detection, one usually wants to know the minimum detectable concentration N_{\min} of a particular molecule by the instrument. For a given molecule of cross section σ and for a given length L of the medium, it is given by

$$N_{\min} = \frac{1}{\sigma L} \ln \left[\frac{1}{1 - (\Delta I / I_o)_{\min}} \right], \quad (1)$$

where $\Delta I = (I_o - I)$ and $(\Delta I / I_o)_{\min}$ is the minimum detectable fractional change in signal. In most cases, $(\Delta I)_{\min}$ is limited by the detectivity (D^*) of the detector used in the experiment. Liquid-nitrogen-cooled HgCdTe detectors are widely used at CO₂ laser wavelengths because of their high detectivity around 9-11 μm region. Room-temperature HgCdTe detectors are suitable for field measurements but they are known to have a detectivity 2 to 3 order of magnitude less than their cooled counterparts.⁴ In the following, the frequency responsivity of a room-temperature HgCdTe detector and the detection limit of the instrument using this detector is presented.

Experimental

As shown in Fig.1(a), the output of a line-tunable cw CO₂ laser is directed to an absorption cell. The beam passes twice inside the cell and a portion of the beam is directed to a room-temperature HgCdTe detector. The input beam is intensity modulated by using

a chopper and phase-sensitive detection is employed by using a lock-in-amplifier. For the initial testing of the system, ethylene in its 99.5% pure form is used as the absorbing medium. Ethylene is a hydrocarbon commonly found in nature and in automobile exhausts. It has absorptions in almost all CO₂ laser lines but that due to 10P(14) line is very strong at atmospheric condition and is used for testing and calibration purposes.^{2,5} In the experiment, six CO₂ laser lines, 9P(12) through 9P(20) in the 9.6 μm band and 10P(14) in the 10.6 μm band, are used for testing purposes.

Results & Discussion

Absorption studies of ethylene with 9P(12) through 9P(20) lines revealed that the 9P(18) line is absorbed strongly, and other lines are absorbed weakly. Figure 1(b) shows the absorbance [$A = \ln(P/P_0)$] of ethylene at 9P(18) CO₂ laser line as a function of ethylene total pressure. It is clear that the Beer-Lambert's law is followed in the low pressure region (0-1 torr), but it deviates as the pressure is increased. The absorption saturates at about 3 torr. The general behavior of the curve reflects absorption within a fixed bandwidth laser line while the absorption bandwidth of the molecule is varied with pressure. Herlemont et al.⁶ made absorption measurements of pure ethylene using 53 lines of a 900 MHz bandwidth waveguide CO₂ laser. They found no reportable absorption at 9P(18) line. In fact, the only absorption they observed in the 9P branch is with the 9P(12) line at a pressure of ~5 torr. The present study supports this latter observation. Absorption studies with 10P(14) laser line showed that the absorption in this line is very low and it is independent of input powers. The latter is found to be consistent with other laser lines studied. The low absorption of ethylene at 10P(14) line is consistent with the waveguide spectra of Herlemont et al.⁶

Figure 1(c) shows the frequency responsivity of the room-temperature HgCdTe detector found in the experiment in the range 0 - 400 Hz. In the experiment, a fixed amount of laser power was directed on to the detector. The chopper was set at a particular frequency and the signal in the lock-in-amplifier (LIA) was maximized by adjusting the phase in the LIA. The two sharp windows at 60 and 120 Hz are due to high attenuation filters used in the lock-in-amplifier to protect from noise due to line frequency and its second harmonic. It is clear that if we neglect these windows, the detector responsivity is generally high in the low frequency (0 - 200 Hz) region, but it drops off as a function of frequency. Above 200 Hz, the responsivity is almost constant. The high responsivity of the detector in the low frequency region was generally associated with more noise as illustrated in Fig. 1(d). These noise values were determined at the same time when the response signals of the detector were determined at each chopper frequency. Comparing Figs. 1(c) and (d), it seems practical to work at a frequency between 200 and 400 Hz.

The most important parameter to be considered in devising an instrument for atmospheric pollution monitoring or gas leak detection, is to find its detection limit (or the minimum detectable concentration) due to a particular molecule. An order of estimate of the detection limit of ethylene can be found by considering the signal-to-noise (S/N) ratio of the instrument. From Figs. 1(c) and (d), the average signal in the range 200 - 400 Hz is ~273 μV , and that of noise in the same range is ~1 μV . This gives $S/N \approx 273$. Let us consider that a signal change equivalent to twice the average noise is detectable. Thus

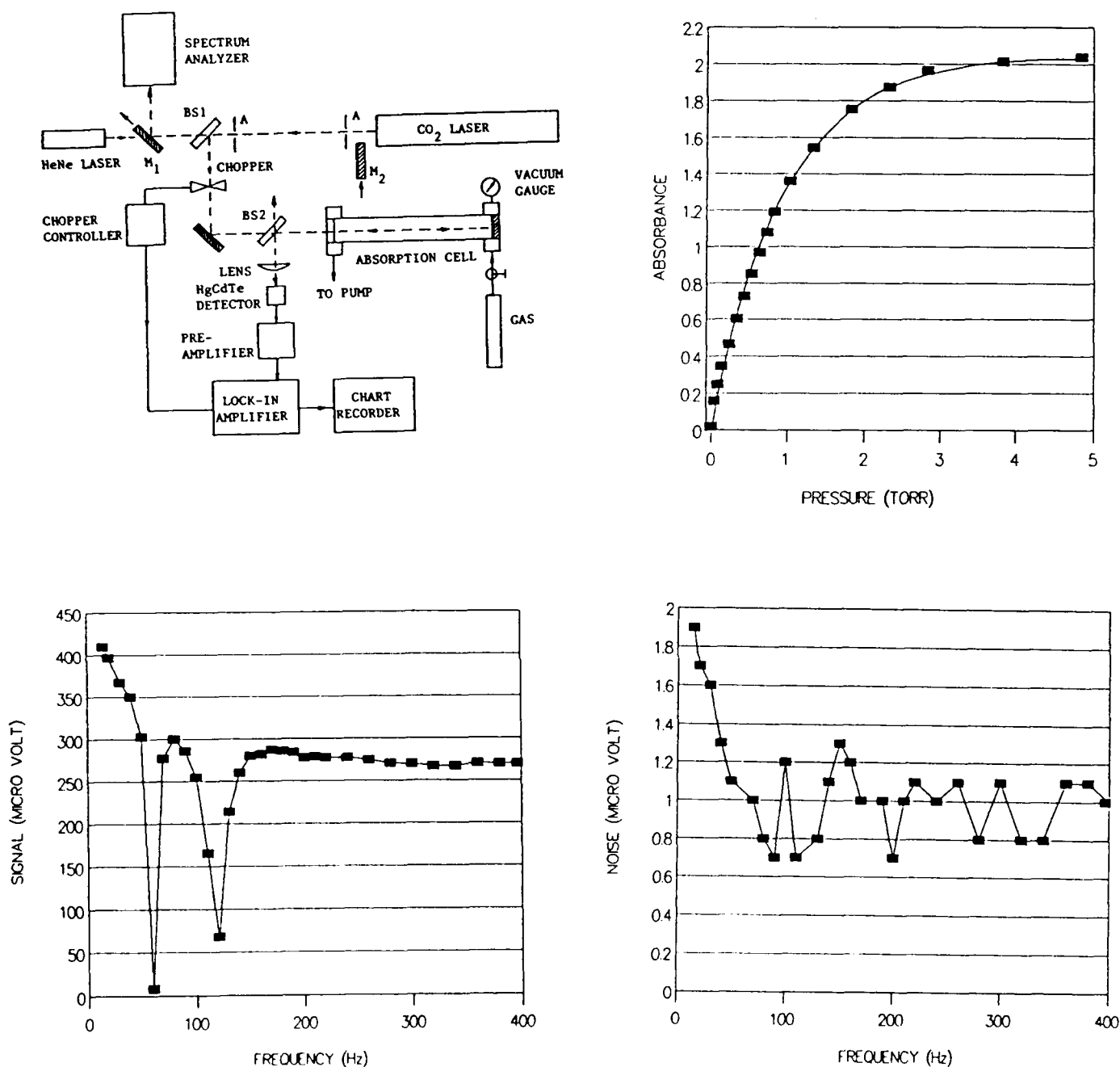


FIG. 1. (a) Experimental arrangement of pollution studies. (b) Absorbance $[\ln P_0/P]$ curve of ethylene at 9P(18) CO₂ laser line. (c) Frequency responsivity of room-temperature HgCdTe detector, and (d) the variation of noise as a function of frequency for the air pollution detection system.

substituting $(\Delta I/I_o)_{\min} = 0.007$, $\sigma = 1.19 \times 10^{-18} \text{ cm}^2$ for 10P(14) CO_2 laser line,⁷ and $L = 180 \text{ cm}$ in eq.1, one gets, $N_{\min} = 3.28 \times 10^{13} \text{ cm}^{-3}$ or 2.2 ppm-m. In finding the ppm-m value for concentration, N in cm^{-3} is divided by the Lochmidt number⁸ $N_L = 2.68675 \times 10^{19} \text{ cm}^{-3}$ (total density of molecules at atmospheric pressure), and then multiplied by $L = 1.8 \text{ m}$. For an outside measurement, this sensitivity scales as 2.2 ppb for a 1-km path. The estimated value will be influenced by atmospheric turbulence, water vapor, temperature, and other factors.

Conclusion

Investigation is performed on the development of a gas analyzer using a cw CO_2 laser which is suitable for detecting atmospheric pollutants or industrial gas leaks. A laboratory system is developed that uses a room-temperature HgCdTe detector. Results of the absorption measurements using ethylene gas and the responsivity of the detector is presented. The instrument has the capability of detecting 2.2 ppm-m of ethylene. A dual-beam CO_2 laser analyzer is under investigation and the results will be presented at the conference.

References

1. P.L. Meyer and M.W. Sigrist, "Atmospheric Pollution Monitoring Using CO_2 -Laser Photoacoustic Spectroscopy and Other Techniques," *Rev. Sci. Instrum.* **61**, 1779 (1990).
2. W.B. Grant, R.H. Kagann, and W.A. McClenny, "Optical Remote Measurement of Toxic Gases," *J. Air Waste Manage. Assoc.* **42**, 18 (1992).
3. W.B. Grant, "He-Ne and CO_2 Laser Long-Path Systems for Gas Detection," *Appl. Opt.* **25**, 709 (1986).
4. W. Galas and F. S. Perry, "High-Speed Room-Temperature HgCdTe CO_2 -Laser Detectors," in *Laser Focus*, (Nov. 1984 issue).
5. R.R. Patty, G.M. Russwurm, W.A. McCleanny, and D.R. Morgan, " CO_2 Laser Absorption Coefficients for Determining Ambient Levels of O_3 , NH_3 , and C_2H_4 ," *Appl. Opt.* **13**, 2850 (1974).
6. F. Herlemont, M. Lyszyk, and J. Lemaire, "Laser Spectroscopy of Ethylene with Waveguide CO_2 and N_2O Lasers," *J. Molec. Spectros.* **74**, 400 (1979).
7. K. A. Fredrikson, "Differential Absorption Lidar for Pollution Monitoring," in *Laser Remote Chemical Analysis*, R. M. Measures, ed., (John Wiley & Sons, New York, 1988) p.273.
8. C. R. Webster, R. T. Menzies, and E. D. Hinkley, "Infrared Laser Absorption: Theory and Application," in *Laser Remote Chemical Analysis*, R. M. Measures, ed., (John Wiley & Sons, New York, 1988) p.196.

OBSERVATION of SEA FOG INCURSION with a DIODE-PUMPED YAG PORTABLE LIDAR

Nobuo TAKEUCHI, Hiroshi OKUMURA, Tadashi SUGITA, Hironori MATSUMOTO,
Shigesumi KUWASHIMA* and Satoshi YAMAGUCHI**

Remote Sensing and Image Research Center, Chiba University
1-33, Yayoi-cho, Inage-ku, Chiba, CHIBA 263, JAPAN
Phone: 81-43-251-1111 Fax: 81-43-253-0272

* OKK Inc.

3-26-12, Kitasenzoku, Ohta-ku, TOKYO 145 Japan

** Electronics Research Laboratory, Nippon Steel Corp.
5-10-1, Fuchinobe, Sagamihara, KANAGAWA 229 Japan

1. Introduction

A portable lidar system has been strongly desired for the measurement of local area air pollution, boundary layer meteorology, plume dispersion and cloud physics. However, so far a compact and convenient lidar system has not been well developed. One of the authors constructed a pseudorandom code lidar (RM-CW lidar) system using a diode laser as a light source[1]. It has a limited performance due to the limited power. We proposed and presented a new system[2-3] based on a high repetitive operation, where we adopted a whole solid system using of a Q-switched diode-pumped YAG laser and an avalanche photodiode(APD). Here we report its application to a sea fog observation.

2. Solid-State Portable Lidar System

The whole system consists of a diode pumped YAG laser, which is Q-switched by an intracavity acoustic optical modulator, a 20cm diameter commercial astronomical telescope on a stable tripod, an avalanche photodiode, a signal processor operating at a high repetition rate and a notebook-type personal computer. The block diagram is shown in Fig.1. The specification of the system is shown in Table 1. The laser itself has a shorter pulsewidth than the sampling time of 50 ns corresponding to the 7.5 m spatial resolution. The beam divergence is reduced to 0.5 mrad using a 20 time beam expander. The received signal is detected by an APD. Initially we used a 0.5 mm diameter element, which was not enough large to collect unfocused signals from a wide range. So in a developed stage, we used a photomultiplier(PMT) as an alternative. We reduced the focal length of the telescope from 2 m to 1.2 m, and switched an APD to a 3 mm diameter one, which covers an illusion circle from measured targets.

The signal processor was specially designed at OKK, Inc. It has the ability to continuously and cyclically accumulate 8-bit digitized signals with a sampling time longer than 30 ns (33 MHz). The largest channel length is 2048 and the accumulation is possible up to 32 bits. After accumulation, the signal is transferred to the CPU of a personal computer. A photo of the whole system is shown in Fig. 2. A further discussion on the SN ratio and the lidar ability can be found in Ref.[2].

3. Observation of Sea Fog — 'YAMASE'

A dense fog gives serious effects on aerotrafic conditions, especially on taking-off and landing at an airport, as well as on agriculture and harvest. Every year in late spring-early summer season in north-eastern Japan, a dense sea fog, Yamase, incurs into land because of the moisture cooled by the northern cold tide current.

We used a portable lidar system for a field measurement of visibility at Misawa Airport, Aomori,(Fig. 3) in late June to early July, 1992. The lidar was set up by the runway (the location marked by X). An A-scope of "Yamase-fog" is shown in Fig. 4, where oscillating structure with a

period of roughly 75 m can be seen on the data. The data was taken every the 11 seconds (10 second accumulation and 1 second transfer). After processing the time sequential data in a personal computer, we can display a time-range chart which shows the fog density by the brightness in Fig. 5. It spans 36 min. The lidar was set toward east. It shows the fog comes in a patched state. The inclination of the brightness signal shows the wind speed of east-west component. From this figure we obtained 4 m/s, which corresponds to the anemometer value.

Here we showed one example of a portable lidar application. This system will promise the realization of a handy compact lidar system, which will exploit wider field of lidar application.

The authors thank Hamamasu Corp. for providing and modifying a C4777 APD unit.

- [1] N.Takeuchi, H.Baba, K.Sakurai, T.Ueno:Diode laser random modulation cw lidar. Appl. Opt. 25-1, 63-67.
- [2] N.Takeuchi, H.Okumura, T.Sugita, H.Matsumoto, S.Yamaguchi:A portable lidar using a diode-pumped YAG laser, Proc. 16ILRC, O4, 695-698 (1992), Cambridge, MA.
- [3] H.Okumura, T.Sugita, H.Matsumoto, N. Takeuchi, S.Kuwashima: A high speed signal processing system for a diode-pumped YAG lidar, Proc. 16ILRC, L18, 537-539.

Table 1 Specification of the developed lidar system.

Specification of the Current System

Laser:	Detector:
Diode Pumped YAG Laser:	Si-APD (Hamamatsu Corp.)
Wavelength 1.064 μm	3.0mm ϕ 20A/W
Pulse Power 70mW aver.	Band Width 10MHz
Pulse Width 25ns	Signal Processor: OKK CHX-01
Repetition 0.5 ~ 10kHz	Continuous Sampling
(1kHz typical)	Data Length 2048 Ch.
Peak Power 3kW@1kHz	Data Size 8 bits
CW LD Power 930mW	Sampling Time 50ns
CW YAG Power 250mW	Averaging up to 32 bits
Modulation: AOM	Control System:
Beam Divergence: 0.5mrad	NEC PC9801NS / T
after 20 times magn.	CPU i386SL (98), 20MHz
Telescope:	FPU i80387, 20MHz
Cassegrain-type (Celestron C-8)	Notebook type
Aperture 20cm	
Focal Length 1.2m	

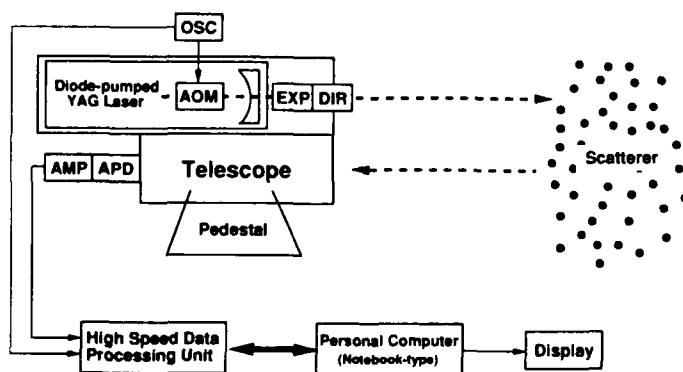


Fig.1 Schematic diagram of the portable lidar system.

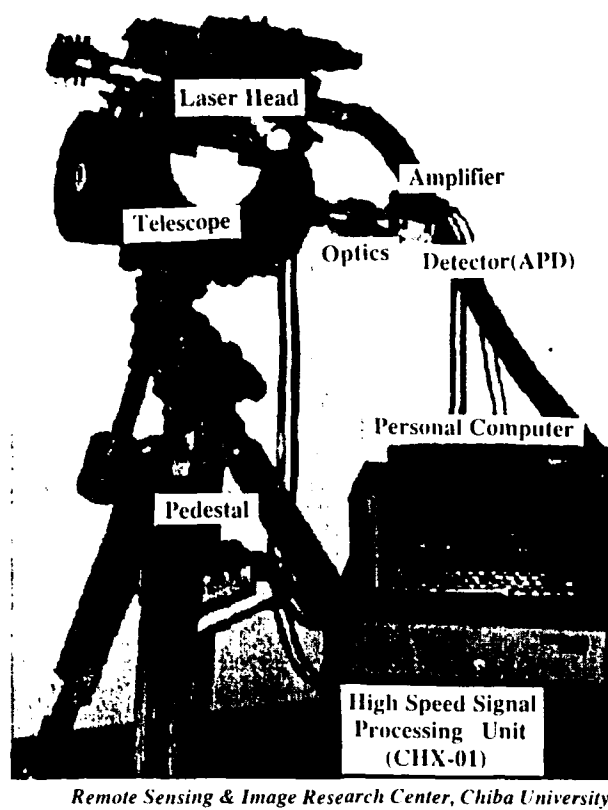


Fig.2 External appearance of the portable lidar system.

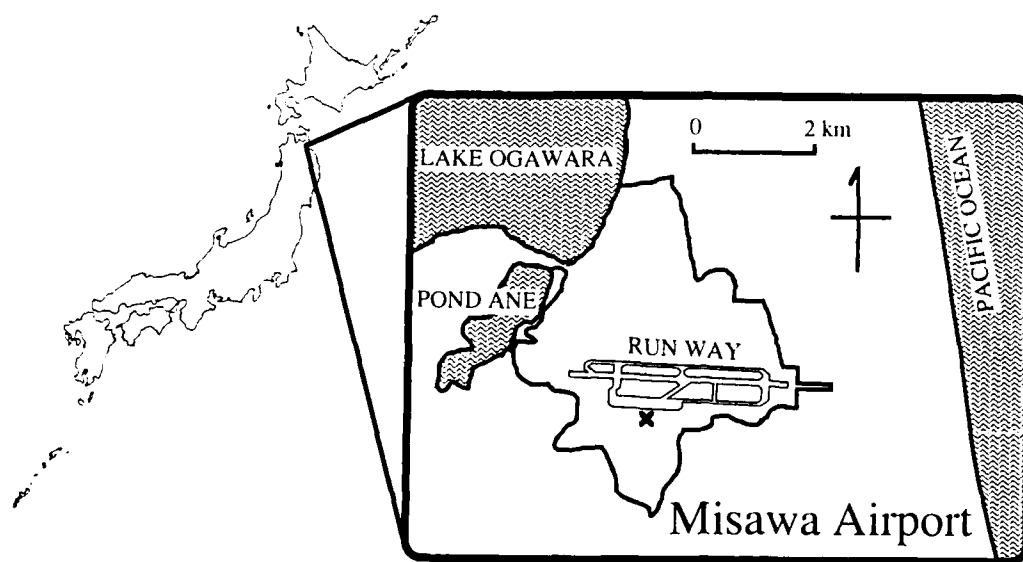


Fig.3 Location of the observation site (Misawa airport).

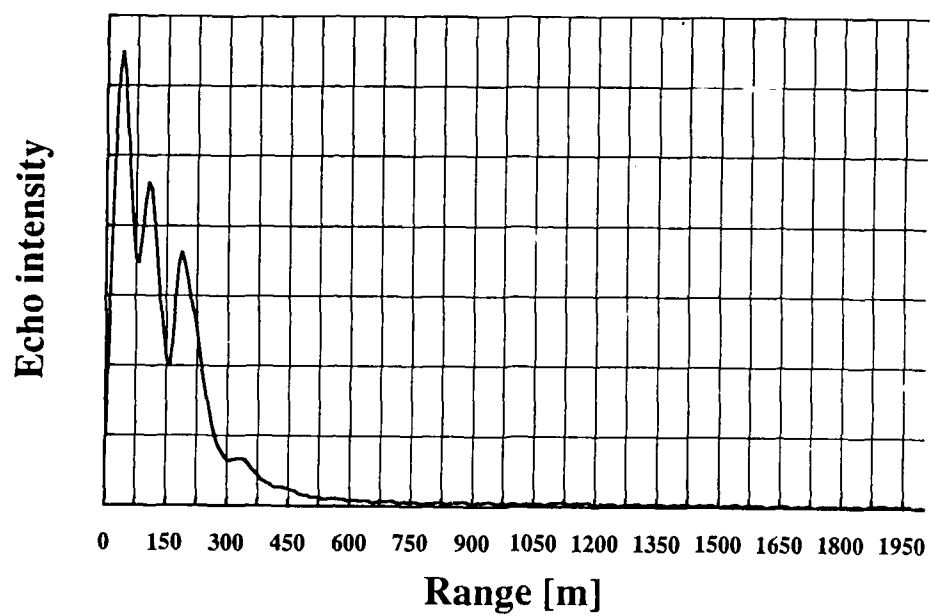


Fig.4 Lidar A-scope of "YAMASE-fog" incursion.

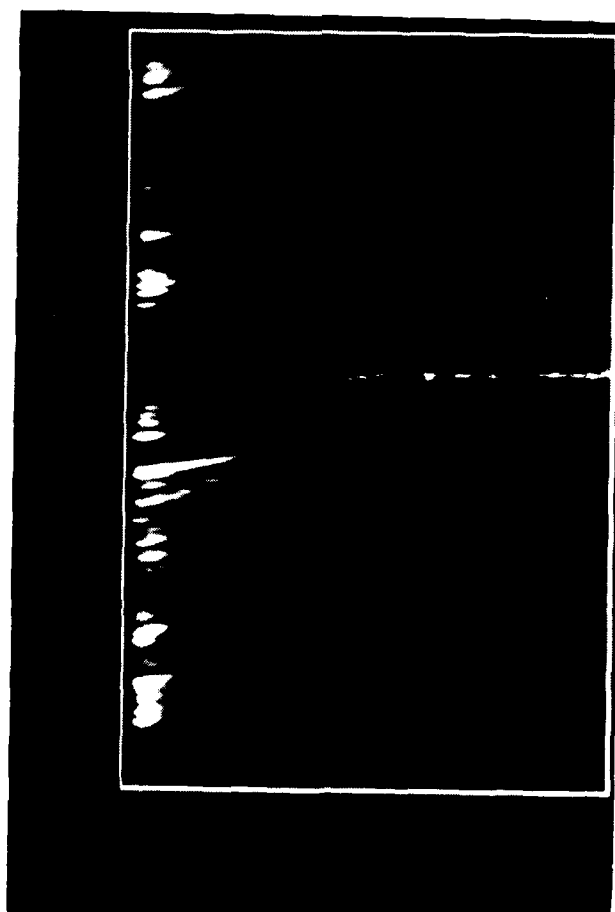


Fig.5 Time series data of "YAMASE-fog".

Simultaneous Inference of Multiple Atmospheric Parameters using Multiple Channels of Information

Benjamin T. Marshall and Larry L. Gordley
G&A Technical Software
28 Research Drive
Hampton, VA 23666
(804) 865-7491

Introduction

The increasing complexity of the new generation of limb viewing atmospheric remote sensing instruments have dictated the need for a robust statistically optimized retrieval method. A common feature of many of these instruments is multiple channels of information with significant contribution from a small number of emitters.

This paper will first present a general approach to the simultaneous retrieval of multiple emitters from multiple channels of information. An implementation for applications which use high resolution spectral data to perform multiple emitter retrievals is then discussed. An example is given for the SAFIRE (Spectroscopy of the Atmosphere using Far Infrared Emission) instrument proposed for EOS. Also discussed is the implementation of this method for the retrieval of temperature, pressure and the volume mixing ratio of molecular species for broadband applications. An example is given of temperature, pressure and O₃ retrieval for the CLAES (Cryogenic Limb Array Etalon Spectrometer) instrument aboard UARS.

General Discussion

The basis of a retrieval is the iterative improvement of a guessed atmospheric state to the point that modeled radiances match the radiances measured by the instrument. A retrieval using a forward iteration approach to perform the inverse, contains steps similar to the following:

1. Input a model atmospheric state (temperature, pressure and mixing ratios).
2. Calculate model total ray radiance (for occultation only total ray transmissions need be calculated).
3. Compare the model results of step (2) to the measured radiance.
4. If necessary, update the atmospheric model and loop to step 2.

Obviously one wishes to arrive at the best guess as efficiently as possible. Numerous techniques exist for getting to this best guess. A review of various methods is given by Rodgers(1976). The basis for the technique used here is what Rodgers refers to as the maximum likelihood method.

The maximum likelihood technique combines multiple measurements of a state by inversely weighting each measurement by its covariance matrix. The assumption of this technique is that the measurement, y , may be represented as a linear transformation of the state, x , or:

$$1) \quad y = Kx .$$

Which leads to the maximum likelihood solution:

$$2) \quad \hat{x} = (S_x^{-1} + K^T S_e^{-1} K)^{-1} (S_x^{-1} x_0 + K^T S_e^{-1} y) ,$$

where \hat{x} is the best estimate of the state vector, x_0 is an a-priori estimate, S_x is the covariance matrix of the a-priori, and S_e is the error covariance matrix of the measurement, y .

A retrieval is not a linear process and equation (1) should really be written as:

$$3) \quad y = F(x), \text{ where } F \text{ is the nonlinear forward model.}$$

If it is assumed that F is close to linear then (3) can be solved by Newtonian iteration which is a matter of expanding (2) as a truncated Taylor series about a guessed value x_i :

$$4) \quad y = F(x_i) + \partial F / \partial x (x - x_i) .$$

The truncated Taylor series is a set of linear equations which can be solved similarly to (1) as:

$$5) \quad x_{i+1} = (S_x^{-1} + K_i^T S_e^{-1} K_i)^{-1} [S_x^{-1} x_0 + K_i^T S_e^{-1} (y - F(x_i) + K_i x_i)] ,$$

where K_i now represents the partial derivative in (4) evaluated at x_i . The evaluation of K at every iteration facilitates convergence even for very non-linear forward radiance functions. Equation (5) may be written as a deviation from x_i as:

$$6) \quad x_{i+1} = x_i + (S_x^{-1} + K_i^T S_e^{-1} K_i)^{-1} [K_i^T S_e^{-1} (y - F(x_i)) + S_x^{-1} (x_0 - x_i)] ,$$

x_{i+1} replaces \hat{x} in equations (5) and (6) since it represents the next iterate in an iterative procedure.

Equation (6) is used to develop a multiple-emitter/multiple-channel onion peel retrieval which includes the ability to retrieve temperature. Beginning with the top level the a-priori x_0 is used as an initial guess of x . This initial guess is iterated upon using equation (6) until convergence. Subsequent levels are determined in the usual onion peel fashion with the initial guess of x equal to the previous ray's retrieved value. For the use of equation (6) on a single level but with multiple emitters and channels it is assumed that there are no inter-emitter correlations so that S_x in this case is a diagonal matrix with the diagonal elements equal to the variance of each emitter at the current level. The terms needed to construct S_x are simply determined from the normal a-priori covariance matrices of each emitter. The error covariance, S_e , of each channel is also assumed to be diagonal with the diagonal terms simply equal to the square of the noise equivalent radiance.

Implementation and Examples

This retrieval technique has been implemented to address two areas of study. Spectral applications and multiple broadband channel applications. Both of these allow simultaneous retrieval of several atmospheric parameters including temperature and pressure. Examples will be given of a study for SAFIRE (Spectroscopy of the Atmosphere using Far Infrared Emission) which demonstrate the feasibility of simultaneously retrieving all major contributing emitters from high resolution spectral data. Examples will also be presented of a study for CLAES (Cryogenic Limb Array Etalon Spectrometer) which show the feasibility of simultaneously retrieving temperature, pressure, and O₃ mixing ratios in the blocker 8 bandpass at 791 cm⁻¹.

References

Conner, B.J and C.D. Rodgers (1989); A Comparison of Retrieval Methods: Optimal Estimation, Onion Peeling, and a Combination of the Two. RSRM-87: Advances in Remote Sensing Retrieval Methods, Ed. A. Deepak, A. Deepak publishing.

Harries, J.E., T.W. Bradshaw, P.F. Gray, P.H.G. Dickinson, J.M. Russell III, J. Park and B. Carli (1987); SAFIRE, A Novel High Resolution Cooled Spectrometer for Atmospheric Research. 38th International Astronautical Congress, Brighton, England, October 10-17, 1987, IAF paper 87-137.

Roche, A.E. and J.B. Kumer(1989); Cryogenic Limb Array Spectrometer (CLAES) - Experiment Overview. Cryogenic Optical Systems and Instruments III: Proceedings of the Meeting, San Diego, CA August 17-19, 1988, Society of Photo-Optical Instrumentation Engineers, pages 324-334.

Rodgers, C.D. (1976); Retrieval of Atmospheric Temperature and Composition from Remote Measurements of Thermal Radiation. Rev. of Geophys. and Space Phys., vol. 14, pages 609-624.

TUNABLE MID INFRARED SOURCE FOR REMOTE SENSING

Norman P. Barnes
Keith E. Murray

NASA Langley Research Center
Hampton, VA 23681

Mahendra G. Jani
Systems Technology Corporation
Hampton, VA 23666

Summary

A tunable mid infrared source could serve a multifunction role for remote sensing of atmospheric constituents such as greenhouse gasses and ozone. While atmospheric constituents which are more plentiful or have a strong dipole moment can utilize weak overtone features in the near infrared, atmospheric constituents which are less plentiful or have smaller dipole moments must rely on the fundamental absorption features in the mid infrared. For lighter gasses, such as the greenhouse gasses, these features are found in the 2.5 to 5.5 μm region. Consequently, NASA Langley is developing the laser technology to provide a tunable mid infrared source suitable for DIAL applications.

An attractive laser source capable of tuning over the mid infrared is a parametric oscillator and amplifier pumped by a 2.0 micrometer solid-state laser. Such a system would consist of a single frequency 2.0 μm solid-state oscillator and amplifier which would pump a single frequency parametric oscillator and amplifier. A single frequency parametric oscillator is required in order to accurately sample the narrow absorption features in a DIAL application. A single frequency parametric oscillator requires, in turn, a single frequency pump laser.

A Ho:Tm:YAG or Ho:Tm:YLF laser could provide a convenient 2.0 μm pump laser. Although lasing occurs on the Ho $^5\text{I}_7$ to $^5\text{I}_8$ transition, Tm is required to provide convenient absorption features which allow pumping by GaAlAs laser diodes. Absorbed energy can be transferred to the Ho with a quantum efficiency approaching 2. By adding Cr to the YAG or Er to the YLF, flashlamp pumping is easily achieved. Such lasers can have a high slope efficiency due to the efficient absorption of the flashlamp or laser diode radiation and the large quantum efficiency. In addition, this Ho transition provides some degree of tuning, enough to access both H₂O and CO₂ absorption features.

Both Ho:Tm:Cr:YAG and Ho:Tm:Er:YLF lasers have been evaluated under flashlamp pumping conditions. An initial analysis of the two materials indicated

that the latter material should be more efficient even though the former has a better spectral match to the flashlamp emission spectrum. Reasons for the better efficiency can be attributed to the higher energy transfer rates and an expected decrease in a deleterious effect often referred to as upconversion. Experimental evaluation of these two materials using similar laser rod sizes as well as similar Ho and Tm concentrations demonstrated that Ho:Tm:YLF had both lower threshold and higher slope efficiency. Performance curves of these lasers with different mirror reflectivities display room temperature thresholds as low as about 70 J and slope efficiencies in excess of 0.04.

An AgGaSe₂ parametric oscillator has demonstrated a threshold as low as 3.6 mJ and a slope efficiency at 1.5 times threshold of 0.31. To obtain this performance, a singly resonant parametric oscillator was used with an Er:YLF pump laser operating at 1.73 μm . It may be noted that this slope efficiency relates the 3.8 μm energy output of the idler as a function of pump energy incident on the nonlinear crystal. As such, the maximum slope efficiency using is limited by the ratio of the pump to the idler wavelength. Consequently, the observed slope efficiency represents approximately 2/3 of the maximum slope efficiency of 0.45.

Narrow linewidth performance of the parametric oscillator has been demonstrated using an injection seeding technique. If injection seeding was not used, the linewidth of the parametric oscillator was approximately 0.016 μm . However, when a single frequency 3.39 μm source was used to seed the parametric oscillator, the linewidth decreased to less than 0.001 μm . In this case, the linewidth is limited by the resolution of the measurement device so the actual linewidth may be considerably lower. Not only did injection seeding decrease the linewidth but it increased the efficiency as well. An increase in the efficiency is expected since seeding decreases the pulse evolution time interval, as demonstrated experimentally.

A parametric amplifier has demonstrated a small signal, single pass, gain in excess of 13. For these experiments, the same Er:YLF pump laser was used and a 23 mm length of AgGaSe₂ was used as the optical parametric amplifier. Energy density on the surface on the nonlinear crystal was maintained at less than 1.0 J/cm² to avoid damage. Even with a long pump pulselength, a single pass gain in excess of 13 was demonstrated at 3.39 μm .

Most of the requisite technologies have been demonstrated for a tunable mid infrared system. A demonstration of higher energies is underway as well as evaluation of other nonlinear optical materials.

REMOTE SENSING TECHNIQUES FOR STRATOSPHERIC AND TROPOSPHERIC GAS MONITORING

P T Woods, B W Jolliffe, M J T Milton, N R Swann, W Bell, N A Martin and T D Gardiner
National Physical Laboratory
Queens Road, Teddington, TW11 OLW
United Kingdom

P F Fogal and D G Murcray
Department of Physics
University of Denver, Co, USA

1 INTRODUCTION

The National Physical Laboratory is involved with the development and utilisation of different laser-based and other spectroscopic remote sensing techniques for a range of different atmospheric monitoring applications. These include:

An infrared laser heterodyne spectrometer and a transportable high-resolution fourier-transform interferometer for ground-based measurements of stratospheric trace gases. These have been employed as part of the European Arctic Ozone Experiment (EASOE), and the European Stratospheric Monitoring (ESMOS) project which constitutes the European component of the Global Network for the Detection of Stratospheric Change.

A mobile high-energy tunable differential-absorption lidar (DIAL) facility has also been developed. This operates in the infrared spectral region (2-5 μm) and the visible/ultraviolet region (220-500 nm). It is capable of remote range-resolved measurements of different atmospheric pollutants. This system has been employed, for example, to monitor the fluxes of volatile organic compounds, including methane, emitted by industrial and landfill sites and agricultural processes.

The current status of the development of these techniques are discussed and some recent measurements presented.

2 STRATOSPHERIC MEASUREMENTS

2.1 INSTRUMENTATION

The instruments used for remote stratospheric gas monitoring operate in the infrared

region and measure the atmospheric absorption of solar radiation in order to detect and quantify the species present. Two types of instrument are available:

- (i) A portable diode-laser heterodyne spectrometer which operates in the 7-13 μm region. This technique enables trace atmospheric gases to be measured with very high spectral resolution ($\sim 0.0005 \text{ cm}^{-1}$) and high sensitivity. It is designed to monitor the concentrations of key stratospheric gases which, because of requirements for high resolution are difficult to detect by other techniques (eg ClONO_2 , HOCl), but which are important to stratospheric chemistry. The high resolution attainable also enables information on the altitude distribution to be obtained.
- (ii) A transportable fourier-transform interferometer (Bruker - 120 M) which is configured to operate in the 2-5 μm and 8-13 μm spectral regions with a resolution of $\sim 0.004 \text{ cm}^{-1}$. A range of different gases are detectable including HCl , HF , O_3 , HNO_3 and the CFC's.

2.2 DATA ANALYSIS TECHNIQUES

Sophisticated computer algorithms are required to translate the measured spectral data into column concentrations or concentration profiles. These algorithms can give rise to systematic biases in the results. Progress with the development of improved algorithms, will be outlined, and the results obtained when different algorithms are used to analyse the same data set will also be presented. The methodology for obtaining altitude profiles of different stratospheric gases from the measurements obtained with the high resolution laser heterodyne spectrometer will also be summarised.

2.3 MEASUREMENT RESULTS

Results have been obtained with the above instruments during two different measurement exercises.

- (i) **The European Arctic Stratospheric Ozone Experiment**
Ground-based measurements were carried out from central Sweden during the period November 1991 - March 1992 [1]. Figure 1 shows the temporal variations in stratospheric HCl and HF during this period. Data on ClONO_2 and HNO_3 trends will also be presented.
- (ii) **The European Stratospheric Monitoring Project (ESMOS)**

A number of field trails have been carried out at the Jungfraujoch Observatory, Switzerland as part of this project [2]. Examples of the results obtained and intercomparisons with other measurement techniques will be presented.

In addition, the NPL transportable fourier-transform interferometer (FTIR) is being employed as a transfer standard to intercompare infrared measurements

carried out in Europe with those at other global network sites. Initial results, where the NPL interferometer was operated alongside FTIR's at Denver University in the USA and by Liege University at the Jungfraujoch Observatory, will be outlined.

3 TROPOSPHERIC DIAL MEASUREMENTS

3.1 INSTRUMENTATION

A mobile DIAL facility has been developed which contains two sets of laser sources [3]. One produces high energy tunable infrared radiation with narrow linewidth ($< 0.08 \text{ cm}^{-1}$) in the range 2-5 μm . The other operates in the visible and ultraviolet regions covering the range 220-500 nm where a number of pollutants including SO_2 , NO_x and aromatic hydrocarbons can be monitored. Currently both systems are based on Nd:YAG laser pumped dye lasers. Tunable infrared radiation is generated using difference frequency mixing and optical parametric amplification is used to achieve the required output energies (~20 mJ per pulse). Research has also been carried out into all solid-state infrared sources and progress in this will be outlined.

3.2 MEASUREMENT RESULTS

The mobile DIAL facility has carried out a large number of different air pollution measurements. Examples include:

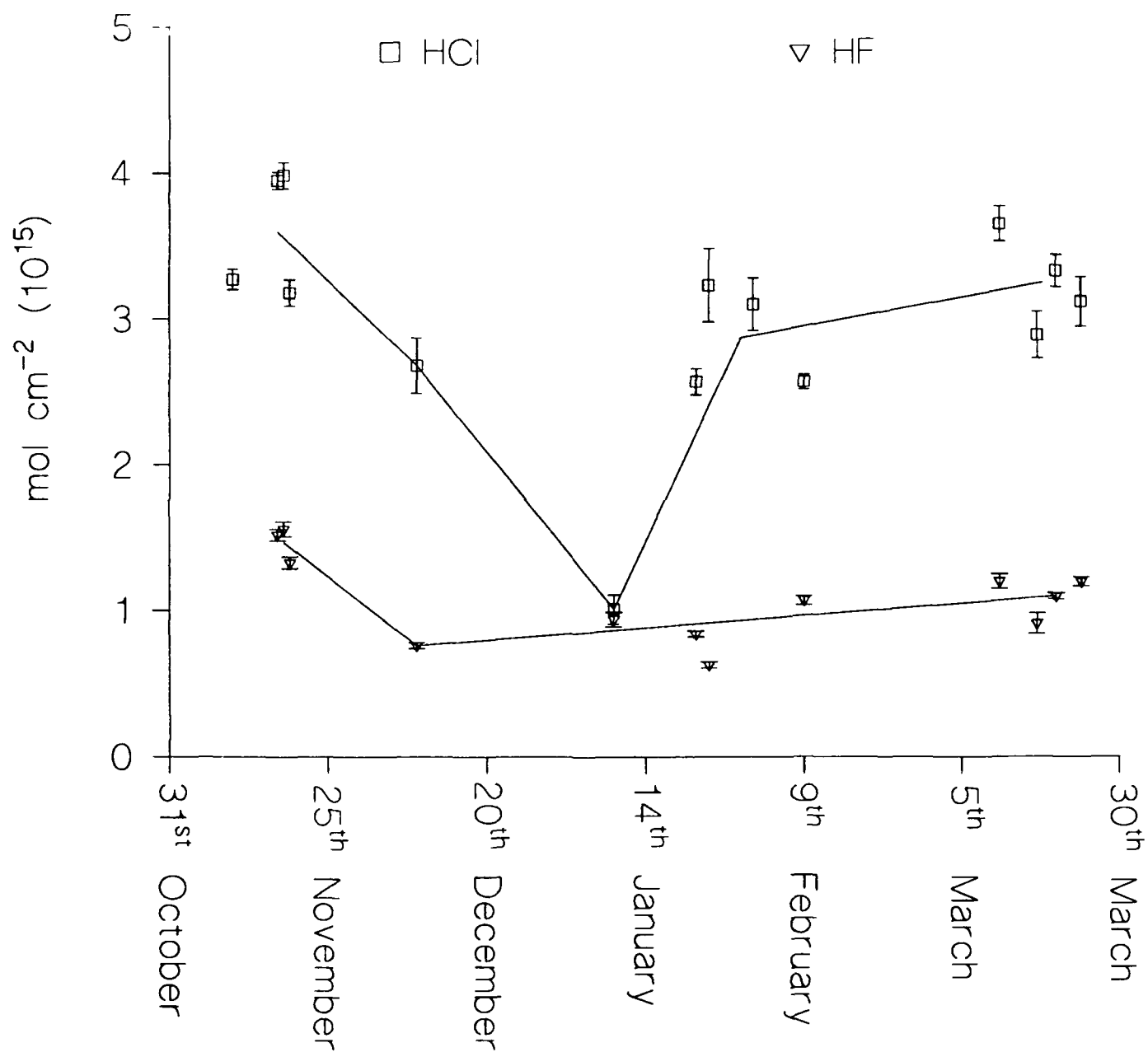
(i) **Measurements of Losses of Volatile Organic Compounds from the Petrochemical Industry**

The DIAL technique enables the fluxes of a wide range of gaseous species, emitted by industrial and other sources to be measured directly without any recourse to dispersion modelling. The technique has been used to monitor the fugitive emissions of volatile organic compounds from the petrochemical industry, including both toxic pollutants and those involved in photochemical ozone production. These results have been used:

- to quantify losses which may be uneconomic to the industries concerned;
- to provide accurate measured data to establish the principal uncertainties in the UK's National VOC Emission Inventory. This data is required for the internationally-agreed UNECE Protocol on the reduction of VOC Emissions.

(ii) **Measurements of Methane Emissions**

The total fluxes of methane emitted from industrial gas processing plant and landfill sites have been measured in order to obtain a more accurate inventory of the emissions from such sources.

Column Content of HCl and HF Measured During EASOE

REFERENCES

- [1] Ground-based Infrared Measurements of Stratospheric Species during EASOE, W Bell, N A Martin, N R Swann, T Gardiner and P T Woods, Proceedings of the Arctic Ozone Workshop, Schliersee, Germany, Sept 1992.

- [2] Stratospheric Monitoring Stations in Europe, P C Simon, M DeMaziere, L Delbouille, G Roland, S Godin, K Kunzie, J de la Noi and P T Woods, Optical Remote Sensing of the Atmosphere Meeting, Optical Society of America, 1990.

- [3] Remote Sensing Techniques for Gas Detection, Air Pollution and Fugitive Loss Monitoring, P T Woods, R H Partridge, M J Milton, B W Jolliffe and N R Swann. J. Air and Waste Management Assn - to be published.

Wednesday, March 10, 1993

Winds 1

WA 8:00am–9:20am
Salon F

John W. Meriwether, *Presider*
Clemson University

Development and Application of Compact Doppler Lidar Systems for Atmospheric Probing

R. Michael Hardesty
NOAA/ERL Wave Propagation Laboratory
325 Broadway
Boulder, Colorado 80303

1. Introduction

For the past several years, scientists at the Wave Propagation Laboratory (WPL) have employed a pulsed Doppler lidar system to observe wind fields and aerosol structure in a variety of scientific investigations. The transverse-excited, atmospheric pressure (TEA) CO₂ lidar produces 1 J energy pulses at repetition rates up to 50 Hz. The system and its associated signal processing and display equipment are mounted in a semitrailer for easy transport to remote field sites.

Evolutionary development of the 1 J lidar system has resulted in an extremely robust, easy-to-use instrument. However, certain fundamental design limitations preclude its application to a class of scientific problems characterized by a need for high-precision velocity measurements and high spatial and temporal resolution. These include measurements of vertical motions in both cloud-free and cloudy regions, measurement of boundary layer turbulence quantities, studies of air/surface exchange mechanisms, and investigation of the relationship between boundary layer structure and ocean surface characteristics. Each of these applications requires a capability to measure winds with an accuracy of about 10 cm s⁻¹ or better, with a range resolution of better than 100 m. The 1 J pulsed lidar, with a measurement accuracy of about 0.5 m s⁻¹ and range resolution of more than 150 m, is not well-suited to this class of problem.

2. Compact, high performance Doppler lidar systems

To address observational needs for future cloud and boundary layer studies, we have begun an effort to develop new lidars with enhanced measurement capabilities. Unlike the existing Doppler system, in which maximizing range was an overriding development goal, the new lidars are (initially) being targeted at improving accuracy even if the overall range must be reduced. This is an acceptable trade-off for many boundary layer and cloud investigations.

Another high-priority goal of the current WPL lidar effort is the development of systems that are compact and robust to extend the range of applications. Most existing lidars, including our 1 J Doppler system, are large, complex, and require nearly constant attention by at least one highly trained operator during measurement periods. Because we plan to deploy these new instruments on both aircraft and ship platforms, a design emphasizing compactness is essential. Over the long term, we also are striving to

produce systems that can operate without operator intervention for extended periods. Such a capability could dramatically increase the scientific impact of lidar measurements.

Two new Doppler lidar systems, employing different technologies and operating at different wavelengths, are currently being developed by WPL to satisfy the atmospheric probing needs of the future. To meet the goals of high velocity accuracy and high temporal resolution, a small, very high pulse repetition frequency (prf) CO₂ laser system has been designed and tested. For high spatial resolution, compactness, and potentially excellent velocity resolution, a Doppler lidar system incorporating a Th:YAG laser transceiver is under development. Operating characteristics of each of these systems is shown in Table 1. More detail on the design of the Th:YAG lidar is also presented elsewhere in this volume (Grund *et al*, 1993).

The compact CO₂ Doppler system (Pearson, 1991) utilizes contemporary diffusion-cooled radio-frequency discharge technology, in combination with a master-oscillator power-amplifier configuration, to achieve good frequency stability and long lifetime. Application of RF excitation technology enables a compact optical design, suitable for operation on a research aircraft or ship. Because the system will be capable of operation for several months between gas refills, we will be able to fill the lasers and amplifiers with relatively expensive rare isotopes of CO₂. This should improve performance by eliminating the attenuation of the optical pulse from ambient atmospheric CO₂ absorption (on the order of 0.5 dB km⁻¹). The combination of high system stability and high prf enables significant averaging to be employed during signal processing to produce the desired velocity measurement accuracy.

The small lidar system was first tested as part of a field program on Porto Santo Island to study the mechanisms associated with transition from stratiform to stratocumulus cloud in the eastern Atlantic. The system was used to measure statistics of vertical velocity and atmospheric turbulence quantities below cloud base. Although limited by a crude data-gathering system, indications are that the results will be useful for relating sub-cloud turbulence parameters to cloud transitions.

At present, the lidar is being redesigned to improve frequency stability by operating the master oscillator in a continuous rather than Q-switched mode. A second gain stage will be added to regain the energy lost by eliminating the Q-switch. This configuration will be simpler, have higher immunity to vibrations, and be much more suitable for differential absorption lidar (DIAL) measurement of species simultaneous with the radial wind measurements. Whereas the previous design incorporated separate master and local oscillator (LO) lasers, a single continuous-wave laser combined with an acousto-optic modulator will be examined in this design to provide both reference and LO signals. This would simplify rapid-wavelength switching for the DIAL applications.

The Th:YAG 2.02 μ m Doppler system is scheduled for testing during the spring of 1993. Primary applications of this lidar are envisioned to be precise boundary layer turbulence measurements, operation from platforms where space is severely limited (such as small research aircraft or ships), and operation in moist regions where water vapor absorption

severely limits CO₂ lidar performance. Diode pumping will enable an extremely compact design and provide high reliability.

3. Measurement of ozone fluxes

In parallel with the two Doppler design efforts, WPL is also developing a compact lidar to measure lower tropospheric ozone profiles. This system is aimed at measuring ozone profiles with good spatial and temporal resolution to heights of 3 km. Because transport of ozone between the boundary layer and the free atmosphere is not well understood, our intention is to combine one of these two new high resolution Doppler systems with the DIAL system to measure the vertical flux of ozone by eddy correlation.

4. Acknowledgements

Chris Grund, Madison Post, Guy Pearson, Wynn Eberhard, Barry Rye, Yanzeng Zhao, and Kin Chan have graciously allowed portions of their work to be summarized here.

References

Grund, C., M. J. Post and K. Chan, "Progress in development of a Th:YAG coherent lidar for high spatial and velocity resolution wind measurement," this volume (1993).

Pearson, G. N., The design and performance specifications of a compact CO₂ Doppler lidar transmitter," Proc. SPIE, vol. 1416, 147-150 (1991).

Table 1 : Performance specifications of the two compact Doppler lidar systems under development at the Wave Propagation Laboratory.

Parameter	Compact CO ₂ lidar	Compact Th:YAG lidar
Operating Wavelength	9.1 - 11.2 μm	2.0218 μm
Pulse Energy	10 mJ	10 mJ
Pulse Repetition frequency	up to 10 kHz	100 - 300 Hz
Anticipated range	5 - 10 km	10 km
Range resolution	100 m (50 m with averaging)	40 m (20 m with multi-pulse averaging)
Velocity accuracy	1-10 cm s ⁻¹	1-10 cm s ⁻¹
Pumping Configuration	RF Discharge-excited	Diode-pumped
Optical design	master oscillator - power amplifier (MOPA)	injection seeded power amplifier

Observations of Winds of the Stratosphere and Mesosphere at Arecibo, Puerto Rico Using a Doppler Rayleigh Lidar

Craig A. Tepley, Arecibo Observatory, Cornell University, P.O. Box 995, Arecibo,
Puerto Rico 00613-0995, Tel: 809-878-2612

Introduction:

At the Arecibo Observatory we use a variety of radar and optical instruments to measure the properties of the Earth's atmosphere and ionosphere. With the incoherent scatter radar we are sensitive to the ionized portion of the upper atmosphere from about half an Earth radius (R_E) down to nearly 60 km during daylight, and 100-150 km during the night when the molecular ionization of this lower part recombines. During both day and night, the winds and turbulent layer structures of the troposphere and stratosphere are accessible up to 25 km with the coherent scatter radar systems. We also use a variety of optical spectrophotometric instruments at Arecibo to study airglow emissions originating from various layers within the atmosphere. Because of the nature of the emitters and their corresponding chemistry, optical remote sensing more preferentially samples the condition of the neutral atmosphere. Thus, by combining simultaneous radar and optical techniques, we can investigate a variety of problems, such as the electrodynamics of the thermosphere, which require data on both the neutral and ionized atmosphere. Much of this instrumentation at Arecibo has been in operation and actively collecting data since the mid-1960s.

Despite this extensive instrumentation for atmospheric studies at Arecibo, we have, until recently, been unable to measure that portion of the atmosphere between about 25 and 60 km using any of the methods described. Not only as a source region for atmospheric tides and gravity waves, it also acts to filter energy and momentum from above and below. Knowledge of the steady-state structure and the dynamic redistribution of various chemical species in the middle atmosphere, particularly at lower or tropical latitudes, is equally important to study the whole atmosphere as a coupled system. Thus, to complete our capabilities for middle atmospheric measurements, we established a Doppler Rayleigh lidar at Arecibo. With the lidar we not only gain new information about the basic temperature and density structure of the middle atmosphere, overlapping with the coherent radar systems at the lower levels, but we also measure the components of the neutral winds, which are important for this region. The addition of Doppler lidar observations makes Arecibo perhaps the only place in the world that could provide a continuous profile of wind measurements, without gaps, from within a couple kilometers near the ground to about $\frac{1}{2}R_E$.

Here, we present an accumulation of neutral wind results made since late 1990, comprising a complete seasonal coverage but over two years of measurements. The coverage is not continuous, month after month, because the general nature of experimental work at Arecibo, dictated by outside proposal demand on the facilities, does not always conform with lidar observations. Yet, with these restrictions we obtained a reasonable seasonal distribution of wind data through most of the middle atmosphere. We present a synopsis of that data set showing the seasonal trends and the day-to-day variability. We also compare our yearly zonal wind measurements with the latest reference model of the middle atmosphere, that is, CIRA 1986.

Instrument and Data Sampling:

Rayleigh lidars, employed to measure the winds of the stratosphere and mesosphere, have only been around for a few years. This is because the required laser transmitter needs to be frequency stabilized, or injection seeded, to narrow the linewidth. This linewidth has to be much narrower than the backscattered molecular return from the atmosphere to not distort or broaden the Doppler shifts and widths of the spectra. A high spectral resolution receiver, such as a Fabry-Perot interferometer (FPI), can then measure these spectral shifts and widths, and from them, determine the winds and temperatures.

Chanin et al. [1989] was the first to demonstrate the Doppler Rayleigh lidar technique for wind observations using an injection seeded, Nd:YAG transmitter and a double FPI receiver. Shortly after that at Arecibo we used a similar laser, but a scanning, single etalon Fabry-Perot to measure the wind components up to an altitude similar to the earlier French measurements. We presented our initial results in Tepley et al. [1991], while a complete description of the instrument at Arecibo was described by Tepley et al. [1993].

For the wind observations presented in this report, we used the same lidar configuration as initially built, that is, a 12 W average power Nd:YAG transmitter coupled with a coaxial 38 cm Newtonian telescope. The telescope is followed by the FPI for spectral selection, and an electronically gated photomultiplier tube for detection. The current power-aperture product is 1.4 W-m^2 , but we plan to increase that significantly in the near future.

During the first year of operation we experimented with various spectral scanning and sky sampling techniques to maximize the effectiveness of the data acquisition process. We settled on a full multiple point spectral scan (as opposed to sampling only the half power points as Chanin et al. [1989] does) measuring at least eight frequency samples for each height. Altitude profiles of the zonal and meridional wind components were sampled at 30° zenith angle and were referenced to interspersed zenith measurements. Much of the data presented here were collected in this mode of observation. The data sampling sequence enables us to measure the full vector wind field from about 10 to 60 km, at 3 km range resolution, in about one hour of real time (about 0.5 s of integration for each spectrum at each height in a single sky direction).

Summary of the Wind Results:

We obviously cannot present all relevant variants of the wind data obtained during the first two years of lidar measurements at Arecibo in this short report. What we will present at the meeting is an extended version of the data set that illustrates the observed seasonal trends and the degree of daily variability of the winds of the middle atmosphere. There is also some suggestion for a year-to-year reversal in the zonal wind patterns from data collected during the same months of the two adjacent years. This may be a characteristic of the QBO, however, the particular effect cannot be verified with such a short data set and the observed differences may be simply part of the normal tropical variations.

For each experimental period, we attempt to measure the winds during several consecutive nights. Figure 1 shows one example of the vector wind field for a late winter, early spring night. The general eastward trend observed in the

stratosphere, reversing in the lower mesosphere, was typical of most of the days during that period. As the meridional wind is generally weaker than the zonal component, the northward surge at higher altitudes near 21:00 AST is atypical, but serves to illustrate some degree of variability. Although these type of plots display much information, they do not convey the extent of error in the measurement. For an individual night we found typical errors of the component winds range from ± 0.5 m/s for altitudes up to 25 km, increasing to about ± 10 m/s near 60 km, as shown in the wind profiles of Figure 2. The backscattered signal is somewhat strong below 25 km due to the presence of dust in the stratosphere recently ejected by Mt. Pinatubo. Although the determination of temperatures would be impossible, we can still measure the winds in this altitude region from the Doppler shift of the Mie scattered spectra.

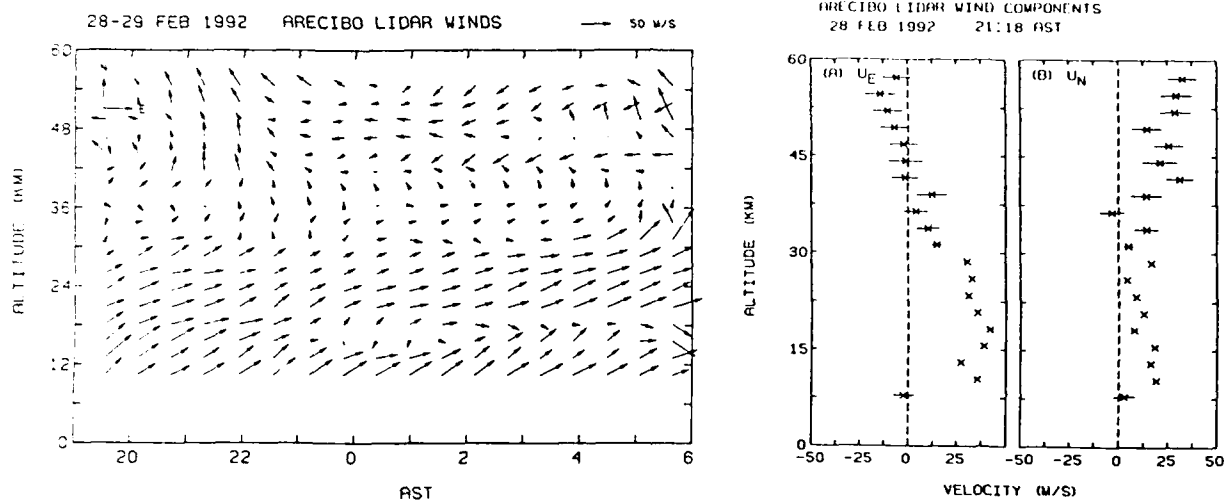


Fig. 1 (left): Vector wind field versus time and altitude for a February night in 1992. As indicated in the upper corner of the figure, an eastward wind is to the right while the northward component is directed upward. A magnitude scale of 50 m/s is also shown on the upper right of the figure.

Fig. 2 (right): Altitude profiles of the zonal and meridional wind components, positive eastward and northward, respectively, for a single time of the map shown in Figure 1.

During the two years of observation, we collected 43 good nights of wind data and averaged individual nights to provide monthly or seasonal representations. Grouping the winds into four quarters resulted in nearly equal coverage during each season. However, the winter is slightly under-represented while the autumn period is oversampled, but each by only a few percent. In Figure 3, we summarize the yearly variation of the zonal wind component and compare it with the zonal wind at 20°N latitude of the CIRA 1986 model atmosphere [Rees et al., 1990]. There is good agreement between our measurements and the model for this time scale, particularly for the strong westward wind in the lower mesosphere during the summer, and the weaker eastward wind in the lower stratosphere in the spring. A summary of the meridional component of the measured neutral winds and details of the observed monthly and daily variations will be presented at the meeting.

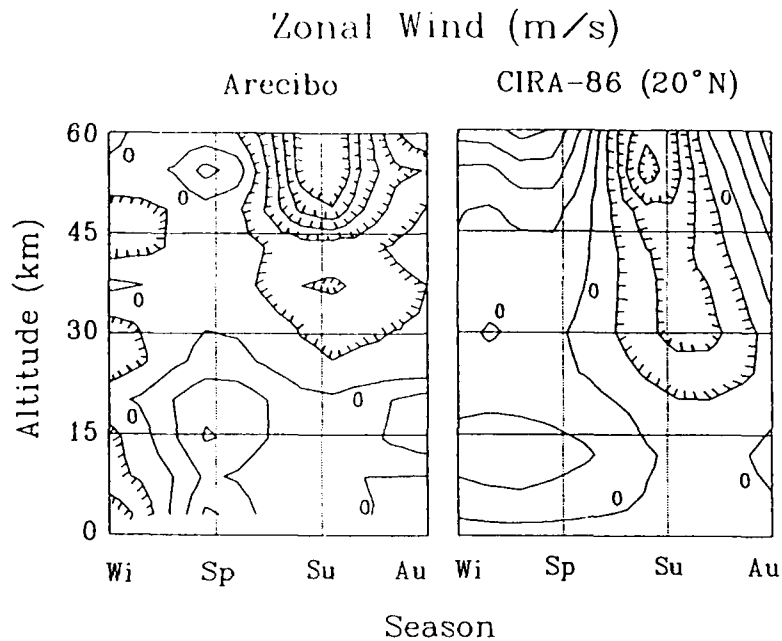


Fig. 3: Yearly average of the measured zonal winds compared with the CIRA-86 model atmosphere. Each contour interval represents 10 m/s with negative (westward) values denoted by hash marks. The zero contours are indicated by a "0".

Discussion and Future Plans:

The wind results presented here just begin to illustrate what can be accomplished with the Doppler Rayleigh lidar technique. It has proven itself as the only method capable of observing the structure and dynamics of the stratosphere and lower mesosphere on a routine basis. We are in the process of improving our capabilities for such measurements by increasing both the size of the telescope for the lidar receiver and the laser transmitter power. We also proposed to augment the Rayleigh measurements with a similar Doppler resonance lidar system to extend these important wind observations up into the lower thermosphere. Finally, at Arecibo we have recently developed a daytime Doppler lidar capability and will apply it to continuous day and night wind observations in an effort to understand the nature of the tidal structure of the middle atmosphere at low latitudes.

References:

- Chanin, M. L., A. Granier, A. Hauchecorne, and J. Porteneuve, A Doppler lidar for measuring winds in the middle atmosphere, Geophys. Res. Lett., **16**, p.1273, 1989.
- Rees, D., J. J. Barnett, and K. Labitzke (eds.), Cospar International Reference Atmosphere: 1986, Pergamon Press, New York, 1990.
- Tepley, C. A., S. I. Sargoytchev, and C. O. Hines, Initial Doppler Rayleigh lidar results at Arecibo, Geophys. Res. Lett., **18**, p.167, 1991.
- Tepley, C. A., S. I. Sargoytchev, and R. Rojas, The Doppler Rayleigh lidar system at Arecibo, in press, IEEE Trans. Geosci. Remote Sens., 1993.

Doppler Lidar Observations of a Frontal Passage in the Vicinity of Steep Topography

**Madison J. Post
Paul J. Nieman
F. Martin Ralph
and
Lisa D. Olivier**

**NOAA Wave Propagation Laboratory
325 Broadway, Boulder, CO 80303
Tel. 303/497-3000**

Introduction

On September 25, 1992, we used NOAA's pulsed CO₂ Doppler lidar (Post and Cupp, 1990) to observe the passage of a dry cold front across northeastern Colorado. This particular front was chosen because of 1) its dry nature, which minimized cloud cover and maximized the utility of the lidar, and 2) its intensity, exhibiting tropopause fold characteristics in the 12 h preceding the period of observations. Because of enhanced backscatter throughout the troposphere and lower stratosphere from the eruption of Mt. Pinatubo (in June, 1991), a much larger than normal volume of the atmosphere was observed.

The lidar was positioned on the high plains of Colorado about 1.7 km above sea level (ASL), approximately 6 km east of the Rocky Mountain foothills and 15 km north of Boulder. From this location the lidar detected both airflow in the mid-troposphere and lower stratosphere [4-20 km above ground level - (AGL)], and in the lower troposphere (below 4 km AGL) over the foothills and in the canyons. The small beam size (2 m at 20 km range) and lack of sidelobes allows for detailed observation of flow near the surface, including perturbations induced by the mountains. Besides measuring such atmospheric flow patterns with plan-position indicators (PPIs), range-height indicators (RHIs), and sector scans, we pointed the lidar beam vertically to observe changes in the aerosol backscatter profiles associated with the ongoing tropopause fold event and measure differential vertical motion induced by stationary and propagating gravity waves.

The lidar observations were supplemented with data taken by a suite of in situ and remote observing systems, including 1) four radar wind profilers equipped with radio acoustic sounding systems (RASS) within 50 km of the lidar, 2) a mesoscale surface network surrounding the lidar and providing 5-min observations of standard meteorological parameters, 3) NOAA's wind profiler demonstration network, 4) the North American rawindsonde and surface networks, and 5) GOES satellite imagery. Preliminary analysis of this rich 12-h data set is presented below, with emphasis on the orographic generation of waves in the frontal environment, and the effect of those waves on frontal structure.

Meteorological Context

On the day of the study an intensifying jet stream-frontal zone (jet-front) system and associated tropopause fold embedded in westerly flow moved eastward over the western United States and Rocky Mountains. This system, which extended downward to the surface as a cold front, formed the "tail" portion of an ~2000-km comma cloud observed by infrared and visible satellite imagery. The wind profiler at Medicine Bow, Wyoming (a region characterized by much less steep terrain than that near the lidar site), documented temporal and vertical changes in wind velocity typically associated with the passage of a jet-front system. As the comma cloud entered Colorado, it developed a distinct ~50-70 km break to the east of the Continental Divide in a region where strong ($>25 \text{ m s}^{-1}$) westerly flow descended from the mountain peaks. In contrast to the observations at Medicine Bow, sensors on the eastern plains of Colorado observed temporal and vertical variations in wind velocity and temperature that were atypical, revealing that the front was modified by the steep terrain to the west of the lidar.

Prior to the onset of cooling associated with jet-front passage, a ~1-km deep layer of enhanced static stability ($\sim 4 \text{ K km}^{-1}$) and warming ($\sim 1.5 \text{ K h}^{-1}$) descended from ~4.5 km AGL at 0000 UTC to ~3 km AGL at 0630 UTC. The veering of winds with height from southwesterly to westerly through this descending stable layer is typically found within warm fronts. At 0800 UTC the RASS initially observed the lower extension of the 1.5-2 km deep jet-front system at ~2.5 km AGL as a layer of enhanced static stability ($3\text{-}4 \text{ K km}^{-1}$) and cooling ($1\text{-}1.5 \text{ K h}^{-1}$). By 1800 UTC the ascending isentropes of the jet-front system linked with the large stability of the descending tropopause at ~6.5 km AGL in a classical tropopause fold configuration. It has been shown (e.g., Shapiro and Keyser, 1990) that stratospheric air is injected into the middle and upper troposphere during tropopause fold episodes. A time series of backscatter profiles from the Doppler lidar revealed that such a stratospheric injection was occurring; backscatter profiles between 0800 and 1300 UTC increased by 1-2 orders of magnitude in the layer between ~6 and 10 km as stratospheric particulates from the Mt. Pinatubo eruptions were transported into the troposphere.

A 1-2-km-deep layer of nearly neutral static stability was situated above the jet-front system and warm front between 0230 and 10 UTC. Following the passage of the jet-front system, RASS observations of θ_v revealed weak cooling ($.25\text{-}1 \text{ K h}^{-1}$) and moderate static stability ($1\text{-}2 \text{ K km}^{-1}$) in the lower and middle troposphere. Aloft, variations in the profiler winds contained a wave-like periodicity of 2-4 h in the lower stratosphere (14-18 km ASL).

Wave Phenomena

Synoptic and mesoscale conditions during this event were conducive to the development of orographically-forced gravity waves (i.e., mountain waves) and to their modulation by the cold front passage. These conditions included a strong westerly component to the background wind both ahead of and behind the advancing cold front, a layer of large static stability between 3-4 km AGL ahead of the cold front, and a sloping stable layer marking the front. In such an environment one would expect the waves to be mostly two-dimensional, mimicking the general north-south orientation of the front range, but that the

three-dimensionality of the terrain could produce significant variations along the mountains. While the gravity-wave response downstream of the mountains is determined primarily by the atmospheric structure, the dominant horizontal scales of the terrain determine the characteristics of the forced waves located directly above the mountains. A unique feature of the lidar's RHI and PPI sector scans, often available every few minutes, is that they allow a more thorough examination of the temporal evolution of the wave response, including vertical structure, than has previously been documented (Ralph, et al., 1992a, 1992b). Other important aspects of the mountain waves being examined are changes in the horizontal wavelength (Ralph, et al., 1992b), dynamic features arising from convective overturning (e.g., Clark and Farley, 1984; Neiman et al., 1988; Scinocca and Peltier, 1989), and Kelvin-Helmholtz (KH) instability (Smith, 1991).

At 0530 UTC the cold front was approaching, and mountain waves were evident over the foothills, but not over the plains. They later extended downstream as the front passed at roughly the same time that a layer of low static stability was located above the front. The waves were manifested by vertical deflections of up to 1 km in a low-altitude jet. Also associated with this jet were systematic variations of the winds with horizontal spacing of 1-2 km that were located in areas of strong vertical shear (up to $20 \text{ m s}^{-1} / 500 \text{ m}$) which moved downstream with time. It is possible that these features resulted from KH instability in the cross-mountain downslope jet, as has been discussed recently by Smith (1991) in the context of linear hydraulic theory (Smith 1985).

By 1200 UTC a layer of clouds appeared over the mountains and later extended out onto the plains. This cloud interrupted the lidar beam and limited the vertical extent of the data to about 6 km AGL, except for occasional breaks through which higher altitudes could be sensed. Although there were no distinct vertical deflections of the low altitude, 35 m s^{-1} jet at this time, the base of the cloud had a distinct undulation with a horizontal wavelength of 30-35 km. This wavelength increased to roughly 40 km within an hour, and continued to show a primarily downward deflection east of the mountains. Hence, the cloud base provided an indirect measure of wave characteristics. The lidar also revealed a layered pattern in the winds in the lower stratosphere over the mountains. Beginning at 0700 UTC and lasting through much of the event, these layers were perturbed vertically in a way suggesting a substantial mountain wave presence in the lower stratosphere above the mountains. There is also a clear indication of phase tilt with height. Such a tilt indicates that the gravity wave is propagating energy upward. This phase tilt is also suggested by the profiles of vertical motion that clearly display changes in sign and amplitude with height.

Before, during, and after frontal passage a sharp transition from downslope to upslope flow was observed over the foothills, although its location and structure varied substantially with time. Such features can take on the characteristics of a hydraulic jump (often observed in the flow of water over a barrier), as suggested (for example) by the observations presented by Neiman, et al. (1988) and by the modeling results of Durran (1986). At 1240 UTC this feature became very pronounced, and separated upslope flow of 5 m s^{-1} from a downslope jet of 30 m s^{-1} at a point over the foothills. This transition occurred over a horizontal distance of $< 1 \text{ km}$, and was associated with a 1-km upward displacement of the downslope jet.

Summary

Doppler lidar proved to be an effective tool for observing the effects of steep topography on the passage of a dry cold front, including modification of the front by mountain-generated gravity waves. By coupling high temporal and spatial resolution lidar measurements with more conventional data from a network of other sensors, it is possible to provide detailed meteorological analyses of the causes and effects of several significant, but seldom observed, atmospheric phenomena. Preliminary interpretations of a few of the more interesting aspects of the lidar data are presented above. More detailed analyses will be provided at the conference.

References

- Clark, T.L., and R.D. Farley, 1984: Severe downslope windstorm calculations in two and three spatial dimensions using anelastic interactive grid nesting: A possible mechanism for gustiness. *J. Atmos. Sci.* **41**, 329-350.
- Durrán, D.R., 1986: Another look at downslope windstorms. Part I: The development of analogs to supercritical flow in an infinitely deep, continuously stratified fluid. *J. Atmos. Sci.* **43**, 2525-2543.
- Neiman, P.J., R.M. Hardesty, M.A. Shapiro, and R.E. Cupp, 1988: Doppler lidar observations of a downslope windstorm. *Mon. Wea. Rev.* **116**, 2265-2275.
- Post, M.J. and R.E. Cupp, 1990: Optimizing a pulsed Doppler lidar. *Appl. Opt.* **29**, 4145-4158.
- Ralph, F.M., M. Crochet, and S.V. Venkateswaran, 1992a: A study of mountain lee waves using clear-air radar. *Quart. J. Roy. Meteorol. Soc.* **118**, 597-627.
- , P.J. Neiman, L.S. Fedor, and B.L. Weber, 1992b: Nonstationary trapped lee waves: Wind profiler, RASS, and satellite observations. *Preprints, Sixth Conf. on Mountain Meteorology*, 29 Sept. - 2 Oct., Portland, OR. Amer. Meteor. Soc., 68-75.
- Scinnoca, J.F., and W.R. Peltier, 1989: Pulsating downslope windstorms. *J. Atmos. Sci.* **46**, 2885-2914.
- Shapiro, M.A., and D. Keyser, 1990: Fronts, jet streams, and the tropopause. *Extratropical Cyclones, The Erik Palmén Memorial Volume*, C.W. Newton and E. Holopainen, Eds. Amer. Meteor. Soc., 167-191.
- Smith, R.B., 1991: Kelvin-Helmholtz instability in severe downslope wind flow. *J. Atmos. Sci.* **48**, 1319-1324.
- , 1985: On severe downslope windstorms. *J. Atmos. Sci.* **42**, 2597-2603.

Wednesday, March 10, 1993

Winds 2

WB 9:50am–11:30am
Salon F

Thomas J. McGee, *Presider*
NASA Goddard Space Flight Center

Lidar and Radar Studies of Dynamics in the Lower Atmosphere

John W. Meriwether

Clemson University, Department of Physics and Astronomy

206 Kinard Laboratory

Clemson, SC 29634-1911

A periodic wave structure with a vertical wave length of about 2 km between 12 and 19 km has been identified in Rayleigh lidar measurements at 589 nm of low altitude relative density profiles that were made by the University of Illinois group during the March/April Arecibo Initiative for Dynamics of the Atmosphere (AIDA) 1989 campaign effort. The equivalent temperature fluctuations are several degrees in magnitude. Also seen in one series of three successive nights were temperature fluctuations of about 10 °K at altitudes of 25 km with a vertical extent of 1 km. Both of these phenomena show a downward phase speed between 1 and 3 cm/s. The lower periodic structure is believed to be the same phenomenon seen previously in 430 MHz measurements of winds obtained at Arecibo Observatory. The identity of this structure remains uncertain. Cornish and Larsen [1989] and Sato and Woodman [1982a] considered this structure to be a quasi-inertial long period wave. Hines [1989] proposed instead the identification of this structure with a stationary wave system generated by orographic waves caused by the interaction of the sub-tropical tradewinds with the mountainous terrain of Puerto Rico. The higher altitude feature seen in the AIDA lidar observations is believed to be a manifestation of a region of clear air turbulence, which is known to occur in the lower stratosphere.

Instrumental

The Illinois lidar instrument that was fielded in Puerto Rico has been described previously [Beatty et al., 1989; Beatty et al., 1992; Senft et al., 1992]. Their sodium lidar in the AIDA configuration used a XeCl excimer laser to pump a dye laser at the wavelength of 308 nm with 100 watts averaged power. The output of the dye laser was tuned to the D₂ Na resonance frequency at 589 nm with a wavemeter which provided a continuous monitor of the dye laser output frequency. Tweaking the dye laser transmitter frequency optimized the resonance scattering signal observed from the Na layer. The telescope was a custom made Fresnel lens with 1.2m aperture. The divergence of the transmitter beam was 1 mrad, and the field of view for this telescope was about 3 mrad.

The transmitter pulse repetition rate was typically 200 pulses/sec, and the averaged power at 589 nm was about 5 watts. The power aperture product was 6 Wm^2 , which is substantial compared with other Na lidar systems in use today. The range resolution of the profiles collected was determined by the temporal resolution of the pulse counting electronics, which was designed for a dwell time of 125 nsecs corresponding to 37.5 m in range. Successive laser shots were averaged over 4500 shots and the averaged profile was recorded on hard disk. For the purpose of this paper, 35 of these profiles were averaged together to improve the statistics, since the temporal resolution of approximately 2 profiles per minute was not necessary for the purpose of our study. Hence, the time separation between these summed profiles was about 15 minutes.

Results

In Figure 1 we present successive profiles showing the results of ratioing the averaged range corrected profiles to the night averaged profile. By averaging together all profiles for one night of observations and then ratioing each 15 minute averaged profile to this nighttime average, we can remove a large part of the exponential variation of the backscattered signal between 10 and 30 km. However, there will still remain the effects of the phototube gain recovery which may vary throughout the night. Moreover, the alignment of the telescope field of view with the laser pointing was changed from time to time, which may account for some of the variation seen below 14 km.

In examining Figure 1, one sees that there also exists small density structure superimposed upon the relative density variation. We believe that this structure is a manifestation of the atmospheric dynamics of the atmosphere. However, we cannot rule out the possibility that fine aerosol structure may also exist to explain our results. Measurements of the aerosol profile structure do not show evidence of fine structure except for cases of volcanic injection [McCormac et al., 1991]. A more sophisticated series of lidar measurements that feature Raman backscatter observations [Kellnut et al., 1991] would provide a definitive indication as to the possible origin of this structure. So that these high frequency oscillations of interest can be discerned more readily, third order polynomial fits to the data were computed for the range between 13 and 30 km. These are indicated in Figure 1 as the thin solid lines. The next step to enhance the ease by which the small oscillations might be examined is to subtract the corresponding polynomial fit from each averaged ratioed profile.

Figure 2 shows these residual results obtained for four nights of lidar measurements in late March, 1989, for the range between 12 and 30 km. It is important in this analysis that the nighttime average profile be smoothed over a vertical wavelength extent to

remove any remnant of the high frequency structure. Otherwise, the division would destroy a portion of the high frequency information in each averaged 15 minute profile, because the periodic structure moves so slowly that averaging over 8 hours is not sufficient to remove traces of this structure from the averaged profile computed. We chose a vertical length of 4.5 km for the width of the boxcar smoothing applied to the data. Also shown in Figure 2 is a bar that represents the extent of 3% fractional density variation. The lidar data below 13 km could not be used because the gain recovery changes were too substantial.

One sees in Figure 2 between 14 and 18 km that these ratioed profiles show oscillations with amplitudes of several % and a vertical wavelength of about 2 km. These changes in density correspond to temperature fluctuations of 5 °K or less. Also there is an interesting feature near 24 km for which the large modulation in temperature amounts to a fluctuation of 8 °K. The noise level runs from about ± 0.3 K at 14 km to ± 2.0 K at 30 km in these profiles. The low frequency variations below 18 km seen for the succession of profiles we attribute to changes in the gain recovery curve throughout the night.

Discussion

The assignation of the temperature oscillations shown in Figure 2 to the dynamics of the tropopausal and lower stratosphere regions must be regarded as somewhat tentative. The possible contamination of the stratospheric density structure by thin layers in the vertical distribution of stratospheric aerosols cannot be disregarded completely. Nevertheless, the detection of the periodic structure in the AIDA lidar observations of relative densities between 13 and 19 km that we see in Figure 2 was expected. Radar doppler observations of atmospheric winds made at Arecibo at 430 MHz between 8 to 24 km have revealed a periodic wave structure near the tropopausal region [Sato and Woodman, 1982a; Cornish and Larsen, 1989]. These radar observations when analyzed to remove the mean profile as described for the temperature perturbations showed marked indications of a wavy structure between 14 and 18 km with an apparent vertical wavelength of 1.5 to 3.0 km and a horizontal amplitude of winds of about 5 m/s. Hence, we conclude that the temperature fluctuations seen in these lidar results represent the thermal manifestation of the tropopausal dynamics depicted by the radar wind measurements.

The author is grateful for the hospitality of Arecibo Observatory during the preparation of this paper.

References

- Barat, Jean, Some characteristics of clear-air turbulence in the middle stratosphere, *J. Atmos. Sci.*, **39**, 2553-2564, 1982
- Barat, Jean, and F. Bertin, Simultaneous measurements of temperature and velocity fluctuations within clear air turbulence layers: Analysis of the estimate of dissipation rate by remote sensing techniques, *J. Atmos. Sci.*, **41**, 1613 - 1619, 1984
- Beatty, Timothy J., Richard L. Collins, Chester S. Gardner, Chris A. Hostetler, and Chalmers F. Sechrist, Jr., Craig A. Tepley, Simultaneous radar and lidar observations of sporadic E and Na layers at Arecibo, *Geophys. Res. Letts.*, **16**, 1019-1022, 1989
- Beatty J. Timothy, Chris A. Hostetler, and Chester S. Gardner, Lidar observations of gravity waves and their spectra near the mesopause and stratopause at Arecibo, *J. Atmos. Sci.*, **49**, 477-496, 1992
- Cornish, C.R. and M.F. Larsen, Observations of low-frequency inertia-gravity waves in the lower stratosphere over Arecibo, *J. Atmos. Sci.*, **46**, 2428-2439, 1989
- Hines, Colin O., Tropopausal mountain waves over Arecibo: A case study, *J. Atmos. Sci.*, **46**, 476 - 488, 1989
- Keckhut Philippe, M.L. Chanin, and A. Hauchecorne, Stratosphere temperature measurement using Raman lidar, *App. Opt.*, **29**, 5182-5186, 1990
- Sato, Toru, and Ronald F. Woodman, Fine altitude resolution radar observations of upper-tropospheric and lower-stratospheric winds and waves, *J. Atmos. Sci.*, **39**, 2539 - 2545, 1982a
- Sato, Toru, and Ronald F. Woodman, Fine altitude resolution observations of stratospheric turbulent layers by the Arecibo 430 MHz radar, *J. Atmos. Sci.*, **39**, 2546 - 2552, 1982b
- Senft, Daniel C., Chris A. Hostetler, and Chester S. Gardner, Characteristics of gravity wave activity and spectra in the upper stratosphere and upper mesosphere at Arecibo during early April, 1989, *J. Atmos. Terr. Phys.*, in press, 1992

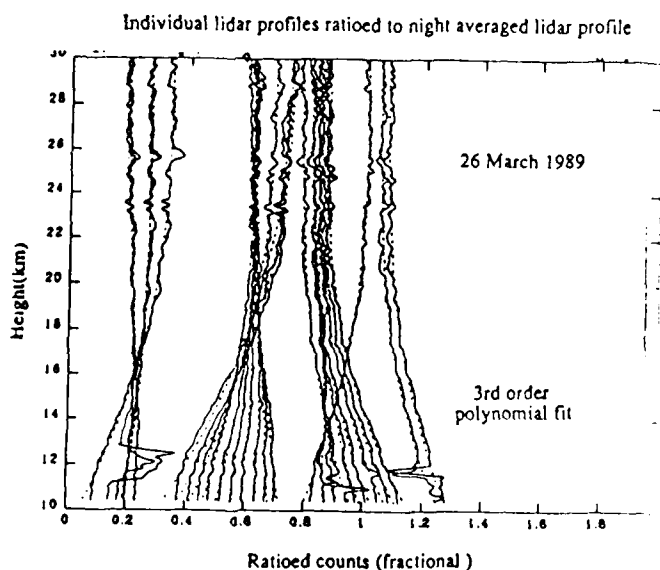


Figure 1

Strong variation at bottomside due to electronic gain changes as well as field of view re-alignments

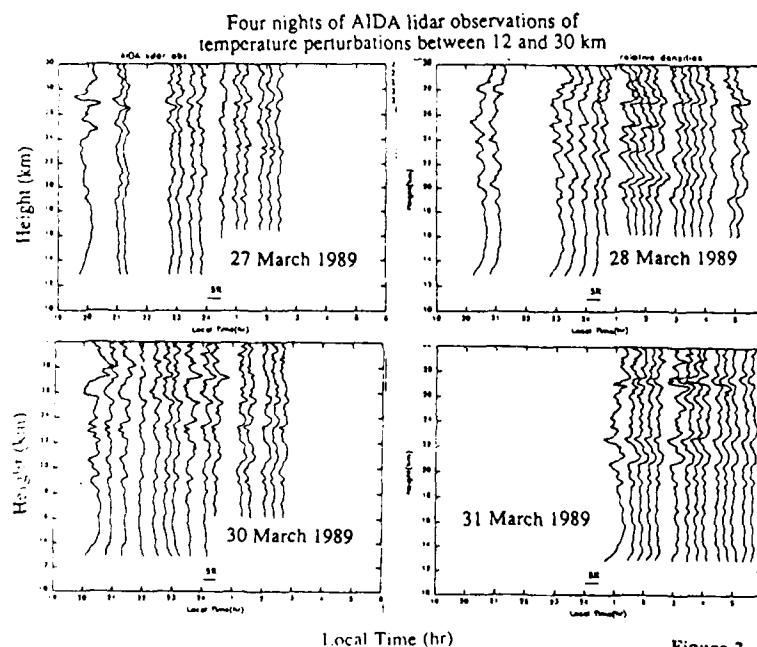


Figure 2

Wind Profiling with the Volume Imaging Lidar: A Comparison with Aircraft and Balloon Based Measurements

A.K. Piironen and E.W. Eloranta
University of Wisconsin-Madison
Department of Meteorology
1225 W. Dayton St.
Madison, WI 53706, USA

The University of Wisconsin Volume Imaging Lidar¹ (VIL) provides vertical profiles of the horizontal wind inside the convective boundary layer. In this paper we outline the VIL wind profiling method and compare results with aircraft-based and balloon-based observations. The methods provide different spatial averages: radiosonde measurements are nearly point measurements, aircraft measurements are flight path averaged, and VIL measurements are area averaged.

The VIL is a scanning lidar capable of detecting aerosol backscattering in $\sim 100 \text{ km}^3$ volumes within a ~ 3 minute volume scan. It employs a 30 Hz, 0.6 Joule Nd:YAG laser as a transmitter and a 0.5 m telescope with APD detector as a receiver. The scanning is done by using a beam steering unit consisting of two rotating mirrors mounted at 45° angles to the optical axis.

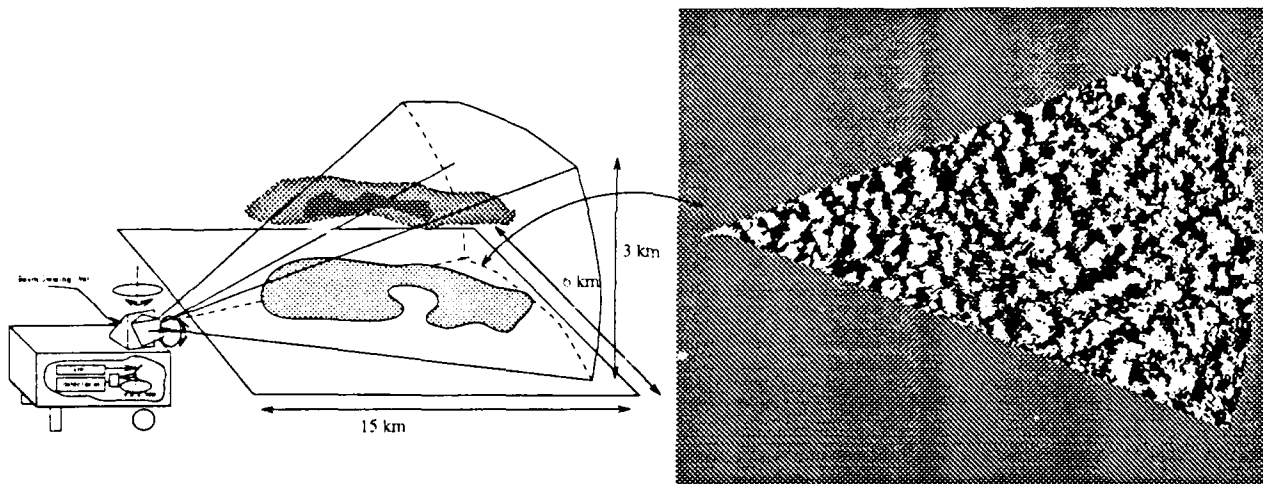


Figure 1: Schematic figure of VIL operation. The right panel shows a CAPPI plane recorded with the VIL. Brighter areas indicate increased aerosol scattering

By observing the movement of aerosols between successive scans we are able to compute area-averaged profiles of the horizontal wind². To compute winds, lidar profiles are mapped onto Constant Altitude Plan Position Indicator (CAPPI) planes after application of a $\sim 2 \text{ km}$ high pass median filter in range. Each pixel in the CAPPI's are then filtered with a high pass, $\sim 1 \text{ hr}$, temporal median filter in order to reject stationary structures. The resulting CAPPI's are histogram normalized to prevent a few bright features from dominating the images. Two-dimensional cross correlations are then used to determine mean aerosol movement between successive scans. The position of the cross correlation function (CCF) peak provides the wind speed and direction. Temporal averaging is performed by averaging CCF's instead of averaging individual wind results together; this improves the statistical reliability of the results. The amplitude and shape of the CCF peak along with the amplitude of random correlations away from the peak position are used to estimate the reliability of each wind measurement.

In July and August of 1989 the VIL was operated in the FIFE experiment near Manhattan, Kansas. Simultaneous wind measurements were recorded from the NAE Twin Otter³

aircraft and also with optically tracked weather balloons by Brutseart et al⁴. The aircraft measurements are averaged over flight legs of 15 to 40 km. We have selected only those aircraft measurements closer than 20 km to the VIL.

The balloon profiles were averaged to match the 50 m vertical resolution of the VIL profiles. The VIL profiles are derived without temporal averaging to provide ~ 3 m temporal resolution. All VIL measurements judged to be statistically reliable are plotted.

Wind speed and direction comparisons between the VIL and balloon based measurements are shown in figure 2. The VIL and sonde results are clearly correlated, however on days with strong surface heating the balloons responded to localized gusts producing a large scatter in the comparison.

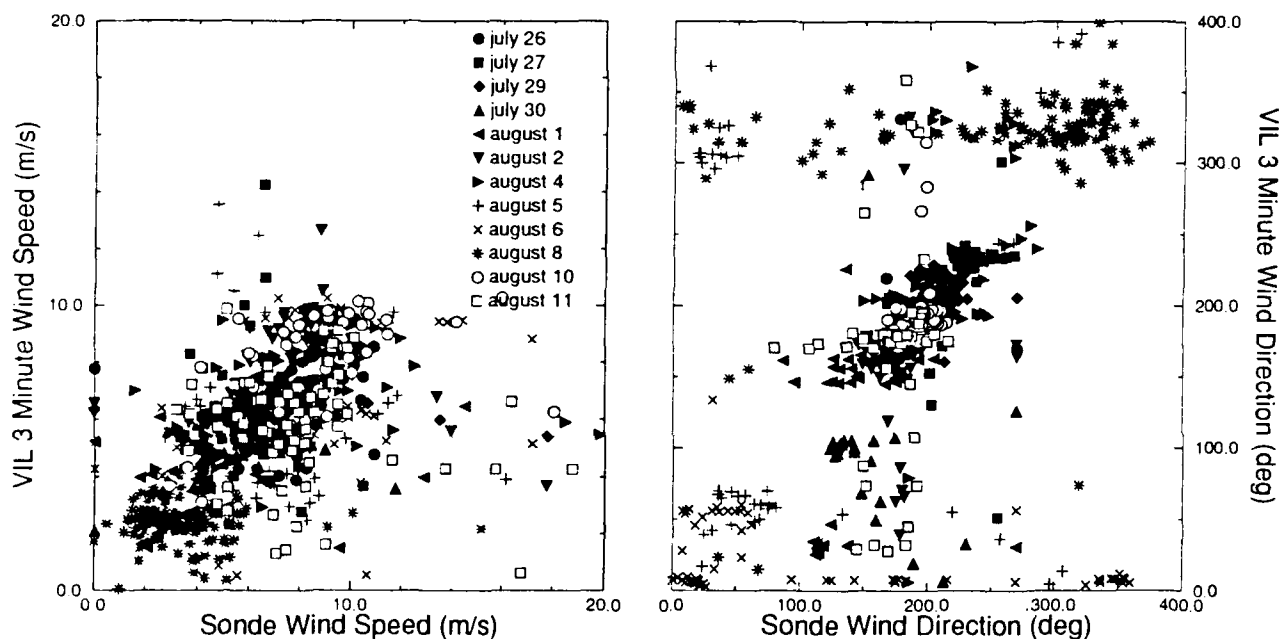


Figure 2: VIL wind results vs. radiosonde wind results during FIFE 1989. Values are less than 10 minutes apart and separated less than 50 m vertically.

A comparison between the VIL and the aircraft measurements shows much better correlation (see Figure 3): A least square fit to a straight line gives a slope of 0.98 ± 0.03 and an offset of $0.30 \pm 0.25 \text{ ms}^{-1}$ for wind speed, and a slope of 0.99 ± 0.02 and an offset of $8^\circ \pm 12^\circ$ for direction. Aircraft flights on July 28, August 2, and August 3, 1989 were directed through the middle of the VIL scan pattern so the aircraft and the lidar were more closely matched. These results show smaller variations between spatially and temporally spaced VIL observations than between adjacent aircraft measurements. This suggests that the VIL results are statistically more stable than the aircraft measurements as a result of area averaging. The aircraft gives flight path line averages over ~ 15 km, while the VIL gives area averages over $\sim 70 \text{ km}^2$.

Figure 4 shows a 9 hour history of wind speeds derived from 15 minute averaged VIL wind profiles with 50 m vertical resolution. Notice the internal consistency of VIL measurements inside the boundary layer even in the presence of strong clear air convection. This indicates the advantages of area averaging. Above the convective boundary layer the VIL winds are quite noisy as a result of very weak aerosol structure at these altitudes.

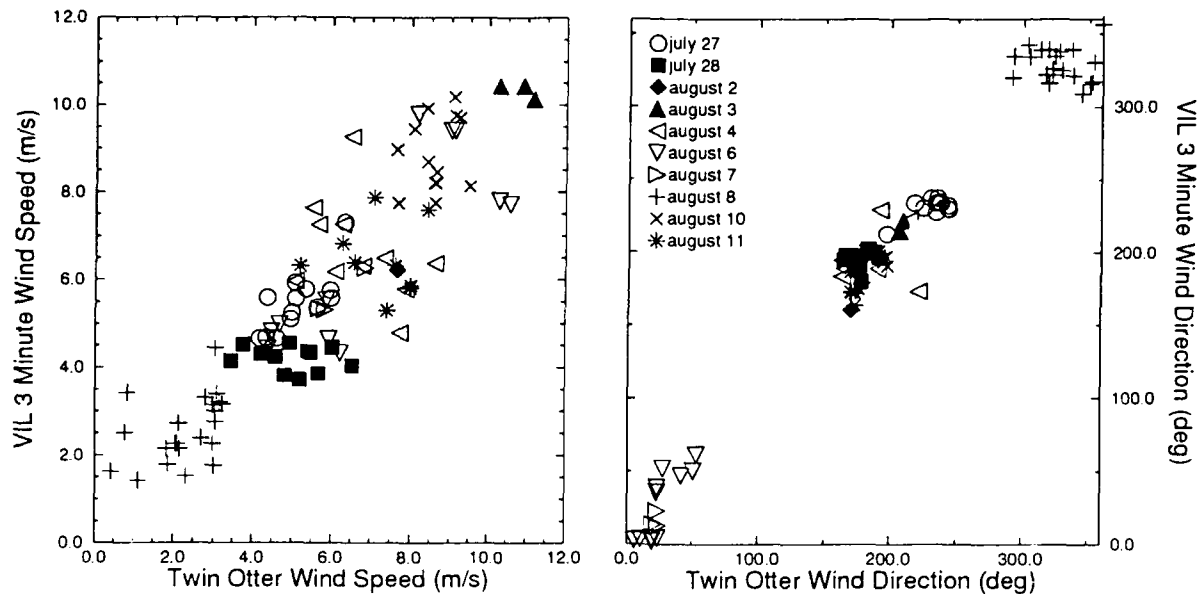


Figure 3: VIL wind results vs. aircraft based wind measurements. Comparisons made with the aircraft path inside the VIL scan volume are marked using solid black symbols.

Speed August 6, 1989

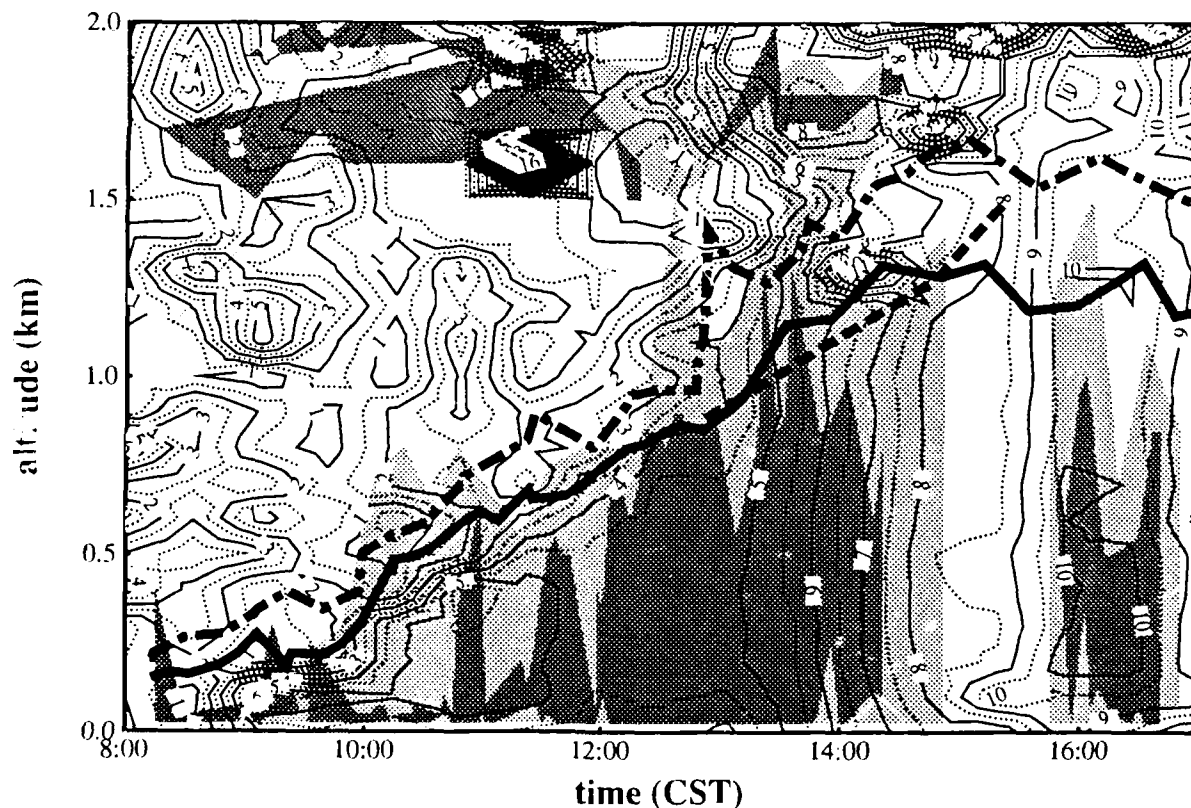


Figure 4: Contour lines represent VIL wind speed as a function of time and altitude. Mean boundary layer heights (solid line), plume tops (dot-dashed line), and cloud bases (dashed line) are also shown. Shading indicates the relative statistical reliability assigned to the VIL measurements with darker shades corresponding to higher reliability.

Figure 5 compares hourly averaged VIL wind profiles with radiosonde-based, aircraft-

based and surface weather station wind measurements between 10:00 and 11:00 CST on July 27, 1989. Surface measurements were generated from 8 National Center for Atmospheric Studies PAM stations using anemometers on 6 meter surface towers. Based on visual inspection of VIL Range Height Indicator planes, the boundary layer mean height was ~ 1 km and cloud base at 1.5 km during this time. Notice that the estimates of VIL wind reliability decrease above the boundary layer. The VIL wind speed profile shows slight wind shear near to ground due to friction. The aircraft measurements are scattered to either side of the VIL profiles due to the smaller averaging volume and shorter averaging times. The radiosonde profiles have large fluctuations due to local wind variations. Ground based measurements are slower in speed and backed in direction due to surface friction. Notice the high degree of internal consistency in the VIL profiles in the convective boundary layer.

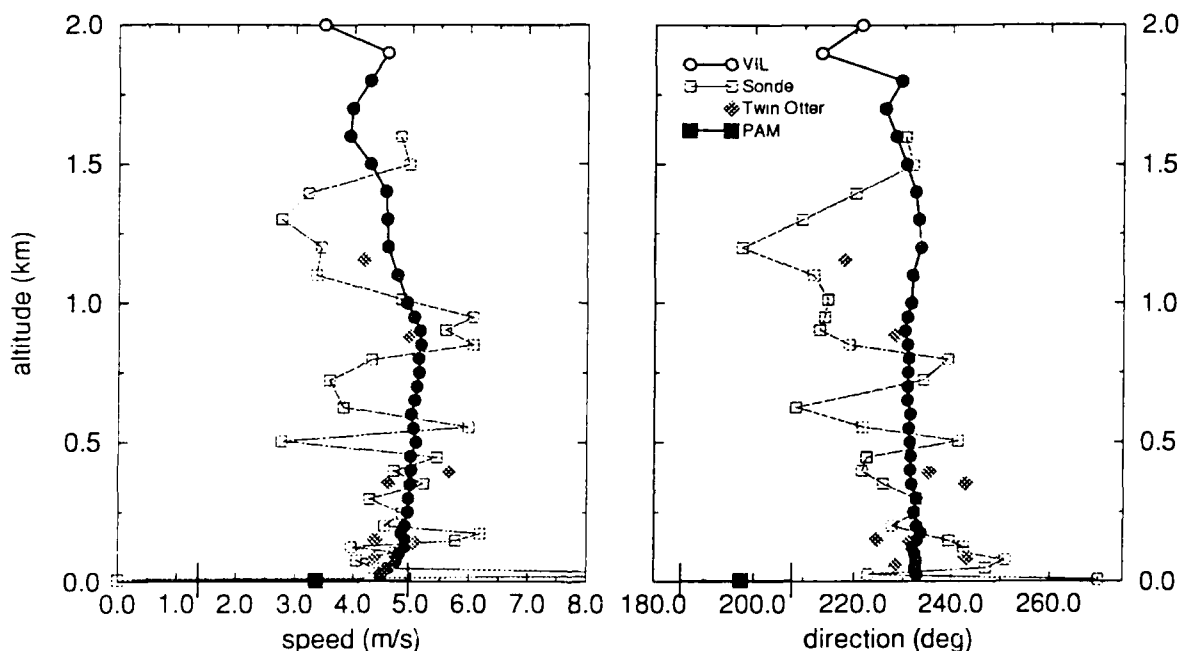


Figure 5: VIL wind profiles are compared with aircraft (Twin Otter), radiosonde (Sonde), and weather station (PAMS) wind measurements. Weather station measurements are averages over one hour and eight stations while the error bars show extremes between station averages. VIL results are separated in three reliability classes, where darker symbols indicate higher reliability.

Acknowledgements:

This research was supported by grants from the Finnish Academy; University of Joensuu, Finland; Suomen Kulttuurin Edistämmissäätiö Foundation, Finland; NASA Grant NAG-5-902; and ARMY Research Office Grants DAAL03-86-K-0024 and DAAL03-91-C-0222.

References:

- ¹ Eloranta, E.W. and J.L. Schols (1990): 'The Measurement of Spatially averaged Wind Profiles with a Volume Imaging Lidar'. *Abstracts 15th International Laser Radar Conference July 1990 Tomsk, USSR*.
- ² Schols, J.L. and E.W. Eloranta: 'The Calculation of the Horizontal Wind Velocity from Volume Imaging Lidar Data'. *Accepted for publication J. Geophysical Research*.
- ³ MacPherson, J.I. (1990), 'NAE Twin Otter Operations in FIFE 1989', National Aeronautical Establishment of Canada, Laboratory Report LTR-FR-113, June 1990.

OPTICALLY-BASED AIR DATA USING DOPPLER-SHIFTED,
HIGH SPECTRAL RESOLUTION LIDAR

W.R. Lempert, J. Forkey, N. Finkelstein, and R. Miles
PRINCETON UNIVERSITY
Department of Mechanical & Aerospace Engineering
Princeton, New Jersey 08544

Optically-based velocimetry techniques have the potential to provide critical data for the maneuverability and control of supersonic/hypersonic aircraft under conditions where conventional sensors are unreliable. For example, at high speed, the calibration of pitot-pressure devices is uncertain. Recently, High Spectral Resolution Lidar (HSRL) incorporating a barium atomic vapor filter has been used to determine atmospheric temperature and backscatter ratio (1). In this paper, we present a concept for an air-born Optical Air Data System (OADS) based on a Doppler-shifted HSRL approach which we have termed Spectrally Filtered Rayleigh Scattering (FRS) (2).

The basic approach is illustrated in Figure 1. When a narrow bandwidth laser is used to illuminate air from a moving vehicle, the detected backscatter is shifted in frequency by an amount proportional to velocity and broadened in linewidth by an amount proportional to $\sqrt{T/m}$, where T is the temperature, and m is the mass. If the laser is tuned into an absorption resonance of an atomic or molecular vapor, and, if the return scatter is detected through a filter constructed from this vapor, then the transmitted signal seen by the detector is a function of velocity and temperature. If the laser is tuned through the absorption band, or, if multiple filters of varying bandwidths are simultaneously employed, then velocity and temperature can be determined from the spectral shape. Additionally, calibration of the absolute detected intensity yields air density. At altitudes less than approximately fifteen kilometers, aerosol scatter contributes significantly to the total backscatter. This improves the velocity measurement, but interferes with temperature and density.

Figure 2 shows sample data obtained from a Mach 4 laboratory-scale wind tunnel flow using the second harmonic from an injection-seeded Nd:YAG laser at 0.532 microns, in conjunction with an optically thick molecular iodine vapor filter. In this case, the laser was formed into thin sheet which was incident

to the flow at an angle of 41° . The scattering was imaged onto an intensified CID camera using a 2" diameter by 3" long vapor filter, in which the iodine pressure was held at ~ 1.5 torr by means of a water-jacketed cold tip held at $\sim 45^\circ\text{C}$. The body of the cell was held at $\sim 80^\circ\text{C}$ with heating tape. The open circles in Fig. 2 represent the digitized integrated intensity from a 10×13 pixel portion of the imaged flow field. The solid curve is a least-squares fit from which a flow velocity of 649 ± 11 m/sec, and a static temperature of 60 ± 9 K is obtained. (The uncertainties are 2σ based on statistics only.) Similar scans were performed in a larger scale Mach 3 wind tunnel in which trace quantities (~ 10 ppm) of residual water vapor are known to condense into a fine "fog" of 10-100 angstrom ice crystals. A least squares fit, analogous to that of Fig. 2, gives a velocity of 566 ± 6 m/sec. The reduced uncertainty is the result of the enhanced intensity and decreased spectral width of the particle scattering.

We will discuss details of a proposed air-borne backscatter system based on single isotope atomic mercury vapor absorption at 253.7 nm (3) in conjunction with the third harmonic of a single frequency Ti:Sapphire (or alexandrite) laser. Critical aspects of the system, including filter design, laser requirements, and potential accuracy as a function of altitude, will be presented.

REFERENCES

1. F.J. Lehman, S.A. Lee, and C.Y. She, Opt. Lett. 11, p. 563 (1986).
2. R. Miles and W. Lempert, Appl. Phys. B 51, p. 1 (1990).
3. H. Edner, W. Faris, A. Sunesson, and S. Svanberg, Appl. Opt. 28, p. 921 (1989).

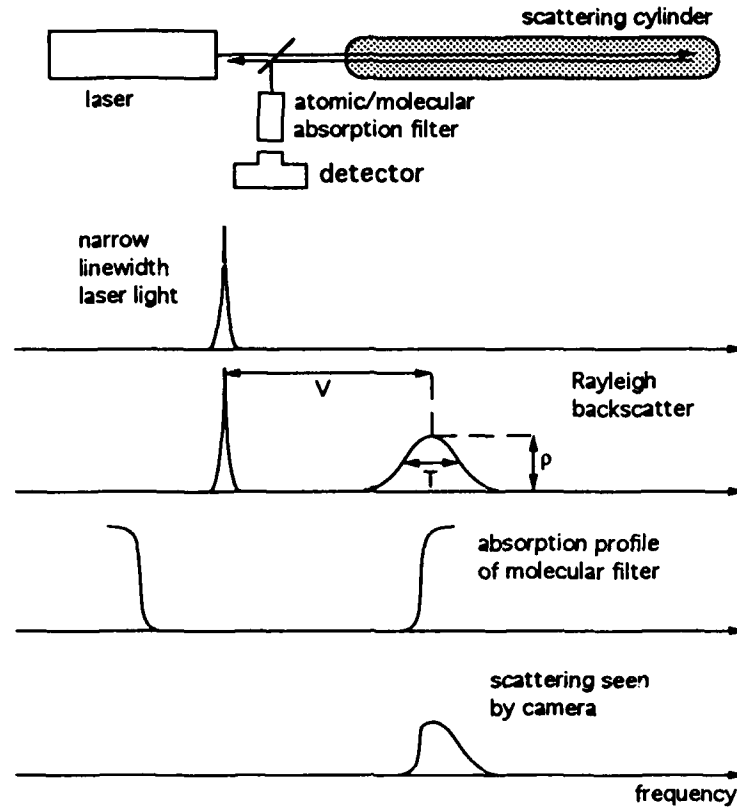


FIGURE 1. FRS Basic Concept

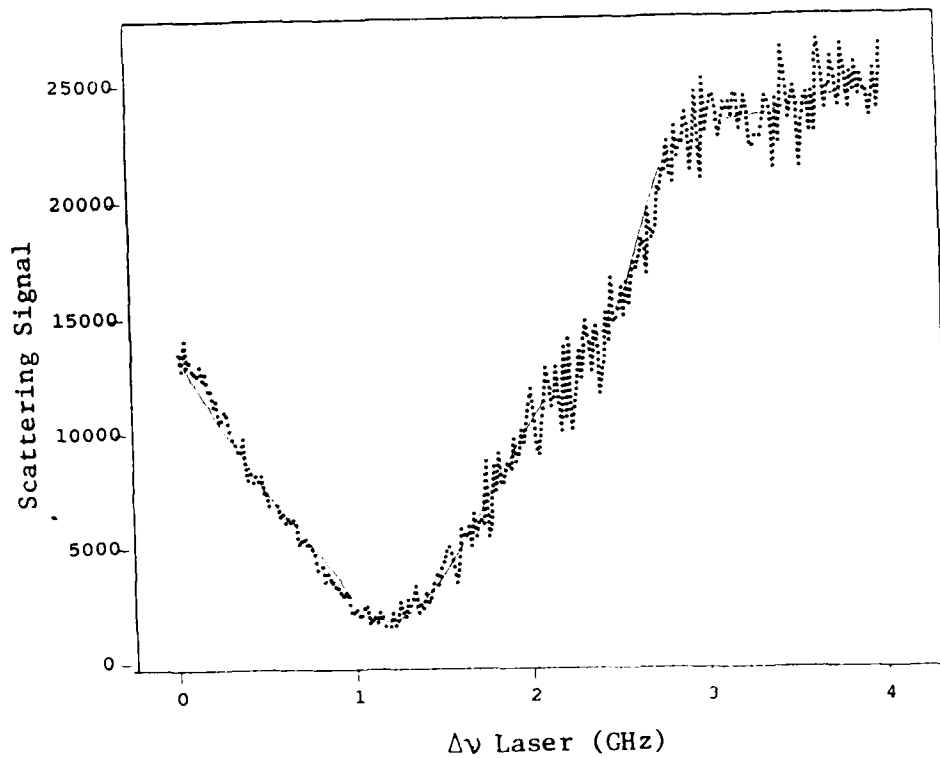


FIGURE 2. Data (Circles) and Best Fit (Solid) from Mach 4 Wind Tunnel Flow.

Multi-center Airborne Coherent Atmospheric Wind Sensor

J. Rothermel, NASA Marshall Space Flight Center, Huntsville, AL 35812
R. M. Hardesty, NOAA Wave Propagation Laboratory, Boulder, CO 80303
R. T. Menzies, NASA Jet Propulsion Laboratory, Pasadena, CA 91109

INTRODUCTION

In Spring 1992 development began for the Multi-center Airborne Coherent Atmospheric Wind Sensor (MACAWS). The four-year project will culminate in an airborne scanning pulsed CO₂ Doppler lidar for multi-dimensional wind and calibrated backscatter measurement from the NASA DC-8 research aircraft. MACAWS is under joint development by the lidar remote sensing groups of the NASA Marshall Space Flight Center (MSFC), National Oceanic and Atmospheric Administration Wave Propagation Laboratory (NOAA), and Jet Propulsion Laboratory (JPL). MSFC is assigned lead responsibility for overall coordination, science definition, and mission planning. Each lidar group is sharing major hardware components and subsystems which, in several instances, have been used in previous ground-based or airborne measurement programs. The principal of operation is similar to that employed by MSFC during previous airborne lidar wind measurements [1-6]. The primary improvements are use of the NOAA Joule-class tunable CO₂ laser transmitter, expanded scanning capability, and improved in-flight instrument control and data visualization systems.

METHOD OF OPERATION

During operation the pulsed lidar beam is directed anywhere within a 64 degree cone using a germanium wedge scanner mounted on the left side of the aircraft. The backscattered, Doppler-shifted radiation is measured to infer the line-of-sight wind velocity, assuming the scattering particles act as passive wind tracers. A dedicated inertial navigation system (INS) is used to measure the aircraft attitude and speed in order to obtain ground-relative line-of-sight velocity. By scanning the lidar beam slightly forward and aft during flight, fields of two-dimensional wind estimates can be obtained within the scan plane, i.e. co-planar scanning. Data from the INS is used to update the scanner settings to ensure the shot pattern is aligned within the desired scan plane. Multiple scan planes, revealing a quasi-three-dimensional view of the velocity and backscatter structure, can be obtained by appropriately directing the scanner.

RESEARCH OBJECTIVES

Following integration and ground test at JPL and successful test flights from the NASA Ames Research Center, MACAWS will begin a series of specialized field measurements addressing two classes of objectives:

1. Atmospheric Dynamics

MACAWS will be capable of specialized measurements of atmospheric dynamic processes in the planetary boundary layer and free troposphere in locations, and over scales of motion, not routinely or easily accessible to conventional wind sensors. Participation is planned for the Global Energy and Water Cycle (GEWEX) Continental-scale International Project (GCIP) in the mid-1990's [7,8]. In the context of GCIP, MACAWS wind measurements will contribute toward improving parameterization schemes for sub-grid scale processes related to the hydrological cycle, necessary for improving climate and general circulation models. Additionally, investigations with MACAWS at critical spatial and temporal scales will improve the understanding of a variety of atmospheric processes and features: orographic windstorms, generation of instability along dry lines, evolution of mesoscale circulations in differentially-heated boundary layers, interaction of thunderstorms with the environment including generation of new convection by thunderstorm outflows, and regional air quality degradation. In short, the unique measurement capability of MACAWS has the potential to improve predictive capabilities for weather and climate.

2. Satellite Instrument Performance

MACAWS is applicable to reduction of uncertainties in performance studies of satellite-borne, lidar-based wind sensors. An example is the NASA Laser Atmospheric Wind Sounder (LAWS), a prospective Doppler lidar system to measure global tropospheric winds. Ground-based lidar studies can provide only limited information, whereas MACAWS can be used to closely duplicate the LAWS measurement perspective using appropriate scanner settings and flight maneuvers. The resulting measurements are expected to improve the validity of LAWS Observing System Simulation Experiments (OSSEs). For example, LAWS data will contain a surface return signal applicable to calibration, atmospheric extinction estimation, and "ground-truth" velocity estimation. During post-processing, these data may be used to minimize biases in LAWS measurements. Observations from MACAWS are also relevant to issues of the impact of spatial variability in velocity and backscatter estimation, detailed assessment of cloud spatial and optical properties, line-of-sight and two-dimensional wind profile estimation (particularly near aerosol gradients), and long-term monitoring of natural surfaces that are potential LAWS calibration targets for backscatter estimation as well as for monitoring instrument health. Of course, an airborne lidar system capable of simulating the LAWS measurement perspective is also applicable to post-launch performance validation studies.

CONCLUSION

The MACAWS airborne Doppler lidar system will have unprecedented atmospheric measurement capability in the planetary boundary layer and free troposphere, with the inherent capability to provide guidance to risk reductions studies for space-borne lidar-based wind sensors. Final integration and ground test will commence in 1994; system test flights and research flights will begin in Spring 1995. It is envisioned that

MACAWS will be re-flown periodically as part of ongoing atmospheric dynamic and satellite performance studies.

ACKNOWLEDGMENTS

The MACAWS development effort would not be possible without the participation of M.J. Post and J. Howell (NOAA), D.M. Tratt (JPL), J.A. Dunkin and W.D. Jones (MSFC), and many others. This work is partially supported by the National Aeronautics and Space Administration. The support of Dr. Ramesh Kakar, NASA Headquarters, is gratefully acknowledged.

REFERENCES

1. Bilbro, J.W., G.H. Fichtl, D.E. Fitzjarrald and M. Krause, Airborne Doppler lidar wind field measurements, *Bull. Amer. Meteor. Soc.*, 65, 348-359 (1984).
2. Bilbro, J.W., C.A. Dimarzio, D.E. Fitzjarrald, S.C. Johnson and W.D. Jones, Airborne Doppler lidar measurements, *Appl. Opt.*, 25, 3952-3960 (1986).
3. Blumen, W. and J.E. Hart, Airborne Doppler lidar wind field measurements of waves in the lee of Mount Shasta, *J. Atmos. Sci.*, 45, 1571-1583 (1988).
4. Carroll, J.J., Analysis of airborne Doppler lidar measurements of the extended California sea breeze, *J. Atmos. Oceanic Tech.*, 6, 820-831 (1989).
5. Emmitt, G.D., Convective storm downdraft outflows detected by NASA/MSFC's 10.6 micron pulsed Doppler lidar system, NASA CR-3898, Marshall Space Flight Center, Huntsville, AL, 46 pp. (1985).
6. McCaul, E.W., Jr., H.B. Bluestein and R.J. Doviak, Airborne Doppler lidar observations of convective phenomena in Oklahoma, *J. Atmos. Oceanic Tech.*, 4, 479-497 (1987).
7. World Climate Research Program, Scientific plan for the Global Energy and Water Cycle Experiment, WMO Tech. Doc. No. 376, 83 pp. (1990).
8. World Climate Research Program, Scientific Plan for the GEWEX Continental-scale International Project (GCIP), WMO Tech. Doc. No. 461, 73 pp. (1992).

Simulation Space-Based Doppler Lidar Wind Measurements Using
Ground-Based Single Shot Observations

G. D. Emmitt, J. Dieudonné, S.A. Wood
and L. Wood

Simpson Weather Associates, Inc.
809 E. Jefferson Street
Charlottesville, VA 22902
Telephone: (804)979-3571

Both single-agency and multi-agency efforts are currently underway to put a Doppler lidar wind sounder into space within the next decade. Justification for this ambitious project rests mainly in the universally recognized need to provide direct measurements of the winds as input to both climate studies and forecast models. Expectations of success are based heavily upon ground-based observations as well as a few airborne observations. While the space-based observations will be taken at 5-10 Hz providing samples with a spatial separation of 50 to 70 kilometers within the earth's atmosphere, both the ground-based and airborne observations have been acquired primarily at 20 to 100 hertz providing a shot density of many samples per square meter resolution. Furthermore, many of the wind velocity estimates derived from these ground-based and airborne instruments have been acquired by using a poly-pulse pair technique involving 20 to sometimes 100 pulses. Currently there is very little in the way of data that is acquired in a single shot mode and processed to achieve resolution, both in space and time, that will approximate that which is achievable with a space-based system.

Over the past year data have been collected at the Marshall Space Flight Center's (MSFC) Ground-Based Doppler Lidar facility. These data have been collected both in the single shot mode as well as in the poly-pulse pair processor mode. These observations were taken with the following objectives:

- 1) to obtain single shot data that could be used to simulate a space-based observing perspective and inter-shot spacing;
- 2) to examine the velocity fields at the cloud boundaries, particularly at the lower boundary of cirrus clouds; and
- 3) to examine single shot statistics in comparison to those derived from the poly-pulse pair statistics.

The MSFC's lidar is a 20 mJ, 10.6 μ m pulsed incoherent Doppler system. During most of our observations, the laser was operated at 110 Hz with the scanner rotating at 3-4 degrees per second. The data was processed by the poly-pulse pair processor

every 50 shots providing line-of-sight (LOS) measurements every .5 sec. Twice per second, a single set of in-phase and quadrature data was recorded - i.e., every 50th shot. The single shot data was then processed with a complex FFT to obtain LOS wind measurements. Figures 1 and 2 are examples of poly-pulse (pp) pair and single shot (ss) observations taken during the same 360° scan.

Construction of vertical soundings was accomplished using a sine-fitting program to the velocity azimuth display (VAD) data for each range gate between 1 and 10 km in slant range. Figures 3 and 4 are examples of sine wave fitting to the 15th range gate of the VADS shown in Figures 1 and 2. The goodness of fit estimates provide a first order expression of the representativeness of LOS observations.

For the presentation we expect to show the results of a study using multiple VADS where the poly-pulse pair product is considered "truth" for the simulation of space-based observations using the single shot data. The effects of spatial separation of space-based observations will be accounted for by combining single shots from ground-based VADS separated in time.

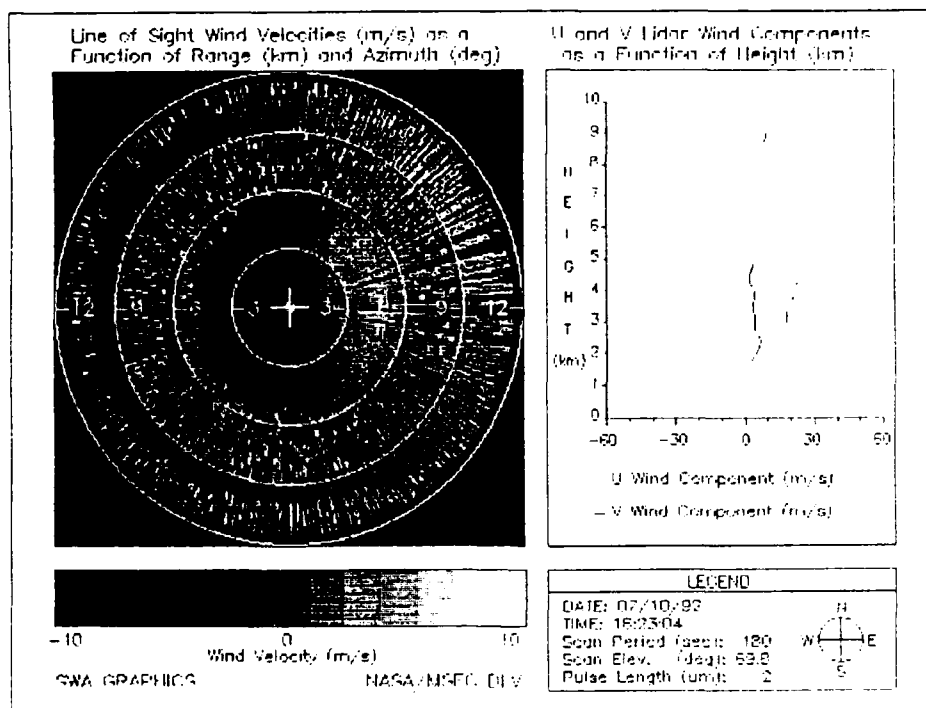


Fig. 1. Display of Doppler lidar data processed with a poly-pulse pair algorithm using 50 sequential shots. Vertical profile is obtained with sine fitting of individual range gates. The lidar was operated at 110 Hz.

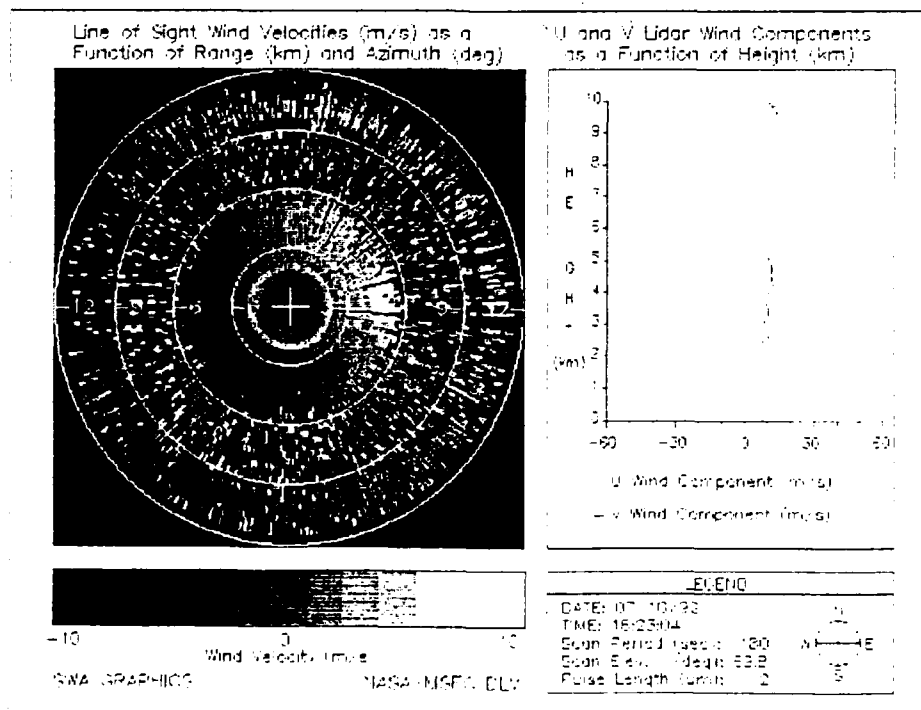


Fig. 2. Display of single shot Doppler lidar data taken at 1.5° azimuthal increments. These data were taken at the same time as those shown in Fig. 1.

SINE FIT TO NASA/MSFC GBDL DATA POLY-PULSE PAIR

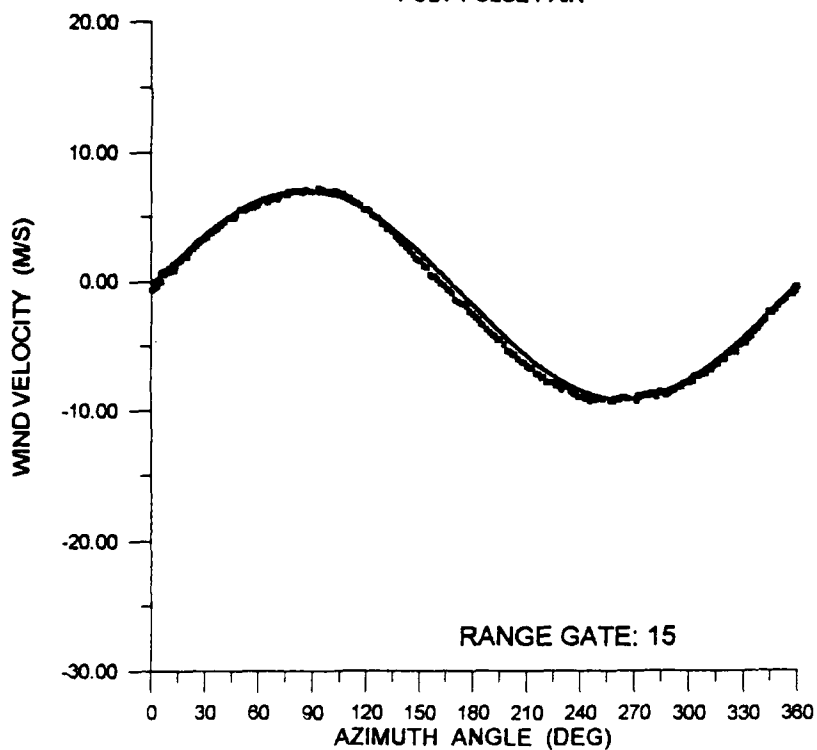


Fig. 3. Velocity Azimuth Display (VAD) for the 15th range gate of the data displayed in Fig. 1. Each data point is derived from a 50 shot poly-pulse pair processing.

SINE FIT TO NASA/MSFC GBDL DATA SINGLE SHOT

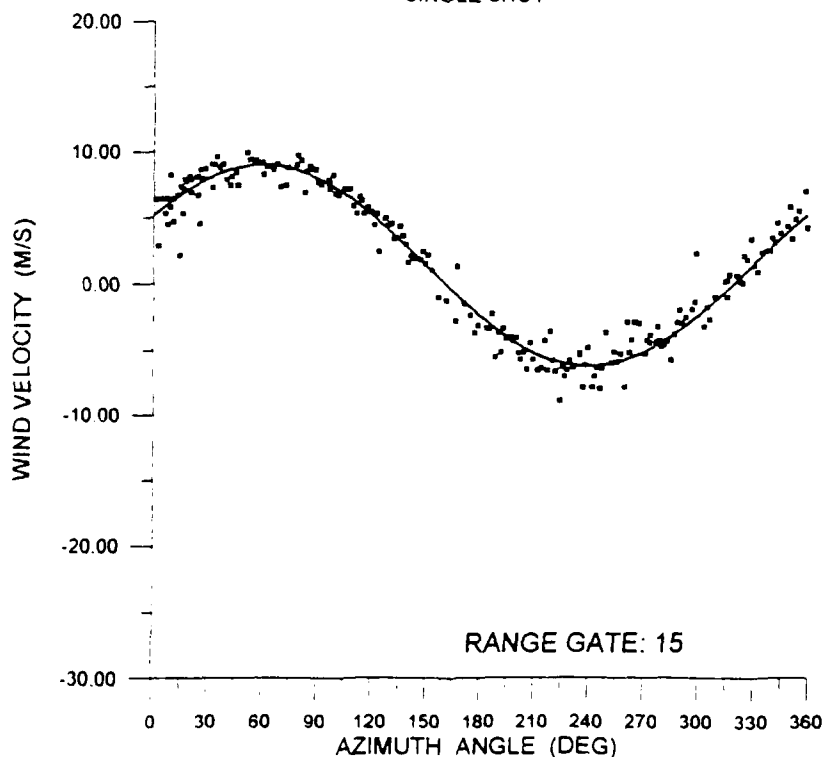


Fig. 4. VAD for the 15th range gate of the single shot data displayed in Fig. 2.

Wednesday, March 10, 1993

Ozone 1

WC 1:00pm-2:30pm
Salon F

I. Stuart McDermid, *Presider*
Jet Propulsion Laboratory

Lidar Developments for Tropospheric Ozone Research in Europe

Jens Bösenberg
Max-Planck-Institut für Meteorologie
Bundesstr. 55, Hamburg, Germany

The TESLAS subproject of the joint European environmental programme EUROTRAC has started an initiative to develop accurate, reliable, and easy to operate lidar systems for measurements of the ozone vertical distribution in the troposphere. The progress is reported.

The TESLAS subproject of the EUROTRAC environmental programme was defined in 1987 as a collaborative initiative to develop DIAL systems for routine use in tropospheric ozone research. The main goal was to improve existing techniques, mostly based on the use of dye lasers, in order to come up with relatively easy to operate, reliable, and accurate systems. Further, the methodology was to be examined in detail to optimize system performance and to yield reliable estimates of the accuracy to be achieved under different atmospheric conditions.

Several systems were developed, all but one operating in the UV wavelength region. The laser sources exploited so far are:

- a special CO_2 -laser in the IR,
- Nd:Yag fourth harmonic plus first order stimulated Raman scattering (SRS) in hydrogen and deuterium (266, 289, 299 nm)
- KrF Excimer laser plus up to second order SRS in hydrogen and deuterium (248, 277, 313, 268, 292, 302 nm),
- dye laser pumped by Nd:Yag second harmonic.

The process of stimulated Raman scattering for use in lidar systems has been studied in detail for the optimisation of system parameters. High conversion efficiencies and high reliability have been achieved. Other components of a lidar system, e.g. telescopes, filter and grating spectrometers, detectors, and data acquisition systems have been studied, and several improved designs have been developed.

Eight different groups have so far built operational systems. Most of them have been operated for an extended period already. Reliability has been increased considerably, routine operation by one technician has been demonstrated.

An intercomparison experiment, TROLIX '91, has been performed at the RIVM in Holland, where four different lidar systems (from The Netherlands, France, Sweden, and Germany) have been compared to each other, to groundbased photometric monitors and a DOAS instrument (with the lidars pointing horizontally), and with helicopter borne ECC-sondes and photometric monitors. The measurements had to be performed under extremely bad weather conditions with rain and low clouds for most of the time. Nevertheless a considerably large data set has been collected, which is still in the process of being analyzed. First results show, that for rather homogeneous atmospheric conditions the agreement is excellent (e.g. $2\mu\text{g} \cdot \text{m}^{-3}$ on the average). For inhomogeneous conditions with large aerosol gradients, present evaluation schemes have their limitations, and the remaining errors are much larger. Results will be presented, differences will be discussed, and possible improvements will be proposed.

**DIAL LIDAR MEASUREMENTS OF
STRATOSPHERIC OZONE
IN THE PRESENCE OF
VOLCANIC AEROSOLS**

Thomas J. McGee
NASA Goddard Space Flight Center
Code 916
Laboratory for Atmospheres
Greenbelt, MD 20771

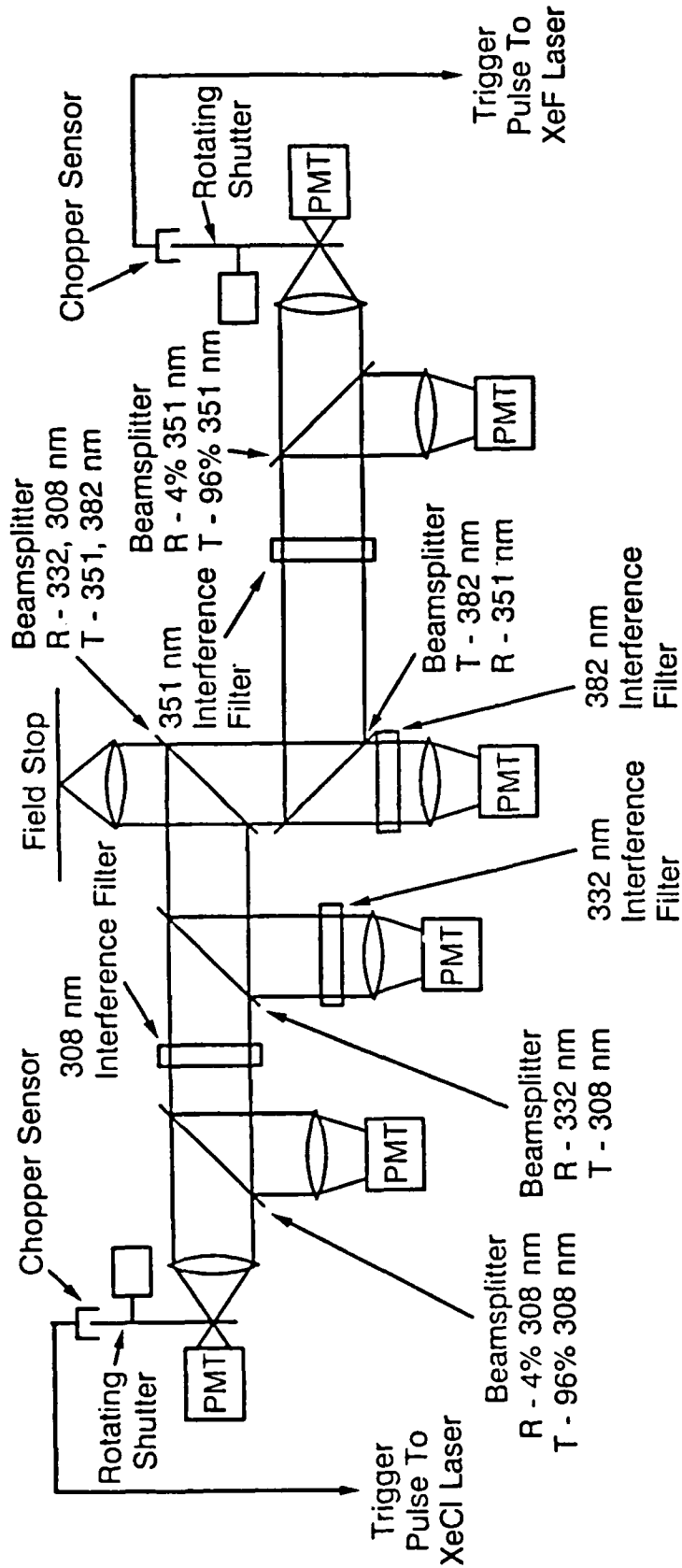
On June 15, 1991, Mt. Pinatubo in the Philippines explosively erupted, injecting large quantities of SO₂ and dust particles directly into the stratosphere. The SO₂ slowly reacted to form a concentrated and fairly thick layer of aerosol particles in the 15 to 32 km region of the stratosphere. When this layer was transported to latitudes at which a number of stratospheric lidars were operating, signals which had been dependent only on molecular scattering began to have a very large component due to Mie scattering from aerosols. Unlike Rayleigh scattering, the wavelength dependence of this Mie component is not well known.

A large fraction of the ozone lidar instruments currently operating worldwide transmit two ultraviolet wavelengths into the atmosphere. One, generally at 308 nm, is absorbed by ozone, and the other, usually above 350 nm, is not. The light is backscattered by atmospheric molecules, and the lidar signals are detected at the same wavelengths. In a clean atmosphere, this large separation of wavelengths is not a problem since Rayleigh scattering is well understood and the wavelength dependence of the scattering is known exactly. Scattering from aerosols, which like scattering from molecules is elastic, is dependent on the composition and the size distribution of the particles. These are not typically well known and therefore the wavelength dependence of the scattering is also poorly known. Ozone measurements based on elastically backscattered laser light show very large errors in the

regions where aerosols are present.

Since the time of the eruption, we have implemented changes in our lidar system to enable the acquisition of lidar returns based on Raman scattering of the transmitted laser light. Since Raman scattering is inelastic, it is detected at a different wavelength from the transmitted radiation. Thus there is no aerosol scattering component to the lidar return. Figure 1 is a schematic of the detector currently in use. Six channels are collected; two Rayleigh channels at each wavelength and one Raman channel. The high sensitivity Rayleigh channels are used to extract ozone information above the aerosol layer; the low sensitivity channels are now being used in conjunction with the Raman channels to generate an altitude-dependent Backscatter/Extinction ratio, which can then be used in an effort to correct the low channel Rayleigh data. The results on the usefulness of this technique to correct for aerosol backscatter will be discussed. The Raman channels are also used to generate an ozone profile below 30 km, where aerosols are still a significant problem.

The majority of the presentation will center on the data returned from two international intercomparisons in 1992; the first in Southern France, and the second at Lauder, New Zealand. Comparisons with data from the UARS instruments and other European lidars will be presented.



BEAM SEPARATION AND DETECTION OPTICAL SCHEMATIC

RIVMs tropospheric and stratospheric ozone lidars for European and Global monitoring networks

Daan P.J. Swart, Arnoud Apituley, Jan Spakman, Eric P. Visser and Hans B. Bergwerff

National Institute of Public Health and Environmental Protection (RIVM),
Laboratory for Air Research, P.O. box 1, 3720 BA Bilthoven, The Netherlands
Tel. +31 30 742677, Fax: +31 30 287531, E-mail: dpjswart@rivm.nl on internet

Background tropospheric ozone levels have doubled since 1900 [1], and are presently increasing at a rate of 1 % per year[2]. Of all trace gases in the lower atmosphere, ozone has reached concentration levels closest to proven toxic levels on man[3]. Crop yield in the Netherlands is estimated to be lower by 3 to 4 % (300-400 million US \$) due to higher ozone levels during the growth season[4]. Column (i.e. mainly stratospheric) ozone levels at northern hemisphere mid latitudes have gone down by 5 to 6 % between 1970 and 1991 [5]. The expected increased exposure of the earth surface to UV-B has many adverse effects on man and environment[6]. The changing vertical distribution of ozone may be reflected in climate changes as well[5].

Clearly, high quality routine monitoring of the vertical profile of ozone in both troposphere and stratosphere is of prime importance in the analysis of trends and their underlying mechanisms. In addition, simultaneous measurement of many other relevant constituents and parameters is mandatory. Both earth observing satellites and monitoring networks on continental and global scale are needed to assess and understand the magnitude of the ozone changes.

RIVM is developing a tropospheric ozone lidar [7] for the *European Tropospheric Ozone Research (TOR) Network*, and a stratospheric ozone lidar for the *Network for the Detection of Stratospheric Change (NDSC)*.

Tropospheric Ozone Lidar

RIVMs tropospheric ozone lidar is presently (Nov 1992) operational and performing regular measurements in the altitude region of 600 to 4.000 meters. The system setup is shown in figure 1 and details are given in table 1. A typical measurement result is shown in figure 2. In the course of 1993 the range of the system will be extended to enable measurements from the lower boundarylayer to the lower stratosphere (100 m to 12 km). In 1994 the instrument is scheduled to be fully automated and to execute routine measurements on an hourly basis whenever the weather permits.

In the TROLIX 91 intercomparison campaign in Bilthoven, the Netherlands, four tropospheric ozone lidars have performed measurements simultaneously with helicopter borne ozone sonde and UV photometric analyzer [8-13]. A typical result is shown in figure 3. As expected for UV DIAL with rather large wavelength separation, aerosol and other interferences can not be neglected in the lower part of the profile. Processing algorithms including corrections for these interferences are under development at this time.

Upon completion, the system will be part of the dutch station *Kollumerwaard* of the TOR monitoring network (figure 4). Table 2 gives an overview of components measured simultaneously at this location. Specific lidar aims in TOR will be the climatology and trend analysis of the tropospheric ozone profile, and the budgets of the ozone exchange between boundarylayer and free troposphere, and between troposphere and lower stratosphere.

Stratospheric Ozone Lidar

RIVM's stratospheric ozone lidar is presently under development in Bilthoven, the Netherlands [14], and will perform its first measurements early 1993. The system setup is shown in figures 5 and 6. Details are given in table 3. The system is designed to perform routine nighttime measurements in the altitude region of 18 to 45 kilometers in the framework of the NDSC and will be installed in Lauder, New Zealand upon completion in 1994. Table 4 gives an overview of the components measured simultaneously at this location.

The goals of the NDSC are explicitly defined in [15]. They include high quality measurements to detect and understand changes in the physical and chemical state of the stratosphere, to provide an independent calibration of satellite sensors, and to obtain data to test and improve multidimensional stratospheric chemical and dynamical models.

References

1. A. Volz & D. Kley, "Evaluation of the Montsouris series of ozone measurements made in the nineteenth century", *Nature* **332**, 240 (1988).
2. J.A. Logan, "Tropospheric Ozone: seasonal behavior, trends, and anthropogenic influence", *Journal of Geophysical Research* **90**, 10463-10482 (1985).
3. W. Slooff, R.M. van Aalst, E. Heijna-Merkus, R. Thomas, "Ontwerp Basisdocument Ozon", RIVM Report 758474002 (1987).
4. L.J. van der Eerden, A.E.G. Tonneijck, J.H.M. Wijnands, "Crop loss due to air pollution in the Netherlands", *Environmental Pollution* **53**, 365-376 (1988).
5. Scientific Assessment of Ozone Depletion: 1991, WMO Global Ozone Research and Monitoring Project Report no. 25.
6. UNEP Environmental effects Panel Report, "Environmental effects of Ozone Depletion: 1991 update" (November 1991).
7. J.A. Sunesson, A. Apituley and D.P.J. Swart, "Differential Absorption LIDAR System for Routine Monitoring of Tropospheric Ozone", in preparation
8. A. Apituley, "RIVM tropospheric ozone LIDAR measurements during TROLIX'91", RIVM-report 222201007 (1991)
9. C.N. de Jonge, "NO₂-DIAL measurements during TROLIX'91", RIVM-report 222201003 (1991)
10. C.N. de Jonge, "Planetary boundary layer measurements during TROLIX'91", RIVM-report 222201004 (1991)
11. J.B. Bergwerff, "Airborne O₃-measurements during TROLIX'91", RIVM-report 222201005 (1991)
12. C.N. de Jonge, "Ground based measurements during TROLIX'91", RIVM-report 222201008 (1991)
13. A. Apituley, "RIVM contribution to TESLAS field campaign TROLIX'91 for intercomparison of Tropospheric Ozone Lidar Systems", RIVM-report 222201009 (1992) in preparation
14. D.P.J. Swart and J. Spakman, "Stratospheric Ozone Lidar for the NDSC, definition study", RIVM-report (1993) in preparation
15. Network for the Detection of Stratospheric Change, Status and Implementation Report (january 1990).

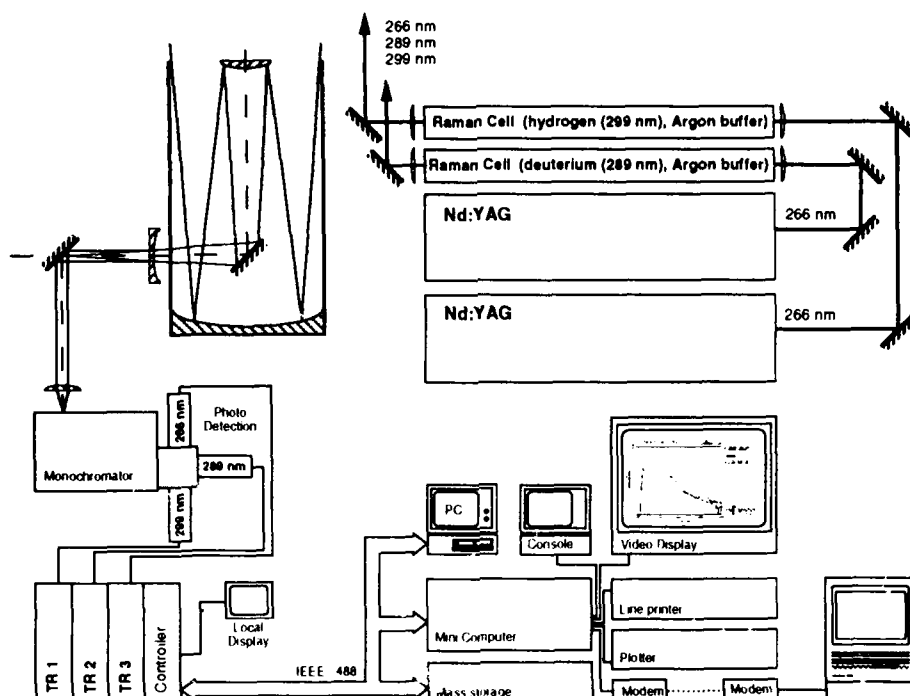


Figure 1. System set-up of RIVM tropospheric ozone lidar. Three wavelengths are emitted in the vertical. Backscattered radiation is collected in a telescope and dispersed in a monochromator. Detected signals are stored and averaged in transient recorders. A mini computer controls the measurement procedure and calculates the resulting ozone profile.

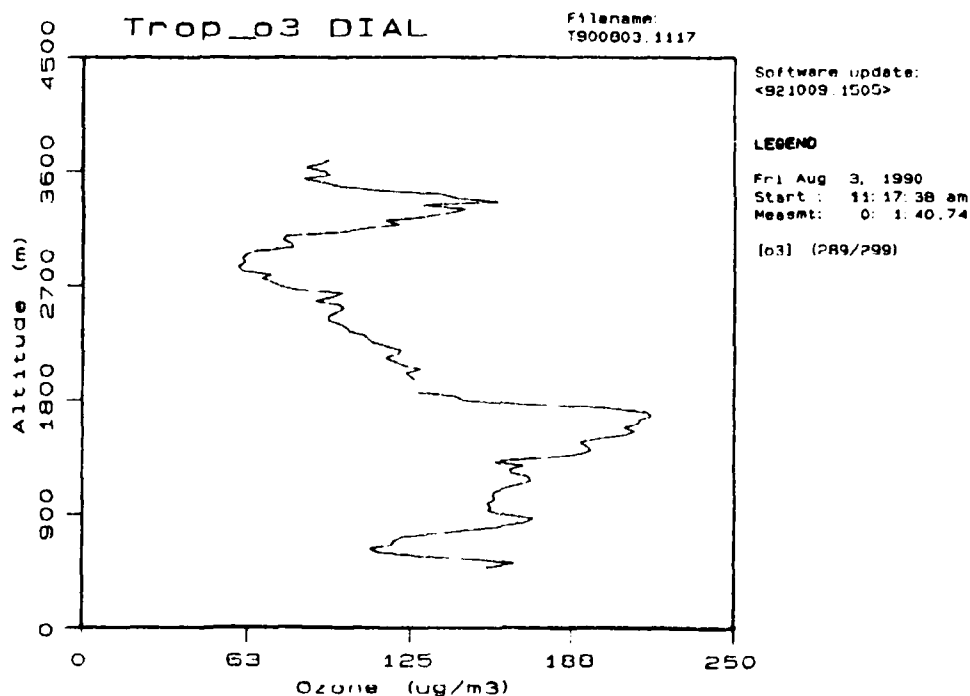


Figure 2. Typical measurement result of RIVM tropospheric ozone lidar. Values for altitudes within the range 600-900 meters are obtained with the 266/289 nm DIAL pair, whereas above 2000 meters the 289/299 pair is used

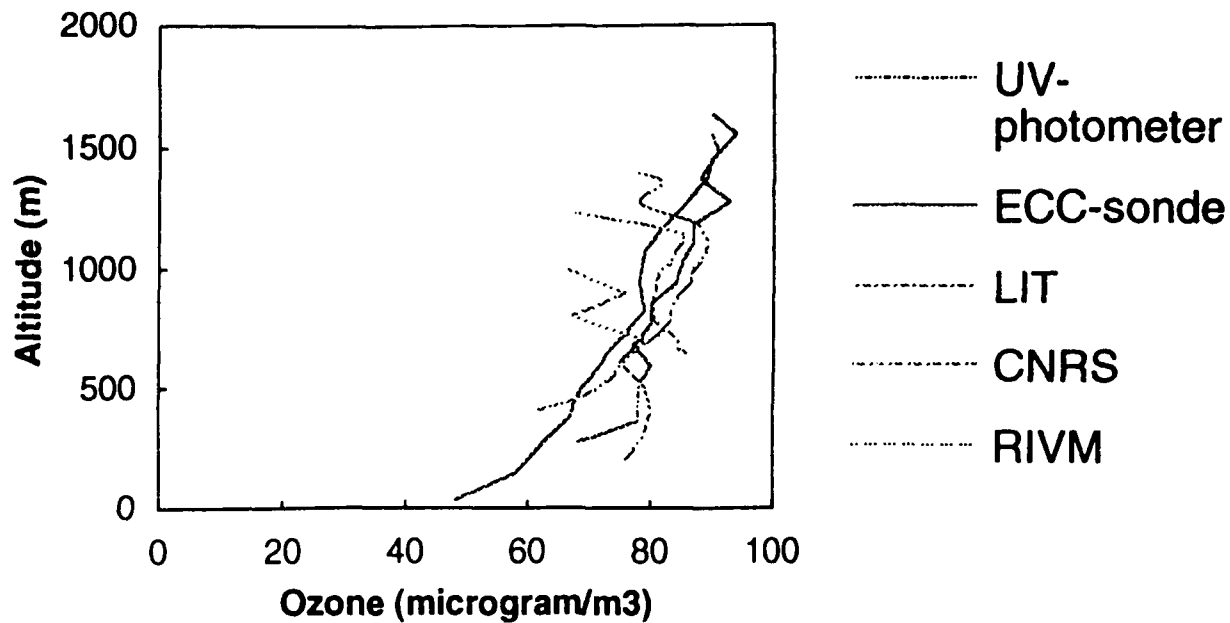


Figure 3. Ozone concentrations above Bilthoven on June 24, 1991, measured simultaneously by three lidars and two helicopter-borne instruments. The non-RIVM lidars presented in this figure are instruments from Lund Institute of Technology (LIT), Sweden, and Centre National de Recherche Scientifique (CNRS), France.

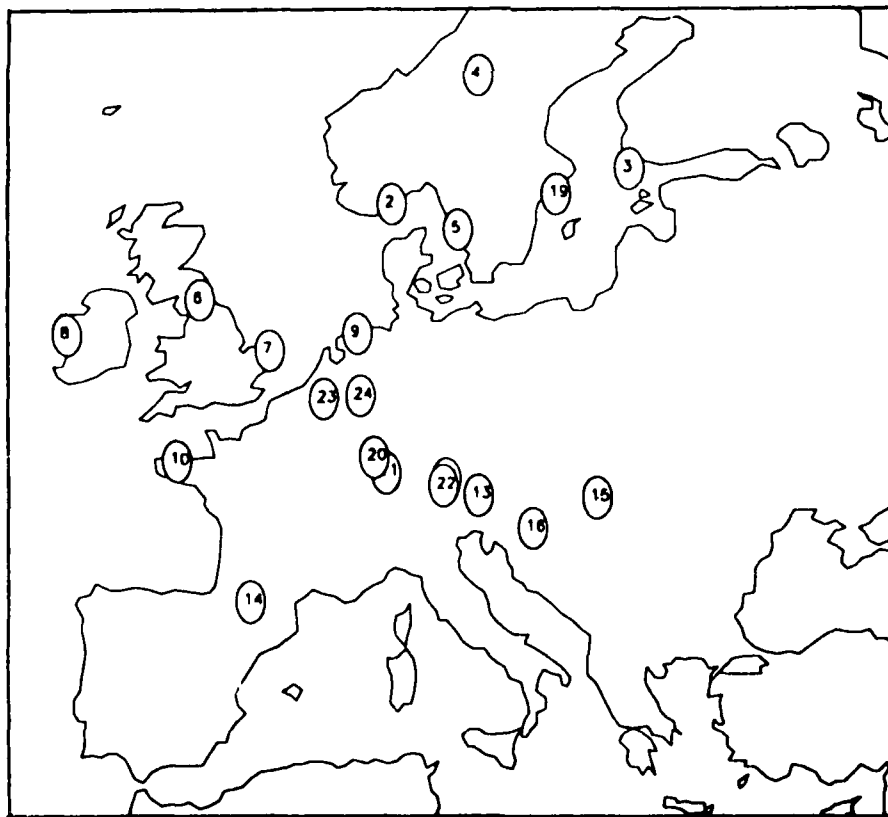


Figure 4. The Tropospheric Ozone Research (TOR) network over Europe. Distribution of sites is rather inhomogeneous; coverage of the south- and east european areas is poor. This map does not show the stations Spitsbergen (79°N) and Tenerife (28°N).

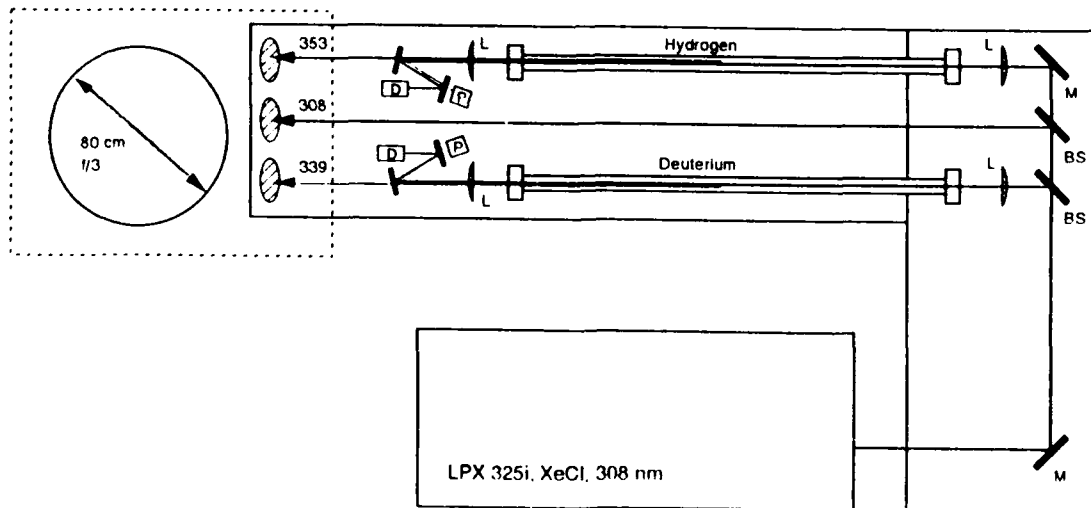


Figure 5. Emitter section of the RIVM stratospheric ozone lidar. The main part of the 308 nm laserbeam (central path) is directly emitted into the atmosphere. Remaining fractions are focused in Ramancells where beams of suitable wavelengths and energies are generated. The direction of the three emitted beams is accurately adjusted by the computer controlled steering mirrors.

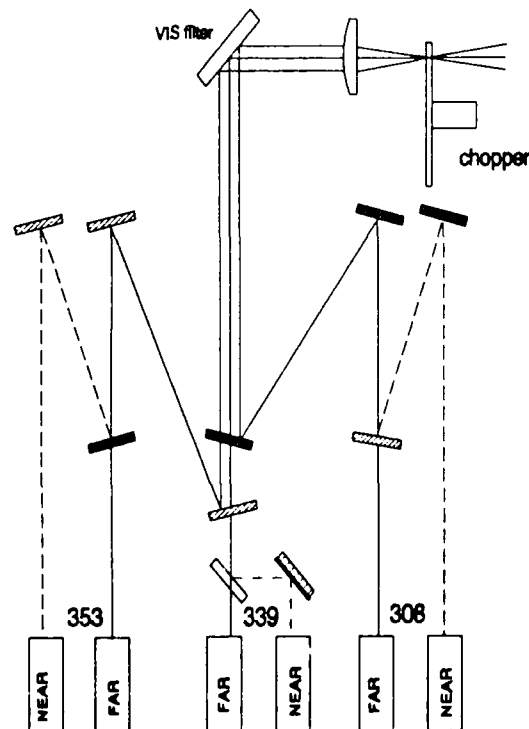


Figure 6. Receiver optics of the RIVM stratospheric ozone lidar. Backscattered radiation is captured by a 81 cm telescope and focused in a field stop/chopper wheel combination. The chopper blocks lidar echoes from the lower altitudes which tend to overradiate the sensitive photomultiplier tubes. After collimation and pre-filtering the wavelengths are separated by dichroids and split in channels of 98% and 2% transmission.

Table 1. Tropospheric Ozone Lidar system detail

Lasers	2x Spectra Physics DCR 3D Nd:Yag, 10 hz, 80-90 mj @ 266 nm each
Raman cells	2 m custom made, focal length 1100 mm, containing H ₂ + Ar and D ₂ + Ar.
Transmitted energies	30 mj/pulse@ 266 nm, 25 mj/pulse@ 289 nm, 40 mj/pulse@ 299 nm, <1 mrad
Telescope	Optical Surfaces, Dall Kirkham type, 600 mm primary, f/12, 2 mrad max full angle
Wavelength separation	Bentham 300 HR Cherny Turner type Monochromator (adapted), f/4.2, 1800 l/mm grating
Detectors	3x EMI 9817 QA, linear focussed type, 12 dynodes BeCu, gain 3 .10 ⁶
Digitizers	3x Lecroy TR6810, 5Mhz, 12 bit, 409.6 mV full scale
Computer	HP 1000 A600+ Minicomputer

Table 2. Measurements at TOR station Kollumerwaard, The Netherlands

Trace gases	O3 (groundlevel + profile 100m to 12 km), NO, NO2, SO2, CO, CO2, CH4, PAN,
Aerosols	VOCs
Wet Deposition	SO4, NO3, NH4, heavy metals
Meteo	acidifying compounds, heavy metals wind speed and direction, temperature, global radiation, jNO2

Table 3. Stratospheric Ozone Lidar system details

Laser	Lambda Physik LPX 325i, 250 Hz, 400 mJ/pulse @ 308 nm, 100 W
Raman cells	2 m custom made, focal length 1200 mm, H2+ Ar and D2 + Ar.
Telescope	Ealing, Newtonian type, 810 mm primary, f/3, 0.5 mrad full angle
Wavelength separation	Dichroic Mirrors and Interference filters
Detectors	6x EMI 9883 QA, linear focussed type, 14 dynodes BeCu, gain 3 .10 ⁷
Digitizers	6x DSP 2190 photoncounters, 100MHz, 500ns dwell
Computer	HP 1000 A400 Minicomputer

Table 4. Measurements at NDSC prime site Lauder, New Zealand

Species	Instrument
O3 column	Dobson
O3 profile	Ozone sonde 0-30 km, Excimer Lidar 18-45 km, Microwave 25-75km
Temperature profile	
H2O profile	Sonde 0-30 km, Nd:Yag Lidar
Aerosols	Sonde 0-30 km, Microwave
NO2 stratospheric column	Nd:Yag Lidar 0-30km, Aerosol backscatter sondes, Dust sondes
HCl, CH4, HNO3, CLONO2 strat. column	UV/Vis spectrometer
Ultraviolet radiation	FTIR
OH	UV spectrometer Etalon spectrometer

Wednesday, March 10, 1993

Ozone 2

WD 3:00pm–4:30pm
Salon F

Yasuhiro Sasano, *Presider*
National Institute of Environmental Studies, Japan

NDSC and Lidar Observations at OHP

Sophie Godin
Universite de Paris VI
T15 E5, 4 Pl. Jussieu
75230 Paris, France

Summary not available at press time.

Errors introduced in Differential Absorption Lidar Measurements of Stratospheric Ozone by Pinatubo Aerosols

W. Steinbrecht and A.I. Carswell

Institute for Space and Terrestrial Science
and Department of Physics and Astronomy, York University
4700 Keele Street, North York, Ontario, Canada M3J 1P3
Tel: 416-736-2100 Fax: 416-736-5516

Differential Absorption Lidars (DIAL) are being used since the early 1980's to measure stratospheric ozone. They allow a routine, drift free, remote optical measurement of the ozone profile. Therefore they have been chosen as one component of the Network for the Detection of Stratospheric change (NDSC, [1]). Unfortunately, like many optical measurements, their precision is affected by the large amount of aerosols in the stratosphere after a major volcanic eruption. Because of this one has to be very careful when using lidar measurements of ozone together with measurements of stratospheric aerosols, although lidars have been used very successfully in the past to characterize the stratospheric aerosol layers following volcanic eruptions (e.g. [2, 3]).

Several papers have investigated the influence of aerosols on differential absorption lidar ozone measurements in the past [4, 5, 6]. Most of them are, however, focused on tropospheric measurements involving wavelengths closer to the ozone absorption peak and aerosols different from stratospheric aerosols. This paper will give results of our careful assessment of the errors introduced by volcanic aerosols in DIAL measurements of stratospheric ozone.

The most common DIAL setup uses the elastic backscattered lidar return signals $P(r, \lambda)$ at the wavelengths 308 and 353 nm, where 308 nm light is strongly absorbed by ozone. The final expression for the ozone concentration, $n_{O_3}(r)$ can be written as:

$$n_{O_3}(r) = \frac{1}{2 \Delta \sigma_{O_3}} \left\{ \underbrace{\frac{d}{dr} \ln \left(\frac{P(r, 353)}{P(r, 308)} \right)}_{(a)} - \underbrace{\frac{d}{dr} \ln \left(\frac{\beta(r, 353)}{\beta(r, 308)} \right)}_{(DBT)} \right\} \quad (1)$$

$$- \frac{1}{\Delta \sigma_{O_3}} \left\{ \underbrace{n_{Ray}(r) \Delta \sigma_{Ray}}_{(b)} - \underbrace{\Delta \alpha_{Mie}(r)}_{(DET)} \right\}$$

Here $P(r, \lambda)$ are the measured return signals, $\Delta \sigma_{O_3} = \sigma_{O_3}(308) - \sigma_{O_3}(353) \approx \sigma_{O_3}(308)$ is the ozone differential absorption cross section and $\beta(r)$ is the atmospheric volume backscatter coefficient for elastic (Mie and Rayleigh) backscattering. $n_{Ray}(r)$ is the number density of Rayleigh scatterers, with differential extinction cross section $\Delta \sigma_{Ray} = \sigma_{Ray}(308) - \sigma_{Ray}(353)$. $\Delta \alpha_{Mie} = \alpha_{Mie}(308) - \alpha_{Mie}(353)$ is the aerosol differential extinction. The term labeled (a) involves the measured signals, and is usually the largest of the four terms. Term (b) describes the difference in Rayleigh extinction from air molecules. It is fairly small above 15 km and can be accounted for using an air density profile from nearby balloonsonde stations or a model atmosphere. The error introduced in the reported ozone concentration is generally less than 1 %.

The two terms labeled (DBT) and (DET) involve aerosols. (DBT) is called differential backscatter term, it describes the different atmospheric backscattering at the two wavelengths. For pure Rayleigh backscattering $\beta(r, 353)/\beta(r, 308) = (308/353)^4$ does not depend on r and the term (DBT) vanishes. When additional Mie scattering from aerosols is present, however, it has to be considered. The last term (DET) describes the difference in atmospheric extinction at the two wavelengths due to aerosols. For the typical low stratospheric background aerosol loading both terms (DBT) and (DET) remain small and can be neglected, however, after a large volcanic eruption especially the term (DBT) can become quite large and both terms cannot be neglected any more. Usually (DBT) is the larger of the two terms.

A variation of the DIAL technique described above uses the Raman shifted returns from Nitrogen at 332 and 385 nm instead of the elastic Rayleigh/Mie returns. In this case the differential backscatter term (DBT) vanishes, as for pure Rayleigh scattering. However the differential extinction term doubles, since significant ozone absorption only takes place on the way from the lidar system to the Raman backscattering event.

Both terms (DBT) and (DET) cannot be estimated from a two wavelength DIAL measurement alone. Additional informations, about aerosol number density and size distribution, or measurements on additional wavelengths are needed. In the following we will estimate how large the terms (DBT) and (DET) typically are, what can be done to correct for them and what errors will remain after an attempted correction.

Stratospheric aerosols resulting from the Pinatubo eruption consist to 99% of $\text{H}_2\text{SO}_4/\text{H}_2\text{O}$ droplets [8] and Mie theory can be used to calculate the single particle Mie cross sections. We calculated the atmospheric Mie backscatter and extinction cross-sections for most wavelengths of interest in stratospheric ozone DIAL measurements: 308 (XeCl), 332 ($\text{XeCl} + \text{N}_2$), 339 ($\text{XeCl} + \text{D}_2$), 353 ($\text{XeCl} + \text{H}_2$), 368 ($(\text{XeCl} + \text{D}_2) + \text{N}_2$) and 385 nm ($(\text{XeCl} + \text{H}_2) + \text{N}_2$), as well as for 532 (Nd:YAG $\times 2$) and 694 nm (Ruby) by integrating over unimodal lognormal size distributions.

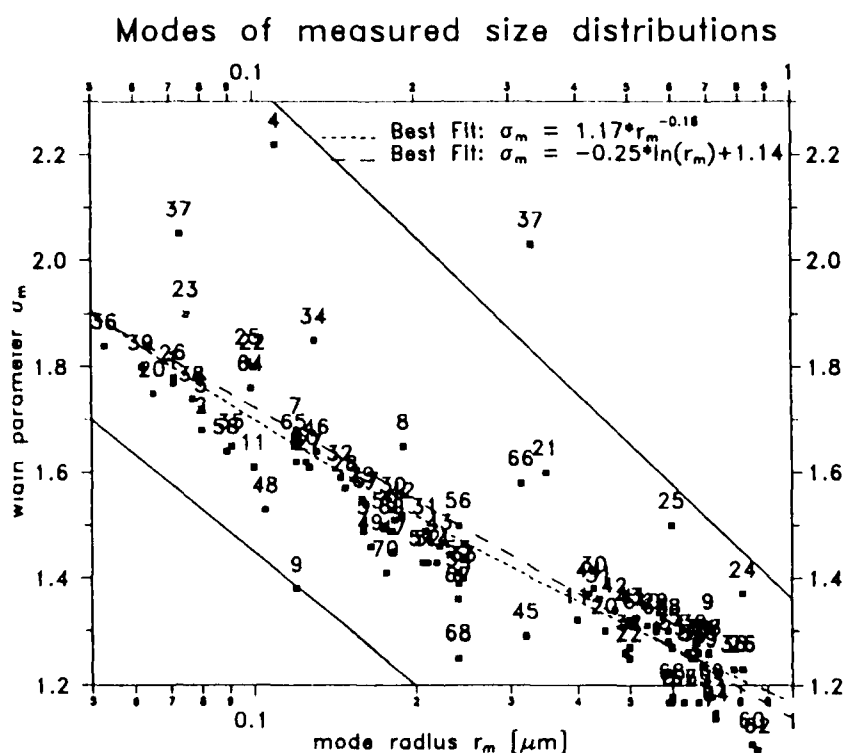


Figure 1: Mode radius and width parameters of lognormal size distributions fitted to distributions measured before and after the El-Chichón and Mt. Pinatubo eruptions. The dashed lines are fits to describe a relation between the width parameter σ_M and the mode radius r_M .

Actual size distributions in the atmosphere can be represented as a combination of unimodal distributions. Figure 1 shows mode radius r_M and width parameter σ_M of unimodal and bimodal distributions that have been obtained by fitting to actually measured distributions [7, 2, 8, 9]. The size distributions fall into two classes: Small particles with a mode radius between 0.05 and 0.25 μm , typical for clear background conditions and enhanced after a volcanic eruption, and large particles with radius between 0.4 and 0.8 μm . The large particles are significant only after a volcanic eruption.

From $\alpha_{Mie}(\lambda)$ calculated at the different wavelengths it is easy to derive the differential Mie extinction and the ozone error resulting from the term (DET). This has been done in Fig. 2 showing the ozone error when the differential extinction term (DET) is neglected, for an aerosol density of 1 cm^{-3} . For the small particle modes neglecting (DET) leads to an overestimation of the ozone concentration. For the larger

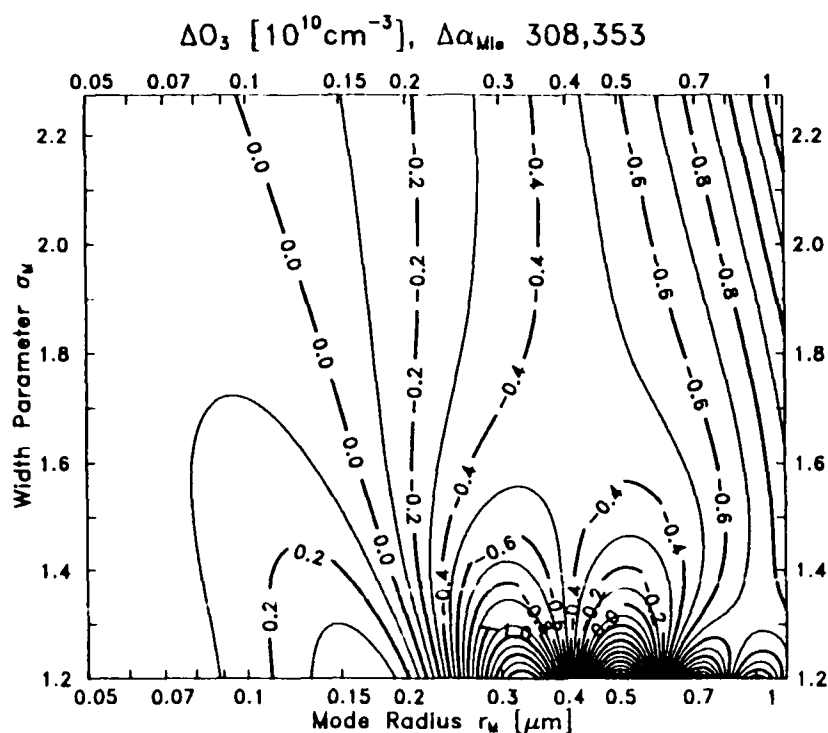


Figure 2: Ozone error when neglecting differential extinction, as a function of mode radius and width parameter. Results are calculated for lognormal size distributions with an aerosol number density of 1 cm^{-3} and a 308/353 nm elastic backscatter DIAL.

particles it can lead to over or underestimation, depending on the exact particle size. Due to oscillations in the large particle region a correction for (DET) is very hard, unless one has very precise knowledge of the particle size distribution or the wavelength dependence of the Mie extinction. Especially for large particles neglecting the differential extinction term seems to be as good as or better than trying to correct for it. Using realistic particle densities we find that for clear stratospheric conditions and a 308/353 nm elastic backscatter DIAL the ozone error when neglecting (DET) is below 5% above 15 km and below 1% above 20 km. In midlatitudes after the Pinatubo eruption the error is rarely above 10% and usually around 5%.

Our results also show that the error due to (DET) is about 30% smaller for a 308, 339 nm elastic backscatter DIAL compared to a 308, 353 nm DIAL. As expected the error for a Raman DIAL transmitting 308, 353 nm is about twice as large as for a 308, 353 nm elastic backscatter system.

Since the differential backscatter term (DBT) depends not only on size and amount of aerosols, but also on their spatial rate of change a more general assessment as for the differential extinction term is not easy. Instead we calculated the size of the differential backscatter term (DBT) for several size distribution profiles measured by balloonsondes over Wyoming [9]. In practice no nearby size distribution profiles will be available, but quite often measurements at a second reference wavelength can be used to estimate the differential backscatter term (DBT) by extrapolation from the two reference wavelengths to the absorption wavelength. As an example Fig. 4 shows the ozone error for a 308/353 nm elastic backscatter lidar when neglecting the differential backscatter term (DBT) completely and when trying to correct for it by using information at a second reference wavelength. Completely neglecting (DBT) can lead to errors over 100%. Trying to correct for (DBT) by using another wavelength will reduce the error to typically under 10%, however at some altitudes the error may still be around 50%.

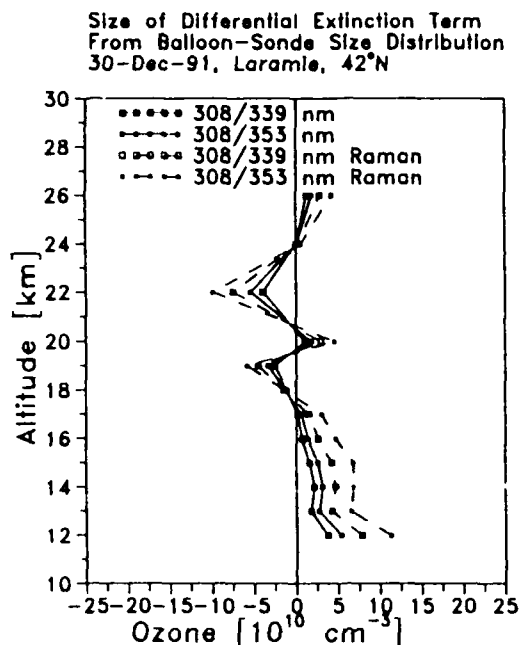


Figure 3: Ozone error when neglecting differential extinction term for different two wavelength DIAL setups. Values have been calculated using a measured size distribution and Mie theory

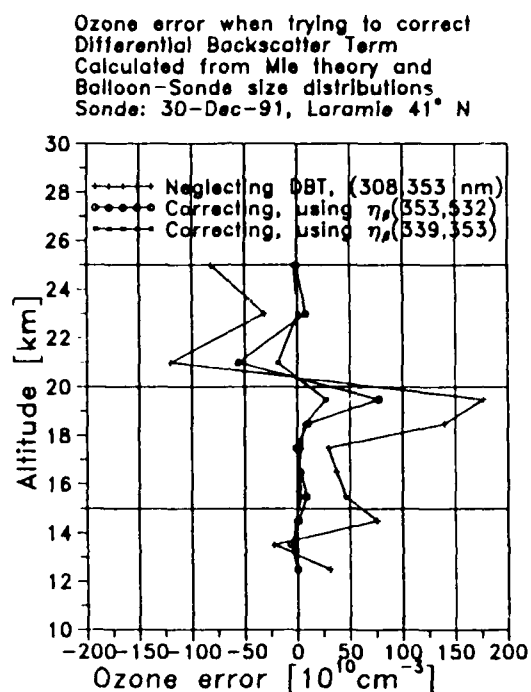


Figure 4: Ozone error when neglecting differential backscatter term and when trying to correct for it, using a second reference wavelength.

References

- [1] M. J. Kurylo and S. Solomon, editors. *Network for the Detection of Stratospheric Change, a Status and Implementation Report*. NASA-UARP and NOAA-CGCP, (1990).
- [2] D. J. Hofmann. "Perturbations to the Global Atmosphere Associated with the El Chichón Volcanic Eruption of 1982". *Rev. Geophys.*, 25(4), 743-759, (1987).
- [3] H. Jäger and W. Carnuth. "The Decay of the El Chichón Stratospheric Perturbation, Observed by Lidar at Northern Midlatitudes." *GRL*, 14, 696-699, (1987).
- [4] Ed V. Browell, Syed Ismail, and S. T. Shipley. "Ultraviolet Dial Measurements of O3 Profiles in Regions of Spatially Inhomogeneous Aerosols" *Appl. Opt.*, 24, 2827, (1985).
- [5] Y. Zhao. "Simplified Correction Techniques for Backscatter Errors in Differential Absorption Ozone Measurements." In *Optical Remote Sensing of the Atmosphere 1991*, pages 275-277, Workshop in Williamsburg, Virginia, Nov. 18-21, 1991, OSA, Washington, D.C.
- [6] A. Papayannis, G. Ancellet, J. Pelon, and G. Mégie. "Multiwavelength Lidar for Ozone Measurements in the Troposphere and Lower Stratosphere." *Appl. Opt.*, 29(4), 467-476, (1990).
- [7] V. R. Oberbeck, E. F. Danielsen, K. G. Snetsinger, and G. V. Ferry. "Effect of the Eruption of El Chichón on Stratospheric Aerosol Size and Composition." *GRL*, 10(11), 1021-1024, (1983).
- [8] T. Deshler, D. J. Hofmann, B. J. Johnson, and W. R. Rozier. "Balloonborne Measurements of the Pinatubo Aerosol Size Distribution and Volatility at Laramie, Wyoming During the Summer of 1991." *GRL*, 19(2), 199 - 202, (1992).
- [9] T. Deshler. Private communication, Sept. 1992.

New Lidar for the Network for the Detection of Stratospheric Change - Mauna Loa Observatory : System Description

T. Daniel Walsh, L. Oscar Lindquist, Mary L. White,
Apostolis Deslis, and I. Stuart McDermid

Jet Propulsion Laboratory
California Institute of Technology
Table Mountain Facility
Wrightwood, CA 92397

Introduction

The development of differential absorption lidar (DIAL) systems for long-term measurements of stratospheric ozone and for potential inclusion in the Network for the Detection of Stratospheric Change (NDSC) [Kurylo and Solomon, 1990] began at JPL in 1986. The DIAL system at the JPL Table Mountain Facility (TMF, 34.4° N, -117.7° W) was developed specifically to have the characteristics suitable for long-term measurements as proposed for NDSC. Regular measurements of stratospheric ozone concentration profiles commenced in February 1988, with temperature measurements beginning in January 1990 and aerosol measurements in July 1991. This system has been fully described elsewhere [McDermid *et al*, 1990]. The new system incorporates some new developments compared to the TMF system and details of the new design are presented.

Mauna Loa Lidar - Mobile Facility

Based on the successful demonstration and evaluation of the DIAL system at TMF, a new lidar was commissioned for deployment at the NOAA Mauna Loa Observatory, Hawaii, station of the NDSC and for participation in the Correlative Measurements Program to support the Upper Atmosphere Research Satellite (UARS). This system is temporarily housed in a mobile facility pending the completion of the new NOAA observatory at Mauna Loa. The mobile laboratory comprises two custom built, 40' long trailers. The layout of the lidar system within these trailers is shown in fig. 1. The laser transmitter and optical receiver systems are located in one trailer and the data acquisition and analysis systems, together with the laser heat exchanger and a general work area, comprise the second trailer. This arrangement helps to isolate the optical components from the vibrations caused by the heat exchanger and by personnel moving about. The design of the trailers allows them to be

moved intact by road or sea and the wheels can be removed for transportation by air or container ship.

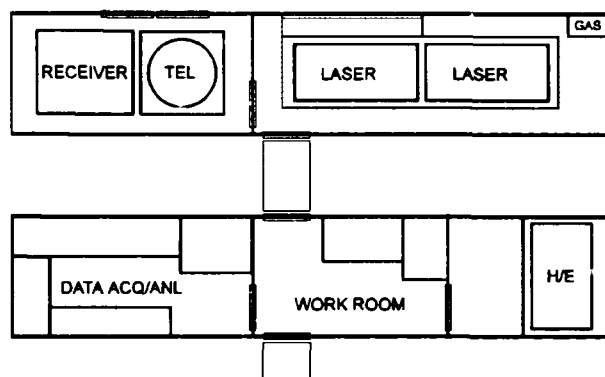


Figure 1. Mobile lidar laboratory layout.

The framework of the laboratories is sufficiently strong that it can be lifted, with the lidar equipment in place, by a helicopter or crane.

Laser Transmitter

Similar to the TMF lidar, the MLO system uses a 100 Watt, tuned, low-divergence, xenon chloride excimer laser for the transmitter. The laser system utilizes two LPX series lasers from Lambda Physik which were specially designed to match the required

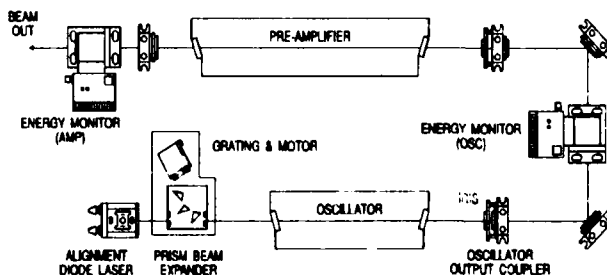


Figure 2. LPX-150 oscillator-amplifier.

specifications for the lidar experiment. Each of the LPX lasers comprises two separate excimer laser discharge units. The first laser, LPX-150, is set up in an oscillator-amplifier configuration, as shown in fig. 2, and offers the capability of tunable, narrow-bandwidth, high-power laser operation. The oscillator, which is based on the Lambda Physik LPX-120 laser, can be tuned in wavelength by a motor controlled grating in conjunction with a prism beam expander. The output from this unit is then used to injection-lock a power amplifier which is based on the Lambda Physik LPX-200 laser and which is designated as the pre-amplifier in Fig. 2. The complete operation of these lasers, including the temporal synchronization, is controlled by a micro-computer (PC) and a fiber-optic local area network (LAN).

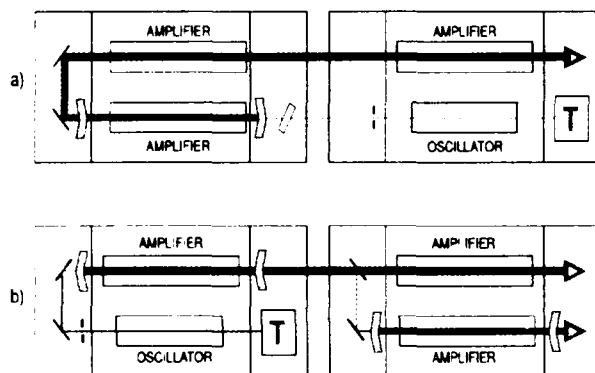


Figure 3. Complete laser system

The second laser unit, LPX-2220, contains two power amplifiers, each based on the Lambda Physik LPX-200 laser. There are a number of possible configurations for the set up of the complete four-laser system but only three are relevant to this experiment. Two of these options are shown in fig. 3. In fig. 3(a) the oscillator injection-locks the pre-amplifier which is then single-passed through two power amplifiers in series. In theory this arrangement should provide the highest output power. However, the same arrangements are possible with the laser system in the TMF lidar [McDermid *et al.*, 1991] and it has been found that losses between the two final amplifiers, caused for example by dirty windows, can severely reduce the final output power and the arrangement shown in fig. 3(b) provides a more consistent output power level. In this arrangement the output from the pre-amplifier is split with the majority of the energy, >95%, being single-passed through the power amplifier. The remaining energy is then used to injection lock the

other power amplifier. The output from the injection locked amplifier is typically about 75% of that from the single-passed amplifier. The configuration in fig. 3(b) is the preferred arrangement when the system is operated with XeCl in all discharge volumes. In this situation the output from the injection locked amplifier is passed through a cell containing high purity hydrogen at approximately 500 psig in order to generate the reference wavelength. The 353.2 nm wavelength is then generated by the first Stokes stimulated Raman shift by hydrogen and photon conversion efficiencies on the order of 50% can readily be achieved. It is possible to operate the LPX-2220 with different gas mixtures in each of the discharges, i.e., a two-color mode. For this application one discharge would act as a single-pass amplifier for XeCl as in fig. 3(b). The second discharge would operate with XeF and an unstable resonator cavity, again similar to fig. 3(b) but with no injection seeding. The two-color mode of operation provides more energy at the reference wavelength at the expense of some energy at 307.9 nm. For the DIAL experiment, normally only about 10% of the energy is required at the reference wavelength compared to the probe wavelength. However, the Raman augmentation technique may require higher energy at the reference wavelength to obtain good signal-to-noise ratios in the Raman reference channel. Since the reference wavelengths from Raman shifting the XeCl fundamental in H₂ or from the XeF fundamental are quite close, the only elements of the optical detection system that need to be changed to switch between these wavelengths are the interference filters.

In order to reduce further the divergence of the output laser beams they are expanded by a factor of 5 before being transmitted into the atmosphere. This is important since it allows the field-of-view of the receiver telescope to be reduced which, in turn, reduces the size of the image in the plane of the chopper.

Receiver System

The receiver foreoptic is a 1-meter aperture Dall Kirkham telescope with a focal ratio of F/8. The obscuration of the primary aperture is less than 10% resulting in an active collection area of approximately 7000 cm². The telescope mirror reflectivities are >90% for all of the UV wavelengths used.

A relay system comprising a field lens and an achromatic triplet is used to focus the telescope output onto the plane of the chopper blade. This is indicated as L1 in fig. 4. A second lens, L2, then collimates the received light. The component wavelengths, 308, 332,

353 and 385 nm, are separated by a series of long-wave pass dichroic beamsplitters and interference filters. While the beamsplitters, S1-S3, are shown to operate at 45° in fig. 4 they actually are used at 15° incidence in order to obtain the sharpest wavelength transition from >98% reflectivity to >80% transmission. The 308 and 353 nm wavelengths are further split in the ratio 99:1 by beamsplitter S4 to provide the high and low intensity channels. The lower efficiency for Raman scattering is largely compensated by not attenuating these channels even though they operate at low altitudes.

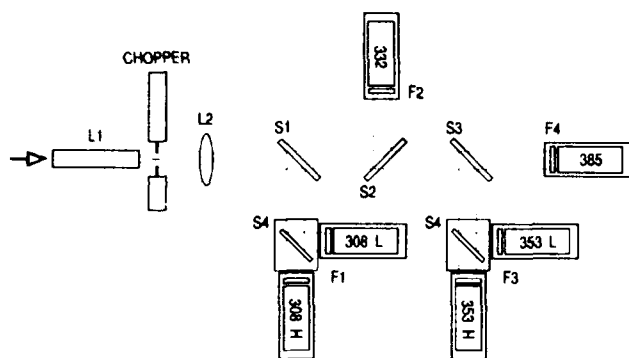


Figure 2. Schematic diagram of the receiver optical detection system.

Data Acquisition System

The lidar returns are detected using photomultipliers, EMI 9883QAM, operating in the photon counting mode. The two photomultipliers for the high intensity channels are electronically gated in addition to the mechanical chopping. A block diagram of the data acquisition electronics is shown in fig. 5.

The data acquisition system employs a PC-based photon counting/MCS system. This allows counting to much higher rates, 250 MHz, than in the TMF system and also ensures absolute synchronization between all of the counting channels.

Various aspects of the lidar system operation and data acquisition are controlled by individual computers. For example, each laser has its own control computer, as has the beam steering and alignment monitoring system, and the photon counting system. These separate computers are connected via an ethernet based local area network so that data can be readily transferred from one machine to another and also allowing real-time analysis of the results using an independent workstation.

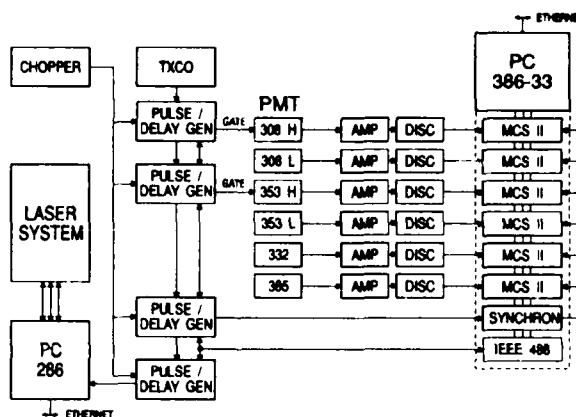


Figure 5. Block diagram of the receiver and data acquisition system electronics.

Summary

This paper will present a detailed description of the design of this new lidar system. Some examples of measurements of stratospheric ozone, temperature and aerosol profiles, and the results of some preliminary intercomparisons will be given elsewhere [McDermid and Walsh, 1993].

Acknowledgment. The work described in this paper was carried out at the Jet Propulsion Laboratory, California Institute of Technology, under a contract with the National Aeronautics and Space Administration.

References.

- Kurylo, M. J. and S. Solomon, 1990, *Network for the Detection of Stratospheric Change - A Status and Implementation Report*, Issued by NASA Upper Atmosphere Research Program and NOAA Climate and Global Change Program.
- McDermid, I. S., S. M. Godin, and L. O. Lindqvist, 1990, Ground-based laser DIAL system for long-term measurements of stratospheric ozone, *Appl. Opt.*, **29**, 3603-3612.
- McDermid, I. S., D. A. Haner, M. M. Kleiman, T. D. Walsh and M. L. White, "Differential Absorption Lidar Systems for Tropospheric and Stratospheric Ozone Measurements," *Opt. Eng.* **30**, 22-30 (1991).
- McDermid, I. S. and T. D. Walsh, "New Lidar for the Network for the Detection of Stratospheric Change - Mauna Loa Observatory: Initial Results," *Optical Remote Sensing of the Atmosphere*, This Volume (1993).

New Lidar for the Network for the Detection of Stratospheric Change - Mauna Loa Observatory : Initial Results

I. Stuart McDermid and T. Daniel Walsh

Jet Propulsion Laboratory
California Institute of Technology
Table Mountain Facility
Wrightwood, CA 92397-0367

Introduction

A new lidar system capable of simultaneous measurements of stratospheric ozone, temperature and aerosol profiles has been successfully built and tested. A detailed description of the design and implementation this new system will be given elsewhere [Walsh *et al.*, 1993]. In this paper we will present some initial measurements made with this lidar and some intercomparisons with the existing stratospheric lidar at the JPL-Table Mountain Facility (TMF). Ozone profiles are obtained using the differential absorption lidar (DIAL) technique extended to include two Raman channels for aerosol correction [Singh *et al.*, 1992]; temperature profiles are obtained from Rayleigh and Raman scattering lidar; aerosol backscatter ratio profiles are obtained from comparison of the elastic and Raman backscattered lidar signals.

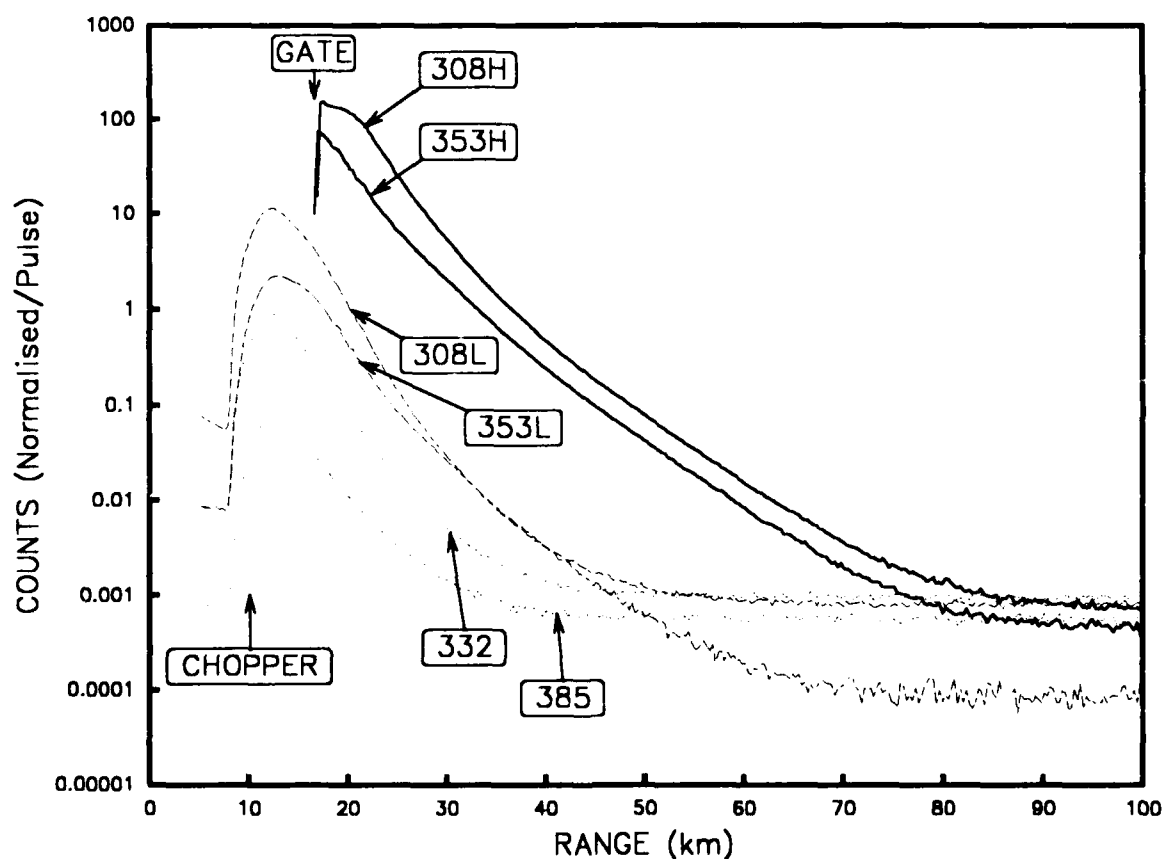


Figure 1. Raw data curves obtained for the six receiver channels, 10/02/92.

Results

Several changes were made in the design of the new lidar compared to the existing system at TMF. Two extra channels were added to the detection system to receive the lidar returns from Raman scattering by atmospheric nitrogen in order to try and eliminate the problems caused by aerosol scattering resulting from the eruption of Mt. Pinatubo. Also, a chopper was implemented in an effort to reduce the signal-induced-noise caused by the intense lidar returns from low altitudes [McDermid *et al.*, 1990]. Figure 1 shows the first signals obtained with this system for each of the six receiver channels. These data are the result of a one hour integration ($\sim 700,000$ laser pulses) using $2 \mu\text{s}$ (300 m) range cells and are normalized by dividing the total counts by the number of pulses. The suffixes, H and L, on the plot labels refer to the high and low intensity receiver channels. In addition to the mechanical chopping of the return signal, the high intensity channels are also electronically gated. The turn on of the chopper and the electronic gates are indicated in figure 1. The 308H channel shows signs of saturation at a normalized count of about 150, figure 1. This corresponds to an overall system response of approximately 200 MHz. The Raman channels, 332 and 385 nm, show sufficient signal intensity to obtain the ozone profile in the region of maximum aerosol scattering, i.e., between 15 and 25 km.

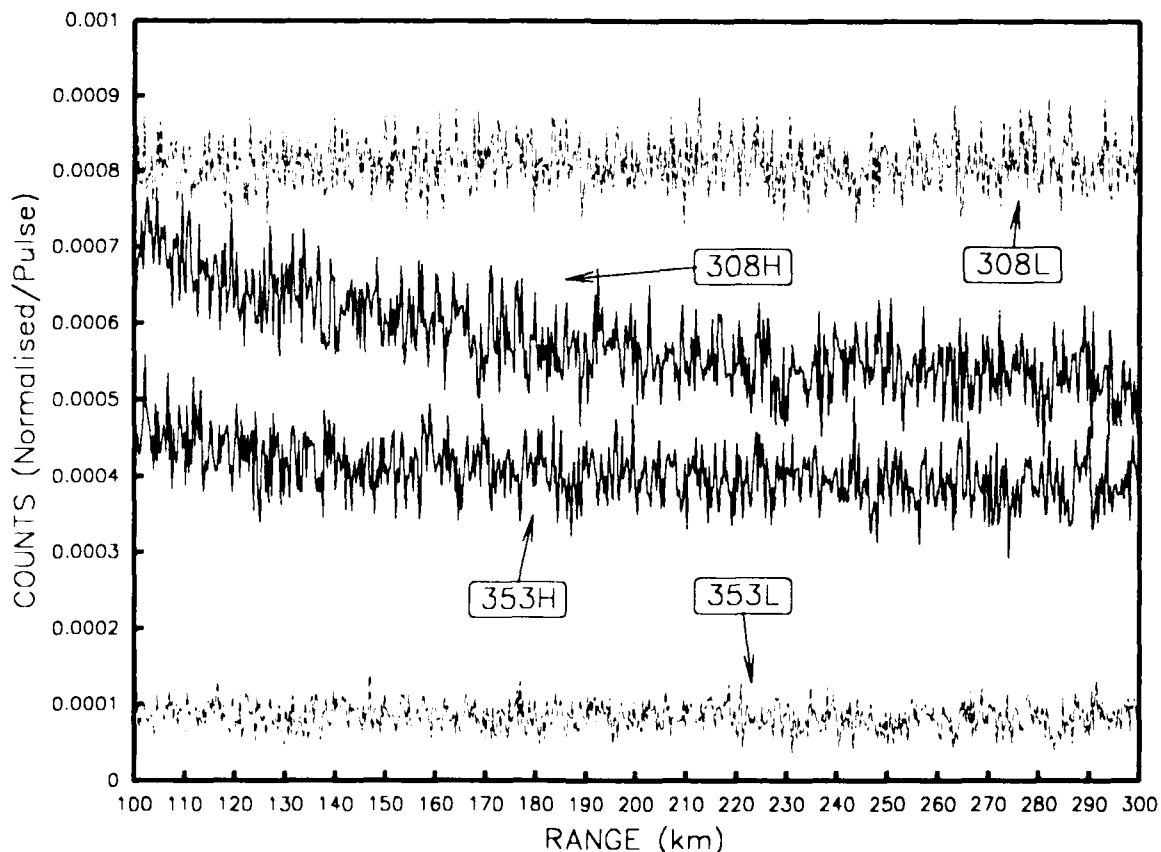


Figure 2. Background signal levels, greatly expanded. The data for the 332 and 385 nm channels have been omitted for clarity but are similar to those for the 308 and 353 nm low intensity channels.

The background signal levels have been significantly expanded and are shown in figure 2. This plot shows that there is still some residual signal-induced-noise in the 308H background but it is greatly reduced, compared to the existing TMF lidar system, by the implementation of the chopper. The background levels in the other channels are completely flat. Further optimization of the chopper and electronic gate timing may reduce the curvature in the 308H background more but even at this level its impact on the ozone profile derivation is negligible.

The ozone profile derived from the 308/353 nm raw data in figures 1 and 2 is shown in figure 3. At this point, the analysis of the 332/385 nm Raman data was not implemented and the aerosol effects below 25 km are clearly evident in this plot. It should be emphasized that this is the very first profile obtained with the new system and the integration time was only 1 hour. The results in figure 3 are very encouraging and it is anticipated that good ozone profiles up to approximately 60 km altitude will be possible with the system.

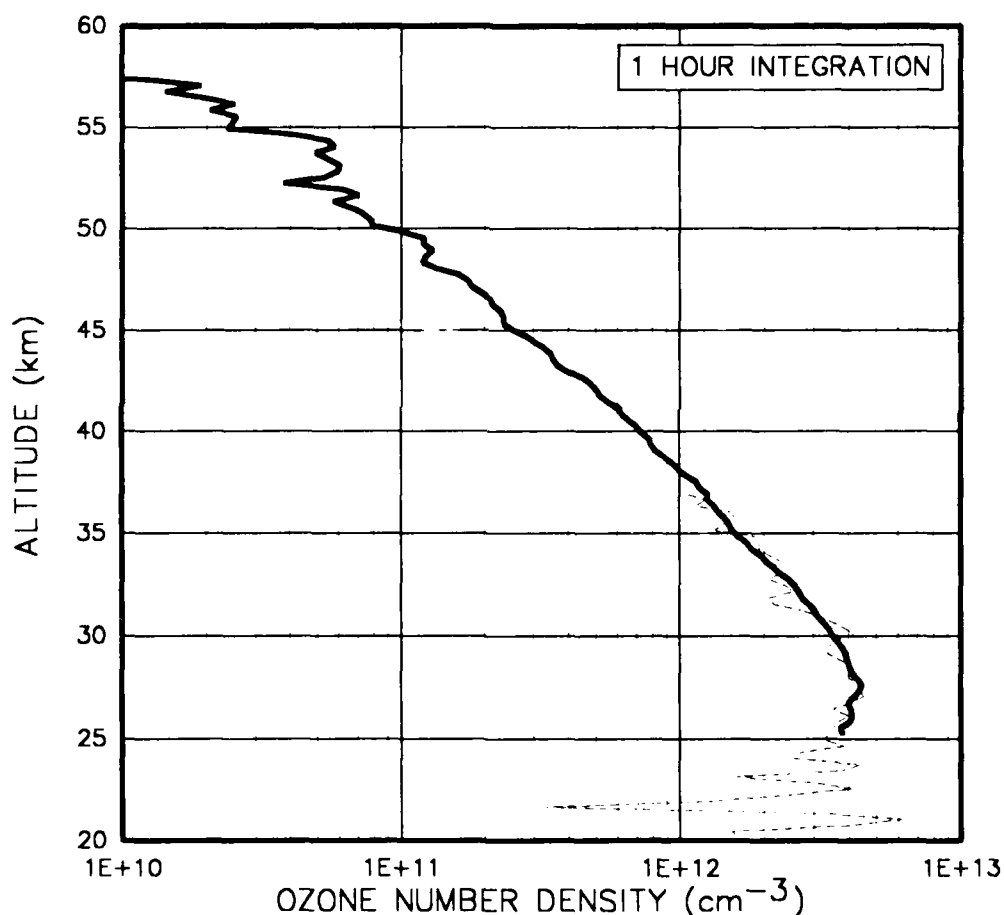


Figure 3. Ozone profile obtained from the raw data in fig. 1, October 2, 1992. Solid line - high intensity 308/353 nm data; dashed line - low intensity 308/353 nm data, note aerosol interference.

A temperature profile derived from the 353 nm raw data in figures 1 and 2 is shown in figure 4. While this profile terminates at 60 km altitude it is anticipated that temperature measurements to significantly higher altitudes, >75 km, will be possible with this system. Preliminary comparison of the results shown in figures 3 and 4 with results from the existing

TMF lidar and with the CIRA model atmosphere show good agreement. The new system will undergo a period of intense intercomparison before it is moved to the NDSC station at Mauna Loa, Hawaii. Some of the results of these intercomparisons will be presented.

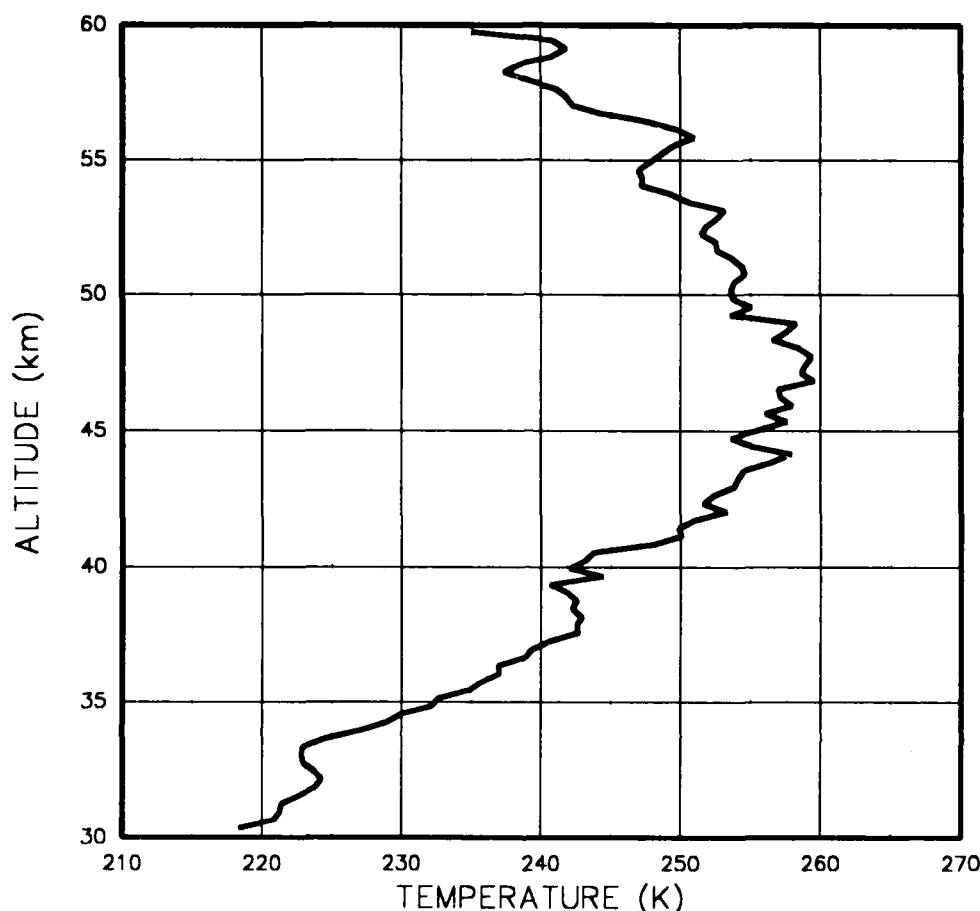


Figure 4. Temperature profile obtained from the 353 nm high intensity data in fig. 1.

Acknowledgments. The work described in this paper was carried out at the Jet Propulsion Laboratory, California Institute of Technology, under a contract with the National Aeronautics and Space Administration. We are grateful for the assistance of Oscar Lindquist and Marty Schmoie in obtaining the results presented here.

References:

- McDermid, I. S., S. M. Godin and L. O. Lindquist, "Ground-based laser DIAL system for long-term measurements of stratospheric ozone," *Appl. Opt.*, **29**, 3603-3612 (1990).
- Singh, U. N., T. J. McGee, M. Gross, W. S. Heaps and R. Ferrare, "A New Raman Lidar Technique for Measuring Stratospheric Ozone in the Presence of Volcanic Aerosols," 16th International Laser Radar Conference, Cambridge, MA, Paper B4 (1992).
- Walsh, T. D., L. O. Lindquist, M. L. White, A. Deslis and I. S. McDermid, "New Lidar for the Network for the Detection of Stratospheric Change - Mauna Loa Observatory: System Description," *Optical Remote Sensing of the Atmosphere 1993*, This Volume.

Thursday, March 11, 1993

Aerosols 1

ThA 8:00am–9:40am
Salon F

Horst Jager, *Presider*
Fraunhofer Institute, Germany

LIDAR MEASUREMENTS OF STRATOSPHERIC AEROSOLS
AT MAUNA LOA OBSERVATORY: 1974 TO PRESENT

T. E. DeFoor and S. Ryan

Mauna Loa Observatory
Climatic Monitoring for Diagnostic Change
National Oceanic and Atmospheric Administration, ERL
Hilo, Hawaii

D. J. Hofmann and E. G. Dutton

Climatic Monitoring for Diagnostic Change
National Oceanic and Atmospheric Administration, ERL
Boulder, Colorado

The measurement of stratospheric aerosols using a ruby lidar system has been an ongoing program at the National Oceanic and Atmospheric Administration, Climate Monitoring and Diagnostic Laboratory, Mauna Loa Observatory (MLO) since 1974. The 18 year MLO stratospheric aerosol record includes measurements of the injection growth and decay of aerosols following two of this centuries more important stratospheric aerosol producing eruptions: El Chichon (Mexico, 1982) and Mt. Pinatubo (Philippines, 1991). Also evident in the MLO lidar record are a number of lesser events which include the 1980 eruption of Mt. Saint Helens, the 1981 eruption of Nyamuragira, and the 1984 eruption of Nevado del Ruiz. Apparent, too, is a relatively quiescent period between 1985 and 1991 during which stratospheric aerosols decayed to near background aerosol levels. During this period, stratospheric aerosol backscatter ranged from as high $1\text{E-}2 \text{ sr-1}$ (El Chichon) to as low as $6\text{E-}5 \text{ sr-1}$.

Precision multi-wavelength aerosol optical depth measurements were also made over much of the same period as the MLO lidar record. Because of MLO's special location in the tropical mid-Pacific at 3400 meters elevation, which is above most of the atmospheric water vapor and aerosols, much useful information can be gained through the comparison of these two records.

THE PINATUBO ERUPTION IN RELATION TO THE EL CHICHON EVENT AND THE STRATOSPHERIC BACKGROUND LOAD

H. Jäger

Fraunhofer Institute for Atmospheric Environmental Research, IFU,
Kreuzeckbahnstr. 19, D-8100 Garmisch-Partenkirchen, Germany, 0049-8821-183-193

INTRODUCTION

Long-term records of the stratospheric aerosol layer exhibit periods of low and high aerosol load. Both, the background periods and the volcanically perturbed periods, are of interest. Long-term lidar records, which cover up to two decades (e.g. DeFoor, 1993), show that the variability of the stratospheric aerosol content spans more than two orders of magnitude. Our interest is not only devoted to spectacular volcanic perturbations of the stratosphere. Of course, such events provide large signals, not only to our lidar systems, but also to atmospheric chemistry and radiation models; but the highly perturbed situation is not the normal state of the stratosphere. This is rather a state of more or less aged volcanic load. But there are also periods which are not affected by the build-up and the decay of volcanic perturbations. Such background periods have to be studied carefully to extract information on other sources of the stratospheric aerosol. Such sources might be the diffusion of sulphurous precursor gases into the stratosphere or convective processes, and, in addition, we cannot rule out sources resulting from anthropogenic activities.

OBSERVATIONS OF PERTURBATIONS

The investigation of the stratospheric sulphate aerosol layer by lidar at Garmisch-Partenkirchen began in late 1976. Since then an almost uninterrupted record exists. Until 1990 a ruby laser was used as the emitter which was then replaced by a Nd:YAG laser. At present backscattering is received by a 52 cm Casssegrain telescope at 532 nm and recorded by photon counting. Figure 1 shows two major perturbations to the stratosphere by the eruptions of El Chichón (4 April 1982) and Pinatubo (15 June 1992).

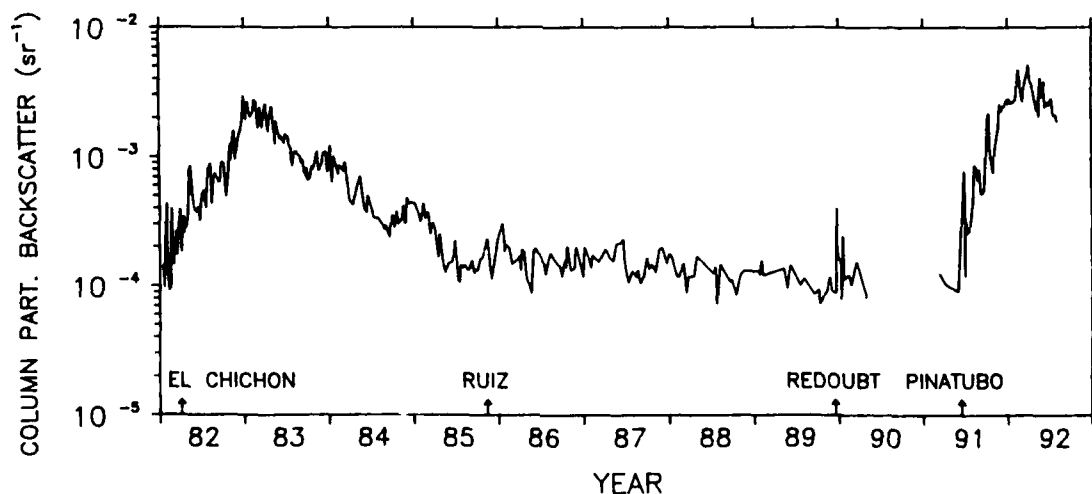


Fig. 1. Time variation of the vertically integrated particle backscattering at 694 nm (integration from tropopause + 1 km to layer top).

The first observation at Garmisch-Partenkirchen of a cloud related to the Pinatubo eruption was seen on July 1, 1991 (Jäger, 1992). Since then the build-up to one of the largest perturbations in the stratosphere in this century was observed continuously. Figure 2 shows a Pinatubo profile from February 1992 when the load from the Pinatubo eruption was at a maximum.

In Figure 3a the period 1991/92 is shown as a contour plot of the lidar backscatter ratio (ratio of measured total backscatter to calculated molecular backscatter) at 532 nm, in contrast to Figure 3b which shows the El Chichón perturbation in 1982/83. In this case the values were originally measured at 694 nm and were recalculated for the 532 nm wavelength to allow a direct comparison. The aerosol model involved in these conversions has been described by Jäger and Hofmann (1991).

A comparison of these two contour plots shows that the Pinatubo effect exceeded the El Chichón effect in northern midlatitudes, as might be expected, in that the Pinatubo eruption injected almost 3 times more SO_2 into the stratosphere than the El Chichón eruption (Bluth et al., 1992); that seems to be the only major difference. There are, however, many similarities: the early arrival, within a few weeks of the respective eruption, in the range below 20 km; the observation of very dense clouds above 20 km after about 4 months during a regime of reversed summer winds (easterlies); the merging into one deep layer after the change to the winter wind regime (westerlies); the maximum appearing after 8 months, for the Pinatubo eruption, and after 9 months for the El Chichón eruption; and finally a parallel downward trend of the lower contours and a stabilization of the maximum at between 18 and 19 km about a year after the respective eruption.

We can conclude that the transport and dispersion of stratospheric injections follow common patterns. The build-up of a perturbation can, therefore, be predicted, based on a knowledge of previous eruptions at similar latitudes and seasons.

THE BACKGROUND PERIOD

The decay of the El Chichón perturbation was terminated by the Ruiz eruption (of secondary magnitude) in Colombia in November 1985. The years following were not affected by volcanism, except for some rather sporadic observations of the marginal Redoubt eruption (Alaska, December 1989), until the Pinatubo event.

This period can be regarded as a background period, although a certain decay trend can be seen in Figure 1 between 1987 and 1990. The higher stratospheric aerosol content during this period in comparison to an earlier background period between 1977 and 1979 has already been discussed (Jäger, 1991). The 1987/90 decay of the stratospheric mass load (derived from lidar measurements applying an aerosol model, Jäger and Hofmann, 1991)

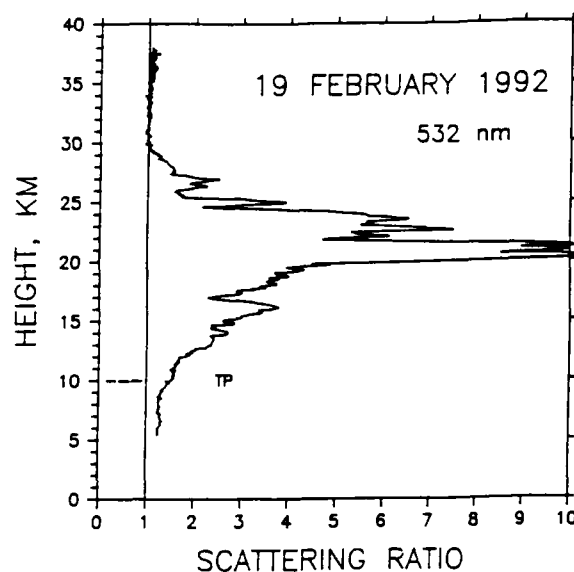


Fig. 2. Profile of the scattering ratio taken at the maximum of the Pinatubo perturbation.

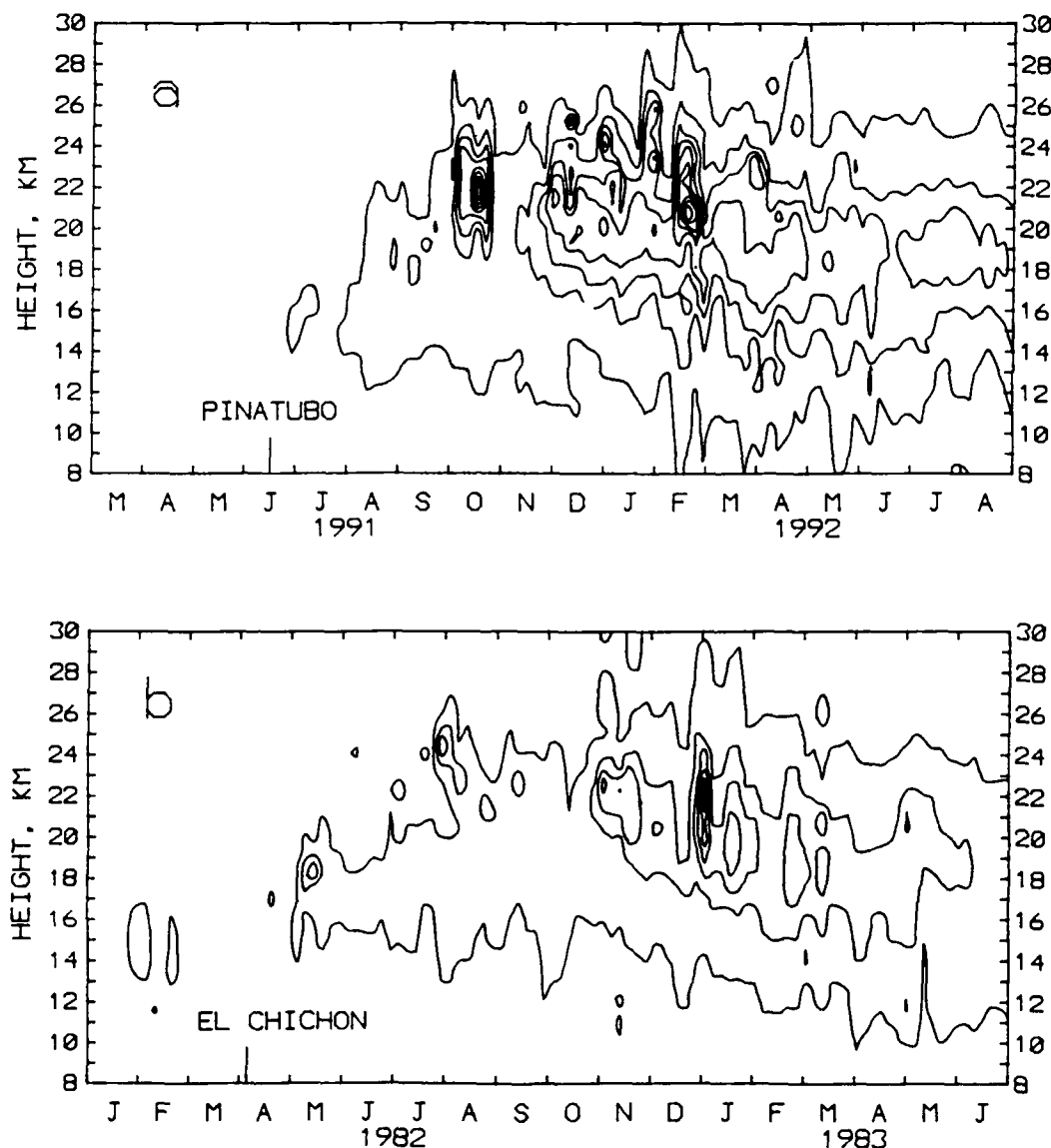


Fig. 3. Contours of the backscatter ratio at 532 nm, starting at 1.3 with increments of 1.

was analysed by comparing the following layers: tropopause up to 15 km, 15 to 20 km, 20 to 25 km and 25 to 30 km. Figure 4 shows the calculated percent-per-year decrease within these ranges; the fastest decay is seen in the uppermost layer, the slowest decay in the lowermost layer.

These findings are not in accord with the fact that the troposphere must be regarded a sink for stratospheric aerosols. The observed decay values, which decrease from the top to the bottom of the stratosphere, indicate that, at least at northern midlatitudes, a source of aerosols or precursor gases might exist in the troposphere or lower stratosphere. Hofmann (1991) recently discussed the possibility that the growing jet air traffic could be responsible for the increase in stratospheric background aerosol load observed over the past three decades. Exhaust gases from kerosene jet fuel are produced mainly at tropopause level or in the lower stratosphere at middle and high latitudes, and contain enough sulphur (up to 0.3% allowed, IATA Amendment No.1, 1988) to increase appreciably the aerosol load.

CONCLUSIONS

Both the equatorial eruptions of El Chichón and Pinatubo have so far followed the same dispersion pattern. This allows us to predict that the decay of the Pinatubo perturbation will still be observable at northern midlatitudes until 1996. Considering the stratospheric mass loads at northern midlatitudes, the Pinatubo eruption exceeded the El Chichón eruption by about 50% and the 1990 background by a factor of about 30. The investigation of stratospheric background periods is likewise important for estimating contributions other than natural ones to the stratospheric aerosol load. An analysis of the period preceeding the Pinatubo eruption indicates that possibly anthropogenic sources are adding to a steady increase in the stratospheric background aerosol load.

There is evidence that stratospheric aerosols not only interfere with the atmospheric radiation budget but also affect the stratospheric ozone layer through heterogeneous reactions on the surface of aerosol particles, involving reactive compounds of anthropogenic origin. Increases in stratospheric aerosols, even at a background level, have to be studied very carefully in order to estimate future effects of the growing anthropogenic contamination in the stratosphere.

REFERENCES

- Bluth, G.J.S., S.D. Doiron, Ch.C. Schnetzler, A.J. Krueger, and L.S. Walter, Global tracking of the SO₂ clouds from the June 1991 Mount Pinatubo eruptions, *Geophys. Res. Lett.*, 19, 151-154, 1992.
- DeFoor, Th.E., Lidar measurements of stratospheric aerosols at Mauna Loa Observatory: 1974 to present, *Technical Digest of Optical Remote Sensing of the Atmosphere*, this volume, 1993.
- Hofmann, D.J., Aircraft sulphur emissions, *Nature*, 349, 659, 1991.
- Jäger, H., Lidar observed trend in stratospheric background aerosol, *Technical Digest of Optical Remote Sensing of the Atmosphere*, 1991 (Optical Society of America, Washington, D.C.), Vol. 18, 153-155, 1991.
- Jäger, H. and D. Hofmann, Midlatitude lidar backscatter to mass, area, and extinction conversion model based on in situ aerosol measurements from 1980 to 1987, *Appl. Opt.* 30, 129-138, 1991.
- Jäger, H., The Pinatubo eruption cloud observed by lidar at Garmisch-Partenkirchen, *Geophys. Res. Lett.*, 19, 191-194, 1992.

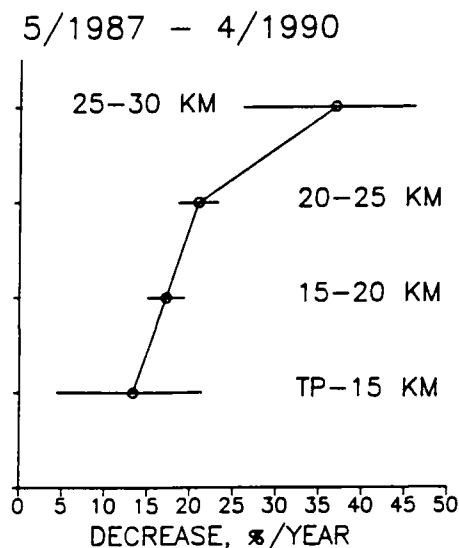


Fig. 4. Decrease in the column particle mass at background level between 1987 and 1990.

Evolution of Pinatubo and Cerro Hudson Aerosol Over the Antarctic During the 1991 Austral Spring

Michael C. Pitts

Science Applications International Corporation (SAIC)

1 Enterprise Parkway

Hampton, VA 23666 [804-864-2693]

Larry W. Thomason

NASA Langley Research Center

Atmospheric Sciences Division, Mail Stop 475

Hampton, VA 23681-0001 [804-864-6842]

William P. Chu

NASA Langley Research Center

Atmospheric Sciences Division, Mail Stop 475

Hampton, VA 23681-0001 [804-864-2675]

Introduction

The eruption of Mt. Pinatubo (15.1°N, 120.4°E) in the Philippines on June 15, 1991, injected large amounts of SO₂ into the stratosphere as high as 30 km (McCormick, 1992). The SO₂ underwent rapid conversion to H₂SO₄/H₂O aerosol, and after the first few weeks following the eruption, the aerosol had dispersed in a band over the tropics between 20°S and 30°N. In subsequent weeks, substantial amounts of aerosol were transported to the mid-latitudes of both hemispheres, and by early September, satellite observations indicated a layer of Pinatubo aerosol centered near 21 km had reached as far south as the outer edge of the Antarctic polar vortex (McCormick and Veiga, 1992). In addition, the Cerro Hudson volcano in southern Chile (45.92°S, 73.0°W) erupted intermittently from August 12-15, 1991, sending significant amounts of SO₂ into the lower stratosphere, primarily below 14 km. Satellite observations indicated that the Cerro Hudson cloud initially became embedded in a predominantly westerly flow, and after two weeks was dispersed in a band between 50°S and 65°S (Doiron et al., 1991). Thus, at the onset of the 1991 Austral spring, two distinct volcanic aerosol clouds were present in the stratosphere over the polar regions of the Southern Hemisphere. In this study, we utilize SAM II and SAGE II data to identify and track the movement of these volcanic clouds and study transport processes associated with the Antarctic polar vortex during the spring.

SAM II and SAGE II DATA

The Stratospheric Aerosol Measurement II (SAM II) and Stratospheric Aerosol and Gas Experiment II (SAGE II) satellite instruments were designed by NASA to monitor aerosols and other constituents of the atmosphere. Both of these experiments use the solar occultation technique to measure vertical profiles of attenuated sunlight through the limb of the Earth during each sunrise or sunset encountered by each respective satellite. The SAM II instrument has been making measurements of aerosol extinction in the polar regions since its launch in October 1978 (McCormick et al., 1979). These measurements have provided valuable information on the stratospheric aerosol layer in the high latitudes, including the effects of volcanic eruptions (e.g.

Kent and McCormick, 1984; Kent et al., 1985), and the occurrences of polar stratospheric clouds (e.g. McCormick et al., 1982). The SAGE II sensor has been making measurements of aerosol extinction since its launch in October 1984 (Mauldin et al., 1985). SAGE II measurements have provided an excellent database for global studies of aerosols (e.g. Kent and McCormick, 1988) and recently have proven invaluable in studies of the evolution of Pinatubo aerosol (e.g. McCormick and Veiga, 1992; Thomason, 1992; Trepte and Hitchman, 1992).

Summary of Results

We have studied the spatial and temporal evolution of the Cerro Hudson and Pinatubo volcanic aerosol clouds over the polar regions during the 1991 Austral spring using the SAM II and SAGE II aerosol extinction data. From these data we have generated analyses of aerosol extinction which depict the aerosol distribution from mid-latitudes well into the polar regions. On the basis of these analyses, the Cerro Hudson aerosol can be clearly distinguished from the Pinatubo aerosol and the movement of these separate aerosol clouds can be observed during this time period. Figure 1 shows a latitude-altitude cross-section of SAM II and SAGE II aerosol extinction data from October 1 through October 20, 1991. Pinatubo aerosol is discernible as a tongue of enhanced aerosol stretching from lower latitudes to roughly 60°S , centered at an altitude of about 21 km. Cerro Hudson aerosol occur as a distinct layer of enhanced aerosol below 14 km stretching across the highest latitudes. The white areas below the aerosol clouds represent regions where the instruments could not "penetrate" due to the large optical thickness of the layers above. In comparison, Figure 2 shows a similar cross-section as in Figure 1, except for October 1 through October 20, 1989, a period when the stratosphere was relatively free of volcanic aerosol. Clearly, both the Pinatubo and Cerro Hudson aerosol represent significant perturbations above the background stratospheric aerosol content.

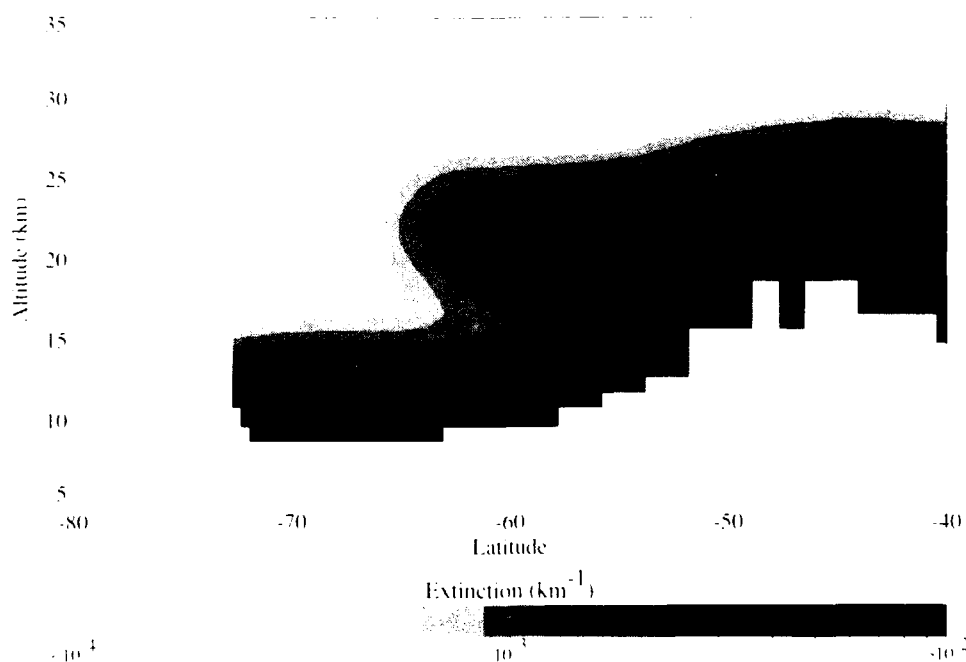


Figure 1. Latitude-longitude cross-section of SAM II and SAGE II aerosol extinction observations from October 1 through October 20, 1991.

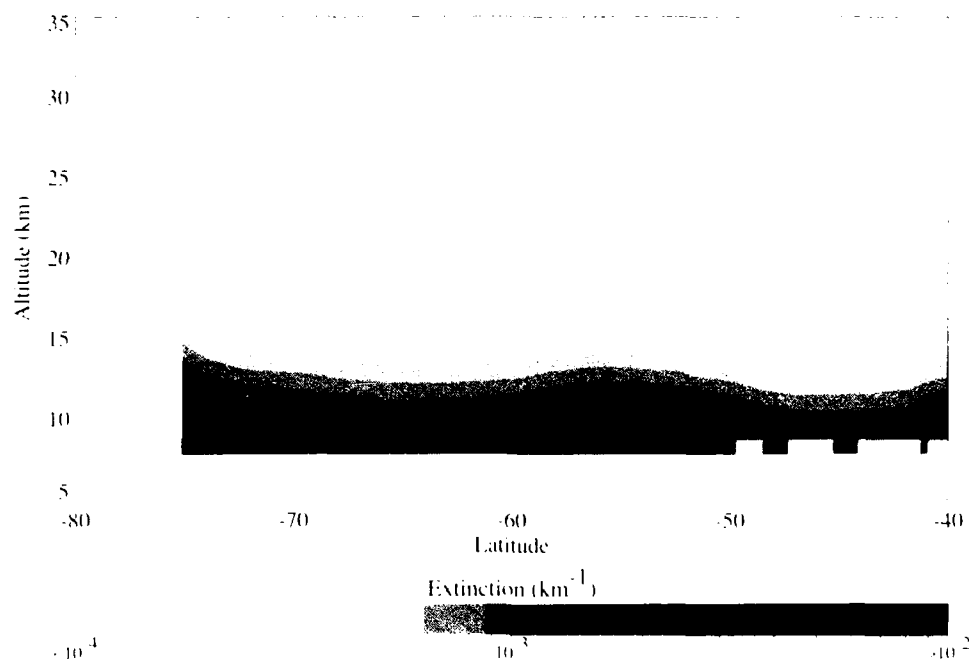


Figure 2. Same as Figure 1, except for October 1 through October 20, 1989.

We have produced latitude-longitude plots of aerosol extinction at various altitudes. These plots, along with daily isentropic potential vorticity analyses derived from NMC data, provide observational evidence that below 14 km, the polar circulation was characterized by an unstable vortex subject to episodes of strong wave activity which transported the Cerro Hudson aerosol to latitudes poleward of 70°S. Above 14 km, however, the vortex was much more stable and there is no evidence of the Pinatubo cloud penetrating the vortex until the final warming began after mid-November. In addition, we have examined the time history of the SAM II aerosol extinction profiles inside the polar vortex throughout the spring. Shown in Figure 3 are the daily medians of all SAM II aerosol extinction ratio profiles located inside the polar vortex at approximately 5-day intervals from September 1 through November 22. The first profile in the figure is typical of the background aerosol inside the vortex in any non-volcanic year. However, by mid-September there is an enhancement below 14 km due to the arrival of the Cerro Hudson cloud. This enhanced layer persists in the SAM II record until the vortex breaks down. Also note that there is no enhancement above 14 km until mid-November, when the Pinatubo cloud is observed above 20 km.

Hofmann and Solomon (1989) hypothesized that volcanic aerosol can initiate ozone destruction by serving as sites for heterogeneous chemical reactions which release reactive chlorine species. We examined SAGE II ozone profiles from inside the polar vortex during September and October and found approximately a 50% decrease in ozone near 13 km when compared with previous years. At this time it is unclear whether the unusually high aerosol extinctions associated with Cerro Hudson are contaminating the ozone measurements, so these results should be considered preliminary.

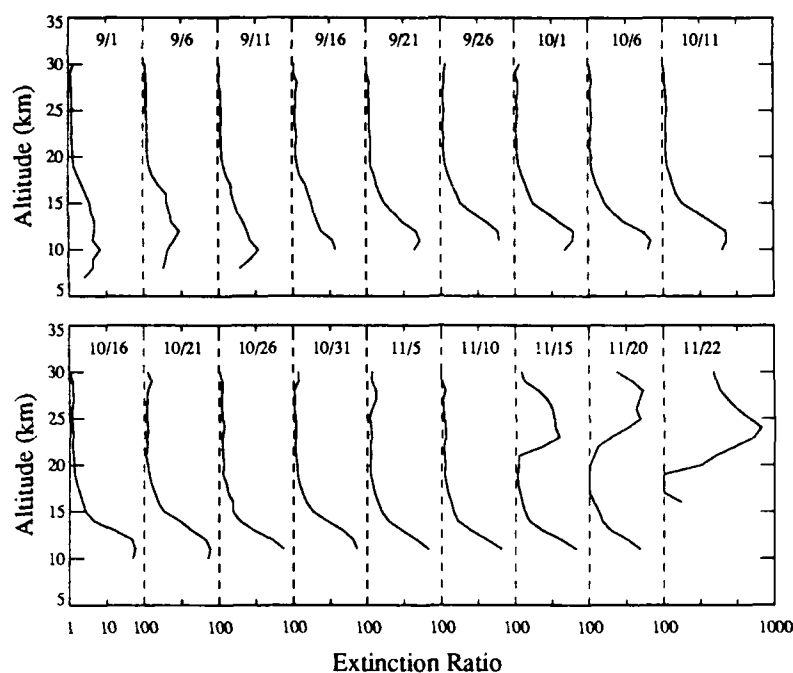


Figure 3. Daily medians of SAM II aerosol extinction ratio profiles from inside the polar vortex between September 1 and November 22, 1991. Aerosol extinction ratio is defined as the ratio of aerosol extinction to molecular extinction.

References

- Doiron, S. D. et al., *EOS*, 72, 489, 1991.
- Hofmann, D. J., and S. Solomon, *J. Geophys. Res.*, 94, 5029-5041, 1989.
- Kent, G. S., and M. P. McCormick, *J. Geophys. Res.*, 89, 5303-5314, 1984.
- Kent, G. S., and M. P. McCormick, *J. Optics News*, 42, 11-19, 1988.
- Kent, G. S. et al., *J. Atmos. Sci.*, 42, 1536-1551, 1985.
- Mauldin, L. E. et al, *Opt. Eng.*, 24(2), 307-312, 1985.
- McCormick, M. P., *Geophys. Res. Lett.*, 19, 149, 1992.
- McCormick, M. P., and R. Veiga, *Geophys. Res. Lett.*, 19, 155-158, 1992.
- McCormick, M. P. et al., *Bull. Am. Meteor. Soc.*, 60, 1038-1046, 1979.
- Thomason, L. W., accepted by *Geophys. Res. Lett.*, 1992.
- Trepte, C. R., and M. H. Hitchman, *Nature*, 355, 626-628, 1992.

Airborne Lidar Measurements of Aerosols

William B. Grant, Edward V. Browell, Bruce E. Anderson, and Syed Ismail
NASA Langley Research Center, MS 401A, Hampton, VA 23681

Introduction

Aerosols are now recognized as having a significant impact on global climate. Aerosols affect climate directly via scattering and absorption, and indirectly through their effect on cloud properties, generally acting in a manner that counteracts the warming induced by greenhouse gases such as CO₂ [Charlson et al., 1992; Fouquart and Isaka, 1992; Penner et al., 1992]. The NASA Langley Research Center's airborne UV DIAL system measures vertical-profile of aerosol scattering at IR, visible, and UV wavelengths at distances up to 25 km above and 12 km below the aircraft. The system has been operated in many different locations around the world during the past decade. The data sets obtained during these field experiments present an opportunity to contribute to the understanding of aerosol optical properties and their distribution, transportation and transformation, all of which bear on how they affect global climate. This paper presents an overview of work being undertaken to analyze and interpret the aerosol data as well as some preliminary results on lidar measurements of aerosols from biomass burning from a variety of locations.

UV DIAL system

The airborne UV DIAL system uses a pair of Nd:YAG-pumped dye lasers to generate wavelengths at 1.06 μm and 576, 600, 288, and 300 nm for tropospheric ozone measurements and 602, 622, 301, and 311 nm for stratospheric ozone measurements [Browell, 1989]. The system is flown on either the NASA DC-8 or the NASA Electra research aircrafts. The laser beams can be sent in both the nadir and zenith directions. Aerosol data are generally recorded with a vertical resolution of 15 m and a horizontal resolution of 300 m. Since both aerosol and ozone profiles are measured simultaneously, air mass characterizations are facilitated. In addition, the system is generally flown with a large complement of in situ instruments so that additional detailed measurements of the atmosphere can be made during the same flight.

Particle measuring system

Aerosol number densities as a function of size diameter are frequently recorded during the airborne missions. These measurements are made using a pair of optical-scattering aerosol probes: a forward-scattering spectrometer probe (FSSP) for 0.5- to 8.0- μm diameter particles, and an active-scattering aerosol spectrometer probe (ASASP) for the 0.12- to 3.1- μm diameter range. Both probes provide total count rates and 15 channels of sizing information. These instruments are calibrated by the manufacturer prior to each mission and are mounted externally on the airframe at locations thought to be minimally affected by aircraft-induced airflow perturbations.

Lidar aerosol data analysis technique

The airborne lidar data are processed through various steps after a mission. The first step is to subtract the background signal level from the profiles. Scattering-ratio calculations first involve an estimation of the molecular density profile. While meteorological data for the

flight are generally available, at times it is more convenient to use model atmospheres, such as those in Jursa [1985], which are given for every 15° latitude in the Northern Hemisphere for the four seasons. The lidar data are examined to identify an aerosol-free region where all the atmospheric scattering is assumed to come from molecular scattering. This is sometimes difficult in the nadir direction since aerosols tend to be ubiquitous in the lower troposphere. In that case, an estimate is made of the amount of aerosol scattering present (on the basis of zenith data or some calibration information), and the data are processed accordingly. Both the IR and visible data are routinely processed for scattering ratio profiles, while the UV scattering ratio profiles are only selectively calculated. On some missions where aerosol shape is expected to be important, such as for volcanic aerosols and polar stratospheric clouds [Browell et al., 1990a], depolarization ratios are also measured.

Extinction calculations are more difficult to make. The best way would be to measure backscatter from a particular target with and without the aerosol layer in between. This technique is not possible from an aircraft. The approach we have taken here is to assume that we know the aerosol type and its index-of-refraction and that we can calculate the extinction using Mie theory from the 180° phase function [e.g., Whitlock et al., 1985]. Admittedly, this approach cannot be used to determine the composition of unknown aerosol types, but should be useful in developing the tools of aerosol analysis.

Lidar determination of aerosol type

Sasano and Browell [1989] performed an analysis of lidar data of aerosols taken using the UV DIAL system. They corrected the wavelength dependence of backscatter measurements for extinction, looked at pairs of lines (1064 and 600 nm, 600 and 300 nm), and showed that on a scatter plot with the wavelength dependences for the two pairs as the two axes, the various aerosol types surveyed were clearly separated from each other. In their analysis, they considered only five aerosol types: Saharan dust, maritime, rain forest, continental, and stratospheric. We have extended their analysis to include aerosols from biomass burning, water clouds, cirrus (ice particle) clouds, volcanic aerosols, and PSCs. Since the UV data are not routinely analyzed for aerosol scatter, we have looked initially at the wavelength dependence using only the visible and near-IR wavelengths. Results of this analysis will be presented at the meeting.

Biomass burn plumes

Biomass burning has been studied on a number of NASA missions including The Amazon Boundary Layer Experiment - Dry Season (ABLE-2B) in Brazil, July-August 1985 [Andreae et al., 1988; Browell et al., 1990b]; the Arctic Boundary Layer Experiment (ABLE-3A) in Alaska, July-August 1988 [Browell et al., 1990b; Browell et al., 1992]; ABLE-3B in eastern Canada, July-August 1990; the Pacific Exploratory Mission - West (PEM-West) in the western North Pacific Ocean, September-October 1991; and the Transport and Atmospheric Chemistry near the Equator - Atlantic (TRACE-A) in Brazil, Africa, and the South Atlantic Ocean, September-October 1992. During the field experiments, a number of in situ instruments were onboard the aircraft for characterization of the aerosol size distribution and molecular species in the directly sampled plumes. The in situ data were used to verify that the plume resulted from biomass burning, and the size distribution of the aerosols and the concentrations of NO_x, NO_y, hydrocarbons, and ozone were used to help determine the age

and nature of the plume.

In situ aerosol data

Aerosol absorption, extinction, and backscatter values were calculated at 300, 585, and 1064 nm from in situ size distributions using the spherical particle assumption and the Mie scattering algorithm described by Bohren and Huffman [1983]. Complex refractive indices for the aerosols of interest were taken from Deepak et al. [1982]. In the cases of multi-modal size distributions, e.g., those with a sulfate accumulation mode and sea salt coarse mode, the distributions were decomposed and the appropriate refractive indices were applied to the individual modes. When a particular mode was comprised of a mixture of aerosol types with significantly different optical properties, e.g., biomass burning aerosols and background sulfate, a refractive index reflecting the fraction of each aerosol type at each size diameter was used in the calculations.

Comparisons between lidar and in situ aerosol measurements of smoke plumes show very good agreement in the few cases where detailed comparisons were possible. Figures 1 and 2 show the vertical profiles from a fresh biomass burn plume in eastern Canada for which lidar (directly) (Fig. 1) and in situ data (via Mie scattering calculations) (Fig. 2) were used to determine the aerosol scattering. Other data also show differences between the aerosol characteristics depending on geographical location, which affects the biomass type being burned and the conditions under which it burns, and age of the plume. The results of this analysis are described in this paper.

Plans for further work

As more confidence is developed with the tools for analysis and interpretation of the data, more extensive studies will be performed on the characteristics and distributions of aerosols from various sources, especially those from biomass burning, using the data sets obtained with the UV DIAL system.

Acknowledgments

The authors thank C. Butler and M. Fenn of SAIC, N. Mayo of Lockheed Eng. and Science Co., and W. McCabe, B. Meadows, and J. Williams of NASA for operating the UV DIAL system; P. Robinette of ST Systems Corp. and G. Nowicki of SAIC for help in processing the lidar aerosol data; and G. Gregory, D. Bagwell, and C. Hudgins of NASA for help in operating the in situ aerosol instruments. This research was funded in part by NASA's Global Tropospheric Chemistry Program.

References

- Andreae, M. O., E. V. Browell et al., Biomass-burning emissions and associated haze layers over Amazonia, *J. Geophys. Res.*, **93**, 1509-1527, 1988.
- Bohren, C. F., and D. R. Huffman, Absorption and Scattering of Light by Small Particles, J. Wiley & Sons, New York, 530 pp, 1983.
- Browell, E. V., Differential absorption lidar sensing of ozone, *Proc. IEEE*, **77**, 419-432, 1989.
- Browell, E. V., et al., Airborne lidar observations in the wintertime Arctic stratosphere: Polar stratospheric clouds, *Geophys. Res. Lett.*, **17**, 385-388, 1990a.

Browell, E. V., C. F. Butler, P. Robinette, S. A. Kooi, M. A. Fenn, and S. Ismail, Airborne lidar observations of aerosols and ozone in plumes from biomass burning over the Amazon Basin and over Alaska, paper presented at the Chapman Conf. on Global Biomass Burning, Williamsburg, March 19-23, 1990b.

Browell, E. V., C. F. Butler, S. A. Kooi, M. A. Fenn, R. C. Harriss, and G. L. Gregory, Large-scale variability of ozone and aerosols in the summertime arctic troposphere, *J. Geophys. Res.*, **97**, 16,433-16,450, 1992.

Charlson, R. J., S. E. Schwartz, J. M. Hales, R. D. Cess, J. A. Coakley, Jr., J. E. Hansen, and D. J. Hofmann, Climate forcing by anthropogenic aerosols, *Science*, **255**, 423-430, 1992.

Deepak, A., G. S. Kent, and G. K. Yue, Atmospheric backscatter model development for CO₂ wavelengths, NASA Contractor Report 3638 for Marshall Space Flight Center, 1982.

Fouquart, Y., and H. Isaka, Sulfur emission, CCN, clouds and climate: A review, *Ann. Geophysicae*, **10**, 462-471, 1992.

Jursa, A. S., ed., *Handbook of Geophysics and the Space Environment*, Fourth Edition, Air Force Geophysics Laboratory, Hanscom AFB, Mass., 1985.

Penner, J. E., R. E. Dickinson, and C. A. O'Neill, Effects of aerosol from biomass burning on the global radiation budget, *Science*, **256**, 1432-1434, 1992.

Sasano, Y., and E. V. Browell, Light scattering characteristics of various aerosol types derived from multiple wavelength lidar observations, *Appl. Opt.*, **28**, 1670-1679, 1989.

Whitlock, C. H., J. T. Suttles, and S. R. LeCroy, Phase function, backscatter, extinction, and absorption for standard radiation atmosphere and El Chichón aerosol models at visible and near-infrared wavelengths, NASA Tech. Memo. 86379, March 1985, avail., NTIS, Springfield, VA, 22161.

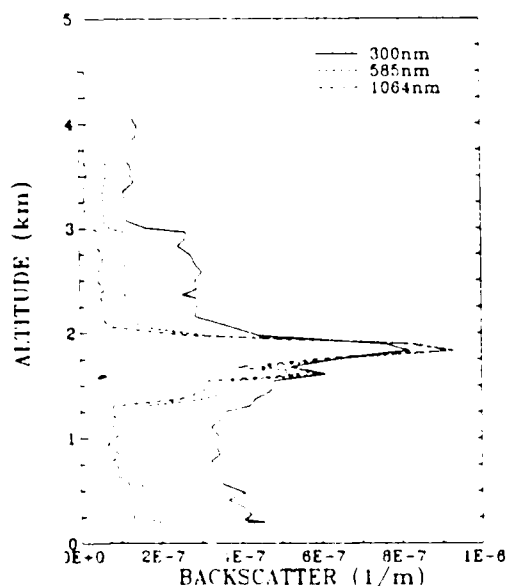


Figure 1. Lidar measurement at 1.064 μm on July 17, 1990 (52°N, 82°W) of the aerosol scattering ratio of the free troposphere (above 3.3 km), mixing-layer sulfate aerosol (0.5-3.3 km), biomass burn plume (1.5-2.3 km), and low-level boundary layer (0-0.5 km).

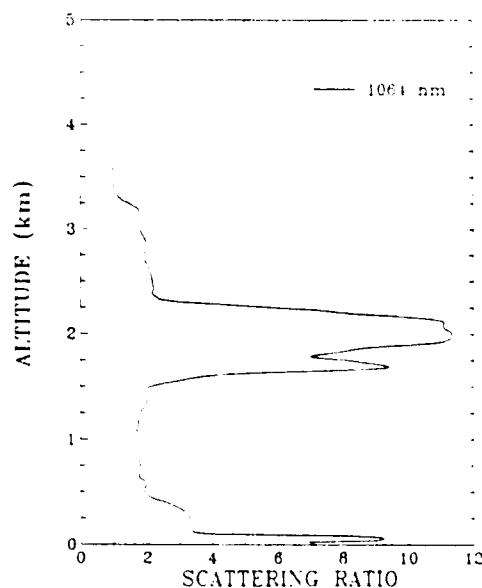


Figure 2. Results of Mie scattering calculations based on in situ aerosol measurements from a spiral near the location probed in Figure 1.

Thursday, March 11, 1993

Aerosols 2

ThB 10:10am–12:10pm
Salon F

Raymond M. Hoff, *Presider*
Atmospheric Environment Service

Time-Dependent Behavior of Mount Pinatubo Aerosol

Joseph Michalsky
Atmospheric Sciences Research Center
University at Albany, State University of New York
100 Fuller Rd
Albany, New York 12205
(518)442-3809

Nels Larson
Pacific Northwest Laboratory
P.O. Box 999
Richland, Washington 99352
(509)376-4333

INTRODUCTION

The 15-16 June 1991 eruption of Mount Pinatubo delivered approximately 20 million metric tons of SO_2 to the stratosphere. This is about three times the estimate for El Chichon (Bluth et al., 1992). While El Chichon's volcanic plume was confined mostly to the northern hemisphere, the SO_2 plume from Mount Pinatubo straddled the equator resulting in a more symmetrical global distribution of the $\text{H}_2\text{SO}_4\text{-H}_2\text{O}$ aerosol that results from the photochemical conversion of the SO_2 . Dutton and Christy (1992) find that the average Mount Pinatubo aerosol cloud as measured at two southern and two northern hemisphere sites exceeds the El Chichon aerosol optical depth for the first 10 months by about 70%. This is consistent with the extra SO_2 loading and more uniform dispersal of the plume between hemispheres. They found the global and northern hemispheric temperatures of the lower troposphere to be 0.4 and 0.7° C below normal, respectively, by June 1992. This is consistent, thus far, with the predictions of Hansen et al. (1992).

This paper follows the aerosol optical depth change over three northern mid-latitude sites for the first sixteen months following the eruption. The technique to derive volcanic aerosol optical depth from ground-based measurements (which are, by their nature, total column aerosol optical depth measurements) follows the technique developed in an earlier paper to examine El Chichon aerosol (Michalsky et al., 1990). The three sites' time-dependent behavior is discussed and compared. Comparison of El Chichon and Mount Pinatubo aerosol optical depth change with time is also discussed for the one site that operated before, through, and after both eruptions.

DATA

Aerosol optical depth measurements are taken at three mid-latitude US sites: Richland, Washington; Boulder, Colorado; and Albany, New York. In Richland the instrument is a sun-

tracking solar radiometer with five filters centered on 428, 486, 535, 785, and 1010 nm. Data have been taken continuously since before 1980 at this site, and an analysis of these data through the El Chichon epoch appear in Michalsky et al. (1990). In Boulder and Albany the data are acquired using the rotating shadowband photometer. This instrument, which measures total and diffuse horizontal illuminances and calculates direct normal illuminance, is not a conventional sunphotometer. Its operation and cross-calibration with a standard sun-tracking radiometer is examined in LeBaron et al. (1989). The photometer measurements are in a single broad band centered on 555 nm.

Direct normal spectral irradiance from the instruments on clear or partially clear days is used with the Langley technique to calculate total column optical depth at each of the wavelengths. The Langley technique assumes exponential extinction with changing air mass, i.e.,

$$I = I_0 * \exp(-\tau * m),$$

where I and I_0 are the spectral irradiances at the bottom and top of the atmosphere, respectively, m is the air mass relative to a value of one in the zenith direction, and τ is the total column optical depth. Plotting the natural logarithm of the measured direct spectral irradiance versus air mass results in a straight line for clear stable conditions. The slope of this line, as determined from a least squares fit, is the total column optical depth. Molecular water and oxygen bands are avoided through judicious filter selection; molecular, or Rayleigh, scattering is a well known function of wavelength and pressure, therefore, it is removed by subtraction; seasonal climatological values for total column ozone are used to subtract ozone optical depth in the Chappuis band of ozone; this yields the aerosol optical depth.

ANALYSIS

The automated measurements permit every clear or partially clear day's data to become a candidate for Langley analysis. On some occasions when there are too few data for a Langley plot, or the Langley plot indicates an unstable condition, previously determined calibrations of extraterrestrial spectral irradiances (the intercept in the least squares fit to the Langley plot) may be used to calculate an average optical depth. These data yield between 135 and 210 data points per year, depending on a site's climatology.

To ascertain the seasonal patterns in the time-averaged optical depth, all data acquired with the stratosphere unperturbed, or minimally perturbed by volcanic aerosols, are superimposed on a single year. The background data from the first half year is appended and data from the second half year is prepended to the data. A lowess smooth of the data (Cleveland, 1979) is applied, in order to obtain approximately monthly averaged data with the influence of outliers deweighted. Fig. 1 contains background data for Boulder, Colorado. As is typical of most sites, there is a maximum during early summer and a minimum in the early winter. The background contains a little more than 16 months' data. As the volcanic perturbation reverts to background levels, we will be able to add more data to our background data set and determine a better averaged behavior.

This smoothed background aerosol optical depth is removed from every point in the data set according to the time of year. Once this differenced data set is formed it is smoothed with the lowess function to reveal perturbations to what we assume is background. Fig. 2 is a plot of the points after removing the background, and the smooth line is the lowess estimate of the perturbation to background aerosol. The extent to which we are successful in removing the background is indicated by the deviations about the zero optical depth line before the onset of Mount Pinatubo's aerosol perturbation. The dashed horizontal lines represent ± 0.01 optical depth about the zero optical depth line. Therefore, we have a reproducible monthly averaged optical depth to about the 0.01 level.

The effect of Pinatubo began to exceed this background level in the last four months of 1991. The peak optical depth of about 0.15 was reached during the February/March 1992 period. During the summer of 1992 the optical depth fell to about 0.06, but since has begun to increase somewhat. This behavior is virtually identical to that of the El Chichon perturbation (Michalsky et al., 1990) with the exception that the Mount Pinatubo optical depths are larger by about 40 to 50%.

Although there is insufficient space to show the results from the other sites, they confirm this behavior in general, but not quite in detail. For example, Richland data show a somewhat higher peak at the same wavelength. Albany has a lower peak. The differences are within the error of the estimate, however. The most recent data from all three sites will be presented at the meeting.

This research was supported by the United States Department of Energy under grant DE-FG02-90ER61072, by the Geosciences Program within the Office of Basic Energy Sciences of the DOE at Pacific Northwest Laboratory, which is operated for DOE by Battelle Memorial Institute under contract DE-AC06-76RLO 1830, and by the New York State Energy Research and Development Authority under grant 1725-EEED-IEA-92.

REFERENCES

- Bluth, G.J.S., S.D. Doiron, C.C. Schnetzler, A.J. Krueger, and L.S. Walter (1992), Global Tracking of the SO₂ Clouds from the June, 1991 Mount Pinatubo Eruptions. *Geophys. Res. Letters*, 19, 151-154.
- Cleveland, W.S. (1979), Robust Locally Weighted Regression and Smoothing Scatterplots. *J. of the Amer. Stat. Assoc.*, 74, 829-836.
- Dutton, E.G. and J.R. Christy (1992), Solar Radiative Forcing at Selected Locations and Evidence for Global Lower Tropospheric Cooling Following the Eruptions of El Chichon and Pinatubo. *Geophys. Res. Letters*, submitted.
- Hansen, J., A. Lacis, R. Ruedy, and M. Sato (1992), Potential Climatic Impact of Mount Pinatubo Eruption. *Geophys. Res. Letters*, 19, 215-218.

LeBaron, B.A., J.J. Michalsky, and L. Harrison (1989), Rotating Shadowband Photometer Measurement of Atmospheric Turbidity: A Tool for Estimating Visibility. *Atmos. Environ.*, 23, 255-263.

Michalsky, J.J., E.W. Pearson, and B.A. LeBaron (1990), An Assessment of the Impact of Volcanic Eruptions on the Northern Hemisphere's Aerosol Burden During the Last Decade. *J. of Geophys. Res.*, 95, 5677-5688.

Fig. 1. Boulder Background Aerosol vs Time of Year

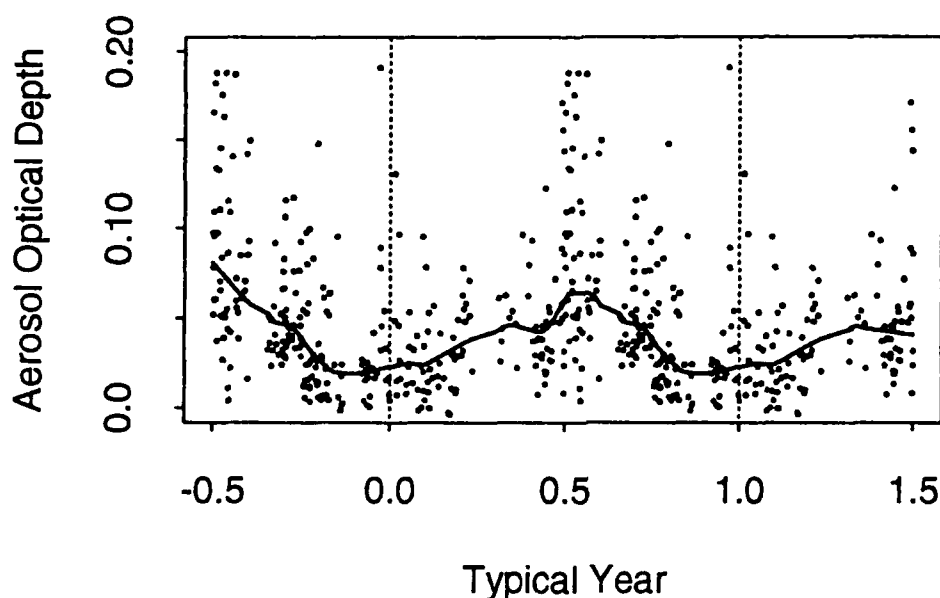
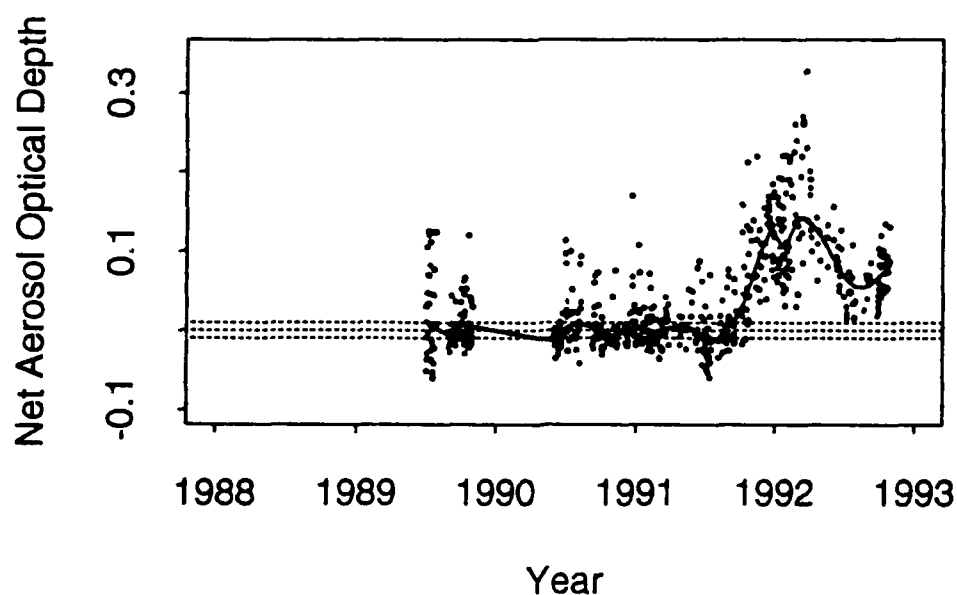


Fig. 2. Pinatubo Aerosol @ Boulder vs Time



OBSERVATIONS OF MOUNT-PINATUBO AEROSOL WITH A RAMAN ELASTIC-BACKSCATTER LIDAR OVER NORTHERN GERMANY AT 53.5° N

Ulla Wandinger and Claus Weitkamp
GKSS Forschungszentrum Geesthacht GmbH,
Postfach 1160, W-2054 Geesthacht, Germany
(Tel. ++49 4152 871854)

Albert Ansmann
Institut für Troposphärenforschung,
Permoserstrasse 15, O-7050 Leipzig, Germany
(Tel. ++49 341 23922460)

The paper presents latest results of lidar observations of the stratospheric perturbation after the strong eruptions of the volcano Mt. Pinatubo on the Philippines in June 1991. A Raman lidar with an additional channel for the measurement of elastically (Rayleigh and particle) backscattered light is used. The combined lidar of GKSS has been described in detail previously (Ref. 1). Table 1 depicts the essential system parameters. An extended discussion of the applied technique is given in Ref. 2. This type of lidar is particularly useful for stratospheric aerosol studies because it allows, in contrast to conventional elastic backscatter lidars, the determination of height profiles of the aerosol extinction coefficient (from the nitrogen Raman signal profile) and of the extinction-to-backscatter ratio (lidar ratio), from which the area-weighted mean or effective radius r_{eff} of the particle size distribution can be estimated (Ref. 3). Experimentally determined extinction-to-backscatter ratios are also needed for the evaluation of data from elastic backscatter lidars, especially for the estimation of aerosol extinction properties.

Table 1. Lidar system parameters

Laser type	XeCl excimer	Detected wavelengths:	
Laser wavelength	308 nm	Elast. backscatter	308 nm
Laser pulse energy	270 mJ	N ₂ Raman	332 nm
Laser repetition rate	250 Hz	H ₂ O Raman	347 nm
Transm. divergence	≤ 0.1 mrad	Dispersion system	Filter polychromator
Receiver diameter	0.8 m	Detection method	300-MHz photon counting
Receiver FOV	0.4 mrad	Range resolution	15 m

The measurements are taken at Geesthacht, 40 km to the southeast of Hamburg (53.5° N, 10.5° E). Each observation lasts two hours during which 1.5 million laser shots are transmitted. The averaged signal profiles are taken for the determination of geometrical and scattering properties of the stratospheric aerosol layer as shown in Fig. 1.

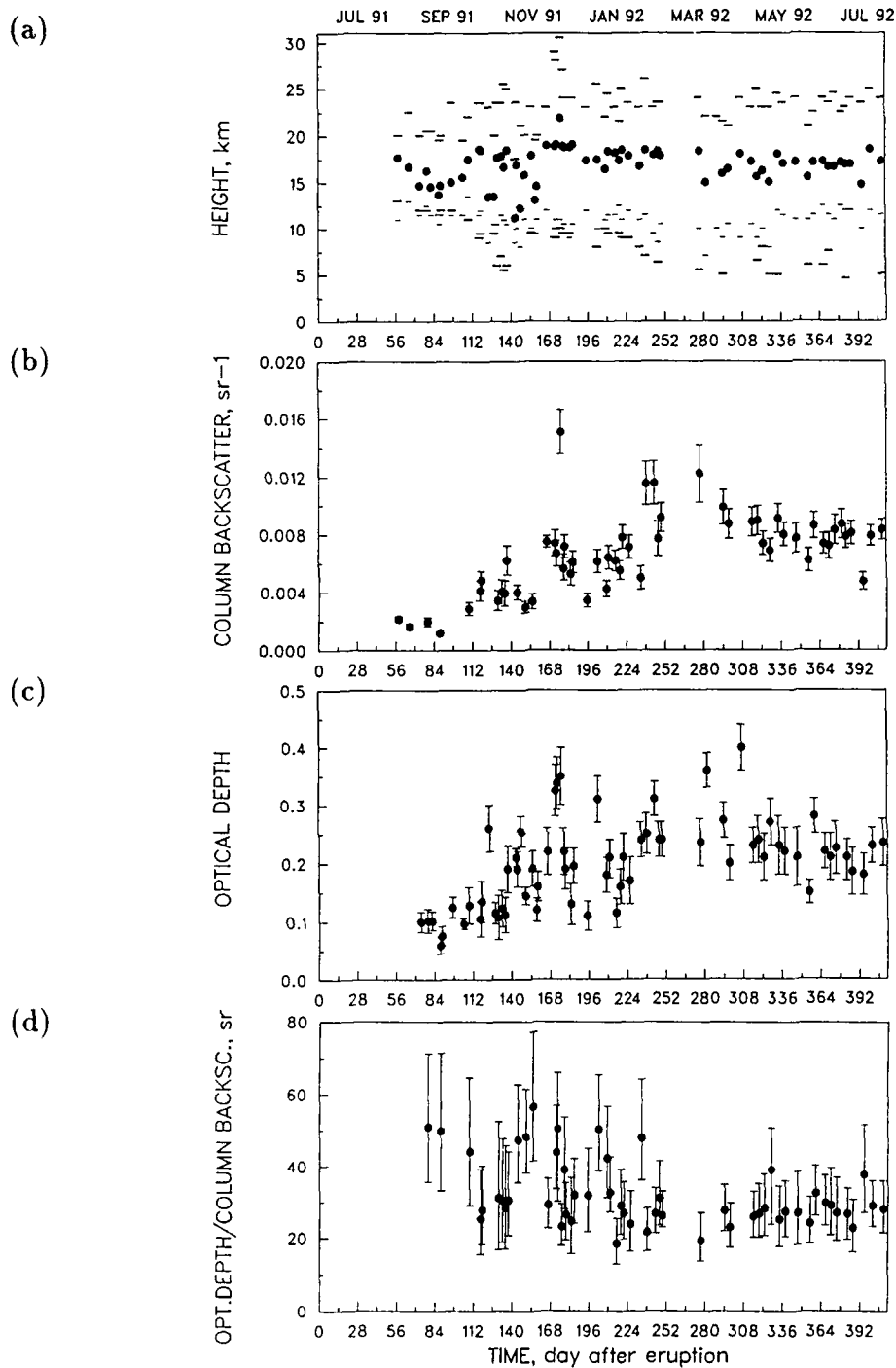


Fig. 1: (a) base and top heights (-), tropopause height (-), and backscatter-weighted mean height of the stratospheric aerosol layer (o), (b) column-integrated aerosol backscatter, (c) optical depth, and (d) ratio of optical depth to column-integrated backscatter as a function of time. Time scale zero is 15 June 1991. Vertical bars indicate the uncertainty due to a $\pm 20\%$ uncertainty in the assumed ozone density profile (monthly-averaged Mt.-Hohenpeissenberg ozone profile).

Mount-Pinatubo aerosol is mainly observed between the tropopause at z_{trop} and a height of 25 km. Traces of stratospheric aerosol are found down to about 5 km height during clear nights. Maximum values of the layer top height z_{top} (30.5 km) and the total-to-Rayleigh backscatter ratio (3.5 for $\lambda = 308 \text{ nm}$) are observed on 8 December 1991. The backscatter-weighted mean layer height varied strongly in 1991. The center of backscattering decreases from 18.8 km in December 1991 to 16.9 km in July 1992. A descent of about 2 km in seven months is consistent with droplet radii of 0.3 to 0.4 μm . Those particles adopt Stokes velocities of 4 km per year at heights between 15 and 20 km.

The column backscatter $\delta_\beta = \int_{z_{\text{trop}}}^{z_{\text{top}}} \beta_{\text{aer}}(z) dz$ and the optical depth $\delta_\alpha = \int_{z_{\text{trop}}}^{z_{\text{top}}} \alpha_{\text{aer}}(z) dz$ with the particle backscatter and extinction coefficients β_{aer} and α_{aer} , respectively, show qualitatively the same trend. The optical depth of the layer has been roughly 0.2 since the end of November 1991. The ratio $\sigma_\alpha/\sigma_\beta$, however, is, on average, larger in 1991 than in 1992. Mie scattering calculations for realistic bimodal lognormal size distributions of the sulfuric acid aerosol (Ref. 4) indicate that extinction-to-backscatter ratios of 50, 35, and 20 sr are caused by droplet size distributions with area-weighted mean radii of about 0.1, 0.2, and 0.4 μm , respectively. Thus, in 1992, the effective radius of the particle size distribution of the total stratospheric aerosol load ranges between 0.2 and 0.4 μm . The mean particle radius is estimated to be between 0.1 and 0.2 μm . The particles in the central region of the layer are larger than 0.4 μm , because lidar ratios between 10 and 20 sr are usually observed around the backscattering center. A strong variation of the extinction-to-backscatter ratio with height, often between 10 and 80 sr, was typical for the winter season 1991/92.

References

1. A. Ansmann, M. Riebesell, U. Wandinger, C. Weitkamp, E. Voss, W. Lahmann, and W. Michaelis, "Combined Raman elastic-backscatter lidar for vertical profiling of moisture, aerosol extinction, backscatter, and lidar ratio", *Appl. Phys. B* **55**, 18-28, 1992.
2. A. Ansmann, U. Wandinger, M. Riebesell, C. Weitkamp, and W. Michaelis, "Independent measurement of extinction and backscatter profiles in cirrus clouds by using a combined Raman elastic-backscatter lidar", *Appl. Opt.* **31**, 1992, in press.
3. A. Ansmann, U. Wandinger, and C. Weitkamp, "One-year observations of Mount-Pinatubo aerosol with a combined Raman elastic-backscatter lidar over northern Germany at 53.5° N", submitted to *Geophys. Res. Letts.*
4. H. Jäger and D. Hofmann, "Midlatitude lidar backscatter to mass, area, and extinction conversion model based on in situ measurements from 1980 to 1987", *Appl. Opt.* **30**, 127-138, 1991.

Lidar Measurements of the Stratospheric Aerosol Layer over Toronto

D.P. Donovan, W. Steinbrecht and A.I. Carswell

Institute for Space and Terrestrial Science and
Department of Physics and Astronomy, York University
4700 Keele Street, North York, Ont., Canada, M3J 1P3
Tel: 416-736-2100 Fax: 416-736-5516

Introduction

Since March 1991, lidar measurements of the stratospheric aerosol layer over Toronto Canada (42.80° N, 79.50° W) have been routinely conducted at wavelengths of 353nm and 532nm. Two separate Lidar systems have been used, one system is an Ozone Differential Absorption Lidar (DIAL) system based on a *XeCl* excimer laser with $\lambda_{off} = 353\text{nm}$ and the other system is an elastic backscatter lidar built around a frequency doubled Nd:YAG laser ($\lambda = 532\text{nm}$). The Nd:YAG lidar sends out a linearly polarized beam and the components of the return signal parallel and perpendicular to the polarization vector of the transmitted beam are detected separately. Both systems are described in detail in [1].

Understanding the characteristics of volcanic aerosols is important for several reasons. Enhanced aerosol loading in the stratosphere will perturb the radiation field, affecting photochemical reaction rates and possibly leading to stratospheric warming [2]. Stratospheric aerosols may also function as reaction sites for ozone depleting heterogeneous chemistry [3]. In addition, significant aerosol levels can adversely affect the accuracy of remote sensing measurements of the stratosphere.

Lidar systems can be used to measure stratospheric aerosol properties with excellent temporal and spatial resolution. In this paper we will present and discuss results of our aerosol measurements.

Aerosol Backscatter

A common parameter in lidar aerosol measurements is the backscatter ratio

$$R(r, \lambda) = \frac{\beta_M(r, \lambda) + \beta_r(r, \lambda)}{\beta_r(r, \lambda)} \quad (1)$$

where, $\beta_M(r, \lambda)$ is the Mie, or aerosol, scattering cross section at range r and wavelength λ and $\beta_r(r, \lambda)$ is the Rayleigh, or molecular, scattering cross section. The aerosol backscatter at two wavelengths can be related by the Mie scattering exponent η , defined by the relation,

$$\frac{\beta_M(r, \lambda_1)}{\beta_M(r, \lambda_2)} = \left(\frac{\lambda_1}{\lambda_2} \right)^\eta \quad (2)$$

In general, η will be a function of the aerosol size distribution and its refractive index. As such, η contains some information on the aerosol extinction-to-backscatter ratio (σ_M/β_M) at both wavelengths. Using standard Mie theory η was related to a range of aerosol extinction to backscatter ratios at 532 nm and 353 nm by calculating both η and σ_M/β_M for a range of expected and measured aerosol size distributions at each wavelength.

Incorporating our η vs σ_M/β_M relationship, $R(r, \lambda)$ can be calculated from the lidar return signal allowing for a range dependent aerosol backscatter-to-extinction ratio, by iteratively solving the following equation for both wavelengths

$$R(r, \lambda) = C_\lambda \frac{r^2 P(r, \lambda)}{\beta_r(r, \lambda)} \exp \left[-2 \int_r^{r_{norm}} (\sigma_r(r', \lambda) + \sigma_M(r', \lambda) + \sigma_{O_3}(r', \lambda)) dr' \right] \quad (3)$$

where $P(r, \lambda)$ is the return signal power from range r and wavelength λ , σ_r is the Rayleigh extinction coefficient, σ_M is the Mie extinction coefficient, σ_{O_3} is the Ozone absorption coefficient and C_λ is a constant chosen to give a particular value of $R(r, \lambda)$ at the normalization altitude r_{norm} . In our case our signal to noise ratio is good enough that we can choose r_{norm} to be above the aerosol cloud, usually $r_{norm} = 35$ km, so that $R(r_{norm}, \lambda) = 1$.

For both wavelengths, $\beta_r(r, \lambda)$ and $\sigma_r(r, \lambda)$ are calculated from molecular density profiles provided by balloon borne radiosondes launched 2 km away from the lidar site. The sondes are launched every weekday by the Canadian Atmospheric Environment Service and usually provide density information up to about 30-35 km.

In Fig. 1 we show an example of the scattering ratios at 532nm and 353nm and the corresponding η as a function of range measured during late April 1992. In Fig. 2 we show the corresponding molecular and aerosol backscatter coefficients at both wavelengths and compare them with backscatter coefficients calculated from a aerosol size distributions measured during mid-April over Laramie, Wyoming (42° N) [4]. For the Lidar data shown here the tropopause height was about 10.5 km. In the Lidar data shown in Fig. 1 and Fig. 2 the absorption due to ozone at 532nm has not accounted for, however, the effect is expected to be on the order of 2%. As can be seen from the figure the match is quite good, especially considering the temporal and spatial separation in the sonde and Lidar measurements.

Depolarization Measurements

The linear depolarization ratio (δ) is defined as the ratio of the power collected by the perpendicular channel to the power collected by the parallel channel i.e.

$$\delta(r) = \frac{P_{perp}(r)}{P_{para}(r)} \quad (4)$$

As is the case here, for low optical depths where multiple scattering is not important, a value of δ above that expected from a molecular atmosphere generally indicates that the aerosols are irregular in shape while a value of δ below the Rayleigh value of about 0.015 generally indicates that the scattering aerosols are of a spherical nature.

In Fig. 3 we show a comparison between the scattering ratio and the depolarization ratio at 532nm for the data shown in Fig. 1 and Fig. 2. A strong correspondence between features in the R profile and the δ profile is evident. The sub-Rayleigh values of δ indicate that the stratospheric aerosol is spherical consistent with small H_2SO_4/H_2O droplets.

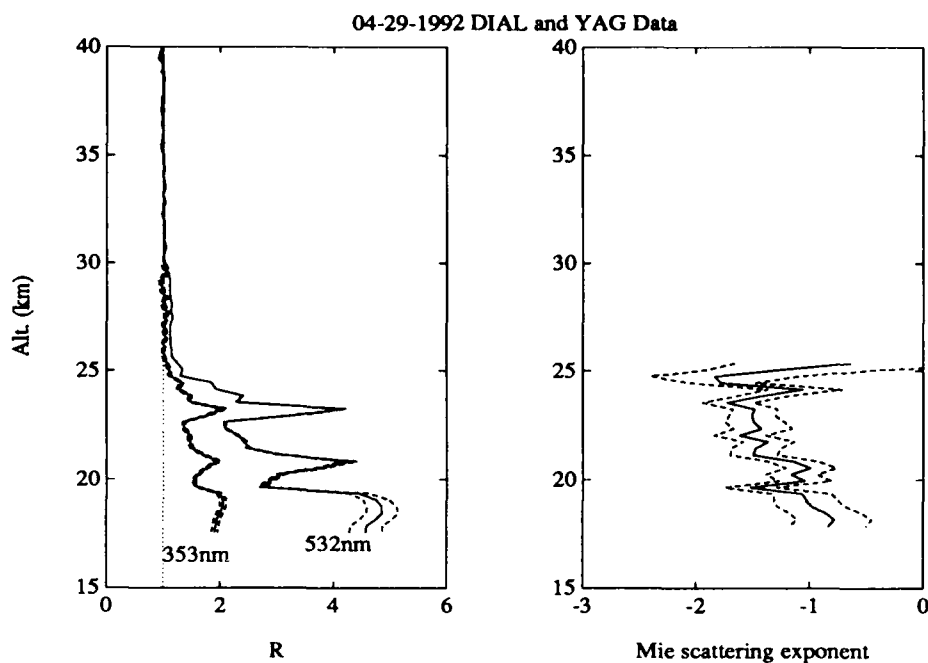


Figure 1: Comparison between observed scattering ratios at 353nm and 532nm (left) and the corresponding Mie scattering exponent η (right). The error bounds shown include the signal error as well as the aerosol and Rayleigh optical depth errors.

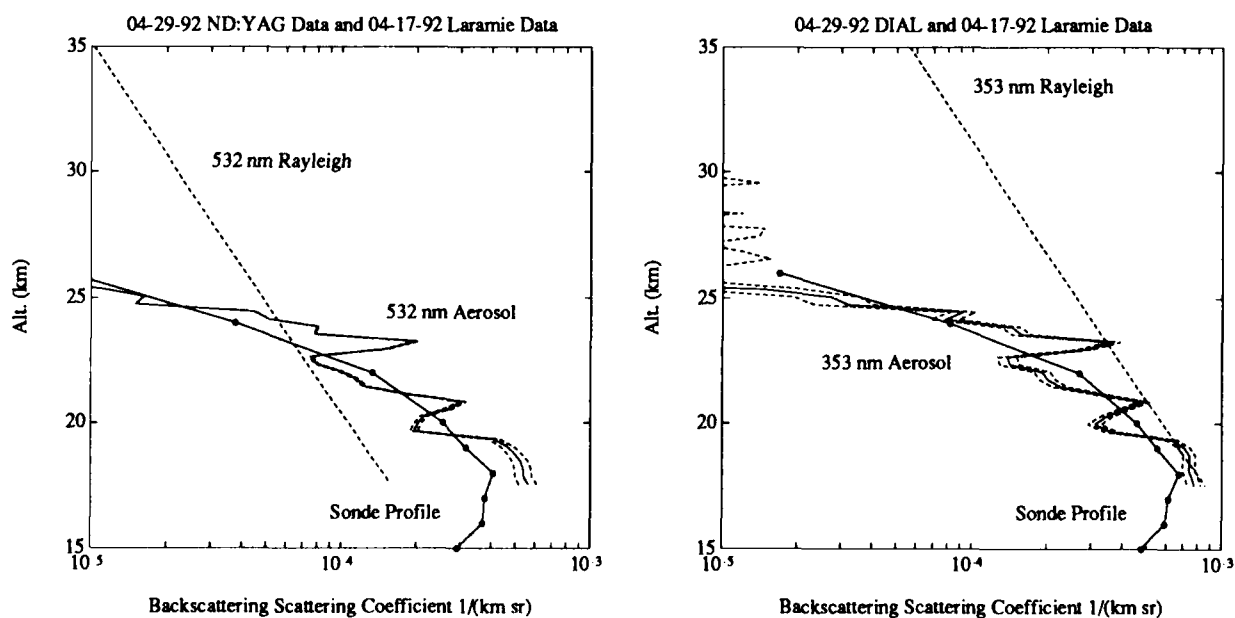


Figure 2: Lidar derived Rayleigh and Aerosol backscattering coefficients (β_r and β_M) corresponding to the data shown in Fig. 1 compared with those calculated from a sonde measured aerosol size distributions measured during mid-April over Laramie, Wyoming (42° N).

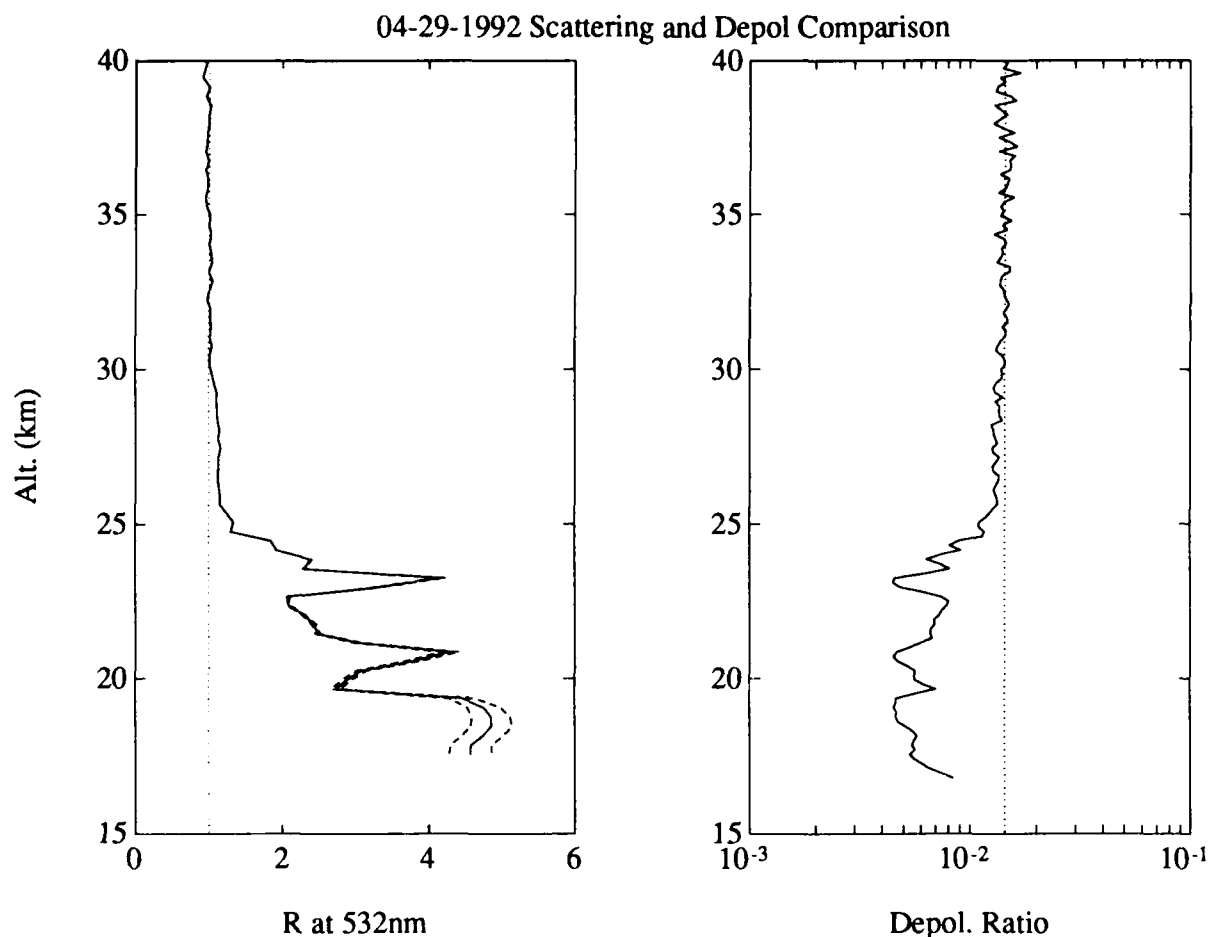


Figure 3: Comparison between R at 532 nm and δ for the data shown in Fig. 1 and 2. The dotted lines correspond, respectively, to the expected Rayleigh scattering and depolarization ratios. Notice that the departure from $R = 1$ corresponds quite well with the departure of the depolarization from the Rayleigh value.

References

- [1] A.I. Carswell, S.R. Pal, W.Steinbrecht, J.A. Whiteway, A. Ulitsky and T-Y Wang, "Lidar measurements of the Middle Atmosphere", *Can.J. Phys.* Vol 69, 1076-1086 (1991)
- [2] Hofmann, D.J. and Solomon, S., "Ozone Destruction Through Heterogeneous Chemistry Following the Eruption of El Chichón", *J. Geophys. Res.*, **94**, 5029-5041 (1989)
- [3] Arnold, F., Bührke, Th. and Qiu, S., "Evidence for stratospheric ozone-depleting heterogeneous chemistry on volcanic aerosols from El Chichón", *Nature*, **348**, 49-50 (1990)
- [4] T. Deshler, private communication (1992)

Particle Size Characterization by means of Depolarization Measurements

C. Flesia

Observatoire Cantonal de Neuchâtel, CH-2000 Neuchâtel, Switzerland

38-24.18.61

and Institut of Atmospheric Physics ETH, CH-8093, Zurich, Switzerland

L. de Schouepnikoff

Observatoire Cantonal de Neuchâtel, CH-2000 Neuchâtel, Switzerland

38-24.18.61

Interest in the light scattering methods for the retrieval of the particle size distribution have grown in the last several years due to the unsatisfactory state of standard methods for the detection of small particles.

A characteristic feature of the inverse problem is the instability of the solution to measurements errors (ill-posed problem). In such problems, measurement errors are usually greatly amplified in the process of extracting the desired information and proper regularization techniques are needed to reduce the error in the desired solution to within acceptable bounds. The essence of regularization procedures consists in adding extra information to the optical data in order to obtain smoothness of the sought-for solution. Regularization requirements are needed in both the analytical and numerical methods. However, because of the complexity of the atmospheric system, the accuracy of the results of the inversion of the lidar equation, which is directly dependent upon the sensitivity of the system to the physical and mathematical assumptions, is generally unsatisfactory.

We have developed a new approach to the inversion problem based on the calculation of the moments M_j (i.e., M_0 = particle concentration, M_1 = mean particle radius, $\sqrt{M_2 - M_1^2}$ = Standard Deviation, etc..) of the size distribution function $n(r)$ from a knowledge of several values of the lidar backscattered energy $E_\nu(R)$ from the distance R . The lidar returns are measured as a function of an experimental parameter (wavelength, polarization, field of view...) chosen as a function of the specific physical quantity of interest.

The extra information needed for the regularization procedure are found in the general properties of the distribution functions describing the particle size. This leads to some

general constraints which can be added to the solution of the lidar equation in order to satisfy the requirements of the regularization procedure [1]

As a part of our development, we have conducted tests on the inversion procedure using numerical values of the lidar backscattered intensity calculated for a known monomodal size probability distribution. The algorithms have then been tested using the so calculated lidar signal as input values for the inversion procedure. Two wavelengths have been used to retrieve the concentration and the mean particle radius and three to calculate in addition the standard deviation. The comparison between the known values of the moments of the size probability distribution and their values resulting from the inversion procedure give the accuracy of the reconstructed moments with a precision comparable to the numerical precision of the simulated input lidar signal. The stability with respect to the measurement noise have been tested by calculating the input lidar signal for different kinds and different levels of noise.

The inversion procedure using the simulated lidar signal at two and/or three wavelengths (for instance $\lambda = 0.355 \mu m$, $\lambda = 0.532 \mu m$ and $\lambda = 1.064 \mu m$) can tolerate measurement errors up to 10-15 %, while the non linear iterative methods need the use of as many as twelve wavelengths from $0.26 \mu m$ to $4.91 \mu m$ to reach the same accuracy [2,3]. Tests performed with a well controlled laboratory experiment using the light intensity scattered by a solution of polystyrene sphere has confirmed the accuracy of the numerical results.

Physically, the indetermination of the problem is often associated with the extreme generality of its formulation; in order to suppress unphysical solutions it is necessary to incorporate in the inversion scheme some constraints, not derived from measurements. However, these restrictions should not be excessive. Finding the proper proportion between them is the main difficulty of the inversion problem. From this point of view, the constraints arising from the general theory of the moments eliminate the inherent instability of the problem without changing its physical content. The advantages of this approach are as follows:

- The constraints, which are derived from the general theory of distribution functions, are independent of the particular particle size distribution considered and then they don't require previous knowledge of the solution.
- The use of a simplified kernel is not required. This allows us to exploit the total information content of the Mie kernels and to include into the inversion procedure some generalization of the scattering theory.
- A minimum number of wavelengths is required to reach a very high accuracy on the inversion results.

Some preliminary tests show that the deviation from the spherical symmetry of the atmospheric particles is equivalent to introducing a statistical noise on the lidar signal. Results show an error of about 10-15 % due to the use of the spherical approximation in the inversion of the lidar signal also for the case of small particles with a mean radius $< 0.5 \mu m$.

Fig. 1 shows the isolevel curves of the percent of difference F between the values of the lidar signals calculated using the optical coefficients (extinction and backscattering) for spherical and non spherical particles respectively. A uniform mixture of prolate spheroids with deformation (i.e., the ellipticity) varying between 1.1 and 3 have been considered. For a monomodal distribution of the sizes of the equivalent-volume-spheres, the difference F depends essentially on the standard deviation: for very small σ varying between $\sigma = 0$ (i.e., the Dirac radial distribution) and $\sigma = 0.05$, F shows, as a function of the mean radius strong fluctuations which disappear as soon as σ increases above $\sigma = 0.05$. The value of F converge then to a constant value of about 10-12 %. This gives an estimation about the error resulting from the use of the spherical approximation on the simulation of the direct lidar signal in the case of small particles.

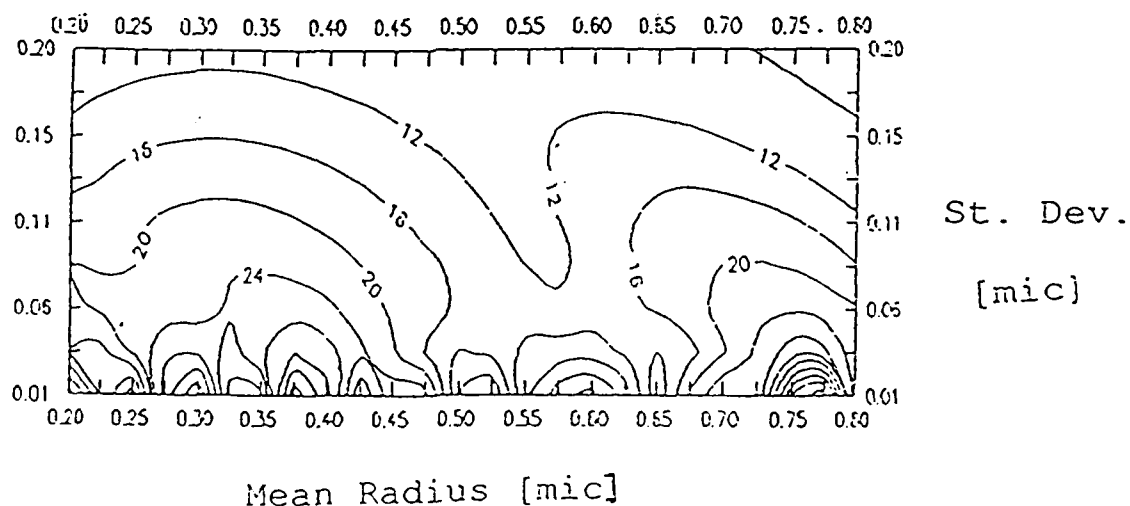


Fig. 1

These results confirm the need to use a depolarization channel in the retrieval of the atmospheric particle size distribution from lidar measurements not only for characterisation of crystal clouds but also in presence of aerosol and small nonspherical particles.

In an attempt to apply these findings, we have used these results to provide an interpretation of the depolarized lidar signal in terms of microphysical characteristics of the Pinatubo aerosol. Because of the strong dependence of the lidar return on the particle shape, the parallel and the perpendicular intensity at a given wavelength have to be used as input values for the inversion procedure.

From the particle size evaluation carried out using depolarization lidar data, by means of Mie computation and with the assumption of spherical particles, in the lower stratosphere, Pinatubo particles with mean radius of 0.5, 0.7 μm should result; if non sphericity is assumed, from theoretical evaluation of the measured depolarization, the equivalent radius for particles of spheroidal form should result in smaller dimension of 0.1, 0.2 μm . The latter result, which is in agreement with in situ measurements [4] is consistent with the existence of frozen particles of sulfuric acid tetrahydrate in the lower stratosphere [5,6].

REFERENCES

- [1] C. Flesia, M. Morandi, L. Stefanutti, Final Report, ESA/ESTEC Contract no. XA/89/171/PK, 1992
- [2] K.S. Shifrin and G. Tonna, Internal Report IFA no. 91/30, 1991
- [3] Ben-David, A. Herman and J.A. Reagan, Appl. Opt., 27,1235-1242, 1985
- [4] T. Deshler, D.J. Hofmann, B.J. Johnson and W.R. Rozier, Geophys. Res. Lett., 19, 199-202, 1992
- [5] L. Stefanutti et al., submitted to Geophys. Res. Lett., special issue EASOE Campaign
- [6] C. Flesia et al., submitted to Geophys. Res. Lett., special issue EASOE Campaign

Lidar Observations of Mt. Pinatubo Aerosols: Effects on the Global Radiation Budget

T. D. Stevens, S. Maruvada, T. J. Kane, and C. R. Philbrick

The Pennsylvania State University
University Park, PA 16802
(814) 863-0851

INTRODUCTION

Significant amounts of stratospheric aerosols can cause a cooling of the earth's surface due to the scattering of solar radiation back into space. Likewise a warming of the stratosphere where the particles reside will occur due to absorption of upwelling infrared radiation [1]. The eruption of the Pinatubo volcano in the Philippines (15.14°N, 120.35°E) on June 15, 1991, produced the largest impact on the stratosphere ever observed by modern airborne, spaceborne, and ground-based scientific instruments. The volcanic aerosols were ejected into the upper troposphere and the stratosphere to heights above 33 km. Due to their long residence time, the volcanic aerosols were transported around the globe in about three weeks [2]. The effects are spread in the meridional direction by the interactions of large scale planetary waves with the reservoir regions about the equator. By September 27 small amounts were observed as far north as Norway.

Estimates, from the SAGE II experiment of NASA, place the aerosol mass injected by this eruption between 20 and 30 megatons, approximately twice the amount produced by El Chichon in 1982 [3]. NASA models also predict a surface temperature decrease, in 1992, of about three times the standard deviation of the annual global mean [1]. This temperature decrease is sufficient to reverse current global warming trends for the next couple of years. It is therefore important to study and understand aerosol distribution and variations in the stratosphere to see how they contribute to the thermodynamic exchange processes in the atmosphere.

INSTRUMENTATION AND DATA COLLECTION

The LAMP instrument was designed to operate as both a middle atmosphere sensor and a lower atmosphere meteorological sounder. To accomplish this task, the profiles of many atmospheric properties including nitrogen concentration, water vapor concentration, aerosols, density, and temperature must be monitored over a large altitude range simultaneously. The LAMP lidar is a rugged self-contained transportable instrument capable of operating in almost any environment, as was demonstrated by its operation aboard the German ice breaker RV Polarstern in Antarctica during December 1991.

The instrument uses a pulsed Nd:YAG laser transmitting near-infrared radiation of 1064 nm, 1.5 joules per pulse at a pulse repetition frequency of 20 Hz. The fundamental output frequency is doubled and tripled by nonlinear crystals to produce outputs at wavelengths of 532 nm and 355 nm with energies of 600 mJ and 250 mJ respectively. The system design is an advanced development from two earlier lidars, the GLINT and GLEAM systems developed by Philbrick at the Air Force Geophysics Laboratory (currently Phillips Laboratory) [4,5]. The five

subsystems, transmitter, receiver, detector, data system, and control/safety system have all been integrated into a standard shipping container, which serves as a field laboratory. The lidar utilizes two independent receivers. The primary receiver is a 41 cm diameter Cassegrain telescope and the secondary receiver is an 20 cm Schmidt Cassegrain telescope. The 41 cm receiver collects the backscattered return from about 500 m to 80 km, while the 20 cm telescope covers the 8 - 35 km region for an independent check on system behavior. Measurements are made at the wavelengths of 355 and 532 nm for molecular scattering (Rayleigh and Raman) and particle scattering.

The Pennsylvania State University, The University of Bonn, and The University of Wuppertal were invited by the Alfred-Wegener-Institut of Germany for the voyage from Tromsø, Norway to Bremerhaven, Germany, to Puerto Madryn, Argentina, to Antarctica, to Punta Arenas, Chile. The voyage covered latitudes from 70°N to 65°S. The LAMP instrument first collected data on September 24, 1991, at the Andøya Rocket Range, Norway. The LADIMAS campaign began with a two-week period of testing and coordinated rocket measurements. The lidar was installed on the helicopter deck of the RV Polarstern at Tromsø, Norway on October 10, 1991. Several profiles of low altitude atmospheric data were collected in hazy and overcast conditions while the ship was in transit to Bremerhaven, Germany. Measurements were obtained on every clear night and several nights of poor weather conditions aboard the RV Polarstern as it sailed from Germany to Argentina, Antarctica and then to Chile.

This voyage provided an excellent opportunity to collect profiles of the Pinatubo cloud as it spread latitudinally. The only other methods capable of measuring this cloud globally are satellite based instruments, such as the SAGE II experiment. However, satellite instruments cannot penetrate into the troposphere because of the large optical depth in limb sounding, and do not offer the spatial or temporal resolution available to lidar.

OBSERVATIONS

The aerosols from the Pinatubo eruption plume were first detected by the Penn State LAMP lidar in Andenes, Norway (69° 17' N, 16° 01' E) on September 27, 1991 [6]. The backscattered return from the laser pulses represents the total scattering, both molecular and aerosol. The backscatter ratio, R , is defined by,

$$R(\lambda, z) = [\beta_a(\lambda, z) + \beta_m(\lambda, z)] / \beta_m(\lambda, z), \quad (1)$$

where β_a and β_m are the volume backscatter cross sections for aerosols and molecules, respectively.

The largest optical thickness and largest backscatter ratio were observed near the equator, as expected. The most optically thick portions of the Pinatubo aerosols covered latitudes from 24°S to 30°N, and altitudes from 20 to 30 km. The aerosol cloud also settles to lower altitudes as it spreads north and south following the stratification contours established by the tropopause. The highest altitudes of enhanced aerosol scatter, above 30 km, are observed near the equator. As the cloud spreads southward it rises to about 33 km at 14°S and then the upper detectable altitude settles to 26 km at 62°S. The cloud's peak altitude steadily descends to 25 km as it spreads northward.

Figure 1 shows a plot of a two-color lidar return from the ground to 40 km on the night of November 22, 1991 during the LADIMAS campaign. These profiles represent a 30 minute average with a 150 m height resolution. The U.S Standard Atmosphere has been corrected for transmission loss using LOWTRAN 7. The profiles are then tied to this modified standard atmosphere above the Pinatubo aerosols where molecular scattering dominates. Since the molecular backscattering cross section is

proportional to $1/\lambda^4$, the cross section for 355 nm is about 5 times the 532 nm backscattering cross section ($532^4/355^4 = 5.04$). The model return for 355 nm has been shifted by this same amount from the model return for 532 nm. The Pinatubo dust layer can be clearly seen on both wavelengths in the lower stratosphere between 20 and 30 km. However, between 7 and 12 km, a cirrus cloud dominates the 532 nm return, but has a much smaller signature in the 355 nm backscattered signal. This is because the molecular backscatter for the 355 nm signal is much stronger than that of the 532 nm signal, and thus the particle backscatter does not dominate the molecular backscatter at the 355 nm wavelength. We can then assume that the cirrus cloud consists of very large particles, maybe ice crystals, because the scattering intensity for both wavelengths has about the same magnitude. The particle backscatter ratio is now defined to add some understanding to the wavelength dependance of particle scattering.

The particle backscattering ratio (PBR) is defined as the ratio of the aerosol backscattering cross section at 532 nm to the aerosol backscattering cross section at 355 nm. The ratio of the aerosol backscattering cross sections for two wavelengths defines a relation that provides information on the particle size and distribution. Figure 2 shows the PBR for the lidar profiles in Figure 1. The PBR through the stratospheric aerosol layer between 19 and 32 km is almost constant at 0.5, while the PBR through the cirrus cloud between 9 and 10 km is clearly not constant. We can assume that the Pinatubo cloud consists of a uniform distribution of particles that remains constant through the region from 19 to 32 km. However, the cirrus cloud must contain a variety of particle shapes, sizes, and/or distributions.

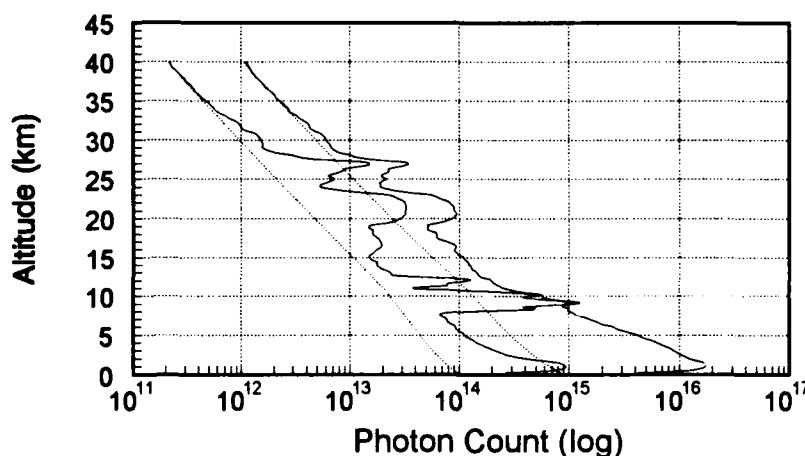


Figure 1. Lidar profiles for 355 and 532 nm wavelengths collected on November 22, 1991.

$$\text{Particle Backscattering Ratio} = \frac{\beta_{a532}}{\beta_{a355}} = \frac{(R_{531}-1)\beta_{m532}}{(R_{355}-1)\beta_{m355}} \quad (2)$$

Because the PBR is constant through the Pinatubo aerosols we can assume that the particle size and distribution are also constant. This allows us to calculate the wavelength dependence of the aerosols using the two wavelength measurements (355 and 532 nm) obtained from the LAMP lidar. The 532 nm lidar profile was tied to the U.S. Standard Atmosphere density at 45 km. Figure 3 is a plot of the Pinatubo layer after the U.S. Standard density was subtracted from the lidar return in the region of the aerosols. The aerosol particle scattering can be expressed in terms of additional molecular scattering at that wavelength. From this information the actual atmospheric transmission at both wavelengths can be calculated. This wavelength dependence is applied to the input solar radiance curve to define the solar radiance that reaches the earth's surface.

The large data base collected aboard the RV Polarstern during the LADIMAS campaign provides measurements of aerosol extinction in the stratosphere between 70°N and 65°S. An estimate of the decrease in the global solar radiance will be calculated.

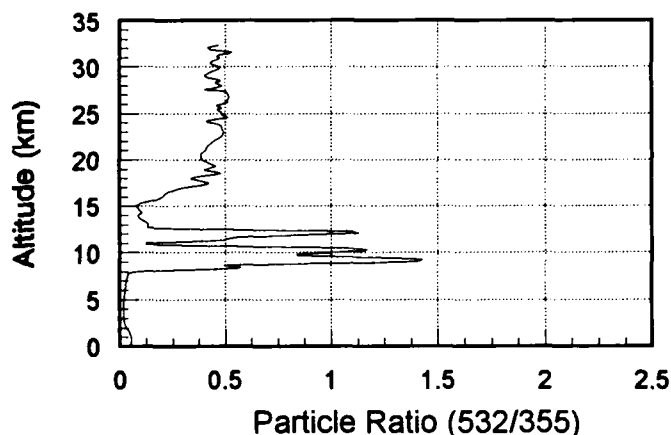


Figure 2. Particle backscattering ratio (PBR) through the Pinatubo aerosols.

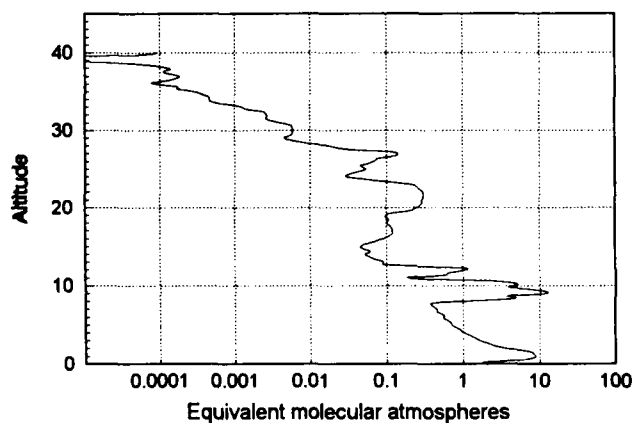


Figure 3. The Pinatubo aerosols scattering at 532 nm plotted in terms of additional equivalent atmospheres.

REFERENCES

1. James Hansen, Andrew Lacis, Reto Ruedy, and Makiko Sato, "Potential Climate impact of Mount Pinatubo eruption," *Geophysical Research letters*, vol. 19, No. 2, pp. 215-218, 1992.
2. L.L. Stowe, R.M. Carey, and P.P. Pellegrino, "Monitoring the MT. Pinatubo aerosol layer with NOAA/11 AVHRR data," *Geophysical Research Letters*, vol. 19, No. 2, pp. 159-162, 1990.
3. M.P. McCormick, R.E. Veiga, "SAGE II Measurements of early Pinatubo aerosols," *Geophysical Research Letters*, Vol. 19, No. 2, pp. 155-158, 1992.
4. C. R. Philbrick, D. P. Sipler, G. Davidson, and W. P. Moskowitz, "Remote sensing of structure properties in the middle atmosphere using lidar," *Proceedings of OSA Meeting on Laser and Optical Remote Sensing*, pp. 120-123, 1987.
5. C. R. Philbrick, D. P. Sipler, B. E. Dix, G. Davidson, W. P. Moskowitz, C. Trowbridge, R. Sluder, F. J. Schmidlin, L. D. Mendenhall, K. H. Bhavnani, And K. J. Hahn, "Measurements of the high latitude middle atmosphere properties using LIDAR," AFGL-TR-87-0053, Environmental Research Papers, no. 967, Geophysics Laboratory, 129 pages, 1987.
6. C. R. Philbrick, D. B. Lysak, T. D. Stevens, P. A. T. Haris, and Y. -C. Rau, "Atmospheric Measurements Using the LAMP lidar during the LADIMAS campaign," *Proceedings of the 16th International laser Radar Conference*, NASA Conference Publication 3158, pp. 651-654, 1992.

Implications of Aerosol Phenomenology on Sensor and Algorithm Design

Steve Westerman
Lockheed Missiles & Space Company
Org. 66-30 Bldg. 572
Sunnyvale, Ca 94088
(408) 742-6109

I. Introduction

Atmospheric haze, or aerosols, can dramatically reduce the horizontal visibility in a region. During pollution outbreaks such haze can be so thick that it appears to hang in the air. Scientists have been studying the detailed composition, dynamics and effects of aerosols on emitted radiation for years. An eventual goal is to produce a global method for the remote determination of aerosol content. To date, results from these studies have had an impact on our understanding of the Earth-radiation budget, pollution source monitoring, and visible image correction. They have also indicated that the influence of aerosols is very difficult to assess because of its tremendous variation in time and space.

In general this natural variability creates a challenge to both algorithm development and sensor design efforts. How aerosol particle size, its level in the atmosphere, viewing and absorption properties produce measured radiance is quite complex. Many of these features are integrated into one value, horizontal visibility. To support algorithm and sensor tasks we propose a study to map relevant atmospheric phenomena to horizontal visibility and to determine their impacts on its remote measurement.

II. Study Objective

Retrieving surface visibility conditions from satellite data requires an understanding of haze phenomenology. The majority of algorithms that address this problem are model-based, table lookup techniques (1,2). These model-based approaches rely on analytic expressions to characterize aerosol variability. As a first step, this study assesses the range of natural aerosol variability contained in radiative transfer models.

Specifically, this paper investigates the sensitivity of modeled satellite received radiance to a broad range of atmospheric and measurement parameters. Atmospheric and aerosol models, surface albedo, and geometry were investigated because of their direct relation to received radiance in the radiative transfer expression. This selection provides a starting point for further isolation of the critical parameters affecting the remote determination of aerosols. The study allows for the development of a measurement envelope based on aerosol phenomenology.

III. Procedure

A set of measurement characteristics was established for the study. The specific parameters and ranges of this set are found in Table 1. We varied these parameters and evaluated their impact on radiance with LOWTRAN 7 (3). LOWTRAN 7, a low resolution spectral band model, gives us an industry accepted, flexible configuration that is well suited to our proposed sensitivity study.

With the model and parameters selected, the next step was to generate data from all the permutations of input parameters specified in Table 1. To do this, we built streamlined access files into LOWTRAN 7 for data creation. This allowed data for a given group of atmospheric and geometry inputs to be varied over the visibility parameter range. This process produced large data files containing the spectral breakdown and integrated values of transmittance and radiance.

Parameter	Range
Aerosol Model	Rural, Urban, Maritime
Surface Reflectance	0.0 to 30.0 %
Solar Zenith Angle	40.0 to 80.0 °
Satellite Look Angle	0.0 to 40.0 °
Wavelength	0.5 to 1.0 μm
Visibility	0.2 to 50 Km
Atmospheric Profiles	Tropical, Mid latitude, Sub Arctic

Table 1 : Study Parameter Space and Ranges

After generating approximately 1000 individual LOWTRAN 7 runs, graphs of total inband radiance as a function of visibility for each set of parameters were drawn. The curves were the basis for preliminary analysis on trends and limits of aerosol phenomenology to received satellite radiance. An example is given in Figure 1 and shows the characteristic effect of two surface reflectivities on radiance over a visibility range 0 to 50 Km. Except at the lowest visibility levels, the total radiance is much lower for smaller surface reflectances.

IV. Results

In our evaluation process, we computed the impact of varying key parameters on received radiance. We were also concerned with parameters which seemed to have the largest impact on the measurement of visibility. By ranking and denoting the trends each parameter plays in the complicated radiative transfer process, we isolated specific areas for further study. Particular interest was paid to wavelength location and bandwidth because of its direct relation to sensor design.

The most significant findings from this sensitivity study were 1) surface reflectivity modulates the received signal greatly, 2) aerosol composition is a critical factor for low visibilities, and 3) broader bands are more sensitive to aerosol loading than narrow spectral bands. From Figure 1, strong flattening of the 30 percent reflectance curve is seen after the 5 Km visibility level. Similar flattening does not occur until ~20 Km in the 7 percent curve. This represents little if any sensitivity to aerosol for high reflectivities and that non-line of sight scattering (adjacency) effects appear to be a dominant source in low visibility cases.

Results from the aerosol composition comparison are quite pronounced in the 0 - 5 Km range. Figure 2 shows the difference of rural aerosol (land) to maritime aerosol (sea) compositions on total return. At the lower visibilities, maritime aerosols produce larger total radiance returns than rural aerosols. This difference is about $1.5 \text{ mW} / \text{Sr cm}^2$ at 0.2 Km and goes to zero at values greater than 5.0 Km. If this separation holds true, algorithms may be able to make a simple land / sea decision before complete processing. By doing this, the algorithm has reduced the number of aerosol models it must represent and potentially the amount of *a priori* information it would require.

Computations for all the parameters in Table 1 were carried out for four wavelength bands. The bands selected were (0.50 - 0.70 μm), (0.70 - 1.00 μm), (.52 - .60 μm), and (0.63 - 0.69 μm). LOWTRAN 7 simulations showed that the broader (0.5 - 0.7 μm) band to be the most sensitive band to visibility in all cases. The narrower, visible bands proved to be slightly less sensitive, while the near-infrared band the least. This finding was assigned to two factors. First, wider bandwidth in the green to red portion of the spectrum captures more signal. Second, increased scattering both from particulates and molecules is expected for this wavelength region.

The results so far have had algorithm implications. To investigate sensor sensitivity, we calculated the slopes ($\delta V / \delta R$) for several curves. This information is used to assess measurement accuracies

needed for visibility determination. Figure 3 plots the potential visibility error for given levels of sensor measurement uncertainty. The plot shows the potential impact of measurement error on a table look-up methods. Results show that radiance measurements require high accuracy if such a technique is to provide good estimates of visibility over all ranges.

V. Implications

This study has produced results that have implications to both visibility algorithm development and sensor design. There is insufficient sensitivity in the visible total radiance signal at either narrow or broad bands to meet future visibility requirements. As seen in Figure 1, this conclusion is particularly true for scenes over highly reflective surfaces with clear atmospheres (visibility > 10 Km). The effect of aerosol composition on radiance has been shown to be large, but isolated in the lower visibility ranges. We have also found that geometry, particularly the solar zenith angle, changes the level of the radiance return significantly. This feature is a smooth, almost constant function that can be compared to a measurement offset. To summarize, we have found that surface reflectance is the most critical parameter affecting haze phenomenology.

Center frequency, bandwidth and measurement accuracy are a few of the factors considered in the sensor design process. The decisions made on such items as bandwidth and wavelength are application dependent. Optimal bands for visibility may not meet needs for cloud imagery or surface reflectance measurements, and design decisions must weigh such considerations. The results from this study have two implications to sensor design. First, broader visible bands are preferred for total radiance measurements. This is still a design issue since other results have shown that path radiance, and not total radiance, might be a better indicator of haze levels. Second, accurate radiometric measurements are required. Figure 3 highlights the need for accurately measured radiances to estimate visibility. The implication on design will be the requirement of improved on-orbit calibration techniques.

VI. Future Plans

This study has identified several key areas for further investigation. Consequently, we plan to (1) conduct a study examining spatial contrast as a measure of horizontal visibility, (2) develop a processing technique for obtaining path radiance that might lead to a more direct relationship and (3) monitor ongoing visible sensor calibration projects.

VII. References

- 1- Richter, R (1990); A fast atmospheric correction algorithm applied to Landsat TM images; Int. J. Remote Sensing, vol.11 no.1, pp. 159-166
- 2- Haggerty, J.A. et al (1990); A comparison of surface and satellite-derived aerosol measurements in the western Mediterranean; Journal Geophysical Research, vol. 95, no. C2, pp. 1546-1557
- 3- Kneizys, F.X. et al (1988); Users guide to LOWTRAN 7; AFGL-TR-88-0177

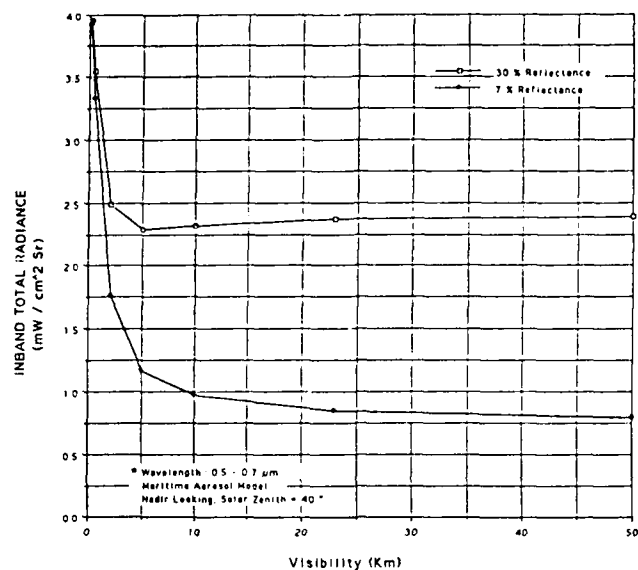


Figure 1 : Data Analysis Curve Exhibiting Impact of Surface Reflectance on Radiance

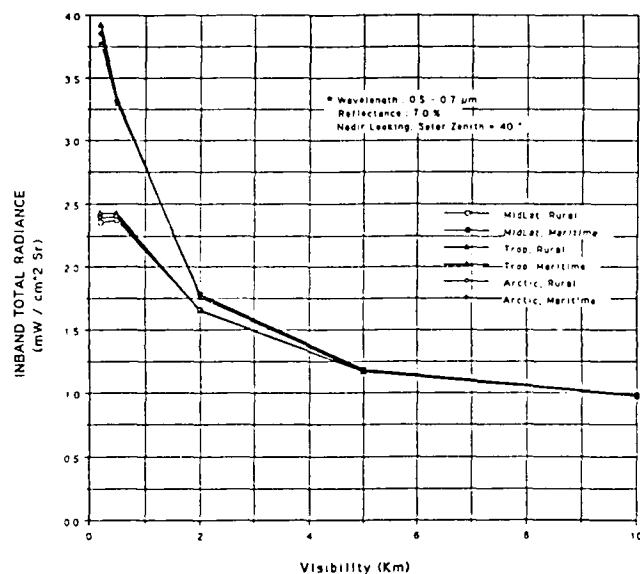


Figure 2 : Aerosol and Atmospheric Model Comparison over Visibility

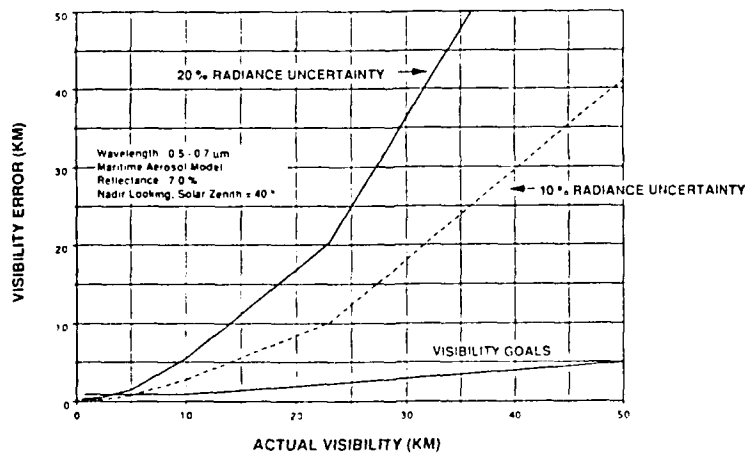


Figure 3 : Measurement Uncertainty Impacts to Visibility Estimates

Thursday, March 11, 1993

Spectroscopy 1

ThC 1:30pm–3:00pm
Salon F

Shepard A. Clough, *Presider*
Atmospheric Environmental Research, Inc.

**The HITRAN Molecular Database:
Enhancements for Remote Sensing**

Laurence S. Rothman
Phillips Laboratory
Geophysics Directorate
Simulation Branch (PL/GPOS)
29 Randolph Road
Hanscom AFB, MA 01731-3010 USA

Telephone: (617) 377-2336

FAX: (617) 377-4451

This paper summarizes some of the major updates, improvements, modifications, and future directions to the spectroscopic molecular database, HITRAN, that enhance its application for remote sensing.

Introduction

The molecular spectroscopic database, known under the acronym HITRAN, has been in existence for two decades to provide the necessary fundamental parameters to represent molecular properties in atmospheric spectroscopic analyses. The original goal of this database was to include the necessary parameters for the requirements of the Lambert-Beer law of attenuation, *i.e.*, the line position (in cm^{-1}), the intensity [(in $\text{cm}^{-1}/(\text{molecule}-\text{cm}^{-2})$], the Lorentzian halfwidth (in $\text{cm}^{-1}/\text{atm}$), and the lower state energy (in cm^{-1}) of each transition. The intensity and halfwidth have been standardized to a temperature of 296K on the compilation, and the halfwidths were chosen to be the air-broadened values. An intensity cutoff criterion was also established: all transitions that yielded at least a 10% absorption through a space-to-space limb-viewing atmospheric path in local thermodynamic equilibrium (LTE) tangent to the surface would be retained.

The HITRAN molecular database¹ currently includes line parameters for 31 species and their isotopomers that are significant for terrestrial atmospheric studies. The line-by-line portion of HITRAN contains about 709,000 transitions between 0 and 23000 cm^{-1} . The most recent compilation also has substantially more information on chlorofluorocarbons and other molecular species that exhibit dense spectra which are not amenable to line-by-line representation. Table 1 is a summary of the molecular species that are currently represented in the line-parameter portion of the compilation. Table 2 summarizes the situation for the cross-section data.

Major Updates

The most recent editions of HITRAN¹ (1991 and 1992) have witnessed a plethora of improvements and extensions to the previous edition² of 1986. The enhancements have been on several fronts: the addition of some molecular species and additional vibrational bands; the inclusion of more parameters for each transition; the implementation of error codes and reference codes; and the improvement of the interface software for the database. We highlight here some of the improvements to molecular bands that would be expected to impact a majority of users whose applications include remote sensing.

Molecule	Isotopes	# of Bands	# of Lines
H ₂ O	4	134	48 523
CO ₂	8	592	60 790
O ₃	3	76	168 881
N ₂ O	5	140	24 125
CO	5	31	600
CH ₄	3	48	47 415
O ₂	3	18	2 254
NO	3		7 385
SO ₂	2	7	26 225
NO ₂	1	9	55 468
NH ₃	2	9	5 817
HNO ₃	1	13	143 021
OH	3	27	8 676
HF	1	6	107
HCl	2	17	371
HBr	2	16	398
HI	1	9	237
ClO	2	8	6 020
OCS	4	6	737
H ₂ CO	3	10	2 702
HOCl	2	6	15 565
N ₂	1	1	120
HCN	3	8	772
CH ₃ Cl	2	6	6 687
H ₂ N ₂	1	2	5 444
C ₂ H ₂	2	9	1 258
C ₂ H ₆	1	2	4 749
PH ₃	1	2	2 886
COF ₂	1	7	46 894
SF ₆	1	1	11 520
H ₂ S	1	1	661

Table 1. Summary of Molecular Species on HITRAN

Molecule	Spectral Range (cm ⁻¹)	No. of Temps	Number of points per T
CCl ₃ F (CFC-11)	830-860	6	2 023
	1060-1107	6	3 168
CCl ₂ F ₂ (CFC-12)	867-937	6	4 718
	1080-1177	6	6 539
CClF ₃ (CFC-13)	765-805	6	2 696
	1065-1140	6	5 056
	1170-1235	6	4 382
C ₂ Cl ₃ F ₃ (CFC-113)	780.5-995	6	430
	1005.5-1232	6	454
C ₂ Cl ₂ F ₄ (CFC-114)	815-860	6	3 034
	870-960	6	6 067
	1030-1067	6	2 494
	1095-1285	6	12 808
C ₂ ClF ₅ (CFC-115)	955-1015	6	4 044
	1110-1145	6	2 360
	1167-1259	6	6 269
N ₂ O ₅	555.4-599.8	4	93
	720.3-764.7	4	93
	1210.1-1274.8	4	135
	1680.2-1764.6	4	176
ClONO ₂	740-840	2	10 371
	1240-1340	2	1 400
	1680-1790	2	1 540
HNO ₄	770-830	1	5 476
CHCl ₂ F (CFC-21)	785-840	1	5 020
CCl ₄	786-806	1	1 826
CF ₄ (CFC-14)	1255-1290	6	2 359
CHClF ₂ (CFC-22)	780-1335	6	11 798

Table 2. Summary of Cross-section Data

Water vapor has had major improvements in the near infrared and visible regions (which has extended the spectral range of HITRAN) as well as a significant improvement in the ν_2 region. Indeed, recent simulations in this latter region demonstrate the success. A long standing program has been in progress to provide improved carbon dioxide parameters. In the latest edition of HITRAN the largest impact will be in the improved intensities and halfwidths. Details of the current status of CO_2 are given in Refs. 3 and 4. There were very significant changes of the ozone line parameters for the 1991 edition. In addition to updates of bands already on previous compilations, many new bands were added. For the first time the bands of $^{16}\text{O}^{16}\text{O}^{18}\text{O}$ and $^{16}\text{O}^{18}\text{O}^{16}\text{O}$ have been calculated based on analyses of high-resolution spectroscopic data which is a vast improvement over the earlier rough estimates that existed on HITRAN for some of the isotopic bands. Details of this work are contained in the article of Flaud *et al.*⁵ as well as Ref. 1. For methane, the major changes were improvements to existing entries at longer wavelength, the inclusion of new weak bands, and the addition of measured widths and shifts in all regions. The article by Brown *et al.*⁶ provides the details of the methane revisions.

Major changes have been made for nitrogen dioxide (NO_2) have been made. These modifications included a total replacement of the ν_2 region and the pure rotation bands.⁷ It should be stated, however, that although these updates represent a significant improvement, much work remains to be done, and is indeed being pursued by groups involved. Another trace gas species that has seen significant improvement is nitric acid. Goldman and Rinsland⁸ detail some of the effort that has gone into this enhancement, which includes new parameters for many bands in the longer wavelength regions of the infrared.

Among species added recently to HITRAN are carbonyl fluoride (COF_2), sulfur hexafluoride SF_6 , and hydrogen sulfide H_2S . These molecules have all been detected in the stratosphere. For additional details, one should consult the papers by Rinsland *et al.*⁹ and May.¹⁰

The chlorofluorocarbons (CFC's) and oxides of nitrogen are examples of species exhibiting dense spectra that have so far, with a few exceptions, eluded representation in the discrete parametrized format used for the molecules shown in Table 1. The approach taken in HITRAN has been to provide cross-sections for several molecular bands derived from high-resolution experimental data. The cross-sections σ are given in units of $\text{cm}^2/\text{molecule}$ corresponding to transmittance of $\exp(-\sigma\eta)$, where η is the gas-column density ($\text{molecule}/\text{cm}^2$). The latest database has many of the important bands observed at six different temperatures that span representative values for the earth's atmosphere (see Table 2). The latest generation of line-by-line codes, make use of this information and can produce quantitative simulations of atmospheric profiles. Future refinements will include data at representative pressures. It is likely that line-coupling effects will also be of interest for the heavy molecules. The cross-sections for the HITRAN91/92 compilation are described in detail by Massie and Goldman.¹¹

As just one representative example of the power that one now has for remote sensing, we cite the recent observations of tropospheric trace gases made by Rinsland and Goldman.¹²

Conclusion

HITRAN is continually evolving to better meet the requirements of a diverse group of users: remote sensing of the atmosphere, planetary atmospheres, energetically disturbed atmospheres, combustion processes, detection of radiant sources through the intervening atmosphere, pollution monitoring, and global climate change monitoring. As new instruments in different spectral regions become operational, HITRAN endeavors to provide the parameters necessary for these tasks. Recently, error criteria have been added to HITRAN. It is hoped that sensitivity studies will be made to better show the effects of the errors on particular simulations.

The current version of the database is available on both floppy diskettes in compressed form and CD-ROM disks (formerly the databases were available only on large magnetic tape). The direction is clearly for PC orientation. There will be made available to the user more powerful tools to rapidly access subsets of data, plot data, and perform various preliminary analyses. Supplemental sets of molecular data will also become accessible.

One must emphasize that the HITRAN project is the result of the efforts of many researchers throughout the world. The megabytes of data result from the often thankless work of numerous spectroscopists analyzing, identifying, calculating, and painstakingly measuring thousands of spectral lines in laboratories and in the field.

The HITRAN92 database can be obtained on magnetic tape from the National Climatic Center of NOAA, Federal Building, Asheville, NC 28801-2696. It is available on floppy diskettes for use on MS-DOS machines from Prof. Dennis Killinger, Dept. of Physics, University of South Florida, Tampa, FL 33620. A version on CD-ROM optical disk can be obtained from the author.

Acknowledgments This program has been funded through the Air Force Office of Scientific Research Task 2310G1. The effort has also been supported by the Atmospheric Radiation Measurement program under the Department of Energy interagency agreement No. DE-AI06-90RL12076.

References

1. L.S. Rothman, R.R. Gamache, R.H. Tipping, C.P. Rinsland, M.A.H. Smith, D. Chris Benner, V. Malathy Devi, J.-M. Flaud, C. Camy-Peyret, A. Perrin, A. Goldman, S.T. Massie, L.R. Brown, and R.A. Toth, *JQSRT* **48**, 469 (1992).
2. L.S. Rothman, R.R. Gamache, A. Goldman, L.R. Brown, R.A. Toth, H.M. Pickett, R.L. Poynter, J.-M. Flaud, C. Camy-Peyret, A. Barbe, N. Husson, C.P. Rinsland, and M.A.H. Smith, *Appl. Opt.* **26**, 4058 (1987).
3. L.S. Rothman, R.L. Hawkins, R.B. Wattson, and R.R. Gamache, *JQSRT* **48**, 537 (1992).
4. R.B. Wattson and L.S. Rothman, *JQSRT* **48**, 763 (1992).
5. J.-M. Flaud, C. Camy-Peyret, A. Perrin, and C.P. Rinsland, *JQSRT* **48**, 611 (1992).
6. L.R. Brown, J.S. Margolis, J.P. Champion, J.C. Hilico, J.M. Jouvard, M. Loëte, C. Chackerian, Jr., G. Tarrago, and D. Chris Benner, *JQSRT* **48**, 617 (1992).
7. A. Perrin, C. Camy-Peyret, and J.-M. Flaud, *JQSRT* **48**, 645 (1992).
8. A. Goldman and C.P. Rinsland, *JQSRT* **48**, 653 (1992).
9. C.P. Rinsland, A. Goldman, and J.-M. Flaud, *JQSRT* **48**, 693 (1992).
10. R.D. May, *JQSRT* **48**, 701 (1992).
11. S.T. Massie and A. Goldman, *JQSRT* **48**, 713 (1992).
12. C.P. Rinsland and A. Goldman, *Appl. Opt.* **31**, 6969 (1992).

Molecular Absorption Parameter Measurements for Remote Sensing Applications

Zhiping Chu, Li Chen and Peter K. Cheo

Electrical and Systems Engineering Department

U-157, University of Connecticut

Storrs, CT 06269

Tel: (203) 486-0624

FAX: (203) 486-3789

Mid-infrared region of the spectrum is rich with vibrational-rotational lines of molecular pollutants within the atmosphere. Differential absorption lidar (DIAL) technique has commonly been used to remotely detect the low concentrations of the pollutants.¹⁻³ This technique depends critically on the assumed molecular absorption line frequency, line strength, linewidth, pressure shift of line frequency and temperature dependence of line width. In the present study, a novel and compact IR tunable laser system with narrow linewidth and wide tunability⁴ in the spectral range from 9.1 to 12.5 μm has been built. Our objective is to measure the line parameters of the atmospheric gases by taking advantage of the high power and wide tunability of this sideband laser. Those parameters are important for remote sensing applications between 9.1-12.5 μm . This paper presents the measurements of absorption line frequencies, frequency shifts due to pressure, line strengths and self-broadened Lorentz linewidths of NH_3 and C_2H_4 transitions which were covered by the CO_2 laser used in the experiment.

In this work, a grating tuned CO_2 laser has been assembled and it provides a limited laser lines in the 9 and 10 μm bands with a single mode spatial distribution and frequency stability less than 100 KHz. To attain an efficient and broadband tuning of the sideband laser frequency, each laser line was sequentially coupled into a CdTe buffered GaAs waveguide modulator. Along the optical path a traveling-wave modulation field at microwave frequencies (8 to 18 GHz) was applied to a 3.5 cm long microstrip electrode. A useful sideband power of 10 to 50 mW was made available with a 5-10 W CO_2 laser in our experiments.

Using this tunable CO₂ laser, we have made a series of high resolution measurements of the molecular absorption parameters. Figure 1 is a schematic diagram of the apparatus. Various gas samples can be measured and analyzed in a similar way. We measured NH₃ and C₂H₄ absorption lines which were covered by the tunable sidebands generated from P(8) to P(40) CO₂ laser lines in the 001→100 transition band. The absorption cell length was chosen such that the line center absorption was always in the optimum range of 20% to 80%.

The microwave synthesized sweeper, the Fabry-Perot interferometer FP2 which was used as a monochromator and the data acquisition were controlled by an IBM 286 computer. With regard to the systematic errors which can arise in fitting calculated and measured line profiles, care was taken to ensure that each scan was obtained at relatively slow speeds to avoid line distortion.

From high-resolution absorption scans we can determine line parameters with a least-square fitting program. For each absorption line the optical depth was determined from three scans, namely, absorption scan, vacuum scan and saturation scan. Absorption scan gave the absorption line shape. Vacuum and saturation scans were taken periodically to check the 0% and the 100% absorption. By least-square fitting Voigt profile with the recorded data we can determine the absorption parameters: line center frequency ν_0 , line strength S , and self-broadened Lorentz linewidth γ_L . Figure 2 shows a typical absorption line scan of NH₃ which is least-square fitted by a Voigt profile. The lower curve is the plot of residuals which is the difference between the measured data and the theoretical curve.

For both the upper and the lower sidebands (± 8 to ± 18 GHz), the absorption line frequency was derived with maximum uncertainty of 1.5×10^{-4} cm⁻¹. Because the CO₂ lines have been well known and tabulated, and in this experiment the microwave resolution is 1 kHz and laser line stability was better than 100 KHz we conclude that the uncertainty in line position determination could be increased by adding more sampling points or reducing the scan range. With the improvement of laser line stability which can reach 1 KHz by using a Lamb-dip frequency stabilizer, the accuracy of the measured line frequency can be achieved to about 1 kHz, e.g., the accuracy will be 1.25 KHz for a 1 MHz scan range and 801 sampling points.

The accurate and easy determination of the absolute line frequency makes the study of line frequency shift due to pressure possible. Absorption spectra were taken

from runs at different pressures. Figure 3 presents the line positions for 3 transitions as a function of NH_3 pressure. The results indicate the expected linear dependence. The slope of the straight line best fit to the dispersed points is the measured frequency shift. In Figure 4, the self-broadened Lorentz linewidths γ_L of 3 transitions are shown also as a function of NH_3 pressure. The measured linear dependence agrees with the collision-broadening theory. The line width measurements are accurate to about 6%.

It is expected that a significant contribution can be made to the basic spectroscopic study by using this tunable sideband laser not only for the direct absorption measurements but also for the coherent measurements in a heterodyne configuration. Because the spectrum region covered by this system lies in the well known 8-13 μm atmospheric window, this technique will be really prominent in the research of the atmospheric spectra and in astrophysical exploration.

The authors are grateful to the Division of Atmospheric Science of National Science Foundation under a grant #ATM 9011067 and the School of Engineering of University of Connecticut for support. The authors wish to thank Paul Dufilie, Weiqun Chen and Mark Castracane for their technical assistance.

REFERENCES

1. A. P. Force, D. K. Killinger, W. E. Defeo, and N. Menyuk, *Appl. Opt.* **24**, 2837-2841 (1985).
2. E. E. Uthe, *Appl. Opt.* **25**, 2492-2498 (1986).
3. T. Itabe, K. Asai, M. Ishizu, T. Aruga, and T. Igarashi, *Appl. Opt.* **28**, 931-934 (1989).
4. P. K. Cheo, *IEEE J. Quant. Electronics*, **QE-20**, 700-709 (1984).

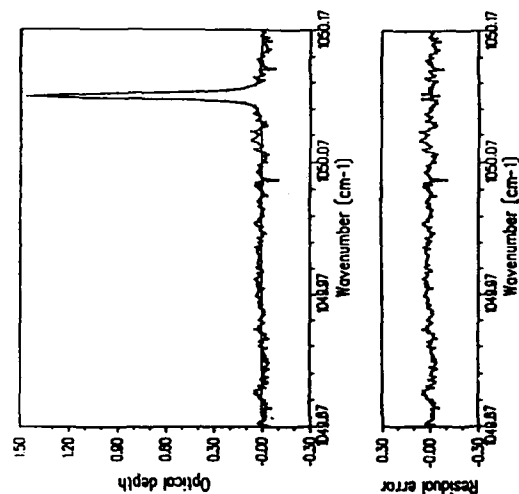


Fig. 2. Upper trace shows the scanned optical depth curve at $p=1.85$ torr, which is least-square fit to a Voigt profile. The bottom trace shows the residual error (meas.-cal.).

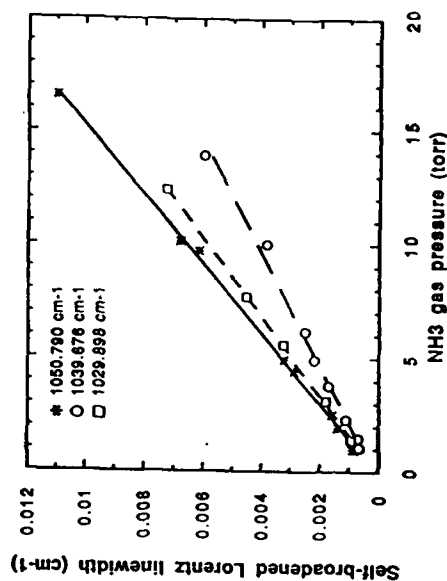


Fig. 4. Self-broadened Lorentz linewidths for three transitions are shown as a function of NH_3 pressure.

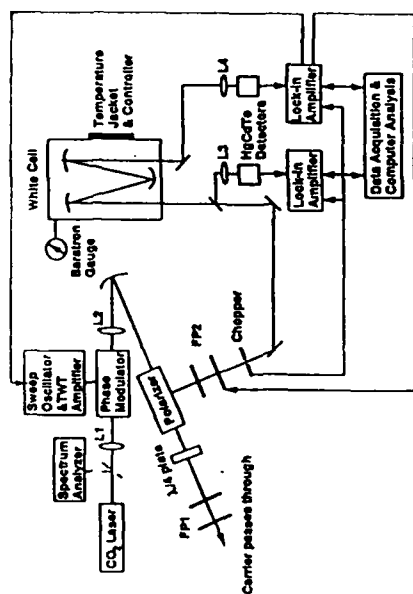


Fig. 1. Experimental setup of the CO_2 sideband laser system for the molecular absorption parameter measurements.

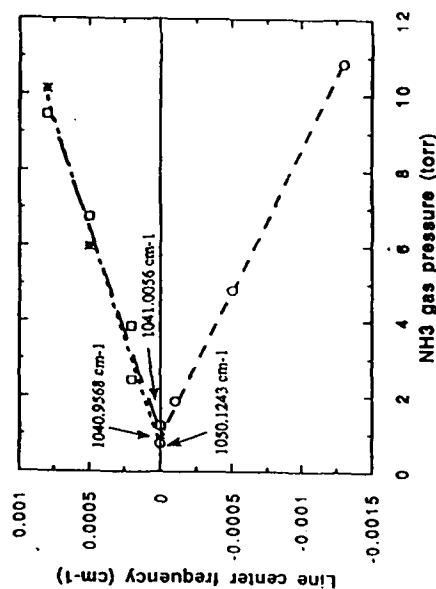


Fig. 3. Line center frequencies for three transitions are plotted as a function of NH_3 pressure. The markers pointed by the arrows indicate frequencies measured at the lowest pressures. The slopes of the straight fitting lines are the frequency shifts due to pressure.

Infrared Spectroscopic Measurements Needed for Atmospheric Remote Sensing

P. Varanasi, U. Shin, and A. Gopalan
Marine Sciences Research Center
The University at Stony Brook
Stony Brook, NY 11794-5000

We have measured the infrared spectra of several atmospheric molecules in our laboratory at low temperatures appropriate for atmospheric remote sensing using the high-resolution of a state-of-the-art Fourier transform spectrometer (FTS) and a tunable diode laser spectrometer (TDLS). However, in order to limit the summary to four pages, we present here only the details of the measurements of the collision-broadened half-widths of $sP(1,0)$, $sP(3,2)$, $sP(4,1)$, $sP(4,2)$, and $sP(4,3)$ in the ν_2^s -fundamental bands of $^{14}\text{NH}_3$ and $^{15}\text{NH}_3$ at 198, 245, and 295 K employing the Doppler-limited spectral resolution ($\sim 10^{-4} \text{ cm}^{-1}$) of the TDLS. The temperature dependence of the collision-broadened half-widths of these lines broadened by N_2 has been determined. In addition, we have also measured the air-broadened linewidths of all of these lines at 295 K and the half-width of the $sP(3,2)$ line of $^{15}\text{NH}_3$ broadened by $^{14}\text{NH}_3$ at 198, 245, and 295 K. Our tunable diode laser spectrometer, the low-temperature absorption cell, and the experimental technique for measuring collision-broadened (Lorentz) linewidths have been described previously.¹

The parameter n appearing in the last columns of Tables 1-2 describes the variation of γ_L^0 with T . It is defined in the well known power-law

$$\gamma_L^0(T)/\gamma_L^0(T_0) = (T_0/T)^n$$

in terms of the line width $\gamma_L^0(T_0)$ at a reference temperature T_0 . A more useful form of the above law for graphical analysis is

$$-\ln \gamma_L^0(T) = n \ln T + \text{constant}. \quad (1)$$

In almost all the N_2 -broadened linewidth measurements, even though the mixtures were quite lean, self-broadening was taken into account. As can be

seen from the values given in Table 3, self-broadened line widths are quite large. Since self-broadening involves samples of pure ammonia and not dilute mixtures, in order to avoid saturation of the line centers, we have measured the half-widths of $^{15}\text{NH}_3$, which is present in its natural abundance as an impurity in $^{14}\text{NH}_3$, broadened by $^{14}\text{NH}_3$. The values of n given in the last column define the power-law dependence of line width on temperature.

Acknowledgements— This work was supported by the Upper Atmospheric Research Program of the Earth Sciences and Applications Division of NASA under Grant-in-Aid No. NAGW-1238.

References

1. P. Varanasi, *JQSRT* 47, 263 (1992).

List of Tables

Table 1. Nitrogen-broadened linewidths, γ_L^0 ($\text{cm}^{-1} \text{ atm}^{-1}$), of several lines in the ν_2^s band of $^{14}\text{NH}_3$ and $^{15}\text{NH}_3$ at 198, 245 and 295 K. The uncertainties quoted are standard deviations in the data. The entries in the last column are values of n which is defined in Eq.(1).

Table 2. The half-width, γ_L^0 ($\text{cm}^{-1} \text{ atm}^{-1}$), of the $P(3,2)$ line in the ν_2^s band of $^{15}\text{NH}_3$ broadened by $^{14}\text{NH}_3$ at 198, 245 and 295 K. The uncertainties quoted are standard deviations in the data. The entries in the last column are values of n which is defined in Eq.(1).

Table 3. Air- and N_2 - broadened linewidths at 295 K. The entries in the last column is $\gamma_L^0(\text{NH}_3\text{-air}) : \gamma_L^0(\text{NH}_3\text{-N}_2)$, the so-called relative broadening efficiency r of air with respect to N_2 .

Table 1.

Isotope	Line	ν (cm ⁻¹)	γ_L^0 (cm ⁻¹ atm ⁻¹)			<i>n</i>
			295 K	245 K	198 K	
¹⁴ NH ₃	<i>sP</i> (1,0)	948.2321	0.1130 ± .0014	0.1274 ± .0034	0.1533 ± .0008	0.77
	<i>sP</i> (3,2)	908.1122	0.1373 ± .0009	0.1515 ± .0018	0.1689 ± .0019	0.52
	<i>sP</i> (4,1)	888.0794	0.1051 ± .0012	0.1239 ± .0015	0.1402 ± .0016	0.72
	<i>sP</i> (4,2)	887.9998	0.1108 ± .0014	0.1272 ± .0021	0.1471 ± .0018	0.71
	<i>sP</i> (4,3)	887.8767	0.1164 ± .0003	0.1268 ± .0024	0.1496 ± .0012	0.63
¹⁵ NH ₃	<i>sP</i> (1,0)	943.0350	0.1115 ± .0039	0.1247 ± .0039	0.1546 ± .0017	0.82
	<i>sP</i> (3,2)	903.0350	0.1320 ± .0013	0.1445 ± .0016	0.1596 ± .0004	0.48
	<i>sP</i> (4,1)	883.0990	0.0993 ± .0009	0.1204 ± .0026	0.1349 ± .0017	0.76
	<i>sP</i> (4,2)	882.9990	0.1134 ± .0014	0.1308 ± .0014	0.1481 ± .0008	0.67
	<i>sP</i> (4,3)	882.8500	0.1122 ± .0004	0.1320 ± .0014	0.1517 ± .0008	0.75

Table 2.

Line	ν (cm ⁻¹)	γ_L^0 (cm ⁻¹ atm ⁻¹)			<i>n</i>
		295 K	245 K	198 K	
<i>sP</i> (3,2)	903.0350	0.4881 ± .0080	0.5771 ± .0190	0.6945 ± .0060	0.99

Table 3.

Isotope	Line	ν (cm ⁻¹)	γ_L^0 (cm ⁻¹ atm ⁻¹)		r
			N ₂	air	
¹⁴ NH ₃	<i>sP</i> (1,0)	948.2321	0.1130 ± .0014	0.0998 ± .0015	0.88
	<i>sP</i> (3,2)	908.1122	0.1373 ± .0009	0.1210 ± .0018	0.88
	<i>sP</i> (4,1)	888.0794	0.1051 ± .0012	0.0868 ± .0039	0.83
	<i>sP</i> (4,2)	887.9998	0.1108 ± .0014	0.0985 ± .0012	0.89
	<i>sP</i> (4,3)	887.8767	0.1164 ± .0003	0.1016 ± .0027	0.87
¹⁵ NH ₃	<i>sP</i> (1,0)	943.0350	0.1115 ± .0039	0.0929 ± .0039	0.83
	<i>sP</i> (3,2)	903.0350	0.1320 ± .0013	0.1109 ± .0020	0.84
	<i>sP</i> (4,1)	883.0990	0.0993 ± .0009	0.0840 ± .0009	0.85
	<i>sP</i> (4,2)	882.9990	0.1134 ± .0014	0.0956 ± .0008	0.84
	<i>sP</i> (4,3)	882.8500	0.1122 ± .0004	0.0966 ± .0016	0.86

NDSC Infrared Observations at Mauna Loa, Hawaii

F.J. Murcray, D.G. Murcray, S.J. David,
R.D. Blatherwick, J.J. Kusters, F.H. Murcray, and A. Goldman

University of Denver, Department of Physics

Denver, CO 80208

(303) 871-3557

C.P. Rinsland

NASA Langley Research Center

Hampton, VA 23665

(804) 864-2699

Since May 1991, the University of Denver is involved in high resolution infrared atmospheric measurements at Mauna Loa, Hawaii, one of the Network for Detection of Stratospheric Change (NDSC) primary sites, using a BOMEM DA3.002 interferometer. Additional measurements for monitoring and intercomparisons are made at Denver, with a BRUKER IFS HR and BOMEM DA3.002 interferometers. More recently, the involvement has been extended to several complementary NDSC sites.

At M. Loa, the high resolution (0.002 cm^{-1}) interferometer is used for infrared solar observations in several wide spectral intervals in the $700\text{--}4300\text{ cm}^{-1}$ region. These intervals cover most constituents of interest to atmospheric chemistry in general and specifically to NDSC, including HCl, CH₄, HNC₃, ClONO₂, O₃, NO, NO₂, HF, N₂O, CO₂, CO, OCS, HCN, C₂H₆, CF₂Cl₂, CHF₂Cl, COF₂, C₂H₂ and CFCl₃.

Measurements are now made on a weekly basis, and retrievals of several species are performed regularly, including HCl, HNO₃, N₂O and O₃ and the analysis of other species is in progress. It is noted that some constituents, such as HNO₃, show large daily variations.

The retrievals are performed with non-linear spectral least squares fitting programs, using the HITRAN92 spectral line parameters with special updates, such as for the HNO₃ and HCl regions. The retrievals provide total column densities above the site, and the analysis is aimed at separating the stratospheric column from the tropospheric column. The retrieval algorithms also require

accurate parameterization of the instrument spectral response function.

In addition to the regular NDSC activities for long-range trend monitoring, the site allows the observations of special events, such as the SO₂ emission from Mt. Pinatubo eruption in 1991, and also provides correlative measurements for space-borne instruments, such as UARS.

The M. Loa site also participates in the traveling calibration cell for intercomparisons and validation among NDSC sites. The analysis of the cell spectra is centered at D.U.

The University of Denver hosted the two NDSC infrared group meetings, in March 1991 and in October 1992. The discussions in these meetings include priority molecules, observing strategy, data intercomparisons and retrieval algorithms. Validation of data and analysis are the main objectives of this group.

The University of Denver is developing the data center for archiving and exchanging infrared spectra from the various primary and complementary NDSC sites.

Activities at the complementary sites include collaboration with several of the new groups on instrumentation and data analysis for solar spectra observations. Atmospheric emission measurements are also planned for some of the sites.

In conclusion, our studies show that atmospheric spectra remain a powerful tool for monitoring our changing atmosphere. Progress in the instrumentation and data analysis provide more accurate quantification of the atmospheric trace constituents.

Thursday, March 11, 1993

Spectroscopy 2

ThD 3:20pm–5:00pm
Salon F

Herbert Fischer, *Presider*
Meteorological Institut Munchen, Germany

338 / ThD1-1

Studies of Atmospheric Constituents from High Resolution
Infrared Atmospheric and Laboratory Spectra

A. Goldman, F.J. Murcray, R.D. Blatherwick, F.H. Murcray,
J.J. Kusters, F.S. Bonomo, S.J. David, and D.G. Murcray

University of Denver, Department of Physics

Denver, CO 80208

(303) 871-2897

C.P. Rinsland

Atmospheric Sciences Division

NASA Langley Research Center

Hampton, VA 23665

(804) 864-2699

High resolution ($0.002\text{--}0.003\text{ cm}^{-1}$) Michelson type interferometer systems have been used at the University of Denver since 1987 to obtain infrared solar absorption spectra of the stratosphere during several balloon flights ($\sim 37\text{ km}$), as well as ground-based solar spectra and laboratory spectra of molecules of stratospheric and tropospheric interest. The stratospheric spectra cover the $700\text{--}2200\text{ cm}^{-1}$ region and show many new spectral features of important atmospheric gases such as O_3 (including ^{18}O and ^{17}O isotopic species), NO_2 , HNO_3 , O_2 , N_2 , COF_2 , ClONO_2 , SF_6 and others. The new spectral features are enhanced by the high resolution and long path spectra obtained during sunrise and sunset. Also, new features appear as the concentrations of some trace gases increases in the atmosphere. An ongoing project of high resolution stratospheric atlas, documents the stratospheric spectral features in selected regions.

In support of the stratospheric and tropospheric spectra, numerous laboratory spectra have been obtained with the same interferometer system. The laboratory spectra cover mostly $700\text{--}3000\text{ cm}^{-1}$ at room temperature, and have also been extended to $500\text{--}5000\text{ cm}^{-1}$ at -50°C . The molecules covered include CCl_4 , CCl_2F_2 , CCl_3F , CF_4 , CHClF_2 , CH_2Cl_2 , CHCl_3 , CH_2O , C_2H_6 , ClONO_2 , COF_2 , COCl_2 , COClF , HCOOH , HNO_3 , H_2O , NO_2 , HNO , N_2O , and others. Spectroscopic analysis of laboratory data is

done in collaboration with several other spectroscopy groups, which provide additional laboratory spectra and molecular constants.

Analysis of stratospheric spectral features combined with analysis of laboratory molecular absorption spectra, improves the spectral line parameters (such as line positions, intensities and pressure broadening) and leads to more complete lines identification and more accurate retrieval quantification of atmospheric gases. The improved line parameters, characterization of the instrument response function and retrievals algorithms, provide a more reliable determination of long-term trends in the concentrations of stratospheric species.

Recently updated line parameters, based on laboratory and stratospheric spectra, include vibration - rotation bands such as HNO_3 ν_2 ; NO_2 ν_3 , $\nu_3 + \nu_2 - \nu_2$; COF_2 ν_6 , ν_2 , $\nu_4/2\nu_5$; SO_2 ν_3 , ν_1 ; N_2 (0-1) eq; O_2 (0-1) eq, md., and ClO (0-1). Ongoing studies include the update of line parameters for HNO_3 $\nu_5/2\nu_9$, ClONO_2 ν_4 , HCl (0-1), and $^{16}\text{O}^{17}\text{O}^{16}\text{O}$, $^{17}\text{O}^{16}\text{O}^{17}\text{O}$ ν_1/ν_3 bands.

Ground-based spectra in the 3-12 μm region are obtained regularly from Mauna Loa (Hawaii) and Denver (Colorado), in support of the Network for Detection of Stratospheric Change (NDSC) and NASA Upper Atmospheric Research satellite (UARS). Analysis of the ground-based spectra provides total column density for most trace gases of interest to atmospheric chemistry down to the ppb range and lower. Some altitude distribution information for species such as O_3 , HCl and HNO_3 can be derived. The observation sites also provide the monitoring of trace gases during special events, such as the July 1991 observations of SO_2 from Mt. Pinatubo eruption.

In addition to ground based solar spectra, we have studied absorption features of several trace gases in infrared spectra recorded over surface level paths of 1 km with very high signal to noise ratio, at the National Solar Observatory on Kitt Peak. These provide measurements of tropospheric O_3 , HCOOH , NH_3 , H_2CO etc.

Our studies indicate that high resolution high signal-to-noise stratospheric and tropospheric spectra will continue to show many new features. With improved line parameters and retrieval algorithms, the analysis of atmospheric spectra will further advance our understanding of atmospheric chemistry and changing composition.

Comparison of Ozone Columns between
FTIR and CLAES over Mauna Loa, Hawaii

Shelle David, Sheryl Beaton, Aaron Goldman, Frank Murcray,
University of Denver, Department of Physics

Denver, Colorado 80208

(303) 871-3557

Aiden Roche, Jack Kumer

Lockheed Missiles and Space Co.

Palo Alto Research Laboratory

Palo Alto, California

Very high resolution infrared solar spectra have been collected from Mauna Loa Observatory by a Fourier Transform Spectrometer (FTS) system. Observations have been made every Wednesday morning (weather permitting) since November, 1991, by the staff of the Observatory, which is operated by the Climate Monitoring and Diagnostics Laboratory of NOAA. The instrument currently covers two spectral regions: 800 to 1200 cm^{-1} and 2800 to 3200 cm^{-1} . Many atmospheric gases have absorptions in these regions which can be used to recover abundance information. Both regions include absorptions due to ozone. For this study, regions near 1146 and 1163 cm^{-1} have been fitted to recover ozone columns.

Spectral fittings to the data were done using the personal computer version of the non-linear least squares routine. Ozone, N_2O , and

H₂O line parameters were taken from the HITRAN 92 database. Radiosonde data from Hilo, Hawaii was merged with a standard atmosphere for temperature and pressure profiles. The shape of the ozone altitude profile used was the monthly average profile from Hawaii (Altmans, NOAA/CMDL, private communication). The least squares fitting program was allowed to vary scale factors multiplying the starting ozone, N₂O and H₂O profiles. In addition, several instrument parameters (wavenumber shift, effective resolution, 100% transmission) were fitted. The resulting ozone profile was summed to produce a total vertical column. This column was compared to the integrated profile obtained from the CLAES instrument on UARS on selected days. These comparisons are of interest because both techniques rely on infrared absorption.

HALOE Observations of Ozone, Halogen, Nitrogen, and Hydrogen Compounds Made from the UARS Platform

J. M. Russell III¹, L. L. Gordley², J. H. Park¹, and S. R. Drayson³

¹Atmospheric Sciences Division, Mail Stop 401B, NASA Langley Research Center,
Hampton, VA 23681-0001, U.S.A., 804-864-5691

²G&A Technical Software, Hampton, VA 23666, U.S.A.

³Research Activities Building, University of Michigan, Ann Arbor, MI 48105, U.S.A.

Experiment and Instrument Approach

The Halogen Occultation Experiment (HALOE) was launched September 12, 1991, by the Space Shuttle Discovery into a 57°, 585-km, near-circular orbit onboard the Upper Atmosphere Research Satellite (UARS). The experiment was allowed to outgas for about 1 month before science observations began on October 11, 1991. The experiment approach is solar occultation. The instrument technique uses the principle of gas-filter radiometry in four channels to measure vertical profiles of HCl, HF, CH₄, and NO, and broadband radiometry in four other channels to measure NO₂, H₂O, O₃, and CO₂. The latter channel is used for pressure registration and temperature versus pressure sounding of the atmosphere. Methane measurements extend to about 70 km, H₂O and temperature to 80 km, O₃ to 90 km, HCl and HF to ≈ 60 km, NO₂ to ≈ 55 km, and NO to 120 km altitude. Results from this experiment have provided the first pressure versus latitude cross sections of HCl, HF, and NO, including continuous measurements of NO from the upper troposphere, in some cases, to the lower thermosphere. The data set will be used to pursue a number of scientific investigations, including stratospheric photochemistry and dynamics studies, evaluation of the impact of natural versus anthropogenic chlorine sources on total chlorine, the effect of volcanic aerosols on the chemistry, and study of Antarctic processes which occur during the ozone hole development and recovery phases.

The HALOE instrument tracks the Sun as it rises and sets at the spacecraft altitude and measures atmospheric attenuation profiles on the Earth limb. Fifteen sunrises and 15 sunsets occur each day, usually in opposite hemispheres. Latitude versus time coverage over the course of a year extends from ≈ 80°N to 80°S. The instrument design allows for the Sun to be acquired over a ± 180° azimuth range, thereby providing the potential for observations to be taken on all solar occultation events. Some events are lost when the UARS spacecraft performs a 180° yaw maneuver approximately every 32-34 days in order to confine the Sun illumination to one side of the spacecraft throughout the mission. During the yaw maneuver, some occultation events are lost due to the need to re-initialize instrument parameters. In addition, a small percentage of events are lost during periods when the orbit precession creates a solar grazing condition in which the Sun is not occultated by the Earth or the period of darkness is small, causing some instrument overheating. A detailed experiment description has been presented by Russell et al. (1992).

During an occultation event, the instrument measures the solar intensity as a function of tangent height, H_0 , which is the point of closest approach of a ray path to the Earth surface. The broadband radiometer channel measurement concept used is illustrated in Fig. 1. By ratioing the endoatmospheric solar signal $V_{\Delta v}$ measured as a function of tangent height, to the exoatmospheric value V_0 , the limb transmittance vertical profile $\tau_a(H_0)$ is obtained in each spectral band (i.e., $2.8 \mu\text{m}$, $6.2 \mu\text{m}$, $6.61 \mu\text{m}$, and $9.85 \mu\text{m}$ for CO_2 , NO_2 , H_2O , and O_3 , respectively). These transmittance profiles are inverted in ground processing to obtain temperature versus pressure and mixing ratio profiles of the gases. Currently, the temperature profiles are measured only above 35 km because of complications resulting from the Mt. Pinatubo aerosol layer. National Meteorological Center (NMC) data are used below 35 km.

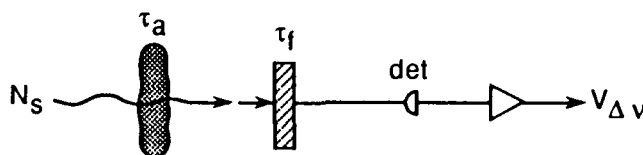


Figure 1. HALOE broadband radiometer measurement concept for NO_2 , H_2O , O_3 , and CO_2 .

The other HALOE measurements of HCl , HF , CH_4 , and NO are made using the much more complicated gas-filter radiometer concept (Fig. 2). In this case, a difference signal, ΔV , between solar energy passing through a gas cell, e.g. HCl , and that which follows a vacuum path through the instrument, is divided by the vacuum path signal, V , at every tangent height to obtain a signal that is sensitive to the gas of interest. The spectral regions used are $2.45 \mu\text{m}$, $3.4 \mu\text{m}$, $3.46 \mu\text{m}$, and $5.26 \mu\text{m}$ for HF , HCl , CH_4 , and NO , respectively.

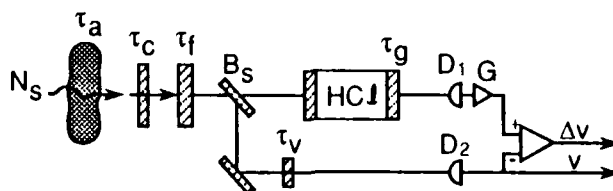


Figure 2. HALOE gas filter radiometer measurement concept for HCl , HF , CH_4 , and NO .

The gas filter approach is required because of strong spectral interference and the tenuous levels (e.g. ppbv) of the gases being observed (Russell et al., 1992). In either approach, broadband or gas filter, the signals are ratioed making the instrument virtually self-calibrating and especially useful in the study of long-term trends, since errors due to unaccounted-for drifts are greatly reduced.

Observations

Pressure versus latitude cross sections have been developed for several periods of HALOE observations for all measured parameters. Examples of these for CH_4 and HF are shown in Figs. 3 and 4, respectively. These cross sections display some obvious and striking similarities. The most notable features are the upward-sloping contours centered slightly southward of the Equator. The larger mixing ratio contours slope upward for CH_4 , and the smaller values do this for HF . This is consistent with the fact that both gases have long lifetimes, are good tracers and, therefore, should be driven by

rising motion due to the Hadley circulation in the Tropics. There is also evidence of poleward transport toward both poles in each cross section. The sharp mixing ratio gradient which appears in CH_4 from $\approx 18^\circ\text{S}$ to 43°S and below ≈ 60 mb is an artifact due to strong aerosol absorption. HALOE has made the first pressure versus latitude cross section measurements of HCl , HF , and NO . The NO data show strong correlations with solar activity. Observations have also been made in two Antarctic spring periods which have revealed important mechanisms which are operative during the ozone hole recovery period. The experiment has shown the presence of very strong vertical descent in the Antarctic vortex center region and has measured the time constant of O_3 , H_2O , and HCl recoveries in the spring. The data also show evidence that low latitude air has been transported inside the vortex in late October when the vortex winds have begun to weaken in places.

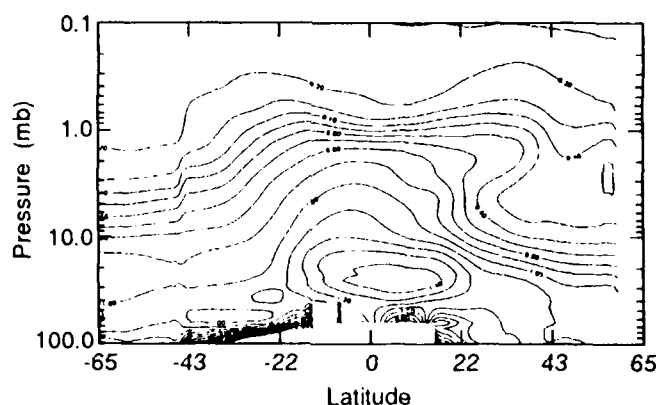


Figure 3. CH_4 (dV) pressure vs latitude cross section, sunset on January 10 to February 10, 1992.

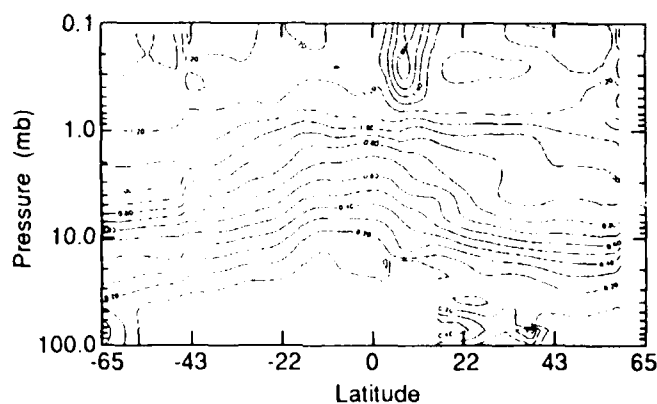


Figure 4. HF (dV) pressure vs latitude cross section, sunrise on January 10 to February 10, 1992.

Conclusions

The HALOE instrument performance in orbit is very good to excellent. Signal drift rates, noise values, gains, and pointing characteristics are well within specifications. The transmission noise, for example, is ≤ 0.05 percent in all channels, and the gas filter noise is equivalent to resolving difference signals of ≤ 1 part in 10^5 . The indicated precision obtained using Southern Hemisphere summer retrievals is on the order of 0.1 to 0.5 ppbv for HCl, HF, NO, and NO₂, and 0.03 to 0.4 ppmv for CH₄, H₂O, and O₃ over most of the measurement altitude range. Comparisons with correlative measurements are encouraging. Zonal mean CH₄ and HF pressure versus latitude cross sections both show features consistent with those expected of tracer molecules. This has important implications for science studies and is an indirect validation of this first HF latitudinal survey. In conclusion, the quality of the HALOE data is very good and will allow all scientific objectives to be obtained.

References

Russell, James M. III, L. L. Gordley, J. H. Park, S. R. Drayson, W. D. Hesketh, R. J. Cicerone, A. F. Tuck, J. E. Frederick, J. E. Harries, and P. J. Crutzen, 1992: The Halogen Occultation Experiment, Submitted to *J. Geophys. Res. Special Issue on UARS*.

Paper withdrawn

Atmospheric Trace Molecule Spectroscopy (ATMOS) Data Analysis Method

M. C. Abrams, M. R. Gunson, L. L. Lowes,
Jet Propulsion Laboratory
California Institute of Technology
4800 Oak Grove Dr., Pasadena, Ca., 91109

R. Zander,
Institute of Astrophysics
University of Liege
B4000, Liege-Cointe, Belgium
and

C. P. Rinsland
Atmospheric Sciences Division,
NASA Langley Research Center
Hampton, VA, 23665

The Atmospheric Trace Molecule Spectroscopy (ATMOS) experiment makes use of a Fourier transform spectrometer to measure solar spectra from the Space Shuttle payload bay. The data analysis strategy and method used during the ATLAS-1 mission will be described.

During the ATLAS-1 mission in March/April 1992, the ATMOS instrument obtained 94 sets of interferograms during solar occultations at latitudes from 55° S to 30° N with tangent height spacings of about 2 km. The interferograms are transformed and ratioed against high sun spectra to produce pure atmospheric transmission spectra covering the spectral region from 2 to 16 μm with signal-to-noise ratios ranging from ~ 250 at 16 μm to 50 at 2 μm . The process of inverting such a large number of measured spectra into profiles of atmospheric constituents requires a data analysis strategy that is both interactive, so that each step can be validated and tested independently, and automatic, so that it can be applied routinely. In refining this process, choices were made based on the need to produce accurate geophysical parameters in a timely manner.

The high resolution, broad-band spectral response of the ATMOS instrument permits an accurate spectroscopic determination of the observing geometry, and of the atmospheric temperature profile,

which are necessary steps before determining the volume mixing ratio profiles of more than 30 telluric constituents.

The observational geometry (the tangent pressure or height of the limb spectrum) is determined between altitudes of 15 and 70 km by inverting CO_2 and N_2 lines whose atmospheric distributions are well known, and coupling these measurements with tangent heights predicted from the spacecraft ephemeris. The later, without other information, was shown to be accurate to only a few kilometers, which was deemed to be an unsatisfactory limit to the accuracy of the retrieved quantities throughout the entire stratosphere and mesosphere. Generally, the spectroscopic determination of tangent pressures, which in conjunction with climatological information on the heights of well determined pressure levels, provided tangent heights to an accuracy of about 200 meters.

In three of the five primary optical filters used by ATMOS it is possible to perform a pressure-temperature retrieval by global fitting of CO_2 absorption features assuming an *a priori* CO_2 distribution. The method provides measured temperature profiles from 10-70 km, which overlap and extend above the profiles provided by meteorological sources, in this case the National Meteorological Center (NMC). In the thermosphere only some spectroscopic retrievals are possible with the CO_2 ν_3 band, and the EMSIS climatological model is used to extend, where necessary, our pressure-temperature profiles. In practice the retrieved pressure-temperature profiles and the NMC profiles have been found to be in good agreement. Due to the computational time involved in the pressure-temperature retrievals, merged NMC-EMSIS profiles have been adopted to proceed with the more rapid constituent retrievals. Sensitivity studies have compared constituent retrievals using various physical models which indicate that the utilization of the merged NMC-EMSIS model is often satisfactory. This is mainly due to the careful selection of telluric absorption features which are insensitive to temperature errors.

Constituent retrievals are performed routinely with an onion-peeling algorithm, results from which have been validated with other global fitting algorithms. A number of studies have been performed to test the sensitivity of the onion-peeling method to modelling of the finite field-of-view effect and the dependence on the *a priori* constituent profile. The onion-peeling approach is particularly attractive for routine analysis because of its large speed advantage.

Each step in the analysis permits validation for self-consistency and sensitivity to the assumptions made in obtaining the results. The merit of a broadband survey instrument is that the reliance on

outside models and input is minimal, and can be verified internally. In addition, the simultaneous measurement of physical conditions and constituent distributions provides a consistent suite of geophysical information.

Thursday, March 11, 1993

Poster Session

ThE 8:00pm–10:00pm
Salon A

MONITOR OF EJECTIONS OF INDUSTRIAL POLLUTANTS IN THE ATMOSPHERE USING A TV CAMERA

V.A.Banakh, *V.L.Mironov, *V.V.Morskii, I.N.Smalikho,
*I.A.Sutorikhin

*Institute of Atmospheric Optics SB Rus.Acad.Sci.,
Tomsk, 634055, Russia
Altai State University, Barnaul, Russia

One of the problems of ecological monitoring of the atmosphere is operative diagnostics of ejection power of pollutants close to pollution sources, for example, plant chimneys [1]. At present, different methods of remote sensing of industrial pollutions have been developed, in particular, the methods based on the optical measurements. In this case, as is shown in [2], the measurements of image brightness of smoke plumes with the use of a TV camera appear to be sufficiently informative.

In the present paper a theoretical analysis is given concerning the possibilities of determination of pollution ejection power and average concentration of smoke plume particles according to brightness of its optical image. The results of theoretical calculations are compared with the data of the experiment made with the use of the TV camera for the case of a model pollution source. Statistical description of the process of pollutants transfer in the atmosphere is presented. The problem of scattering of solar and background light by the smoke plume particles taking into account the turbulent particle mixing due to the wind velocity fluctuations is considered within the framework of the theory of light multiple scattering. The influence of irregularity of smoke outflow from chimneys (fluctuation of ejection power) on the characteristic of optical images is under study. The results obtained make it possible to propose a number of methods for determining the pollution ejection power and average concentration of the smoke plume particles.

References

1. G.I. Marchuk, Mathematical Modeling in the Problem of Environment. (M. Nauka, 1982), 210p.
2. V.L. Mironov, V.V. Morskii, I.A. Sutorikhin, Atmospheric Optics, 1990, v. 3, No. 4, p. 447.

DETERMINATION OF EJECTION POWER OF POLLUTANTS ACCORDING TO OPTICAL RADIATION BACKSCATTERING

V.A.Banakh, I.N.Smalikho

*Institute of Atmospheric Optics SB Rus. Acad. Sci.,
Tomsk 634055, Russia*

The paper presents a method for remote determination of ejection power of a local source of pollution from the measurements of backscattering intensity when sounding the smoke plumes using a directed cw optical beam. For the light intensity distribution along the coordinate x in the image plane of smoke plume we can write the following formula [1]:

$$V(x) = \frac{1}{2} T\beta [1 - e^{-2\mu(x)}] / \mu, \quad (1)$$

where T is the geometric factor, β is the backscattering coefficient, μ is the summarized parameter, depending on the ratio of smoke particles to the wavelength and on the scattering albedo.

$$\tau(x) = \sigma_0 \int_{-\infty}^{\infty} dz \rho(z, x) \frac{z_0}{F} \quad (2)$$

is the optical depth, σ_0 and ρ are the total cross-section of scattering and particle concentration, respectively; z_0 is the distance to the plume; F is the focal length of the telescope receiving lens.

The formula for ejection power of pollutants M is of the form:

$$M = \theta_y \int_{-\infty}^{\infty} dz dx \rho(z, x), \quad (3)$$

where θ_y is the component of the average wind velocity perpendicular to the plane zx . As a result, from Eqs. (1)-(3) one can obtain:

$$M = \frac{z_0 \theta_y}{F 2\mu\sigma_0} \int_{-\infty}^{\infty} dx \ln \left[\frac{1}{1 - \frac{2\mu}{T\beta} V(x)} \right], \quad (4)$$

which makes it possible to determine the ejection power according to the measured intensity distribution $V(x)$.

References

1. V.A. Banakh, I.N. Smalikho, *Atmospheric Optics*, 1991, v. 4, No. 10, pp. 1048-1053.

Demonstration of a New GFCR Method with
CH₄ Measurements at 2.3 microns

Liang-guo Wang
College of William and Mary, Williamsburg, VA 23185

Glen Sachse, Peter LeBel, Andrew Wallio, and Stephanie Vay
NASA Langley Research Center
Hampton, VA 23665

Over the past 20 years, gas filter correlation radiometers (GFCR's) have made important contributions to our knowledge of the atmosphere by providing remote measurements of a number of gas species from aircraft, balloon, and spacecraft platforms. Though GFCR's have many attractive features, these instruments are generally mechanically complex, often requiring rapidly moving mechanical parts. A new GFCR concept has been reported by Sachse et al.¹ According to this concept a polarization modulator is used in conjunction with a polarization beamsplitter as a solid-state optical switch to rapidly alternate the path of incoming radiation between the two GFCR's optical paths (i.e., the paths containing the gas correlation and vacuum cells). Because this concept does not require rapidly moving parts, it has several potential advantages for remote sensing from space, including high reliability, efficiency and long operational life time.

We have developed and demonstrated a breadboard non-mechanical GFCR instrument using a photo-elastic polarization modulator. With this breadboard instrument we have carried out laboratory measurements of methane in the 2.3 μm region simulating atmospheric conditions with various methane concentrations and total pressures. A simple theoretical model using the Air Force Phillips Lab (formerly AFGL) HITRAN database has also been developed to study GFCR remote measurement of tropospheric trace species in the 2 to 3 micron region. The results of laboratory measurements and comparisons with analytical-calculations will be presented.

The experimental set-up using the breadboard GFCR instrument is shown in figure 1. A blackbody source is used to simulate reflected solar radiation. The blackbody at 900 °C gives a peak radiation near 2.3 microns. A sample cell of 40 cm length was filled with a mixture of methane and air at various concentrations and total pressures to simulate the atmosphere. The breadboard instrument is composed of the optical switching element, two optical paths, spectral filters and a common detection element for the two optical paths. Incoming radiation from the sample cell is band-limited and polarized by an interference band pass filter and a polarizer respectively. The band filter was specially chosen to cover a part of the methane band in the 2.3 micron region while minimizing interference from other species such as CO and water vapor. The polarized radiation is then incident on a photoelastic polarization modulator that modulates the output between vertical and horizontal polarization at rate of 38 kHz. A polarizer used as a beamsplitter

reflects vertically polarized light and transmits horizontally polarized light. Thus, non-mechanical radiation switching is achieved: the radiation beam is rapidly alternated between the two optical paths - one containing a vacuum cell and the other containing a correlation gas cell. A correlation cell having an optical pathlength of about 2" was filled with methane at 500 torr. A second polarizer beamsplitter is used to recombine the two beams and direct the combined beam to a liquid nitrogen cooled InSb detector. The differential signals between the GFCR's two paths were measured and normalized by total radiation signals through both paths.

Methane was chosen for our laboratory demonstration because it is an important green-house gas. In the past century the atmosphere CH₄ concentration has doubled to 1.7 ppm. We have measured the absorption signals for CH₄ partial pressures up to 22.5 torr in the sample cell. This is equivalent to 1.7 ppm methane in 7 km of atmosphere. Figure 2 shows our experimental results of methane measurements in the 2.3 micron band. For three fixed methane mixing ratios, the normalized differential signals are plotted as a function of total sample cell pressure. Calculated results, also plotted in the same graph, show good agreement with experimental values.

In conclusion, we have proven a non-mechanical GFCR concept by laboratory demonstration of CH₄ measurement at 2.3 microns. Both experimental data and theoretical calculations show that measurements at 2.3 microns have a higher sensitivity in the lower troposphere, a region not detectable by current tropospheric remote sensors.

References

1. Glen W. Sachse and Liang-Guo Wang, "Gas Filter Correlation Radiometer Concept Utilizing a Photo-Elastic Modulator", OSA Technical Digest, 4, 188-189, 1990.

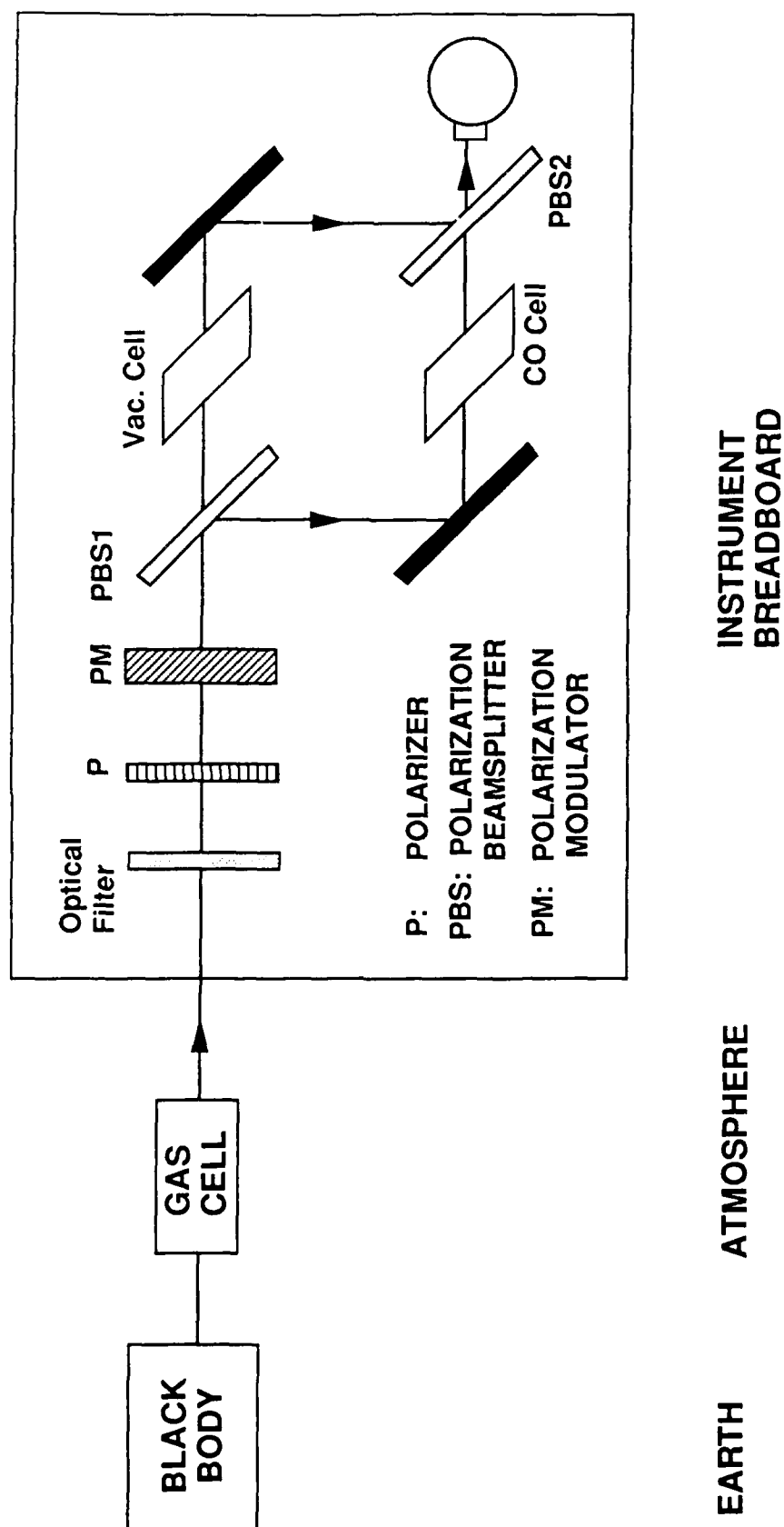


Figure 1 Laboratory GFCR Demonstration

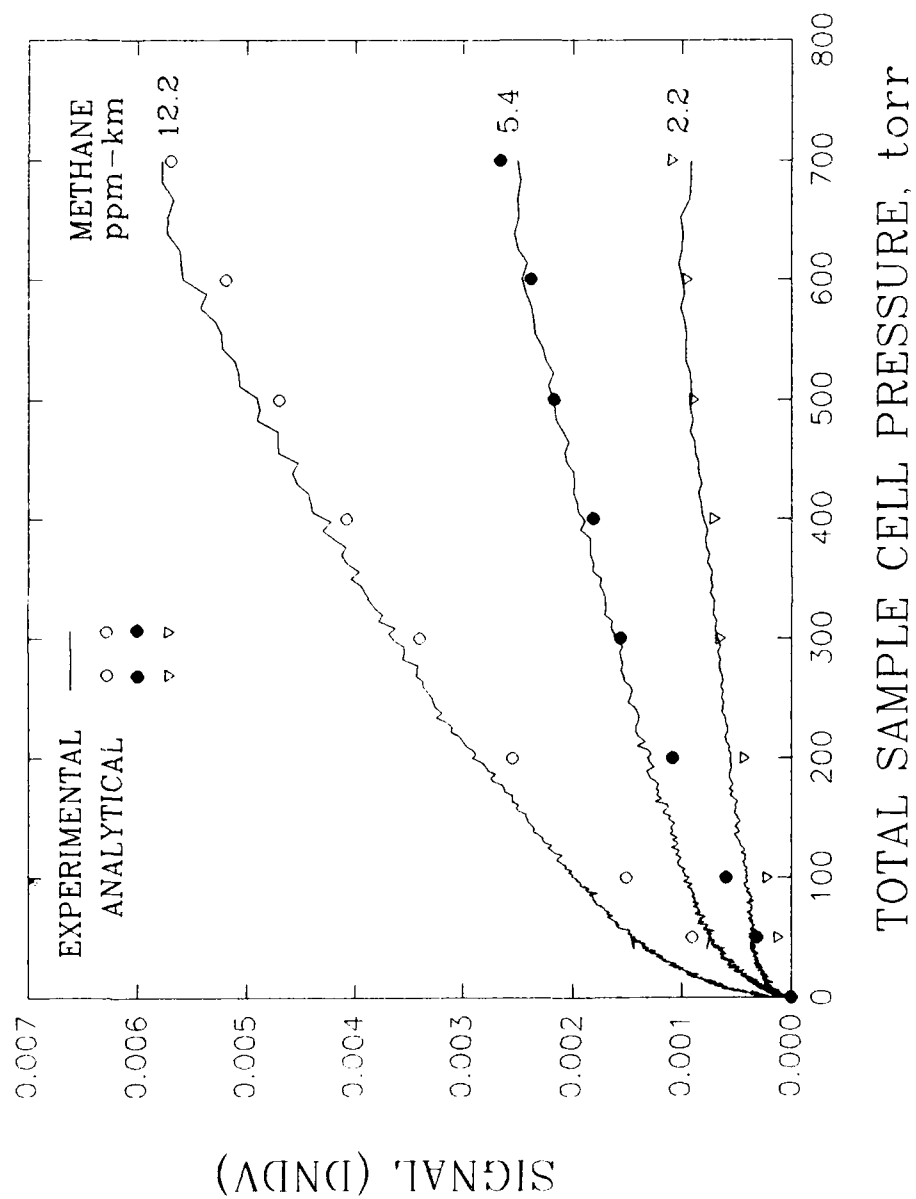


Figure 2 - Comparison of Experimental and Analytical Results

HNO₃ Profiles Obtained During EASOE

F.J. Murcray, J.R. Starkey, W.J. Williams

University of Denver, Department of Physics

Denver, Colorado 80208

(303) 871-3557

W.A. Matthews

NIWAR

Lauder, New Zealand

U. Schmidt

Institut fur Chemie, KFA Julich

Ulrich, Germany

P. Amedieu

Service D'Aeronomie du CNRS

Paris, France

C. Camy-Peyret

Laboratory Physics Molecular et Atmospherique

Paris, France

The detection of the Antarctic ozone hole by Farman et al¹ has led to increased interest in obtaining data at high latitudes on the altitude distribution of many of the constituents involved in the photochemistry of the ozone layer. Data concerning the altitude profile of constituents at stratospheric altitudes is generally obtained using instruments flown on large balloons. Launch and recovery of the instrumentation flown on such balloons at remote sites is difficult. In order to reduce these difficulties we have developed a small grating spectrometer system which can be flown on

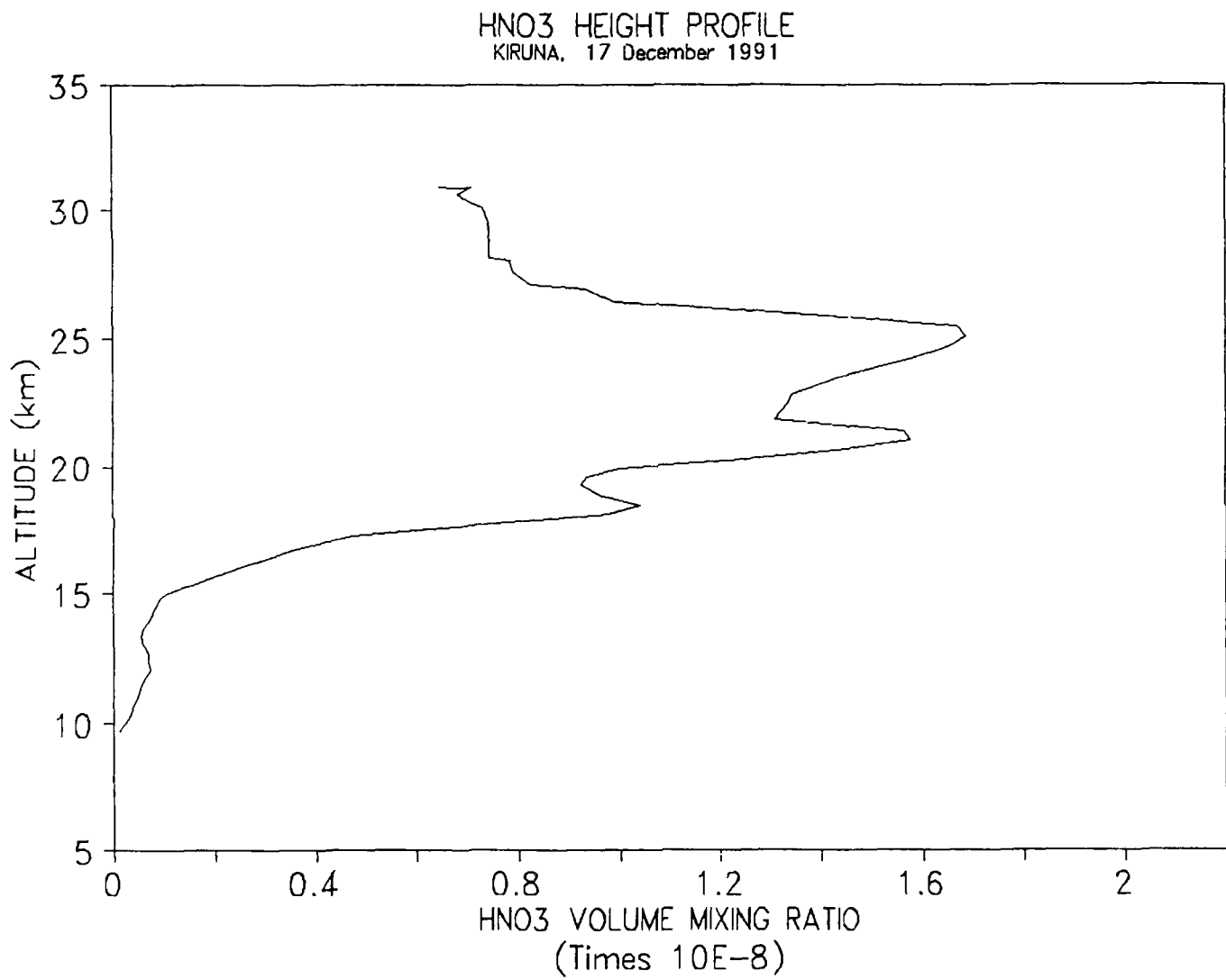


Figure 1. HNO₃ height profile, 17 December 1991.

small balloons. HNO_3 is of particular interest in high latitude photochemistry since it is involved in the heterogeneous reactions occurring during the winter. The spectrometer was designed specifically to obtain data on HNO_3 however the spectral region scanned (8μ to 13μ) includes features due to CH_4 , N_2O , O_3 , F12 and F11. The system is used to measure the atmospheric spectral emission and its change with altitude as the balloon ascends. The change in spectral radiance with altitude is used to obtain profile data on the constituents of interest.

While the instrument was designed for use as a sonde it's lightweight, low power and low data rate make it suitable for piggyback operation on larger gondolas. It was employed in this fashion for the EASOE campaign. Units were flown on gondolas operated by U. Schmidt (KFA), P. Amedieu (CNES) and C. Camy-Peyret (LPMA). They were flown a total of nine flights. HNO_3 profiles have been determined for flights made December 17, 1991, January 9, 1992, January 22, 1992, February 5, 1992 and March 14, 1992. An example of a profile obtained during the flight of December 17, 1991 is given in Figure 1. The profiles exhibit considerable structure.

The profiles along with other data obtained by other investigators during the experiment are being examined to see how well the observations can be explained.

REFERENCES:

Farman, J.C., B.G. Gardiner and J.D. Shanklin, "Large Losses of Total Ozone in Antarctica Reveal Seasonal ClO_x/NO_x Interaction," *Nature*, 325, 207, 1985.

On Determining the Carbon Budget (CO_2 and CO) of the Lower Thermosphere from Non-Equilibrium Infrared Radiance

Jeremy R. Winick and Richard H. Picard, Phillips Laboratory/GPOS, Hanscom AFB, MA 01731, (617)377-3619.

Peter P. Wintersteiner, A.J. Paboojian, and R.A. Joseph, ARCON Corporation, Waltham, MA.

The high resolution (1 cm^{-1}) limb emission spectra taken with the CIRRIS 1A interferometer on STS-39 over tangent heights from 50 to 200 km provides an opportunity to test the detailed non-LTE models of the emission and investigate methods for determining the carbon budget of the lower thermosphere from coincident measurement of the $4.3\text{ }\mu\text{m}$ CO_2 ν_3 band and the $4.7\text{ }\mu\text{m}$ CO band. Earlier theory (Kumer and James, 1977, López-Puertas *et. al.*, 1986, López-Puertas and Taylor, 1989) did not have high resolution spectral data to thoroughly validate their theories. López-Puertas and Taylor (1989) compared their models to SAMS data, a situation that needed an additional line-by-line model to filter their model results in a manner similar to the pressure modulated radiometer measurement. The high resolution spectra provide a much more stringent test of the theoretical non-LTE infrared emission models. We limit our discussion to the daytime spectra for a number of reasons. (1) The solar excitation leads to a large increase in signal, increasing the altitude to which good spectra can be obtained, (2) the domination of solar excitation simplifies the determination of the CO and CO_2 densities since other non-local earthshine processes become less important, and (3), the solar excitation of the CO_2 ν_3 states yields a rich spectrum including isotopic and hot-band emission.

The 32K interferograms are apodized with a Kaiser-Bessel line-shape function yielding spectra with resolution of 1.03 cm^{-1} FWHM. This resolution clearly separates the rovibrational lines in the CO (1-0) sequence which have a mean spacing of 4 cm^{-1} and the lines in the P-branch of the CO_2 626 and 636 band, but only the lower rotational quantum number lines of the R-branch. Since the non-symmetric isotopes, 627 and 628 have twice the number of lines and thus half the line spacing, the rovibrational structure cannot be resolved. This resolution, however, is good enough to clearly determine that many weak bands are important contributors to the limb spectra for tangent altitudes below 100 km.

Figure 1 shows a limb spectrum at tangent height of 65 km. We have identified the prominent signatures of many component bands. The 626 ν_3 fundamental is so optically thick that the expected band shape with the band origin at 2349 cm^{-1} is not evident among the other "weaker" bands. The 636 fundamental with band origin at 2283 cm^{-1} is also optically thick, as can be seen from the flattened band-shape. The various solar "pumped" bands, excited by solar flux at 2.7- and $2.0\text{-}\mu\text{m}$ are prominent. At higher altitudes as the optical depth of CO_2 lessens, the weaker bands become less important, but at 95 or even 105 km the $2.7\text{ }\mu\text{m}$ excited state still is very important. Above 110 km the 626 fundamental is optically thin and dominates the limb emission. Figure 2 for a tangent altitude of 121 km shows a spectrum that is dominated by the fundamental. Another set of lines spaced at about 4 cm^{-1} is now present throughout the range $2250\text{-}2450\text{ cm}^{-1}$. These lines have been identified as NO^+ (1-0) and possibly (2-1) lines. At these high altitudes the CO_2 limb radiance is most strongly dependent upon on the local CO_2 density and the solar zenith angle (which determines the excitation rate). In fact at these altitudes the solar excitation rate is quite

insensitive to the SZA for $\text{SZA} < 70$ ($\text{SZA} < 80$ for 140 km altitudes), so that the limb emission is a good indicator of the CO_2 density.

The CO daytime non-LTE emission is also predominantly produced by solar excitation. The situation is somewhat simpler than for CO_2 for three reasons; (1) there is only one important band excited and (2) the limb emission is optically thin above 80 km, and (3) the rovibrational lines are all clearly resolved (line spacing about 4 cm^{-1}). Below 95 km the $4.8 \mu\text{m}$ ozone combination band underlies the CO P-branch, but the R-branch lines can be well fitted using a synthetic spectrum. Figure 3 shows the CO spectral lines and the underlying ozone band for a tangent altitude of 86 km. Since the opacity of CO is considerably less than CO_2 , the CO limb emission is proportional to the local CO density for tangent altitudes above 90 km and $\text{SZA} < 89$.

For the high altitude conditions specified above, we have compared the limb radiance at high and low latitudes. For the high latitude case we have data for tangent altitudes at 121, 127, 131, and 140 km at 62-67 North and $\text{SZA} \sim 50$. For the low latitude case at tangent altitudes of 120 and 140 km at ~ 10 North and SZA of 59 and 66 (actually coadded scans). Spectral fitting routines indicate that the CO_2 and NO^+ limb radiances are at least a factor of two higher at the high latitudes as seen in Table 1. SZA differences cannot account for more than at most 25%. The CIRRIS data were taken during a period of highly elevated geomagnetic activity which could account for increased CO_2 at high altitudes especially at high latitudes where joule heating is maximized. The CO radiance, however, does not show any clear indication of a latitude effect at 120 and 140 km.

Table 1:

Tangent Altitude	Latitude	SZA	CO_2 Limb Radiance	CO Limb Radiance	$\text{NO}^+(\nu=1)$ Limb Radiance
118-122	15N-6N	62-69	1.3×10^{-8}	3.2×10^{-9}	9.6×10^{-10}
139-141	3N-5S	70-78	9.0×10^{-10}	1.2×10^{-9}	9.0×10^{-10}
121	63N	48	3.4×10^{-8}	3.2×10^{-9}	2.8×10^{-9}
127	67N	53	2.3×10^{-8}	2.4×10^{-9}	1.7×10^{-9}
131	62N	47	1.3×10^{-8}	2.0×10^{-9}	2.6×10^{-9}
140	67N	52	6.1×10^{-9}	1.2×10^{-9}	1.9×10^{-9}
144	60N	46	5.2×10^{-9}	---	2.7×10^{-9}

References

1. Kumer, J. B. and T.C. James, J. Geophys. Res., **79**, 638-648, (1977).
2. López-Puertas, M., R. Rodrigo, J.J. López-Moreno, and F.W. Taylor, J. Atmos. Phys., **48**, 749-764 (1986).
3. López-Puertas, M. and F.W. Taylor, J. Geophys. Res., **94**, 13045-13068 (1989).
4. Wintersteiner, P.P., R.H. Picard, R.D. Sharma, J.R. Winick, and R. A. Joseph, J. Geophys. Res., **97**, 18083-18118 (1992).

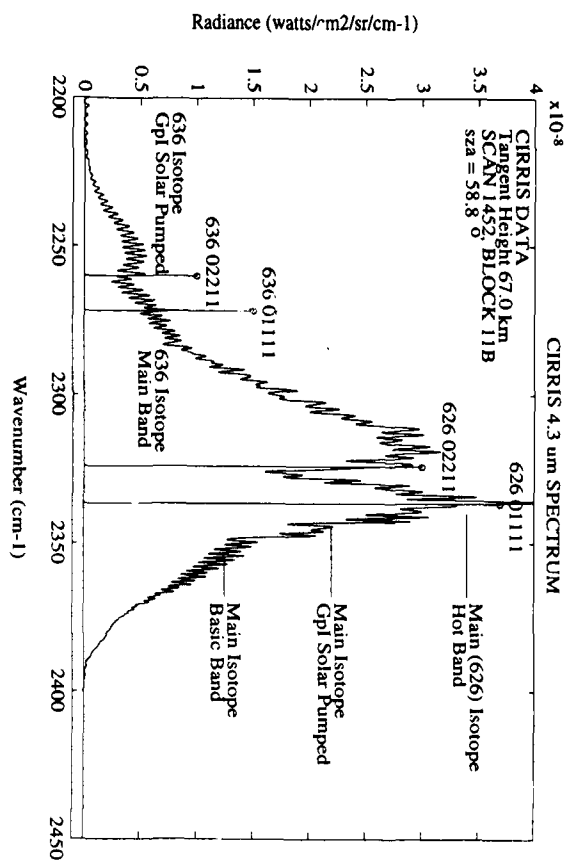


Fig. 1. CIRIS 1A spectrum of CO_2 4.3 μm region at tangent height of 65 km showing the contribution of many weak and solar pumped bands. Note that 626 (00011-00001) fundamental is not dominant

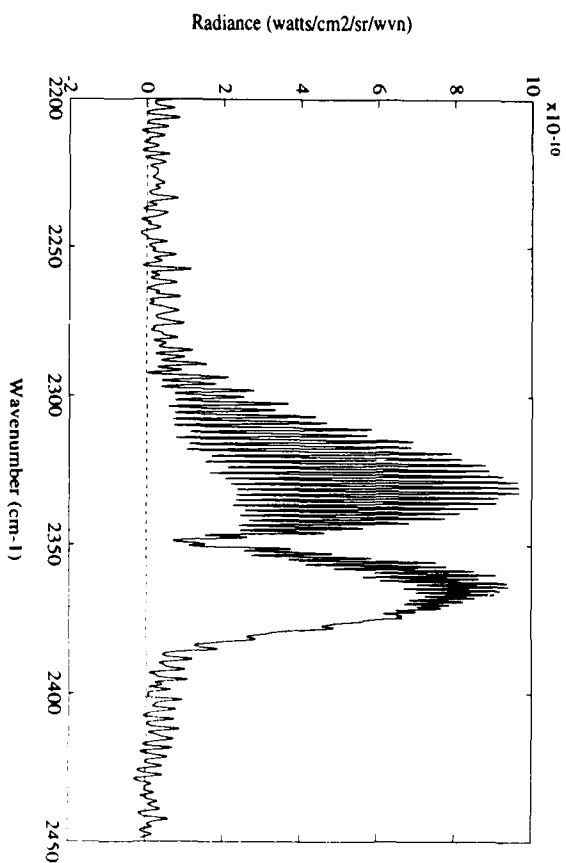


Fig. 2. CIRIS 1A spectrum of CO_2 4.3 μm region at tangent height of 121 km is dominated by 626 fundamental and clearly show NO^+ (1-0) emission.

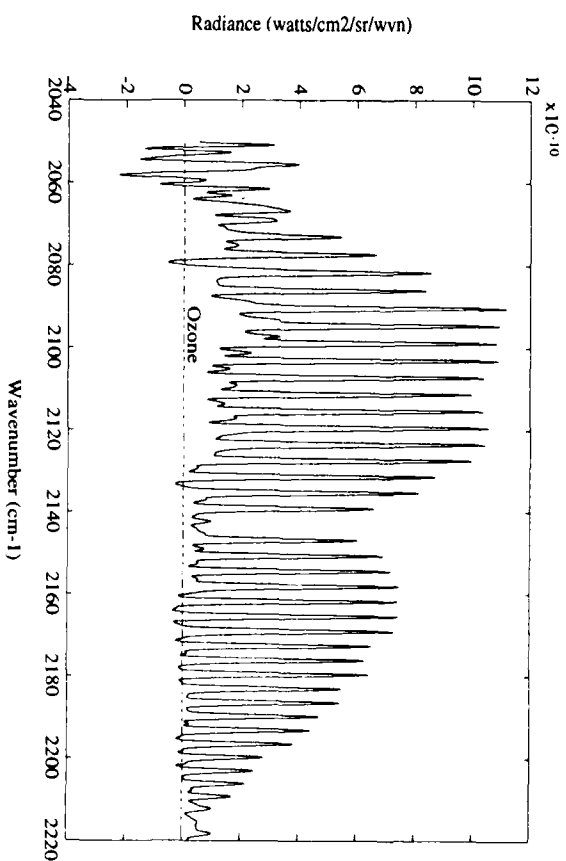


Fig. 3. CIRIS 1A CO spectrum at 86 km tangent altitude shows evidence of the ozone 4.8 μm band underlying the P-branch.

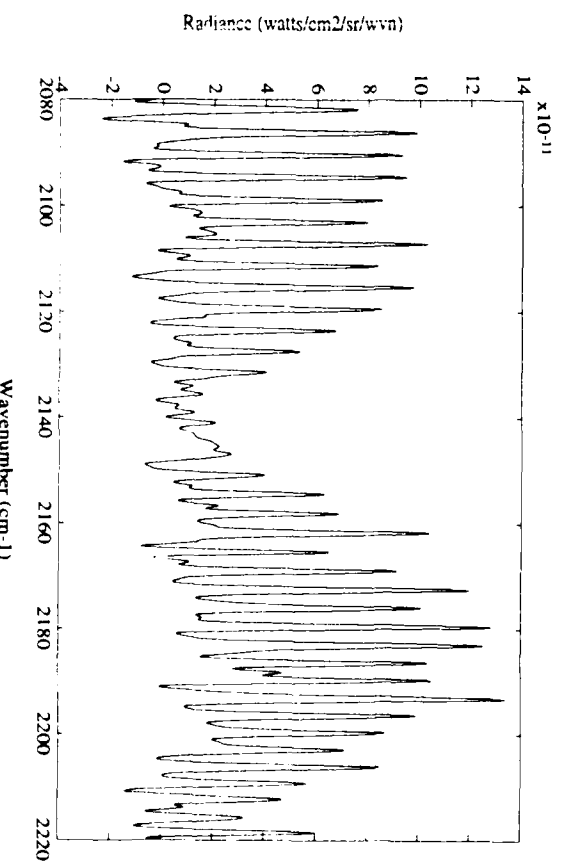


Fig. 4. CIRIS 1A CO spectrum at 121 km tangent altitude (same as Fig. 2) with clear, but somewhat noisy CO signature.

**Flight Results for the Balloon Borne Ozone
Profiler with Variable Footprint**

by

**William S. Heaps
NASA Goddard Space Flight Center
Code 916.0
Greenbelt, Maryland 20771
(301)286-5106**

A prototype of the balloon borne ozone profiler with variable footprint has been developed and was flown from Fort Sumner, New Mexico and September 30, 1992. The instrument was composed of a 100 mm grating spectrograph with an intensified diode array detector covering a spectral range from 250 nm to 350 nm. Scanning of the horizon was accomplished with a right angle dichroic mirror driven by a stepper motor. The viewing direction was determined by a shaft encoder on the scanning mirror and a magnetic compass fixed to the balloon gondola. Altitude was determined using a global positioning system (GPS) receiver.

The following measurement scenario was followed: The azimuth pointing system was set to a given position and ten scans of the diode array were recorded. The azimuth was incremented by fifteen degrees and another ten scans were recorded. After this process had been repeated six times for a total of sixty scans at six different azimuth angles a data file including the sixty scans plus housekeeping and position data from the GPS was written to the hard disk drive on board. One cycle of data taking required approximately 28 seconds. A smaller file containing one spectrum plus the housekeeping and position data was telemetered to the ground so system performance could be monitored in real time. This cycle was repeated continuously during the ascent of the balloon obtaining over fifty thousand spectra between ten and twenty-five kilometers in altitude.

Figure 1 shows a representative spectrum obtained at an altitude of 22.93 kilometers viewing at an azimuth of 298.3 degrees. The great decrease in intensity between 310 nm and 290 nm arises from absorption by atmospheric ozone. The spectral intensity data between these two wavelengths can be used to determine the ozone altitude profile both locally and at increasing ranges from the instrument as longer wavelengths are employed. Figure 2 gives a preliminary altitude profile obtained using spectra over the wavelength range from 295.5 nm through 316.4 nm for an azimuth angle in the range between 105 and 120 degrees.

Additional ozone profiles obtained with more refined algorithms will be presented as well as modifications and improvements to the system which will be made before another flight.

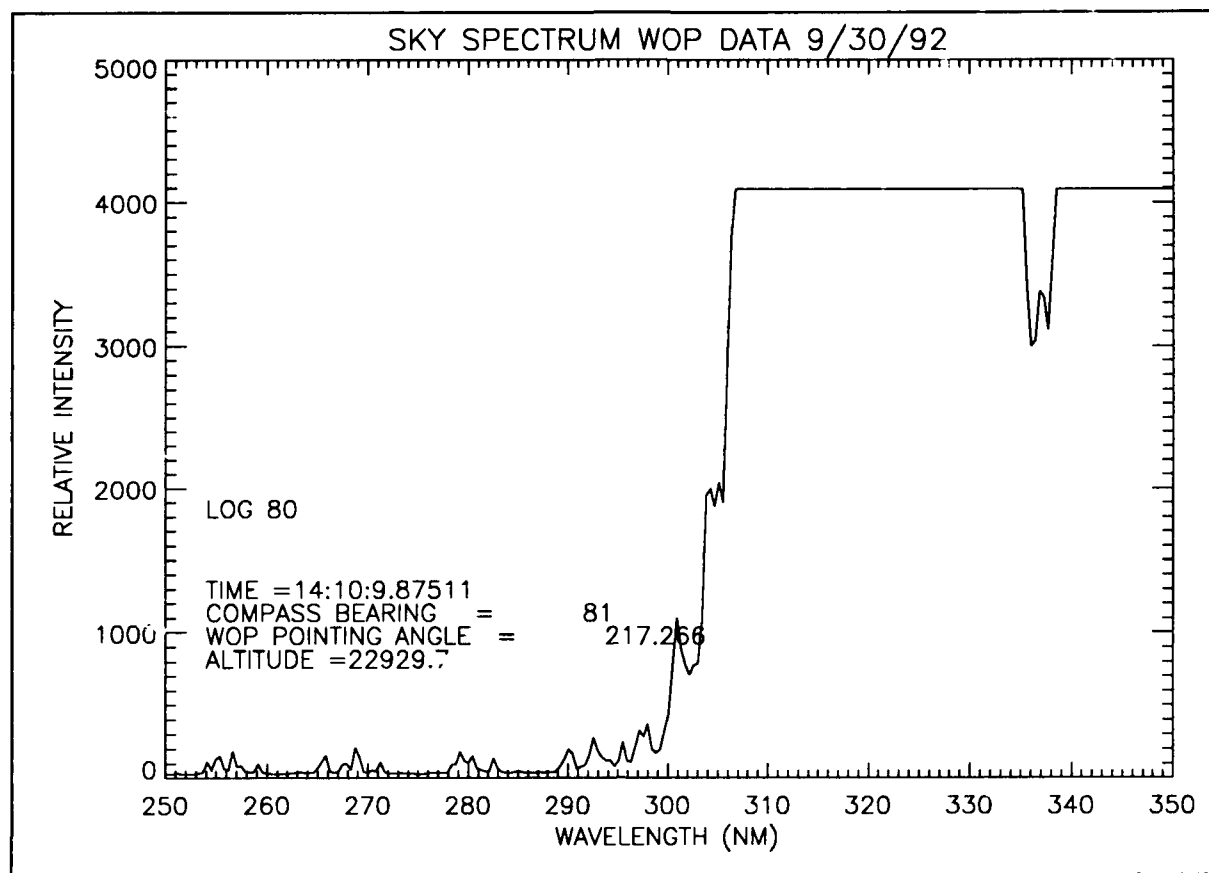


FIGURE 1. A TYPICAL SPECTRUM OBTAINED DURING THE FLIGHT. INFORMATION ABOUT THE OZONE PROFILE IS CAN BE OBTAINED FROM THE DATA BETWEEN 290 NM AND 320 NM.

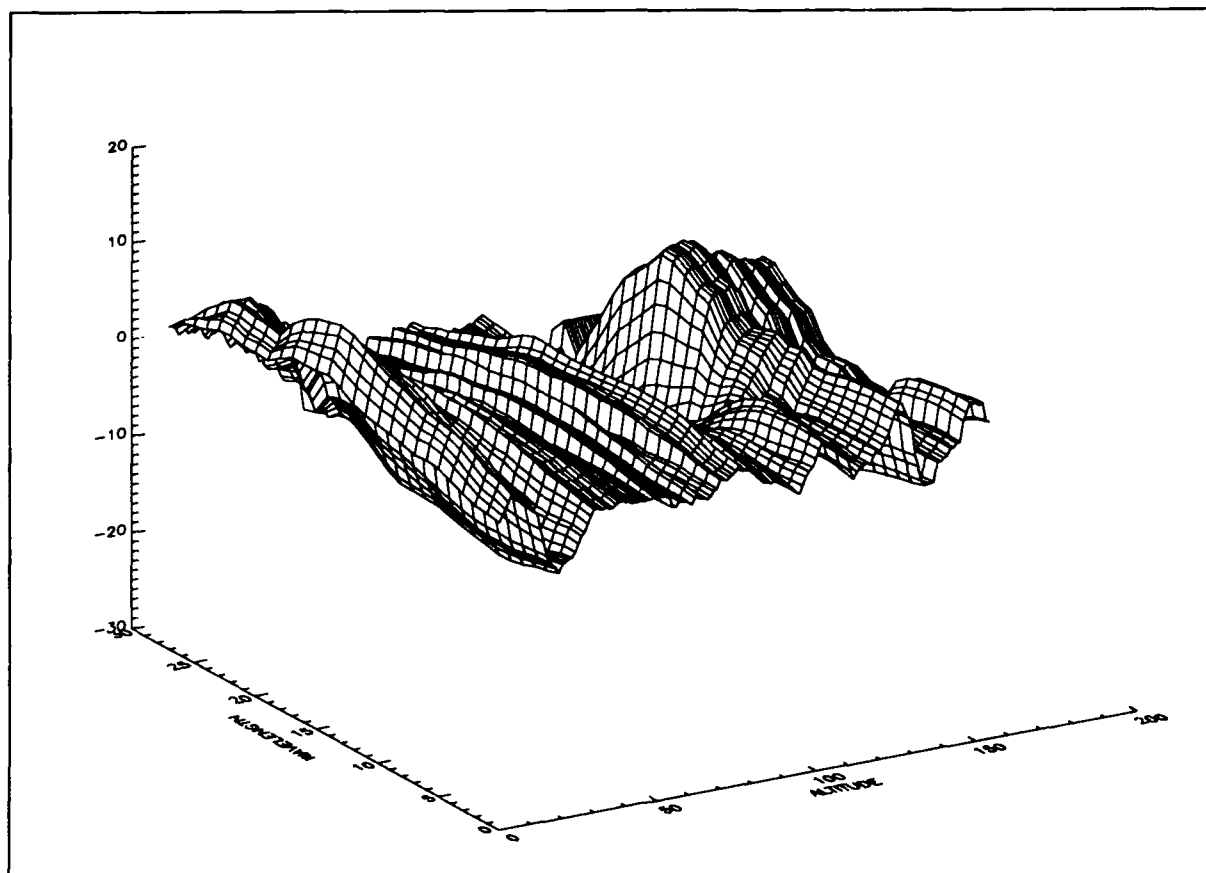


FIGURE 2. A PRELIMINARY OZONE PROFILE. THE VERTICAL SCALE IS OZONE CONCENTRATION IN UNITS OF 10^{12} MOLECULES PER CUBIC CENTIMETER.

The Remote Sensing of Tropospheric Gases by Thermal Emission Spectroscopy,

W.F.J. Evans and E. Puckrin,
Environmental Resource Studies,
Trent University,
Peterborough, Ontario K9J7B8
(705) 748-1622

Introduction

A technique for the remote sensing of tropospheric gases for air pollution and global warming has been developed. Models of global warming depend on the measured laboratory absorption spectra of Radiatively Active Gases, yet the atmosphere works on the radiative transfer of thermal emission. An outstanding question is then: are there discrepancies between calculations of radiation codes and atmospheric fluxes? Models of the global warming use laboratory absorption spectra of gases as a basis for radiative transfer calculations. In the atmosphere, the greenhouse effect actually arises through the emission of Planck blackbody radiation from atmospheric gases and aerosols. The measurement of atmospheric gases by thermal emission spectroscopy with FTIR technology is described using a technique which has recently been developed for measuring the thermal emission spectra of gases in an infrared cell in the laboratory. In particular, CFC11, CFC12, HNO₃, NO₂, SO₂, C₂H₄, CH₄, C₄H₁₀ and N₂O₅ have been measured in the laboratory. These gases are of importance for investigations of the tropospheric chemistry of air pollution and global warming. The gases measured in the atmosphere include CFC11, CFC12, CFC22, ethylene and nitric acid. As an example, the thermal emission spectrum of CFC11 has been measured in detail. This is compared with the measured laboratory absorption spectrum and with the spectrum of CFC11 from an atmospheric observation. Atmospheric spectra indicating the presence of the several gases have been measured. It is shown that absorption spectra of these gases may not be adequate for detailed radiative transfer calculations in greenhouse models and for satellite thermal emission analysis.

It was the discrepancies between observed atmospheric thermal emission spectra and laboratory absorption spectra led us to try to measure thermal emission spectra of gases in the laboratory. These measurements should be of high interest to modellers of the global warming effect of gases, particularly the CFCs. These new measurements may affect the calculations of global warming potentials (IPCC; 1990). The authors would like to thank Consumers gas for major contract support and the Atmospheric Environment Service for the loan of the BOMEM model 100 instrument.

Experimental Techniques

A BOMEM model 100 emission interferometer with two entrance beams was used to observe the atmospheric spectra. One beam is pointed at the zenith sky and the other at a cold liquid nitrogen target. It was used in a similar experimental setup to measure the thermal emission spectra of gases in the laboratory cell. The laboratory cell has IRTRAN windows and a filling tube with a valve; the optical path length of the cell is 7.5 cm and the pressure can be varied from 1 atmosphere to .02 atmospheres. Mixtures of the relevant trace gas with nitrogen can be easily measured. Many different gases have been investigated in the cell including chlorofluorocarbons, nitrogen oxides, hydrocarbons and natural gas.

Results

Atmospheric emission spectra of the zenith sky have been measured at Peterborough since May, 1990. In regions of the spectrum where there is strong atmospheric absorption, the atmosphere emits thermal emission as a Planck black body. In these observed atmospheric spectra, O_3 , H_2O , HNO_3 , CFC11 and CFC12 are prominent emission features.

A series of laboratory spectra at different pressures from 1 atmosphere to 0.1 atmospheres were measured for CFC11. A series of laboratory spectra at different amounts of CFC11 and constant pressure of 1 atmosphere were also measured. These cover the approximate range of atmospheric measurements.

Discussion

Discrepancies between observed thermal emission spectra and laboratory absorption spectra led us to try to measure thermal emission spectra of gases in the laboratory. A comparison of the measured thermal emission spectrum of CFC11 and a laboratory absorption spectrum after Murcray (1987) showed that there are discrepancies between the measured emission and the absorption spectrum.

On the other hand, a comparison of our laboratory emission spectrum and the atmospheric emission spectrum observed in January, 1992 indicate that there is excellent agreement between the two types of emission spectra.

Models of the global warming use laboratory absorption spectra of gases as a basis for band models in radiative transfer calculations.

In the atmosphere, the greenhouse effect actually arises through the emission of Planck blackbody radiation from atmospheric gases and aerosols. Since there are discrepancies between measured laboratory emission spectra and published laboratory absorption spectra, then the absorption spectra of these gases may not be adequate for detailed radiative transfer calculations in greenhouse models. These new measurements should be of high interest to modellers of the global warming effect of greenhouse gases, particularly the CFCs, since these new measurements may affect the calculations of global warming potentials (IPCC; 1990).

Conclusions

The measurement of atmospheric gases by thermal emission spectroscopy with FTIR technology is described. In particular, CFC11, CFC12, HNO₃, NO₂, N₂O₅, CH₄ and C₂H₄ have been observed in atmospheric emission spectra at Peterborough. These gases are of high importance for investigations of the tropospheric chemistry of air pollution and global warming.

A technique has recently been developed for measuring the thermal emission spectra of gases in a infrared cell in the laboratory. As an example, the thermal emission spectrum of CFC11 as measured in the laboratory was investigated in detail. This was compared with the measured laboratory absorption spectrum and with the spectrum of CFC11 from atmospheric observations. The other gases measured include CFC11, CFC12, CFC22, SO₂, ethylene, propane and nitric acid. Atmospheric spectra indicating the presence of many of the same gases have been measured.

It was found that absorption spectra of these gases may not be adequate for detailed radiative transfer calculations in greenhouse models. These new measurements should be of interest in the analysis of satellite remote measurements of gases and in models of the global warming effect of gases, particularly the CFCs, since these new measurements may affect the calculations of global warming potentials.

References

IPCC; Scientific Review of Global Warming,
ed J. Houghton, Oxford University Press, London (1990).

Murcay, D.J.,
CRC Handbook of Spectra of Atmospheric Interest,
CRC Press (1987).

A Signal-Processing Approach for the Retrieval of Global Tropospheric CO Using the Atmospheric Infrared Sounder (AIRS)

L. Larrabee Strow
Department of Physics
University of Maryland Baltimore County
5401 Wilkens Avenue
Baltimore, Maryland 21228
USA
(410) 455-2528

1. Introduction

One goal of the Earth Observing Systems (EOS) is to measure concentrations of key atmospheric gases on a global scale in order to understand biogeochemical cycles in both the natural, unpolluted atmosphere, and in regions where anthropogenic activities have perturbed concentrations of gas-phase species. A particular concern in tropospheric chemistry is that increasing levels of carbon monoxide (CO) may lead to a decrease in atmospheric hydroxyl (OH) which would reduce the atmosphere's ability to scavenge other trace gases.

CO has an approximate residence time of 2 months in the atmosphere and consequently is not uniformly mixed. Seasonal variations in the unpolluted atmosphere are on the order of 100 ppb. A large series of in-situ measurements of CO using aircraft flights found a number of regions with CO concentrations in the first two kilometers of the atmosphere ranging from a low of approximately 50 ppb to highs of 200-300 ppb (Marenco et al. 1989). (Much higher levels measured near urban areas were omitted to improve the reliability of the data.) The 200-300 ppb concentrations are widespread, but can be attributed to weather patterns bringing in polluted air from urban areas. Boundary layer levels of CO can reach 20 ppm in urban areas, far above natural variations.

CO is an ideal candidate for satellite measurements, given its temporal and geographic variations. Global measurements may allow a better understanding of: (1) the sources and sinks of CO, (2) long-term trends in the globally averaged CO concentrations, and (3) trends in regional CO pollution.

This paper examines the capability of the Atmospheric Infrared Sounder (AIRS) (AIRS 1991) to perform scientifically useful global measurements of the CO column content. AIRS is primarily a temperature and humidity sounder for EOS as well as a prototype for the next generation operational NOAA sounder. However, AIRS may potentially provide complete spectral coverage of the 1-0 vibration-rotation band of CO at 2140 cm^{-1} at a resolving power of 1200, which is sufficient to resolve individual CO lines. We present here a technique for the retrieval of the CO column content based on a signal processing technique known as the Welch method.

2. CO Signal Characteristics

AIRS is a grating spectrometer that operates between 650 and 3000 cm^{-1} with a resolving power of 1200. It has a 1.1° field-of-view (FOV) which corresponds to a 13.5 km diameter footprint at nadir. Scan lines sweep between $\pm 49^\circ$. The AIRS design goal is for maximum noise equivalent temperature variations ($NE\Delta T$) of 0.20K RMS per spectral resolution element, or 0.28K per detector element (two detectors per spectral resolution element), at a 250K scene temperature. The detector outputs will have a nominal digitization level of 0.1K.

We performed simulations at both the 0.20K RMS noise level and for a noise level of 0.07K RMS, which is the projected *detector* noise in the CO spectral region. In the CO region higher scene temperatures will be the norm and consequently the 0.20K noise level is conservative, although other system noise may preclude reaching the 0.07K noise figure.

The CO algorithm assumes that all of the standard atmospheric and surface parameters have been retrieved over a nominal 50 by 50 km area that includes 9 AIRS FOV's and one AMSU FOV. We also assume that a cloud clearing algorithm has been applied to the CO channels that effectively averages the radiances in the 9 FOV's and reduces the noise by a factor of 3. This noise reduction may be optimistic.

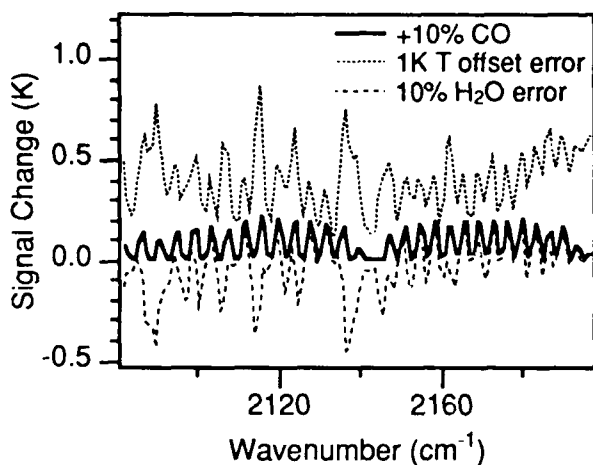


Fig. 1. Effect of a 1K offset in the temperature profile and a 10% error in H₂O amount on the CO signal.

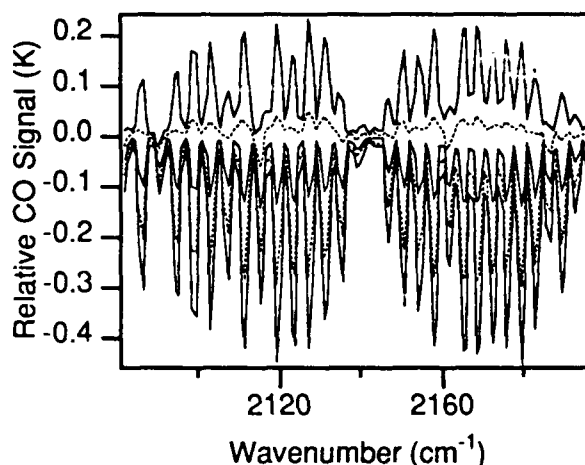


Fig. 2. Effect of varying the surface temperature (in 5K steps) from -12K to +8K of the first air layer temperature. The -12K contrast is at the top of the figure.

The CO profiles used in these simulations were varied from a standard profile by either increasing the CO amount at all altitudes by 10% or by doubling the CO amount at the ground to 300 ppb with lower amounts at higher altitudes up to 4 km, where this profile then matches the CO amount in our standard profile. The 300 ppb CO concentrations were commonly observed by Marengo et al. (Marengo et al. 1989) in a large series of aircraft in-situ measurements over the ocean.

The sensitivity of the CO signal to uncertainties in the temperature and humidity profile is shown in Fig. 1. Expected errors in the AIRS retrieved H₂O profile of 10% were modeled by changing the H₂O amount by 10% at all altitudes. Similarly, the sensitivity to temperature was modeled by changing the temperature profile by a constant 1K offset at all altitudes. H₂O lines dominate the signal changes caused by varying both the temperature and H₂O.

Figure 2 shows the sensitivity of the CO signal to the temperature contrast between the surface and the first air layer, for the profile with an increase in CO between 0–4 km. Clearly, the temperature contrast between the surface and the first several air layers must be well characterized and will generate a significant spread in the accuracy of the individual CO retrievals. These variations in the CO signal are comparable to the AIRS noise level and will be difficult to retrieve using individual channels. The effect of random detector noise is shown in Fig. 3 where we see that the 0.20K RMS noise completely overwhelms the CO signal. The low-altitude CO profile variation was used in this plot.

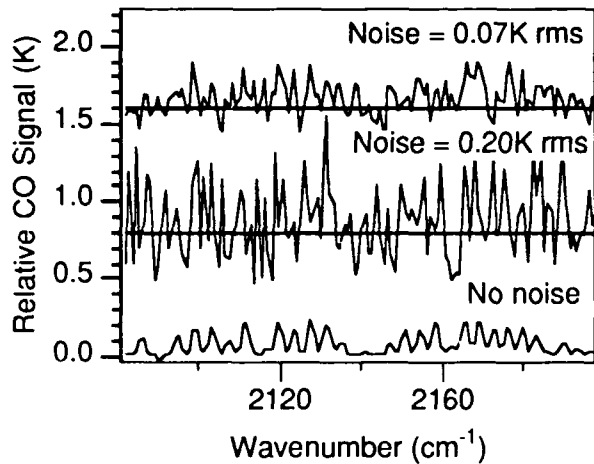


Fig. 3. Effect of noise on the CO signal for the -12K surface contrast.

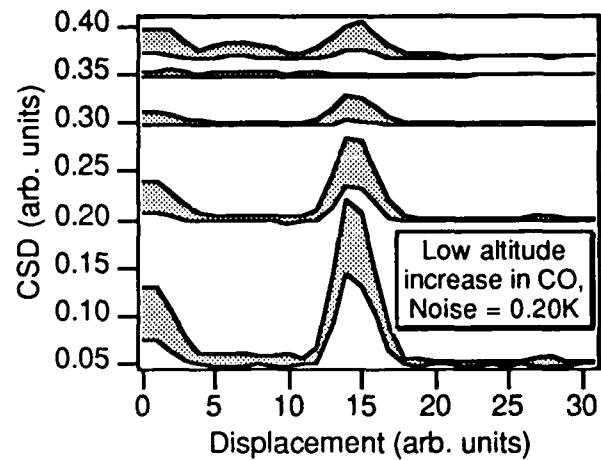


Fig. 4. The CSD and its standard deviation for various surface temperature contrasts, 0.20K RMS noise, using the low altitude CO profile change.

3. Cross Spectral Density and Retrieval Results

The striking feature of the noise-free CO signals is their sinusoidal appearance. This characteristic, coupled with the high noise of AIRS relative to the expected variations in the CO signal, suggests the use of signal processing techniques for the extraction of a single frequency out of a noisy time series. Our equivalent time series becomes the (infrared) frequency dependence of the difference between a brightness temperature spectrum calculated using a reference CO profile and the observed brightness temperature spectrum.

We investigated a CO retrieval based on a standard technique in signal processing called the Welch method (Candy 1988), which estimates the power spectral density of a signal in random noise. We form the following vectors

$$\mathbf{X}_\nu = B(\nu, T)^{calc} - B(\nu, T)^{calc+\gamma\%CO} \quad (1)$$

and

$$\mathbf{Y}_\nu = B(\nu, T)^{calc} - B(\nu, T)^{measured} \quad (2)$$

where $B(\nu, t)$ is the brightness temperature, ν the frequency, and T the temperature. The $+\gamma\%$ in $B(\nu, T)^{calc+\gamma\%CO}$ indicates that this calculation of the brightness temperature should be for an atmosphere with a perturbed amount (γ) of CO over the standard profile. $B(\nu, T)^{measured}$ is the AIRS observed brightness temperature. Now cut \mathbf{X} and \mathbf{Y} into k (possibly overlapping) sections, \mathbf{x}_k and \mathbf{y}_k , of length m . Hanning window \mathbf{x}_k , \mathbf{y}_k to produce \mathbf{x}_k^h and \mathbf{y}_k^h . The cross-spectral density (CSD), which we use as our measure of the CO column content, is given by

$$CSD = \sum_k FFT(\mathbf{x}_k^h) * FFT(\mathbf{y}_k^h)^* \quad (3)$$

The spectral region studied here contains 130 points (or equivalently 65 spectral resolution elements). Through trial and error testing, we chose $m=64$, which gives $k=17$ sections that have

considerable overlap. This set of parameters is a compromise between signal-to-noise and resolution of the main CO "bump" in the CSD. Figure 4 shows the CSD for a 0.20K RMS detector noise and the low-altitude CO profile change. The peak in the CSD near 14 displacement units, which is due to the "sinusoidal" feature of the CO spectrum, is linearly related to the increase in CO amount over the chosen standard CO profile. The shaded area in each curve is the ± 1 standard deviation range. Each graph has 5 CSD's representing the different thermal contrasts between the surface and first air-layer temperature examined in Fig. 2. This result, combined with those for the 0.07K RMS noise figure, show that variations of 150 ppb in low-altitude CO can be measured by AIRS at a FOV of 50 by 50 km with a signal-to-noise varying from zero to 10, depending upon the instrument noise and thermal contrast. Our preliminary simulations to determine the sensitivity of our CO retrieval algorithm to errors in the temperature and humidity profile and to a nominal undetected cloud fraction of 3% indicate that these errors are comparable to the random measurement error of the CSD technique.

4. Conclusions

Measurements on the order of the natural background variations of CO are possible with AIRS by using the cross-spectral density technique to lower noise and sensitivity to systematic errors. Commonly occurring levels of CO pollution in urban areas should be detected with ease since they are far above the natural background variations examined here. This technique lowers the effects of noise on the measurement to a magnitude similar to the level of systematic errors caused by uncertainties in the state of the atmosphere.

The disadvantage of this technique is the lack of any profile information. However, most observed increases in CO are in the first several kilometers, and thus the lack of profile data is probably not a severe hindrance to the scientific utility of these data. The advantages of using AIRS for CO measurements are several. First, AIRS will provide a better knowledge of the state of the atmosphere than any other satellite instrument making routine global measurements. This means that our measurement of CO may have smaller systematic errors than those due to MOPITT (Drummond 1991), which cannot directly use the AIRS retrievals for the atmospheric state. Secondly, AIRS is a prototype for a NOAA operational sounder and may fly over a much longer time period than other instruments measuring CO. This may provide a much longer, and more consistent, measurement of CO than those provided by several specialized, and different, instruments. Thirdly, AIRS will provide partial redundancy for MOPITT, should it fail, at a very low incremental cost over what is required for temperature and humidity sounding using AIRS.

References

- AIRS (1991) Atmospheric Infrared Sounder: Science and Measurement Requirements. Technical Report D6665 Rev. 1, Jet Propulsion Laboratory, Pasadena, CA
- Candy JV (1988) *Signal Processing, The Modern Approach*. McGraw-Hill Book Company
- Drummond JR (1991) In *Optical Remote Sensing of the Atmosphere*. Optical Society of America, 1991 Technical Digest Series, Volume 18, November 18-21
- Marengo A, Macaigne M, Prieur S (1989) *ATMOS Envir.*, (23):185-200

Analyses of the potential of tropospheric trace gas observations from satellites.

R. de Winter-Sorkina¹, H. van der Woerd¹, M. Roemer²¹ National Institute of Public Health and Environmental Protection, Laboratory of Air Research, P.O. Box 1, 3720 BA, Bilthoven, The Netherlands, tel: 31 30742677² TNO Institute of Environmental Sciences, P.O. Box 6011, 2600 JA, Delft, The Netherlands

The trace gas observations from satellites can be the powerful tools for the validation of tropospheric models, because of their global coverage in space and time. For verification of tropospheric models GOME spectrometer [1], which will be launched on ERS-2 satellite in 1994 should be able to measure the changes in tropospheric column densities of species occurring in the atmosphere. The trace species for which the tropospheric columns could be observed by GOME spectrometer are: ozone O₃, nitrogen dioxide NO₂, sulfur dioxide SO₂ and formaldehyde HCHO. In this study we tried to answer the question: what is the sensitivity of GOME spectrometer for the measurement of changes in the tropospheric column densities of these species. We applied only forward modeling to see how large should be the changes in tropospheric column densities of these species to cause the change of GOME signal which will exceed the noise level of the instrument. Though, it is the lowest boarder of detectibility, we tried to find out, and the error caused by the retrieval procedure must be added to our results.

In this study the model of radiation transport in the Earth atmosphere [2] developed at the Dutch National Institute of Public Health and Environmental Protection is used. This model uses isotropic two stream method for calculations of the solar photon flux in the atmosphere. Spectral resolution of the model is 1nm for wavelength range 250-350 nm or 5nm for wavelength range 350-660 nm. The tropospheric ozone, NO₂, SO₂ and HCHO column densities for altitudes up to 16.75 km are introduced from the two-dimensional TNO-Isaksen troposphere model. The tropospheric column densities are divided into 4 layers (0-2 km, 2-4.75 km, 4.75-9.75 km and 9.75-16.75 km). The altitude profiles of the stratospheric ozone and NO₂ densities are introduced from the two-dimensional Cambridge model. The stratospheric density profiles for SO₂ and HCHO are taken from [3].

The photon flux in the upwards direction above the atmosphere is converted into the signal at GOME spectrometer F_c (in electrons per pixel) using the known instrument parameters. The signal to noise ratio for the measurement of changes in signal is

$$dS/N = (F1_c - F2_c) / (F1_c + F2_c + 2 \cdot N_c^2)^{1/2}, \text{ where}$$

N_c in electrons per read out, is the number of electrons which are noise.

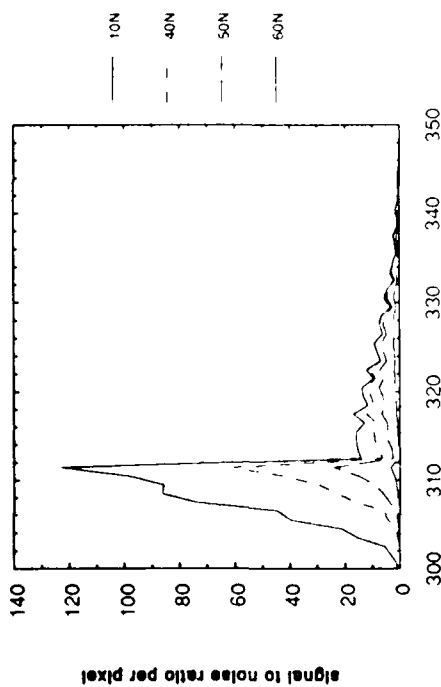
In order to test our model on ability to predict right signal to noise ratios of GOME spectrometer, comparison of results calculated with our model, with the radiation transport model from the University of Utrecht and with the PCTTRAN7 radiance code was carried out. The model of the University of Utrecht uses delta-Eddington approximation and includes anisotropy for scattering by cloud droplets and aerosols. For comparison the case of 20% reduction in the total column of ozone for solar zenith angle of 80 degrees and two seconds integration time was used. The difference in photon flux at GOME due to ozone depletion and the signal to noise ratio dS/N obtained by these three models are in a good agreement with each other. Contrary to PCTTRAN7, which is a ray-tracing program calculating radiances, our model is isotropic and calculates fluxes (radiances averaged over 2π sterad). Comparison of radiances calculated by PCTTRAN7 for nadir viewing mode with the averaged radiances calculated with our model shows considerable differences. But

even for the cases when there are considerable differences in the signal at GOME instrument, the signal to noise ratios dS/N for the measurement of changes in species density are in reasonable agreement, because of quite week dependence of difference in signal to noise ratio dS/N on signal value. We estimate that for the cases of substantial deviation of our radiances the error caused to our results on signal to noise ratio dS/N does not exceed 30% and for some cases is negligible.

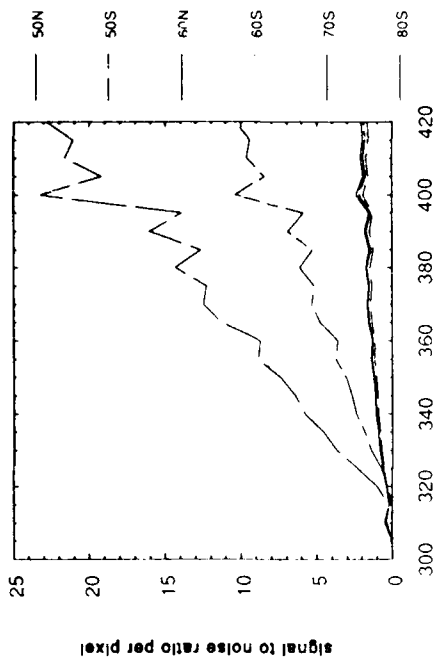
Calculations of the GOME signal to noise ratios per pixel for changes in tropospheric ozone, NO_2 , SO_2 and formaldehyde columns were carried out for selected four month, corresponding to different seasons and for various latitudes. It was shown that the signal to noise ratio dS/N is proportional to the changes in tropospheric species column density. We determined sensitivity for trace gas measurement as the change in the tropospheric column density (in percents), which causes signal to noise ratio $dS/N=1$. The typical signal to noise ratio dS/N spectra for 20% changes in the tropospheric ozone column, for 200% changes in the tropospheric NO_2 column (for January, 15th and for a number of latitudes), for 20 times changes in the tropospheric SO_2 column (for the latitude of $50^\circ N$ and for different seasons), and for 40 times changes in the tropospheric formaldehyde column (at the equator and for different seasons) are shown in the Figure. A number of Huggin's vibrational absorption bands of ozone giving the best value for the sensitivity and with $\lambda > 312$ nm was used. A number of stronger vibrational bands of formaldehyde was used for the sensitivity calculation. In conclusion, the sensitivities of GOME spectrometer for the measurements of tropospheric ozone, NO_2 , HCHO (corresponding to 1.5 s integration time) and SO_2 (30 s integration time) for different seasons and latitudes are shown in Table 1. The sensitivity of measurements is low or measurements are not possible in nothern polar regions in autumn and winter with change to the worse in winter. Same is valid for southern polar regions in spring and summer with change to the worse in summer. In this case solar zenith angle is larger, than about 80 degrees, the light pathlength through the atmosphere is longer, light is scattered before reaching the troposphere. We calculated also the sensitivity of GOME for the measurements of summer smog in Europe, when the density of ozone near the Earth ground can exceed the normal values up to 5 times. The sensitivity of GOME for the measurements of changes in ozone density for altitudes from 0 to 2 km in July for latitude $50^\circ N$ is 17%. Thus, it is quite likely that the summer smog episodes can be observed by GOME. In general, the changes in the tropospheric column of ozone up to 20% occur in the atmosphere. In the nothern hemisphere the changes of the tropospheric NO_2 column density up to 8-10 times can occur. Therefore, there are good prospects for the detectibility of tropospheric ozone and NO_2 by GOME instrument, however we should not forget to add the error caused by the retrieval procedure to our sensitivities of GOME. The changes of the tropospheric SO_2 column density in the nothern hemisphere up to 8-10 times can occur in relatively small areas, but the peak value of the signal to noise ratio corresponds to 30 seconds of integration time and therefore to a large area, where such a large changes can't occur. Thus, SO_2 can be observed by GOME only in regions with relatively high densities, especially in cases of industrial pollution in spring and summer at the latitude of about $50^\circ N$. In case of formaldehyde it is unlikely that it can be observed by GOME instrument with reasonable accuracy.

1. The Interim GOME Sciense Report, ESA, 1992.
2. F.A.A.M. de Leeuw Model calculations of fotolyses rates for tropospheric chemistry, RIVM, 1988.
3. G. Brasseur, S. Solomon Aeronomy of the Middle Atmosphere, 1986, p. 288 and 221.

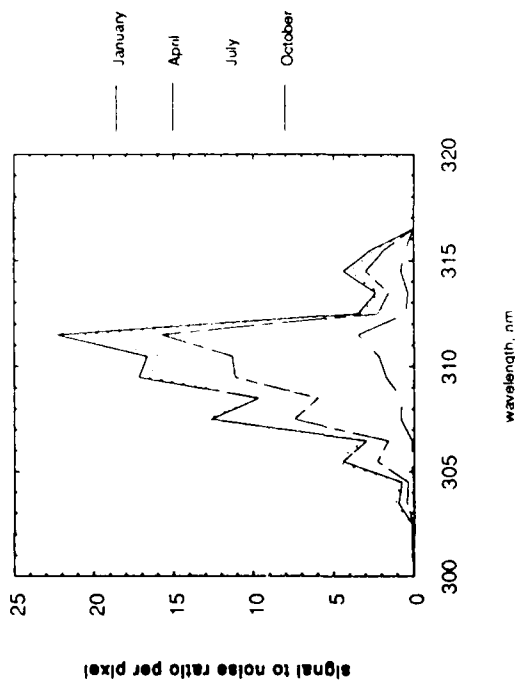
GOME S/N for changes in troposph. ozone
January 15, 20% change



GOME S/N for 200% change in tropos. NO2
January 15



GOME S/N for changes in troposph. SO2
50N, [SO2]trop*20



GOME S/N for changes in troposph. HCHO
ONS, [HCHO]trop*40

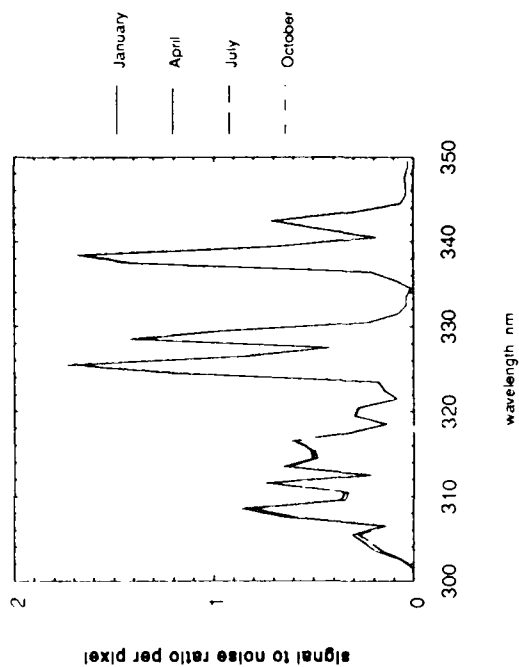


Table 1. Sensitivity of GOME spectrometer for tropospheric ozone, NO₂, SO₂ and HCHO measurements. Stratospheric densities from Cambridge 2D model. Tropospheric densities from TNO-Isaksen 2D model.

Latitude	Sensitivity for ozone, %				Sensitivity for NO ₂ , %			
	January	April	July	October	January	April	July	October
80° S	0.7	-	-	0.7	91	-	-	83
70° S	0.8	3.9	-	0.8	93	134	-	95
60° S	0.9	2.2	7.4	0.7	89	145	51	86
50° S	0.9	1.3	1.4	0.6	105	116	50	79
40° S	0.7	1.0	0.9	0.5	85	84	54	67
30° S	0.7	0.8	0.7	0.6	85	80	60	68
20° S	0.9	0.9	0.7	0.6	85	82	63	74
10° S	1.2	1.1	0.8	0.9	90	82	74	84
0°	1.1	1.3	1.1	1.2	78	78	74	88
10° N	0.8	0.9	1.2	1.2	61	66	70	83
20° N	0.7	0.7	1.0	1.0	42	53	65	71
30° N	0.7	0.6	0.8	0.8	28	34	43	44
40° N	0.9	0.6	0.7	0.9	15	26	28	28
50° N	1.5	0.6	0.7	1.0	9	19	25	20
60° N	7.2	0.6	0.7	1.4	19	29	34	30
70° N	-	0.6	0.7	3.1	-	46	54	62
80° N	-	0.7	0.7	-	-	44	59	-

Latitude	Sensitivity for SO ₂ , %				Sensitivity for HCHO, %			
	January	April	July	October	January	April	July	October
80° S	-	-	-	-	-	-	-	-
70° S	-	-	-	-	-	-	-	-
60° S	-	-	-	-	-	-	-	-
50° S	-	-	-	-	-	-	-	-
40° S	-	-	-	-	2705	-	-	-
30° S	1459	1564	-	1608	1534	2633	-	2373
20° S	-	-	-	-	1471	1724	1868	1575
10° S	-	-	-	-	1390	1533	1635	1489
0°	1753	-	-	-	1446	1412	1435	1459
10° N	870	1451	1430	1370	1694	1465	1492	1552
20° N	441	782	731	684	1932	1564	1580	1714
30° N	214	190	199	189	2397	1403	1157	1410
40° N	254	109	119	130	1851	1709	1229	2286
50° N	549	85	92	121	-	1859	1433	3829
60° N	-	174	193	357	-	-	-	-
70° N	-	591	1061	-	-	-	-	-
80° N	-	1248	-	-	-	-	-	-

Derivation of CLAES Filter Shapes

J.L. Mergenthaler, J.F. Potter, J.B. Kumer, T.C. James, and A.E. Roche
Lockheed Palo Alto Research Laboratory
Palo Alto, California, 94304

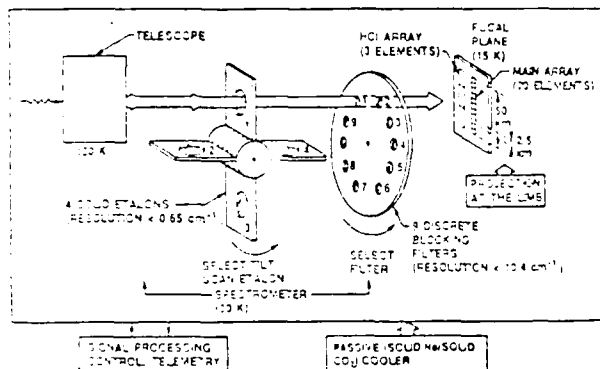


Figure 1: CLAES Functional Diagram.

1 Introduction

The Cryogenic Limb Array Etalon Spectrometer, CLAES, was launched on September 12, 1991 aboard the NASA Upper Atmosphere Research Satellite (UARS) and has been acquiring data on stratospheric composition since October 1, 1991. Overviews of the CLAES experiment and hardware are given by Roche et al (1) and Burriesci et al. (2). In the OSA Topical Meeting on Optical Remote Sensing of the Atmosphere in 1990 we presented three papers, (3,4,5) that described our progress up to that time in defining the system spectral transmission. In this paper, we describe refinements to CLAES characterization since then. These have come from further work with the pre-launch cold test data and from on-flight data. The spectral transmission characterization described here is currently being used in CLAES retrieval software. Figure (1) shows a schematic diagram of the spectrometer. In normal operation the CLAES instrument achieves a $0.2\text{-}0.65 \text{ cm}^{-1}$ spectral resolution by passing the radiation through one of nine passband blocking filters (FWHM $\sim 10 \text{ cm}^{-1}$) mounted in a filter wheel, and one of four Fabry-Perot etalons which are mounted in a paddle wheel to provide for spectral scanning by tilting. The transmitted radiation then falls on a focal

plane array consisting of a main array of 20 elements and an HCL array of 3 elements. The main detector array is used by eight spectral channels from 5.3 to $12.8 \mu\text{m}$ and takes atmospheric data in $20\text{-}2.5 \text{ km}$ vertical increments. The 3-element HCL array is used only by the $3.5 \mu\text{m}$ channel where each detector spans approximately 16 km for S/N augmentation.

This paper describes two aspects of instrument characterization; the first is the refinement of the spectral calibration of the instrument, i.e. defining the relationship between etalon resolver and the wavenumber positions of the etalon transmission peaks; the second is the determination of the shape of the system spectral transmission.

2 Spectral Registration

The relationship between the wavenumber, ν , at which a given order is transmitted by an etalon and the angular tilt is given by

$$\nu = \nu_0 / (1 - \sin^2(\theta/n))^{1/2} \quad (1)$$

where ν_0 is the wavenumber position for normal incidence radiation, θ is the etalon tilt angle, and n is the index of refraction of the etalon material. Spectral calibration involves the determination of the relationship between etalon resolver readout and θ , ν_0 , focal-plane dispersion, and the etalon free-spectral range. The pre-launch spectral characterization from gas cell transmission data and other laboratory methods is described in James(4 and 6). The observation of atmospheric features has the obvious advantages over laboratory studies in that long paths and low gas pressures (sharp features) are achieved while reactive gas handling is not a problem. In the normal science mode a passband filter is rotated into the optical train, then the etalon paddle wheel is positioned at several angles to transmit radiation from targeted spectral features on to the focal plane array. The number of targeted features is kept small to fit the time constraints imposed by the requirement to sample all blocking regions in 65 seconds. In addition to the normal science mode a special scan mode is run periodically which is very useful for

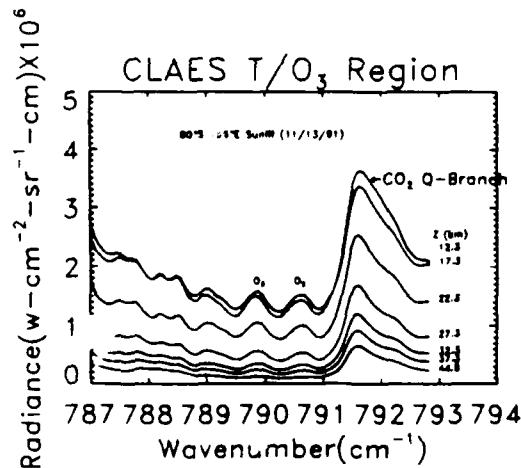


Figure 2: CLAES scan of the 792cm^{-1} CO_2 Q-branch on several detectors.

spectral calibration. In this mode the blocking filter is rotated into position and the etalon is rotated in small angular steps through more than a free-spectral-range. This process takes 65 seconds for each blocking filter region and produces a continuous scan of all spectral features on the blocking filter region. A portion of a wavenumber-registered multi-detector plot of a scan over the temperature/osone region is shown in Figure (2). The interpretation of this plot is complicated somewhat by the fact that at a given angle, more than one spectral feature is transmitted corresponding to different etalon orders.

Figure (3) demonstrates one of the first uses of the spectral calibration mode which arose immediately upon observing the atmosphere. The dashed curve is the CLAES measured spectrum whose spectral registration is based on the pre-launch resolver to angle conversions. The solid curve is a simulation based on FASCODE2 (7) and the HITRAN (8) spectral line data base with a spectral calibration based only on Eq.(1). Note that the wavenumber scale of the measured spectrum was contracted compared to the simulated spectrum. This contraction was observed in all spectra. The dotted curve shows the measured spectrum after an offset of 0.3° was added to the resolver number to angle conversion table. Once the scale contraction was adjusted the modeled and the measured spectral features in all regions aligned much better. The positions of spectral lines on the HITRAN database for the features of interest are known to better the 0.001 cm^{-1} and thus are very suitable for adjusting the set of ν_0 for

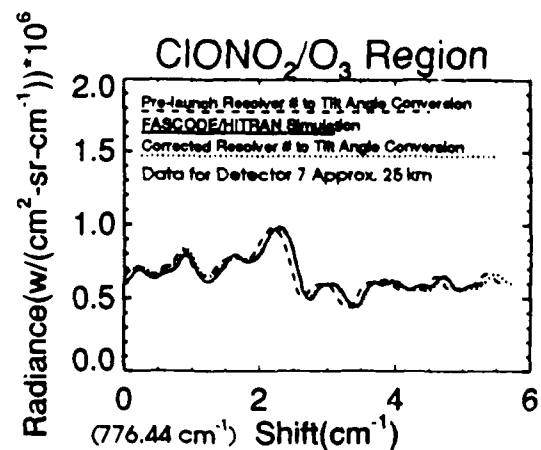


Figure 3: Spectral registration refinement.

CLAES by sliding the measured spectrum with respect to the modeled spectrum until identifiable features coincide.

The spectral continuous scan data is also useful in examining instrument resolution and free-spectral-range. Figure (4) shows FASCODE/HITRAN fits to the CO_2 laser lines in the CFC-12 channel at 925 cm^{-1} . These lines are part of a band and are distributed at approximately 2 cm^{-1} intervals all across the region of the band-pass filter. The wavenumber positions of each line have been labeled as a reminder that in this case at least three orders of etalon transmission are contributing to the CLAES measurement. These data give a very good check of the laboratory determination of the etalon free-spectral-range and resolution for this blocker. This particular etalon is used for the 5 long-wavelength channels so this test provides a limited check on etalon characterisation for those channels as well. Another aspect of spectral calibration is focal plane dispersion. Isolated osone and carbon dioxide lines in the CFC-12 and CFC-11 regions were traced up and down the array to measure the angle at which a particular feature appeared on each detector.

3 System Filter Envelope

This work expands on the previous work with a comparison of two methods of determining system filter functions.

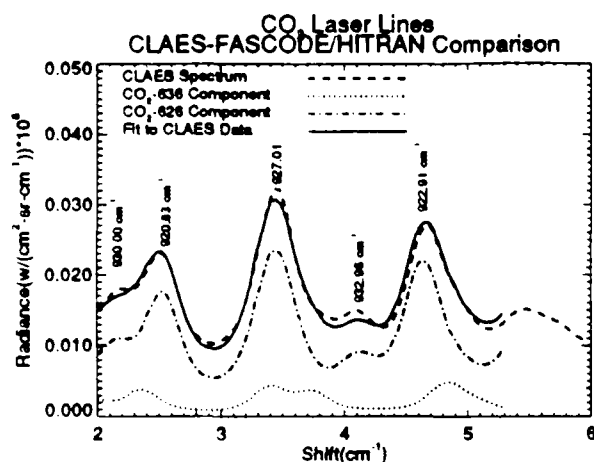


Figure 4: Claes spectral scan vs model in CO_2 laser lines $\sim 925cm^{-1}$.

3.1 Derivation from "Matched" Data

Laboratory data has been analyzed in which a grating spectrometer was used as quasi-monochromatic source for CLAES. System filter functions were mapped by repeated CLAES scans across the grating spectrometer output which was stepped across the CLAES band-pass filter range. CLAES was operated with "matched" etalon/blocking filter combinations as in normal operation. (Previously (5) a "mismatched" analysis was described.) The "matched data" appears as a spike superposed on a gray background. A Glo-bar source was used for the spectrometer, the radiance level of the was monitored so that any variations in the source intensity could be accounted for in reduction of the data. The grating spectrometer was driven by a stepping motor and the angular position was recorded from the output resolver attached to the grating mounting shaft. Spectral calibration of the spectrometer was done using various orders of a 6328 Å He-Ne laser. As the spike was stepped in frequency across the blocking filter, between CLAES scans, the background remained constant, this allowed for the subtraction of the background leaving only the spikes the map out the blocking filter. A spline was used to connect the maxima of the peaks and map the filter shape. Figure (5) shows the background-subtracted grating data and the filter envelope for detector 10 in the CFC-12 region blocker 5.

3.2 Blackbody Fit

A major finding of the work on system spectral transmission (3,4,5) was that CLAES spectral scan of the internal blackbody source could be better reproduced by an instrument model if etalon-like behavior or channeling was ascribed to the silicon detectors. Another

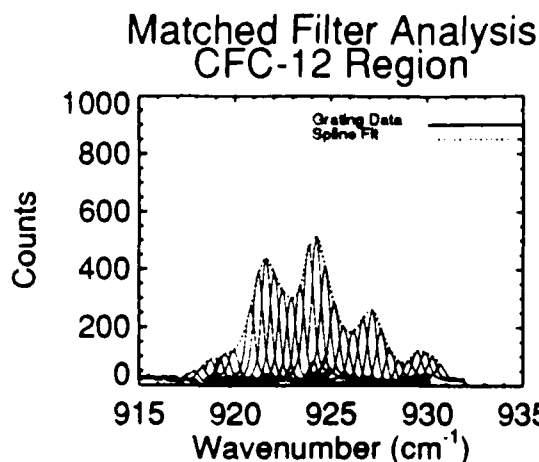


Figure 5: System filter shape mapped by grating spectrometer data.

method for deriving system filter functions was devised which uses a non-linear least squares method to fit CLAES blackbody scan data with a model consisting of a blackbody function, a detector channeling parameterization, an etalon model, and filter shapes measured by the manufacturer, the Optical Coating Laboratory Incorporated (OCLI). Let $M_s(\nu)$ be a simulated spectral scan of the internal CLAES blackbody source with radiance $B_T(\nu)$ where $F(\nu)$ is the stand-alone filter envelope, $E(\nu)$, the etalon model and $C(\nu)$, the detector channeling model described below.

$$M_s(\nu) = \int B_T(\nu') C(\nu') E(\nu, \nu') F(\nu' + \Delta\nu_s) d\nu' \quad (2)$$

The detector channeling function, $C(\nu)$, has been modeled as a Airy function with modulation, A , phase ν_p , and free-spectral-range, ν_f .

$$C(\nu) = \frac{1.0}{1. + A \sin^2(\pi(\nu - \nu_p)/\nu_f)} \quad (3)$$

The free spectral range, $\nu_f = 2.93cm^{-1}$ has been determined from the "mismatched" data analysis (5) and conforms to the detector thickness and index of refraction (3). The channeling parameters A and ν_p are determined independently by the non-linear least squares fit for each detector. The peak position of the filter is observed to vary as a function of position on the filter for this reason a shifting parameter, $\Delta\nu_s$, was introduced into the fit to reposition filter shape since each detector receives radiation through a different part of the filter. Figure (6) shows the result of the channeling non-linear least squares fit analysis compared the matched data analysis. Although the approaches are quite different the results are quite similar. To ensure exact reproduction of the CLAES blackbody scan, the

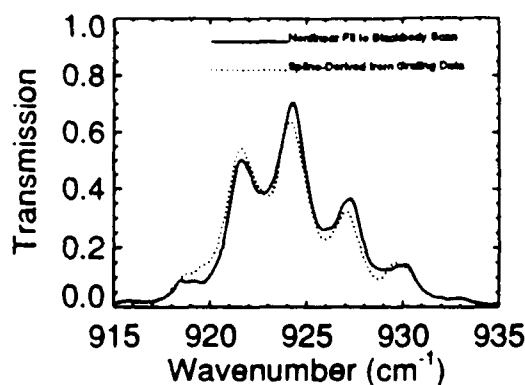


Figure 6: Comparison of system filter shapes derived from two methods.

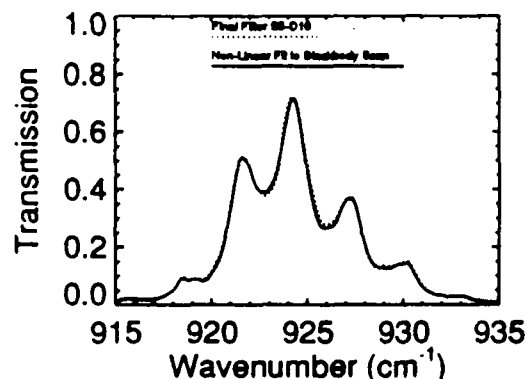


Figure 7: Comparison of system filter shapes before and after final adjustment.

filter model from the above analysis is adjusted iteratively until exact reproduction of the measured black-body continuous is achieved. The final filter shape is compared with the channeling filter shape before adjustment in Figure (7)

4 Further Discussion

Additional material pertaining to spectral characterization and data products the CLAES instrument will be presented. This will include discussion of spectral system parameters for other channels, model fits to the continuous scan data, and some examples of CLAES data products.

5 References

1. A.E.Roche and J.B.Kumer, "Cryogenic Limb Array Etalon Spectrometer (CLAES): Experiment Description," *Remote Sensing of Atmospheric Chemistry*, Orlando, Florida, 1-3 April, 1991, SPIE Proceedings Vol. 1491, pp 91-103.
2. L.Burriesci, L.Naes, L.Springer, and B.Steakley. "Cryogenic Limb Array Etalon Spectrometer (CLAES): Instrument Overview," SPIE Proceedings, Vol. 973, pp 335-341, 1988.
3. J. B. Kumer *et al.*, "Detector Channeling Hypothesis for Enhanced Structure Observed in CLAES System Blocker Filter Functions," *OSA Topical Meeting on Optical Remote Sensing of the Atmosphere*, Incline Village, Nevada, 12-15, Feb. 1990, page 164.
4. T. C. James *et al.*, "Spectral Calibration of the CLAES," *OSA Topical Meeting on Optical Remote Sensing of the Atmosphere*, Incline Village, Nevada, 12-15, Feb. 1990, page 172.
5. J. L. Mergenthaler *et al.*, "Retrieval of CLAES Filter Shapes from Spectral Calibration Data," *OSA Topical Meeting on Optical Remote Sensing of the Atmosphere*, Incline Village, Nevada, 12-15, Feb. 1990, page 180.
6. T. C. James *et al.*, "Model Calculations of the Spectral Transmission of the CLAES Etalons," SPIE Proceedings Vol. 973, 1988.
7. S. A. Clough *et al.*, "Atmospheric Radiance and Transmittance: FASCOD2" in *Sixth Conference on Atmospheric Radiation* (American Meteorological Society, Williamsburg, VA, May 1986), pp.141-146.
8. L. S. Rothman *et al.*, "HITRAN Database: 1986 Edition", Appl. Opt. **26**, 4058-4095(1987).

A NOVEL COLLECTOR FOR HIGH ALTITUDE AIRCRAFT OBSERVATIONS OF SOLAR ULTRAVIOLET FLUX

J. BURRIS

Code 917

Laboratory for Atmospheres

Goddard Space Flight Center

Greenbelt, Md. 20771

(301) 286-7473

An inexpensive technique to quickly and reliably collect the integrated solar flux over a hemisphere is described.

Radiation in the near ultraviolet (280-400nm) is a driver for several important stratospheric processes¹ which impact upon the loss of polar ozone. O₃ can be destroyed by reactions controlled through the photodissociation of certain halogen containing molecules such as OCIO/BrO thereby releasing highly reactive Cl/Br. O₃ removal can also be significantly enhanced by the presence of polar stratospheric clouds through the accelerated release of active chlorine. The presence of PSCs is sensitive to stratospheric temperature which is in turn controlled by the absorption of ultraviolet radiation.

In order to rapidly measure the solar flux over this spectral region from a high flying aircraft or drone, a novel collector has been constructed consisting of a fiber optic array with the end surfaces embedded on a hemispheric surface such that each fiber views a known portion of the sky (figure 1). Fifty fibers (with a core diameter of $\sim 50\mu$ and total diameter [core+cladding] of $\sim 65\mu$), uniformly distributed over the surface, allows complete, simultaneous, coverage over 2π steradians. Data can be acquired throughout the entire flight without any special effort on the part of the aircraft/drone. Two collectors make the measurement insensitive to the orientation or flight path of the platform. This is a significant improvement over existing techniques which require either that the detector be mechanically scanned or that the aircraft alter its flight track so as to physically scan the instrument through the entire field of interest. Energy deposition within this spectral region is dependent upon the solar zenith angle due to both absorption and scattering with significant attenuation expected for high zenith angles; simulations^{2,3} show that at an altitude of 20km significant count rates can be expected between 290-400nm for a solar zenith angle of 85 degrees (see Table 1). Signals from fibers positioned to view reflections off the aircraft surface can be masked out. Using special silica fibers with high transmission in the UV ($t \sim 0.95/\text{meter}$ at 280nm) the collector can be positioned so as to optimize the desired signal without the constraint of colocating the detector/electronics. The detector consists of an 0.125m Ebert-Fastie double monochromator with 3600l/mm grating

blazed for 250nm, an effective resolution of 0.3nm and a measured efficiency of 2.5%. Radiation will be coupled into the instrument using a lens assembly and detected using a high gain PMT. A stepping motor scans the system over the wavelength region of interest. Scans would take ~two minutes. A discriminator, photon counter and microcomputer complete the detector package. Replacement of the PMT, discriminator and counter by a CCD array would allow the entire spectrum to be acquired simultaneously.

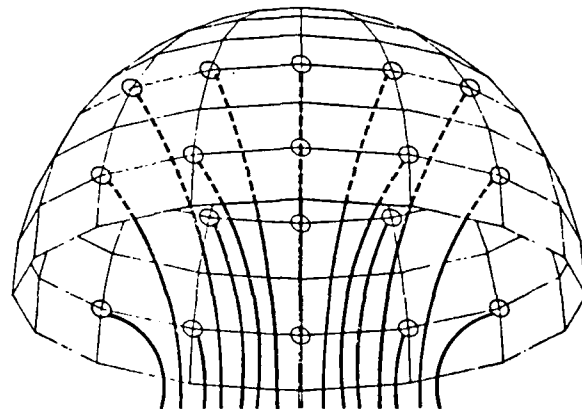
References:

1. G. Brasseur and S. Solomon, *Aeronomy of the Middle Atmosphere*, D.Reidel(Dordrecht), 1986.
2. E. Smith and D. Gottlieb, "Solar flux and its variations," *Space Sci. Rev.*, **16**, 771(1974).
3. F. Smith and C. Smith, "Numerical evaluations of chapman's grazing incidence integral $ch(X,\chi)$," *J. Geophys. Res.* **77**, 3592(1972).

Table I

λ	counts/sec
280nm	< < 1
290nm	~ 0.1
300nm	~ 20
310nm	~ 600
320nm	~ 7000
330nm	~ 17000
340nm	~ 20000
360nm	~ 22000
380nm	~ 20000
400nm	~ 26000

FIGURE 1
HEMISPHERIC COLLECTOR



Optical fibers embedded within a hard hemispheric surface to form a collector of solar flux.

Expected count rates from 100 fibers, 5 meters in length with a 50μ core. PMT QE is 0.2, monochromator thruput ~0.025 and fiber thruput is ~0.7. The aircraft altitude is 20km and the solar zenith angle is 85 degrees.

FROM 'ONION PEELING' TO 'CUTTING ONION CUBES'

Thomas v. Clarmann

Institut für Meteorologie und Klimaforschung
 Kernforschungszentrum Karlsruhe GmbH und Universität Karlsruhe
 Postfach 3640
 W-7500 Karlsruhe 1
 Federal Republic of Germany
 Phone 07247/825946

Long horizontal paths and rapid changes of observer position combined with large horizontal gradients in mixing ratios of trace gases of interest are the reason for the need of a two-dimensional approach for analysis of limb emission spectra from space-borne experiments. A data evaluation concept is described and discussed which is based on classical one-dimensional 'onion peeling' approach, but avoids the assumption of spherical homogeneity.

INTRODUCTION

Most limb sounding spectroscopy experiments are evaluated with algorithms which are based on the assumption of spherically homogeneous layers. Neither the 'onion peeling' retrieval method <1>, <2>, <3> nor most of the more sophisticated methods for evaluating limb sounding data, like the Mill-Drayson-method <4> and the global fit method <5> take into account horizontal gradients in mixing ratios of trace gases. This approach may be appropriate for evaluating data from balloon-borne measurements, where the small number of elevation scans does not permit a two-dimensional approach.

In the case of a continuously operating limb emission experiment, e.g. the MIPAS instrument <6>, which is planned to be operated from the first ESA polar platform, there is no need to reduce the horizontal resolution of the experiment by the assumption of spherically homogeneous layers. Furthermore this restriction would cause instabilities in the retrieved profiles, especially at regions of high horizontal gradients like in the edge region of the polar vortex or at the NO₂ Noxon cliff.

ANALYSIS OF INSTABILITIES

The following example illustrates how the horizontal inhomogeneity of mixing ratio can lead to instable solutions for the retrieved trace gas profile. For example, a high value for a certain trace constituent may be retrieved from the uppermost tangent altitude and is taken to calculate the radiative transfer through this layer during the analysis of the spectrum of the second tangent altitude from the top. Thus, variations of this certain gas in the uppermost layer will be compensated by the retrieval algorithm when evaluating the second spectrum from the top (Fig. 1).

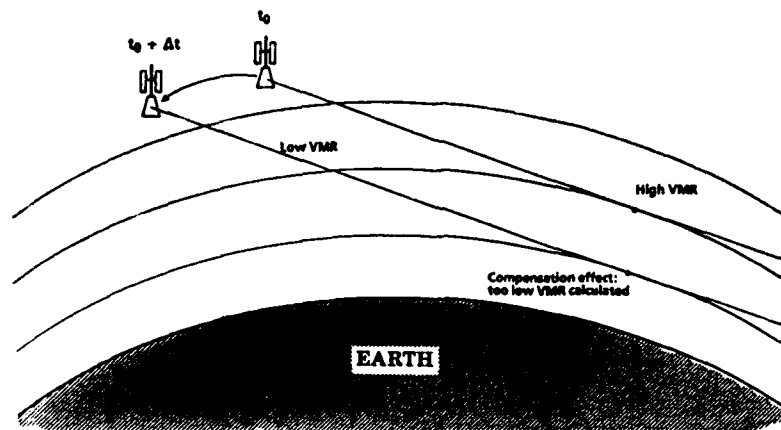


Fig. 1. Compensation mechanism of one-dimensional retrieval algorithms.

Test calculations based on synthetic spectra generated by FASCOD2 <7> show that an assumed HNO_3 volume mixing ratio variation of 20% within 250 km horizontal distance in 23 km altitude triggers an additional retrieval error of 11 % in the next layer (20 km), provided 3 km layering. In this case study the distance of 500 km is assumed to be the subsatellite distance covered during one altitude scan. Figure 2 shows instabilities caused by the assumption of spherical homogeneity of the onion peeling method. Other sources of errors like noise are not included.

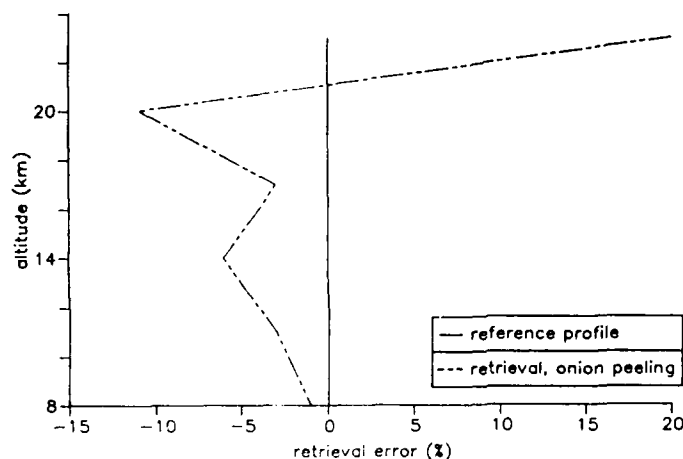


Fig. 2. Onion Peeling retrieval instabilities, due to invalid assumption of spherical symmetry.

A NEW TECHNIQUE

The following approach, which is based on the classical onion peeling method, avoids this type of instabilities and improves the horizontal resolution of limb sounding results in the case of rear-looking instruments like MIPAS.

Let j be the index of the uppermost tangent height within one elevation scan, and M the number of a certain elevation scan within one orbit. The lowest tangent height is denoted by 1. Increasing M indicates later elevation scans in case of a rear pointing instrument. Then evaluation of spectra is done according to the following order (Fig. 3):

M th spectrum of height j
 $M-1$ st spectrum of height $j-1$
 $M-2$ nd spectrum of height $j-2$

 \vdots
 $M-j_{\max}+1$ st spectrum of height 1
 $M+1$ st spectrum of height j
 M th spectrum of height $j-1$

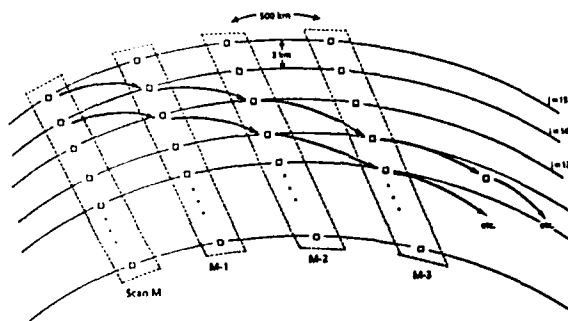


Fig. 3. Stationary state evaluation scheme for a typical rear scanning instrument. Arrows indicate the order of evaluation.

By ray tracing, those points are determined, where the ray intersects layers above the tangent layer. For these points mixing ratios of atmospheric gases are interpolated from adjacent gridpoints of the same layer. The order of evaluation guarantees that the ray passes only air volumes which can be described by interpolation of results achieved at former steps, except the target air mass at the tangent height. Only when initializing the retrieval procedure, a priori information has to be used. For initialization the following order of evaluation is applied:

1st spectrum of height j
2nd spectrum of height j
1st spectrum of height $j-1$
3rd spectrum of height j
2nd spectrum of height $j-1$
1st spectrum of height $j-2$
4th spectrum of height j

\vdots

1st spectrum of height 1

After this step the stationary state order is used, unless that air volumes behind the tangent point are still characterized by a priori information for another handful of steps. As soon as the ray passes only air volumes, for which gas mixing ratios have been retrieved in previous steps, no more a priori information on the target gas distribution is needed.

CONCLUSION

The proposed retrieval scheme might increase the spatial resolution and the stability of the solution of any inverse radiative transfer problem connected with rapid-moving rear scanning limb sounders. On the analogy of 'onion peeling', the expression 'cutting onion cubes' might characterize the method in a self-explaining way. This method is not applicable on solar occultation experiments, because only one profile can be measured during one sunrise or sunset situation.

REFERENCES

1. T.B. McKee, R.I. Whitman, J.J. Lambiotte, Jr., "A Technique to infer Atmospheric Water-Vapor Mixing Ratio From Measured Horizon Radiance Profiles," NASA TN D-5252 (U.S. GPO, Washington, D.C., 1969).
2. J.M. Russell III, S.R. Drayson, "The inference of Atmospheric Ozone Using Satellite Horizon Measurements in the 1042 cm⁻¹ Band," J. Atm. Sci. Vol. 29, pp. 376-390 (1972).
3. A. Goldman, R.S. Saunders, "Analysis of Atmospheric Infrared Spectra for Altitude Distribution of Atmospheric Trace Constituents - I: Method of Analysis," J.Q.S.R.T., Vol. 21 (2), pp. 155-162 (1979).
4. J.D. Mill, S.R. Drayson, "A Nonlinear Technique for Inverting Limb Absorption Profiles," in: Developments in Atmospheric Science, 9, Remote Sensing of the Atmosphere and Applications, A.L. Fymat and V.E. Zuev, Elsevier Scientific Publishing Company, Amsterdam, pp. 123-135 (1978).
5. M. Carlotti, "Global Fit Approach to the Analysis of Limb-Scanning Atmospheric Measurements," Applied Optics, Vol. 27 (15), pp. 3250-3254 (1988).
6. H. Fischer, C. Blom, H. Oelhaf, "Michelson interferometer for passive atmospheric sounding," in Technical Digest on Optical Remote Sensing of the Atmosphere, 1991 (Optical Society of America, Washington D.C., 1991), Vol. 18, pp. 323-325 (1991).
7. S.A. Clough, F.X. Kneizys, E.P. Shettle, G.P. Anderson, "Atmospheric Radiance and Transmittance: FASCOD2," Sixth Conference on Atmospheric Radiation, May 1986, Williamsburg Va., p. 141 (American Meteorological Society, Boston, Mass., 1986).

Forward model comparisons with the High-resolution Interferometer Sounder (HIS)

R.O. Knuteson, H.E. Revercomb, W.L. Smith

University of Wisconsin-Madison CIMSS
1225 W. Dayton St., Madison, WI 53706
(608) 263-7974

Introduction

A subject of continuing interest is the accuracy of current line-by-line transmittance models in the description of atmospheric radiative transfer. The most direct way to investigate this question is to compare accurate measurements of atmospheric radiation with calculations based upon good in-situ measurements of atmospheric state parameters. This summary brings up to date the results of earlier comparisons of observations with calculations to illustrate the outstanding issues remaining. The earlier results were summarized in the 1990 Incline Village meeting of the Optical Society.[Revercomb 1990]

Measurements

The High-resolution Interferometer Sounder (HIS) has been developed at the University of Wisconsin with high absolute accuracy in mind. The instrument is a Michelson interferometer with laser sampling for wavenumber accuracy and onboard precision blackbodies for radiometric accuracy. The HIS has been operated both from aircraft looking down and from the surface looking upward to measure the emitted atmospheric radiance. The five observations presented here compared to calculations are over a range of atmospheric conditions; two are from the NASA U2 at about 20 km altitude (14-15 April 1986), two are from the ground at Denver Stapleton Airport (31 Oct - 1 Nov 1988), and one is from the NOAA P3 aircraft over the Gulf of Mexico (18 Nov 1988) at 8 km altitude.

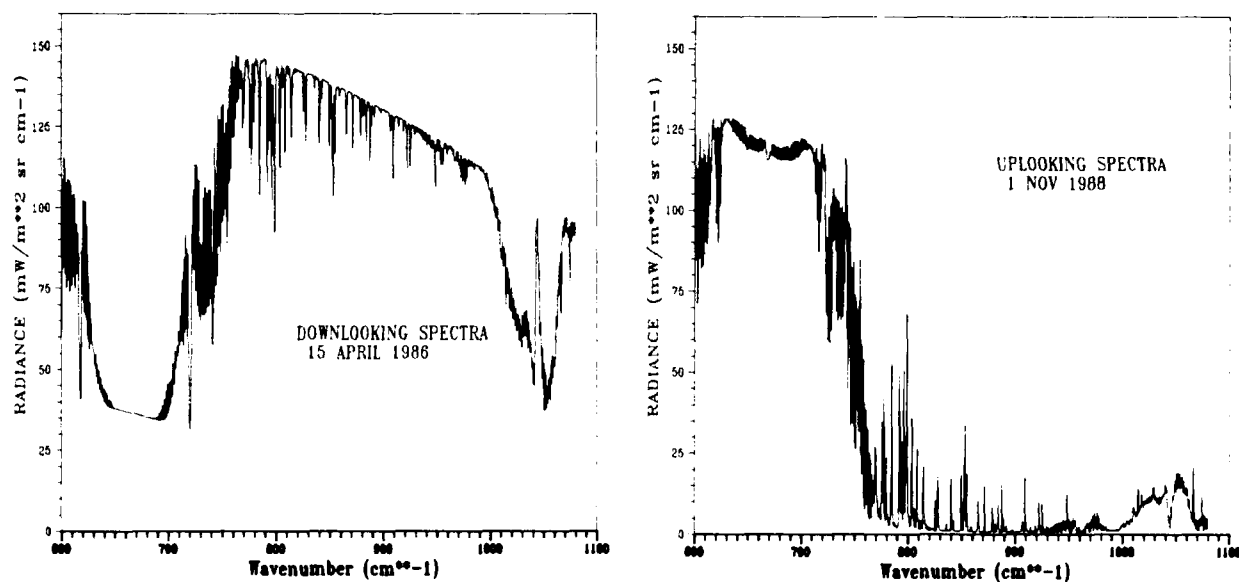


Figure 1. Calculated downlooking radiance at 20km altitude (left) and uplooking radiance at the surface (right).

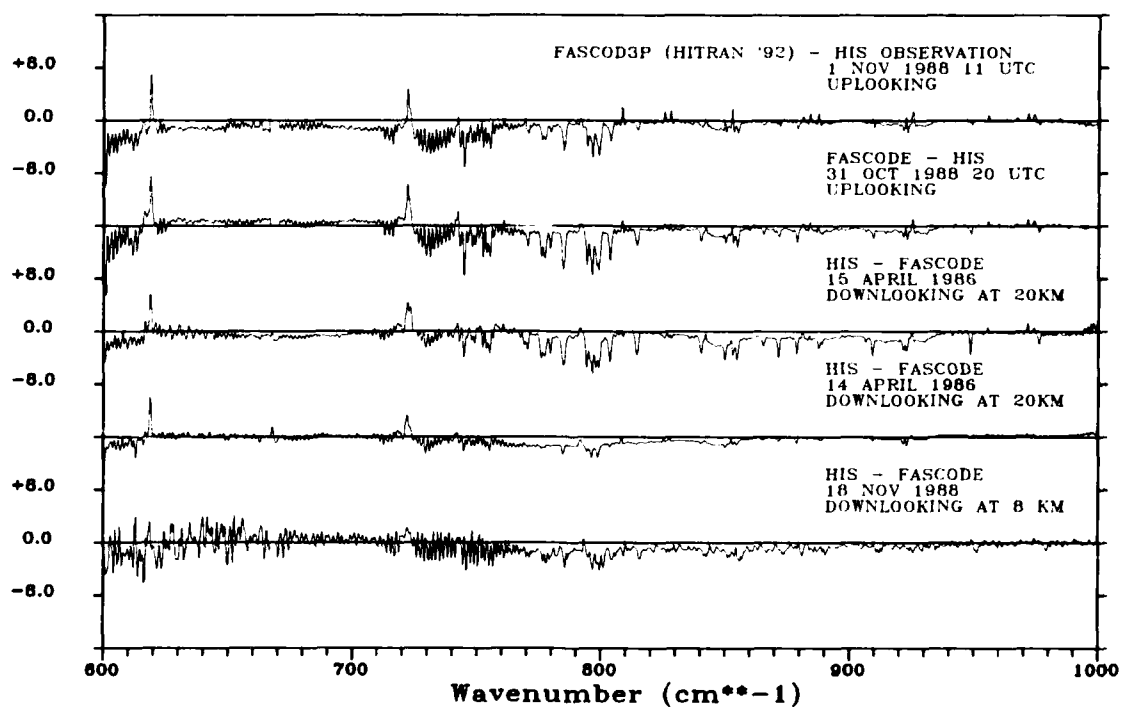


Figure 2. Radiance differences between observation and calculation for a set of different atmospheres illustrating the remaining spectroscopic issues in this spectral region.

Results

Figure 1 shows two of the five calculations; one example of downlooking and one of uplooking. The result of calculating the radiance using temperature and moisture profiles obtained from radiosonde launches, reducing the calculations to the HIS resolution, apodizing the result and differencing from the observations is summarized in Figure 2. The calculations have been done using FASCOD3P (March 1992) and HITRAN '92 with a line mixing parameter of 1.0. The effect of CFCs and CCl₄ have not been accounted for in the calculations to facilitate comparison to previous results.

Conclusions

Figure 2 shows that some differences still remain in the CO₂ region that have not yet been resolved. Several of these cases will be studied in more detail as part of the International Radiation Commission ITRA working group. More recent observations may also shed light upon these issues by improving the characterization of the atmospheric state and by providing a wider range of atmospheric conditions (particularly moister cases).

References

- (1) Revercomb, H.E., R.O. Knuteson, W.L. Smith, H. M. Woolf, and H.B. Howell, 1990: Spectroscopic Inferences from HIS Measurements of Atmospheric Thermal Emission. Optical Remote Sensing of the Atmosphere, 1990 Technical Digest Series, Vol 4, from Topical meeting, Incline Village, Nevada, 12-15 February, published by the Optical Society, Washington, DC, 590-593.
- (2) Anderson, G., et al., FASCOD3P (1992), Phillips Lab, Hanscom AFB, MA
- (3) Rothman, L., et al., HITRAN (1992), Phillips Lab, Hanscom, AFB, MA

CO₂ Non-LTE Excitation and Emission at 4.3 μ m from a Line-by-Line Radiative Transfer Model

Henry Nebel,*^x P. P. Wintersteiner,[#] R. H. Picard,*
R. D. Sharma,* J. R. Winick*

* Phillips Laboratory, Geophysics Directorate (OPS), Hanscom AFB, MA 01731

[#] ARCON Corporation, 260 Bear Hill Road, Waltham, MA 02154

^x Permanent address: Alfred University, Alfred, NY 14802

In this report, infrared radiative excitation of the asymmetric stretch (ν_3 mode) vibrationally excited states of CO₂ in the non-LTE region of the quiescent atmosphere is considered using a line-by-line (LBL) radiative transfer model¹. A set of codes known collectively as Atmospheric Radiance Code (ARC) is used to calculate (1) the vibrational populations of states that emit at 4.3 μ m, and (2) the resulting earthlimb radiance. The model calculations are then compared to earthlimb radiance data from the Spectral Infrared Rocket Experiment, or SPIRE². The approach has previously been used to model CO₂ 15 μ m emission³.

The vibrational energy levels of CO₂ used in the present calculations are shown in Fig. 1, where the level notation is that of the HITRAN database⁴. The transitions near 4.3 μ m involving emission of one ν_3 quantum are very strong, with Einstein A coefficients ~ 400 s⁻¹. The states in groups 1 and 2 are populated by transitions at 4.3 μ m and 2.7 μ m in sunlight, while those in group 3 are populated by 2.0 μ m transitions from the ground state. Absorption at 2.7 μ m and 2.0 μ m is followed, with high probability, by emission at 4.3 μ m. These solar fluorescent processes are very important in the daytime.

Vibrational temperatures for both nighttime (no solar excitation) and low-sun daytime conditions are presented in order to emphasize the importance of solar excitation processes. Fig. 2 shows the calculated vibrational temperature profiles of the CO₂(00011) state for the principal 626 isotope and the three most important minor isotopes assuming no solar excitation. Fig. 3 gives the same vibrational temperature profiles for low-sun daytime conditions with a solar zenith angle of 78°, simulating the daylight scans of the SPIRE experiment. Solar flux absorption in the 4.3 μ m bands accounts for the large differences between the sunlit results of Fig. 3 and the nighttime results shown in Fig. 2. It is responsible for most features of the daytime profiles above 60 km.

The minor isotope bands have smaller opacity than the band of the principal (626) isotope due to much smaller number densities. Thus the solar flux penetrates to lower altitudes in the minor species bands in the daytime and the stratospheric earthshine penetrates more effectively into the mesopause region at night. This results in higher vibrational temperatures for the minor isotope levels in the mesosphere and lower thermosphere.

Vibrational temperature profiles are also calculated for the 01111 state and for the higher-lying group 1, 2 and 3 states shown Fig. 1. These latter states are very effectively populated in the daytime by the short-wave solar flux at 2.7 and 2.0 μ m. The calculation therefore neglects airglow (earthshine) absorption contributions to the populations of these states in the daytime.

Integrated radiance in a limb view is calculated for each spectral line within a band for selected tangent heights, and the results are summed to obtain total band radiance. This must be done for each band and each isotope separately. The results for the daytime case, using all the bands shown in Fig. 1 and a solar zenith angle of 78° , are shown in Fig. 4, which also includes data points for the sunlit scans of the SPIRE experiment. As can be seen in Fig. 4, the model calculations agree very well with the daytime experimental results, which is regarded as confirmation that the model properly accounts for the processes that are important for exciting $\text{CO}_2(\nu_3)$ states in the daytime.

In the sunlit case, the major contribution to the total limb radiance for tangent heights of 55-95 km is made by the group 1 fluorescent states near 3500 cm^{-1} , indicating that solar pumping dominates the excitation processes in the daytime. The 626 fundamental plays a relatively unimportant role in this region because it is strongly self-absorbed. For tangent heights above 100 km where the atmosphere is thin, the 626 fundamental dominates the radiance as expected. Contributions from individual bands or groups of bands to the total radiance will be presented, and the implications of the results will be discussed. Certain results from the radiative transfer calculation will also be presented to illustrate the exchange of radiant energy between various regions of the atmosphere.

The SPIRE instrument also took several scans which looked across the dawn terminator. These have been modeled such that the limb path is partially sunlit and partly in darkness. The calculated limb radiance is shown in Fig. 5, along with the experimental data points for the terminator scans of the SPIRE experiment. The model underpredicts the experimental results to some extent, although the shape of the curve is basically correct. The calculation that underlies these model results will be discussed, showing how the various components of the total predicted radiance are affected by the assumptions made. In particular, the partitioning of the limb path into segments will be discussed along with the role of radiative excitation at various points along the path. The role played by the hydroxyl radical in the mesopause region will also be discussed.

References

1. Wintersteiner, P. P., R. H. Picard, R. D. Sharma, H. Nebel, A. J. Paboojian, J. R. Winick, and R. A. Joseph, CO_2 Non-LTE Effects in a Line-by-Line Radiative Excitation Model, *Technical Digest, Topical Meeting on Optical Remote Sensing of the Atmosphere*, Opt. Soc. Am., 1990 Series, Vol. 4, pp. 615-618, 1990.
2. Stair, Jr., A. T., R. D. Sharma, R. M. Nadile, D. J. Baker, and W. F. Grieder, Observations of Limb Radiance with Cryogenic Spectral Infrared Rocket Experiment, *J. Geophys. Res.*, 90, 9763-9775, 1985.
3. Wintersteiner, P. P., R. H. Picard, R. D. Sharma, J. R. Winick, and R. A. Joseph, Line-by-Line Radiative Excitation Model for the Non-equilibrium Atmosphere: Application to CO_2 $15\text{ }\mu\text{m}$ Emission, *J. Geophys. Res.*, 97, in press, 1992.
4. Rothman, L. S., R. R. Gamache, A. Goldman, L. R. Brown, R. A. Toth, H. M. Pickett, R. L. Poynter, J.-M. Flaud, C. Camy-Peyret, A. Barbe, N. Husson, C. P. Rinsland, and M. A. H. Smith, The HITRAN Database: 1986 Edition, *Appl. Opt.*, 26, 4058-4097, 1987.

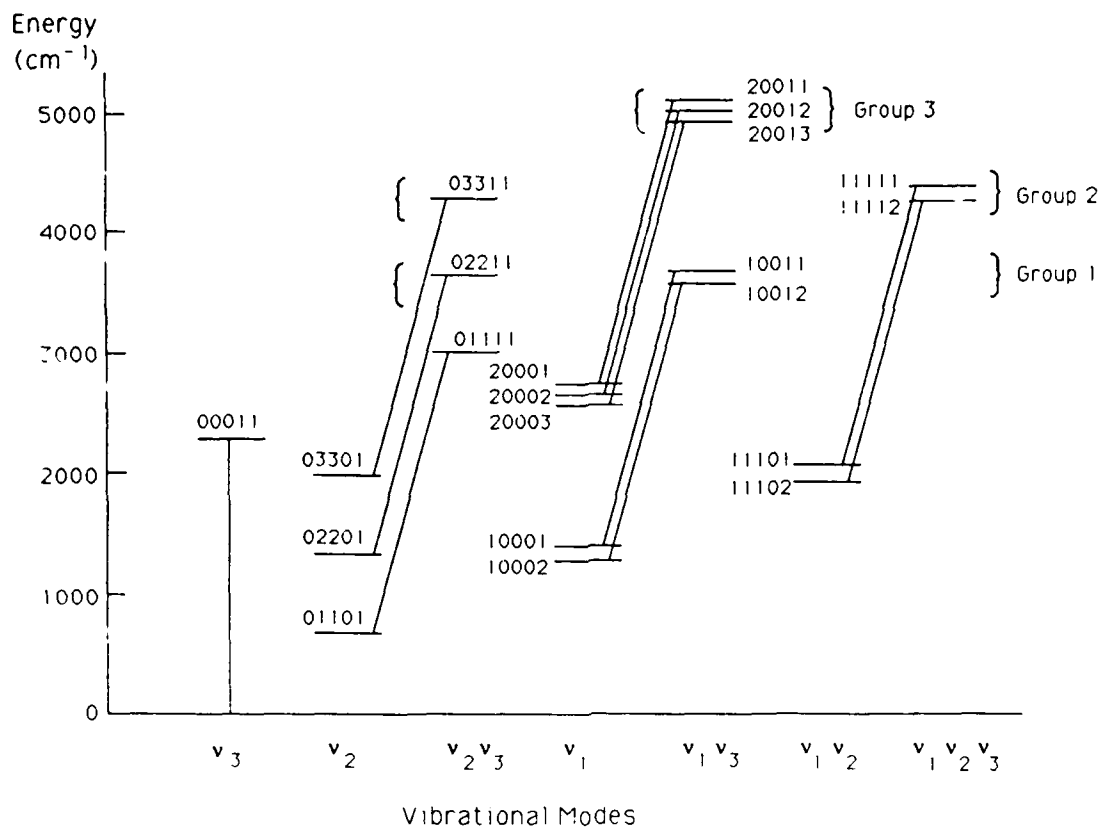
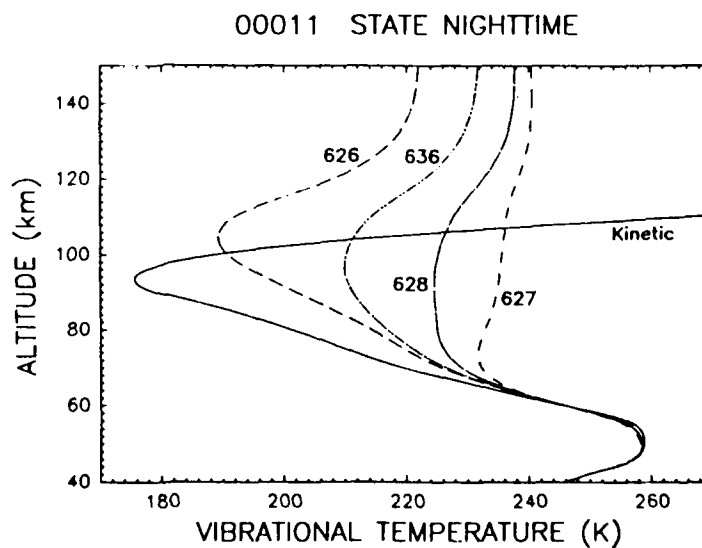


Fig. 1 CO₂ vibrational levels contributing to 4.3 μ m absorption and emission.

Fig. 2 Vibrational temperatures of the lowest excited v_3 state, 00011 , for four isotopes of CO₂ and no solar excitation.



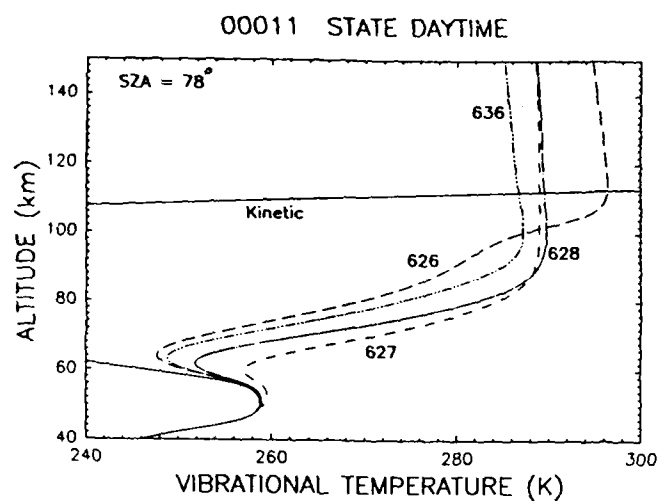
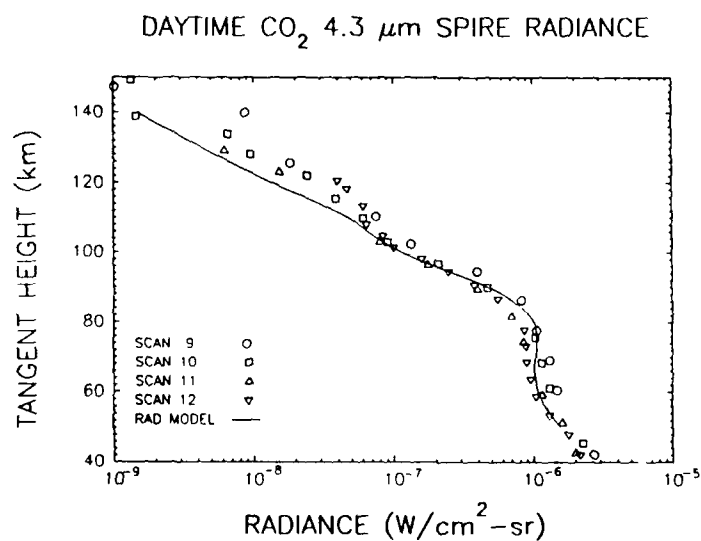


Fig. 3 Vibrational temperatures of the lowest excited v_3 state, 00011, for four isotopes of CO_2 and a solar zenith angle of 78 degrees.

Fig. 4 Comparison of $4.3 \mu\text{m}$ SPIRE daytime limb radiance with the model calculation.



$4.3 \mu\text{m}$ SPIRE RADIANCE, TERMINATOR SCANS

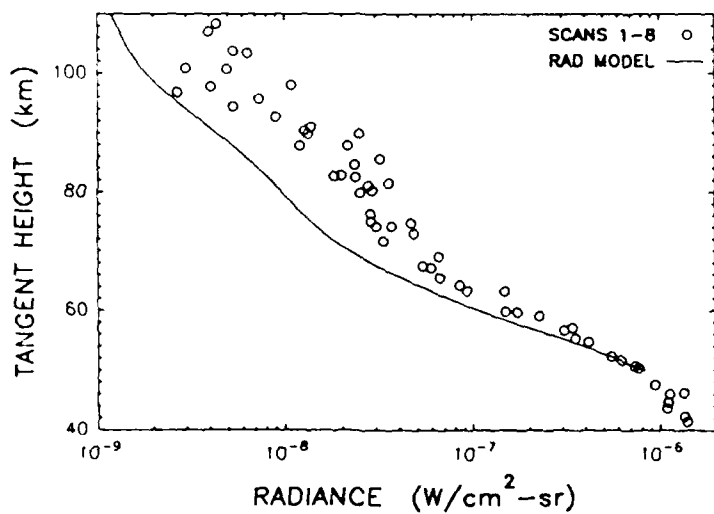


Fig. 5 Comparison of $4.3 \mu\text{m}$ SPIRE terminator limb radiance with the model calculation.

Daytime Measurements Of The Atmospheric Boundary Layer Using An Alexandrite Lidar

Cyrille N. Flamant
Institute for Physical Science and Technology, University of Maryland
College Park, MD 20742-2431
(301) 286-5770

Thomas D. Wilkerson
Institute for Physical Science and Technology, University of Maryland
College Park, MD 20742-2431
(301) 405-4850

Coorg Prasad
Science and Engineering Service Incorporated
4040 Blackburn Lane, Burtonsville, MD 20866
(301) 286-2157

Joseph Famiglietti
NASA Goddard Space Flight Center, Code 917
Greenbelt, MD 20771
(301) 286-5764

1. Introduction and Background

On the behalf of the Maryland Air Management Administration, lidar measurements are being made of the daytime evolution of Planetary Boundary Layer (PBL) height over Prince Georges County, MD. This paper describes the first week of observations, August 3-10, 1992. Data were taken most days around 11:00 AM (EDT), and in the afternoon when the lidar was available at various times. The PBL heights cited here are given in meters above the Goddard lidar station altitude which, in turn, is 65 meters above sea level. Coordinates at GSFC are approximately 39°00'N by 76°51'W.

The lidar measurements will provide qualitative and quantitative information on the height of the PBL over the state of Maryland during summer periods, and make possible important correlations with the behavior of pollutants, in particular urban ozone and its precursors.

The Mie-backscatter lidar, employs one tunable Alexandrite laser. The chosen wavelength is 760.37 nm, and the laser pulse energy is 30 mJ at a pulse repetition rate of 10 Hz (average optical power 3/10 Watt). To operate in the presence of daytime skylight background, we filter the photomultiplier detector with 1 nm wide interference filter centered on the wavelength 760.3 nm. The lidar telescope is a 44 cm diameter Newtonian telescope. Lidar return signals are digitized and recorded on tape in files 12 minutes in length. Display of the processed data is in a one-dimensional (1-D) form, namely a graph of the range squared corrected signal *versus* altitude, or in a two-dimensional (2-D) form, in which the strength of the backscattered signal is plotted using a false-color code image, as a function of time and altitude.

In most cases the PBL is manifested as a well-defined layer of high aerosol backscatter that suddenly diminishes in strength at altitudes of, nominally, 200-2000 meters depending on the time of day and the meteorological conditions. Particles and humidity are trapped in this layer because of a capping inversion, which one usually finds at the top of the layer. Humidity adds to the optical

prominence of the layer by virtue of its contribution to particule growth.

2. Observations

A. 08/05/92, 10:40 (1-D graph, Figure 1) Since it is still early in the day, the BL has not yet attained its full depth. The top of the layer lies near 900 meters, and the transition zone of about 100 meters depth indicates strong activity in the entrainment zone and a rapidly growing BL. One can also see, above the BL up to 2000 meters, the residual layer from the previous day, which is gradually incorporated in the growing BL. The remaining temperature inversion at the top of the residual layer weakens as the day goes on. As a result, if it is not entirely incorporated in the BL by midday, what is left will mix into the free troposphere and vanish.

B. 08/05/92, 10:40 (2-D false color image, Figure 2) The advected BL above GSFC is shown here for a 12-minutes interval. The weakest backscatter signal is indicated in black and the strongest in white. The mixed layer is identified as the region where the signal is strong, but is very little spread on the color scale over the entire depth (a high concentration of well mixed particles). The entrainment zone is identified by a sharp decrease in signal leading to a large color spread over a short range of altitudes. Two strong thermals are visible; they are, as it were, the forcing that drives the growth of the BL. As the ground warms up under solar illumination, convection occurs and lifts particulates and humid air up to higher altitudes. The top of the mixed layer above is not well defined and has a relatively constant height in contrast to the top of the BL. Stronger backscatter signal arises from above each of the thermals, as more humid and particle-rich air is being pushed up from the surface by the growing BL before being incorporated in the mixed layer.

C. 08/05/92, 16:25 (1-D graph, Figure 3) The BL is well developed, and its top now reaches 1800 meters. It is still growing, as indicated by the entrainment zone (1800-2000 meters). The signal from the mixed layer is much stronger than in the free troposphere.

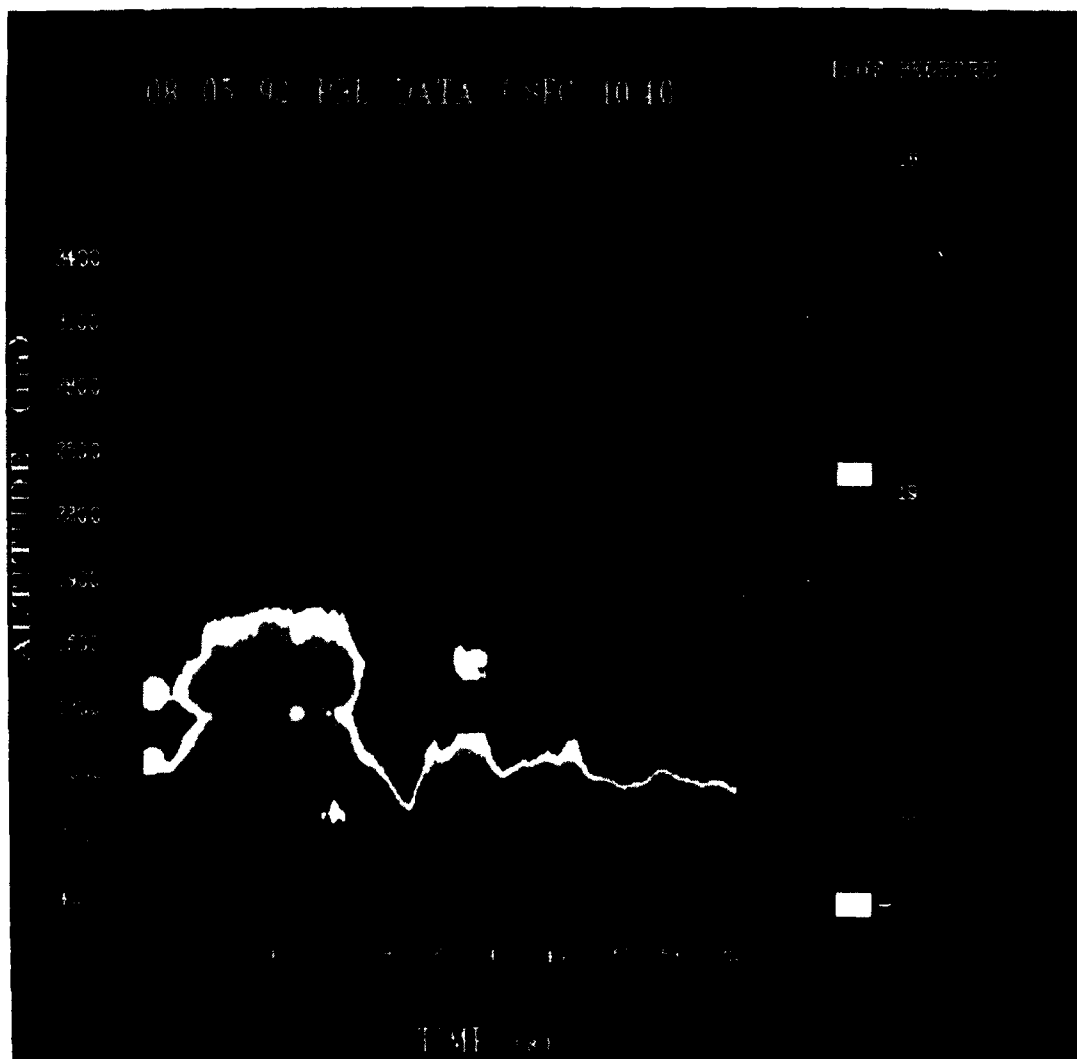
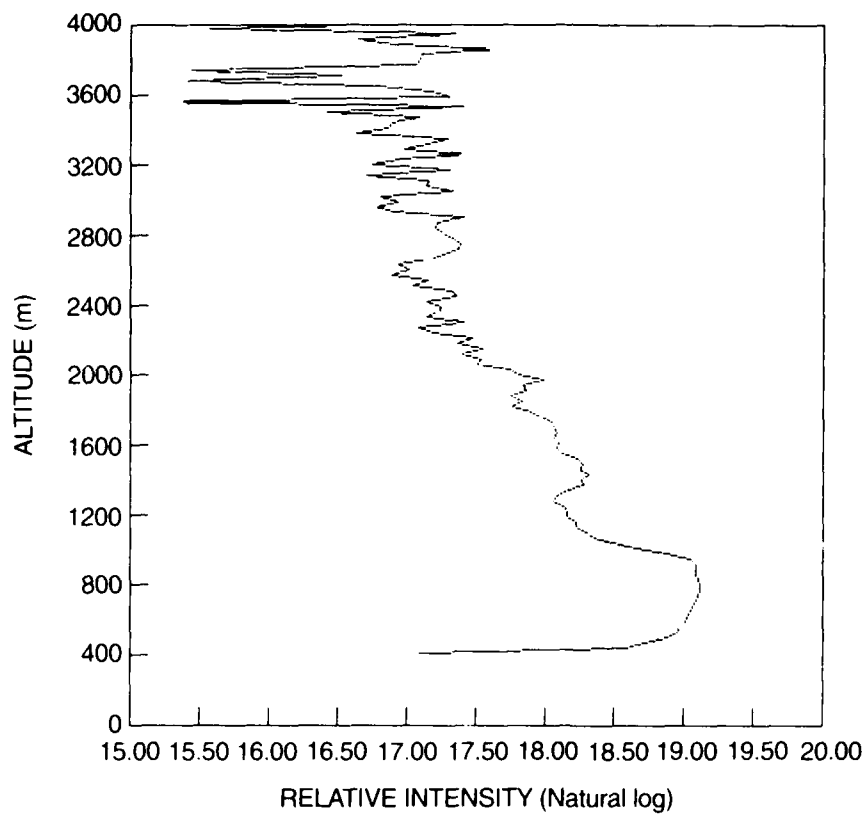
D. 08/05/92, 16:25 (2-D false color image, Figure 4) As with the previous graph, this picture confirms that the BL height is about 1800 meters. Moreover, we see the presence of clouds at the top of the BL which has now reached the lifting condensation level where the upward motion of moist air is still strong enough to create small, fair weather cumulus.

3. Conclusion

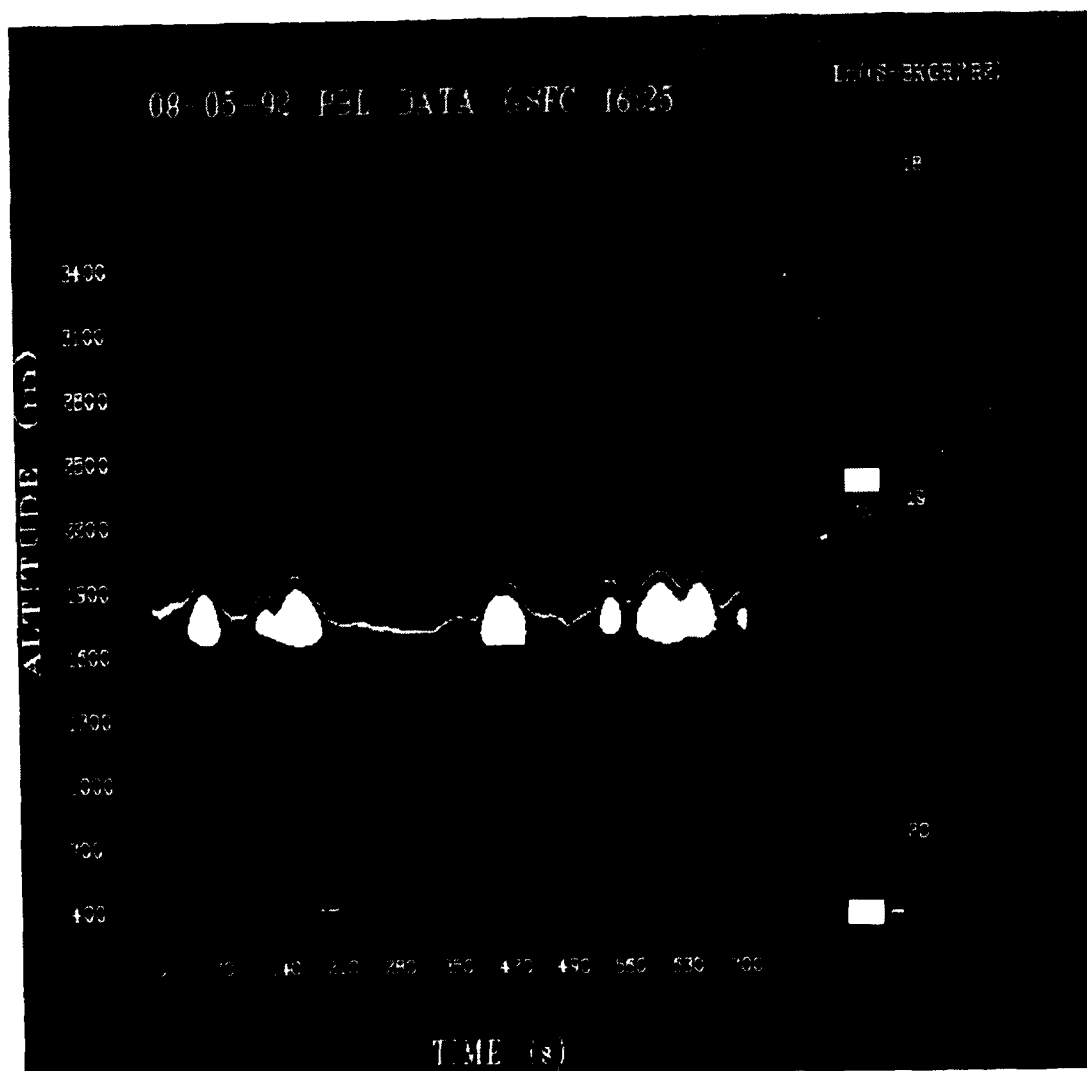
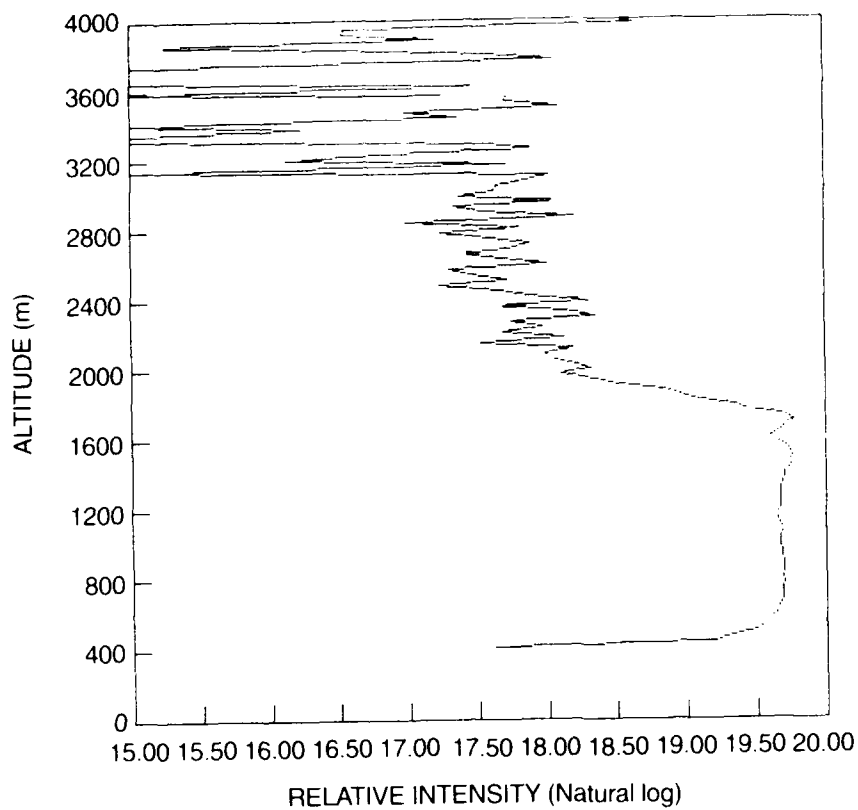
The near-infrared Alexandrite lidar, operating at a fraction of a Watt (average output power) with a narrow filter to reduce daylight background, is capable of providing near-continuous coverage of the atmospheric BL that would be difficult and very labor-intensive to obtain by other means. The daytime growth of the BL is readily observed, as are the entrainment zone, convective phenomena, and formation of cumulus at the lifting condensation level. The combination of altitude profiles of backscatter plus altitude-time images of the aerosol kinematics enables a number of observations of BL meteorology to be made that are useful and perhaps essential for accurate air pollution modelling.

References

1. Schwemmer, G.K., M. Dombrowski, C.L. Korb, T. Milrod, H. Walden, and R.H. Kagann, A Lidar System for Measuring Atmospheric Pressure and Temperature Profiles, *Review of Scientific Instruments*, **58**, 2226, 1987.



R2 CORRECTED SIGNAL 08-05-92 10:40



SAGE II Measurements of Volcanic Aerosols

Robert E. Veiga

Science Applications International Corporation

1 Enterprise Parkway
Hampton, Virginia 23666
(804)-864-2679

Introduction

Volcanic injections of gaseous and crustal constituents directly into the stratosphere occur with low frequency. The mineralogical aerosols quickly settle out while the gases, primarily SO_2 , are converted into aerosols. Once in the stratosphere, the optical properties and the global dispersion of volcanic aerosols can be inferred using in situ particle samplers, photometers, lidars, and satellite instruments. Satellite remote sensing offers the opportunity to study atmospheric dynamics over the short term using the aerosols as a quasi-conserved tracer.

SAGE II Aerosol Measurements

Since October 1984 the Stratospheric Aerosol and Gas Experiment II (SAGE II) has yielded a data set of aerosol extinction profiles at the wavelengths of 385, 453, 525, and 1020 nm. The instrument makes slant-path transmission measurements in the atmosphere at the terminator as the satellite transits in or out of the Earth's shadow. Each day, 30 profiles (15 in each hemisphere) are retrieved from cloud-top to the upper stratosphere with a vertical resolution of 1 km. SAGE II has detected volcanic aerosols from the eruptions of El Chichón (1982), Ruiz (1985), Etna (1987), Kelut (1990), Pinatubo (1991), and Hudson (1991) (Kent and McCormick, 1988; Yue et al., 1991; Brogniez and Lenoble, 1991; McCormick and Veiga, 1992). The data set also indicates that several other unreported volcanic eruptions may have placed material into the lower stratosphere.

Global Optical Depth

Stratospheric optical depth at 525 nm was computed by integrating each SAGE II extinction profile from 2 km above the tropopause to 40 km over the 8 year period from October 1984 through September 1992. For periods after the June 1991 eruption of Pinatubo, the aerosol loading in the lower stratosphere was high enough to diminish the slant-path transmission below the threshold sensitivity of SAGE II, thereby causing loss of information between the peak of the Pinatubo aerosol cloud and the tropopause. For such profiles, optical depth was estimated by extending the profile down to the tropopause in a manner such that the extinction at the altitudes where no measurements were available was set equal to the extinction at the lowest altitude at which data was available. This method of profile extrapolation can cause the optical depth to be overestimated by about 10-20% (M. T. Osborn, personal communication); however only the period from June 1991 through September 1992 is affected. The ensemble of optical depth estimates were mapped onto a regular

latitude-time grid and smoothed to produce Fig. 1. The dominant aperiodic features seen in Fig. 1 are the tropical volcanic aerosol intrusions due to Ruiz (November 1985 - 5°N), Kelut (February 1990 - 5°N) and, Pinatubo (15°N). Superposed on the background before 1991 is an monotonic decrease from the residual El Chichón aerosols. This decrease is modulated by annual variations extending from the subtropics to the high latitudes. The annual optical depth peak occurs during local winter and may be due to a combination of temperature-induced particle growth, the large annual variation in the tropopause altitude, and the relatively high level of eddy transport during winter. Notice that after 1989, in the northern latitudes between 10° and 35°, that the stratospheric optical depth had decreased to a relative minimum such that immediately before the eruption on Pinatubo the optical depths were equal to those encountered ten years earlier (Kent and McCormick, 1984). A prominent feature evident in Fig. 1 is a region of relative minimum optical depth centered at the latitudes of 30°N and S. At these latitudes the occurrence of tropopause breaks and folds would allow stratosphere-troposphere exchange of aerosols. It is also a region where annual large-scale anticyclones, such as the Asian monsoon, have been observed to penetrate into the lower stratosphere to effect material exchange from the tropics to the mid-latitudes (McCormick and Veiga, 1992).

Dispersion of the Pinatubo Aerosols

The paroxysmal eruption of Pinatubo injected a large quantity of gas and aerosols into the stratosphere. Within two weeks the bulk of the resulting volcanic cloud had circled the planet while spreading to the tropical latitudes bounded between 20°S and 30°N [McCormick and Veiga, 1992, Stowe et al., 1992]. During this early period the cloud was composed of SO₂ gas [Bluth et al., 1992], crustal particles, and sulfate droplets [Deshler et al., 1992]. The sulfate aerosols were produced by the rapid conversion of SO₂ gas to sulfuric acid [McKeen et al., 1984]. Fig. 1 shows the order of magnitude increase in optical depth caused by Pinatubo and that the highest values occurred during late 1991 to early 1992. In contrast to Ruiz aerosols 6 years earlier, the Pinatubo aerosols were rapidly advected to the southern hemisphere. Fig. 1 shows that Ruiz aerosols affected predominantly the northern latitudes while Kelut aerosols had essentially no northern migration. Fig. 1 also shows that the tropical optical depth by September 1992 had decreased by a factor of 2 from the levels in January.

A vertical cross-section, computed from the SAGE II 1020 nm extinction ratio data, detailing the spread of the Pinatubo aerosols is shown in Fig. 2. Altitudes below tropopause + 2 km are blacked-out and the SAGE II saturation altitudes are plotted as small triangles. Lidar data from two separate campaigns, one in December 1991 and the other in May 1992, were used to obtain estimates of the extinction ratio below the saturation altitudes (Philbrick et al., 1992; M. P. McCormick personal communication, 1992). Fig. 2a shows the early structure of the cloud it spread zonally, and the transport of low altitude aerosols into the northern hemisphere. Four months later, as seen in Fig. 2b, most of the SO₂ had converted to sulfuric acid aerosol and had spread to the southern hemisphere at altitudes near 23 km, extending to 50°S by mid-November. During this same period an asymmetry over the tropics had developed with a lobe of high extinction ratio immediately

to the south of the equator. Fig. 2c shows penetration of extinction ratios greater than 100 to the South Pole by austral summer whereas transport to northern latitudes is blocked by the northern polar vortex. This period also shows the lobe of relatively high extinction ratio immediately south of the equator persisting since its inception 4 months earlier. Also, during February-March 1992 the aerosol perturbation reached its highest altitudes approaching 40 km. Fig. 2d shows the Pinatubo aerosol 1 year after the eruption. Note that the equatorial lobe present in Figs. 2b and c has disappeared and that the tropical saturation altitudes have dropped almost uniformly to 20 km indicating that sedimentation has caused the peak of the aerosol layer to drop several km relative to early 1992.

References

- Bluth, G. J. S., S. D. Doiron, C. C. Schneetzler, A. J. Krueger, and L. S. Walter, Global tracking of the SO₂ clouds from the June 1991 Mount Pinatubo eruptions, *Geophys. Res. Lett.*, **19**, 151-154, 1992.
- Brognez, C. and J. Lenoble, Analysis of 5-year aerosol data from the SAGE II, *J. Geophys. Res.*, **96**, 15,479-15,497, 1991.
- Deshler, T., D. J. Hofmann, B. J. Johnson, and W. R. Rozier, Balloonborne measurements of the Pinatubo aerosol size distribution and volatility at Laramie, Wyoming during the summer of 1991, *Geophys. Res. Lett.*, **19**, 199-202, 1992.
- Kent, G. S. and M. P. McCormick, SAGE and SAM II measurements of stratospheric aerosol optical depth and mass loading, *J. Geophys. Res.*, **89**, 5303-5314, 1984.
- Kent, G. S. and M. P. McCormick, Remote sensing of stratospheric aerosol following the eruption of El Chichón, *Optics News*, **14**, 11-19, 1988.
- McKeen, S. A., S. C. Liu, and C. S. Kiang, On the chemistry of stratospheric SO₂ from volcanic eruptions, *J. Geophys. Res.*, **89**, 4873-4881, 1984.
- Philbrick, C. R., D. B. Lysak, T. D. Stevens, P. A. T. Haris, and Y. C. Rau, Atmospheric measurements using the LAMP lidar during the LADIMAS campaign, Sixteenth International Laser Radar Conference, *NASA Conference Publication 3158*, July 20-24, 1992.
- Stowe, L. L., R. M. Carey, and P. P. Pellegrino, Monitoring the Mt. Pinatubo aerosol layer with NOAA/11 AVHRR data, *Geophys. Res. Lett.*, **19**, 159-162, 1992.
- Yue, G. K., M. P. McCormick, and E. W. Chou, Stratospheric aerosol optical depth observed by the SAGE II: decay of the El Chichón and Ruiz volcanic perturbations, *J. Geophys. Res.*, **96**, 5209-5219, 1991.

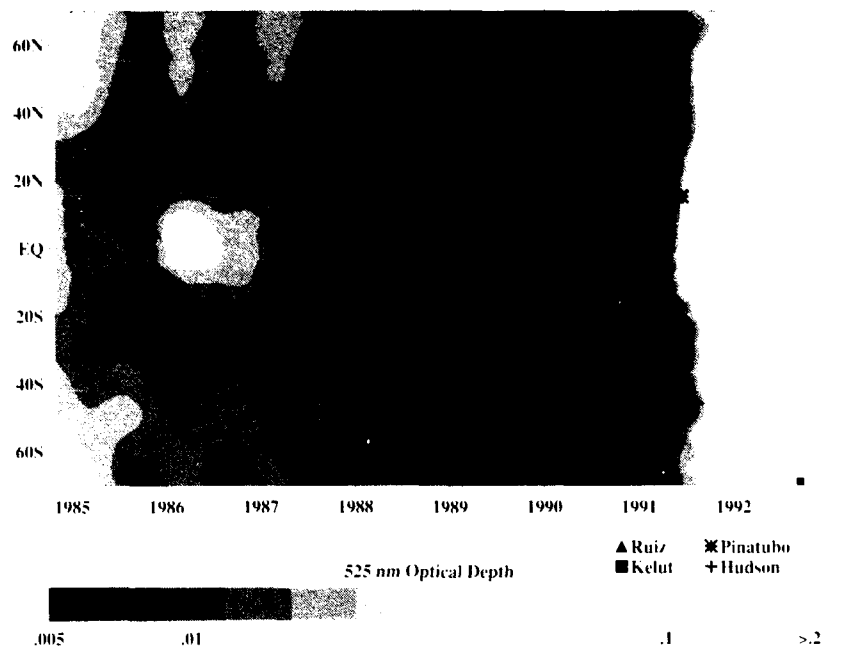


Figure 1. SAGE II 525 nm stratospheric optical depth. Years marked at January 1.

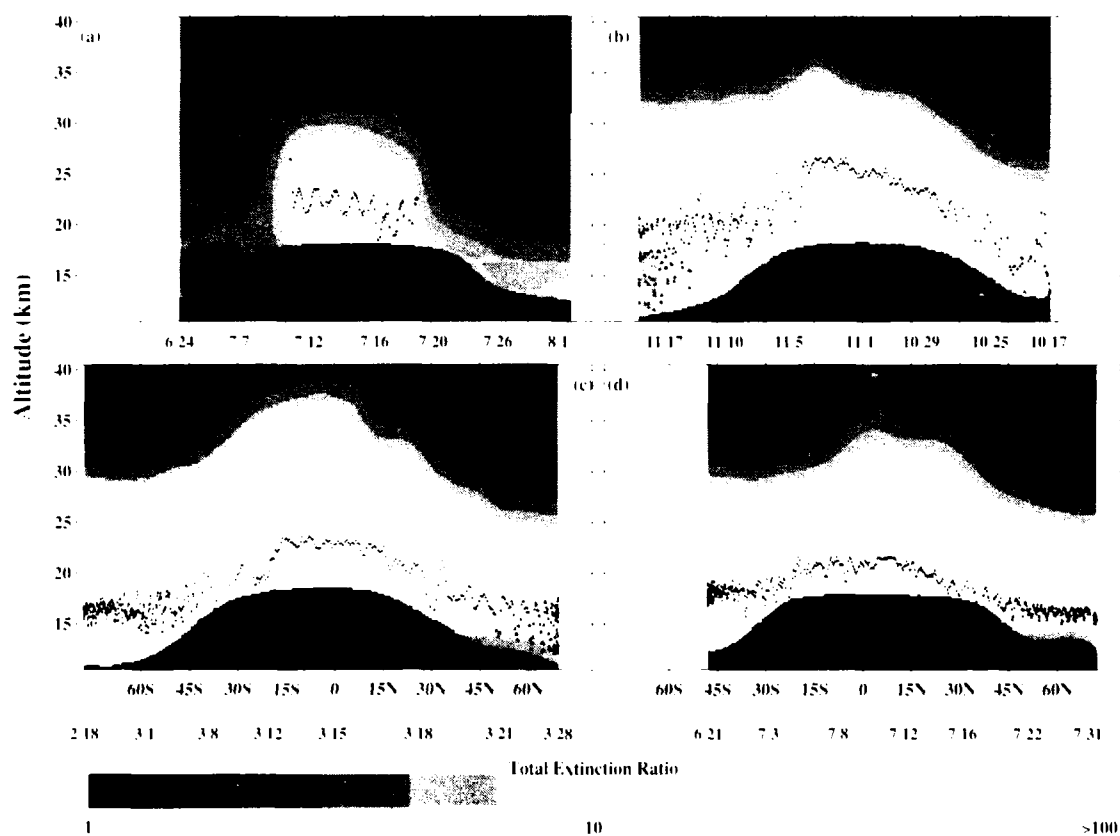


Figure 2. SAGE II 1020 nm extinction ratio. (a) 23 Jun - 8 Aug 1991. (b) 16 Oct - 23 Nov 1991. (c) 17 Feb - 28 Mar 1992. (d) 20 Jun - 1 Aug 1992.

COMPARISON OF REMOTELY MEASURED MULTISPECTRAL SCATTERING PARAMETERS FOR TROPOSPHERIC AEROSOLS.

D. R. Cutten

Earth System Science Laboratory, University of Alabama in Huntsville, Huntsville, AL 35899

E. W. McCaul, Jr.

Universities Space Research Association
4950 Corporate Drive, Huntsville, AL 35806

J. D. Spinhirne

NASA/Goddard Space Flight Center, MS 617, Greenbelt, MD 20771

R. T. Menzies

NASA/Jet Propulsion Laboratory, MS 169-214, Pasadena, CA 91109

R. Pueschel

NASA/Ames Research Center, MS 245-4, Moffett Field, CA 94035

A. D. Clarke

Department of Oceanography
University of Hawaii, 1000 Pope Rd, Honolulu, HI 96822
and

D. A. Bowdle

Earth System Science Laboratory, University of Alabama in Huntsville, Huntsville, AL 35899.

INTRODUCTION

In Fall 1989 and Spring 1990 the National Aeronautics and Space Administration (NASA) conducted a number of survey flights on the NASA DC-8 aircraft over the Pacific Basin as part of the GLOBal Backscatter Experiment (GLOBE). The main objective of these flights was to collect data on tropospheric aerosol backscatter, either by direct measurement or modeled from measurements of selected aerosol microphysical properties that cover a wide range of spatial and temporal scales. The primary intent of collecting these data is to predict the performance of space-borne lidar systems such as the Laser Atmospheric Wind Sounder (LAWS). Other goals of the GLOBE missions were to characterize the source and properties of aerosols in the middle to upper troposphere over the remote ocean regions.

Data visualization techniques have been used to provide data quality control and to undertake analysis on selected data sets within the GLOBE database. Results of this analysis have provided further information on the types of aerosol and their physico-chemical properties in the middle and upper troposphere over the remote Pacific Ocean.

APPROACH

The GLOBE database contains data sets from several collocated aerosol sensor systems which allow empirical links to be developed between direct aerosol backscatter data at different wavelengths and to provide aerosol physico-chemistry which can be used to derive aerosol backscatter at any wavelength.

These data sets have been compiled into a central system and examined for quality and consistency. The Hierarchical Data Format (HDF) was selected as the common format from which the data can be accessed because it is used by several data visualization programs. One of the programs being extensively used for this analysis is the LinkWinds program developed by Jet Propulsion Laboratory (JPL). This interactive program allows the display and manipulation of scientific data in an image format as well as allowing some basic statistical analysis and scatter plots on selected areas between two coregistered data sets from separate sensors. The data are displayed in a false-color 2-dimensional altitude-time cross-section plot. The analysis performed on these plots was designed to isolate, identify and characterize aerosol types (eg., background (Rothermel et al, 1989)) and their properties (eg., effective particle size) in the tropospheric region.

The approach taken in the analysis presented here was to examine the ratio of backscatter data at any two wavelengths for a particular flight where common data existed and to look at the histogram of the ratio values and the averaged ratio. In the case of the GLOBE lidar dataset six backscatter ratios were examined after the data had been preprocessed to produce a set of 2-D cross-sectional plots. The nature of the histogram plot immediately indicated if there was a monomodal or bimodal tendency in the ratio data either for the whole flight or a selected region. The averaged value for the ratio within a selected region provided a conversion factor between the two wavelengths. These ratios indicated what aerosol size range was dominating the backscatter for the selected regions of interest in the troposphere, such as convective features or dust plumes. Scatterplots also allowed empirical conversion factors to be estimated for backscatter wavelength relationships. The LinkWinds program can provide relationships between aerosol backscatter and selected meteorological parameters (eg., relative humidity) along a particular transient flight when the meteorological data are also coregistered. Results of these analyses are presented in companion paper (McCaul et al, 1993).

To facilitate the concentration-dependent aerosol backscatter analysis, backscatter (β) data are expressed in terms of the aerosol mixing ratio $\beta_{mr} = \beta(z)/\rho(z)$. Here mr denotes "mixing ratio", z the altitude and ρ the air density. In many situations mixing ratios tend to be conserved during air mass processes such as vertical and horizontal transport. This approach aided the identification, quantification and correlation analysis of aerosol features within and across the data sets.

The availability of aerosol size distribution data ($dn/d\log D$) along a flight track and the LinkWinds visualization program allowed one to see which size range dominated the aerosol backscatter for a particular wavelength. By combining the size distribution image with a coregistered image of single particle backscatter computed with a generic composition, a new image is created which represents the differential backscatter ($d\beta/d\log D$). This parameter immediately indicated which type of aerosol process could lead to maximising the backscatter.

INSTRUMENTATION

Instrumentation used in the survey flights (Bowdle et al, 1991) consisted in part of two lidar systems operating from the visible to the infrared wavelengths to measure aerosol backscatter, and aerosol sampling systems which could measure aerosol size distributions and chemical composition. Data analysed for this paper were obtained from the following instrumentation. Aerosol backscatter data were obtained from the NASA/Goddard Space Flight Center (GSFC) Nd:YAG pulsed lidar system operating at 0.53, 1.06 and 1.54 μm wavelengths and the NASA/JPL pulsed coherent lidar system operating at 9.25 μm . Aerosol size distribution data were measured with (i) the NASA/ARC Particle Measuring Systems (PMS) Forward Scattering Spectrometer Probe (FSSP) mounted on a wing tip pylon and (ii) the University of Hawaii's thermally pre-conditioned PMS Laser Optical Particle Counter (LOPC) which also provided physico-chemical data on the aerosols (Clarke, 1991). All data from these sensors have been calibrated

by procedures appropriate for each sensor. The data sets which cover the Pacific Ocean basin were of sufficient size to minimize sample biases, and to allow locating and examining aerosol features.

PRELIMINARY RESULTS

Tables 1 and 2 show example data obtained for backscatter ratio, conversion factors and correlation coefficients from two GLOBE transient flights at six lidar wavelengths. Data for the middle troposphere and convective plume aerosols were taken from the latter stages of the Tokyo to Honolulu flight on June 3, 1990. The convective plume was located by examining areas of the $1.06\mu\text{m}$ β_{mr} cross-sectional plot immediately above remote tropical regions of the marine boundary layer for high backscatter. The dust plume data were selected from the Darwin to Tokyo flight on 31 May, 1990 where a strong dust region, possibly associated with a jet stream was encountered near Tokyo. This dust plume was diagnosed from the physico-chemical data obtained from LOPC measurements at flight level. The size of the regions selected were approximately 156km by 0.9km for the middle troposphere, 86km by 4.1km for the convective plume aerosols and 160km by 1.6km for the dust plume. Mid point altitudes of the selected regions are given in Table 1. Various pairs of backscatter were checked to ensure internal consistency. All histograms for the regions studied were observed to be essentially monomodal.

The ratio values in Table 1 for the middle troposphere aerosol except for the last value, show typical wavelength dependence which is indicative of a size distribution dominated by small particles such as sulfuric acid. The unity $\beta_{1.06}/\beta_{1.54}$ value may have arisen from the fact that the $1.54\mu\text{m}$ backscatter data were noisier data and have been averaged over a longer period. The convective plume aerosol which is expected to be dominated by larger particles originating from the marine boundary layer, also showed wavelength dependence that is commensurate with that particle range. However, the $\beta_{1.06}/\beta_{9.25}$ and $\beta_{1.54}/\beta_{9.25}$ values are a little lower than expected. In the case of the dust plume the wavelength dependence is not typical for 1 micrometer dust particles. Several other regions examined in the dust plume also gave similar values. The dust encountered could be mixed with a free troposphere aerosol (such as ammonium sulfate or sulfuric acid) and/or industrial soot to form an external mixture. Hence a composite refractive index is involved and the backscatter ratio no longer followed a simple relationship based on particle size alone.

Table 1. Example of backscatter ratios for middle troposphere, convective plume and dust plume aerosols.

Backscatter Ratio	Middle Troposphere (4.1km)	Convective Plume (2.4km)	Dust Plume (6.3km)
$\beta_{0.53}/\beta_{9.25}$	109.6	12.4	38.2
$\beta_{1.06}/\beta_{9.25}$	13.7	3.8	16.0
$\beta_{1.54}/\beta_{9.25}$	12.3	2.3	6.1
$\beta_{0.53}/\beta_{1.06}$	7.8	3.2	2.3
$\beta_{0.53}/\beta_{1.54}$	8.3	6.7	4.9
$\beta_{1.06}/\beta_{1.54}$	1.0	2.0	2.3

Correlation coefficients derived from 9.25 μ m backscatter versus visible/near infrared backscatter plots and from cross-plots of backscatter within the visible/near infrared wavelengths are given in Table 2. In most cases the correlation is significant, particularly those involving 9.25 μ m backscatter, which is indicative of some linearity in the data. Assuming linearity, an estimate of a conversion factor is made. In most cases these values are found to be similar to the corresponding ratio values in Table 1.

Table 2. Conversion factors (CF) and correlation coefficients (r) at selected wavelength pairs for middle troposphere, convective plume and dust plume aerosols covering the same regions used for Table 1.

	Middle Trop.		Convective Plume		Dust Plume	
	r	CF	r	CF	r	CF
9.25 vs 0.53 μ m	-0.106	~ 100	0.484	~ 10	0.648	~ 40
9.25 vs 1.06 μ m	0.453	~ 15	0.847	~ 5	0.871	~ 15
9.25 vs 1.54 μ m	0.322	~ 12	0.378	~ 3 - 4	0.689	~ 8
1.06 vs 0.53 μ m	0.180	~ 10	0.441	~ 5	0.782	~ 2
1.54 vs 0.53 μ m	0.169	~ 10	0.141	~ 8	0.497	~ 6
1.54 vs 1.06 μ m	0.447	~ 1	0.232	~ 3	0.727	~ 3

These preliminary results suggest that backscatter data can be used to extract information about aerosol properties. However, they also showed that the analysis has to be done on extensive datasets that include many aerosol regimes before any substantive conclusions can be made. The GLOBE dataset should achieve this objective as it sampled data over a large portion of the Pacific Ocean during two different seasons. Further results will be presented based on this dataset.

REFERENCES

- Bowdle, D.A., S.F. Williams, J. Rothermel, and J.E. Arnold, 1991, "The global backscatter experiment (GLOBE) Pacific Survey Mission", Tech. Digest, Coherent Laser Radar: Tech. and Applications, Snowmass, CO, 290 - 292.
- Clarke, A.D., 1991, "A thermo-optic technique for in situ analysis of size-resolved aerosol physicochemistry", Atmos. Environ., 25A, 635 - 644.
- McCaul Jr., E.W., D.A. Bowdle, D.R. Cutten, R.T. Menzies and J.D. Spinhirne, 1993, "Relationship between lidar backscatter and meteorological fields", Submitted to Sixth Topical Meeting Opt. Remote Sens. of the Atmos., Salt Lake City, UT, USA.
- Rothermel, J., D.A. Bowdle, J.M. Vaughan, and M.J. Post, 1989, "Evidence of a tropospheric aerosol backscatter mode", Appl. Opt., 18, 1040 - 1042.

Relationships Between Lidar Backscatter and Meteorological Fields

by

Eugene W. McCaul, Jr.

Institute for Global Change Research and Education
Universities Space Research Association
4950 Corporate Drive, Suite 100, Huntsville, AL 35806
205-544-5298

David A. Bowdle

Earth System Science Laboratory
University of Alabama in Huntsville, Huntsville, AL 35899
205-544-1682

Dean R. Cutten

Earth System Science Laboratory
University of Alabama in Huntsville, Huntsville, AL 35899
205-544-3327

Robert T. Menzies

NASA/Jet Propulsion Laboratory, MS 169-214, Pasadena, CA 91109
818-354-3787

and

James D. Spinhirne

NASA/Goddard Space Flight Center, MS 617, Greenbelt, MD 20771
301-286-9099

1. Introduction

A primary concern in the design of satellite-borne Doppler lidar wind sensors is the extent to which atmospheric aerosol concentrations are sufficient to produce backscatter intense enough for accurate retrieval of wind estimates. Although some climatological data regarding the large-scale spatial and seasonal evolution of the global tropospheric aerosol field have become available within the past decade (Kent *et al.*, 1991), our knowledge of the structure of aerosol fields on the synoptic scale and mesoscale remains inadequate. In an effort to investigate the structure of these fields and their relationships to meteorological phenomena, lidars operating at several wavelengths were flown aboard the National Aeronautics and Space Administration's (NASA) DC8 on a number of flights in the Pacific Ocean basin during late 1989 and early 1990 as part of the Global Backscatter Experiment (GLOBE; Bowdle *et al.*, 1991).

Observing system simulation experiments (Krishnamurti *et al.*, 1991) are currently being used to study the efficacy of various design choices and tradeoffs for the Laser Atmospheric Wind Sounder (LAWS), a satellite-borne Doppler lidar under consideration for launch by NASA as part of the Earth Observing System (EOS). A crucial input to the simulation experiments is the distribution of aerosol backscatter throughout the atmosphere. Inasmuch as the simulation of LAWS wind measurements is complex and computationally intensive, and the real initial conditions describing the aerosol field are unknown, it is not yet feasible to simulate directly the generation, transport and removal of aerosols within the model. Rather, what is sought is a parameterization of the aerosol

backscatter field in terms of basic meteorological fields already carried in the model calculations.

The purpose of this work is to examine the lidar backscatter fields measured during the GLOBE flights, compare them with spatially and temporally co-registered estimates of meteorological data fields, and examine the statistical relationships between the backscatter and meteorological fields. The problem is complicated by the extreme variability of the lidar backscatter, which easily encompasses six orders of magnitude, by the sparsity and irregular coverage of the lidar data fields, and also by the fact that the meteorological data are available only at scales much larger than those resolved by the lidar data.

2. Data Reduction

The lidar data were obtained from the Jet Propulsion Laboratory's (JPL) $9.25\ \mu\text{m}$ CO_2 system (Menzies and Tratt, 1991), and from the multi-wavelength (0.532 , 1.064 , and $1.54\ \mu\text{m}$) Nd:YAG system operated by Goddard Space Flight Center (GSFC; Spinhirne *et al.*, 1991), during a series of 13 flights by the NASA DC8 in the Pacific basin region during late Spring 1990. The flights consisted of a mix of transits and local excursions. These lidars probed the atmosphere at either nadir or zenith incidence, sampling the same regions simultaneously whenever feasible. Cruising altitudes for the transit flights were usually between 8 and 12 km.

Although each system collected data with fine time resolution, logistical considerations forced this investigation to examine only data averaged over time intervals of 100 s for the JPL data, and 60 s for GSFC. The JPL and GSFC data were furnished with nominal vertical resolutions of 30 m and 75 m respectively. Backscatter measurements contaminated by cloud returns or attenuated due to obscuration of the beam by intervening cloud were excluded from both backscatter datasets. In addition, the lidars were unable to obtain useful data within approximately 1 km range of the aircraft. The locus of points where lidar data were available thus assumed the form of an irregular "curtain" partly above and partly below the aircraft flight level. However, because of discontinuities in lidar operation and limitations in range, the lidar data curtains usually achieved only about 10-20% of the maximum possible spatial coverage.

For display and study purposes, the lidar data were remapped to a standard time-height cross-section grid having 20 s time resolution and 30 m altitude resolution. Displays of the data on this standard grid are approximately equivalent to those on a flight-distance versus altitude grid, because fluctuations of aircraft groundspeed were relatively small on most transit flights.

Meteorological data were collected and archived by sensors on board the DC8, but these gave conditions only at flight level, not in the regions of space probed by the lidars. For direct comparison with the curtains of lidar data, co-registered full-height curtains of meteorological data were created using large-scale gridded model analyses produced at the European Centre for Medium Range Weather Forecasts (ECMWF). These data were available daily at 00 and 12 UTC on a latitude-longitude (ϕ, λ) grid with 2.5 degree spacing, and at 14 standard levels p_k from 1000 hPa to 10 hPa in the vertical. For each flight, standard pressure level data at $(\lambda(t), \phi(t), p_k(t))$ in each column of lidar data taken at time t were "advected" to new positions $(\lambda(t_0), \phi(t_0), p(t_0))$ valid at the nearest ECMWF analysis time t_0 . Then the gridded ECMWF data were interpolated to the advected data positions. The interpolations were accomplished with the aid of a circularly symmetric distance-dependent weighting function in the horizontal, and cubic splines in log-pressure in the vertical.

The data advection scheme used estimates of all three local wind components furnished by ECMWF at the analysis time. The advection was accomplished iteratively over 30 min steps, accounting in each step for streamline curvature and stretching/shrinking. Because most flights straddled 00 UTC, advection was rarely needed for more than 6 h, so that it was not unreasonable to assume the 00 UTC ECMWF winds to be steady-state throughout the advection process. Potential temperatures and water vapor mixing ratios were assumed to be conserved during advection, and other quantities such as temperature and relative humidity were computed at the original unadvected positions by application of the Poisson and Clausius-Clapeyron equations. The end result is the deduction of the meteorological variables at the original unadvected standard-level

points $(\lambda(t), \phi(t), p_k(t))$ within the lidar curtains, from which further spline interpolation in $\log-p$ produces a vertical profile at equivalent 30-m resolution. The gridded curtains of meteorological data thus obtained could be compared directly with the gridded lidar data.

3. Results

The lidar and meteorological data curtains were inspected and compared for each flight, to see which meteorological variables, if any, showed promise as a possible predictor of backscatter. Cross-correlations between the logarithm of lidar backscatter and the various meteorological variables were also routinely computed. The cross-correlations were computed in three principal forms: (1) single coefficients describing the cross-correlation between pairs of variables over the full slab of lidar data points in each entire flight; (2) cross-correlations between the vertical profiles of variables as a function of time; and (3) cross-correlations between time series of variables as a function of altitude. In addition, separate cross-correlation computations were made using "LinkWinds" and other data visualization software in specific regions within flights exhibiting heterogeneous conditions.

The assessment of degree of correlation between backscatter and meteorological fields was complicated by the large differences in spatial and temporal resolution of the two types of data, and by the sparsity and irregularity of coverage of the lidar data. Ideally, comparison of the lidar backscatter fields, available at a typical horizontal resolution of less than 5 km and vertical resolution of less than 100 m, with the meteorological fields, derived from data having approximately 250 km horizontal resolution and roughly 1 km vertical resolution, would require considerable low-pass filtering of the lidar data to insure compatibility of scales for the highest wavenumber features in each field. However, it was not generally feasible to apply filtering techniques or spectral analysis to the lidar backscatter fields because of their intermittence and variable spatial coverage. Thus, the cross-correlation computations were conducted straightforwardly on the available lidar data points, with the full knowledge that some decorrelation is inevitable owing to the absence of fine-scale features in the interpolated ECMWF-derived meteorological fields.

Several regimes of statistical relationships between backscatter and meteorological fields have emerged from study of the data, with only a few meteorological variables showing promise of serving as possible bases for parameterizing the backscatter field. In this paper the emphasis is on two of the most important regimes.

The most prominent statistical regime occurred in maritime tropical air masses, where there was generally a positive correlation, usually ranging from 0.5 to 0.9, between the vertical variations of backscatter and moisture. Two moisture fields were studied, relative humidity and specific humidity. When considering the entire troposphere, the correlation between backscatter and relative humidity was higher than that between backscatter and specific humidity. This is because both backscatter and relative humidity typically showed high amplitude in both the boundary layer and in moist layers that generate cirrus clouds in the upper troposphere. In the lower troposphere, correlations between backscatter and specific humidity were comparably large, but in the upper troposphere specific humidity was inevitably small and poorly correlated with the backscatter. The correlations between backscatter and moisture were generally high only for the large-amplitude vertical variations in the fields; horizontal correlations were much smaller and less consistent in character. Occurrences of local negative correlation between backscatter and moisture were not infrequent in this regime. They were apparently attributable in many cases to vertical or horizontal phase errors in the positions of the edges of moist layers represented in the ECMWF data. In other cases, high wavenumber details in the backscatter field were simply not resolved by the ECMWF data. In some of these cases, important features of the backscatter field below clouds were obscured, leading to incomplete sampling along the vertical, and to further decorrelation.

A second important statistical regime occurred in the vicinity of jet streams just downwind of large land masses, where backscatter correlated better with windspeed rather than with moisture. In this regime, correlation coefficients were often in excess of 0.6. This pattern was very evident along the east coast of Asia in midlatitudes. The aerosols in this region appeared to be a mixture of dust and other constituents (Cutten *et al.*, 1993), which experience long-distance transport only

when winds are strong. This correlation was large and positive for both vertical and horizontal fluctuations of the fields.

4. Conclusions

The positive correlation between lidar backscatter and moisture appears to be relatively common in maritime tropical airmasses, and derives mainly from the covariance of the large-amplitude vertical fluctuations of the variables. Physically, these correlations may be related to the fact that many maritime aerosols consist of hygroscopic sea salt and sulfate species whose growth is encouraged by moderate or high ambient relative humidity. However, the smaller amplitude horizontal fluctuations show correlation only in localized layers, with little evidence of any systematic relationship between variables. To investigate the relationship between lidar backscatter and atmospheric moisture in more detail, it will be necessary to deploy collocated, calibrated backscatter lidars and Raman or differential absorption lidars capable of sensing the detailed structure of the moisture field. To infer the relative humidity field, an estimate of the temperature field will also be needed.

In jet stream flows located downwind of large land masses, diverse aerosol populations prevail, and the lidar backscatter correlates well with windspeed in and near the jet core. The existence of what appear to be a limited number of regimes of statistical relationships between the backscatter and meteorological fields offers hope that conditional parameterizations of backscatter suitable for input to simulations of instruments such as LAWS can be devised based solely on model-derived knowledge of the local meteorological context.

5. Acknowledgments

The authors acknowledge the support provided by Dr. Ramesh Kakar of NASA Headquarters for this work. The lead author was funded through Universities Space Research Association grants NAS8-38769 and NAS8-37135.

6. References

- Bowdle, D. A., J. Rothermel, J. E. Arnold, and S. F. Williams, 1991: The Global Backscatter Experiment (GLOBE) Pacific Survey Mission: Results and Implications for LAWS. *Technical Digest on Coherent Laser Radar: Technology and Applications*, Vol. 12, 290-292, Opt. Soc. Amer., Snowmass, Colo.
- Cutten, D. R., E. McCaul, J. D. Spinhirne, R. T. Menzies, R. Pueschel, A. D. Clarke, and D. A. Bowdle, 1993: Comparison of Remotely Measured Multispectral Scattering Parameters for Tropospheric Aerosols. submitted to Sixth Topical Meeting Opt. Remote Sens. Atmos., Opt. Soc. Amer., Salt Lake City.
- Kent, G. S., M. P. McCormick, and S. K. Schaffner, 1991: Global Optical Climatology of the Free Tropospheric Aerosol From 1.0- μ m Satellite Occultation Measurements. *J. Geophys. Res.*, 96, D3, 5249-5268.
- Krishnamurti, T. N., J. Xue, G. Rohaly, D. Fitzjarrald, G. D. Emmitt, S. Houston, and S. Wood, 1991: Using a Global Spectral Model in an Observing System Simulation Experiment for LAWS - an EOS Wind Measuring System. *Preprints*, Second Symp. Global Change Studies, 23-27, Amer. Meteor. Soc., New Orleans.
- Menzies, R. T., and D. M. Tratt, 1991: Aerosol and Cloud Observations with a CO₂ Backscatter Lidar on the NASA DC8 GLOBE Pacific Missions. *Preprints*, Seventh Symp. Meteorol. Obs. Instrument., J265-J267, Amer. Meteor. Soc., New Orleans.
- Spinhirne, J. D., S. Chudamani, and J. F. Cavanaugh, 1991: Visible and Near IR Lidar Backscatter Observations on the GLOBE Pacific Survey Missions. *Preprints*, Seventh Symp. Meteorol. Obs. Instrument., J261-J264, Amer. Meteor. Soc., New Orleans.

A Practical Model for the Calculation of Multiply Scattered Lidar Returns

Edwin W. Eloranta
University of Wisconsin
1225 W. Dayton
Madison, Wisconsin 53706

Introduction

Lidar results are typically analyzed using an equation which assumes all photons contributing to the return have been singly scattered. Lidar pulses returned from clouds often encounter large optical depths within a short distance of the cloud boundary and many of the received photons are likely to result from multiple scattering. This paper presents an equation to predict the multiply scattered return. The equation is easy to solve on a small computer and allows specification of the scattering cross section and the scattering phase function as a function of penetration depth into the cloud. Atmospheric clouds are made of particles large compared to the wavelength of visible and near infrared lidars. Optical absorption by particles is typically negligible at these wavelengths. The solution derived in this paper applies to these conditions. The derivation is an approximation which considers only the contribution due to multiple small angle forward scatterings coupled with one large angle scattering which directs the photon back towards the receiver.

Scattering phase function

The phase function is approximated as a Gaussian function of scattering angle for forward scattering events. This choice is convenient because after a series of small angle scatterings the spatial (or angular) distribution of photons remains a Gaussian. This fact considerably simplifies integration of the multiple scattering equations. A Gaussian phase function is specified by two parameters: a value at a scattering angle of zero, $P(0)$, and a mean square angular width, Θ_s^2 . When a computed, or measured phase function, $P_{true}(\theta)$, is available the parameters of the Gaussian approximation can be defined as:

$$\frac{P(\theta)}{4\pi} = \frac{P_{true}(0)}{4\pi} \exp\left(-\frac{\theta^2}{\Theta_s^2}\right) \quad (1)$$

where:

$$\Theta_s^2 = \frac{2}{P_{true}(0)}$$

This approximation provides a particularly robust description of the forward phase function since it provides correct values in the limiting cases. The phase function at zero scattering angle exactly matches the true value, $P(0) = P_{true}(0)$, and the area under the forward peak matches the value of expected by diffraction theory: $\int_0^{4\pi} \frac{P(\theta)}{4\pi} d\Omega = \frac{1}{2}$. The result of applying this approximation to the C1 model phase function calculated by Deirmendjian(1969) is shown in figure 1.

Near the backscatter direction the phase function is assumed to be isotropic. The value is a function of the order of scattering and is computed from a weighted average of the actual phase function values near 180°.

$$P_{n\pi}(R) = \frac{1}{n\pi} \int_0^\pi P(\pi - \theta, R) \int_{-d}^d \frac{1}{\Theta_s(x)^2} \exp\left(-\frac{\theta^2}{n\Theta_s(x)^2}\right) \beta_s(x) x dx d\theta \quad (2)$$

Where: n is the order of scattering, $\tau = \int_0^d \beta_s(x) dx$ and β_s is the scattering cross section per unit volume.

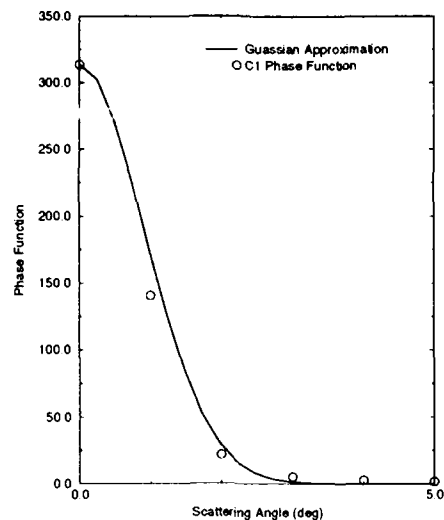


Figure 1. A comparison of the Gaussian approximation to the forward scatter phase function and the exact values computed by Deirmendjian for the C1 model particle distribution illuminated by a wavelength of 450 nm.

Multiple scattering geometry

This model assumes the lidar geometry shown in figure 2.

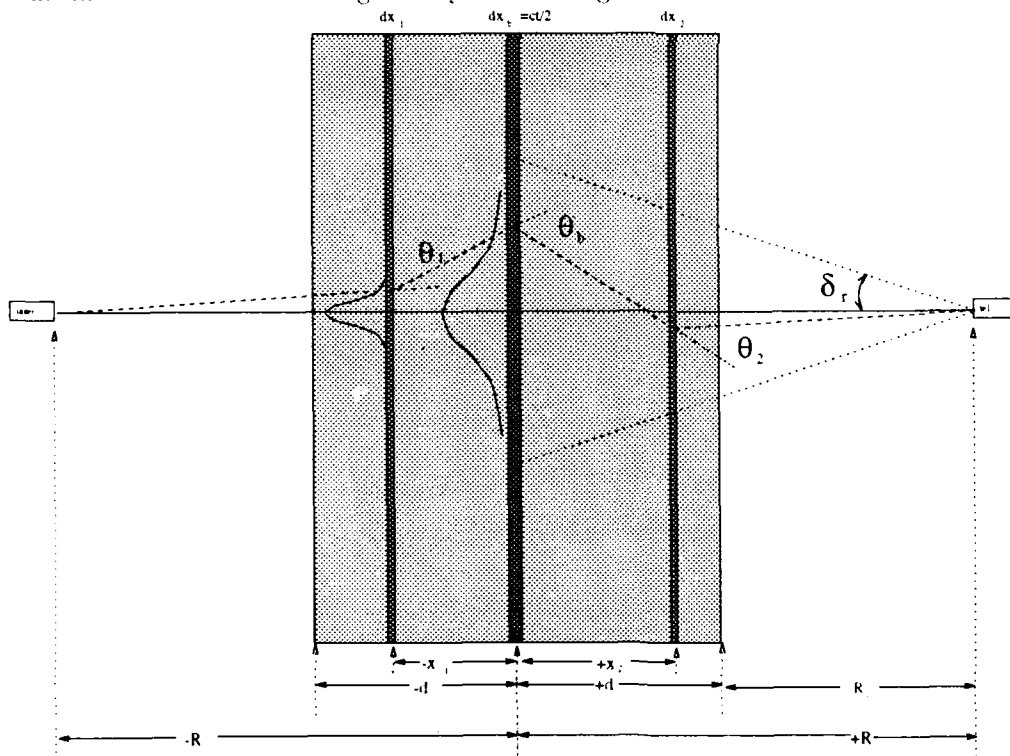


Figure 2. Multiple scattering geometry for a cloud located at a distance R_c from the lidar. For clarity of presentation the propagation path has been unfolded such that the photon return path is separated from the path of the outgoing pulse. In this coordinate system the single scattering slab is placed at the origin, the laser at $-R$ and the receiver at R .

δ_r = Receiver half angle field of view.
 $R = ct/2$ = Distance from the lidar to the single scatter event.
 t = Time after emission of the laser pulse.
 R_c = Distance from the lidar to the cloud base.
 Θ_s^2 = Mean-square angle for single scattering.
 d = Penetration distance into cloud = $R - R_c$.

Equation 3 describes the ratio of n^{th} order scattering, $P_n(R)$, to single scattering, $P_1(R)$. The derivation of this equation assumes: 1) a Gaussian forward scatter phase function described by equation 1. 2) a backscatter phase function which is isotropic near 180° and has a value given by equation 2. 3) the extra path length produced by the small angle deflections is negligible such that the multiply scattered return is not delayed with respect to the single scatter return. 4) the transmitted laser beam is a Gaussian function of angle. 5) multiply scattered photons returned to the receiver have encountered only one large angle scattering event.

$$\frac{P_n(R)}{P_1(R)} = \frac{P_{n\pi}(R)}{P(\pi, R)} \frac{1}{2^{n-1}} \int_{-d}^d \beta_s(x_1) \int_{x_1}^d \beta_s(x_2) \int_{x_2}^d \beta_s(x_3) \cdots \int_{x_{n-2}}^d \beta_s(x_{n-1}) \int_{x_{n-1}}^d \beta_s(x_n) \left(1 - \exp \left(- \frac{\delta_r^2 R^2}{x_1^2 \Theta_s^2(x_1) + x_2^2 \Theta_s^2(x_2) + \cdots + x_{n-1}^2 \Theta_s^2(x_{n-1}) + \delta_t^2 R^2} \right) \right) dx_1 dx_2 dx_3 \cdots dx_{n-1} \quad (3)$$

Where: $P(\pi, R)$ is the phase function at range, R , and a scattering angle of 180° and where the angular distribution of the laser beam is $\propto \exp(-\frac{\theta^2}{\delta_t^2})$.

Figure 3 shows calculations of lidar returns from a cloud with a base altitude of 5 km. The scattering cross section varies with penetration depth while the scattering phase function is assumed to be given by the Deirmendjian C1 model illuminated with a wavelength of 700 nm. The lidar is assumed to have a 5 mrad receiver field of view and a transmitter divergence of 1 mrad (both full angles).

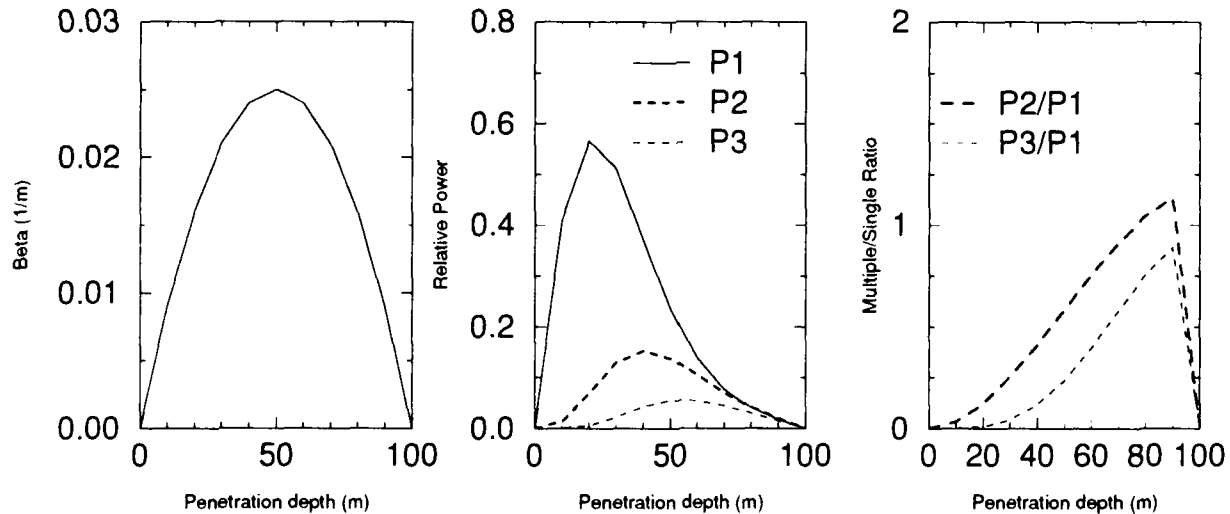


Figure 3. The first three orders of scattering from a cloud with a parabolic range distribution of scattering cross section. The left panel shows the range dependence of the scattering cross section. The center panel shows relative return powers in the first three orders of scattering and the right panel shows the ratios of second and third order scattering to single scattering. The backscatter phase function values for this case are independent of range and have values $\frac{P(\pi)}{4\pi} = .05$, $\frac{P_{2\pi}}{4\pi} = .035$ and $\frac{P_{3\pi}}{4\pi} = .034$

Second order multiple scattering can be computed by an exact integration over all possible double scatter combinations. The model presented above has been used to compute the double scatter contribution for the exact computations presented by Eloranta (1972). The results of this comparison are shown in figure 4.

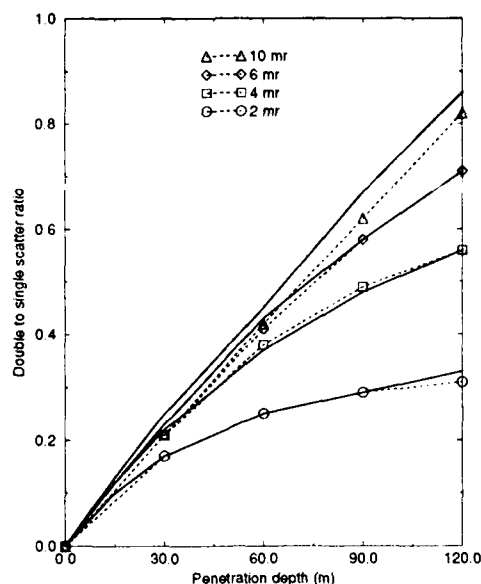


Figure 4. A comparison of small angle approximations and exact double scatter calculations for several receiver fields of view. The double scatter calculations are from Eloranta(1972). Results are for the following case: a cloud base altitude of 1 km, Deirmendjian C1 model phase function, transmitter full angle divergence of 1 mr, and a wavelength of 700 nm. The solid lines are the results of the current model with curves shown for receiver fields of view of 2 mr, 4 mr, 6 mr and 10 mr. Overlaid dashed lines with symbols show the exact values for the same fields of view.

Results obtained from equation 3 provide remarkable agreement with the exact calculations even though this model does not include contributions due to photons which encounter more than one large angle scattering. This is partially due to the fact that lidar receivers typically view a spot on the cloud base with a transverse dimension which has an optical depth of less than 1. Thus, photons scattered laterally are very likely to be outside of the field of view before a second scattering. The small value of the phase function for scattering angles near 90° makes their return into the field of view unlikely. For the narrow angular acceptance angles used in most lidar systems this approximate model for multiple scattering is also expected to provide accurate results for higher order scattering. In cases where the receiver views a spot on the cloud which has a transverse optical depth larger than 1, this approximation is expected to provide a lower bound to the contribution of each order of scattering.

Acknowledgements

Support for this work has been provided by Department of Energy grant DE-FG02-90ER61058 and Office of Naval Research grant N00014-91-J-1558.

References:

- Deirmendjian, D., 1969: *Electromagnetic Scattering on Spherical Polydispersions* Elsevier, New York
- Eloranta, E.W., 1972: *Calculation of Doubly Scattered Lidar Returns*. PhD thesis, University of Wisconsin, 115pp.

Application of a New Iterative Technique for Determining Particulate Extinction Profiles from Airborne Lidar Data Obtained in Clear Tropospheric Conditions

Vladimir A. Kovalev

U.S. Environmental Protection Agency
P.O. Box 93478
Las Vegas, Nevada 89193-3478, (702) 798-3246
Permanent Address: Main Geophysical Observatory
Karbysheva St. 7, 194018 St. Petersburg, Russia

Ramesh Viswanathan

Center for Environmental Studies
University of Nevada
4505 Maryland Parkway
Las Vegas, Nevada 89154, (702) 798-2268

Introduction

In this paper we present preliminary results of the application and potential of a new iterative extinction profile retrieval technique for lidar measurements. Lidar data were collected during May 11-14, 1992, in the Detroit, Michigan area, using a compact airborne nadir looking UV-DIAL.^{1,2} The system was developed for making simultaneous measurements of ozone, sulfur dioxide, and aerosol distributions in the lowest 3-4 km. of the troposphere. The aerosol data are used to obtain semi-quantitative information relating to the atmospheric boundary-layer structure and to develop correction procedure for the DIAL-derived concentrations that are influenced by differential scattering and extinction effects.

Method

The particulate extinction coefficient profile retrieval technique is based on specifying the value of particulate-to-molecular extinction ratio at a specific point in the lidar operation region. In order to derive the particulate extinction profile, the iterative technique first transforms the shape of the lidar signal by normalizing the backscatter term.^{3,4} This simple operation then allows the implementation of the lidar equation solution for the single-component atmosphere to the lidar signal measured in a two-component atmosphere, i.e., one composed of particles and molecules. Subsequently, the inversion procedure is performed using both constant and range-dependent phase functions.

The above described procedure first locates the specific region at which the aerosol extinction coefficient is a minimum. Some reasonable boundary value, i.e., particulate-to-molecular scattering ratio, had to be defined for the particulate extinction profile retrieval. The selection of the appropriate boundary value is the key operation that determines the accuracy of the lidar equation solution, and hence this study is devoted to this problem. The feature of this approach is that the boundary conditions are determined not for a single lidar signal return, but for a whole set of the successive lidar signals. The main components of this approach are as follows: the minimum par-

ticulate-to-molecular scattering ratio is chosen as the preliminary boundary value for selected successive sets of lidar data; subsequently, a continuous extinction profile "image" is generated. From such images it is possible to determine the location of the specific ranges where the particulate component is a minimum, how the presence of cloudy layers affects this location, values of the particulate extinction at the far end of lidar signal (i.e. near the ground), the vertical total optical depth, and how the above factors vary amongst the selected sets.

The described procedure was applied to the UV-DIAL data taken in Detroit. A visual examination of the particulate extinction profile images revealed information on the characteristics of the aerosol extinction profile structure, the values of the extinction, and also provided an understanding of the effect of boundary conditions on the determination of the extinction coefficient. A mechanism for testing the choice and validity of boundary values was investigated by applying the inversion procedure to various sets of lidar returns. Figures 1 and 2 illustrate the preliminary result of applying the inversion procedure to two separate but successive returns of the lidar signal measured at 360 nm. Every extinction profile is obtained from an average of 20 single lidar shots over a 1 second period. The grey-scale chart on the right side of the image relates the derived particulate extinction values to the grey-scale.

Future Prospects

Future plans include a comprehensive investigation of data from lidar measurements taken under various atmospheric optical conditions and the development of criteria for boundary value selection, which can be used when processing data taken under similar atmospheric conditions. It is hoped that this will result in the development of an automated procedure for boundary condition determination. The appropriate choice of the phase functions should also be examined by correlating the extinction values near the ground to *in situ* measurements whenever possible. Further insights may also be gained by investigating how different range dependencies of the particulate phase function influence the extinction profile behavior.

References

1. H. Moosmüller, D. Diebel, D.H. Bundy, M.P. Bristow, C.M. Edmonds, R.M. Turner, V.A. Kovalev, R.P. Haas, and J.L. McElroy, "The U.S. EPA airborne UV-DIAL system," Technical Digest on Optical Remote Sensing of the Atmosphere, (Optical Society of America, Washington, D.C., 1991), 18, 253-255 (1991).
2. H. Moosmüller, D. Diebel, D.H. Bundy, M.P. Bristow, R.J. Alvarez II, V.A. Kovalev, C.M. Edmonds, R.M. Turner, and J.L. McElroy, "Ozone measurement with the U.S. EPA UV-DIAL: Preliminary results," in Proceedings of the Sixteenth International Laser Radar Conference Pt. 2, (Mass. Inst. of Tech., Cambridge, Mass. July 20-24, 1992), pp. 95-98.
3. V.A. Kovalev and H. Moosmüller, "A variable phase function approach for the inversion of lidar return signals," in Proceedings of the Sixteenth International Laser Radar Conference Pt. 2, (Mass. Inst. of Tech., Cambridge, Mass. July 20-24, 1992), pp. 607-610.
4. V.A. Kovalev, "Determination of particulate extinction profiles from lidar signals for a wide range of atmospheric conditions," (Submitted to Applied Optics).

FIGURE 1. Aerosol extinction profile derived for lidar signal taken between 14:37:10 and 14:40:02 hours

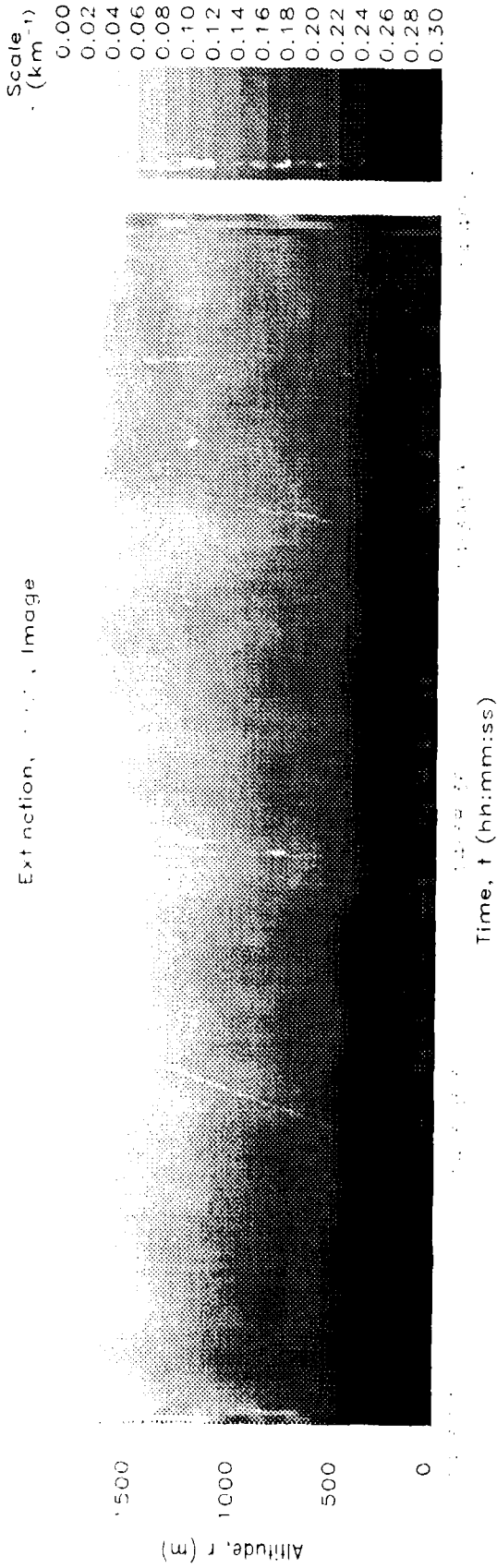
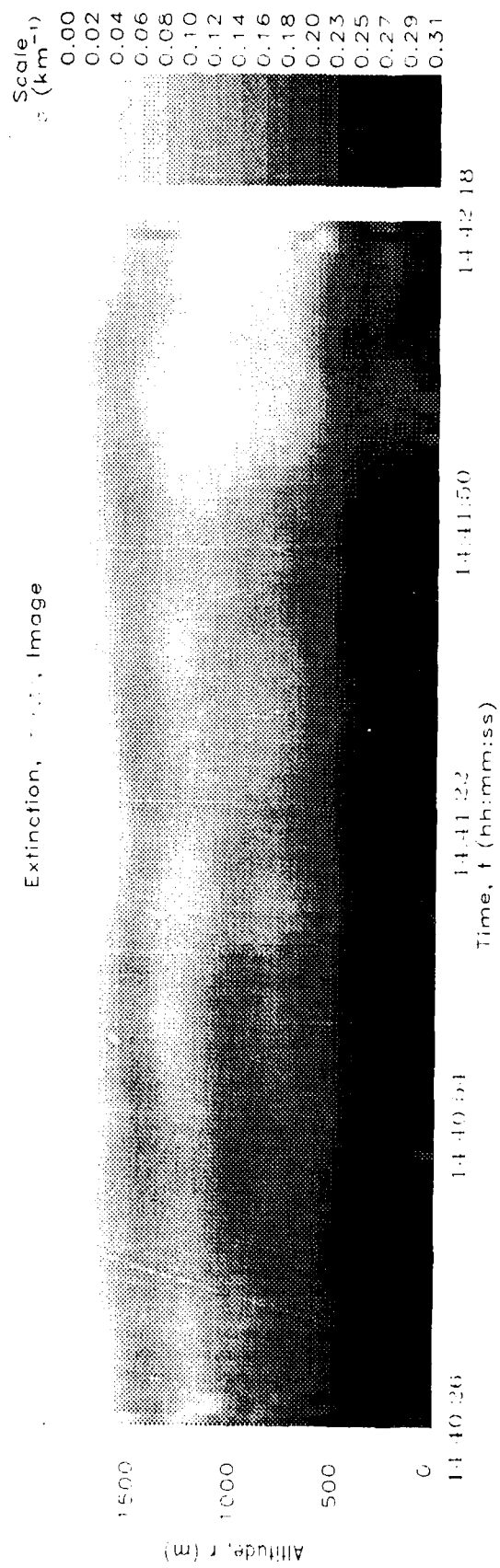


FIGURE 2. Aerosol extinction profile derived for a lidar signal taken between 14:40:26 and 14:42:18 hours



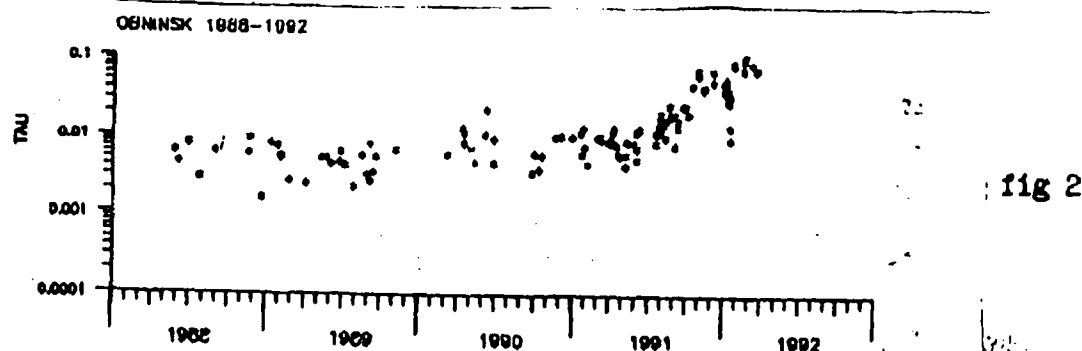
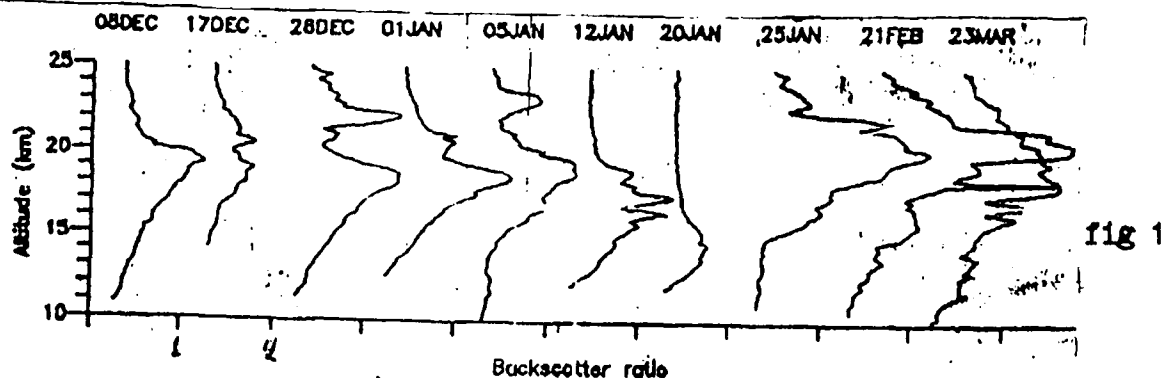
Stratospheric aerosol measuring from Obninsk lidar station following the volcano Pinatubo eruption

S.S. Khmelevtsov, Yu.G. Kaufman

The eruption effect on stratospheric aerosol was first observed during lidar sounding at Obninsk station (55°N , 37°E) in 37 days following the eruption, 22 of July, 1991. The devices used for sounding are described in [1]. The speed of cloud movement, computed on the given measurements, has been found to be more than 1 degree per twenty four hours. 21 of February, 1992 the integral backscatter reached the value $3.67 \cdot 10^{-3} \text{ sr}^{-1}$ (the measurements were carried out at the wavelength of 532 nm) in the layer of 15-30 km and then began to decrease. According to preliminary results, the time of relaxation of the stratospheric aerosol in latitude 55°North is close to 10 months, i.e. just less than the relaxation time of the stratospheric aerosol formed following volcano El Chichon in 1982.

Stratospheric aerosol was most variable from December, 1991 to March 1992. In January large decrease of integral aerosol mass was observed in the layer of 15-30 km and the maximum value of backscatter dropped to 13 km. The possible causes of such stratospheric aerosol decrease are now investigated.

Optical thickness of stratospheric aerosol reached 0.12 in February, 1992 and then also began to decrease (Fig. 2). The calculations of the optical thickness are carried out, using ratios, given in the papers of D.Hofman and H.Jager.



1. V.M. Zakharov, O.K. Kostko, S.S.Khmelevtsov, Lidars and Climate Investigation L, Gidrometeoizdat, 1990.

Evolution of the Pinatubo Volcanic Cloud Over Hampton, Virginia

Mary T. Osborn
Science Applications International Corporation (SAIC)
1 Enterprise Parkway
Hampton, VA 23666 [804-864-2692]

David M. Winker
Atmospheric Sciences Division
NASA Langley Research Center, Mail Stop 475
Hampton, VA 23681-0001 [804-864-6747]

David C. Woods
Atmospheric Sciences Division
NASA Langley Research Center, Mail Stop 475
Hampton, VA 23681-0001 [804-864-2672]

Robert J. DeCoursey
Science Applications International Corporation (SAIC)
1 Enterprise Parkway
Hampton, VA 23666 [804-864-5371]

Introduction

A series of eruptions of the Philippine Mt. Pinatubo volcano in June 1991 climaxed in cataclysmic eruptions on June 15-16, which greatly perturbed the stratospheric aerosol layer. These eruptions yielded an estimated 20 megatonnes of SO₂, which is nearly three times the amount produced by the eruptions of El Chichon in 1982 (Bluth et al., 1991). Lidar measurements taken at 694 nm by the 48-inch lidar system at Langley Research Center (LaRC) in Hampton, Virginia, show the vertical distribution, intensity and spread of the Pinatubo aerosol layers over this mid-latitude location. The peak stratospheric aerosol burden, which occurred in late February 1992, is equivalent to an optical depth of approximately 0.2 at 694 nm. In the subsequent nine months, the stratospheric loading has decreased with an 1/e decay rate of 7.3 months. The magnitudes, transport times, and decay rates of the volcanic aerosol layers following Pinatubo and El Chichon are compared.

48-Inch Lidar System

Routine ground-based ruby lidar measurements have been taken at LaRC, Hampton, Virginia (37.1°N, 76.3°W), since May 1974. These lidar measurements provide high-resolution vertical profiles of the stratospheric and upper tropospheric aerosols. The lidar system, often referred to as the 48-inch lidar system because of its 48-inch telescope, has evolved over the years and provides a valuable long-term history of the mid-latitude stratospheric aerosol (Fuller et al., 1988).

The telescope primary and secondary mirrors were polished and recoated and the system was reassembled in a laboratory setting in late spring of 1991. Routine observations commenced on June 13. A new data acquisition system became operational on August 6, just a few days after the first aerosol layers from the Pinatubo eruption were observed. The new system employs 12-bit CAMAC-based digitizers controlled by a PC clone computer. The new system replaced a 10-bit Biomation transient recorder, providing greatly improved stability and accuracy.

Observations

The lidar scattering ratio, defined as the ratio of the aerosol plus Rayleigh backscattering function to the Rayleigh backscattering function, is the primary result of the analysis of the lidar measurements. The Rayleigh backscatter is obtained from pressure and temperature profiles from radiosondes launched at Wallops Island, Virginia (120 km northeast of the lidar system). Lidar profiles, consisting of approximately 100-400 laser shots, are averaged to a vertical resolution of 0.15 km and normalized to a scattering ratio of 1. All profiles are adjusted iteratively for transmission losses due to aerosol extinction.

An aerosol layer from Pinatubo was first detected at LaRC on August 3, 1991. The last observation showing background conditions was made on July 18. Clouds prevented observations between July 18 and August 3. Between August 3 and October 20, 1992, 65 sets of lidar measurements were taken and analyzed, showing the vertical distribution, intensity, and

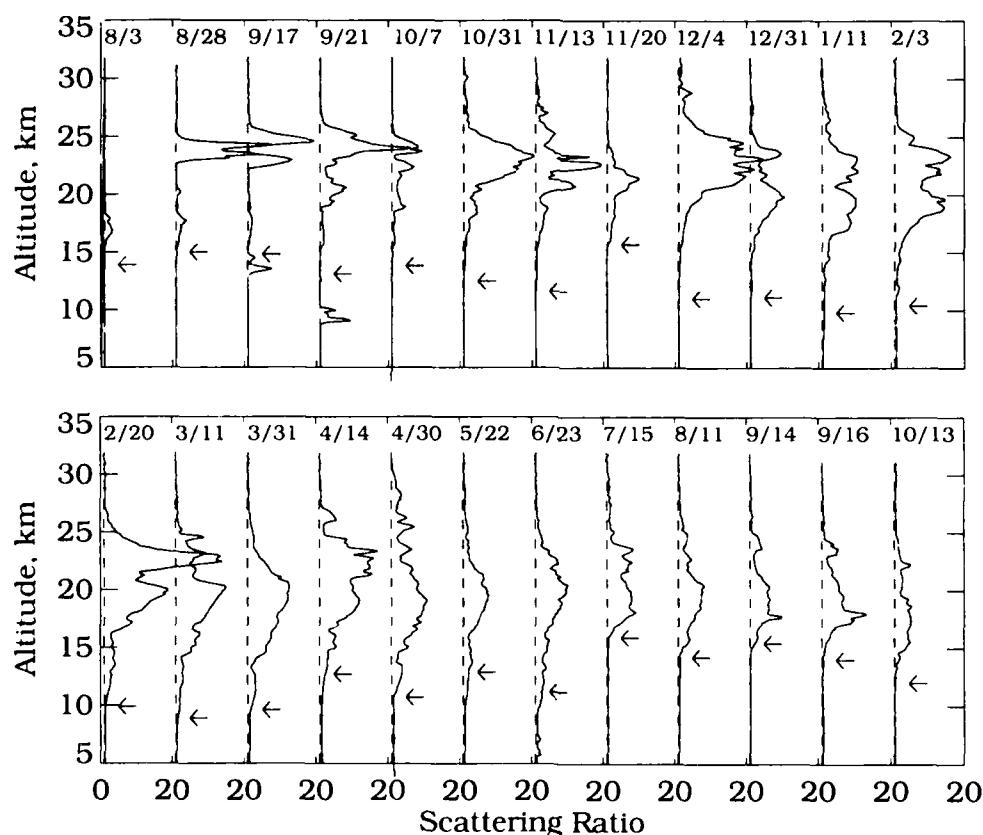


Figure 1. Lidar scattering ratio profiles taken by the LaRC 48-inch lidar system between August 3, 1991, and October 13, 1992.

spread of the Pinatubo aerosol layers over this mid-latitude location. Figure 1 summarizes these measurements by showing the scattering ratio profiles obtained on 24 of the measurement dates. As can be seen in this figure, low altitude layers (< 20 km) from Pinatubo were the first to arrive over LaRC. The first sighting of a layer above 24 km occurred on August 28. The magnitude and vertical distribution of the aerosol layers varied widely from one measurement date to the next, but there is a general increase in the amount of aerosol detected throughout the fall and winter. Pinatubo aerosol layers above 30 km were first detected on October 31. Starting in about December it was necessary to normalize scattering ratio profiles above 30 km, since there was a

significant amount of aerosol in the troposphere. Typical minimum tropospheric scattering ratios were greater than 1.2, a value which corresponds to the maximum stratospheric scattering ratio obtained just prior to the eruption of Mount Pinatubo. The lidar measurement on February 20 was the largest observed, exhibiting a peak scattering ratio of 34 at 22.4 km. It is likely that this relatively high altitude layer was tropical in origin and combined with lower altitude Pinatubo layers present throughout the winter. Beginning in about May of 1992, the Pinatubo layer decreased significantly as it became more Gaussian in shape. The sharp layers detected at 17.8 km on September 14 and 16, 1992, are thought to be from the eruption of Mt. Spurr in Alaska on August 18, 1992.

A contour plot of scattering ratio versus altitude and time (months since eruption on June 15) is shown in Figure 2. This figure includes all of the lidar profiles obtained through October 20, 1992, and illustrates the gradual descent and broadening of the Pinatubo aerosol layer during the first ten months, followed by a gradual decrease in intensity.

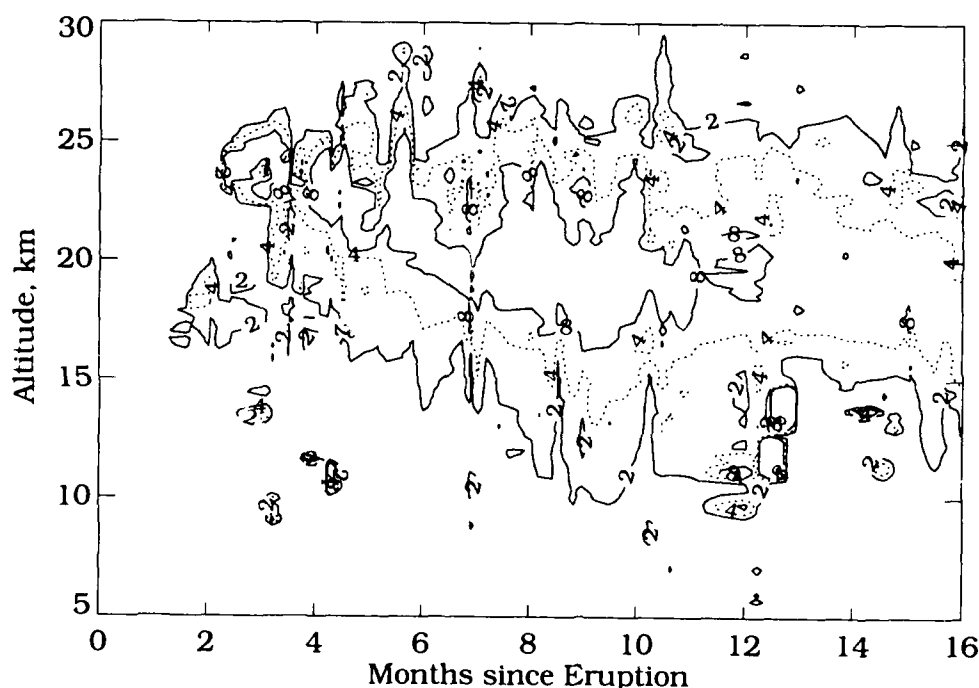


Figure 2. Contour plot of 48-inch lidar scattering ratio vs. altitude and months since the eruption of Mt. Pinatubo on June 15, 1991.

The integrated aerosol backscatter, defined here as the integral of the aerosol backscattering function from the tropopause to 30 km, provides a good measure of the amount of stratospheric aerosol loading at a given location. Figure 3 compares the time history of integrated backscatter at LaRC following the eruptions of both Pinatubo (15.1°N, 120.4°E) and El Chichon (17.3°N, 93.2°W). The increase seen is due to a combination of aerosol formation and growth via gas-to-particle conversion, and a general poleward transport of the aerosol from its initial concentration in the tropics. The background aerosol level preceding the eruption of El Chichon was higher than the level preceding Pinatubo due to several smaller volcanic eruptions in 1980 and 1981. The first volcanic aerosol layer from El Chichon reached Hampton on May 10, 1982, approximately 42 days after the first major eruption on March 28, 1982, whereas the first volcanic aerosol layer from Pinatubo was measured 48 days after the eruption. These transport times are very similar, especially since the first Pinatubo aerosol layer may have arrived a few days earlier. The integrated

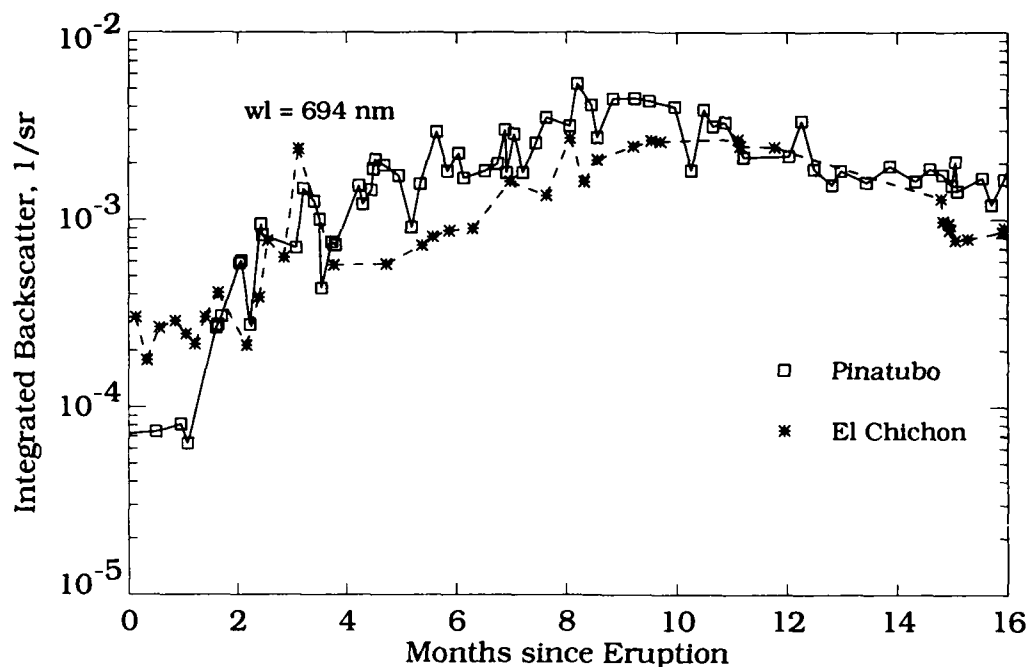


Figure 3. Time history of integrated stratospheric aerosol backscatter measured at LaRC following the eruptions of El Chichon and Pinatubo.

backscatter measured for the first 100 days after each eruption is similar. However, after approximately four months, the Pinatubo integrated backscatter consistently exceeds the values measured after El Chichon for the next six months. The largest Pinatubo integrated backscatter, .0053 1/sr, occurred on February 20, 1992, 250 days after the eruption. Using an extinction-to-backscatter conversion factor of 40 sr, the equivalent peak optical depth is approximately 0.2 at 694 nm. This is approximately twice the maximum loading due to El Chichon, which occurred 245 days after the eruption. The 1/e decay rates, for the nine months following their respective peak loadings, are approximately 7.3 months for Pinatubo and 6.7 months for El Chichon.

References

- Bluth, Gregg J. S., Scott D. Doiron, Charles C. Schnetzler, Arlin J. Krueger, and Louis S. Walter, Global tracking of the SO₂ clouds from the June 1991 Mount Pinatubo eruptions, *Geophys. Res. Letts.*, **19**, 151-154, 1992.
- Fuller, W. H., Jr., M. T. Osborn, and W. H. Hunt, 48-inch lidar aerosol measurements taken at the Langley Research Center: May 1974 to December 1987, NASA RP 1209, October 1988.

The Wavelength Dependence of the Total Extinction Coefficient

Under Volcanic Conditions

Rene Rodriguez and Scott D. Johnson

Idaho State Univ., Dept. of Chemistry, Pocatello, ID 83209 (208) 236-2613

John Burris and Thomas McGee

NASA Goddard Flight Center, Code 916, Greenbelt, MD 20771 (301) 286-5645

SUMMARY

The use of the wavelength ratio as a value for the ratio of the total extinction coefficients at the Raman and Rayleigh wavelengths:¹

$$\epsilon_{\text{Ram}} / \epsilon_{\text{Ray}} = (\lambda_{\text{Ram}} / \lambda_{\text{Ray}})^c \quad (1)$$

has been recently used in the Rayleigh LIDAR equation to determine temperatures or ozone concentrations in the stratosphere. The wavelength dependence of the total scattering coefficient could also be useful for the inversion of LIDAR data to get the particle distribution.² This work examines the dependence of the exponent c , referred to as the Power for the Total Extinction Coefficient Ratio (PTECR), on the index of refraction of the medium, the modal radius of the particle distribution, and the width or shape of the particle distribution. These parameters are expected to be significantly different from the normal atmospheric parameters during volcanic conditions. A Mie code, developed by Dave³ and modified for use on a PC, served to theoretically examine this dependence.

The starting point for the calculations was to choose standard distribution parameters based upon experimental determinations under volcanic conditions.⁴ These standard distributions are termed: 1) background stratospheric (BS), 2) fresh volcanic (FV), and 3) aged volcanic (AV). All are modified gamma distributions of the form:

$$n(r) = a r^\alpha \exp(-b r^g) \quad (2)$$

The particular values of the parameters of gamma distribution for the standard distributions are presented in Table 1.

Particle Distribution	a	α	b	g
Fresh Volcanic	341.3	1	0.5	8
Aged Volcanic	5461.3	1	0.5	16
Background Stratospheric	324.0	1	0.5	18

Table 1 Listing of the parameters of the three particle distributions.

The parameter a is related to the particle density, α and g are related to the shape of the particle distribution, and the parameter b is related to the modal radius of the distribution.

The index of refraction was then varied to reflect various concentrations of sulfuric acid in water. The following refractive index

values, 1.30-0i, 1.41-0i, and 1.52-0i were used.⁵ The b parameter of the size distributions was varied systematically to determine how the wavelength dependence of the total extinction coefficient varies with the modal radius of modified gamma-type particle size distributions:

$$b = \alpha / (g r_c^g) \quad (3)$$

This was facilitated by changing the b parameter for each of the three standard distributions. To determine extinction coefficient wavelength dependence on the width or shape of the size distribution, the g parameter of the modified gamma distribution was varied from the values defined in the three standard distributions.

The results of these studies are summarized in terms of the calculated values of the PTECR (the value of c in eqn. 1) for the various wavelength ratios defined to match common laser and Raman shifted wavelengths currently used in LIDAR experiments. In Figure 1 the value of the PTECR is plotted as a function of the particular distribution used in the Mie scattering calculation for $n = 1.30$.

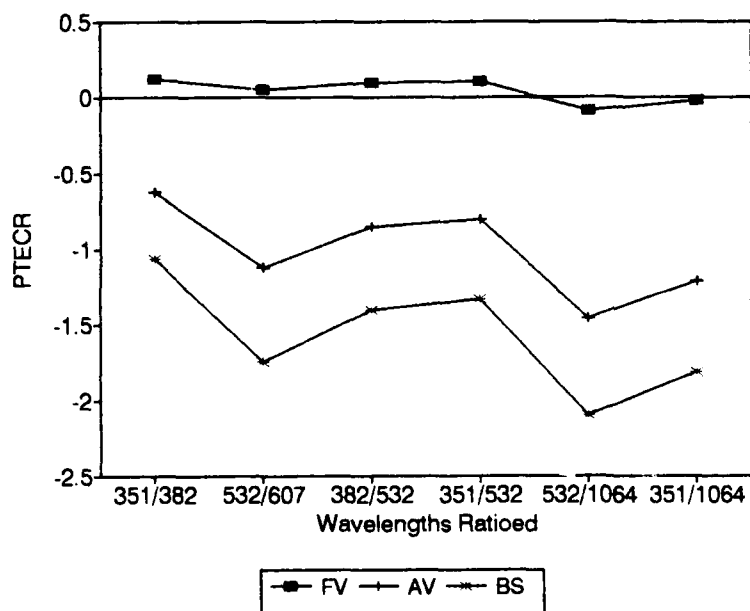


Fig. 1 Plot of the PTECR at index of refraction of 1.30 for the three types of particle distributions studied. Note that the value of the PTECR can range anywhere from +0.2 to -2.0 depending upon the volcanic conditions in the atmosphere.

Note that the value of the PTECR varies from about positive 0.1 to negative 1.6 even for the wavelength ratios which are related to the Rayleigh/Raman wavelengths such as 532nm/607nm. What is responsible for this large change in the value of the PTECR. From the information presented in Table 1 it is apparent that it is directly related to the value of the modal radius, and perhaps the shape parameter g since the difference between the PTECR of the Fresh Volcanic distribution and the Aged Volcanic and Background Stratospheric distributions is the values of the b and/or g parameters. There is no dependence on the value of the particle number since the value of "a" cancels when the ratio is taken.

Figure 2 shows the dependence of the PTECR on the value of b for the

FV distribution at an index of refraction of 1.30. Note that the value of the PTECR changes dramatically from a small positive value to a very relatively large negative value. Indeed the value of the modal radius has a large effect on PTECR.

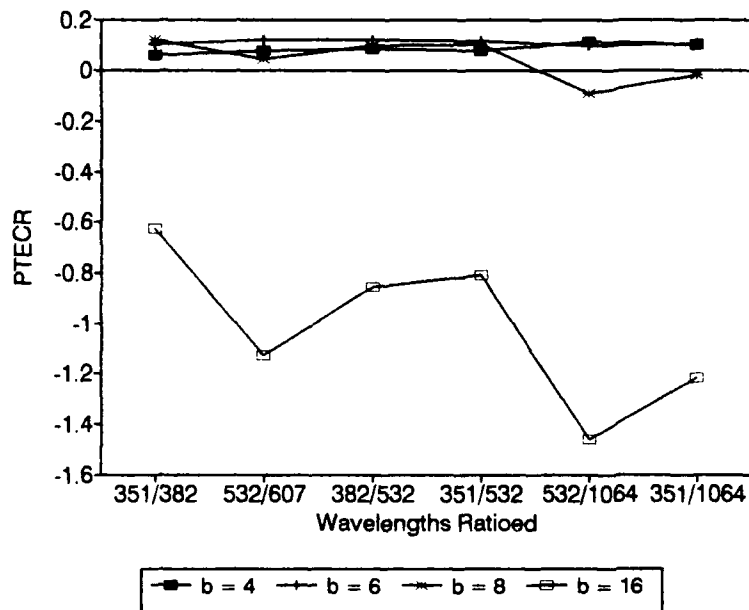


Fig. 2 Plot of the PTECR as a function of the b parameter of the modified gamma distribution for the Fresh Volcanic particle distribution. Note that the value seems to vary little with b at values below $b = 8$, but changes dramatically between $b = 8$ and $b = 16$. This is characteristic at

In figures 3(a-b) the dependence of the PTECR on the shaping parameter and the index of refraction for the FV distribution is apparent. The change in the value of the PTECR with increasing g is minimal for the largest index of refraction, and becomes almost as large as the change in the PTECR with increasing b .

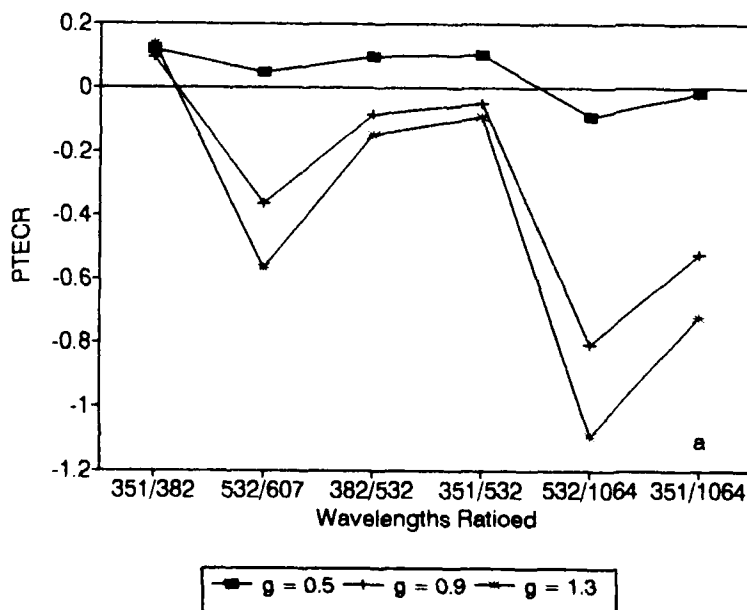


Fig. 3(a-b) Plot of the PTECR as a function of the g parameter for the FV particle distribution at three indices of refraction. Figure 3a corresponds to $n = 1.30$

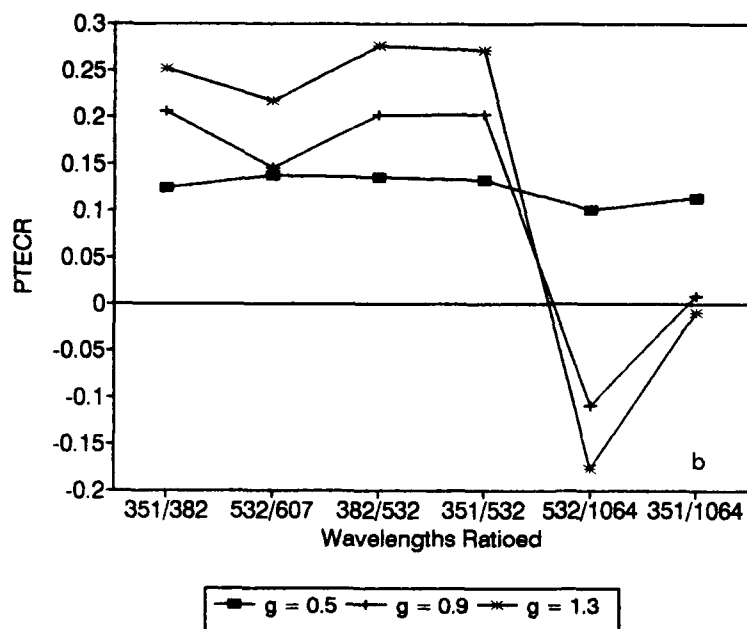


Figure 3b
corresponds to
 $n = 1.52$.

In summary, the examination of the dependence of the total extinction coefficient on wavelength is seen to be a relatively strong function of the value of the modal radius of the particle distribution. In addition, depending on the value of the index of refraction of the medium, the total extinction coefficient can be highly dependent on the value of the shaping parameter in the gamma distribution used in the Mie code to calculate the values of the total scattering coefficient for a given distribution. Thus one expects that the value of the PTECR used to invert the LIDAR data to determine atmospheric concentrations, is going to change significantly under volcanic conditions, and may even switch signs. This work was motivated by the effect on the atmosphere of recent volcanic eruptions such as Mt. Pinatubo in the Philippines.

References

1. A. Ansmann, M. Riebesell, and C. Weitkamp, *Optics Letters*, **15**(3) 746, 1990.
2. J. Heintzenberg, H. Mueller, H. Quenzel, and E. Thomalla, *Applied Optics*, **20**(8) 1308, 1991.
3. J. V. Dave, *Applied Optics*, **9**(8) 1888, 1970.
4. E. P. Shettle and R. W. Fenn, *The Infrared Handbook*, Atmospheric Scattering, W. L. Wolfe and G. J. Zissis (Eds.), Office of Naval Research, Dept. of the Navy.
5. P. B. Russell, T. J. Swissler, M. P. McCormick, W. P. Chu, J. M. Livingston, and T. J. Pepin, *Journal of the Atmospheric Sciences*, **38** 1279, 1981.

Lidar Observations of Mt. Pinatubo Aerosols at Table Mountain (34° N)

David A. Haner, Eric W. Sirko and I. Stuart McDermid

Jet Propulsion Laboratory
California Institute of Technology
Table Mountain Facility
Wrightwood, CA 92397-0367

Introduction

The stratospheric aerosols resulting from the eruption of Mt. Pinatubo have been observed using the JPL-Table Mountain Facility aerosol lidar [McDermid *et al.*, 1991].

There is interest in obtaining lidar derived parameters which describe the microphysical characteristics of the aerosol as well as the bulk distribution of the aerosol in the atmosphere. The lidar backscatter ratio as a function of altitude provides a detailed description of the aerosol distribution in the atmosphere. The comparison of this ratio for two or more wavelengths produces an estimation of the exponent for the wavelength dependence of the volume backscattering coefficient which relates to the size distribution and the composition of the aerosol. In order to summarize the aerosol distribution with altitude, the center of gravity of the backscatter coefficient was calculated for the stratosphere between 12 km (tropopause estimate) and 26 km (aerosol content small and signal above noise). Further, the integrated backscatter coefficient within the same interval was calculated.

Lidar System

The TMF aerosol lidar system is based on a dual-beam Nd:YAG laser using the 1064 nm fundamental and 532 nm second harmonic for the aerosol measurements. The laser is transmitted coaxially with the 40 cm diameter Cassegrainian receiver telescope. Two photomultipliers, one gated, are used to detect the 532 nm return signal and channels and a single gated avalanche photodiode (APD) is used for the 1064 nm detection channel. This arrangement permits measurements from the ground up to approximately 30 km altitude at 532 nm and from 4 km to approximately 26 km at 1064 nm. Transient digitizers (20-MHz, 12-bit) and a PC-computer controlled signal averager are used to monitor the signals.

Observations

The backscatter ratio,

$$R(\lambda, Z) = [\beta_a(\lambda, Z) + \beta_m(\lambda, Z)] / \beta_m(\lambda, Z)$$

was calculated using the received backscatter signal and the molecular volume backscatter coefficient based on the U. S. Standard Atmosphere (1976).

The wavelength power law exponent γ can be found by solving the expression,

$$R(\lambda_2, Z) = 1 + [R(\lambda_1, Z) - 1] \left(\frac{\lambda_2}{\lambda_1} \right)^{4-\gamma}$$

for two wavelengths for the same range. The backscatter ratio can be corrected for the aerosol extinction using an iterative correction or by solving the Bernoulli equation for the backscatter coefficient.

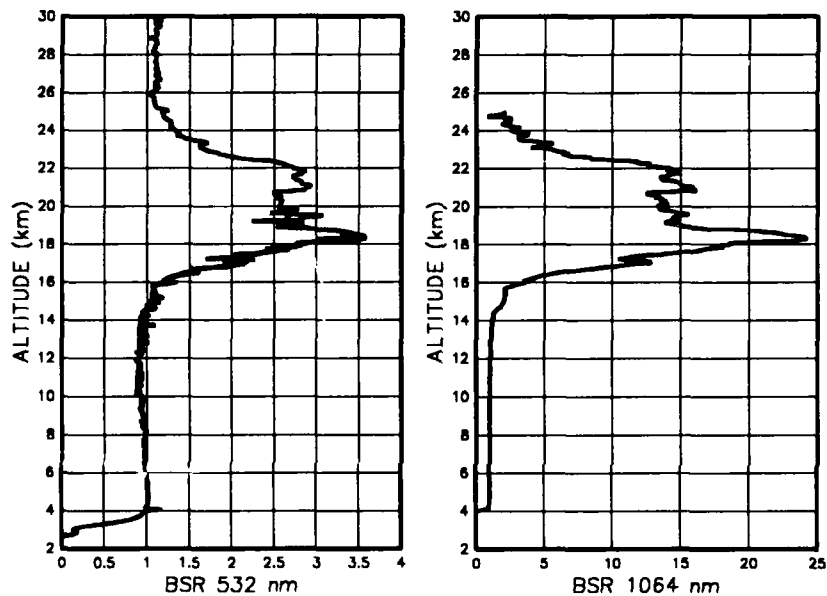


Figure 1. Aerosol backscatter ratio profiles for September 17, 1992.

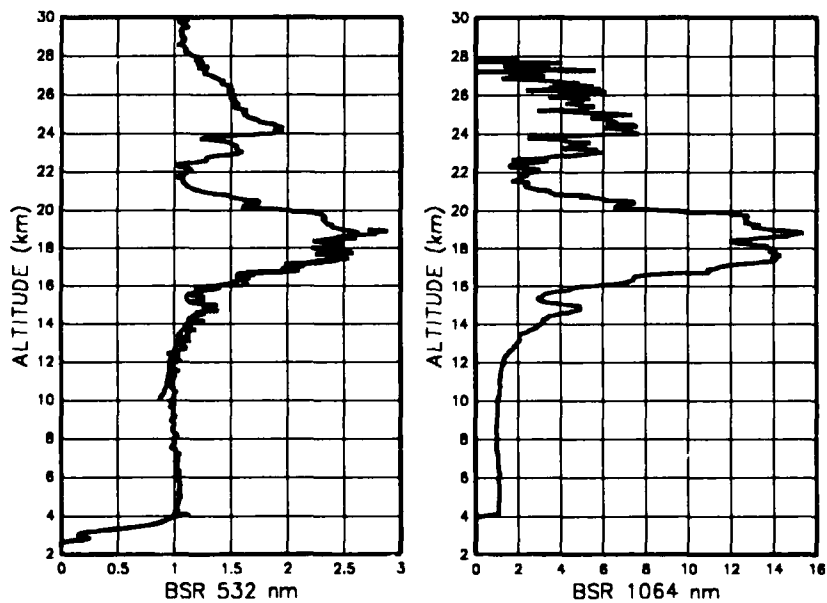


Figure 2. Aerosol backscatter ratio profile for October 14, 1992.

Figures 1 and 2 show two examples of the aerosol backscatter ratio for each of the wavelengths and which demonstrate the high degree of variability in the aerosol profile.

Date	532 nm		1064 nm		γ
	IBSC ($\times 1000$)	CG (km)	IBSC ($\times 10000$)	CG (km)	
6-Aug-92	2.54	18.6	4.55	18.7	1.7
20-Aug-92	2.02	18.9	4.47	18.9	1.9
25-Aug-92	2.97	17.9	6.74	18.2	1.9
26-Aug-92	5.02	17.6	7.21	18.2	2.5
28-Aug-92	1.85	18.7	4.34	18.8	1.9
1-Sep-92	4.75	17.9	6.83	18.6	1.4
5-Sep-92	1.26	19.2	5.93	18.8	1.3
9-Sep-92	1.64	18.4	7.77	17.7	1.1
11-Sep-92	1.57	18.9	6.53	18.8	1.3
15-Sep-92	1.32	19.5	6.36	19.0	1.1
16-Sep-92	1.60	19.4	6.97	19.2	1.0
17-Sep-92	1.40	19.3	7.39	19.1	0.9
18-Sep-92	1.79	19.3	4.65	18.3	1.7
22-Sep-92	2.32	18.5	5.77	18.7	1.6
23-Sep-92	1.47	18.9	6.02	18.8	1.2
25-Sep-92	1.11	19.4	6.90	19.0	0.8
26-Sep-92	2.24	18.6	5.29	19.1	1.5
27-Sep-92	2.39	18.6	6.62	18.9	1.6
28-Sep-92	1.16	19.2	1.91	19.1	
30-Sep-92	1.59	18.9	6.26	18.9	1.1
1-Oct-92	1.85	18.5	5.23	18.4	1.3
2-Oct-92	1.41	18.8	5.79	18.4	1.2
3-Oct-92	1.06	19.3			
6-Oct-92	1.23	18.3	6.23	18.2	0.9
7-Oct-92	1.09	18.5	5.53	18.3	1.0
9-Oct-92	1.80	17.6	7.39	17.6	1.2
10-Oct-92	1.44	18.2	4.67	18.2	1.3
13-Oct-92	1.18	18.6	6.02	18.3	0.9
14-Oct-92	1.11	18.4	6.55	18.0	0.9
16-Oct-92	(3.67)	(13.53)	(25.50)	(13.57)	(0.50)
Average	1.86	18.7	5.93	18.6	1.3

Table 1. IBSC = Integrated backscatter coefficient; CG = the 1st moment of the backscatter coefficient over the altitude range from 12 to 26 km; γ for the peak layer near 18 km.

Table 1 summarizes the range of parameters selected to characterize the aerosol distribution as well as the average values. The γ value in the table was calculated at the peak value of the scattering ratio in order to reduce the uncertainty due to subtraction. The scattering ratios presented are not corrected for extinction.

Conclusions

Our results for the power law exponent for the stratospheric aerosol are in general agreement with other observations at other times and locations [e.g. Kent *et al.*, 1992; Post *et al.*, 1992; Steinbrecht *et al.*, 1992; Sasano *et al.*, 1992]. The integrated backscatter coefficient results for 532 nm also compare well though there are some differences in the range of integration (altitude) that were selected.

Acknowledgments. The work described in this paper was carried out at the Jet Propulsion Laboratory, California Institute of Technology, under a contract with the National Aeronautics and Space Administration. We are grateful for the assistance of Dan Walsh and Marty Schmoe in obtaining the results presented here.

References:

- Kent, G. S., G. M. Hansen and K. M. Skeens, "Multi-wavelength Measurements of the Stratospheric Aerosol Layer Made at Hampton, Virginia (37° N, 76° W)," *Abstract Volume-16th International Laser Radar Conference*, Cambridge, MA, 71-74 (1992).
- McDermid, I. S., T. D. Walsh, M. Schmoe, R. Hoff and D. A. Haner, "Lidar Observations of Pinatubo Aerosols at Table Mountain (34° N) and their Effect on Ozone DIAL Measurements," *Optical Society of America Topical Meeting on Optical Remote Sensing of the Atmosphere*, Williamsburg, VA, 1991.
- Post, M. J., C. J. Grund, A. O. Langford and M. H. Proffitt, "Observations of Pinatubo Ejecta Over Boulder, Colorado by Lidars of Three Different Wavelengths," *Geophys. Res. Lett.*, **19**, 195-198 (1992).
- Sasano, Y., I. Matsui and S. Hayashida, "Three Wavelength Lidar Measurements of Pinatubo Aerosol and its Optical Properties," *Abstract Volume-16th International Laser Radar Conference*, Cambridge, MA, 75-78 (1992).
- Steinbrecht, W. and A. I. Carswell, "Correction for Interference of Mt. Pinatubo Aerosol on DIAL Measurements of Stratospheric Ozone," *Abstract Volume-16th International Laser Radar Conference*, Cambridge, MA, 20-24 (1992).

Friday, March 12, 1993

New Developments 1

FA 8:00am–9:50am
Salon F

Dennis K. Killinger, *Presider*
University of South Florida

Development of Laser Altimeter Sensors for Earth and Planetary Observations

Jack L. Bufton, David J. Harding, J. Bryan Blair, and James B. Garvin
 Laboratory for Terrestrial Physics
 Goddard Space Flight Center, Greenbelt, MD 20771
 301-286-8591

Laser altimeter sensors are a class of devices, developed for airborne and space-based applications, with a primary role of measuring the topography of the Earth and other planetary surfaces. Laser altimeters are mounted for nadir observation on aircraft or spacecraft platforms and provide a high-resolution, high-accuracy measurement of the elevation and horizontal variability of planetary surfaces. The basis of the altimeter measurement is the timing of the round-trip propagation of short-duration pulses of laser radiation between the platform and the surface. Vertical (i.e. surface elevation) resolution of the altimetry measurement is determined primarily by laser pulsewidth, surface-induced spreading in time of the reflected pulse, and the timing precision of the altimeter electronics. With conventional (~ 10 nsec wide) gain-switched pulses from solid-state lasers and sub-nsec resolution electronics, sub-meter vertical range resolution is possible from aircraft altitudes (0.5 km - 20 km) to orbital altitudes of several hundred kilometers. Laser divergence angle and altimeter platform height above the surface determine the laser footprint size at the surface, while laser pulse repetition-rate, laser transmitter beam configuration, and altimeter platform velocity determine the spacing between successive laser pulses. Typical sensor footprint diameters for an aircraft altimeter application are 1-10 m and are ~ 100 m for a spacecraft altimeter. Ideally, the pulse-rate is adjusted to make a contiguous profile of topography so that horizontal resolution is equal to the sensor footprint size. Successful operation of the laser altimeter sensor requires additional information on the laser altimeter platform pointing attitude and position¹. Recent major advances in laser gyros, star cameras, and kinematic positioning with the Global Positioning System permit recovery of platform effects to a sufficient level (e.g. 5-500 μ rad for pointing angle and 10 cm - 1 m for position) to enable sub-meter laser altimetry for the operating altitudes and velocities of both aircraft and spacecraft platforms.

Laser altimeter sensors are in actuality a specialized class of lidar sensors that share many of the same technology requirements and implementation issues involved with active laser sensors that look down from an aircraft or spacecraft at the Earth's atmosphere. This commonality is evident in the design of the Geoscience Laser Altimeter System (GLAS) planned for space-based observations of the Earth as part of the NASA Earth Observing System. Primary data from GLAS are the start (transmitted pulse) detector output and the pulse waveform of the receive detector that is located at the focus of the collecting telescope. The processing of sensor data involves: (1) timing electronics to measure time-interval between laser pulse output and the distorted pulse of the surface backscatter; (2) a high-resolution (nsec-sampling) digitizer to perform a range-resolved lidar function on the surface backscatter; and (3) a more conventional lidar set of electronics composed of a low-resolution (μ sec-sampling) digitizer that provides range-resolved backscatter sampling for cloud measurements and a photon-counter that provides aerosol layer detection at the signal shot-noise limit.

The high-resolution digitizer is the piece of technology that bridges between the altimeter functions of distance measurement and the lidar functions of range-resolved amplitude measurement². Its output is used to correct the laser altimeter timing data for time-walk and pulse distortion effects and is used to infer characteristics of the surface under observation. In the former application the pulse peak and pulse width of the distorted surface return are often enough information to make the timing corrections. The best illustration of the later application is the sensing of vegetation height and structure for the Earth's surface. Fig. 1 is a nadir profile of tree heights superimposed on the ground profile from analysis of pulse waveform data that were acquired in recent aircraft observations of forested areas in the western U.S. Individual pulse waveforms in these data nearly all exhibit dual peaks, the first from the vegetation canopy and the second from the ground surface. Fig. 1 was constructed by simply plotting the time-of-occurrence of the two peaks in successive waveforms along the aircraft nadir track. Fig. 2 illustrates two sample waveforms from airborne laser altimeter data records of tree height and vegetation canopy structure. Similar analysis can be applied to

determine the sub-pixel (i.e. within one sensor footprint) vertical height distribution of bare ground returns. Here the pulse distortion can be used to infer surface slope and surface roughness at the meter-level. An analytical expression has been developed by Gardner³ to express pulse spreading (mean square pulse width) in terms of the laser altimeter system parameters (e.g. timing and digitizer resolution), beam curvature, nadir angle of observation, surface slope, surface roughness, and laser receiver operating signal-to-noise ratio. This expression forms the basis for design and analysis of the technology and techniques of these hybrid lidar sensors.

Multiple laser transmitters in a single altimeter instrument can provide across-track as well as along-track coverage that can be used to construct a range image (i.e. topographic map) of the Earth or planetary surface. This represents a further refinement of technology applicable to the altimeter class of lidar sensors. We are now studying a pushbroom laser altimeter instrument measurement concept that utilizes a number of modular laser pulse transmitters, but only a single receiver⁴. This Multi-Beam Laser Altimeter (MBLA) contains 30 modular laser sources arranged in a linear, across-track array. Simultaneous or near simultaneous measurements of range to the surface are possible by independent triggering of the multiple laser pulse transmitters and reception by a single telescope that is staring at nadir and is equipped with a multi-element linear detector array in its focal plane. The MBLA is designed to produce a strip-image topographic map of the Earth's surface near the nadir track of the Global Topography Mission Earth Probe. Possible modifications in the design include variation of footprint size and/or footprint spacing both along-track and cross-track in order to produce the desired coverage or sampling density within the sensor swath width. The addition of waveform digitization to one or more of these sensor channels can augment the timing data in order to provide the vegetation and surface roughness measurement capability. The pulse width (or rms pulse spreading) data taken together with along-track and across-track slope information provided by adjacent range pixels, enables calculation of the surface slope and roughness.

The integrated area of the received pulse is proportional to pulse energy and is a measure of surface reflectivity at the monochromatic 1 μm laser wavelength of the laser altimeter. Effective use of this reflectivity data requires normalization by laser transmitter energy and consideration for atmospheric transmission. Reflectivity data acquired with the pushbroom scan pattern of the MBLA can provide an imaging capability that supplements the ranging functions. Since this image is acquired with an active sensor that transmits and receives only near nadir (i.e. backscatter geometry), the surface illumination angle is fixed within 1° of zenith and the resultant image is free of bidirectional reflectance effects that exist in passive images with variable solar illumination geometries.

The full capability for along-track and across-track lidar measurement of the Earth and planetary surfaces has not yet been realized in a single instrument in either airborne or space-based applications. A good example of current progress toward this capability in a spacecraft instrument is contained in the Mars Observer Laser Altimeter (MOLA) which was developed and successfully launched in the 1992 Mars Observer Mission. The MOLA laser transmitter generates a pulse of ~ 8 nsec duration at a wavelength of 1064 nm. In operation on the Mars Observer spacecraft, MOLA will transmit this pulse toward the Martian surface from a 400 km polar mapping orbit and utilize a 0.5 m diameter reflector telescope to collect laser pulse backscatter from the surface for measurement of pulse time-of-flight and received pulse energy. The MOLA Instrument will produce a sensor footprint of ~ 120 m diameter on the Martian surface and has a range precision varying between 1 m and 10 m. Each pulse is utilized without averaging for a continuous measure of the range to the surface at a rate of 10 pps along the nadir track of the spacecraft. This yields a horizontal along-track sampling resolution of ~ 330 m. Laser altimetry data derived from MOLA over the two-year mission lifetime of Mars Observer will be utilized to construct: (1) a gridded topographic map of the Martian surface with grid spacings ranging from 0.2° to 1.0° at the equator; (2) high-resolution topographic profiles along the spacecraft nadir track for studies of geology, geophysics, and atmospheric circulation; and (3) laser backscatter profiles related to surface reflectivity and atmospheric transmission at the 1064 nm wavelength. Accuracy in determination of Martian surface elevation is a function of MOLA instrument performance, Mars Observer orbit determination from radio beacon tracking, and MOLA pointing knowledge. The overall measurement goal is 30 m surface elevation accuracy for the gridded topography.

The MOLA instrument payload consists of an optical assembly, electronics package, and support structure. The dominant feature of the instrument is the relatively large aperture (0.5 m diam.) telescope that is used as the altimetry receiver "photon bucket". A cross-sectional view of the MOLA optical assembly is illustrated in Fig. 3. A circular shroud surrounds the telescope in order to provide a solar shield and radiator surface. The laser transmitter is located beneath the telescope and wraps around the telescope central support column that contains the optical detector. The laser transmitter output exits the instrument through the beam guide tube at the periphery of the solar shield. The low mass, optical alignment stability, and the superior thermal diffusivity (heat transfer) of beryllium drove the MOLA optical design toward all-beryllium, athermal construction. In addition to the existing beryllium telescope, beryllium is used for the interface plate (optical bench) and the laser housing. Optical assembly mass is only 10 kg, due in large part to the ultra-lightweight (3 kg) receiver telescope. Details of the MOLA instrument and electronics are provided by Zuber et al.⁵ The diode-pumped Nd:YAG laser transmitter developed at McDonnell Douglas Electronic Systems Corp. was the major enabling technology for the MOLA Instrument. Further details of this laser and the MOLA optical assembly are reported by Ramos-Izquierdo, Bufton and Hayes⁶.

References:

1. Bufton, J. L., "Laser Altimetry Measurements from Aircraft and Spacecraft", *Proceedings of the IEEE*, 77(3): 463-477, March 1989.
2. Bufton, J.L., Garvin, J.B., Cavanaugh, J.F., Ramos-Izquierdo, L., Clem, T.D., and Krabill, W.B., "Airborne Lidar for Profiling of Surface Topography", *Opt. Engr.*, 30(1):72-78, January 1991.
3. Gardner, C.S., "Generalized Target Signature Analysis for Laser Altimeters", *IEEE Trans. on Geo. and Rem. Sens.*, 30, 1992.
4. Bufton, J.L., D.J. Harding, L. Ramos-Izquierdo, "Multi-Beam Laser Altimeter", *Proc. of the Eighth Int'l. Workshop. on Laser Ranging Instrumentation*, Annapolis, MD, May 18-22, 1992.
5. Zuber, M.T., D.E. Smith, S.C. Solomon, D.O. Muhleman, J.W. Head, J.B. Garvin, J.B. Abshire, and J.L. Bufton, "The Mars Observer Laser Altimeter Investigation", *J. of Geo. Res.*, 97(E5):7781-7797, May 25, 1992.
6. Ramos-Izquierdo, L., J.L. Bufton, and P.A. Hayes, "Optical System Design and Integration of the Mars Observer Laser Altimeter", submitted to *Applied Optics*, September 1992.

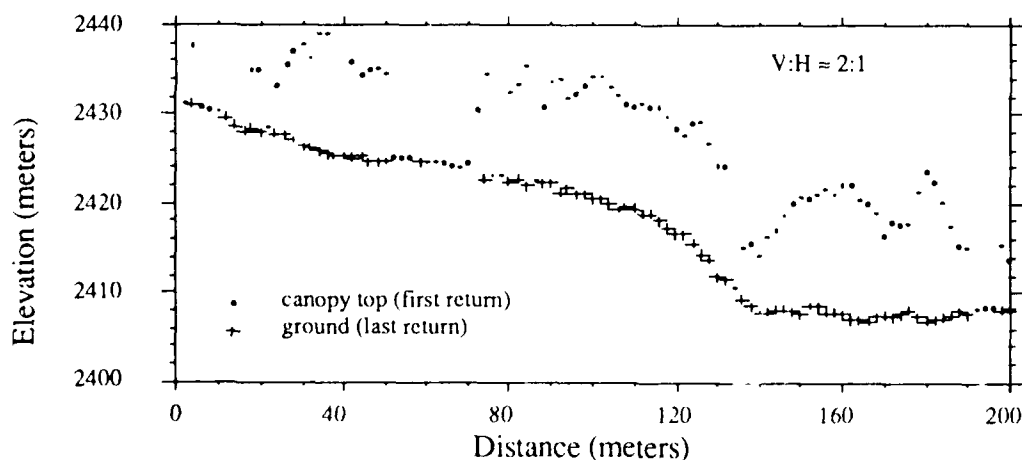


Fig. 1 Airborne Laser Altimeter Data: Mt. Humphreys, AZ 11:55 a.m. 9/12/92

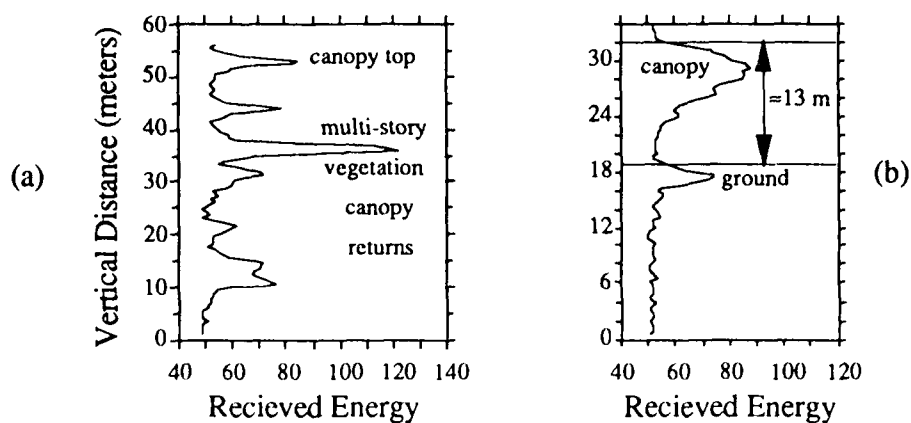


Fig. 2 Airborne Laser Altimeter Pulse Waveforms of Big Basin Redwoods State Park, CA (a) and Mt. Humphreys, AZ (b) September 1992

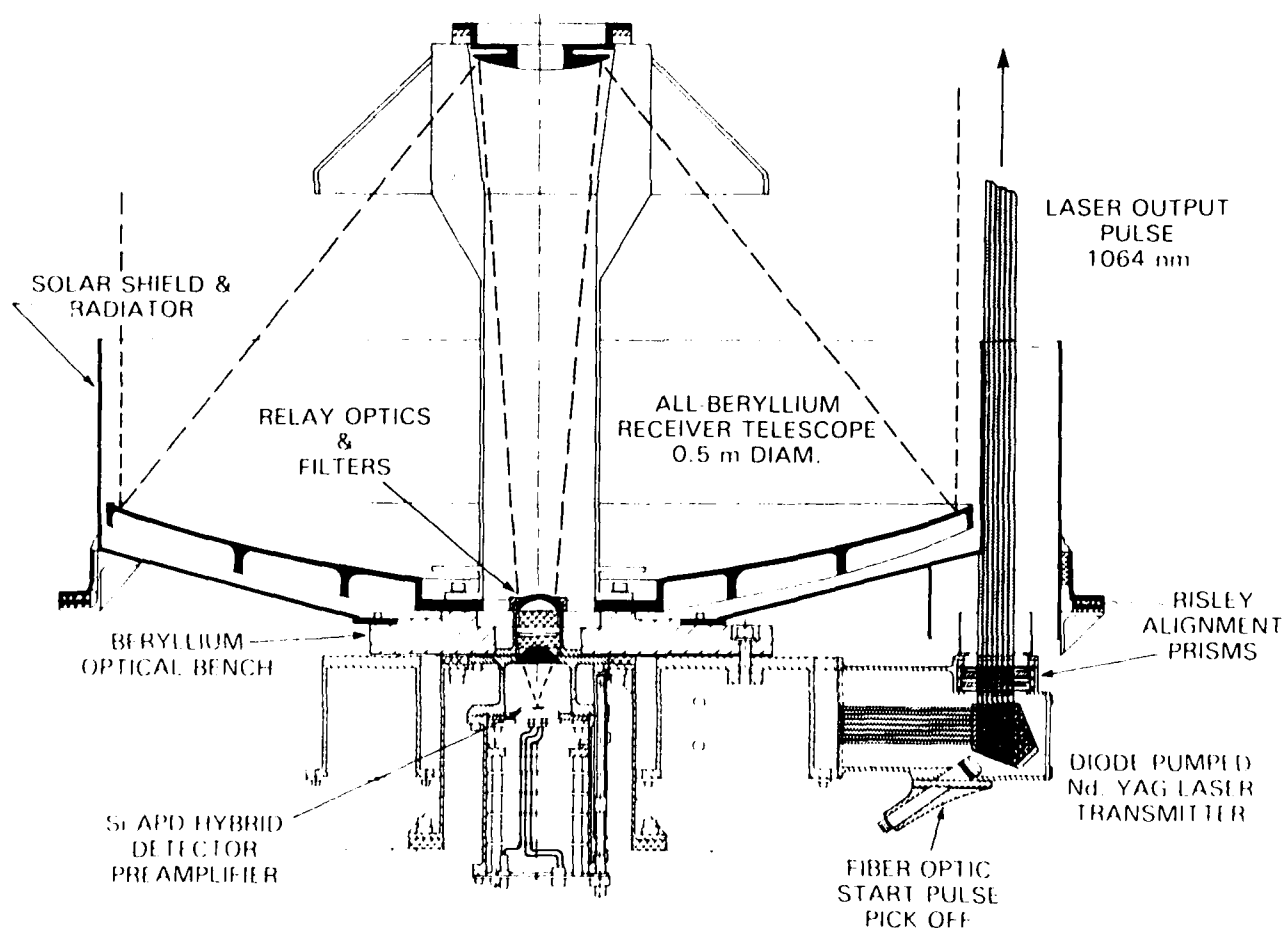


Fig. 3 Optical Assembly of the Mars Observer Laser Altimeter Instrument

PERFORMANCE CALCULATIONS AND TEST OF SCIAMACHY DETECTOR MODULES

A.P.H. Goede¹, R.W.M. Hoogeveen¹, R.J. van der A², and J. de Vries²

¹ *SRON-Utrecht, Sorbonnelaan 2, 3584 CA UTRECHT, the Netherlands, tel. +31 30 535600, fax +31 30 540860*

² *SRON-Leiden, P.O. Box 9504, 2300 RA LEIDEN, the Netherlands, tel. +31 71 275817, fax +31 71 275819*

SUMMARY

1. Scientific Objectives

SCIAMACHY (SCanning Imaging Absorption spectroMeter for Atmospheric CartographY) has been selected by ESA to fly on the first ENVISAT mission (1998). The Instrument Requirements originate from the Max Planck Institut für Chemie in Mainz under principal investigator J.P. Burrows /1/. The instrument comprises an imaging spectrometer operating in the wavelength range of 240-2385 nm, at a resolution of ~0.2 nm. Measurements will be performed in the nadir mode, in the limb mode and in the sun/moon occultation mode.

The main scientific objective of SCIAMACHY is to measure atmospheric trace gas abundances and profiles on a global scale in the stratosphere as well as in the troposphere with emphases on the ozone chemistry and on the greenhouse effect.

The following trace gases are targetted:

- In the stratosphere: O₃, O₂, O₂(¹Δ_g), NO, NO₂, NO₃, N₂O, CO, CO₂, CH₄, H₂O and BrO. Under ozone hole conditions measurements of ClO and OCIO are also possible.
- In the troposphere: O₃, O₂, O₄, NO₂, N₂O, CO, CO₂, CH₄ and H₂O. Under polluted conditions measurements of HCHO, SO₂ and NO₃ are possible.

Two retrieval algorithms will be employed: Differential Optical Absorption Spectroscopy (DOAS) /2/, and backscattered ultraviolet measurement (BUV) /3/. The DOAS technique has the advantage that it does not rely on absolute radiometric calibration as required for the BUV technique.

2. Optical Unit

The optical unit comprises a double spectrometer which disperses the light into eight individual channels each equipped with a detector module (DM) of generic design, see Table 1. The optical unit consists of two scan mirrors for nadir ($\pm 22^\circ$) and limb (2 km resolution) scan. A telescope (off-axis parabola, dia 31 mm, FOV 0.023°x2.3°) collects the incoming radiation, which is subsequently pre-dispersed by a prism and directed to the individual channels for high-resolution dispersion by grating/echelles. This method provides for the required high resolution over the wide spectral range. In addition the optical unit contains a polarisation measurement device in six spectral bands. Polarisation measurement is necessary for radiometric calibration of incoming radiation which is polarised and for scientific studies based on polarisation properties (clouds, aerosols). For further details on the optical design see /4/.

3. Noise Analysis

The performance of the SCIAMACHY instrument has been assessed by calculating the signal to noise ratio using a simple instrument model:

$$S = SR * E * T * \Delta\lambda * \eta * t_{int}$$

here S is the signal (in electrons), SR the spectral radiance (in ph/(s.cm².sr.nm), E the etendue (in cm².sr), T the transmission of optics, $\Delta\lambda$ the wavelength interval/pixel (in nm), and t_{int} the integration time (1.5 or 30 s).

As noise sources were taken: the shot noise of signal, noise of the dark current (shot noise and T fluctuations), Johnson noise of the detector, reset (kTC) noise of detector (not suppressed by Correlated Double Sampling (CDS)), preamp noise, ADC noise, and thermal background radiation (shot noise and T fluctuations). These noise sources have different contributions to the two kinds of detectors used in the SCIAMACHY instrument and are treated separately.

Table 1. SCIAMACHY Baseline Channel Definition

Ch	λ [nm]	used pixels	$\Delta\lambda$ [nm]	Material	T_{det} [K]
1	240- 295	512	0.22	Si	200
2	290- 405	1024	0.22	Si	200
3	400- 605	1024	0.40	Si	235
4	590- 810	1024	0.44	Si	235
5	790-1040	1024	0.49	Si	235
6	1000-1700	1024	1.37	In _{0.53} Ga _{0.47} As	235
7	1940-2040	1024	0.20	In _{0.71} Ga _{0.29} As	150
8	2265-2385	1024	0.22	In _{0.82} Ga _{0.18} As	150

3.1 Si detectors

These detectors are used for the UV and visible part of the spectrum. The noise is dominated by the reset (kTC) noise of the detector which can not be suppressed by CDS as is done with the kTC noise of the videoline. A smaller contribution originates from the preamplifier. Finally, there is a contribution from the 16 bits AD Converter which digitises the signal for further digital processing. The ADC noise is of the order of one LSB (least significant bit) and can therefore be minimised by increasing the gain of the preamp. Since this is at the expense of the integration capacity of the detector it is only employed in the UV channel 1 where signal levels are low.

3.2 InGaAs detectors

Above 1000 nm the sensitivity of Si drops dramatically. Therefore the smaller bandgap material InGaAs was selected for the IR channels. Due to the relatively large dark current these detectors will be operated at nearly zero bias, with each pixel having its own charge integrator and amplifier. The noise characteristics are therefore different. Here noise is dominated by kTC noise which originates from the reset FET and from the detector itself. The preamp and the ADC also contribute, albeit less than the Si detectors since the integration capacity is smaller (1.6 pC versus 10 pC). Finally, in the IR channels there is a noise contribution from the self-generated thermal photons. The number of thermal photons can exceed the signal since the field of view (fov) of the detector is large (60°*70°) in comparison with the fov of the instrument (1.3°*0.023°). Thermal radiation has been suppressed by lowering the temperature of the instrument from 20°C to 0°C and by applying a optical (IR) bandpass filter with a transmission window of 20 nm in front of the detector. The transmission window is graded since the wavelength range of a detector array is larger (200 nm).

The resulting noise figures for both the Si and the InGaAs detectors have been summarized in Table 2. As will be shown in most cases the shot noise of the signal is the dominating noise source.

Table 2. Noise figures for SCIAMACHY's channels 1-8

Ch.	kTC	ADC	preamp	th.backg.	I_{dark}
1	660	76	470		
2	660	760	470		
3	710	760	470		
4	710	760	470		
5	710	760	470		
6	500	100	180		95
7	400	100	180	160	80
8	400	100	180	800	260

4. Detector test results

A breadboard set-up was built to verify the performance of the channel 1-5 detectors design. The set-up has an adjustable detector temperature (190-300 K). An extensive series of tests was performed and the results were interpreted using numerical modelling. Figure 1 shows the measured noise as a function of temperature for the UV (Ch 1) and VIS (Ch 2-5) wavelength bands. In the UV band the lower radiance level of the solar spectrum requires increased gain of the preamplifier. This reduces the ADC noise contribution and therefore the measured noise values. The higher values in the figure represent the VIS channels. The drawn lines in the figure are the modelled noise values, based on design parameters. The noise sources taken into account are the kTC noise, the preamplifier noise sources (voltage, current and 1/f) and the ADC contributions (quantisation, differential non-linearity and a white noise). These noise sources are taken into account using the relevant transfer functions.

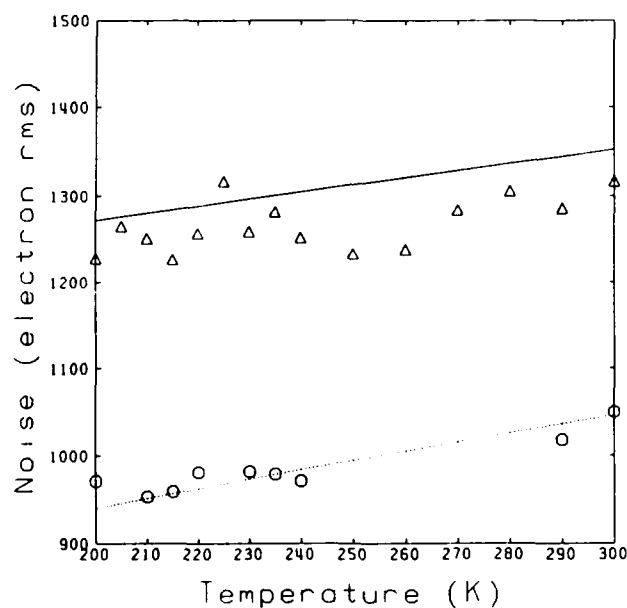


Fig. 1. Measured and modelled noise figures as a function of temperature. The circles denote the UV channel 1, the triangles the visible channels (2-5), whereas the lines result from the model.

Pixel cross-talk was measured using the virtual channel concept of our design, which enables the use of different exposure times within one detector array. Using this method, pixel cross-talk can be measured. Figure 2 shows the results as a function of the charge accumulated in the pixels. Three mechanisms were considered to explain the results; diffusion from the dead layer into the pixels, diffusion from the channels stops and simple overload of the pixels. Because no dependence on temperature was found, it was concluded that the latter mechanism is dominant. The drawn line in the figure is the modelled pixel cross-talk. Apart from these features, results were obtained for dark current, linearity and saturation levels, annealing of the detectors and a line-reset mode. The latter is a special feature in the design which allows exposure times down to 20 μ s.

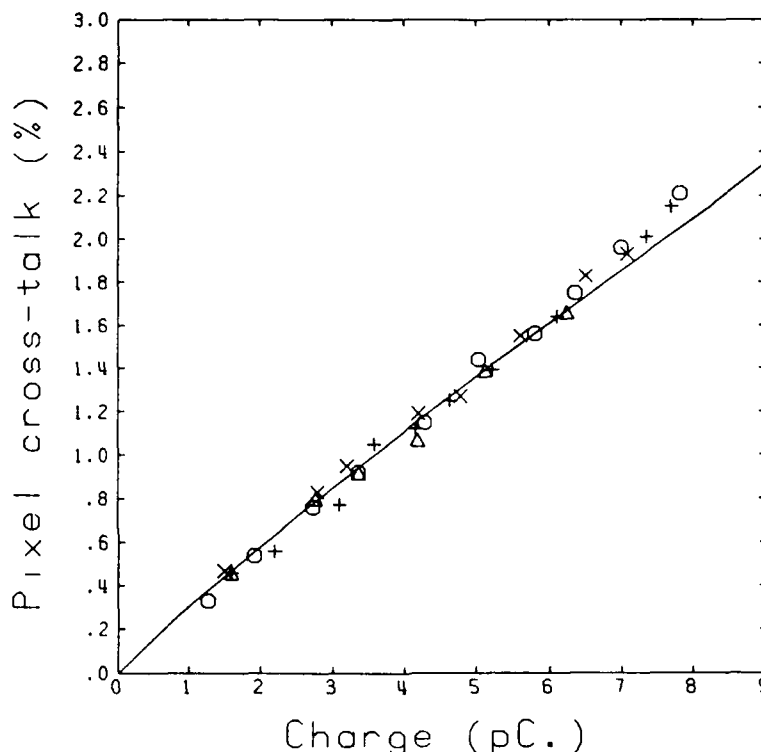


Fig. 2. Measured pixel crosstalk figures as a function of pixel charge for 4 temperatures ($x = 200$ K; $\Delta = 235$ K; $O = 235$ K; $+ = 300$ K). The line results from the model.

5. Conclusion

Measured noise values are close to the theoretical minimum and agree with our theoretical modelling. Further breadboard measurements are in hand to demonstrate the NIR channels 6-8 performance.

References

1. J.P. Burrows et al., SCIAMACHY Phase A study - Scient. Req. Spec., April 1990.
2. U. Platt and D. Perner, J. Geophys. Res. **85** (1980) 7453.
3. S.F. Singer and P.C. Wentworth, J. Geophys. Res. **62** (1957) 299.
4. C. Smorenburg and H. Visser, Proc. of the Int. Symp. on Opt. Syst. Design, Berlin, 1992.
5. A.P.H. Goede, P. de Groene, R.W.M. Hoogeveen, J. de Vries, R.J. van der A, C. Smorenburg, H. Visser - World Space Congress - 29 COSPAR - p.A.2-S.7.34.X -Washington (1992).

Laser Diode Characterization for Optical Remote Sensing Applications

Thomas H. Chyba¹, L.-G. Wang², G. Sachse³, L. Mayo⁴, and Alene W. Heuser⁵

¹National Research Council Research Assoc., M/S 401A, NASA LaRC, Hampton VA 23681 (804)864-7506

²College of William and Mary, Williamsburg VA 23185 (804) 864-1565

³Flight Electronics Division, M/S 468, NASA LaRC, Hampton VA, 23681 (804) 864-1566

⁴Science Applications International Corp., M/S 474, NASA LaRC, Hampton VA 23681 (804) 864-1608

⁵Atmospheric Sciences Division, M/S 401A, NASA LaRC, Hampton VA, 23681, (804) 864-5370

INTRODUCTION

Laser diodes are being utilized with increasing frequency in optical remote sensing applications. Their attractive features include small size, low cost, low power consumption, good output power, high modulation speed, good reliability, and good wavelength tunability. However, their optical properties vary significantly even during the same manufacturing run. Therefore, when the application places stringent requirements on their optical properties, diodes need to be individually characterized and evaluated. This paper discusses our present efforts to characterize laser diodes for use in a Differential Absorption Lidar (DIAL) instrument which imposes very tight requirements on diode behavior.

REQUIREMENTS

NASA's Laser Atmospheric Sensing Experiment (LASE) will measure atmospheric water vapor (H₂O) with an airborne DIAL instrument.¹ A diode laser serves as the injection-seed source for its Ti:Sapphire laser transmitter. For each H₂O absorption line chosen, a computer will tune the laser diode to that line, lock on the line, and then switch the diode wavelength rapidly between on resonance (λ_{on}) and off-resonance (λ_{off}). Requirements imposed upon the diode laser seed source are summarized in Table 1.

PROPERTY	REQUIREMENT
Optical Power	> 50mW, CW
Wavelength Tunability	813-818 nm
Linewidth	≤ 0.5 pm (225 MHz)
Beam Steering Tolerance	$\leq \pm 80$ μ radians
In-flight H ₂ O Line Selection	Autonomous Search/Lock on 2 Lines
λ_{on} to λ_{off} Switching Time	≤ 400 μ sec
Accuracy of λ_{on} , λ_{off}	≤ 0.35 pm, ≤ 2 pm
Difference Between λ_{on} and λ_{off}	20 to 70 pm

Table 1. Requirements for the laser diode seed source.

LASER DIODE CHARACTERIZATION

An extensive characterization of each laser diode is needed to verify that it meets these specifications. Before the characterization process can begin, however, sources of optical feedback on the laser diode must be eliminated or reduced. To accomplish this, we have found it necessary to remove the window from the laser

diode package, carefully select antireflection-coated collimating lenses, and provide the laser diodes with ~ 90 dB of optical isolation.

The first test is to measure the optical power as a function of temperature T and injection current I in order to define an operating region with sufficient optical power for injection seeding. The second test is to measure the side-mode suppression of the laser in the operating region. In order to increase the side-mode rejection beyond the nominal 25 dB intrinsic to our Spectra-Diode laser diodes, a Fabry-Perot filter is incorporated into the flight instrument.

The remainder of the characterization procedure for each diode is to: (1) determine the mode spacing and the λ tunability with T and I , (2) determine the coefficients in the Taylor Expansion for the mode surfaces and number the modes, (3) map the mode surfaces, including exit and entry information, (4) determine the locations of the H_2O lines on each mode surface, (5) choose which locations have enough power for seeding and are sufficiently far from mode edges to allow reliable switching between λ_{on} and λ_{off} , (6) find reliable paths from below the lasing threshold to each H_2O line, and (7) update these paths if the laser diode characteristics change with age. The focus of this paper is this 7 step process.

Typical dependence of λ upon T and I for a single-mode laser diode is shown in Figure 1. At a given T , I is increased from zero until cavity mode N has sufficient gain to lase. If T or I is varied further, mode N will continue to lase until its losses become so great that mode M is preferred and the laser mode-hops to mode M . In the figure, this mode hop corresponds to the operating point of the laser crossing the edge of mode surface N and jumping up to reside on surface M . Thus, the exit point of a mode is a point along its edge, but an entry point for a mode is typically near its center. Neighboring modes are separated by the cavity mode spacing. For a given mode, λ varies with both T and I so that the mode surfaces are tipped relative to the T - I plane. Any plane parallel to the T - I plane is a plane of constant λ and its intersection with a mode surface forms a line of constant wavelength (an iso- λ line). Since the mode surfaces are limited in extent, an iso- λ line may intersect many modes. Hence, once the mode surfaces and the water vapor iso- λ lines on them are mapped, we can choose T and I to tune to a selected H_2O absorption line with optimum power and distance from mode edges. Figure 1 also demonstrates that the attempt to retrace a path in T , I space can lead to hysteresis if a mode edge is crossed.

The laser diode characterization apparatus used to map the laser modes is shown in Figure 2. A computer is connected to a Burleigh wavemeter and an ILX Lightwave controller via a GPIB bus. In-house software has been written to control the laser diode temperature and current and to record T , I , λ , and the corresponding mode number. The software allows the user to specify arbitrary paths for the diode in T , I space which can be autonomously executed at a later time in batch mode. In this manner, simple T or I scans or more complicated mode mapping is performed.

An initial series of scans of I and T is performed to determine the λ -tuning characteristics of the laser diode. These data are analyzed to determine the mode spacing $\Delta\lambda$ and the constants a_i in the expression

$$\lambda(T, I) = N\Delta\lambda + a_0 + a_1T + a_2I + a_3T^2 + a_4I^2 + a_5IT.$$

This expression is used to compute the mode number N corresponding to each measured λ . The constant a_0 is fixed by tuning the laser to a chosen T_0 and I_0 , measuring λ , and arbitrarily assigning the mode number N_0 to that lasing mode.

To map all accessible modes, the computer executes a series of finely-stepped I and T scans in a zig-zag pattern throughout the allowed I, T space. For each mode, the computer records its entry points, exit points, and the locations of all selected H_2O lines found on it. Afterward, a second program analyzes these data and plots the mode surfaces. A plot of mode surface #103 of an SDL 5412-H1 diode is shown in Figure 3. An entry location is shown as a triangles, an exit location is shown as a circle, and a "+" designates a turning point of the zig-zag scan. An "x" marks the location of one of the 16 preferred H_2O transitions selected for the LASE measurements. Iso- λ lines are drawn through the x's. An enlarged view of the high T /high I boundary of this mode is shown in Figure 4. Here, the program has also appended the mode number from which mode 103 was entered or to which mode 103 exited, as well as the direction of the path that caused this mode hop to occur. For example, near $T = 25^\circ C$ and $I = 137mA$, a mode hop occurred in which mode 103 was exited and mode 112 was entered as I was increased at constant T .

Once the modes are mapped in sufficient detail, reliable paths to H_2O lines need to be determined. From the entry/exit mode information, the user can deduce which modes can be entered from below threshold with high reproducibility. Often there are temperature ranges or "windows" such that if T is fixed to a value in such a window and the laser is repeatedly brought up from below threshold to a certain I value, the same laser mode is always entered. Usually a laser mode surface has a window along a portion of its edge such that if that window is traversed, the same mode is consistently entered. In this manner, trial paths to water vapor lines are established. These paths are programmed into the computer, which repeats them many times to attach a probability of success to each path.

Occasionally mode competition is strong and no reliable entry window for a specific desired mode can be found. To solve this problem, the computer can make the diode execute a path in T, I space which lies within the boundary of the desired mode, but walks near the edges of that mode. If the diode hops onto the desired mode, it will stay on it since its mode edges are not crossed. If the diode is in another mode, then, unless the other mode completely covers the desired mode, it will eventually cross a mode edge and hop to a different mode. If the path is followed long enough, eventually the diode will end up lasing on the desired mode. This technique has been successfully used in the lab to consistently enter mode 103 which has no single reliable entry window from below threshold.

We have found that laser diode mode surfaces can be reproducibly entered (and H_2O lines reliably found) for long periods of time. At present, the longest period of time over which a single diode has been tested has been 1-2 months. During this time, its mode surfaces and paths to those surfaces were highly reproducible.

We gratefully acknowledge contributions by Addison Inge and Curt Banziger.

REFERENCES

1. J.C. Barnes, L.G. Wang, N.P. Barnes, W.C. Edwards, W.A. Cheng, R.V. Hess, G.E. Lockard, and P.L. Ponsardin, Injection Seeding of $Ti:Al_2O_3$ in an Unstable Resonator

Theory and Experiment, *OSA Proceedings on Advanced Solid State Lasers 1991*, vol. 10, pp. 136-141 (1991).

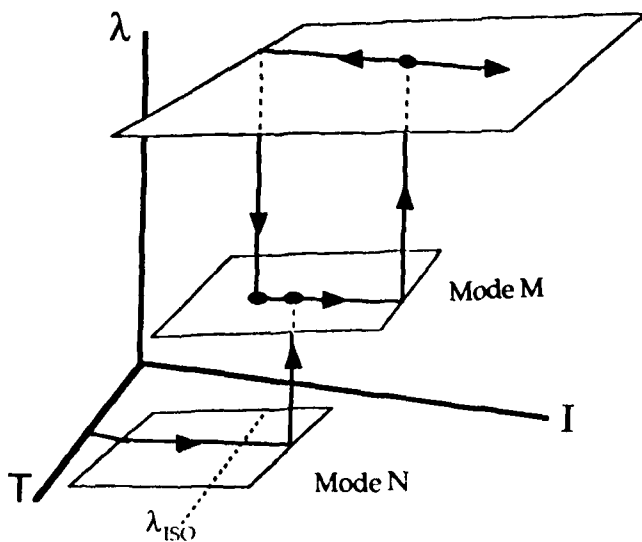


Figure 1. Laser diode mode surfaces

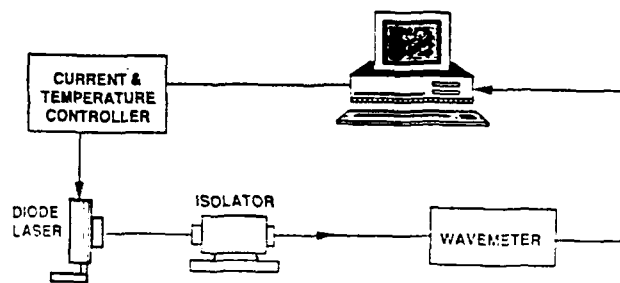


Figure 2. Diode characterization apparatus

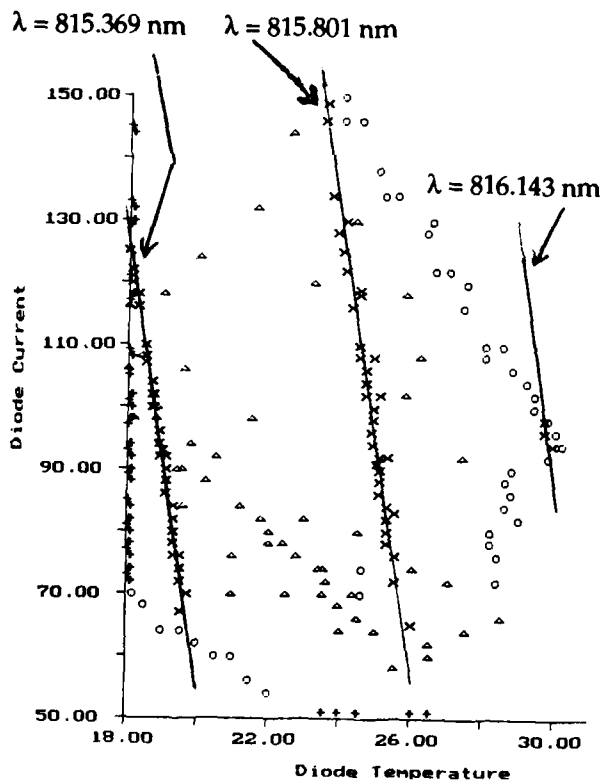


Figure 3. Map of mode surface 103 for an SDL 5412-H1 diode

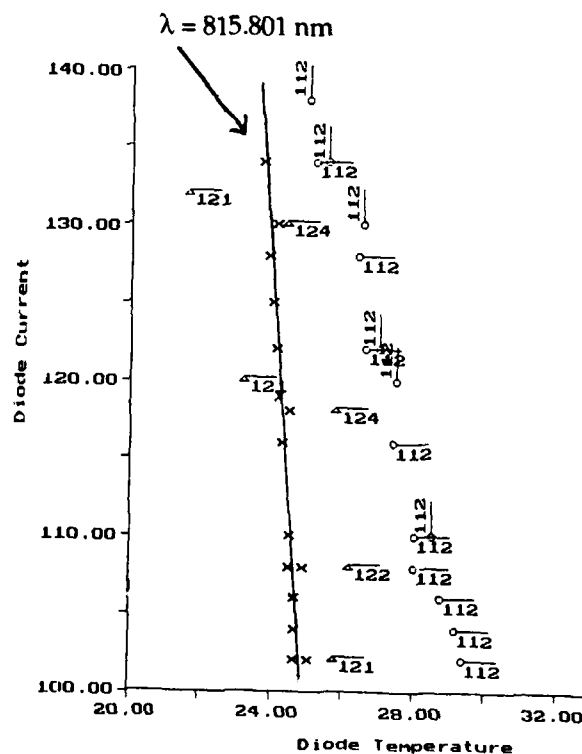


Figure 4. The high T/high I edge of mode 103, showing exit and entry information

Charge-Coupled-Device Detection for a Doppler-Rayleigh Lidar

Jonathan S. Friedman, NAIC Arecibo Observatory, P.O. Box 995, Arecibo, PR 00613-0995, (809)878-2612

Mark W. Robison, Astronomy Department, University of Minnesota, 116 Church St. SE, Minneapolis, MN 55455, (612)626-2067

Craig A. Tepley, NAIC Arecibo Observatory, P.O. Box 995, Arecibo, PR 00613-0995, (809)878-2612

Paul Castleberg, Cornell University, Department of Electrical Engineering, 351 Engineering and Theory Center, Ithaca, NY 14853, (607)255-8298

Francisco Garcia, Cornell University, Department of Electrical Engineering, 351 Engineering and Theory Center, Ithaca, NY 14853, (607)255-8298

1. Introduction:

The use of a charge-coupled device (CCD) camera together with a Fabry-Perot etalon (FP) to measure neutral winds in the thermosphere using 630 nm airglow has been proposed by Hays [1990]. In principle, the same technique is used for lidar winds with the sole difference being that a lidar provides its own light source, whereas airglow relies on a naturally occurring emission in the atmosphere. Hays [1990] showed that a CCD array detector attached to an etalon has more than an order of magnitude higher sensitivity than a photomultiplier tube (PMT). Particular advantages of using a CCD are: (1) It can record the whole fringe pattern at once, thus retaining the photons from multiple rings. (2) Because the FP etalon is not scanned, drifting of the location of the fringe pattern is eliminated. (3) The CCD has higher sensitivity to red light than a PMT. This paper is a report on the usefulness of a CCD array to record the fringes from a Doppler-Rayleigh lidar Fabry-Perot etalon for measuring winds and to compare the obtained results with those obtained using a scanning etalon and a PMT.

2. Comparison between the CCD and PMT:

It is important to understand how data taking using the CCD differs from that using the PMT. The differences rest in the fact that a CCD preserves the intensity distribution of the light incident on it, while a PMT records the amount of light incident on it without any spatial resolving power. Instrumentally, these are fundamentally different techniques both optically and in the electronics following the detector. These differences strongly affect how data is recorded with each.

A PMT produces a current that is directly proportional to the rate at which photons strike its cathode. That current is read by a multichannel scaler in which the channels are sequentially gated so that each corresponds to a specific time delay and integrates only until the next channel begins to integrate. This produces both the range and range resolution information. The PMT response is much faster than that of the electronics, so the data taking rate is dependent on how fast the scaling electronics can record the data. In general, each pulse out of the laser results in a temporal profile of backscattered light. The return is thus a function of backscattered intensity versus height. In a Doppler-Rayleigh experiment, the return light is transmitted through a FP, so the recorded intensity is scaled by the FP transmission function. The transmission function is scanned across the Rayleigh-broadened signal to obtain an intensity profile as a function of frequency. More than 1000 shots are averaged to produce an intensity versus altitude profile corresponding to one

position on the Rayleigh-broadened backscattered signal with a suitable signal-to-noise ratio (SNR) for measuring winds to 60 km altitude with 1.5 km range resolution. Usually seven frequency positions of the transmission function are used to map out the fringe. Thus, to acquire a complete spectral profile of the Rayleigh-broadened return between 10 and 60 km takes 10 to 20 minutes. Three directions are needed to get both horizontal wind components, so the winds can be mapped out every 30 to 60 minutes.

The CCD determines altitude and range resolution using a gated intensifier. This is necessary because the CCD cannot download data quickly enough to do continuous detection. Thus, with the CCD, the data contains information from a single altitude with a range resolution determined by the gate-width of the intensifier. Although all of the spectral information is gathered at one time without having to scan the FP, the information only refers to a single range. The number of shots needed to obtain suitable signal to noise depends on altitude, and ranges from 10s of shots at the lower altitudes up to 1000 shots above 50 km. To measure winds continuously from 10 km to 60 km requires about twice as much time as pressure scanning the FP with a PMT, but more signal information is collected, thus improving the frequency resolving power. This may ultimately extend the range of measurements.

While the final form of raw data from the PMT experiment maps an intensity versus frequency distribution from each range, the CCD data gives images of the rings which must be integrated to produce the spectrum from which winds can then be extracted. Figure 1a shows the raw spectrum recorded by the CCD array, and figure 1b is the integrated line spectrum.

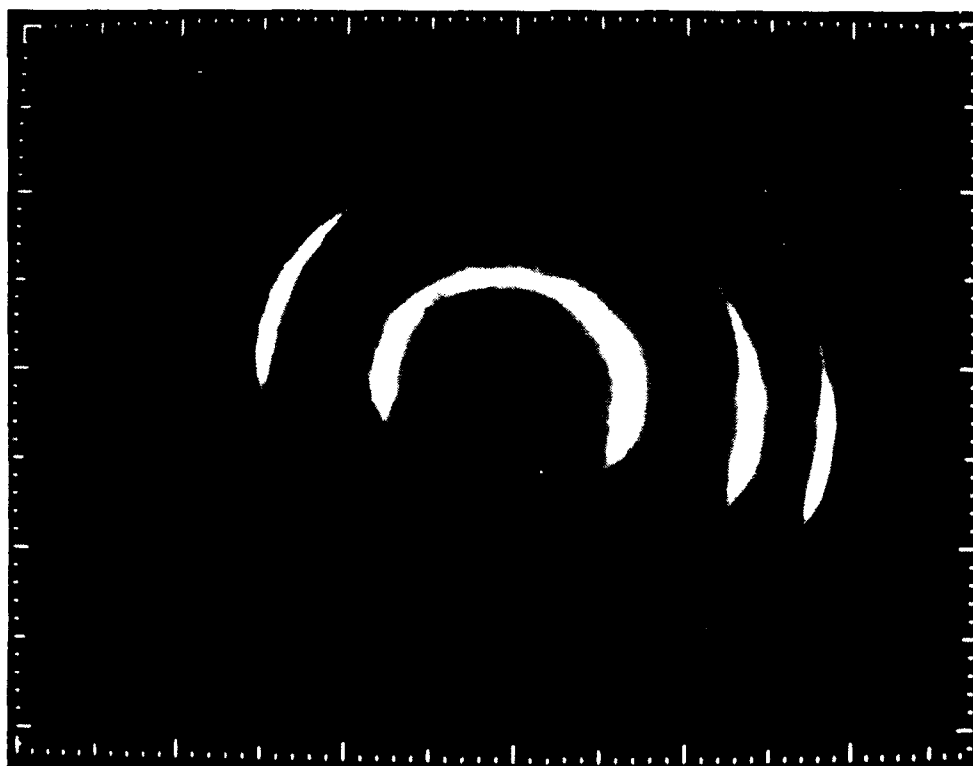


Figure 1a The image of Fabry-Perot interferometer fringes from the Rayleigh-scattered return of the Doppler-Rayleigh lidar as recorded by the CCD array

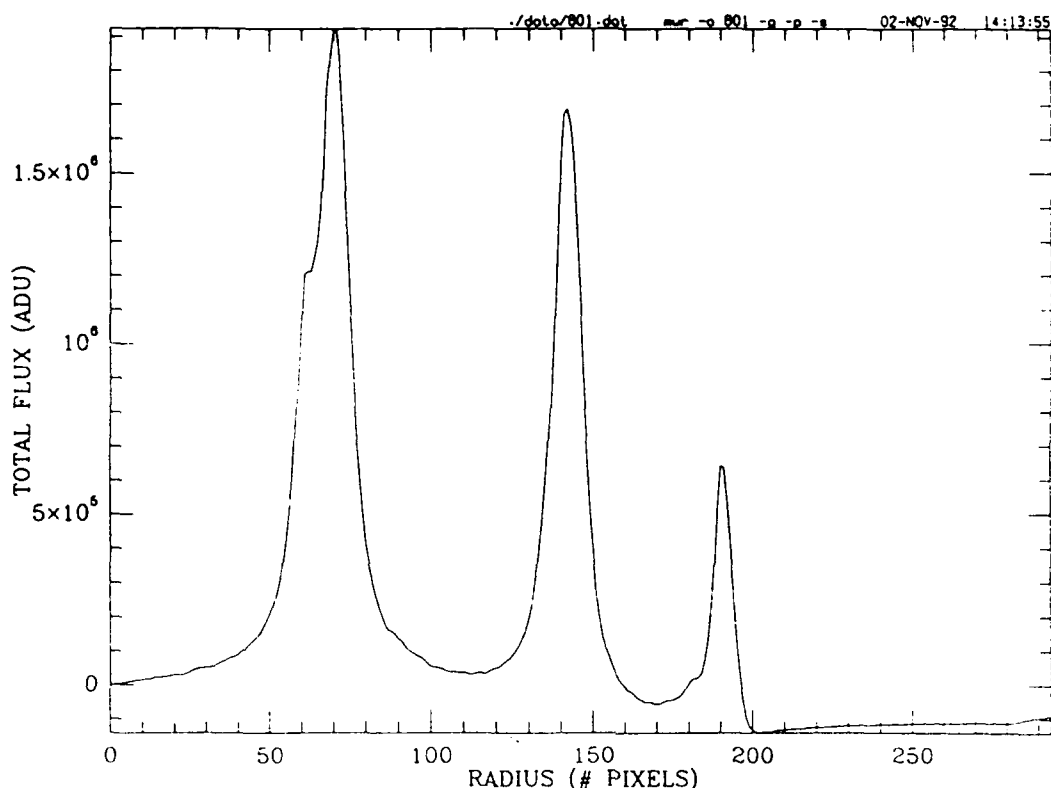


Figure 1b The integrated intensity versus radius plot of the image in 1(a).

3. Data Analysis Method:

As mentioned earlier, to analyze the fringes recorded with the CCD they need to be integrated so as to produce spectra of intensity vs. frequency. Figure 2 gives a flow chart of the algorithm used to do this integration. The image data file created by the CCD controller is read in along with flat-field information that allows the program to compensate for variable sensitivity of different regions of the device. The image is expanded by a factor designed to compensate for pixels over which the light intensity drops off rapidly. This expanded image is then integrated by annuli about the center of the rings which is determined manually. Because each integrated fringe from a FP should contain the same amount of energy, the resulting plot of integrated signal strength versus radius is a set of equal-height fringes that conform to an Airy function. At this point the background is subtracted to improve the contrast and the resulting data is written to a file. Reducing an image containing 578×385 pixels to a line plot requires 45 seconds on a Sun Sparcstation IPX.

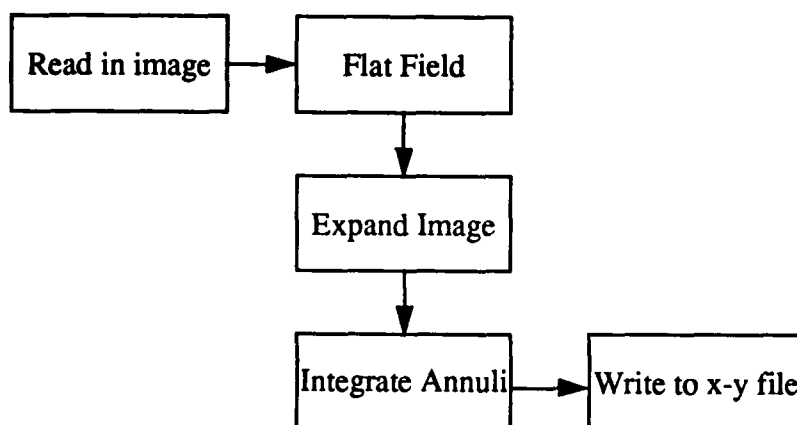


Figure 2. Flow diagram of the algorithm to convert the CCD images of Fabry-Perot interferometer fringes to an x-y plot.

To determine winds from the x-y spectrum, measurements are obtained by pointing the laser vertically to ascertain the zero-horizontal wind component and then north (or south) and east (or west) to get those components respectively. The frequency shift of the spectrum is related to the wind velocities by the factor 0.532 m/s per 1MHz shift, given a laser wavelength of 532nm and a 30° zenith look angle.

4. Discussion and Conclusions:

We have measured winds in the stratosphere and mesosphere with Doppler-Rayleigh lidar since spring of 1990 using the scanning FP and PMT detection [Tepley et al., 1993]. Initial experiments using fixed FP and CCD detection were begun during the summer of 1992. Currently, we are preparing to conduct comparative wind measurements with both techniques.

The CCD detector-based Doppler lidar has several obstacles to overcome. Among them is etalon drift, which is unavoidable, but its effects can be minimized by collecting data from a single altitude in all directions before moving on to other altitudes. This minimizes the time and thus the amount that the etalon can drift. The etalon drift problem is exacerbated by pressure scanning, which will need to be done to compare CCD with PMT results. This can be avoided by completing all of the CCD experiments before collecting PMT data.

Finally, the CCD should benefit the daytime lidar because the shape of the spectrum it records is unaffected by changes in background light intensity. Fluctuations in background intensity caused by aerosols drifting through the field of view make render results with a scanning FP plus PMT questionable.

References:

Hays, P.B., "Circle to line interferometer optical system," *Appl. Opt.*, **29**, p. 1482, (1990).

Tepley, C.A., S.I. Sargoytchev, and R. Rojas, "The Doppler Rayleigh Lidar System at Arecibo," *IEEE Trans. Geosci. Remote Sensing*, (1993 in press).

The Automated Rotating Shadowband Spectroradiometer

Lee Harrison, Mostafa A. Beik, and Joseph J. Michalsky

Atmospheric Sciences Research Center
University at Albany, State University of New York
100 Fuller Road
Albany, NY 12205

Introduction

We are developing a photodiode array rotating shadowband spectroradiometer (RSS) as part of the Instrument Development Program (IDP) of the Atmospheric Radiation Measurement (ARM) Program of the United States Department of Energy (DOE). This instrument uses the automated rotating shadowband technique to separate and measure the spectrally resolved direct-normal, total horizontal, and diffuse horizontal irradiances in the 360 to 1060 nm wavelength region. It is intended as an instrument for the central facility of each of the cloud and radiation testbed (CART) sites, and will complement the array of multi-filter rotating shadowband radiometers (MFRSR) currently being deployed by ARM and other research programs including TOGA/COARE.

I. The Automated Rotating Shadowband Technique

The RSS uses the technique developed for the automated rotating shadowband radiometer (RSR) (Michalsky et al. 1986), and builds on the experience gained first with single passband instruments (LeBaron et al. 1989), and subsequently with multiple filter instruments (Harrison et al. 1993), to measure surface irradiances and atmospheric optical depths. The basic rotating blocking-band method was introduced by Wesely (1982). Instruments have been developed by Guzzi et al. (1985), and by Ascension Technology Inc. (Stoffel et al. 1991) to automate the Wesely method. A RSR differs from these in that it uses a computed ephemeris to position the band for the blocking measurements, rather than depending on the detection of a minimum irradiance. The RSR method permits much longer integration times for each measurement because it needs measurements at only four positions rather than a "continuous" scan across the sky.

The longer measurement duration (and fewer required measurements) of the automated RSR technique permits the development of narrow passband and spectrometric instruments. This substantially improves measurement precision, and permits what would otherwise be impossible wavelengths or passbands. This is critical to the RSS instrument; without the use of this method the scan times would be too long.

The automated RSR technique also improves accuracy. It implements a first-order correction for "excess sky blockage" caused by the shadowing band, which is necessary to obtain correct optical depths, and also significantly improves the measurement accuracy under skies with fractional cloud coverage. A disadvantage of the RSR technique is that the instrument must be accurately aligned, however the accuracy needed for the method to operate properly is also required of any Lambertian detector intended to make total horizontal irradiance measurements to an accuracy of better than 5% (Harrison et al. 1993).

II. The RSS

The instrument is shown in Fig. 1. Light enters the instrument through the integrating cavity diffuser. This design is derived both from the MFRSR instruments, and work in progress on the development of high accuracy Lambertian fore-optics for ultraviolet spectroradiometers. The diffuser is coupled to an integrating cavity that improves both light-throughput, and Lambertian

response. The slit is a 250 μm by 5 mm airgap followed by the spectrometer's controlling slit that is 50 μm wide and 3.0 mm long. Light exiting the slit passes through an electronically controlled shutter, a double prism spectrograph, and is focussed on the 256 channel silicon photodiode array. The RSS shadowband position, shutter control, sampling strategy and data acquisition and storage are controlled by a microprocessor-based data acquisition system.

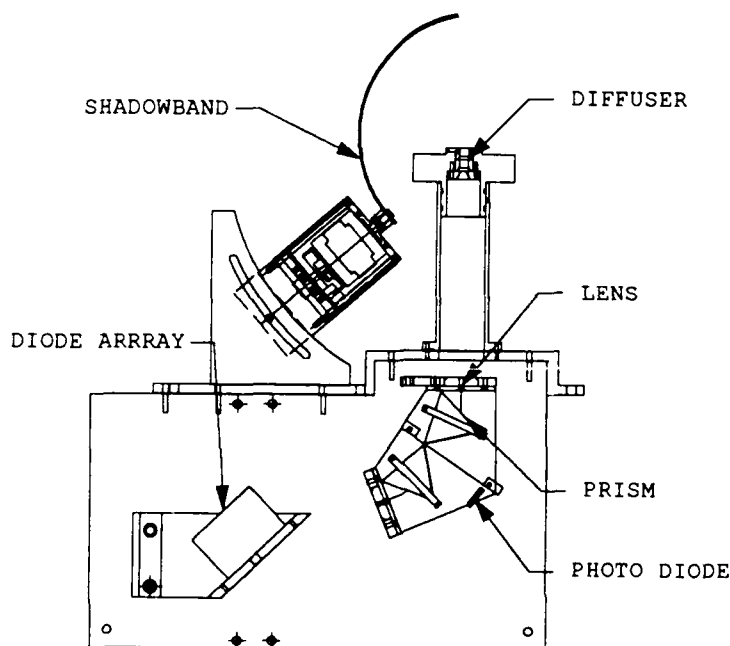


Fig. 1. The rotating shadowband spectroradiometer (RSS)

The RSS uses a double-prism spectrograph; all optical elements are fused silica. This all-quartz design permits observations below 400 nm. This design has been chosen for simplicity, the extreme stability and ruggedness of the optical elements, and because the non-linear dispersion of the system is advantageous for the intended measurements.

Neither flint achromats nor flint dispersing prisms can be employed, and careful optical trade-off studies were necessary to arrive at an acceptable design. A solution was found that is very straightforward to construct; it uses only simple plano-convex lenses. Coma and spherical aberrations are controlled by making the f -number of the system ≈ 7 . Chromatic aberration "controls itself" because the prism material is identical to that of the lenses, and the lenses *are not* chromatically corrected. The result is that the entire effect of chromatic aberration manifests itself as a planar tilt in the focal surface of the dispersed spectrum, which can be readily accommodated simply by tilting the detector. In contrast to high-resolution diode array spectrographs this instrument has only one diode per slit-width at the image plane. Thus the geometric limiting resolution of the instrument is set by the pixel width and the mapping of the spectrum across the array, rather than the theoretical resolving power of the spectrograph. The geometric spectral resolution ranges from 0.6 nm at 360 nm to 8 nm at 1060 nm; the real instrument resolution is slightly degraded by the electronic "cross-talk" between neighboring pixels.

The RSS uses a Hamamatsu NMOS silicon photodiode array model S3901-256Q detector with a Hamamatsu model C4350 amplifier/driver assembly. The diodes have 50 μm center-to-center spacing and a width of 2.5 mm. We have developed a microprocessor controller/data-

interface that uses an Analog Devices AD1380KD 16-bit analog-to-digital converter. Each pixel's analog-to-digital conversion takes 20 μ s and therefore a total of 5.12 ms is required to convert all of the 256 channels. The microprocessor generates the timing signals needed by the array and the analog-to-digital converter, and stores the data. It also controls the shutter.

When operated as an RSR a measurement is made at each of the four positions needed for the RSR algorithm. Each measurement starts with the shutter closed and three rapid "destructive readouts" of the diode array. These data are not stored; the purpose is to refresh the charge state of the diode array pixels. An integration is then made for the planned exposure duration, read out, and stored temporarily by the diode controller. The shutter is then opened for the exposure; the exact shutter interval is monitored by the controller to an accuracy of 1 μ s using a photodiode that sees a reflection from a face of the second prism. The shutter is closed, and the measurement readout is performed. The data can then be corrected by dark subtraction, and normalized for the exposure.

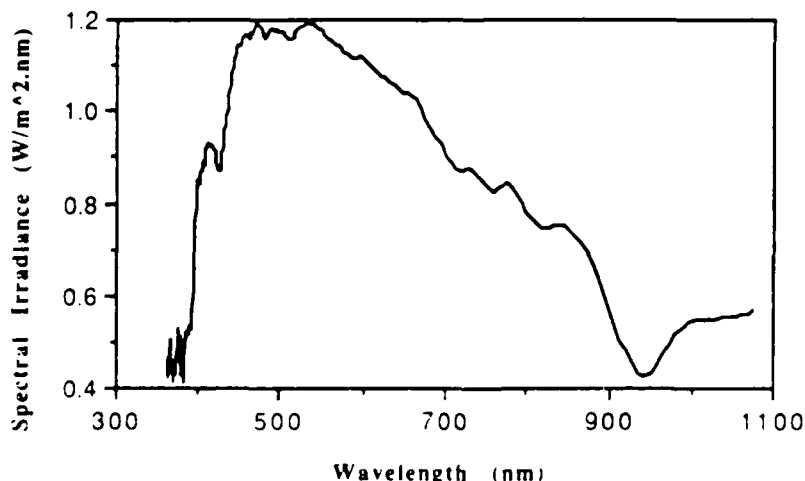
Maximum exposures are limited to less than 3 seconds by the charge leakage of the array, that is not cooled below ambient. However the system light throughput is sufficiently high that exposure times longer than 1 second will saturate the near-infrared pixels even on an overcast day. Longer exposures are needed only for the ultraviolet under dim circumstances.

III. Testing, Calibration, and Preliminary Data

We are starting to operate the RSS. The spectral calibration is performed using standard low pressure gas discharge lamps. Our selection of lamps allow us to find spectral lines over most of the spectral range covered by the instrument. The mercury lines, ranging from 366 to 1014 nm are particularly useful. These lines provide sufficient data to map the geometric passbands of all remaining pixels using a least-squares fitting process and the known refractive index of fused silica as a function of wavelength. The actual slit-functions can be directly determined from the apparent linewidths. Our irradiance calibrations to date have been done using a LI-COR 1800-02 Optical Radiation Calibrator, with a limiting accuracy of $\approx 5\%$.

A total horizontal spectral irradiance plot for a partially overcast day is shown in Fig. 2. This represents our first calibrated solar spectrum from this instrument. Better calibration of the instrument for wavelengths shorter than 400 nm is required. The LI-COR calibrator has a very low output for those wavelengths and therefore is not suitable for this task.

Fig. 2. Response of the RSS to Solar Radiation



VI. Conclusions

Our prototype has demonstrated the necessary throughput and spectral performance needed for this instrument, and all the basic subsystems are developed and working to the predicted levels of performance. Many engineering problems not discussed here have been overcome. Nonetheless we have considerable work remaining. We are currently redesigning the housing and optical mount system to improve stability (a critical requirement for a field instrument). We must also complete the software needed for the instrument to operate autonomously.

The principal reason for developing the rotating shadowband spectroradiometer has been to improve the measurements of absolute spectral irradiance in the shortwave spectral region. The RSS provides fast time resolution, wavelength resolution, and simultaneous data on the direct normal, diffuse horizontal, and total horizontal components of shortwave radiation. The data that this instrument gathers will enable us to develop improved models of the cloud radiation properties and provide information on water vapor, aerosols and cloud and ground albedos using inversion methods (King et al. 1978, King et al. 1979, Shaw et al. 1979). Additionally we hope to test inversion methods to extract ozone abundance from the Chappuis band by comparing such efforts against a high-accuracy UV spectroradiometer to be deployed at the first CART facility.

Acknowledgements: This work has been supported by the United States Dept. of Energy under grant DE-FG02-90ER61072, by the Pacific Northwest Laboratory which is operated for the Dept. of Energy by Battelle Memorial Institute under contract DE-AC06-76RLO 1830, and by the New York State Energy Research and Development Authority under grant 1725-EEED-IEA-92.

References

- Guzzi, R., G.C. Maracci, R. Rizzi, and A. Sicardi (1985) *Spectroradiometer for Ground-Based Measurements Related to Remote Sensing in the Visible from a Satellite*, *Applied Optics*, **24** pp 2859-2863
- Harrison, L., J.J. Michalsky and J. Berndt (1993) *The Automated Multi-Filter Rotating Shadowband Radiometer: An Instrument for Optical Depth and Radiation Measurements* Submitted to *Applied Optics*
- King, M.D., D.M. Byrne, B.M. Herman, and J.A. Reagan (1978) *Aerosol size distributions obtained by inversion of spectral optical depth measurements*, *J. Atmos Sci* **35**: 2153-2167
- King, M.D. and B.M. Herman (1979) *Determination of the ground albedo and the index of absorption of atmospheric particles by remote sensing, part 1: theory*, *J. Atmos Sci* **36**: 163-173
- LeBaron, B.A., J.J. Michalsky and L. Harrison (1989) *Rotating Shadowband Measurement of Atmospheric Turbidity: A Tool for Estimating Visibility*, *Atmos. Environ.* **23**: 255-263
- Michalsky, J.J., J.L. Berndt and G.J. Schuster (1986) *A Microprocessor based Rotating Shadowband Radiometer* *Solar Energy* **36**: 465-470
- Shaw, G.E. (1979) *Inversion of optical scattering and spectral extinction measurements to recover aerosol size spectra* *Appl. Opt.* **18**: 988-993
- Stoffel, T., C. Riordan, and J. Bigger (1991) *Joint EPRI/SERI Project to Evaluate Solar Energy Radiation Measurement Systems for Electric Utility Solar Radiation Resource Assessment* Proceedings of the IEEE Photovoltaics Specialist's Conference, Las Vegas, NV Oct 1991
- Wesely, M.L. (1982) *Simplified Techniques to study Components of Solar Radiation under Haze and Clouds*, *J. Appl. Met.* **21**: 373-383

Friday, March 12, 1993

New Developments 2

FB 10:20am–11:50am
Salon F

D. P. J. Swart, *Presider*
RIVM, Holland, The Netherlands

NEW LASER SOURCES AND DETECTORS FOR INDUSTRIAL EMISSION AND OPEN PATH AIR MONITORING

by

Dennis Killinger
Department of Physics
University of South Florida
Tampa, FL 33620
Ph(813) 974-3995

Many advances in lasers and optical technology for remote sensing of the atmosphere can also be applied to the newly emerging field of environmental and industrial emission monitoring. This paper will cover recent work in the development of new, solid-state and tunable laser sources, and their potential utility for remote sensing of atmospheric or environmental/industrial emissions and gases. In addition, the use of several new detectors or optical (fiber) routing applications will be covered. Examples include the development of tunable Ho lasers for the detection of CO₂ and H₂O in the atmosphere, new GeSb diode lasers for the detection of HF and NH₃, new OPO laser sources, that cover the 3 to 3.5 μm "C-H stretch" spectral region, and grating tunable Diode Lasers. The utility of wide tunability and moderate linewidth makes these lasers important for the future remote detection of many hydrocarbon and pollutant species in the atmosphere, as well as for industrial process control instrumentation.

DIAL in the 3.1 - 3.7 μ m Spectral Region Using Two Simultaneously Pumped Optical Parametric Oscillators.

Scott Taylor
246 GB
Phillips Petroleum Company
Bartlesville, OK 74004
918-661-1610

Introduction

A mobile differential absorption coaxial LIDAR system has been constructed (Petrolaser/LaSen and Titan/Spectron general and subcontractors, respectively) operating in the 3.1 - 3.7 micron range. This instrument is the first of its kind; although, the use of lithium niobate optical parametric oscillators (OPOs) in LIDAR instruments is not new¹⁻³, there have been none that have successfully probed the atmosphere in this spectral region on a consistent basis. The C-H stretching frequency is found in this spectral region thus making this eye safe LIDAR system of intense interest to the petroleum industry for which it was constructed. The primary goals of this device are exploration and environmental monitoring of methane, ethane, and propane.

LIDAR Transmitter and Receiver

The mid-IR source is a pair of lithium niobate (INRAD, 30 mm length, 10 mm width) singly resonant optical parametric oscillators (mirrors are custom made from ARO) pumped at 10 Hz by a single Nd:YAG laser (Continuum 681) operating on the fundamental at 1.06 microns. The OPOs are kept at a constant temperature of 37 °C and are angle tuned. This arrangement allows the simultaneous broadcast of a signal (on-line) and reference (off-line) pair of frequencies which removes the temporal nature of the atmosphere. The beams are combined by rotating the signal frequency polarization 90° from the reference and passing it through a custom made beam combining optic which reflects the reference beam off the exit face. A 4 to 1 expansion occurs before broadcast into the atmosphere (see figure 1). A 12 inch diameter Newtonian telescope collects the return radiation for a pair of liquid N₂ cooled 2.4 MHz InSb detectors (Cincinnati Electronics). A custom made beam splitter in the receiver train separates the returns. Subsequent signals are then digitized by either a pair of 12 bit Colorado Data Systems 10 MHz digitizers or an 8 bit 500 MS/s 2440 dual channel Tektronix digital scope. A real-time UNIX based software acquisition program controls laser triggers, signal processors, and data collection.⁴ The device is designed as a Mie scatter detector in this region, but for preliminary tests operates topographically to increase the sensitivity.

The output energy of each shot is simultaneously monitored by a pair of Molelectron joulemeters (one each for the signal and reference beams) located in the transmitter train. Wavelength calibration is accomplished by angle tuning the signal OPO output through a series of photoacoustic cells containing methane, ethane, and propane. Normally, methane is used to calibrate the OPOs since its spectrum is well known and easily assigned (see figure 2). Wavelengths are assigned to "motor position" units and a tuning curve is generated.

Experimental

A hill side served as a convenient topographic target for a simple experiment which was conducted at Las Cruces, NM. From the top of this hill, propane (from a conventional gas grill container) was released and allowed to flow down the hill side a few inches into the path interrogated by the LIDAR system approximately 71 meters away. The results of the experiment are shown in figure 3. A 64 shot average of the hard target return was obtained before, during, and after the release of gas. The wind was quite calm with very low humidity present in this arid region of the country. The path integrated propane concentration was calculated from:

$$C R = \frac{1}{2\alpha} \left(\ln \left(\frac{P^{ref}}{P^{sig}} \right) + \ln \left(\frac{\rho^{sig}}{\rho^{ref}} \right) + \ln \left(\frac{\epsilon^{sig}}{\epsilon^{ref}} \right) \right)$$

where P^{sig} and P^{ref} are the normalized return power for the signal and reference frequencies respectively and α is the absorption coefficient of propane ($5.6517 \times 10^{-4} \text{ ppm}^{-1} \text{ m}^{-1}$). C is the concentration of propane in ppm and R is the range in meters. The $\ln(\rho^{sig}/\rho^{ref})$ and $\ln(\epsilon^{sig}/\epsilon^{ref})$ quantities are a measure of the differential albedo of the target material at these wavelengths, measured before any gas was released, and detector responsivity respectively. The wavelength selected to detect propane was 3.750 microns and was used for no other reason in that it was between the P(4) and P(5) lines of methane. This selection ruled out absorption due to methane.

Figures

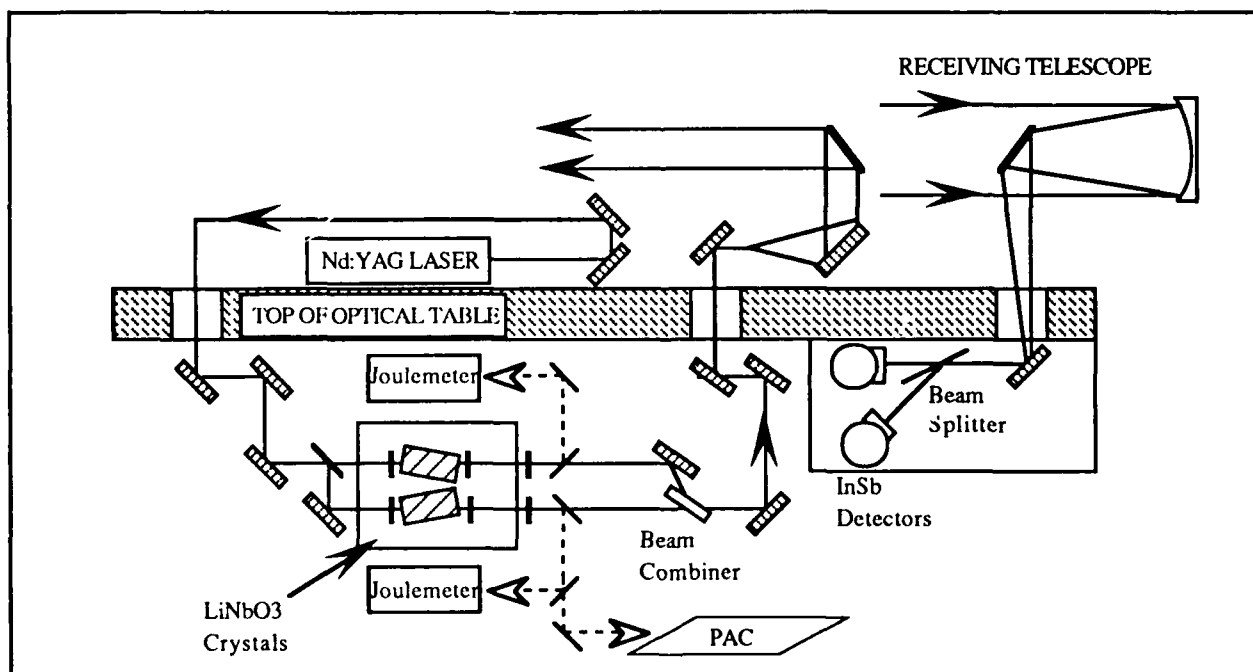


Figure 1. A highly schematic optical layout of the DIAL instrument transmitter/receiver train. Various electronic hardware, signal processors, etc. are not shown. In the truck, which houses the instrument, the optical bench is installed vertically and both sides are used to mount optics. The transmitter components have been "swung out" 90° to give a better feel for how they are actually mounted on the optical bench.

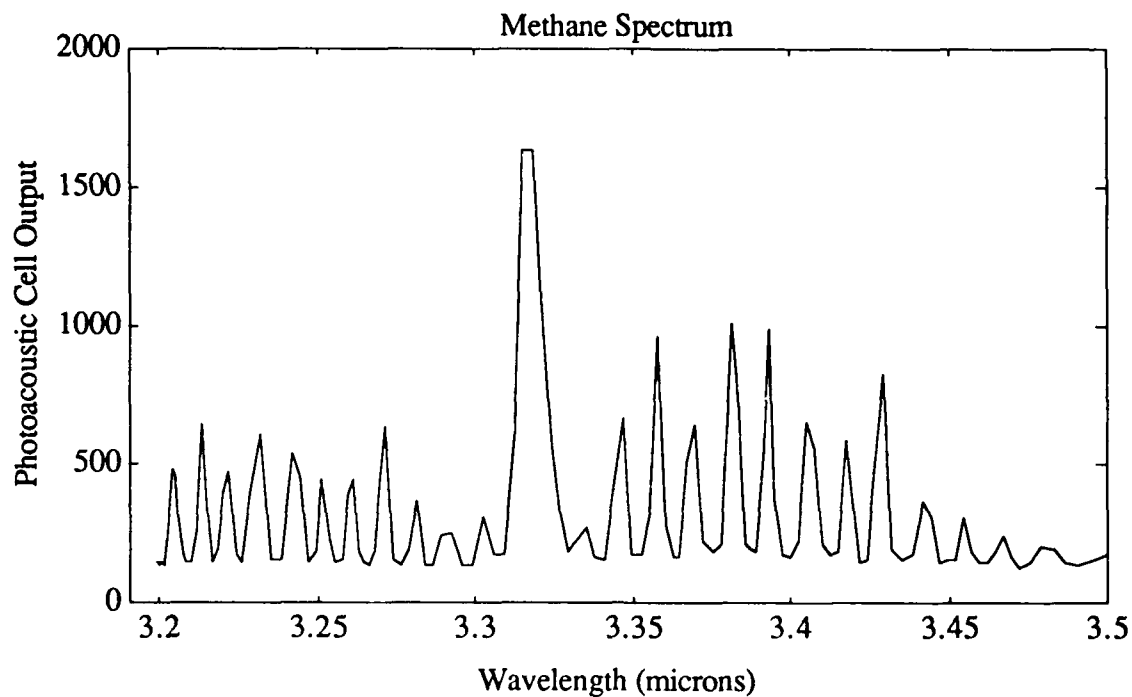


Figure 2. Output of the photoacoustic cell containing methane as the signal OPO is angle tuned. The quality of the spectrum is good enough to easily assign wavelengths to the R, Q, and P branches. No attempt is made to narrow the OPO linewidth and is estimated between 2 and 4 cm^{-1} .

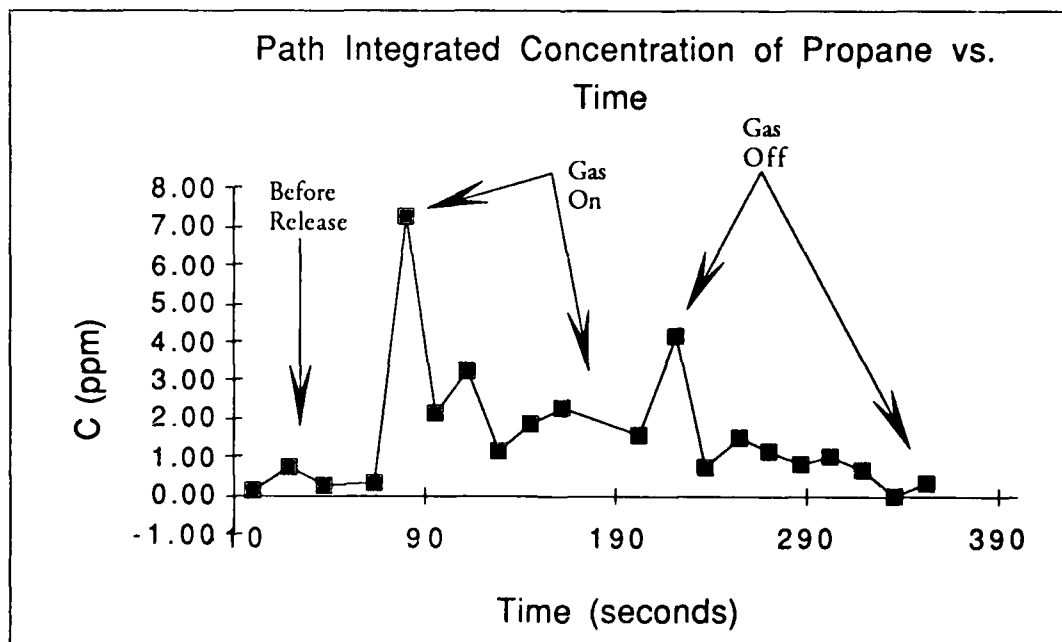


Figure 3. Path integrated propane concentration before, during, and after a release of the gas over a natural target 71 meters away from the LIDAR instrument. The measurable amount of propane

before the release is probably due to propane remaining in the area from previous experiments a few minutes before this one. An error of 20% is estimated for each of the data points. The atmospheric conditions were low humidity with very calm winds that hindered rapid dispersal of the propane cloud from previous experiments.

References

1. Baumgartner, R. A., and R. L. Byer, "Continuously tunable ir lidar with applications to remote measurements of SO₂ and CH₄", Appl. Opt. 17, 3555 (1978).
2. Baumgartner, R. A., and R. L. Byer, "Remote SO₂ measurements at 4 microns with a continuously tunable source", Optics Letters, 2, 163 (1978).
3. Brassington, D. J., "Differential absorption lidar measurements of atmospheric water vapor using an optical parametric oscillator source.", Appl. Opt. 21, 4411 (1982).
4. Fugelso, D., and M. Michnovicz, "Real-Time Data Acquisition", C Users Journal, 9, 48, (1991).

NASA Lidar Atmospheric Sensing Experiment's Titanium-doped Sapphire Tunable Laser System

James Barnes, William Edwards, NASA Langley Research Center, Hampton, VA 23665-5225; Larry Petway, Science Applications International Corp.; Liang-Guo Wang, College of William and Mary

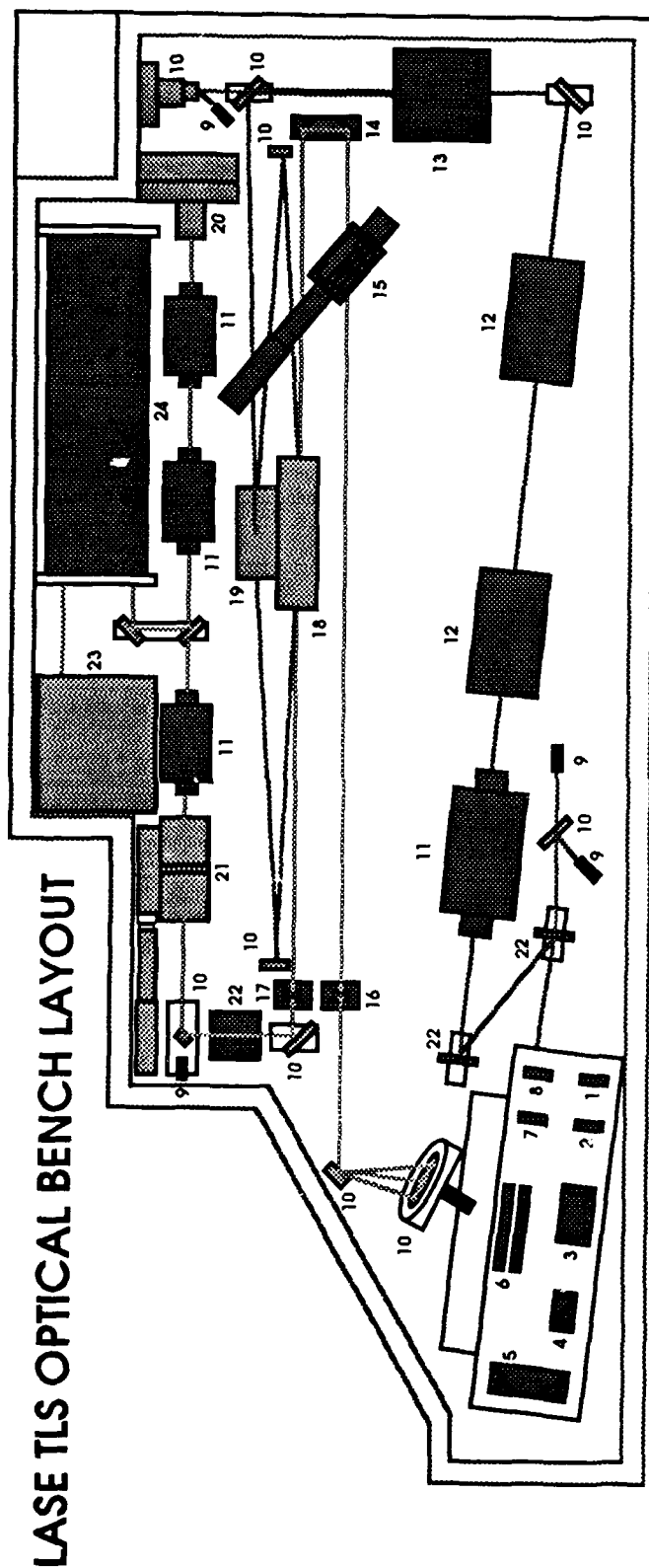
NASA has undertaken an aggressive effort to develop the first fully autonomous airborne DIAL, **D**ifferential **A**bsorption **L**idar, instrument. The LASE, **L**idar **A**tmospheric **S**ensing **E**xperiment, will be deployed on NASA's ER-2 aircraft at altitudes of 52,000 to 70,000 feet. The science objective is to measure tropospheric H₂O and aerosols in phase I and adds O₂ for pressure and temperature determination in phase II. The major subsystems of the instrument including the telescope receiver, control and data system, and the laser transmitter are being constructed and tested at Langley Research Center. This paper describes the LASE laser transmitter's requirements, designs, development, and testing.

The LASE TLS, **T**unable **L**aser **S**ystem, major performance requirements are listed in table 1. A prototype engineering TLS has been designed, assembled, and characterized with respect to the LASE lidar transmitter requirements. Figure 1 is a schematic representation of the optical layout of the TLS laser components. The TLS is comprised of frequency-doubled, Nd:YAG pump laser, a Ti:Al₂O₃ power oscillator, and a diode laser. The pump laser has a nominal 650 mJ per pulse, 532 nm output. It operates at 5 Hz in a double pulse format. The power oscillator, which has been demonstrated to produce 250 mJ per pulse of near diffraction limited output at the gain center of the laser around 790 nm, is an unstable resonator design. The 100 mW continuous wave, single longitudinal mode, laser diode is used to injection seed the power

oscillator. The injection seeding technique used in this work allows wavelength control of the TLS from 810 to 820 nm with a resolution of better than 0.25 pm and achieves a laser linewidth of 0.5 pm. A detailed description of the laser subsystems will be presented.

Table 1. TLS Laser Performance Requirements

PARAMETER	REQUIREMENT
1. Pulse Repetition Modes: Normal Flight Mode Test Mode Test mode	On- and Off-line pulse firing at 5 Hz. On-line pulse firing at 5 Hz for n shots. Off-line pulse firing at 5 Hz for n shots.
2. Pulse Sequence	Off-pulse follows on-pulse after a delay of 400 $\mu\text{sec} \pm 10 \mu\text{sec}$.
3. Pulse Repetition Period	Pulse repetition period is 0.2 sec $\pm 100 \mu\text{sec}$ between pulse pairs.
4. Pulsewidth	≥ 95 percent of the total pulse energy must occur within $\leq 300 \text{ nsec}$.
5. Mean Pulse Energy	≥ 150 millijoules.
6. Energy per Pulse Stability	± 10 percent shot to shot.
7. Tuning Range	813 nm to 819 nm.
8. Injection-Seeded Tuning	The TLS shall be capable of autonomous tuning to within 0.35 pm, 1σ , of commanded wavelengths.
9. Spectral Distribution	$\geq 99\%$ of the total energy in each pulse shall reside within a spectral interval $\leq 1.06 \text{ pm}$, ie., $\approx 0.015 \text{ cm}^{-1}$.
10. Polarization	The output shall be $\geq 90:1$ linearly polarized.
11. Beam Direction Stability	The beam direction shall remain to within 100 μrad of its adjusted direction.



Nd:YAG oscillator

1. HR end mirror
2. 1/4 waveplate
3. Q-switch
4. Wave polarizer
5. Corner cube
6. Rod and flashlamp
7. 1/13 waveplate
8. Flat output coupler

Energy monitor fiber

9. Energy monitor fiber
10. Dichroic turning mirror
11. Faraday isolator
12. Amplifier
13. CD*A SHG w/oven
14. Hollow retroreflector
15. Birefringent filter
16. GRM output coupler

97% R end mirror

17. 97% R end mirror
18. Ti:Sapphire crystals
19. Beam splitter
20. Diode seed laser
21. Thin etalon
22. Telescope
23. Line locking detector/electronics
24. Reference White cell

Figure 1. The optical layout of the LASE titanium-doped sapphire tunable laser system.

**DIODE LASER INJECTION SEEDED, RAMAN SHIFTED
ALEXANDRITE LASER TUNABLE NARROWBAND LIDAR SOURCE**

**S. SCHMITZ
U. VON ZAHN
University of Bonn
Germany**

**T. WILKERSON
University of Maryland
College Park MD 20742**

**D. F. HELLER
J. C. WALLING
Light Age, Inc.
2 Riverview Dr.
Somerset NJ 08873-1150**

**J.C. WALLING
Light Age, Inc.
6 Powder Horn Dr.
Warren NJ 07059-5105**

The immediate purpose of this work is to develop robust, reliable, spectrally narrow light sources for optical remote sensing and specifically for certain atmospheric Lidar studies. One application is the study of the mesospheric sodium layer (80-100 km altitude) to determine altitude profiles of atomic density and temperature. For this purpose we have undertaken comparison of the Na (D₂) radiation at 589.159 nm produced by either anti-Stokes or frequency doubled first Stokes conversion of alexandrite laser wavelengths. A second application is the profiling of atmospheric water vapor by means of differential absorption Lidar (DIAL) utilizing alexandrite fundamental and Stokes shifted outputs in the 730 nm, 940 nm and 1140 nm bands of water vapor. The 1.4 μ m water vapor band also is accessible using output from the Second Stokes shift of alexandrite (at 760 nm) radiation in D₂ gas.

In these and many other lidar applications, minimizing the linewidth of the lidar source is of paramount importance. Typically linewidths for these applications need to be in the 100-500 MHz range. For these applications adequate suitable narrowband laser sources have not previously been available. Here we describe the technical development of one very promising laser source. Concomitant with the source development certain fundamental issues regarding the physics of narrowband light generation with broadly tunable laser materials have been addressed as have concerns regarding limits to the faithfulness of narrowband Raman conversion processes.

Ring and standing-wave diode laser injection seeded alexandrite lasers have been Raman shifted in hydrogen, deuterium, and other gases and their outputs characterized. The fundamental output consists of single axial mode or few axial mode contributions depending on configuration. Most exciting is the ability of these laser sources to provide high average power, extremely narrowband light at most wavelengths in the UV, visible, and IR spectral regions. These sources appear to be extremely well-suited for most atmospheric Lidar applications especially those requiring some degree of ruggedness and reliability.

Preliminary studies of the spectral output of the laser source were conducted at wavelengths near 780 nm using various commercially available, internal cavity

diode lasers. The diode lasers produced between 5 and 100 mW of single frequency output and were continuously tunable, both by temperature and current, over ranges of a few to a few tens of GHz more. One particular (multi-quantum well design) diode has a continuous tuning range of approximately 150 GHz. Typical diodes have linewidths measured to be below 50 MHz. The output of the diode injection seeded alexandrite laser typically consists of between one and 4 longitudinal modes, depending on cavity configuration and seeding conditions. The single mode linewidth was measured to be below 80 MHz, limited by the resolution of our equipment. [The transform limited linewidth for pulses ranging from 30-100 ns in duration is 5-15 MHz.] The longitudinal mode spacing for both ring and standing-wave cavities is about 200 MHz. In these experiments no attempt was made to synchronize the laser cavity length to the diode frequency. Consequently the output typically consisted of contributions from a few cavity modes - dominantly one or two. High frequency mode beating was observed as modulation on the Q-switched pulse waveform and provided a signature for injection seeding. The sporadic single frequency pulses had the expected smooth pulse envelope. More than 200 mJ of pulse energy was obtained using multi-mode resonators and more than 30 mJ was obtained in a single transverse (TEM₀₀), single longitudinal mode beam. Pulse repetition frequencies were varied up to 25 Hz.

The output of the Q-switched, injection seeded alexandrite laser was Raman shifted in hydrogen and deuterium gases. The dominant characterization was done using hydrogen. Commercial Raman cells of a novel design (Light Age, Inc. 101 PAL/RC) were used. The cells could be varied in length up to 1 meter and had integral focusing lenses that were nominally half the cell length. Cell pressure was varied but not necessarily optimized during these studies. The Raman shifted output consisted of several output (Stokes and anti-Stokes) beams at frequencies differing by 4155 cm⁻¹, the Q(1) vibrational spacing in hydrogen. These beams were all collinear and tuned with the alexandrite pump laser frequency. Up to 5 orders of anti-Stokes beams and 2 orders of Stokes beams could be observed by using hand held fluorescent cards and/or IR viewers. In many cases about 50% of the incident light was depleted in the conversion. More than 30% conversion into the first Stokes could be achieved. Conversion into the first anti-Stokes was more modest, but exceeded 5%.

The spectral output of the Stokes and anti-Stokes beams was extremely narrow, below our resolution limit. Our Fabry-Perot could easily resolve adjacent cavity modes of the alexandrite laser (200 MHz) but was limited in the determination of spectral bandwidth to about 350 MHz. This limit was about a factor of 4 smaller than the (spontaneous) Raman linewidth of hydrogen gas at the pressures used and demonstrates that substantial gain narrowing occurs in the conversion process. We expect but cannot yet resolve the transform limited Raman shifted pulses that may occur from time to time as found by MacPherson et al using fixed frequency laser pumps. These experiments demonstrate that diode injection seeded alexandrite lasers are robust and convenient sources useful for a great number of Lidar applications. Work is progressing to obtain linewidths below 100 MHz at 589 nm for atmospheric sodium studies of mesospheric winds and for operation in the 725-735 nm and 940 nm regions for water vapor Lidars.

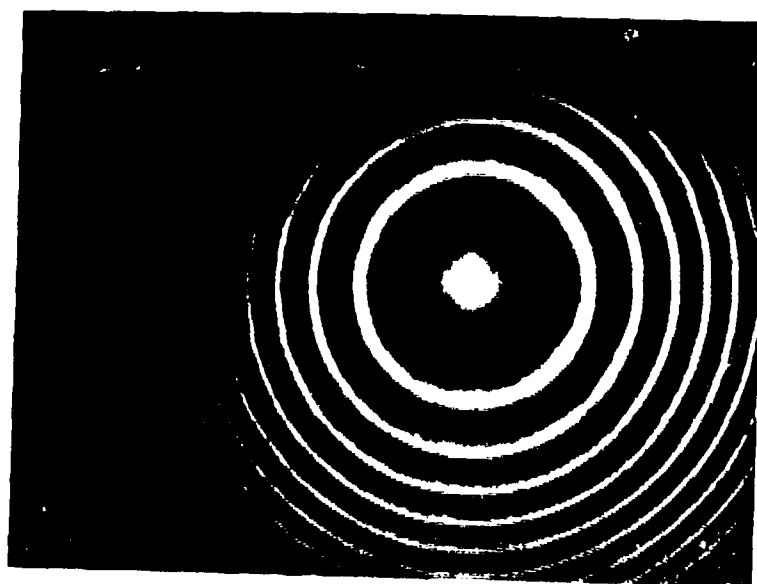


Figure 1: Fabry-Perot pattern from frequency double second Stokes output
Free Spectral Range = 5 GHz.

Abrams, M. C. — MA4, ThD5
Ackerman, Steven A. — MD2
Adler-Golden, Steven M. — TuB2
Adrian, G. P. — TuA4
Aimediou, P. — ThE5
Alvarez, R. J., III — TuD14
Anderson, Bruce E. — ThA4
Anderson, G. P. — TuA5
Ansmann, Albert — ThB2
Aptuley, Arnoud — WC3

Banakh, V. A. — ThE1, ThE2
Barnes, James — FB3
Barnes, Norman P. — TuD25
Baumann, M. — TuA4
Beaton, Sheryl — ThD2
Beik, Mostafa A. — FA5
Bell, W. — TuD26
Bergwerff, Hans B. — WC3
Best, F. A. — TuA6
Bevilacqua, R. M. — TuA3
Bien, Fritz — TuB2
Bisson, Scott E. — MB3, MB4
Blair, J. Bryan — FA1
Blatherwick, R. D. — ThC4, ThD1
Bloom, Hal J. — ThD4
Bonomo, F. S. — ThD1
Bösenberg, Jens — WC1
Bowdle, David A. — ThE18, ThE19
Browell, Edward V. — TuD10, ThA4
Bulton, Jack L. — FA1
Bundy, D. H. — TuD14
Burris, John — ThE12, ThE24
Burrows, J. P. — TuD6

Camy-Peyret, C. — ThE5
Carswell, Allan I. — MB, TuC, TuC4, WD2, ThB3
Casey, Leah W. — TuD2
Castleberg, Paul A. — TuD18, FA4
Chaboureau, J. P. — MB5
Chalfant, Michael W. — TuD2
Chedin, Alain — MB5, MC1, TuA
Chen, Li — ThC2
Cheo, Peter K. — ThC2
Cheruy, F. — MC1
Chetwynd, J. H. — TuA5
Chu, William P. — MB6, ThA3
Chu, Zhiping — ThC2
Chyba, Thomas H. — FA3
Clarke, A. D. — ThE18
Clarmann, Thomas v. — TuB5, ThE13
Claud, C. — MB5
Clough, Shepard A. — TuA1, ThC
Cloutier, M. — TuA5
Cutten, Dean R. — ThE18, ThE19

David, Shelle J. — ThC4, ThD1, ThD2
DeCoursey, Robert J. — ThE23
Dedecker, R. G. — TuA6
DeFoor, T. E. — ThA1
de Schouepnikoff, L. — ThB4
Deslis, Apostolis — WD3

de Vries, R. J. — FA2
de Winter-Sorkina, R. — ThE10
Diebel, D. — TuD6
Dieudonné, J. — WB5
Dighe, Kalpak A. — TuD15, TuD18
Dirkx, T. P. — TuA6
Donovan, D. P. — ThB3
Drayson, S. Roland — ThD3
Dutton, E. G. — ThA1

Eberhard, Wynn L. — TuC1
Edmonds, C. M. — TuD14
Edwards, William — FB3
Eloranta, Edwin W. — MD4, WB2, ThE20
Elouragini, S. — TuC5
Emmitt, G. D. — WB5
Escobar, J. — MC1
Evans, Keith D. — MB2, MB3, TuD11, TuD12
Evans, W. F. J. — ThE8

Farmer, C. B. — MA4
Famiglietti, Joseph — TuD8, ThE16
Ferrare, Richard A. — MB2, MB3, TuD11, TuD12
Finkelstein, N. — WB3
Fischer, Herbert — MA1, TuB5, ThD
Flamant, Cyrille N. — TuD8, ThE16
Flamant, P. H. — TuC5
Flesia, C. — ThB4
Flint, John H. — TuD20
Fogal, P. F. — TuD26
Fong, A. Y. — TuC4
Forkey, J. — WB3
Frank, E. — TuA4
Friedl-Vallon, F. — TuB5
Friedman, Jonathan S. — TuD15, TuD18, FA4
Fritzsche, Ch. — TuB5

Garcia, Francisco I. — FA4
Garcia, Raul — TuD15
Gardiner, T. D. — TuD26
Gardner, Chester S. — MA2
Gardner, Tim J. — TuD2
Garvin, James B. — FA1
Gimmestad, G. G. — MD5
Gimmestad, S. C. — MD5
Glaccum, W. J. — TuA3
Godin, Sophie — WD1
Goede, A. P. H. — FA2
Goldman, A. — ThC4, ThD1, ThD2
Goldsmith, J. E. M. — MB3, MB4
Goldstein, Neil — TuB2
Gooch, W. — MC4
Gopalan, A. — ThC3
Gordley, Larry L. — TuD5, TuD24, ThD3
Grant, William B. — ThA4
Gualtieri, J. Anthony — TuD1
Gunson, M. R. — MA4, ThD5

Haario, Heikki — TuD3
Hahn, J. F. — TuD13
Haner, David A. — ThE25

Hardesty, R. Michael — WA1, WB4
 Harding, David J. — FA1
 Harrison, Lee — FA5
 Heaps, William S. — ThE7
 Heller, D. F. — FB4
 Herbsleb, R. A. — TuA6
 Heuser, Alene W. — FA3
 Hiromoto, N. — TuD21
 Hoff, Raymond M. — TuB1, TuD13, ThB
 Hofmann, D. J. — ThA1
 Hoogeveen, R. W. M. — FA2
 Hornstein, J. S. — TuA3
 Howell, H. B. — TuA2, TuA6
 Huang, Hung-Lung — MD3
 Husson, N. — MB5

Inomata, S. — TuB3
 Inoue, Toshiro — MD2
 Ismail, Syed — TuD10, ThA4
 Itabe, T. — TuD21
 Iwagami, N. — TuB3

Jäger, H. — ThA, ThA2
 James, T. C. — ThE11
 Jani, Mahendra G. — TuD25
 Jankevics, Andrew J. — TuD20
 Johnson, Scott D. — ThE24
 Jolliffe, B. W. — TuD26
 Joseph, R. A. — ThE6

Kane, T. J. — ThB5
 Kaprielov, B. — TuC8
 Kaufman, Yu. G. — ThE22
 Kelley, Michael C. — TuD18
 Khmelevtsov, S. S. — TuC7, TuD9, ThE22
 Killinger, Dennis K. — FA, FB1
 Knuteson, R. O. — TuA2, TuA6, TuB4, ThE14
 Kolev, I. — TuC8
 Korb, C. Laurence — TuD8
 Kusters, J. J. — ThC4, ThD1
 Kovalev, Valdimir A. — ThE21
 Krigman, S. S. — TuA3
 Kumer, Jack B. — ThD2, ThE11
 Kuwashima, Shigesumi — TuD23
 Kyrölä, Erkki — TuD3

Larsen, J. C. — MB6
 Larson, Nels — ThB1
 LeBel, Peter — ThE4
 Lee, Jamine — TuB2
 Lee, S. C. — TuB4
 Lehman, F. J. — TuA3
 Lempert, W. R. — WB3
 Linden, A. — TuB5
 Lindner, Bernhard Lee — TuD7
 Lindquist, L. Oscar — WD3
 Liou, K. N. — MC3, MC4
 Lo, James — TuD1
 Lowes, L. L. — MA4, ThD5
 Lumpe, J. D. — TuA3

Mankin, William — MA
 Manson, P. J. — TuC3
 Marshall, Benjamin T. — TuD24
 Martin, N. A. — TuD26
 Martinsen, Robert J. — TuD20
 Maruvada, S. — ThB5
 Matsumoto, Hironori — TuD19, TuD23
 Matthews, W. A. — ThE5
 Mayo, L. — FA3
 McCaul, Eugene W., Jr. — ThE18, ThE19
 McDermid, I. Stuart — WC, WD3, WD4, ThE25
 McElroy, J. L. — TuD14
 McGee, Thomas J. — WB, WC2, ThE24
 McMillin, Larry M. — TuD1, ThD4
 Megie, Gerard J. — MA3
 Melfi, S. Harvey — MB1, MB2, MB3, TuD11, TuD12
 Menenger, L. — TuC5
 Menzies, Robert T. — WB4, ThE18, ThE19
 Mergenthaler, J. L. — ThE11
 Meriwether, John W. — WA, WB1
 Michalsky, Joseph J. — ThB1, FA5
 Miles, R. — WB3
 Milton, M. J. T. — TuD26
 Minato, A. — TuD21
 Mironov, V. L. — ThE1
 Montgomery, Harry E. — TuD4
 Moosmüller, H. — TuD14
 Morskii, V. V. — ThE1
 Motteler, Howard E. — TuD1
 Murcay, D. G. — TuD26, ThC4, ThD1
 Murcay, F. H. — ThC4, ThD1
 Murcay, Frank J. — ThC4, ThD1, ThD2, ThE5
 Murphy, E. — TuA5
 Murray, Keith E. — TuD25

Nakane, Hideaki — MD1
 Nebel, Henry — ThE15
 Neiman, Paul J. — WA3

Oelhaf, H. — TuA4, TuB5
 Oikarinen, Liisa — TuD3
 Okumura, Hiroshi — TuD19, TuD23
 Olivier, Lisa D. — WA3
 Osborn, Mary T. — ThE23
 Ou, S. C. — MC3, MC4

Paboojian, A. J. — ThE6
 Pal, S. R. — TuC4
 Park, Jae H. — ThD3
 Parvanov, O. — TuC8
 Patterson, E. M. — MD5
 Patterson, G. R. — TuC3
 Pelon, J. — TuC5
 Petway, Larry — FB3
 Philbrick, C. R. — ThB5
 Picard, Richard H. — ThE6, ThE15
 Piesch, Ch. — TuB5
 Piironen, A. K. — MD4, WB2
 Pitts, Michael C. — ThA3
 Platt, C. M. R. — TuC3
 Plum, Charles P. — TuD20

Porch, W. M. — TuC2
 Post, Madison J. — WA3
 Potter, J. F. — ThE11
 Prasad, Coorg R. — TuD8, ThE16
 Puckrin, E. — ThE8
 Pueschel, R. — ThE18
 Purser, R. J. — MD3

Qu, Y. — TuA5

Ralph, F. Martin — WA3
 Rao, N. X. — MC3, MC4
 Reale, Anthony L. — ThD4
 Revercomb, H. E. — TuA2, TuA6, TuB4, ThE14
 Rieu, H. — MC1
 Rinsland, C. P. — MA4, ThC4, ThD5
 Rob, Mohammad A. — TuD22
 Roberts, D. W. — MD5
 Robison, Mark W. — FA4
 Roche, Aiden E. — ThD2, ThE11
 Rodriguez, Rene — ThE24
 Roemer, M. — ThE10
 Rothermel, J. — WB4
 Rothman, Laurence S. — ThC1
 Rozanov, V. V. — TuD6
 Russell, James M., III — TuD5, ThD3
 Ryan, S. — ThA1

Sachse, Glen — TuD10, ThE4, FA3
 Sasano, Yasuhiro — MD1, TuD21, WD
 Schmidt, U. — ThE5
 Schmitz, St. — FB4
 Schwemmer, Geary K. — TuD8
 Scott, N. A. — MB5, MC1
 Seefeldner, M. — TuB5
 Sharma, R. D. — ThE15
 Shaw, W. — TuC2
 Shenk, William E. — TuD4
 Sheppard, A. — TuD13
 Shettle, E. P. — TuA3
 Shin, U. — ThC3
 Short, J. F. — TuA6
 Sihvola, Elina — TuD3
 Sirko, Eric W. — ThE25
 Smalikho, I. N. — ThE1, ThE2
 Smith, A. — TuA5
 Smith, Craig A. — TuD17
 Smith, William L. — MC, MD3, TuA2, TuA6, TuB4, ThE14
 Spakman, Jan — WC3
 Spinhirne, James D. — ThE18, ThE19
 Spurr, R. J. D. — TuD6
 Stankov, B. B. — MC2
 Starkey, J. R. — ThE5
 Steinbrecht, W. — WD2, ThB3
 Stevens, T. D. — ThB5
 Strow, L. Larrabee — TuD1, ThE9
 Sugimoto, Nobuo — MD1, TuD21
 Sugita, Tadashi — TuD19, TuD23
 Sutorikhin, I. A. — ThE1
 Svetogorov, E. D. — TuD9

Swann, N. R. — TuD26
 Swart, Daan P. J. — WC3

Tai, Hideo — TuD16
 Takabe, M. — TuD21
 Takano, Y. — MC4
 Takeuchi, Nobuo — TuD19, TuD23
 Tamminen, Johanna — TuD3
 Taylor, Scott — FB2
 Tepley, Craig A. — TuD15, TuD18, WA2, FA4
 Thériault, J.-M. — TuA5
 Thomason, Larry W. — ThA3
 Thompson, Robert E., Jr. — TuD5
 Tiwari, S. N. — MB6
 Tomova, Y. — TuC8
 Toriumi, Ryoichi — TuD16
 Turner, R. M. — TuD14
 Turner, V. — TuA5

Uehara, Kiyoji — TuD16

Valentin, R. — TuC5
 van der A, R. J. — FA2
 van der Woerd, H. — ThE10
 Varanasi, P. — ThC3
 Vay, Stephanie — ThE4
 Veiga, Robert E. — ThE17
 Visser, Eric P. — WC3
 Viswanathan, Ramesh — ThE21
 Völker, W. — TuB5
 von Zahn, U. — FB4

Walling, J. C. — FB4
 Wallio, Andrew — ThE4
 Walsh, T. Daniel — WD3, WD4
 Wandinger, Ulla — TuC6, ThB2
 Wang, Liang-guo — TuD10, ThE4, FA3, FB3
 Weitkamp, Claus — TuC6, ThB2
 Weng, Chi Y. — TuD8
 Westerman, Steve — ThB6
 Westwater, E. R. — MC2, MD
 White, Mary L. — WD3
 Whiteman, David N. — MB2, MB3, TuD11, TuD12
 Wilkerson, Thomas D. — ThE16, FB4
 Williams, W. J. — ThE5
 Winick, Jeremy R. — ThE6, ThE15
 Winker, David M. — ThE23
 Wintersteiner, Peter P. — ThE6, ThE15
 Wood, L. — WB5
 Wood, S. A. — WB5
 Woods, David C. — ThE23
 Woods, P. T. — TuD26

Yamaguchi, Satoshi — TuD23
 Young, S. A. — TuC3

Zander, R. — MA4, ThD5



Sponsored by
Optical Society of America

In Cooperation with
American Meteorological Society

OPTICAL REMOTE SENSING OF THE ATMOSPHERE POSTDEADLINE PAPERS

- PD1 **Progress in Development of a Tm:YAG Coherent Lidar for High Spatial and Velocity Resolution Wind Measurement**, Christian J. Grund, Madison J. Post, and Kin Pui Chan 473
- PD2 **Spectroscopy and Photochemistry of Nitrogen Dioxide and AB-Initio MRD-CI Study**, Carolina Godoy and Gabriel J. Vazquez 476
- PD3 **Measurements of Pinatubo Aerosols at Southern Midlatitudes**, M. R. Gross, T. J. McGee, U. N. Singh, R. L. McKenzie, and J. M. Rosen 479
- PD4 **Correlation Spectrometer Observations of SO₂, CO and OCS Emitted from Galeras Volcano, 9-10 January 1993**, A. Charland, W. H. Morrow, R. W. Nicholls, and John Stix 483
- PD5 **To What Extent Can Routine Ozone Lidar Measurements Provide a Representative Data Set in View of the Restricted Operation Time Due to Cloud Cover?** Hugo De Backer, Eric P. Visser, Dirk De Muer, and Daan P. J. Swart 487
- PD6 **Characteristics of Clear-Sky Upper Tropospheric Water Vapor Content Determined From SAGE II Observations**, Er-Woon Chiou, M. P. McCormick, and W. P. Chu 491
- PD7 **Temperature Structure of Midlatitude Mesopause Observed by a Narrowband Na Fluorescence Lidar**, C. Y. She, J. R. Yu, and H. Chen 495
- PD8 **Atmospheric Monitoring for Carbon Monoxide**, Dyan N. Seville-Jones, Ronald J. Martinez, Robert K. Sander, and Joe J. Tiee 498
- PD9 **AlGaAs Aerosol Lidar - Theory & Measurements**, James B. Abshire and Jonathan A. R. Rall 502
- PD10 **Spectral Calibration of the Improved Stratospheric and Mesospheric Sounder**, P. E. Morris, F. W. Taylor, and J. Ballard 506
- PD11 **A Mobile Remote Sensing Laboratory for Water Vapor, Trace Gas, Aerosol, and Wind Speed Measurements**, Dennis Slaughter, William White, William Tulloch, and Daniel DeSlover 510

PD12 Techniques Used for Simultaneous 1.064um and 2.036um Airborne LIDAR Utilizing an Optical Parametric Oscillator, J. Bryan Blair, Robert S. Afzal, and James D. Spinhirne514
PD13 A Technique for Measuring Winds in the Lower Atmosphere Using Incoherent Doppler Lidar, Daniel H. DeSlover, Dennis R. Slaughter, William M. Tulloch, and William E. White517
Postdeadline Author Index521

Progress in Development of a Tm:YAG Coherent Lidar for High Spatial and Velocity Resolution

Wind Measurement

Christian J. Grund, Madison J. Post, and Kin Pui Chan

NOAA/ERL Wave Propagation Laboratory

325 Broadway, Boulder, CO 80303

(303) 497 - 6870

I. Introduction and Background

The changing thermodynamic and chemical properties of the atmosphere are largely controlled by the exchange of heat, moisture, and momentum within the land and ocean boundary layers. Understanding anthropogenic impacts on air quality and the climate requires knowledge of the sources, sinks, and turbulent exchange processes for pollutants and greenhouse gases. Present knowledge of these processes largely depends on flux measurements acquired using in situ sensors on aircraft, towers, and tethered balloons, or by radar, sodar, and lidar remote sensors. Large eddy simulation models (Moeng and Wyngaard, 1988) have added significantly to current understanding of these turbulent exchange processes, but significant improvements in the spatial, temporal, and velocity resolution of current measurement capabilities for wind and concentration fluctuations are needed to provide adequate data sets from which improved theories and models of turbulent transfer can be developed and verified. Remote measurement instruments with sufficient resolution would enable flux measurements by eddy correlation techniques, satisfying these needs.

To meet the temporal, spatial, and velocity accuracy requirements for observing boundary layer turbulence fields, the NOAA Wave Propagation Laboratory has designed and is constructing a coherent Doppler lidar based on a CW diode-pumped, injection seeded Tm:YAG laser operating at $\sim 2.02 \mu\text{m}$. In addition to turbulence measurements, we are planning to run this system alongside the NOAA ozone DIAL (Differential Absorption Lidar) system (Zhao, et al., 1992) and a CO_2 coherent Doppler system (Pearson, 1992) modified to measure water vapor by DIAL technique. Water vapor DIAL operation of the $2 \mu\text{m}$ system is feasible and is being considered as a future option.

II. Design considerations

Details of the design of the system and design tradeoffs have been considered in detail elsewhere (Grund and Post, 1992). Briefly, the operating wavelength was chosen because the Doppler frequency shift, Δf_{Dop} , for a given wind velocity, V , is inversely proportional to the laser wavelength ($\Delta f_{\text{Dop}} = 2V / \lambda$), while the Fourier transform width of a fixed pulse length, τ_p , is constant with wavelength ($\Delta f_p = 1 / 2\pi\tau_p$), suggesting that operation at shorter wavelengths improves velocity estimates for a given range resolution (providing the outgoing pulse frequency is known). Eye-safe wavelength operation is required to allow unrestricted scanning in the vicinity of aircraft suggesting operation at wavelengths longer than $1.4 \mu\text{m}$. Also, at shorter wavelengths, background skylight can pose some additional noise problems, and loss of coherence in the beam due to propagation through

moderate turbulence would cause severe reductions in signal-to-noise ratio under average boundary layer conditions. Operation in the 1.5-1.7 μm or 2.0 -2.3 μm wavelength regions minimizes atmospheric absorption and improves maximum range.

To provide good spatial resolution during volume sector scans while allowing profiles to be averaged to reduce speckle noise requires a relatively high laser repetition rate. Thus, CW diode-pumping and acousto-optic Q-switched operation were chosen for the laser transmitter. This approach also minimizes the cooling requirements on the laser crystal and the thermal lensing and birefringence effects on the laser cavity. A large cooling water demand could cause troublesome cavity vibration leading to frequency jitter.

The power oscillator is injection-seeded to provide the narrow bandwidth and frequency stability needed to implement coherent detection in the receiver. Injection-seeded, Q-switched lasers and transmitters for coherent lidar systems using Tm:YAG and similar materials have been demonstrated (Kane et al., 1990; Henderson et al., 1991). Injection seeding was chosen over a master-oscillator power-amplifier design because diode-pumped Tm:YAG is a relatively low gain system making, amplifier design difficult.

Tm:YAG is preferred over Tm,Ho:YAG primarily because the latter system requires significant cooling to achieve good efficiencies. Room temperature operation is an important consideration for field operation in the presence of high-humidity and other adverse environmental conditions.

Details of the design of the system will be given in our talk at the Optical Remote Sensing Meeting.

III. Specification goals

Radial velocity measurement range	$\leq 1 \text{ cm s}^{-1}$ to $\geq 50 \text{ m s}^{-1}$
Velocity measurement accuracy	$\pm 0.5 \text{ cm s}^{-1}$ (averaging applied)
Measurement range	$\geq 10 \text{ km}$
Range resolution	$\leq 30 \text{ m}$
Pulse repetition frequency	100-300 Hz
Operating wavelength	2.0218 μm , Th:YAG
Transmitted pulse energy	10-20 mJ

In addition to the turbulence measurement capabilities of this system, the lower extreme for wind speed measurements will allow direct observations of synoptic-scale subsidence and divergence from aerosol backscatter in relatively clear air and ice crystal fall speeds in cirrus. With the anticipated frequency-purity and stability of this system, we expect to achieve the specified velocity resolution by incoherent accumulation (~ 625 profiles or $\sim 3.2 \text{ s}$ at 200 Hz, and 0 dB wide-band SNR per shot; see Rye and Hardesty (1992) for estimation procedure). The GL HITRAN database suggests that the required atmospheric transparency can be reached at 2.0218 μm , and potential future DIAL operations can be conducted near the water vapor line at 2.02165 μm . The operational wavelength is set and maintained with a commercial Michelson interferometer-based wavemeter.

IV. Current Status

Because a laser transmitter meeting our specifications has not yet been demonstrated, budgetary considerations required us to develop the power oscillator in-house, while obtaining from private vendors the reference oscillator/seed laser and diode laser pump assemblies built to meet our specifications. Procurement and testing of all major and most minor components is now complete and

development has begun on the power oscillator. At this time, the thermoelectrically cooled laser head and pump light fiber-to-rod coupling assemblies have been completed and substantial small-signal gain has been observed. With 10 W of pump power at 785 nm entering each end of the 13-mm-long Th:YAG rod, the current configuration results in ~ 1 m focal length intracavity thermal lensing effect. The power oscillator resonant cavity is under construction and CW operation is expected at any time. Q-switched and seeded operation is anticipated in the near future and a demonstration of a preliminary version of the lidar system is planned for within the next few months.

Acknowledgements

This work is jointly supported by NOAA internal funds and Army Research Office contract no. ARO117-92. K.P. Chan is supported by a National Research Council Senior Research Associateship.

References

- Grund, C.J., and M.J. Post, "Design of a near-IR coherent lidar for high spatial and velocity resolution wind measurement", Proc. 16th International Laser Radar Conference, NASA Conf. Pub. CP-3158, part 2, 405 - 408 (1992).
- Henderson, S.W., C.P. Hale, J.R. Magee, M.J. Kavaya, and A.V. Huffaker, "Eye-safe coherent laser radar system at $2.1 \mu\text{m}$ using Th:Ho:YAG lasers," *Opt. Lett.* 16, 39-44 (1991).
- Kane, T.J., T.S. Kubo, and R.W. Wallace, "Diode-pumped Eye-Safe Coherent Laser Transmitter," Final Report, Geophysics Lab. GL-TR-90-0316 (GL/OPA, Hanscom AFB, MA 01731), 56 pp (1990).
- Moeng, C.H., and J.C. Wyngaard, "Spectral analysis of large-eddy simulations of the convective boundary layer," *J. Atmos. Sci.* 45, 3573-3587 (1988).
- Pearson, G.N., "A pulsed CO_2 Doppler lidar for boundary layer monitoring", Proc. 16th International Laser Radar Conference, NASA Conf. Pub. CP-3158, part 2, 409-411 (1992).
- Rye, B.J., and R.M. Hardesty, "Incoherent accumulation and the Cramer-Rao lower bound for discrete spectral peak estimators in Doppler lidar," submitted to Jan. 1993 special issue *IEEE Trans. Geosci. Remote Sens.*
- Zhao, Y., J.N. Howell, and R.M. Hardesty, "Transportable lidar for the measurement of ozone concentration and flux profiles in the lower troposphere", Proc. 16th International Laser Radar Conference, NASA Conf. Pub. CP-3158, part 1, 185-187 (1992).

SPECTROSCOPY AND PHOTOCHEMISTRY OF NITROGEN DIOXIDE AN AB-INITIO MRD-CI STUDY

Carolina Godoy¹ and Gabriel J. Vázquez^{1,2}

¹ Instituto de Física, UNAM, Laboratorio Cuernavaca
AP-139 B, 62191 Morelos, MEXICO

² National Center for Atmospheric Research
Atmospheric Chemistry Division
P.O. Box 3000, Boulder, Colorado 80307, USA

The spectroscopy and photochemistry of nitrogen dioxide has been the subject of numerous experimental and theoretical studies; yet, these efforts have been little rewarding so far. Regarding the spectroscopy, the ground electronic state \tilde{X}^2A_1 is the only state which has been reasonably well characterized through EPR, ESR, LMR, MW and IR studies; equilibrium geometry, the three vibrational fundamentals, dipole moment, rotational constants, force and anharmonicity constants, and various others fine and hyperfine constants, are now known. Conversely, most of these data are unknown or controversial for the four lowest excited electronic states of NO₂, namely, \tilde{A}^2B_2 , \tilde{B}^2B_1 , \tilde{C}^2A_2 and $1^2\Sigma_g^+$, lying in the far-IR, visible and near-UV regions; it is particularly striking that even the equilibrium geometries and vibrational frequencies of these states are still being sought for. Perhaps the best known of the excited states is 2^2B_2 , which lies in the near-UV, for which equilibrium geometry, vibrational frequencies, rotational constants and T_0 are known. At higher energies, in the near-UV and VUV, there are various valence states: three quartets, 1^4A_2 , 1^4B_2 and 1^4A_1 , and a number of doublets; these states have been predicted theoretically, yet none of them has been observed so far. In addition, a number of fragments of Rydberg series have been observed in the VUV and EUV regions, but only few features have been assigned unambiguously.

The most studied spectral region spans from 10000 to 3200 Å, encompassing the far-IR, visible and near-UV. The spectrum in this region is extremely complex, i.e., consists of a great number of lines densely packed, with no regular pattern in the fine, rotational or vibrational structure. Most of the spectral features are still unassigned; only tiny pieces of the spectrum have lent themselves to spectroscopic examination. The following facts are at the origin of the complexity of the spectrum: 1) three excited states, \tilde{A} , \tilde{B} and \tilde{C} exist in

this region and overlap between themselves and with the ground state \tilde{X}^2A_1 ; 2) NO_2 possesses fine structure due to the spin $s=\frac{1}{2}$ of the unpaired electron, and hyperfine structure due to the nuclear spin $I=1$ of ^{14}N ; 3) there exists a Renner–Teller interaction between \tilde{X}^2A_1 and \tilde{B}^2B_1 , components of the linear $1^2\Pi_u$ state; 4) there exists a conical intersection between \tilde{X}^2A_1 and \tilde{A}^2B_2 along the bending coordinate; 5) in the Franck–Condon region, along the O–NO coordinate, \tilde{B} interacts with \tilde{A} and \tilde{C} , which might result in predissociation and diffusivity in the spectrum. Understandably, these effects could add up to strongly disrupt the rovibronic structure.

In the present contribution we report ab-initio MRD-CI electronic structure calculations on the NO_2 molecule. We have focused our attention on a relatively large number of low-lying excited states, whereby for the sake of computational feasibility some simplifications had to be made, e.g., cores of five and six MO's were chosen. All calculations were carried out in C_s symmetry. An extended basis set of DZ + POL quality augmented with s - and p -type Rydberg functions has been employed, together with an extensive treatment of electron correlation. We report cuts of the potential energy surfaces of the lowest ten doublet ($5^2A', 5^2A''$) and six quartet ($3^4A', 3^4A''$) states along the O–N–O bending and ON–O stretching coordinates. Dipole moments and oscillator strengths for transitions from the X^2A_1 ground state to the excited doublet states were calculated, for all states and geometries. The vertical excitation spectrum and related transition moment properties are given in Tables 1 and 2, respectively.

Table 1 Vertical excitation spectrum of NO_2^a

State	Occupation number								Excitation	T_v
C_{2v}	$3b_2$	$5a_1$	$1b_1$	$4b_2$	$1a_2$	$6a_1$	$2b_1$		C_{2v}	
C_s	$7a'$	$8a'$	$1a''$	$9a'$	$2a''$	$10a'$	$3a''$			
3^2A_1	2	2	1	2	2	1	1	$2b_1 \leftarrow 1b_1$		9.19
4^2B_2	2	2	2	2	1	1	1	$2b_1 \leftarrow 1a_2$		8.34 ^b
2^2B_1	2	2	1	2	2	2	0	$6a_1 \leftarrow 1b_1$		7.85
3^2B_2	1	2	2	2	2	2	0	$6a_1 \leftarrow 3b_2$		7.71 ^b
2^2A_1	2	1	2	2	2	2	0	$6a_1 \leftarrow 5a_1$		7.62
3^2A_2	2	2	2	1	2	1	1	$2b_1 \leftarrow 4b_2$		6.93
2^2B_2	2	2	2	2	1	1	1	$2b_1 \leftarrow 1a_2$		5.89
2^2A_2	2	2	2	1	2	1	1	$2b_1 \leftarrow 4b_2$		5.44
1^2A_2	2	2	2	2	1	2	0	$6a_1 \leftarrow 1a_2$		3.46
1^2B_2	2	2	2	1	2	2	0	$6a_1 \leftarrow 4b_2$		3.17
1^2B_1	2	2	2	2	2	0	1	$2b_1 \leftarrow 6a_1$		3.11
\tilde{X}^2A_1	2	2	2	2	2	1	0	—		0.00

^a Employing the MO's of 1^4B_2 ; ^b MO's of \tilde{X}^2A_1

Table 2 Transition moment properties of NO₂^a

State	μ (Debyes)	τ (μ s)	f
$5^2A'(4^2B_2)$	0.462	0.0013	0.2506
$5^2A''(2^2B_1)$	0.628	0.0583	0.0064
$4^2A'(3^2B_2)$	0.762	0.0154	0.0244
$4^2A''(3^2A_2)$	0.482	305.379	0.1458×10^{-5}
$3^2A'(2^2B_2)$	0.685	0.1209	0.0051
$3^2A''(2^2A_2)$	0.324	309.252	0.2252×10^{-5}
$2^2A''(1^2A_2)$	1.856	1055.76	0.1623×10^{-5}
$2^2A'(1^2B_2)$	1.420	0.1544	0.0128
$1^2A''(1^2B_1)$	1.252	1.340	0.0016
$\tilde{X}^2A'(X^2A_1)$	0.429	---	---

^a For transitions between \tilde{X}^2A_1 and the excited doublet states

The present ab-initio study provides a considerable amount of new information on the excited states, which is employed to discuss the spectroscopy and photochemistry of NO₂. In particular, the O-NO stretching curve shows the correlation of the molecular states to the first dissociation limits, thus shedding light on an issue which had been controversial for some time. The \tilde{A}^2B_2 state is found to be repulsive in this particular cut of the potential energy surfaces and to correlate to NO($\tilde{X}^2\Pi$) + O³P. Therefore, direct dissociation seems a viable photofragmentation mechanism of NO₂^{*}; yet, the curves also suggest alternative or competitive predissociation mechanisms as a result of interactions between \tilde{A} , \tilde{B} and \tilde{C} , right in the Frank-Condon region. The following topics, among others, are also addressed: the electronic excitation spectrum, the ground state dissociation energy and the "anomalous" fluorescence lifetime of NO₂^{*}.

MEASUREMENTS OF PINATUBO AEROSOLS AT SOUTHERN MIDLATITUDES

M.R. Gross¹, T.J. McGee², U.N. Singh¹, R.L. McKenzie³ and J.M. Rosen⁴

¹Hughes STX Corporation, Lanham, Maryland

²Laboratory for Atmospheres, NASA/Goddard Space Flight Center, Greenbelt, Maryland

³DSIR Physical Sciences, Lauder, Central Otago, New Zealand

⁴University of Wyoming, Department of Physics & Astronomy, Laramie, Wyoming

INTRODUCTION

NASA Goddard's Stratospheric Ozone Lidar Trailer Experiment (STROZ-LITE) was designed to utilize the DIAL (Differential Absorption Lidar) technique in measuring atmospheric ozone. After the 1991 eruption of Mt. Pinatubo, it became impossible to make accurate measurements of ozone in the region most contaminated by volcanic aerosols (10-30km). The system formally collected light returns at only the emitted laser wavelengths (308 and 351nm). It has since been modified so that the respective signals at 332 and 382nm produced by Raman scattering from nitrogen molecules could also be acquired. This was done so that ozone could be calculated in the aerosol affected region of the atmosphere. Using the same DIAL scheme, but now with the Raman channels at 332nm and 382nm as the on and off-line wavelengths, an accurate ozone measurement can be made between 10 and 30km (McGee et. al, 1992). In making these modifications, a measure of atmospheric aerosol backscatter can be obtained quite simply. With careful normalization, the ratio of 351 to 382nm return signal can directly give the 351nm aerosol scattering ratio (ASR), defined as the Rayleigh plus Mie backscatter divided by only Rayleigh backscatter, since the 351nm signal contains components of both aerosol and molecular backscatter while the 382nm signal contains only molecular backscatter from nitrogen. Whiteman et. al. (1992) describes this procedure in greater detail. With available ancillary atmospheric pressure and temperature data, an Aerosol Volume Backscatter Cross Section profile at 351nm can be quickly calculated from ASR profiles since the Rayleigh cross section at 351nm is well known. The STROZ-LITE system is also now able to determine a measure of aerosol extinction from the 382nm channel. Transmission at this wavelength contains a term for the sum of 351nm plus 382nm aerosol extinction, which can be solved for directly. By assuming a reasonable wavelength dependence, aerosol extinction profiles at 351nm can be computed.

OBSERVATIONS

From October 31, 1992 through December 14, 1992, the STROZ-LITE system was deployed in Lauder, NZ (45.05S, 169.68E) in conjunction with a joint UARS (Upper Atmosphere Research Satellite) and NDSC (Network for the Detection of Stratospheric Change) sponsored Intercomparison Campaign. Eighteen nights of cloud free data were collected during that time. On the night of November 24-

Figure 1: Aerosol Scattering Ratio for 351 nm Lidar Measurements and 480nm,940nm Backscatter Sonde Data for November 24,1992 in Lauder, NZ (45.0S,169.7E).

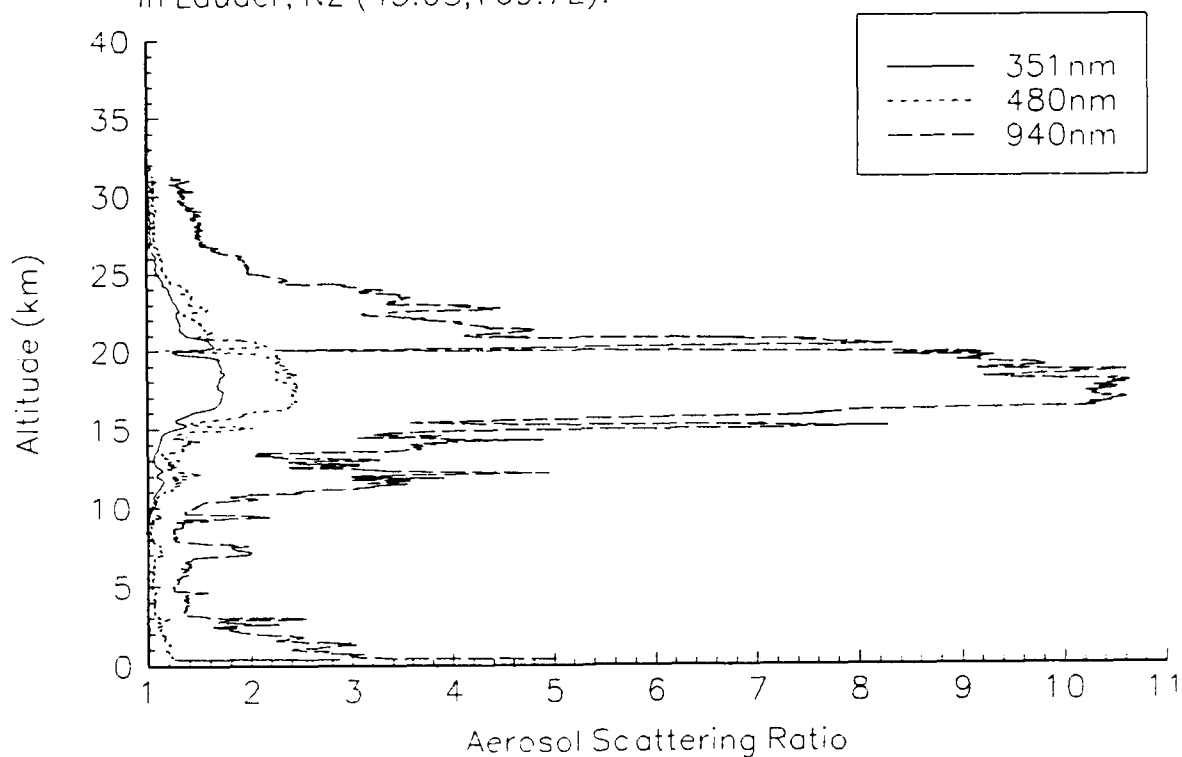


Figure 2: 351 nm Lidar Derived Aerosol Backscatter Profiles for November 1992 in Lauder, NZ (45.0S,169.7E).

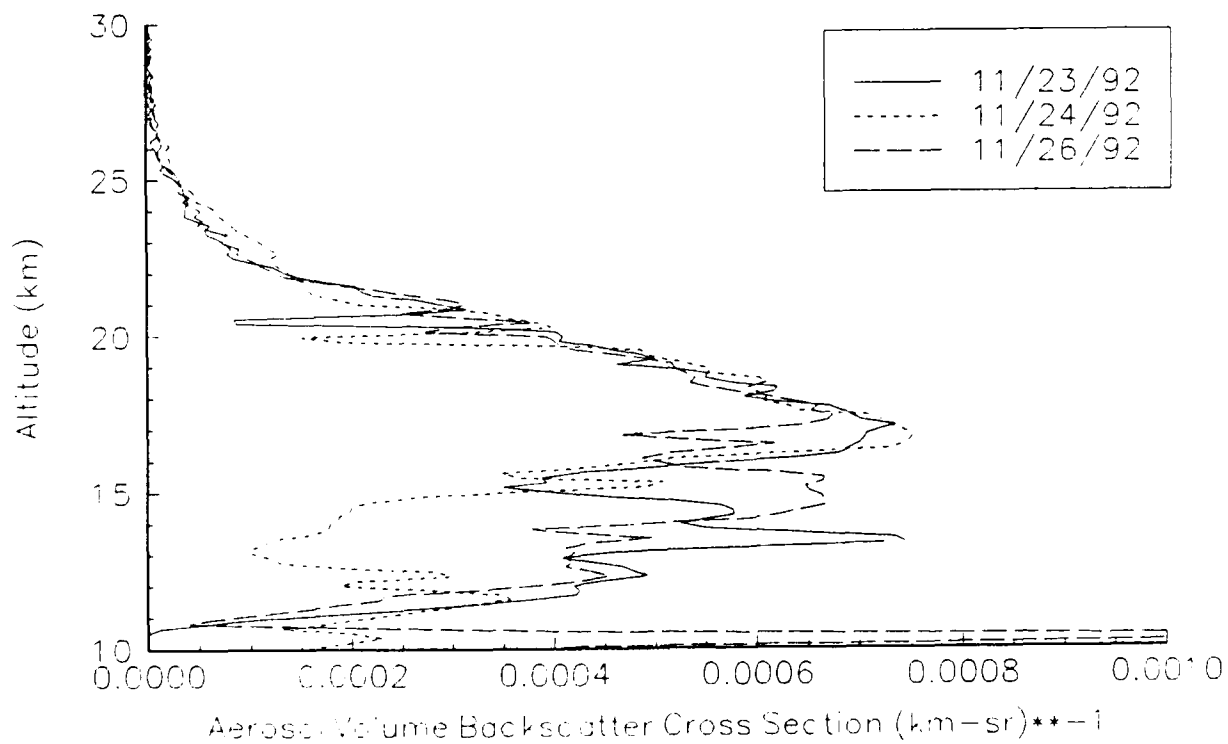


Figure 3: 351 nm Lidar Derived Aerosol Extinction Profiles for November 1992 in Lauder, NZ (45.0S,169.7E).

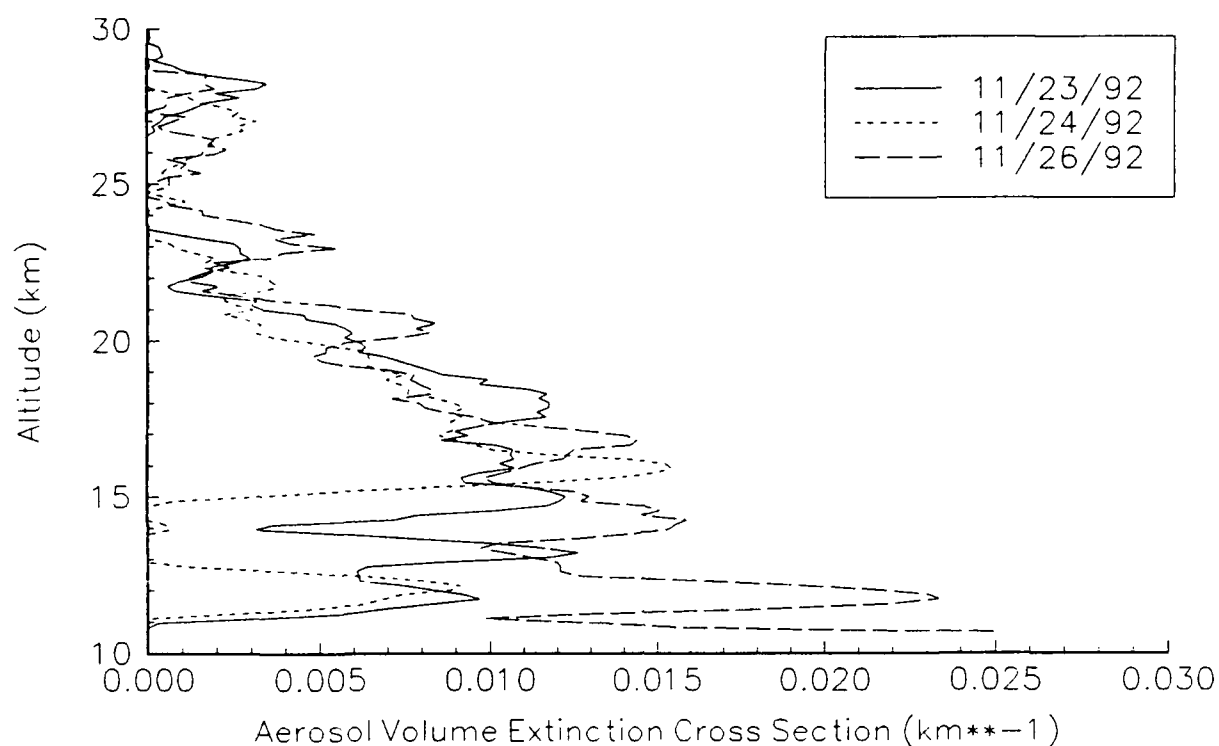
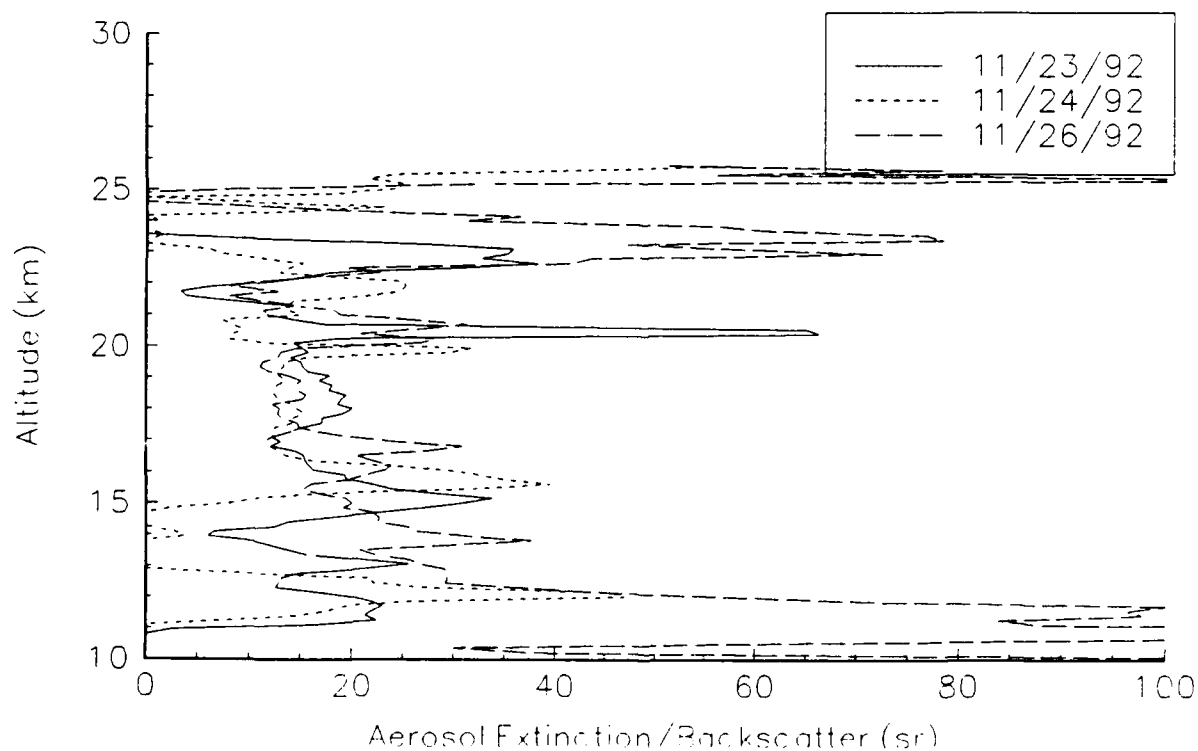


Figure 4: 351 nm Lidar Derived Aerosol Extinction/Backscatter Ratio Profiles for November 1992 in Lauder, NZ (45.0S,169.7E).



25, the GSFC Lidar acquired nearly 5 hours (11:30PM-4:30AM NST) of atmospheric data. At approximately 9:00PM NST on November 24, a balloon borne backscatter instrument (*Rosen and Kjome, 1991*) was released from the Lauder site. This instrument measures aerosol scattering information at both 940nm and 480nm from the ground to approximately 30km. A comparison of ASR at the three available wavelengths for November 24th is shown in figure 1. Lidar system constraints limit the collection of 351nm data below approximately 10km thus restricting the lidar ASR profile to heights above 10km. Good agreement is seen between all three profiles, especially at the feature near 20km. A dynamical study of this night is continuing. Assuming Rayleigh scattering scales as $\lambda^{-4.0}$, the ASR wavelength dependence between 351nm and 470nm is approximately $\lambda^{-2.0}$ near the aerosol peak. The lidar derived Aerosol Volume Backscatter Cross Section profile for the 24th is shown in figure 2 along with profiles from November 23 and 26. Figure 3 and 4 show respectively the Aerosol Volume Extinction Cross Section and the Aerosol Extinction/Backscatter Ratio profiles for these same days. An aerosol extinction wavelength dependence of $\lambda^{-0.6}$ was used to derive extinction at 351nm. (*Ferrare et. al., 1992.*)

CONCLUSION

The modified NASA Goddard STROZ-LITE system was deployed for nearly two months in Lauder, NZ. Nighttime stratospheric aerosol information was gathered when weather permitted lidar operation. Aerosol scattering ratio information at three wavelengths (351nm, 480nm and 940nm) was obtained on November 24 from both the lidar system and from a balloon borne backscattersonde instrument. Lidar derived aerosol extinction, aerosol backscatter and aerosol extinction/backscatter ratio profiles are reported for three days in November, 1992.

REFERENCES

- Ferrare, R.A., S.H. Melfi, D.N. Whiteman, and K.D. Evans, Raman Lidar Measurements of Pinatubo Aerosols over Southeastern Kansas During November-December 1991, *Geophysical Research Letters*, 19, No. 15, 1599-1602, 1992.
- McGee, T.J., M.R. Gross, U.N. Singh, R.A. Ferrare, and W.P. Heaps, Raman Lidar Measurements of Stratospheric Ozone in the Presence of Volcanic Aerosols, submitted to *Geophysical Research Letters*, November 1992.
- Rosen, M.R., and N.T. Kjome, Backscattersonde: a new instrument for atmospheric aerosol research, *Applied Optics*, 30, No. 12, 1552-1561, 1991.
- Whiteman, D.N., S.H., Melfi, and R.A. Ferrare, Raman lidar system for the measurement of water vapor and aerosols in the earth's atmosphere, *Applied Optics*, 31, No. 16, 3068-3082, 1992.

Correlation Spectrometer Observations of SO₂, CO and OCS Emitted from
Galeras Volcano, 9-10 January 1993

A. Charland
Dept. of Earth and Planetary Sciences
McGill University
3450 University Street
Montreal, QC
H3A 2A7, Canada
514 398 6767

W. H. Morrow
Resonance Ltd.
171 Dufferin St. S.
Unit 7
Alliston, Ontario
L0L 1L0, Canada
705 435 2577

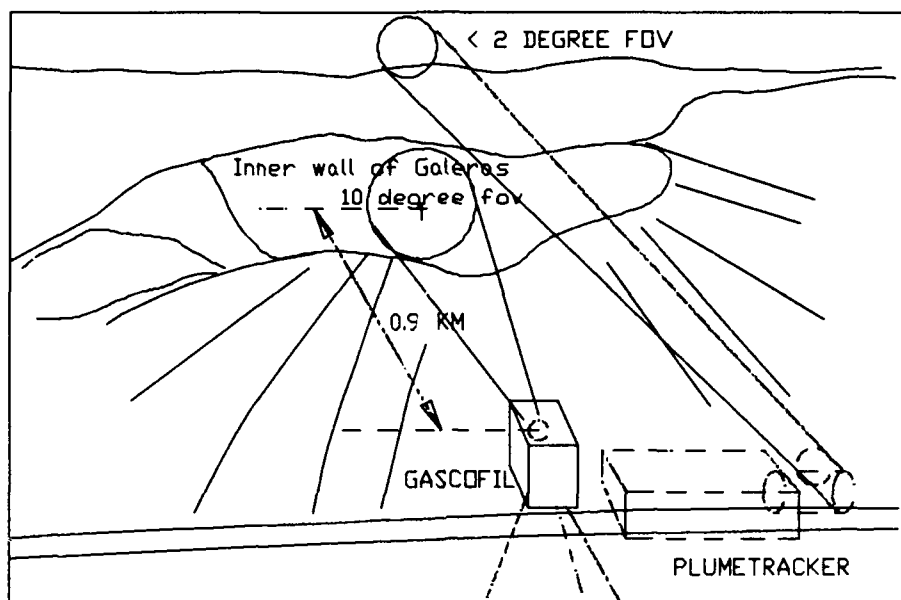
R. W. Nicholls
Centre for Research in Earth and Space Science
York University
4700 Keele Street
Downsview, Ontario
M3J 1P3, Canada
416 736 5247

John Stix
Département de géologie
Université de Montréal
Montréal QC
H3C 3J7, Canada
514 343 6832

This paper describes remote sensing measurements of gasses emitted by Galeras volcano in the Colombian Andes prior to its eruption on 14 January 1993. In all, approximately eight hours of observations were made on 9-10 January in the UV and thermal IR. SO₂ was observed with a dispersive correlation spectrometer (Plumetracker) operating at 310 nm. OCS and CO were observed with a non-dispersive correlation spectrometer (GASCOFIL) operating at 4.8 microns. Preliminary analysis indicates SO₂ levels of the order of 100 ppm-m just above the volcano, CO levels of 150 ppm-m and OCS of 6 ppm-m inside the inner cone of the volcano.

Two correlation spectrometers, GASCOFIL and Plumetracker were used for this field study.

Figure 1 shows the geometry of the observations.



GASCOFIL has been described in a previous paper (Morrow and Nicholls, 1990) so only a brief description appears below. Light from the atmospheric target is collected by a telescope and directed through the gas cell chopper. The transmitted light from the chopper is sent through an interference filter and focused onto a detector. The analogue time dependent detector signal is amplified by a preamplifier and sampled by a 12 bit A to D converter attached to a microcomputer data buss. After processing by the microcomputer the signals were relayed to a notebook computer via a 9600 baud serial link. The data was saved to an ascii file and later reduced with Quattro 4.0.

For the Galeras observations GASCOFIL was outfitted with a 50 torr pure OCS gas cell, a 450 torr pure CO cell, and two reference clear cells, all with MgF2 windows. A spectral band that included both CO and OCS absorption was selected with an interference filter centered at 4.8 microns with 0.11 micron FWHM. A thermoelectrically cooled lead selenide detector operated at 250 K was used to detect the incoming IR radiation. In order to average out the thermal variations in the field of view the sensor was operated without its cassegrain telescope giving it a 10 degree cone angle.

GASCOFIL produces a signal S for each of the four cells of the wheel, two clear and two gas cells. The concentration path of the target gas in the path of the sensor was found by processing the data with the following algorithm:

$$pl = pl_{cal} \frac{1 - k \frac{S_{clear}}{S_{gas}}}{(1 - k \frac{S_{clear}}{S_{gas}})_{cal}}$$

Where:

pl = The "concentration path" of the target gas remotely sensed in the field of view of the sensor in ppm-m.

k = A normalizing constant that forces the numerator to zero when there is no target gas in the field of view of the sensor. k is determined by placing reference black bodies in the field of view of the sensor.

The numerator represents the "correlation signal" from the target gas in the field of view of the sensor and the denominator represents the "correlation signal" from a calibration gas cell placed in the field of view of the sensor.

Plumetracker is an Ebert spectrometer with a rotating mask chopper that modulates the light signal between two slit apertures, one on a peak and one on a valley of the SO₂ absorption spectrum in the 300 to 340 nm region. The output consists of two signals ΔS and S which are the differences between the slit signals and the difference between one slit signal and no light, respectively. By taking the ratio of ΔS to S the signal can be corrected for variations in the light intensity not caused by SO₂ absorption. The system is calibrated by the inclusion of a 1 cm thick 900 ppm-m quartz SO₂ filled gas cell in the optical path. Zero was found by frequently scanning from side to side of the volcanic plume.

The concentration path of the target gas in the path of the sensor was found by processing the data with the following algorithm:

$$pl = pl_{cal} \frac{\frac{\Delta S}{S}}{\frac{\Delta S}{S}_{cal}}$$

Where:

pl = The "concentration path" of the target gas remotely sensed in the field of view of the sensor in ppm-m.

Average column densities of 100 ± 20 ppm-m SO₂, 155 ± 40 ppm-m CO (with atmospheric component removed) and 6 ± 2 ppm-m of OCS were observed over a 0.9 km path extending into the actively outgassing volcanic crater. Since these were the first GASCOFIL measurements made inside a volcanic crater no baseline data were available. However, the OCS/CO ratio of 0.039 ± 0.023 at Galeras is the same order of magnitude as that from fumaroles at Augustine volcano (0.15) (Symonds et al., 1992). Both ratios were measured during periods of passive outgassing. The higher OCS/CO ratio at Augustine may be caused by hotter fumaroles there (870 C) than at Galeras (200-600 C) (cf. Belviso et al., 1986). On the other hand, OCS/CO ratios at Galeras and Augustine during times of passive outgassing are higher than those at Mt. St. Helens and Soufriere (St. Vincent) during explosive eruptions (Cronn and Nutmagul, 1982a; 1982b). This difference may result from OCS being absorbed on ash during eruptions and thus its removal from the gas phase (Rasmussen et al., 1982).

References:

Belviso, S., Nguyen, B.C., and Allard, P., 1986. Estimate of carbonyl sulfide (OCS) volcanic source strength deduced from OCS/CO₂ ratios in volcanic gases. *Geophys. Res. Lett.*, 13: 133-136.

Cronn, D.R., and Nutmagul, W., 1982a. Characterization of trace gases in 1980 volcanic plumes of Mt. St. Helens. *J. Geophys. Res.*, 87: 11153-11160.

Cronn, D.R., and Nutmagul, W., 1982b. Volcanic gases in the April 1979 Soufriere eruption. *Science*, 216: 1121-1123.

Morrow, W.H., and Nicholls, R.W., 1990. Some recent measurements of CO overburden and forest fire emissions with gas filter correlation spectrometers, Gascofil and Gascoscan. *Optical Remote Sensing of the Atmosphere, 1990 Technical Digest Series*, 4: 332-335.

Rasmussen, R.A., Khalil, M.A.K., Dalluge, R.W., Pewnnett, S.A., and Jones, B., 1982. Carbonyl sulfide and carbon disulfide from the eruptions of Mount St. Helens. *Science*, 215: 665-667.

Symonds, R.B., Reed, M.H., and Rose, W.I., 1992. Origin, speciation, and fluxes of trace-element gases at Augustine volcano, Alaska: Insights into magma degassing and fumarolic processes. *Geochim. Cosmochim. Acta*, 56: 633-657.

To what extent can routine ozone lidar measurements provide a representative data set in view of the restricted operation time due to cloud cover?

Hugo De Backer, Eric P. Visser*, Dirk De Muer, and Daan P.J. Swart*

Royal Meteorological Institute (KMI), Ringlaan 3, 1180 Brussels, Belgium. Tel: (32) 2 3730594, Fax: (32) 2 3751259, e-mail: hugo@meteo.oma.be

**National Institute for Public Health and Environmental Protection (RIVM), Laboratory for Air Research, P.O. Box 1, 3720 BA Bilthoven, the Netherlands. Tel: (31) 30 742678, Fax: (31) 30 287531, e-mail: ericv@rivm.nl*

INTRODUCTION

For a proper understanding of long term trends in atmospheric ozone concentrations, the availability of high quality data sets is of great importance. At present, total ozone column densities are routinely measured by the ground based Dobson, Brewer and M-83/124 filter ozonometer networks, as well as by satellite based instruments such as the Total Ozone Mapping Spectrometer (TOMS). Vertical concentration profiles are obtained by ground based Umkehr methods, balloon borne electrochemical ozone sondes and by satellite based limb path atmospheric extinction measurements, such as the Stratospheric Aerosol and Gas Experiments (SAGE I/II).

In addition to these techniques, a global ozone lidar network would be of high value. Whereas the frequency of balloon borne ozone soundings is restricted to, typically, several soundings per week, lidar measurements can in principle be carried out continuously. Compared to satellite based instruments, a lidar network has the advantage of state of the art technology and continuous re-calibrations. Initiatives have been taken for routine ozone lidar networks: Stratospheric systems are currently being developed in the context of the Network for the Detection of Stratospheric Change (NDSC). In Europe, several tropospheric lidar groups are cooperating in the Tropospheric Environmental Studies by Laser Atmospheric Sounding (TESLAS) project.

The frequency at which ozone profiles will be available depends on the specific lidar system performance and the vertical resolution required. Typical acquisition times t_a range from 5 to 15 min for tropospheric profiles, and from 2 to 6 h for stratospheric ones. Care should be taken, however, with regard to the representativity of future lidar ozone data bases. Since lidar profiles can only be obtained without precipitation and fog, and are truncated at the cloud base, a meteorological bias could be introduced. In the present work, this problem is studied by statistical analyses on the long term data set of ozone profiles above Uccle (50°48' N, 4°21' E) measured by balloon borne electrochemical ozone sondes. We investigate the possible differences in ozone profiles for soundings with varying degree of cloud cover. The results are interpreted in terms of requirements to lidar systems for routine ozone monitoring.

THE OZONE SOUNDING DATA SET OF UCCLE

At the Meteorological Institute of Belgium, routine ozone soundings started in January 1969. In the present study, 2728 soundings until December 1992 were used. Normally soundings are performed three times a week, with launch times between 8 and 12 UT. Throughout the whole period the Brewer-Mast sonde [1] was used. All ozone values of a certain profile were multiplied by a correction factor in order to bring the vertically integrated ozone amount to the same value as the total ozone column density measured with the Dobson spectrophotometer 40, located at Uccle. The ozone values of this Dobson instrument were re-evaluated and corrected for SO₂ interference [2].

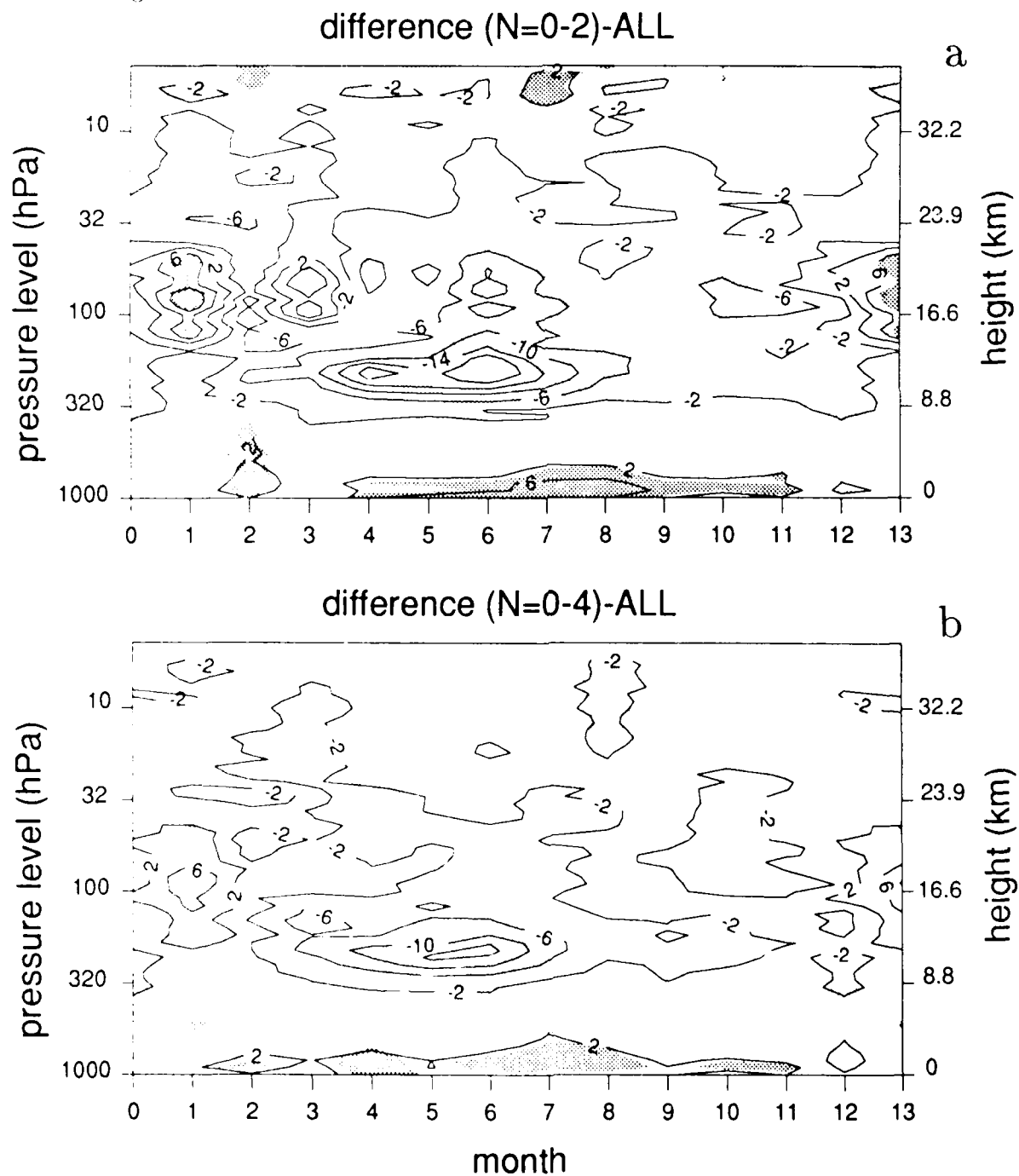
STATISTICAL ANALYSIS

The synoptic data base of Uccle (WMO station 06447) was used to retrieve the amount of cloud cover corresponding to each individual ozone sounding. The cloud data can be used to obtain the subset of the total ozone sounding data set for which lidar measurements *could* have been performed,

i.e. the "lidar subset". The aim of our study is to analyze to what extent this "lidar subset" contains statistically significant differences as compared to the total set of ozone soundings.

The problem is to exactly define the subdivision of the ozone sounding data set into the lidar subset and the non-lidar subset. The most straightforward procedure would be to define the lidar subset as consisting of soundings with clear sky conditions. However, a certain amount of cloud cover is still acceptable, since the lidar can "shoot in between the clouds". In order to correlate the cloud cover N (expressed in octa's) to the available acquisition time t during a period t_0 , we assume that $t = t_0 \times (1 - N/8)$. This will of course not be true for every individual case, but it seems likely to hold when averaging large numbers of observations.

In the statistical analysis, several lidar subsets are chosen with increasing amount of cloud cover. We compare the characteristics of the data sets with $N = 0 - 2$ (746 soundings = 27%), $N = 0 - 4$ (1137 soundings = 42%) and $N = 0 - 6$ (1753 soundings = 64%) to the complete data set comprising all soundings.



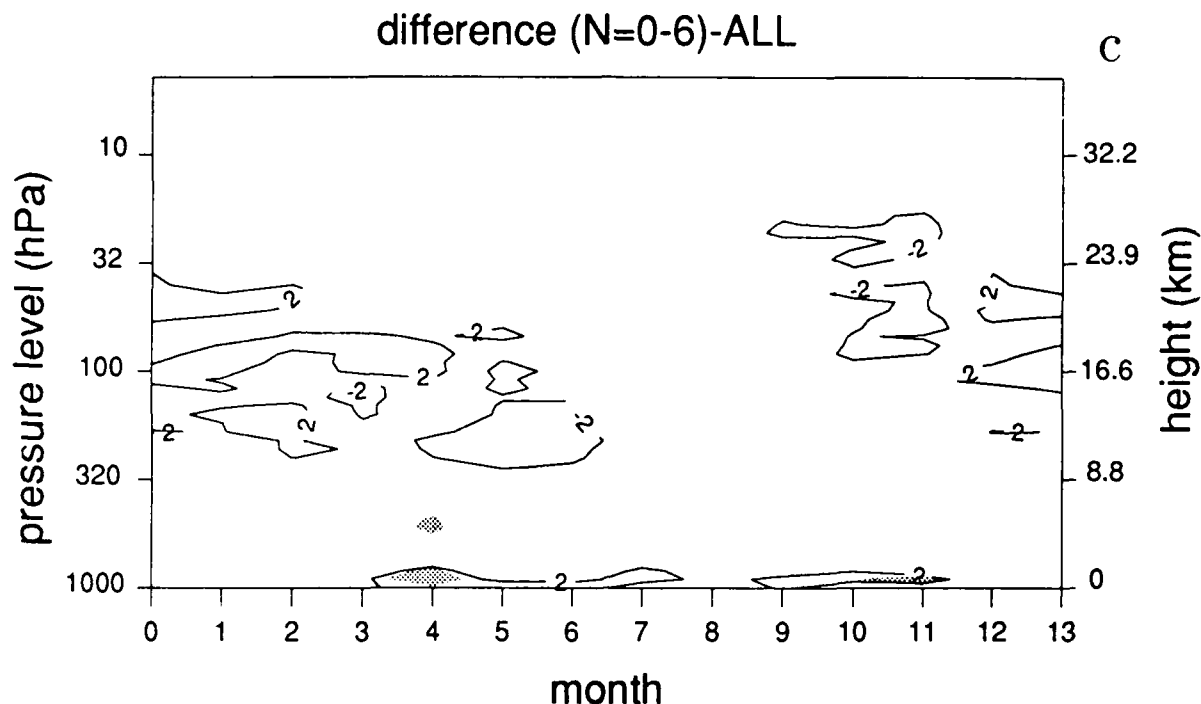


Figure 1. Differences in ozone partial pressure (in nbar) between 3 selected subsets with increasing cloud cover and the complete group of soundings as a function of month and altitude. The horizontal axis shows the months 1-12, where 0 (December) and 13 (January) have been added to obtain cyclic boundary conditions. The dark gray shade indicates regions with significant positive deviations from zero, and the light gray shade corresponds to significant negative deviations. (a) Differences between subset with cloud cover $N = 0 - 2$ and total set; (b) $N = 0 - 4$; (c) $N = 0 - 6$.

RESULTS AND DISCUSSION

Figures 1a-1c show the differences in ozone partial pressure between the 3 selected groups of soundings and the complete set. The values are given as a function of month and altitude. In these figures, the zones where the null hypothesis of equal means is rejected at the 95% confidence level by a two tailed Student's *t*-test are shaded. As expected, we note that the differences become smaller and less significant when more clouds are allowed. If observations with cloud cover up to 6/8 are included (fig. 1c), we find no statistically significant differences any more.

The main features of fig. 1a can be explained as follows. There are two important zones of differences. First, the higher ozone values at low altitudes during the summer months on clear days obviously can be attributed to photochemical production in the boundary layer. Second, there is a zone with lower ozone concentrations on clear days near the tropopause level and the lower stratosphere during spring and summer. This may be explained by the fact that in this period, clear days are more associated with (sub)tropical air masses. These have a higher tropopause, and lower stratospheric temperatures and ozone concentrations. This is further illustrated in fig. 2, which shows the average temperature and ozone profiles for June of the total data set and the set with $N = 0 - 2$. During the winter months the behavior is different and no clear picture is seen.

CONCLUSIONS

Translated to lidar observations it may be concluded that in order to have a good sampling of the tropopause level and the lower stratosphere, especially during summer, routine observations up to at least 6 octa's of cloud cover are required. The same conclusion emerges for the lower troposphere.

Here the requirement is perhaps somewhat less stringent because even with 8/8 clouds the lidar can measure from the ground up to the cloud base.

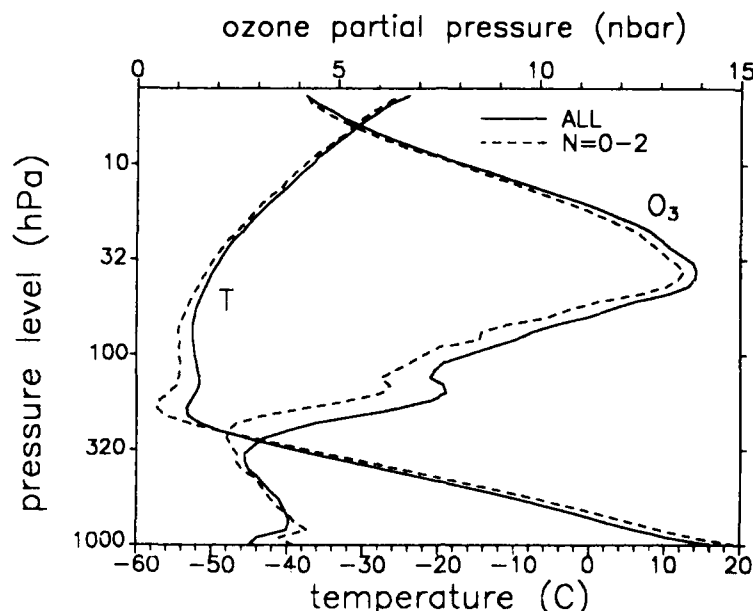


Figure 2. Average temperature and ozone profile for June for clear days ($N = 0 - 2$, dashed lines) and for the total data set (solid lines).

Implications for tropospheric lidar systems.

Given the typical characteristics of tropospheric ozone lidars, these systems would be suitable to provide hourly profiles on a 24 hour basis. This requires that for each valid profile, there should exist t_a minutes within the specific hour during which the zenith is cloudless. In view of our previous assumption, this would allow (on the average) a cloud cover of $N = 8 \times (1 - t_a/60)$ (t_a in min). For measurements still being possible at cloud cover of $N = 6$, the allowable acquisition time equals $t_a = 15$ min. Thus a tropospheric lidar system, able to provide hourly ozone profiles on a routine basis, should have an acquisition time not exceeding 15 min. Strictly speaking, this can only be concluded for a lidar facility located at Uccle. For stations with different climatology, separate studies should be done with regard to the representativity of lidar data bases.

Implications for stratospheric lidar systems.

Stratospheric lidar systems differ from tropospheric ones in the sense that their acquisition times are longer and they usually operate at nighttime. Therefore, the idea of supplying hourly ozone profiles reflecting a diurnal cycle is not well applicable to these systems. A more appropriate objective seems to provide one single profile during each night with long enough cloudless periods. So a routine stratospheric system typically monitors annual or longer cycles of ozone profiles.

In figs. 1a-1c it is seen that the differences in ozone concentrations in the stratosphere (except for the lower part just above the tropopause) are smaller than those in the two regions discussed before. However, in fig. 1a there are still significant deviations up to several nbars in regions well above the tropopause. If these differences cannot be tolerated, then also for stratospheric lidar systems routine sampling at cloud cover up to $N = 6$ should be required. However, in view of the long acquisition time and the restriction of nighttime operation, this could imply that stratospheric lidar facilities at typical West European lowland sites will not be able to provide non-biased data bases of ozone profiles.

REFERENCES

- [1.] A.W. Brewer and I.R. Milford, Proc. R. Soc. London, Ser. A, 256, 470-495, 1960
- [2.] D. De Muer and H. De Backer, J. Geophys. Res. 97, no D5, 5921-5937, April 20, 1992

CHARACTERISTICS OF CLEAR-SKY UPPER TROPOSPHERIC WATER VAPOR CONTENT DETERMINED FROM SAGE II OBSERVATIONS

Er-Woon Chiou
Science Applications International Corp. (SAIC)
Hampton, VA 23666

M.P. McCormick and W.P. Chu
NASA Langley Research Center
Hampton, VA 23681-0001

1. INTRODUCTION

Water vapor is one of the most important components of the atmosphere and is a key factor in shaping weather and climate. The demand for better water vapor measurements, especially in the upper troposphere, was pointed out by London (1957). With the increasing concern over the role of water vapor feedback in global warming, the need for a global water vapor data set with higher vertical resolution has become more acute (Arking, 1990).

It has long been recognized that the present upper air sounding network (radiosonde) has several shortcomings: (1) inadequate coverage, especially over ocean; (2) inadequate vertical resolution in the middle troposphere; (3) almost no data in the upper troposphere; (4) variation in sensor type, calibration, and data analysis leading to regional differences and further uncertainty in data quality. Satellite water vapor measurements provided by current operational sounding systems (for example, NOAA/TOVS, GOES/VAS) are still quite limited in vertical resolution because of the use of only a few relatively broadband infrared channels. Thus, it was strongly recommended that the efforts to construct a vertically-resolved (1 km) global climatology of water vapor in the upper troposphere based on solar occultation measurements from SAGE-II (and the planned HALOE and SAGE-III instruments) be continued (Starr and Melfi, 1990). The lack of other accurate moisture information at these climatically sensitive altitudes places a very high priority on continuing to examine the characteristics of upper tropospheric moisture content derived from SAGE-II observations.

The purpose of this paper is to discuss the seasonal and latitudinal variability of clear-sky upper

tropospheric moisture content through examination of relative humidity between 500mb and 100mb, and upper tropospheric integrated columnar water vapor content (for 500-100mb layer and 300-100mb layer) derived from SAGE-II water vapor data set. Comparisons with the corresponding information obtained from HIRS/MSU retrieval (Susskind et al., 1993), GOES 6.7 μm -derived relative humidity (Soden et al., 1993), and ISCCP C1 water vapor burden (Darnell et al., 1992) are presented to illustrate the complementary nature of various satellite remote sensing techniques.

2. RESULTS AND DISCUSSIONS

Four years (1986-89) of SAGE II water vapor data were archived at the National Space Science Data Center (NSSDC). Various aspects of the validation and application of SAGE II water vapor products have been discussed in Rind et al. (1993) and a series of companion papers. For this study we used the individual archived profiles to derive relative humidity at 50mb intervals between 500mb and 100mb, and integrated water vapor content for the 500-100mb layer and 300-100mb layer in units of gm/cm^2 (equivalent to precipitable centimeters of water). It should be noted that our results represent a clear-sky climatology only.

Figures 1(a) and 1(b) show examples of JUN-JUL-AUG and DEC-JAN-FEB frequency distributions of SAGE-II derived zonal mean relative humidity at 300mb for 0° - 150°W . The curves for 0 - 30°N and 0 - 30°S are not included in Figures 1(a) and 1(b), respectively, because the averages for those two cases might not represent true zonal means due to the small sample size and inhomogeneous geographical distribution. It is worth noticing that the results in the two figures support the

findings based on METEOSAT observations that the values of clear-sky upper tropospheric relative humidity typically range from 5% to 60% (Van de Berg et al., 1991). Furthermore, comparisons of Figure 1(a) with the upper tropospheric relative humidity histogram for July 1987 derived from the GOES 6.7 μ m channel (Soden et al., 1993), show very good quantitative agreement with the exception that SAGE II's peak relative humidity for 30°S–60°S is lower by 10%.

The annual variations of SAGE II-derived integrated columnar water vapor content (500–100mb layer) are depicted in Figures 2(a) and 2(b) for the eastern hemisphere (following Susskind et al.'s (1993) definition as 30°E eastward to 150°W) and the western hemisphere (150°W eastward to 30°E), respectively. Susskind et al. (1993) has shown the annual variations of clear-sky precipitable water using HIRS/MSU retrieval. A number of common features, representative of the upper troposphere, emerge upon intercomparison of these results: (i) In the tropical region, the eastern hemisphere shows considerably higher moisture content than the western hemisphere; (ii) The variations in the tropical eastern hemisphere exhibit a fairly uniform annual cycle characterized by regions of maximum moisture occurring between 0° and 15° in the summer hemisphere; (iii) For the tropical western hemisphere, high moisture is found over a narrow range of latitudes, located mostly north of the equator, and the maximum south of the equator during northern hemispheric winter is weak and diffuse.

Geographical distributions of the SAGE-II derived integrated columnar water vapor (100 to 300mb) are plotted in Figures 3(a) and 3(b) for DEC-JAN-FEB and JUN-JUL-AUG, respectively. During the northern hemisphere winter months, the area of high moisture content centers at the Indonesian region extending westward to Malaysia and eastward into the mid Pacific. The other area of high moisture content covers eastern Brazil to southern tropical Africa. The distributions for northern hemisphere summer months indicate that the centers of high moisture content, which are along the inter-tropical convergence zone (ITCZ), have all moved northward. The regions of maximum moisture content for these months include the bay of Bengal, central Africa and the equatorial Pacific over central America.

As pointed out by Arking (1990), climate is just as sensitive to percentage changes in upper tropospheric water vapor, where the mixing ratio is very small, as it is to percentage changes in the planetary boundary layer, which contains the bulk of the total

column water vapor. Hence, the capabilities of SAGE II observations to provide global distributions of moisture content, especially in the tropical upper troposphere, as shown in Figures 3(a) and 3(b), have very important implications. The range of total columnar water vapor burden obtained from ISCCP-C1 data set falls between 1.0 to 4.5 gm/cm^2 (Darnell et al., 1992). The precipitable water for 500mb to top of the atmosphere, derived from HIRS/MSU retrieval, ranges from 0.03 gm/cm^2 to 0.36 gm/cm^2 . Interestingly, SAGE II solar occultation measurements have allowed us to examine the global variability of moisture content in the uppermost layer of the troposphere, where the range of values (0.002 gm/cm^2 to .01 gm/cm^2) is smaller than the above mentioned quantities by a factor of 10 to 1000.

3. CONCLUDING REMARKS

Using the four year (1986–89) archived SAGE II water vapor data set, we have presented important information on the seasonal variations and geographical distributions of clear-sky water vapor content for the upper troposphere where measurements have previously been very difficult. Comparisons with water vapor measurements from nadir viewing satellite instruments have demonstrated the usefulness of various remote sensing techniques in a complementary manner. An improved SAGE instrument, SAGE III, which is being scheduled for flight as part of EOS mission, will measure water vapor with increased spectral resolution and dynamic range. In addition to making measurements during solar occultation, SAGE III will also make measurements during lunar occultations which greatly increase the latitude and time of day coverage in comparison to SAGE II. In combination, these satellite observations should be valuable in helping us improve our understanding of the role of water vapor in meteorological, hydrological, and climatological processes through improved knowledge of water vapor and its variability on all scales.

REFERENCES

- Arking, A., 1990: Feedback Processes and Climate Response, "Climate Impact of Solar Variability", NASA Conf. Publ. 3086, K.H. Schatten and A. Arking (Eds.), NASA, Washington, D.C., 219–226.
- Darnell, W., W.F. Staylor, S.K. Gupta, N.A. Ritchey, and A.C. Wilber, 1992: Seasonal Variation of Surface Radiation Budget Derived From International Satellite Cloud Climatology Project C1 Data, J. Geophys. Res., Vol. 97, 15,741 – 15,760.

London, J., 1957: A Study of the Atmospheric Heat Balance, Final Report, Contract AF 19(122) - 165 (AFCFC - TR - 57- 287), New York Univ., 99pp.

Rind, D., E.W. Chiou, W.P. Chu, S. Oltmans, J. Lerner, J.C. Larsen, M.P. McCormick, and L.R. McMaster, 1993: SAGE II Water Vapor Observations, J. Geophys. Res. (submitted).

Soden, B.J., and F.P. Bretherton, 1993: Upper Tropospheric Relative Humidity From GOES 6.7 μ m Channel: Method and Climatology For July 1987, J. Geophys. Res. (submitted).

Starr, D. O'C, and S.H. Melfi, 1991: The Role of Water Vapor in Climate, NASA Conf. Publ. 3120, NASA, Washington, D.C., pp50.

Susskind, J., M.T. Chahine, L. Iredell, 1993: Monitoring Climate From NOAA Sounder Using An Interactive Forecast- Retrieval - Analysis System, J. of Climate (submitted).

Van de Berg, L., A. Pyomjamsri, and J. Schemtz, 1991: Monthly Mean Upper Tropospheric Humidities in Cloud-Free Areas From METEOSAT Observations, Int. J. of Climatology, Vol. 11, 819-826.

Fig.1(a)

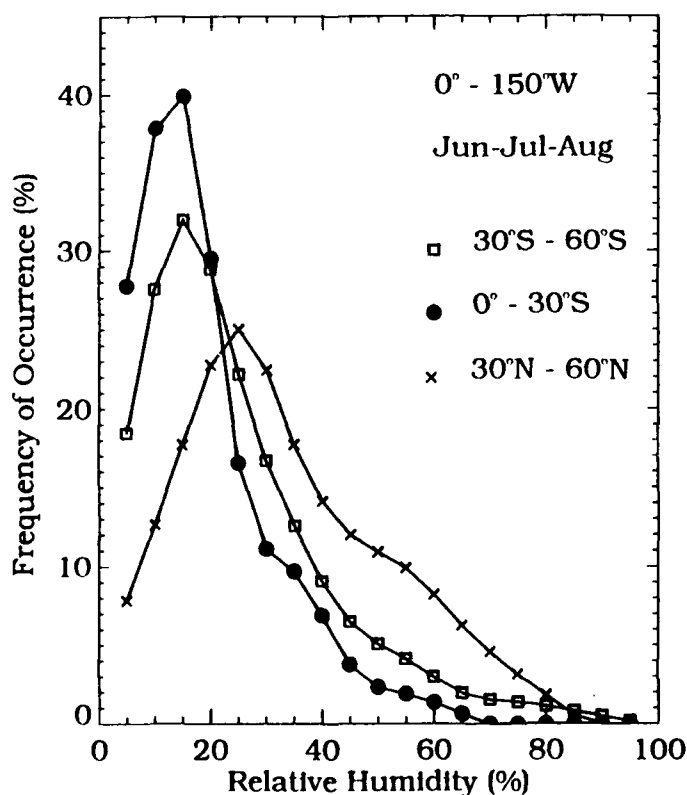


Fig.1(b)

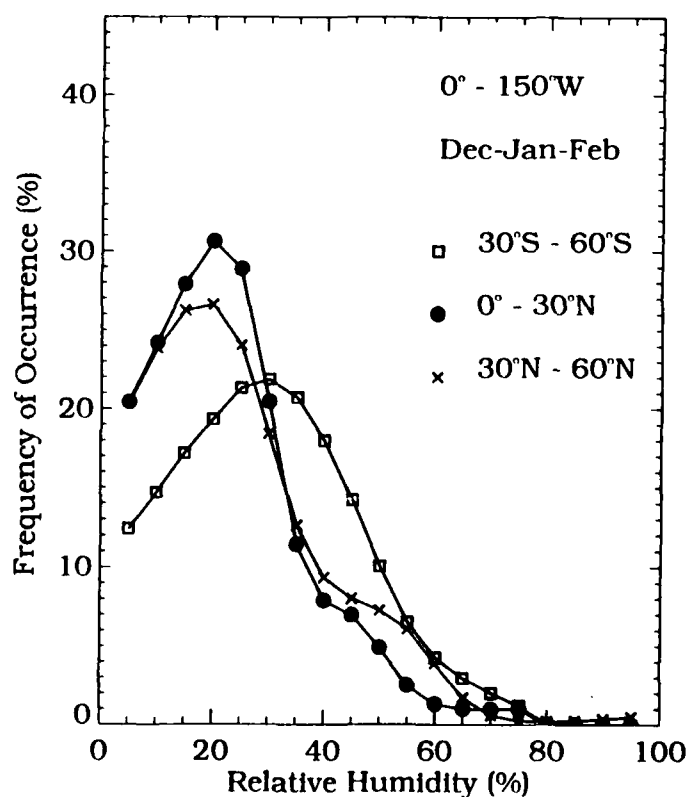
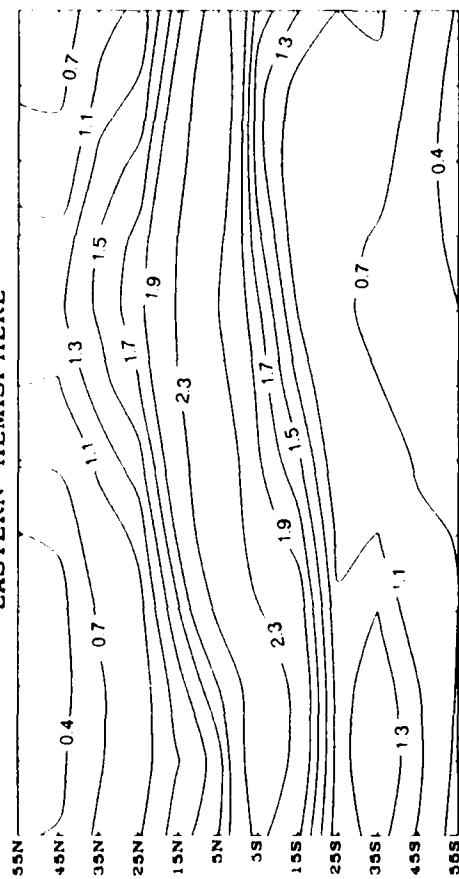


Fig.2(a)

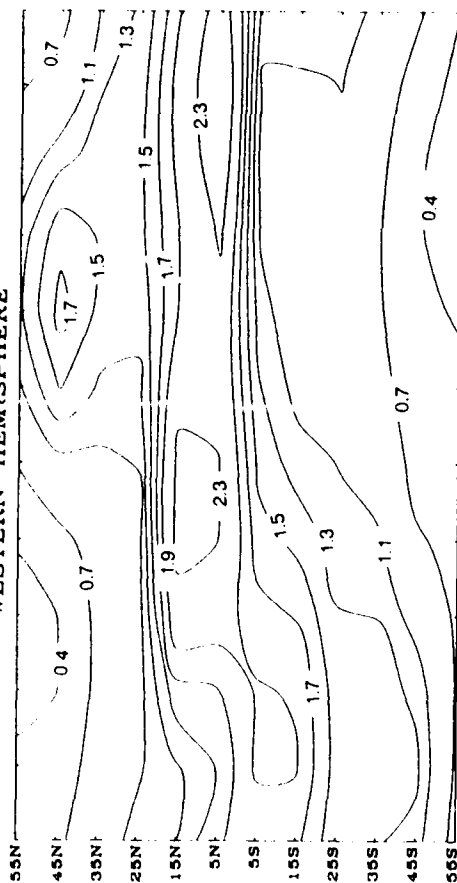
SAGE II-DERIVED COLUMNAR WATER VAPOR
500mb to 100mb Zonal Mean (gm/cm^2)
EASTERN HEMISPHERE



DEC JAN FEB MAR APR MAY JUN JUL AUG SEP OCT NOV

Fig.2(b)

SAGE II-DERIVED COLUMNAR WATER VAPOR
500mb to 100mb Zonal Mean (gm/cm^2)
WESTERN HEMISPHERE



DEC JAN FEB MAR APR MAY JUN JUL AUG SEP OCT NOV

Fig.3(a)

SAGE II-DERIVED COLUMNAR WATER VAPOR
300MB TO 100MB (KG/M^2)
DEC-JAN-FEB

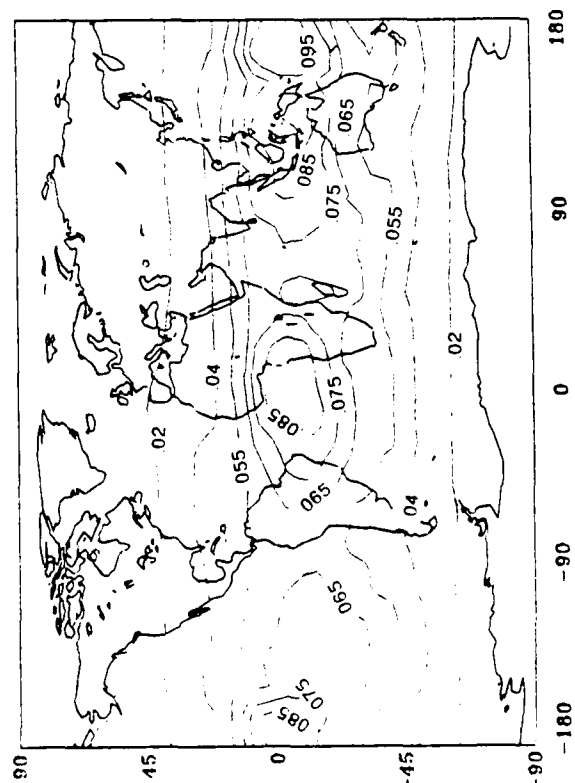
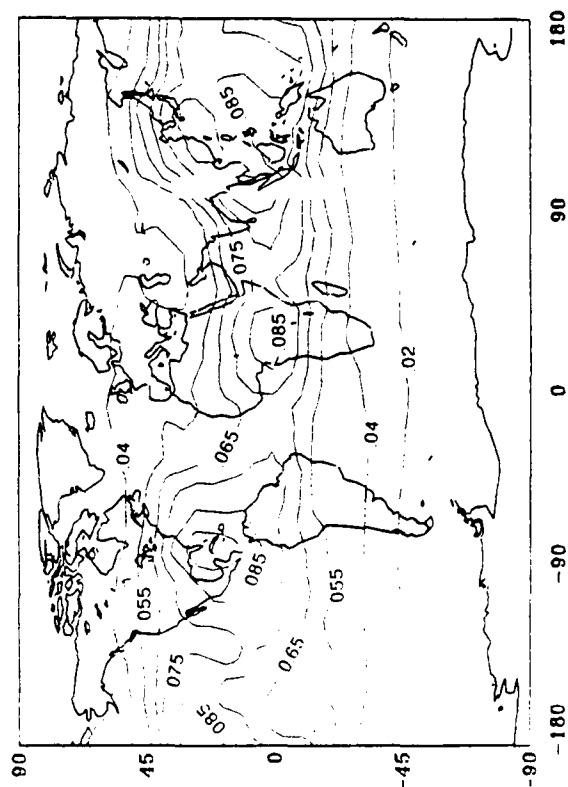


Fig.3(b)

SAGE II-DERIVED COLUMNAR WATER VAPOR
300MB TO 100MB (KG/M^2)
JUN-JUL-AUG



Temperature Structure Of Midlatitude Mesopause Observed by a Narrowband Na Fluorescence Lidar

C. Y. She, J. R. Yu, and H. Chen

Department of Physics, Colorado State University, Fort Collins, CO, USA

Telephone: (303) 491-6261 FAX (303) 491-4947

Summary

Since the first report on the temperature measurements in the mesopause region using the new two-frequency narrowband Na temperature lidar [1], active research continues and several publications have already appeared in the literature [2, 3]. In order to reveal the seasonal variations and the thermal structure of the mesopause region, long-term routine Na temperature measurements at different locations should be made. Unlike at polar latitudes, investigations of the nighttime temperature structures of the mesopause region on regular basis are possible year-round at a midlatitude. Such investigations are now in progress at both Fort Collins, CO (40.60N, 1050W) and Urbana, IL (400N, 880W) [4], using a new two-frequency narrowband Na temperature lidar in each location. From 1991 to the end of 1992, 106 nights of observations (22,138 files) have been conducted at Fort Collins, CO. In this paper, we report the results deduced from 88 nights of quality data with 4 to 9 hours of observation each night. Our data set covers a nearly continuous period of two years. The thermal structure of the mesopause region at a midlatitude location and its seasonal variation can be established from our observations.

A general picture on the temperature structure of the mesopause region at Fort Collins, CO may be obtained from the seasonally averaged temperature profiles. We adopt the practice in Chinese calendar and divide each year into four seasons with spring equinox (~3/21), summer solstice (~6/21), fall equinox (~9/23) and winter solstice (~12/22) being the center of the respective seasons. Under the normal operation of the Na temperature lidar [2], weather permitting, a temperature profile of the mesopause region may be deduced from the photocount profiles of lidar returns in a pre-determined time interval, typically 75 s. Nightly averaged temperature profiles are then deduced from which a seasonally averaged temperature profile is calculated for the nights in the season defined above. Including only the nights with more than four hours of high quality data, six seasonally averaged profiles, summer '91 (11 nights), fall '91 (13 nights), winter '91-'92 (10 nights), spring '92 (17 nights), summer '92 (8 nights), and fall '92 (16 nights) have been computed and they are shown in Fig. 1, along with the COSPAR International Reference Atmosphere (CIRA 1986) profiles. Considerable disagreement exists between the CIRA profiles and the measured profiles; for example, the CIRA profile is seen to be 25 K too cold in the fall (Fig. 1c). Contrary to CIRA 1986, two prevailing temperature minima exist in the mesopause region. The summer profiles contain a weak upper temperature minimum near 97 km and a strong cool (~ 178 K) lower temperature minimum near 86 km. Going into the fall, the lower temperature minimum warms up considerably, while the upper temperature minimum changes only slightly giving rise to a profile with twin temperature minima. The more robust lower temperature minimum continues to warm up and disappears into the mean profile in the winter leading to a profile with a weak mesopause (~ 190 K) at the upper edge (~ 100 km) of the Na layer. As spring comes, the lower temperature minimum develops again resulting in a profile with twin temperature minima very much like the fall profile. The upper temperature

minima in both spring and fall, which are slightly colder than the lower ones, become the mesopause for the respective seasons.

From the 88 nights of nightly averaged temperature and Na density profiles, the temperature structure in the mesopause region may be deduced and clear patterns of repeatable seasonal changes can be observed. Figure 2 displays the mesopause temperature of nightly averaged profiles plotted sequentially over a period of two years. The day number starts from January 1, 1991, UT as Day #1. The bar on the data point, typically ± 10 K, is not the measurement error but the standard deviation indicating the range of measured values, due mainly to gravity wave and tidal perturbations through the night. To aid the eyes, we draw horizontal lines to mark the averaged local low and high values in the figure. The mesopause temperatures rise and fall in a complicated manner between the lows (~ 175 K) and the highs (~ 191 K). The 16 K mesopause temperature difference within a year at 40°N is, as expected, much smaller than the corresponding difference of 60 K observed at 69°N [5]. Although the lows of the mesopause temperature are centered near summer solstices, the mesopause temperature reaches its high a perplexing three months ahead of winter solstice. In order to explain these observed patterns in a more satisfactory manner, we propose to search for related quantities (indicators) that exhibit more direct correlation with seasonal changes.

Since the seasonally averaged profiles show prominent temperature minima at two (a upper and a lower) altitudes, we explore the seasonal dependence of these two temperature minima separately. Figure 3 is the seasonal dependences of the temperatures at the lower minimum. A clear, large seasonal temperature change is evident. To guide the eyes, we again draw horizontal lines around summer solstices (Day # 172 and 538) and winter solstices (Day # 356 and 721) to mark, respectively, the lows at ~ 175 K and the highs at ~ 210 K. The trend of the lower temperature minimum is seen to vary monotonically between a low at summer solstice and a high at winter solstice. The annual temperature change of nearly 40 K is much larger than the nightly temperature variation due to gravity wave and tidal perturbations. The lower temperature minimum, which directly correlates with the annual cycle of seasonal change, is thus regarded as a basic indicator for investigating the thermal structure in the mesopause region. Although the exact functional dependence of the lower minimum temperature trend is not known at this point, the rapid transition of 7.3 K/month in the mean between summer and winter solstices is a clear consequence of the wave-driven diabatic circulation observable at midlatitudes. Without an apparent seasonal pattern, the temperatures (188 ± 8.4 K) and altitudes (99.2 ± 2.9 km) of the upper minimum (not shown) fluctuate to conform with gravity wave activity and tidal perturbation propagated through the lower minimum. Based on the seasonal variations of these two temperature minima, the observed annual patterns of mesopause altitude and temperature can be explained. Since only the lower temperature minimum exhibits the annual oscillation reflecting the balance between radiation and dynamics, we suggest that the lower temperature minimum in the mesopause region actually plays the role of the mesopause as it is commonly known. Its seasonal variation as shown in Figs. 5 represents the thermal structure of the mesopause in midlatitudes which can be used to aid model calculation and to quantify gravity wave induced circulations.

References

1. She, C. Y., H. Latifi, J. R. Yu, R. J. Alvarez II, R. E. Bills, and C. S. Gardner, Res. Lett. 17, 929, 1990.
2. She, C. Y., J. R. Yu, H. Latifi, and R. E. Bills, Appl. Opt., 31, 2095, 1992.

3. Bills, R. E., C. S. Gardner, and S. J. Franke, J. Geophys. Res., 96, 22701, 1991.
4. Bills, R. E., and C. S. Gardner, J. Geophys. Res. (In Press).
5. Lubken, F. J. and U. von Zahn, J. Geophys. Res., 96, 20841, 1991.

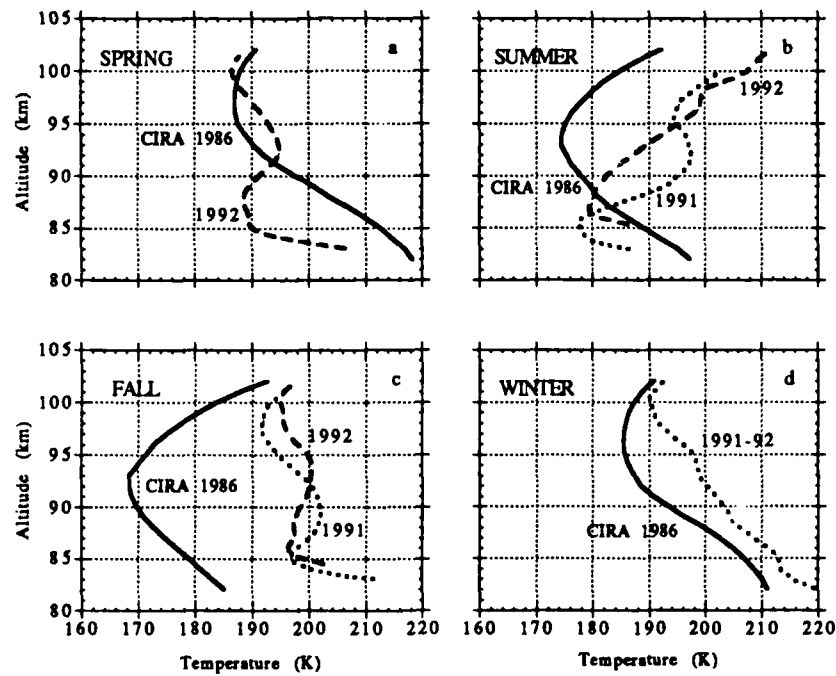


Fig. 1

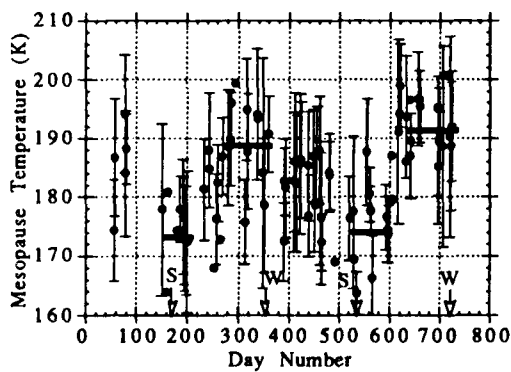


Fig. 2

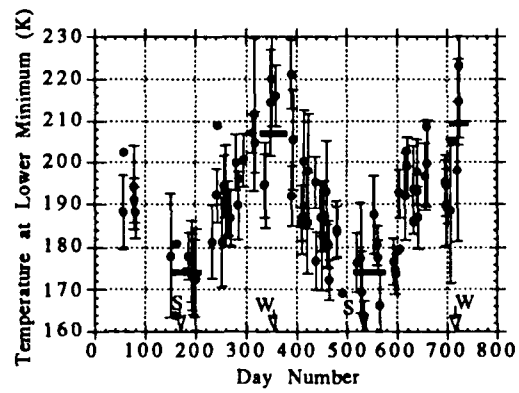


Fig. 3

Atmospheric Monitoring for Carbon Monoxide

Dyan N. Seville-Jones, Ronald J. Martinez, Robert K. Sander and Joe J. Tiee

Chemical and Laser Sciences Division

Los Alamos National Laboratory

Mail Stop J567

Los Alamos, NM 87545

(505) 667-6137

A preliminary study of the flow and concentration of CO over urban intersections is discussed. Results from a tunable diode laser monitoring system are presented.

Atmospheric Monitoring for Carbon Monoxide

The distribution and concentration of carbon monoxide (CO) in the lower levels of the atmosphere have important implications for pollution and non-compliance regulations in urban areas. Currently, EPA air quality sensors record daily averages in certain parts of US cities, but lack the capability to identify the major pollution sources. The mobile source nature of CO emissions exacerbates regulation and control.

In this experiment, long path absorption of carbon monoxide offers an advantage over point sensors by showing mobile source flow patterns and concentrations over several different paths. Since CO has a large cross section and narrow linewidth, it provides short time resolution, and low concentration measurement capabilities. Fluctuations may be distinguished on second by second time scale if required.

The apparatus consists of a laser diode operating near 4.8 μm , an InSb infrared detector, a collimating lens, a scannable mirror, and a set of three retro-reflectors shown in Figure 1. A tunable diode laser enables one to observe the full line absorption of CO and remove any absorption by any unknown interferences. The diode is wavelength tuned by current and ramped across the 2090.6 cm^{-1} (P13) CO absorption line and also the 2090.1 cm^{-1} H_2O absorption line at a rate of 2000 scans per second. A helium-neon laser is used to trace the infrared beam path for alignment to each of the corner cubes. The signal is continuously averaged using a digitizing oscilloscope, and the data is processed and stored on a Macintosh running a Labview data acquisition program. A typical scan of the return signal containing the two absorption lines is shown in Figure 2. To calibrate the system, a 10-cm cell containing 1 torr of carbon monoxide is opened to allow in ambient air pressure at the experiment site. This guarantees the reference cell pressure will correspond in pressure broadened linewidth to the data collected.

In order to complete preliminary testing, the experiment was run at a busy intersection (San Mateo & Menaul) in Albuquerque, New Mexico, in early 1993. The apparatus was positioned at one corner about 2.1 m high, enabling the laser to clear approximately 90% of the traffic. Three retroreflectors were positioned at each of the other corners at distances of 32 m, 36 m, and 56 m. After the corner cubes have been aligned, the scanning mirror, mounted on a motorized controller, scans between each position within a matter of seconds. The aligned system may be run continuously for several hours.

In the data of Figure 2, the laser diode power changes with wavelength (the horizontal axis); a linear fit to laser power is multiplied by Beer's law for the two absorption lines.

$$I_{\text{observed}} = (a + bx) e^{-(\sigma_1 n_1 + \sigma_2 n_2)l} \quad \text{where } \sigma_1 = \text{H}_2\text{O}, \sigma_2 = \text{CO}, n_i = \text{number density.}$$

Due to the proximity of the H_2O absorption band, the overlapping tail effects must be fitted to ensure the concentration of CO is correct. This is done by fitting a Lorentzian pressure broadening lineshape to the H_2O peak. Although the calibration cell gave reproducible results, these results are subject to systematic effects such as temperature changes, air pressure fluctuation, and etalon effects on various window surfaces. Figure 3 shows a typical data set over one path late in the afternoon. Each data point represents a 1.5 minute average of 4600 scans. The aim of this approach is to estimate the real-time concentration in each path through the intersection. Although the concentration is integrated over the entire path length, patterns appeared between the individual paths, indicating that traffic positions affected the measurements.

Future plans include synchronizing the measurements with the traffic lights and the traffic flow.

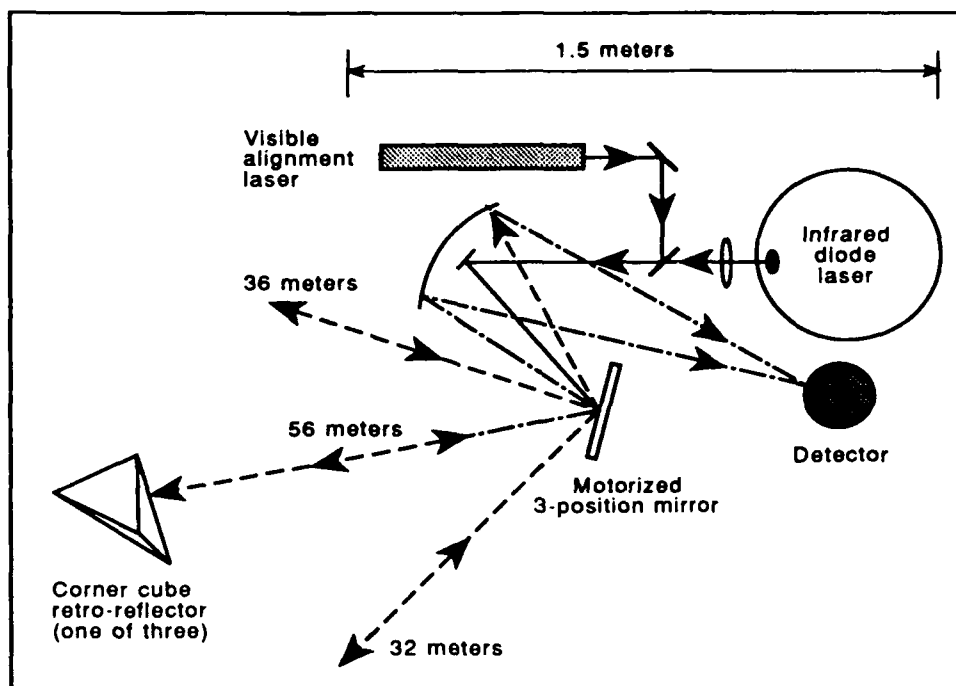


Fig. 1. Schematic of the atmospheric CO monitor.

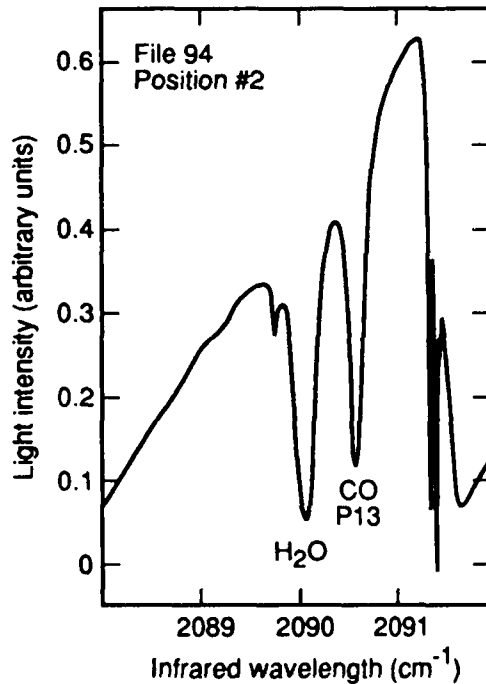


Fig. 2. The trace is the returned signal to the detector showing the power-gain curve of the diode laser with molecular absorption down to the baseline across the 32-m path. Identified are the 2090.1 cm^{-1} H_2O and the 2090.6 cm^{-1} CO lines.

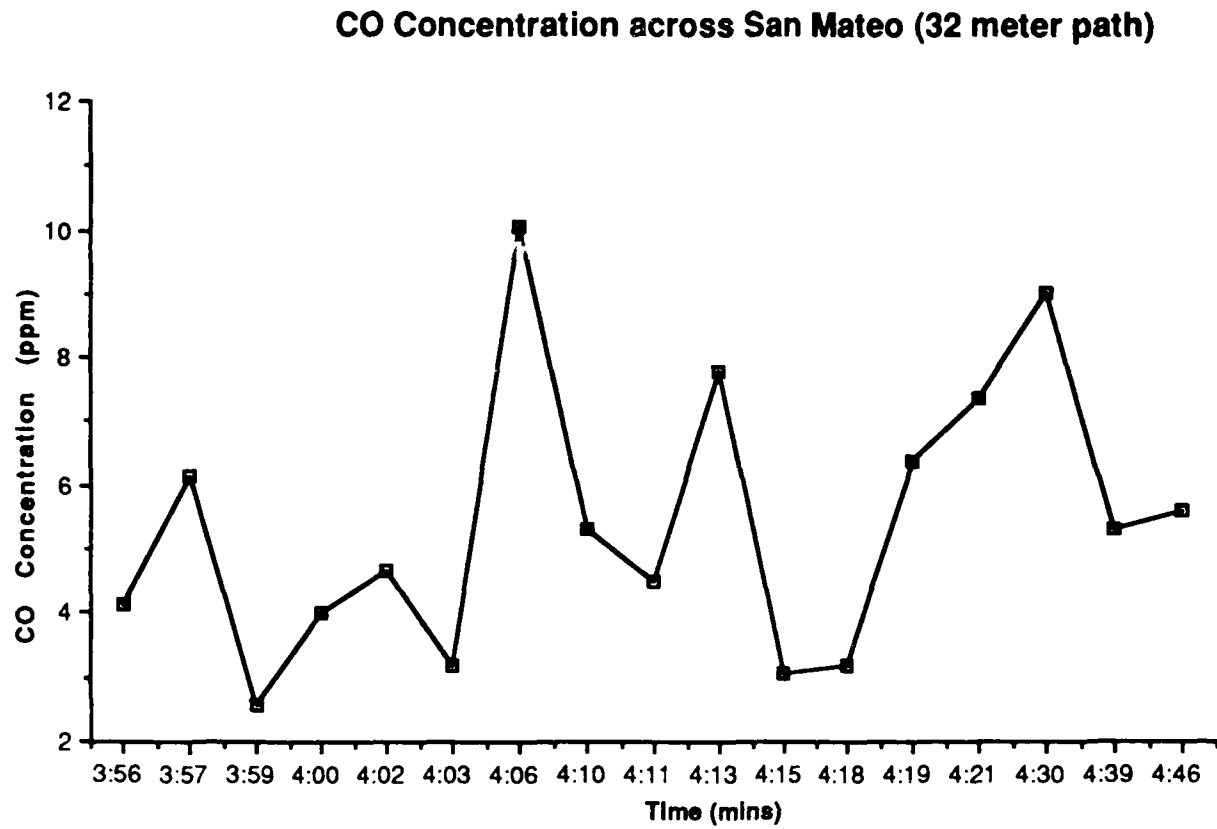


Fig. 3. Average carbon monoxide concentration over specified time interval.

AlGaAs Aerosol Lidar - Theory & Measurements

James B. Abshire
Jonathan A.R. Rall

NASA-Goddard Space Flight Center
Experimental Instrumentation Branch, Code 924
Greenbelt MD 20771
(301) 286-2611

February 24, 1993

Background - In 1983, Takeuchi et al. [1] demonstrated a pseudo-noise (PN) lidar using an externally modulated Argon laser. In 1986, Takeuchi et al. [2] reported PN aerosol lidar measurements using a single AlGaAs laser as a transmitter. We recently reported the design and initial measurements [3,4] made with our AlGaAs lidar which uses a Si APD photon counting detector with a histogram-correlate signal processor.

AlGaAs Lidar Design - Our lidar is shown in Figure 1 and its characteristics are summarized in Table 1. The transmitter is a single AlGaAs laser diode, whose intensity is digitally modulated with a maximal length PN code [5]. The modulated laser signal propagates through the atmosphere, where it is scattered by atmospheric constituents, or by any solid objects (i.e. terrain) in the beam. The receiver telescope focuses the backscattered signal and background light onto the photon counting detector. Optical background is reduced by using a narrow optical bandpass filter and field-of-view. The detector's electrical pulses are passed through a threshold circuit and accumulated in a histogram circuit. The receiver histogram has one range bin per transmitted bit and accumulates the received photon counts synchronously with the transmitted code.

AlGaAs Lidar Theory - The PN lidar detected signal can be derived by considering a laser which is intensity modulated with a maximal-length (m-bit) PN sequence. The PN sequence has $(m+1)/2$ ones and $(m-1)/2$ zeros, and its generator polynomial determines the value (0 or 1) of c_i , which is the i^{th} bit in the PN sequence. The transmitted laser power sequence can be written as

$$p_i = 2P c_i = \begin{cases} 2P, & c_i = 1, \\ 0, & c_i = 0 \end{cases} \quad (1)$$

The transmitter operates at a bit frequency f_b , with a time duration for each bit of $t_b = 1/f_b$. The receiver's range resolution is one bit, which corresponds to $\Delta R = (c/2)t_b$.

An expression for the detected lidar signal can be derived by initially considering only a single scattering region, and then extending the results to multiple ranges. The lidar transmits its sequence through the atmosphere. A fraction of the transmitted photons are scattered backward at some range $R_j = j \Delta R$. Some of the backscatter is captured by the lidar system's receiver telescope and detected. The detected signal produces a sequence of photoelectron emissions, which lag the transmit sequence by the range delay. The mean value of the detector's count rate is governed by the lidar equation, and can be written as

$$\langle \dot{N}_i(R = j\Delta R) \rangle \equiv \langle \dot{N}_{i,j} \rangle = p_{i-j} \gamma \frac{\beta_{\pi}(R) \Delta R f_o(R)}{R^2} \exp\left\{-2 \int_0^R \alpha(r) dr\right\} + \langle \dot{B} \rangle. \quad (2)$$

This can be abbreviated as

$$\langle \dot{N}_{i,j} \rangle = p_{i-j} \gamma \xi_j + \langle \dot{B} \rangle, \quad (3)$$

where $\dot{N}_{i,j}$ denotes the photoelectron rate at the i^{th} bit in the sequence caused by the signal scattered from range cell j , β_π is the atmospheric backscatter coefficient, α is the atmospheric extinction coefficient, f_0 is the lidar overlap function and $\langle \dot{B} \rangle$ is the expected rate from background and detector dark counts. The subscript $(i-j)$ denotes the j -bit range delay to distance R_j and is modulo- m , and ξ_j is an effective "lidar reflection coefficient" for range R_j . The lidar system constant is $\gamma = \eta \tau_{\text{sys}} A_r / (hc/\lambda)$, where η is the detector quantum efficiency, hc/λ is the laser photon energy, τ_{sys} is the system transmission and A_r is the area of the receiver telescope.

For each cycle of the PN code, the histogram integrates each bit of the detected signal for a time duration t_b . If the receiver integrates for L cycles of the PN sequence, each bit in the histogram is integrated for $L t_b$ seconds. The expected histogram count sequence accumulated during this time $T = L m t_b$ can be computed by using (2) and (3) yielding,

$$\langle H_{i,j} \rangle = 2P \gamma \xi_j L t_b c_{i-j} + \langle \dot{B} \rangle L t_b. \quad (4)$$

The receiver histogram is a range delayed version of the transmitted code, with an average count per bin governed by the lidar equation. If the sequence $A_i \equiv 2c_i - 1$, then the expected lidar profile for the single reflector can be computed as the correlation function,

$$\langle N_n \rangle = \sum_{i=0}^{m-1} \langle H_{i,j} \rangle A_{i-n} = \begin{cases} P \gamma \xi_j L(m+1) t_b + \langle \dot{B} \rangle L t_b, & n=j \\ \langle \dot{B} \rangle L t_b & \text{otherwise} \end{cases} \quad (5)$$

The received lidar signal from scatterers at range R_j occurs only at range bin j in the correlation function. The amplitude of the correlation peak is the received signal plus background photoelectron count, which is governed by the lidar equation (2-4). At all other range bins, the expected correlation values are equal and due to background noise alone.

For most lidar measurements, there are scatterers at many range bins. In this case, the expected histogram is the sum of all reflected sequences, each at their respective range delay. The expected correlation function is

$$\langle N_n \rangle = \sum_{i=0}^{m-1} \langle H_i \rangle A_{i-n} = \sum_{i=0}^{m-1} \left\{ \sum_{j=0}^{m-1} \langle H_{i,j} \rangle \right\} A_{i-n}. \quad (6)$$

After exchanging the order of summation and evaluating the outer sum, the result is

$$\langle N_j \rangle = \{ P \gamma L (m+1) t_b \} \xi_j + \langle \dot{B} \rangle L t_b. \quad (7)$$

The noise-like properties of the correlation function "sift out" the received lidar photoelectron count at each range bin, yielding the desired lidar profile.

Performance - The AlGaAs lidar performance is determined by the statistics of the N_j . The counts in each H_j have a Poisson distribution with the mean equal to the variance. The variance of each range bin in (5) is the sum of the variances of each histogram bin. Since the mean equals the variance, this is simply the sum of all signal and background counts

accumulated during T . Consequently all AlGaAs lidar range bins have the same variance, and the SNR for the j^{th} range bin is

$$\text{SNR}(R_j) = \frac{\langle N_j \rangle}{\sqrt{\text{var}(N)}} = \frac{P \gamma L (m+1) t_{b_j}^2}{\sqrt{\left\{ \sum_{j=0}^{m-1} N_j \right\} + \langle B \rangle T}} \quad (8)$$

Measurements - Recent nighttime altimeter and lidar measurements made with our AlGaAs lidar are shown in Figures 2-4. The data has not been overlap corrected or inverted. Figure 2 shows altimetry measurements made over a 12.6 km horizontal path to a terrestrial target, which is likely a power line tower. This measurement was made with a 1 second integration time and has a signal-to-noise (SNR) ratio exceeding 200. Figures 3 and 4 show consecutive lidar profiles measured with 1200 second integration times with the system pointed 75° above the horizon. The overlap function and aerosol attenuation to approximately 7 km are evident in both figures. A very strong subvisible cirrus cloud return appears at 12.9 km in Figure 3 and a second lower layer appears at 10.2 km in Figure 4. These profiles have been smoothed with a 2-bit running average and are range corrected.

References

1. N. Takeuchi, N. Sugimoto, H. Baba, and K. Sakurai, "Random modulation cw lidar," *Applied Optics*, Vol. 22, 1382 (1983).
2. N. Takeuchi, H. Baba, K. Sakurai and T. Ueno, "Diode-laser random modulation cw lidar," *Applied Optics*, Vol. 25, 63 (1985).
3. J.B. Abshire, J.A.R. Rall, S.S. Manizade, "Altimetry and Lidar Using AlGaAs Lasers Modulated with Pseudo-Random Codes," 16th International Laser Radar Conference, Boston MA, July 1992.
4. J.A.R. Rall, J.B. Abshire, S.S. Manizade, "Lidar Measurements using AlGaAs Lasers Modulated with Pseudorandom Codes," *Optcon'92*, Optical Society of America, Boston MA, November 1992.
5. R. C. Dixon, *Spread Spectrum Systems* (Wiley, New York, 1976).

Table 1 - GSFC AlGaAs Lidar - 11/92 Characteristics

Laser	AlGaAs Laser Diode, Spectra Diode Labs 5410
Laser Power	35 mW average, 70 mW peak (typ.)
Laser Modulator	Negative Drive, Current Steering
Collimating Lens	3 element, NA=0.5
Beam Expander	x 8 ratio nominal
Transmitter div. angle	~ 100 urad
PN code generator	255 & 4095 bit, maximal length, 1 MHz bit rate
Range Resolution	150 meters/bit
Telescope	20 cm diameter Schmidt-Cassegrain, f6.3
Interference filter	810 nm, 10 nm bandpass
Field-of-view	160 urad
Detector	Geiger Mode Si avalanche photodiode, EG&G
Discriminator	Leading edge type, Tennelec
Signal Processor	1-bit histogram circuit sync'd to transmit code
Controller - Computer	Gateway 486/33

Figure 1

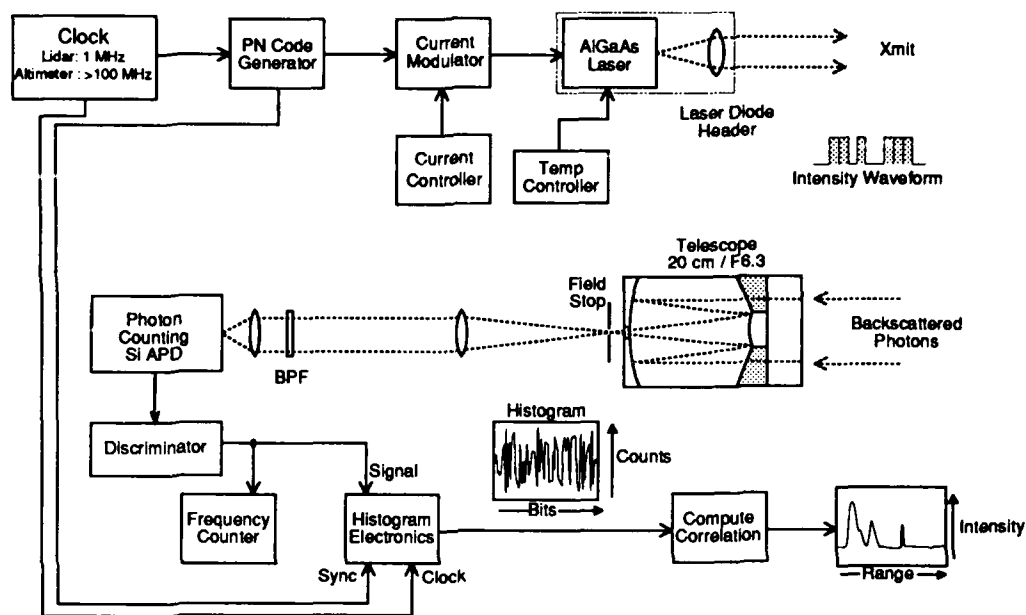


Figure 2

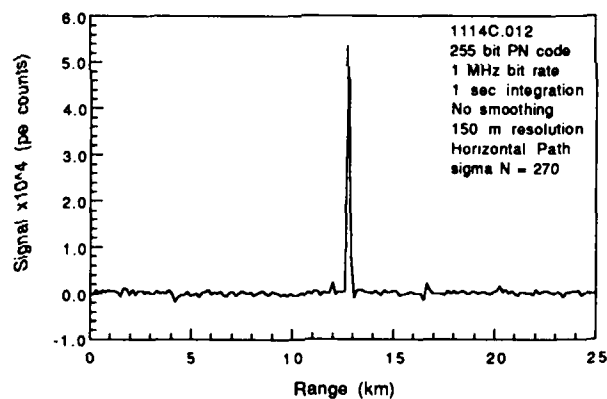


Figure 3

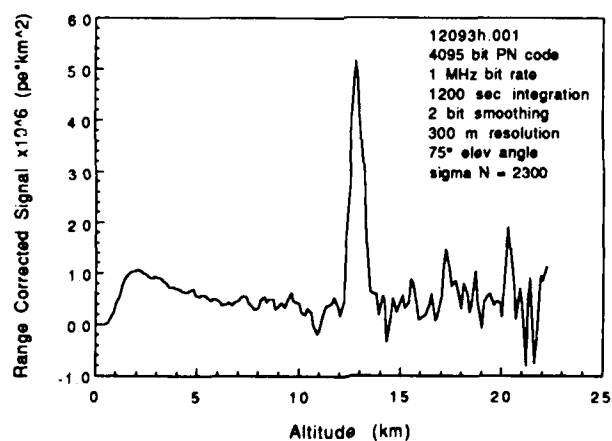
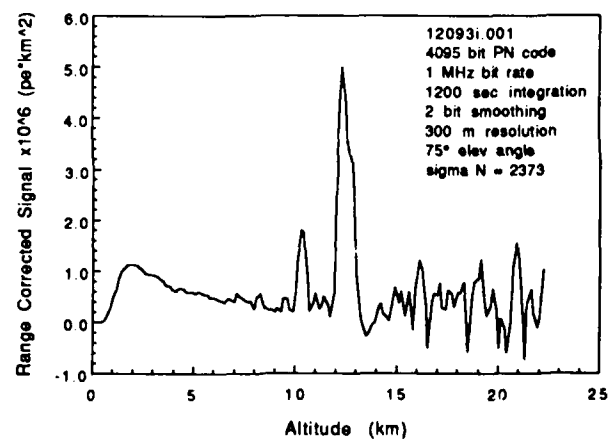


Figure 4



Spectral Calibration of the Improved Stratospheric and Mesospheric Sounder

P. E. Morris, F. W. Taylor, J. Ballard†

Department of Atmospheric Physics, University of Oxford,
Parks Road, Oxford OX1 3PU, U.K. (0)865 272901

†Rutherford Appleton Laboratory, Science and Engineering Research Council,
Chilton, Didcot, Oxfordshire OX11 0QX, U.K. (0)235 445132

1. Introduction and Scientific Objectives

The Improved Stratospheric and Mesospheric Sounder (ISAMS) is a limb-viewing infrared radiometer which measures thermal emission in 24 spectral bands, using both wideband (WB) and pressure modulator radiometer (PMR) techniques (Taylor, 1983). This enables the daily mapping over much of the Earth of temperature, the concentrations of 8 chemical species (water vapour, methane, ozone, nitric acid, nitrogen dioxide, nitric oxide, dinitrogen pentoxide, carbon monoxide) and aerosol opacity in the stratosphere and mesosphere. The instrument has eight separate focal planes, each consisting of a 4-element detector array, which are cooled by two mechanical coolers.

2. Pre-launch Calibration

Pre-launch calibration and characterisation took place over two periods of four months in 1989 and 1990. During these periods the instrument spent about half of the total operating time under vacuum and cryogenic conditions. Tests were carried out semi-automatically with ISAMS in a large space environment simulation chamber. An unusual aspect of the procedure was that the test equipment was in most cases controlled by programs running within the ISAMS instrument microprocessor, the equipment being interfaced to the instrument data bus to allow commands to flow to the test equipment and data to return.

2.1 Spectral Calibration

Each ISAMS channel consists of a number of spectrally selective optical components, including cooled interference filters on lenses, room temperature filters on flat substrates, beam splitters, and antireflection coatings which contribute to the overall channel response (Hawkins *et al.* 1987). The calibration of the ISAMS flight instrument required the use of an infrared monochromator to measure the relative spectral response of each instrument channel. The task of making these spectral measurements fell into two parts:

- (i) determination of the WB and PMR in-band spectral response at a resolution of about 2cm^{-1} over each channel passband;
- (ii) determination of the out-of-band spectral response over the range 4.3 to $18\mu\text{m}$ at a lower resolution to detect spectral leaks;

The monochromator formed part of a customised calibration assembly, known as the Collimator

Monochromator System (CMS). This consisted of a paraboloid mirror mounted on a 2-axis gimbal-frame assembly with the choice of a polychromatic globar source for field of view mapping, or a monochromatic source used for the spectral calibration. The resulting parallel infrared beam was directed into the ISAMS viewing aperture, forming an image in the composite detector element plane. The monochromatic radiation was obtained from a grating spectrometer based on the Fastie-Ebert design with adjustable globar assembly, slits, order sorting filters and grating turret which could all be remotely controlled from outside the vacuum chamber.

With the use of different diffraction orders it was possible to obtain a spectral range from the monochromator of 3 to $20\mu\text{m}$, allowing measurements of all ISAMS channels. An estimated maximum uncertainty in the centre wavelength of a given ISAMS spectral interval was 0.5cm^{-1} . The relative spectral response of each channel was determined by centering the image of the monochromator exit slit onto one detector element and scanning in wavelength. The monochromatic light was alternatively 'chopped' every two seconds by moving a shutter in front of the globar assembly, so that detector responsivity drifts and stray background emission from within the test chamber could be eliminated. The wavelength scale of the monochromator was calibrated using orders from a helium neon laser as well as gas absorption lines in the ISAMS pressure modulator cells. The monochromator's own spectral response was removed using a spectrally flat pyroelectric (TGS) detector.

The in-band spectral scans were limited to just the main filter response and extended to 0.1% of the peak transmission, whereas the lower resolution out-of-band spectral scans provided near-continuous coverage in the filter stop-bands down to relative transmission levels of approximately 0.01%.

The results indicated that the transmission measurements of the multilayer filters placed on curved germanium lens surfaces differed significantly from the spectral responses of flat test pieces coated at the same time, as well as from theoretical calculations. This was believed to be due to non-uniform deposition of the interference layers onto the curved substrate. This only affects 6 of the 14 WB channels, with the remaining filters all being located on flat germanium substrates. These results highlight the importance of measuring the spectral response of the instrument in its final flight configuration. As a result of this work, it must be emphasised that the spectral measurements of individual filters will not necessarily provide an accurate representation of their transmission properties when used in combination with other optical components.

3 Simulated Radiance Calculations

A line-by-line radiative transfer model (GENLN2, Edwards 1992) and a representative climatology (Anderson *et al.* 1985) were used to calculate monochromatic target and contaminant gas infrared emission in each ISAMS channel. These spectra were convolved with the measured filter responses and a theoretical pressure modulator response function to obtain simulated radiances. These results show the contribution to the ISAMS radiance from the target gas, as well as from the contaminants in that channel, expressed as a function of limb tangent height. The GENLN2 calculations were also used to validate the forward-model radiances used in the temperature and constituent retrievals.

3.1 The Spectral Results in Terms of Instrument Performance

The wavelength error resulting from the measurement of the ISAMS filter responses with the grating monochromator was approximately $\pm 0.5\text{cm}^{-1}$. Using this figure for all channels, convolved GENLN2 radiances, which included the emission from the target gas and contaminant species, were calculated using the measured filter response shifted by $+0.5\text{cm}^{-1}$ and -0.5cm^{-1} for all WB and PMR channels. The resulting radiances (scaled to a 290K black body viewed through the same shifted filter) could then be compared to the results from the nominal filters to produce fractional changes in radiance with tangent height.

These radiance changes were then compared to the change in radiance (again scaled to a 290K black body) resulting from perturbing the whole target gas volume mixing ratio (VMR) profile by $\pm 5\%$, while leaving the VMR profiles of the contaminant gases unchanged, and using the nominal filter position. In this way signal changes resulting from the filter uncertainties could be expressed as an equivalent change in constituent amount. For the ISAMS CO_2 temperature sounding channels a $\pm 1\text{K}$ perturbation of the atmospheric temperature profile was made, instead of a change to the (constant) CO_2 VMR with height.

The results suggest that, in the case of some WB channels, the equivalent filter VMR error is in excess of 5%. The channels most affected are nitrous oxide, nitrogen dioxide, and dinitrogen pentoxide, with the magnitude and sign of the errors varying with tangent height. In general, the filter errors in the PMR channels are equivalent to less than a 1% change in VMR, although below 15km they are seen to increase dramatically (15km represents the approximate lower limit for ISAMS limb-sounding measurements). The equivalent filter temperature errors in the CO_2 channels are between 0.0–1.0K (WB), and 0.0–0.3K (PMR). Figure (3.1) shows the results for two ISAMS channels. These filter uncertainties will form an important part of the overall instrument retrieval error budget.

4 References

- ANDERSON, G.P., CLOUGH, S.A., KNEIZYS, F.X., CHETWYND, J.H., SHETTLE, E.P., 1986: Atmospheric Constituent Profiles (0-120km), *Report AFGL-TR-86-0110, Air Force Geophysics Laboratory*
- EDWARDS, D.P., 1992: GENLN2 A General Line-by-Line Atmospheric Transmittance and Radiance Model (v3.0), *NCAR Technical Note TN-367+STR*
- HAWKINS, G., HUNNEMAN R., SEELEY, J.S., 1987: Design and disposition of infrared optical multilayer coatings for the Improved Stratospheric and Mesospheric Sounder, *Proc SPIE*, **868**, pp52-62
- TAYLOR, F.W., 1983: Pressure Modulator Radiometry. Spectrometric Techniques Vol 3, *Academic Press (New York)*

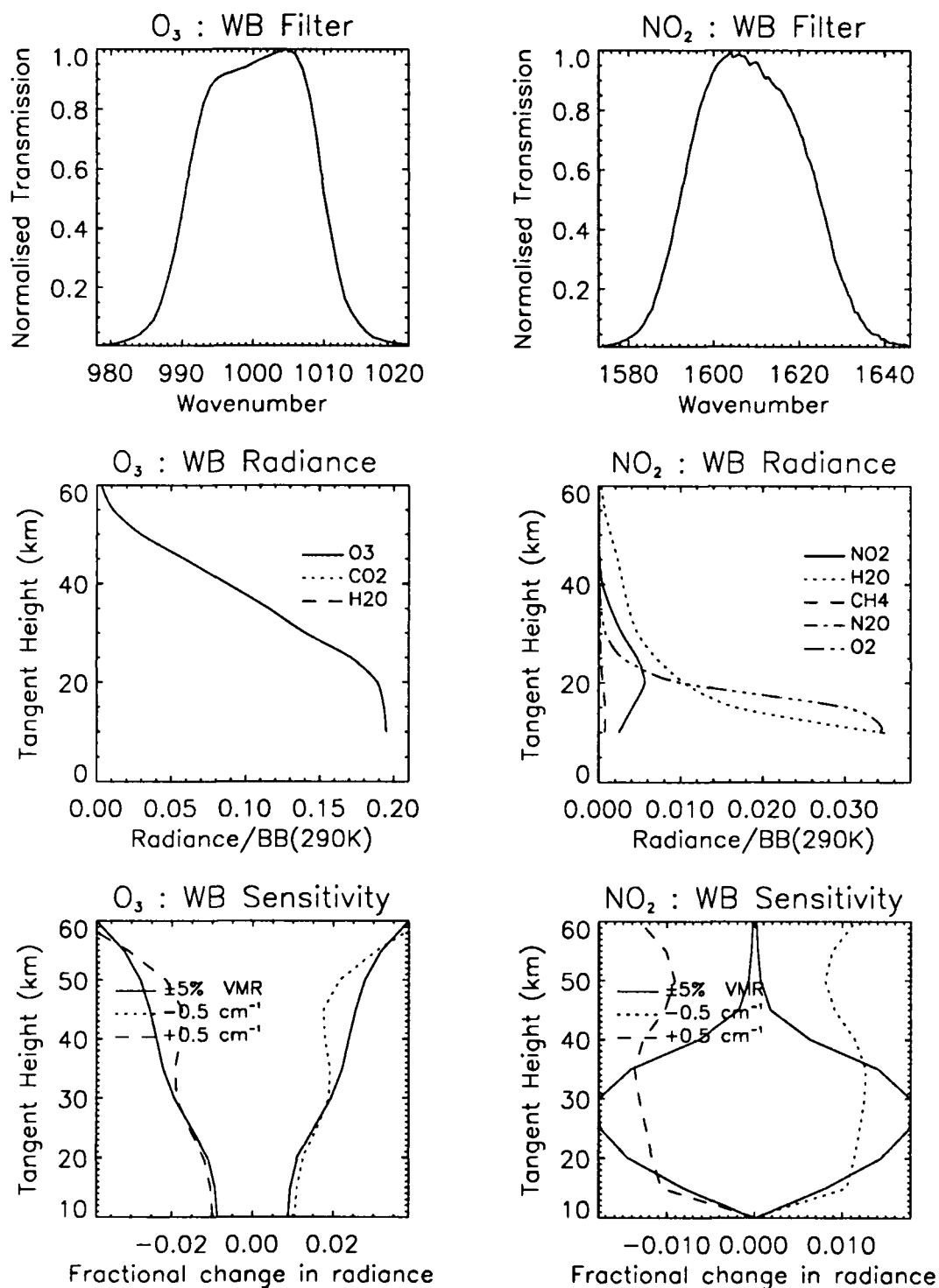


Fig.3.1 (1) measured filter transmission, (2) simulated radiances (expressed as a fraction of a 290K black body), (3) 5% increase/decrease in target gas concentration, compared to radiance changes resulting from a ± 0.5 cm⁻¹ movement of the wideband filter for the ISAMS ozone and nitrogen dioxide channels.

A mobile remote sensing laboratory for water vapor, trace gas, aerosol, and wind speed measurements

Dennis Slaughter, William White, William Tulloch, Daniel DeSlover, University
of California, *Lawrence Livermore National Laboratory*, Livermore, CA 94550, (510)-
422-6425

Introduction

The Lawrence Livermore National Laboratory has developed a mobile field laboratory for remote measurement of atmospheric processes and observables that are important in global climate change, dispersal of hazardous materials, and atmospheric pollution. Specific observables of interest are water vapor, trace gases, aerosol size and density, wind, and temperature. The goal is to study atmospheric processes continuously for extended periods in remote field locations. This laboratory has just reached field ready status with sensors for aerosol and trace gas measurement based on established techniques. A development program is underway to enhance the sensor suite with several new techniques and instruments that are expected to significantly extend the state of the art in remote trace gas analysis. The new sensors will be incorporated into the lab during the next two years.

At the present time the mobile laboratory is just beginning its first experimental campaign using FTIR spectroscopy to measure trace gas distributions and a multiple wavelength, Nd:YAG backscatter lidar to measure aerosol distributions. Instruments being developed for later experiments include: a) a hyperspectral sensing instrument based on an imaging FTIR spectrometer, b) a tunable mid-IR lidar system, c) a broad-band DIAL system in both the visible and mid-IR, and d) a direct-detection Doppler lidar. All of the instruments view the sky through a 50 cm aperture, cassegrain f3 telescope and a two-axis roof-top optical scanner with 50 cm aperture that allows scanning the whole sky from 15° below the horizon to zenith. When fully implemented the sensor suite will include the laser sources in the table below.

Laser	Wavelength $\lambda(\mu\text{m})$	Pulse duration (ns)	Pulse energy (mJ)	Repetition rate (Hz)
Nd:YAG	1.06	9	320	10
"	0.532	9	155	10
"	0.355	9	70	10
"	1.54	9	80	10
alexandrite	0.725	20	200	20
Ho:Tm:YLF	2.1	20	5	1000

The following sections will describe the existing capabilities as well as the goals and approach of the development program.

Water vapor

Two lasers are being developed for water vapor DIAL measurements. They are a Q-switched alexandrite laser at 725 nm and a Ho:Tm:YLF laser at 2.1 μm . Initial experiments are to determine the accuracy and sensitivity of DIAL measurements based on a single broad-band laser pulse and high resolution spectroscopic detection. These experiments are to be carried out both in a laboratory environment with calibrated cells and in field experiments.

Aerosol

The mobile laboratory now includes a Nd:YAG laser whose output may be doubled or tripled. A 100 cm long CH₄ Raman cell at 300 psi will soon provide an output at 1.54 μm . Three additional lasers are currently under development. They include an alexandrite laser at 725 nm, a Ho:Tm:YLF at 2.1 μm , and a tunable OPO laser based on ZnGeP and pumped at 2.1 μm with output wavelength tunable from 2.1-5 μm . All of these laser sources will be used in a backscatter lidar configuration to map aerosol distributions, and to infer aerosol density and size to the extent possible.

Experimental characterization of aerosol distributions will rely on measurement of the spatial profile of backscatter light at several wavelengths in the range 355 nm to 5 μm . Particle size and density measurements have been made successfully by others using multi-wavelength backscatter lidar such as the Nd:YAG system above¹⁻⁴. However, this technique is complex when applied to the measurement of aerosol size and density due to the difficulty of separating the effects of particle size and density from those of extinction, refractive index, and atmospheric propagation^{5, 6}. The backscatter lidar system with several wavelengths spanning more than a decade in range and overlapping the sizes of particular interest to global climate will be evaluated in field experiments to determine its utility and accuracy in determining particle density and size distributions. It is hoped that the additional wavelength range and additional wavelength samples will simplify the inference of aerosol size and density from measured backscatter light intensities.

Wind speed

A Fabry-perot interferometer has been installed on the 1.06 μm lidar return signal for direct-detection Doppler measurement of wind speed. This technique has been used successfully by others to measure wind speed^{7, 8}, sometimes with accuracy at short range^{9, 10} as good as 0.1 m/s and at long range as good as⁸ 0.3 m/s. Simulations indicate the possibility of wind speed measurements with 2 m/s accuracy even at ranges of 100 km or more^{10, 11}. Experimental

demonstration of minimum detectable wind velocity less than 1 m/s remains elusive and is one of the goals of the experimental program undertaken by this laboratory. A development program is underway to optimize interferometers for direct-detection Doppler wind speed measurements at 1.06 μm and 2.1 μm .

Trace gas

An FTIR sensor at the focus of the 50 cm aperture telescope is used to scan the whole sky using sunlight as the illumination source. It is sensitive in the range 200 nm to 40 μm . Incorporation of an imaging capability into this instrument to provide hyperspectral sensing for the spatial mapping of pollutants and trace gas plumes is currently in progress.

A broad-band DIAL system is under development to provide high sensitivity remote measurements of trace gas constituents of the atmosphere. While traditional narrow band DIAL systems have very good sensitivity for some gases their sensitivity in thin plumes is generally limited by low absorbance along the optical path rather than by photon intensity. These systems generally do not reach Poisson limited sensitivity due to pulse to pulse variations in the speckle pattern, in propagation due to turbulence, and in the aerosol distributions, all of which change over times scales of tens or hundreds of milliseconds. It has been theoretically predicted¹² and shown by experiments¹³ that a broad-band laser DIAL system is capable of measurements at low absorbance and of obtaining Poisson limited sensitivity. In that case laser power is the principal limit to useful sensitivity and range. This technique will be evaluated for remote measurement of many low abundance species with vibrational structures in the mid-IR.

Conclusion

The mobile laboratory described here has just become operational and many of its most interesting capabilities will be installed over the next two years. The initial experiments are directed toward field experiments to apply many wavelength backscatter lidar to the characterization of aerosol distributions and to determine sensitivity limits in the field for several new spectroscopic trace gas sensors.

References

1. L. Stefanutti, F. Castagnoli, M. Del Guasta, M. Morandi, V. M. Sacco, V. Venturi, L. Zuccagnoli, J. Kolenda, H. Kneipp, P. Rairoux, B. Stein, D. Weidauer, J. P. Wolf, **Appl. Phys.** **B55**, 13-17 (1992).
2. G. S. Kent, G. M. Hansen, K. M. Skeens, **Sixteenth International Laser Radar Conference**, July 20-24, 1992, Massachusetts Institute of Technology, Cambridge, MA, **NASA, Conference Publication 3158**, pp. 71-74.

3. R. T. Menzies, D. M. Tratt, J. D. Spinhirne, S. Chudamani, **Sixteenth International Laser Radar Conference**, July 20-24, 1992, Massachusetts Institute of Technology, Cambridge, MA, NASA, **Conference Publication 3158**, pp. 63-65.
4. Y. Sasano, I. Matsui, S. Hayashida, **Sixteenth International Laser Radar Conference**, July 20-24, 1992, Massachusetts Institute of Technology, Cambridge, MA, NASA, **Conference Publication 3158**, pp. 75-78.
5. V. E. Zuev, I. E. Naats, in **Remote Sensing of the Atmosphere: Inversion Methods and Applications**, A. L. Fymat, V. E. Zuev, Eds., Elsevier Scientific Publishing Company, New York (1978), pp. 257-261.
6. V. E. Zuev, I. E. Naats, **Inverse problems of lidar sensing of the atmosphere**, Springer-Verlag, New York (1983), pp. 80-162.
7. C. A. Tepley, S. I. Sargoytchev, C. O. Hines, **Geophys. Res. Lett.** **18**, 167-170 (1991).
8. G. Benedetti-Michelangeli, F. Congeduti, G. Fiocco, **J. Atmos. Sci.** **29**, 906-910 (1972).
9. F. Congedutti, G. Fiocco, A. Adriani, C. Guarrella, **App. Opt.** **20**, 2048-2054 (1981).
10. V. J. Abreu, J. E. Barnes, P. B. Hays, **App. Opt.** **31**, 4509-4514 (1992).
11. V. J. Abreu, **App. Opt.** **18**, 2992-2997 (1979).
12. F. A. Theopold, C. Weitkamp, W. Michaelis, **Sixteenth International Laser Radar Conference**, July 20-24, 1992, Massachusetts Institute of Technology, Cambridge, MA, NASA, **Conference Publication 3158**, pp. 671-674
13. G. H. Mount, **SPIE** **1491**, 26-32 (1991).

Techniques Used for Simultaneous 1.064 μ m and 2.036 μ m Airborne LIDAR Utilizing an Optical Parametric Oscillator

J. Bryan Blair
Robert S. Afzal
NASA/Goddard Space Flight Center, Code 924
(301) 286-9809

James D. Spinhirne
NASA/Goddard Space Flight Center, Code 917

The Goddard Visible and Near IR Lidar(VIRL)¹ has been modified to the 2.1 μ m region by replacing the Raman cell previously used to generate the 1.54 μ m pulse with an Optical Parametric Oscillator (OPO)² that can efficiently convert the 1.064 μ m output of the system Nd:YAG laser to generate a pulse at 2.1 μ m. The initial test and application of the 2.1 μ m measurements was during a deployment of the lidar on the NASA DC-8 for the TOGA/COARE project in January-February 1993. For T/C, the DC-8 was flown to and out of Townsville, Queensland. The T/C flights were north to the region of the equator and back. From the transit and local flights, a data set of significant coverage is to be generated.

Previously, the calibrated VIRL system was operated successfully at 1.064, 0.532, 1.54 μ m during the 1989 and 1990 GLOBE(Global Backscatter Experiment) DC-8 aircraft missions. The primary objective of the GLOBE missions, which included 9 μ m backscatter and in situ particle measurements, were to redress the lack of knowledge for aerosol scattering distributions needed to determine the performance of space borne laser wind sensors. The GLOBE project was largely successful, but a problem was the lack of direct backscatter measurements at 2.1 μ m. The interest in 2.1 μ m is from its potential application for LAWS(Laser Atmospheric Wind Sounder) or other doppler lidar instruments. Currently a CO₂ lidar operating at 9 μ m is envisioned as the primary choice, but solid state 2.1 μ m lidar is a competing technology. At present there are no significant direct measurements of 2.1 μ m backscatter. The T/C experiment was an excellent opportunity for an initial test and application of the 2.1 μ m OPO based lidar backscatter measurement. Using the modified VIRL lidar simultaneous backscatter returns were collected at 2.036 μ m and for both the parallel and perpendicular polarizations of 1.064 μ m.

System Overview

The transmitter used was a flashlamp pumped, Q-switched Nd:YAG laser providing highly polarized 240mJ, 14nsec pulses at 50Hz of 1.064 μ m light with a 1.4mrad beam divergence. The backscatter returns were collected with a 16 inch cassegrain telescope that was modified to allow for zenith or nadir orientation. The signal from the telescope was then directed horizontally along the rotation axis of the telescope assembly and split using a dichroic and a polarizing beam splitting cube. Finally, the signals were bandpass filtered and focused on to Si:APDs for the 1 μ m channels and an enhanced InGaAs pin diode, Epitaxx, Inc., for the 2.1 μ m channel. The 2.036 μ m light was generated using an optical parametric oscillator pumped by the 1.064 μ m from the Nd:YAG laser. The OPO, obtained from Schwartz Electro-Optics, Orlando FL, was tested at Goddard (GFSC) before deployment.

The data system consisted of a 80486-based PC interfaced to a CAMAC crate via a high speed parallel interface. Backscatter returns were sampled at 2MHz with 12 bits of digital precision. Running sums of from 1 to 15 shots were recorded on an Exabyte, Inc. 8mm tape drive along with transmitted energy levels for both frequencies and aircraft ephemeris. The transmitted energy levels were sampled using detectors similar to those in the receiver package. The energy monitors receive radiation through optical fibers from an integrating sphere containing a coated flat(anti-reflective@1.06 μ m) set at an angle in the laser output path. The coated flat reflects ~0.5% of the 1 μ m and ~8% of the 2.1 μ m, which were sufficient light levels for detection.

During the field deployment, the laser and the OPO needed to be in a mechanically stable environment free of thermal stresses, shock, and high frequency vibration to prevent misalignment of their respective resonant cavities. A typical flight day in Australia would begin at 90 degrees F with 90% humidity and after several hours of flight, the temperature would be 65 degrees F with 10% humidity. To accommodate these conditions, the laser and the OPO were tightly coupled on a custom nickel-steel bed with an extremely low coefficient of thermal expansion. The vibration environment of the DC-8 is most severe during takeoff and turbulent flight conditions. The entire lidar was mounted on coil springs to isolate the system from the aircraft.

Laser Modifications

A Continuum YG660A-50 laser cavity was unfolded and the graphite bed was replaced with an INVAR slab, 1" x 4" x 65". These modifications allowed us to achieve greater thermal, laser power, and mechanical stability. Also mounted on the INVAR base were the OPO, the laser polarization defining optics, and a beam aperture. This base provided a tightly controlled, thermally insensitive alignment environment between the laser and the OPO. The precise alignment requirements and mechanical sensitivity of the OPO required that it be mounted on the INVAR table with the laser. A tight(6mm) aperture with surrounding beam catch was installed between the laser and the OPO to prevent any OPO back reflections from damaging mounts or optics in the laser cavity.

OPO

The OPO consisted of an uncoated KTP (KTiOPO₄) crystal in a flat-flat resonator ~5cm long. Wavelength selection was achieved by angle tuning the KTP crystal. In order to avoid water vapor absorption lines, the OPO was operated at 2.036 μ m with a FWHM linewidth of ~3nm. The idler wavelength of 2.229 μ m was not detected by the system. The unfocused 1.064 μ m beam(~6mm diameter) entered the OPO through a dichroic mirror(high-reflector@2.1 μ m, high-transmitter@1 μ m.) The OPO output coupler was 80%-reflector@2.1 μ m and 80%-transmitter@1 μ m.

Since the same laser provided the outgoing 1 μ m light for the lidar and pumped the OPO, it was important that the OPO be as minimally invasive as possible. Therefore, certain compromises were made in the OPO implementation in order not to adversely affect the 1 μ m lidar. For example, the 1 μ m and 2.1 μ m beams were made non-collinear by pumping the OPO off the resonator axis in order to avoid back reflections from the OPO's optical surfaces into the Nd:YAG laser. Feedback into the laser was found to cause instabilities in the laser that resulted in damage to the OPO optics. The 1 μ m and 2.1 μ m beams were recombined using dichroic optics and additional turning prisms installed external to the laser enclosure, as shown in figure 1. The orientation of the splitoff and recombining dichroics allowed the 1 μ m beam to pass through unaffected. No noticeable change to the 1 μ m output beam position or pointing angle were observed when the dichroics were adjusted through the angular range needed to compensate for the 2.1 μ m beam. By splitting off the 2.1 μ m, we could adjust the OPO and redirect the 2.1 μ m beam without affecting the operation of the 1 μ m system.

The OPO was pumped with ~240mJ of highly(500:1) polarized 1.064 μ m light. At the final laser output of the lidar, the transmitted beam consisted of ~120mJ of 1.064 μ m and ~2-3mJ of 2.036 μ m. Although it would have been possible to generate more 2.1 μ m energy by using a stable OPO resonator with a mode matched beam waist, this would have led to a more complicated optical train needed to compensate for the changes in beam divergence of the 1 and 2.1 μ m beams. The majority of the loss in the 1 μ m beam is due to scattering losses from the OPO optical surfaces. During the TOGA/COARE deployment, the Nd:YAG laser system was operated at these very conservative energy levels to maximize its lifetime. Over 120 hours of in-flight laser operation in the harsh and dirty aircraft environment were required for this field experiment and running the laser at full capability, as one typically would in the laboratory, would undoubtedly lead to some hard failure in the cavity.

Power stability problems with the OPO output were due to the low pump power and small fluctuations in the 1 μm power level. The OPO is operating near threshold and small input power changes result in larger changes in the output of the OPO. Although excellent alignment between the laser and the OPO was maintained, the OPO performance is extremely sensitive to the pump laser quality and power level. A stable and more powerful pump laser with better beam quality would eliminate this problem. Further improvements to the system would be the addition of a Faraday isolator between the laser and OPO to eliminate feedback problems

Simultaneous Operation

The optical layout of the lidar table allowed the separate alignment of the 1 μm and 2.1 μm beams. The 1 μm beam path consisted of 7 turning prisms, including the boresight prism, in order to redirect the laser light from the laser to the boresighting prism. The 2.1 μm path included two additional turning prisms to allow the separate positioning and pointing of the 2.1 μm beam. The dichroics used to split off and recombine the 1 μm and 2.1 μm beams did not affect the 1 μm beam position or pointing angle. To achieve simultaneous boresighting of the 1 and 2.1 μm beams, the 1 μm beam path was aligned through pinhole apertures in the optical path at two of the turning prisms. Then, the 1 μm beam was boresighted with the telescope and detector package. The 2.1 μm beam was repositioned and realigned to pass through these two pinholes. With the now nearly collinear 1 and 2.1 μm beams we were able to use the 2.1 μm turning prisms to properly boresight with the telescope. At this point, we were able to collect simultaneous 1.064 μm and 2.036 μm lidar returns. Data sets containing simultaneous 1 μm and 2.1 μm cloud returns were collected. Calibration data sets from $\sim 3\text{km}$ above the ocean surface in the nadir viewing configuration with the detectors in a special integrate mode were recorded.

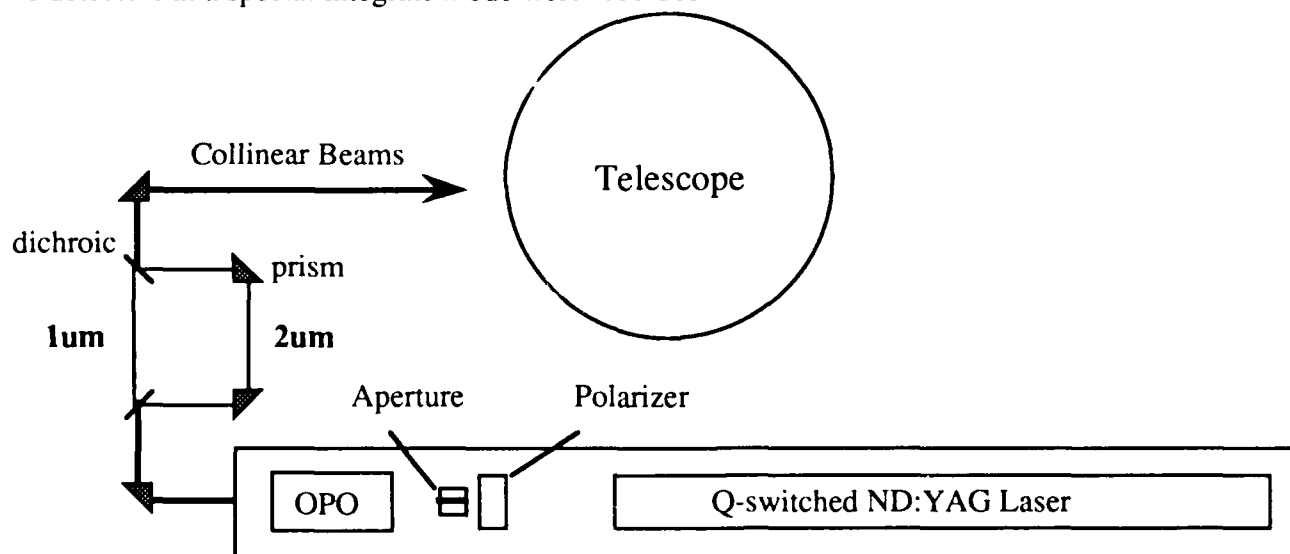


Figure 1: Schematic of Simultaneous 1 and 2 μm lidar

References:

- 1) J.D. Spinhirne, S. Chudamani, J.F. Cavanaugh, "Visible and Near IR Lidar Backscatter Observations on the GLOBE Pacific Survey Missions," Seventh Symposium on Meteorological Observations and Instrumentation and Special Session on Laser Atmospheric Studies J14.3, Jan. 14-18, 1991, New Orleans, LA. p. J261
- 2) There are many good descriptions of OPO's in the literature. Some reference books are: R.W. Boyd, Nonlinear Optics, Academic Press, San Diego, CA, 1992. and F. Zernike and J.E. Midwinter, Applied Nonlinear Optics, John Wiley and Sons Inc., New York, 1973

A Technique for Measuring Winds in the Lower Atmosphere Using Incoherent Doppler Lidar

Daniel. H. DeSlover, Dennis R. Slaughter, William M. Tulloch, William E. White
University of California, *Lawrence Livermore National Laboratory*
Livermore, CA 94550, (510) 423-9691

Introduction

Wind speed is useful from a meteorological standpoint, in atmospheric modeling, and assessment of trace gas dispersal. A continuing effort is involved in improving the sensitivity of such measurements, and is exemplified by the literature.^[1-10] The Mobile Atmospheric Research Laboratory (MARL) at Lawrence Livermore National Laboratory (LLNL) is currently developing a method to improve the sensitivity of wind sounding in the lower through middle atmosphere using a pair of Fabry-Perot interferometers in parallel. This technique, first described by Chanin, et al.^[4], for the middle atmosphere using Doppler Rayleigh lidar, can be applied to the lower atmosphere where Mie (aerosol) backscatter is strong. Elastic events, inherent in both Rayleigh and Mie backscatter, dominate the return signal throughout the atmosphere. Both are susceptible to local wind vectors; which will Doppler shift the laser frequency proportional to the wind velocity. A pair of Fabry-Perot interferometers, tuned to either side of the laser frequency, will provide necessary data to determine the shift in frequency of the backscattered signal. Spectral drift and jitter of the laser and a lack of data points to determine the wind vector place limits on the sensitivity of the system. A method to minimize each of these will be presented.

Fundamentals

The return signal will be Doppler shifted due to the velocity of the particle. According to the familiar equation,

$$v(r) = \frac{\lambda \Delta \nu}{2 \sin \theta}, \quad (1)$$

where the horizontal velocity, $v(r)$, varies with altitude; c , the speed of light; $\Delta \nu$, the frequency shift; and θ , the angle that the beam is pointed with respect to the zenith. The range, r , is determined by time of flight determined by the round trip distance-- ct .

Whereas the aerosol has negligible thermal broadening, the less massive molecular component will be broadened in addition to maintaining a frequency shift. From statistical mechanics, one can

show that molecules are moving at a temperature dependent velocity; which acts in all directions to yield a Maxwellian spread rather than a shift

$$\Delta v_{\text{mol}} = \sqrt{\frac{2 \ln(2) RT}{m \lambda^2}}, \quad (2)$$

where R is the gas constant; T, the temperature; m, the average mass [kg/mole] of the particles. For example, a 532 nm beam will be broadened 1.2 GHz (1064 nm, 600 MHz) due to the molecular constituent. Using Eq. 1, the frequency-doubled line will shift a factor of 2 greater than the Nd:YAG fundamental (2.6 versus 1.3 MHz, for a 1 m/s horizontal velocity component).

Configuration and Technique

The transmitter (injection seeded, Q-switched Nd:YAG; 1064 nm, 320 mJ; 532 nm, 155 mJ; 10 Hz, 9 ns pulse) is monitored on a shot-to-shot basis through a known-response atomic vapor absorption edge filter (Fig. 1). Absolute output power is referenced following transmittal through a pair of calibrated beam splitters. The second splitter sends the signal to another detector via the edge filter. A difference in expected intensity throughput corresponds to a spectral shift in the laser. The drift can be determined and used to correct the measured frequency shift of the backscattered return. Korb, et al., have reportedly used this method to successfully maintain a resolving power, $\nu / \Delta \nu$, of 2.8×10^6 .^[7]

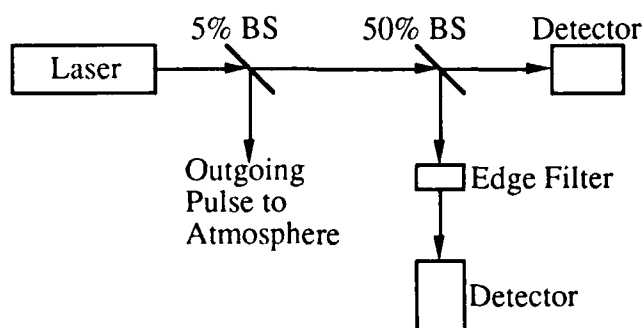


Figure 1. Frequency shift due to laser instability can be corrected by monitoring transmission through an atomic absorption edge filter.

Background noise is partially removed by a sequence of filters (bottom right of Fig. 2). First, a 0.3 nm (320 GHz) FWHM interference filter (55% T), centered around 532.08 nm, will eliminate most unwanted radiation, enough for night-time operation. A pair of low-finesse, Fabry-Perot interferometers in series act to further reduce the background signal. Their spacing (0.2 and

0.5 cm, yielding FWHM's, centered around the laser frequency, of 4.8 and 1.9 GHz, respectively) are nearly incommensurate within the bandpass of the interference filter; thereby canceling additional orders of the opposite interferometer. Preliminary calculations reveal that daytime operation should be possible with a moderate integration time (< 1 hour) when using this pre-filter system. A high-speed digitizer (1 GSample/sec) collects data at each photomultiplier tube (PMT).

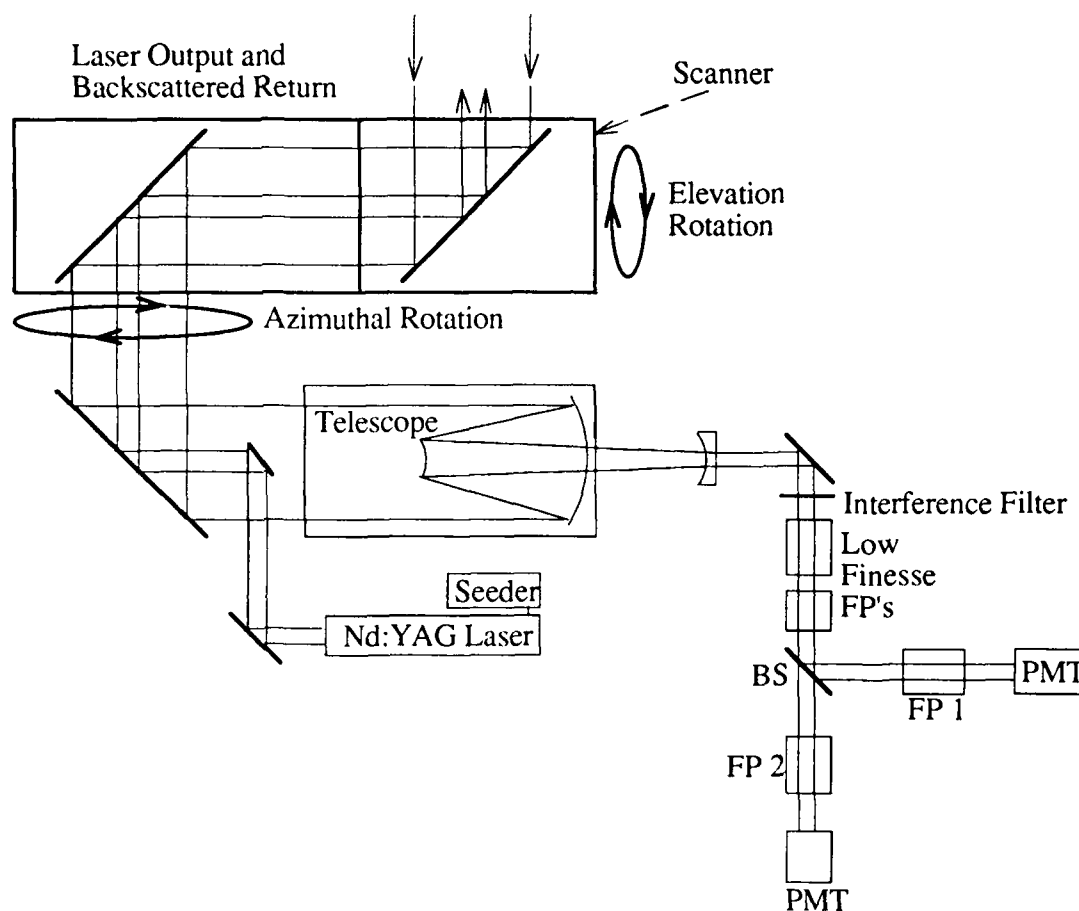


Figure 2. Schematic diagram of LLNL's MARL wind sounding facility. The diagram illustrates the possible motion of the computer controlled scanner, collection telescope, and background filter scheme prior to sampling of data.

The MARL facility incorporates a 3-mirror, 50 cm aperture scanner with continuous azimuth and elevation control; thus affording full hemispherical scan capability (upper portion of Fig. 2). Garnier showed that three points (zenith and two orthogonal tilted view) are sufficient to determine the horizontal wind vector (and a balloonsonde to set a reference for systematic drift)^[3, 5]. With the functionality of the scanner a continuous conic scan can be achieved; whose data will result in a sine wave from which the amplitude, phase, and mean value of the wind vector can be calculated. Sensitivity should be improved after fitting the data to a natural sinusoidal. A balloonsonde will

not be required, aside from comparison purposes, since systematic frequency drift is monitored in an absolute sense.

Conclusion

An extension of a proven technique, using Doppler Rayleigh lidar (25 - 60 km) to monitor wind speeds, is being applied to the lower atmosphere based on aerosol backscatter. The dual Fabry-Perot system is under development and is nearly ready for field test. Suggestions have been made that will improve sensitivity in the wind speed calculation by correcting for frequency instabilities in the laser (use of an atomic vapor absorption filter) and scanning the sample volume (conic scan to create sinusoidal array of wind vector information) to better fit the data. This should prove to be a functional system to determine wind speeds--from the ground to 60 km.

Work performed under the auspices of the U.S. Department of energy by Lawrence Livermore National Laboratory under Contract #W-7405-Eng-48.

References

1. V. J. Abreu, et al., "Observations of Winds with an Incoherent Lidar Detector," *Appl. Opt.*, **31**, 4509-14.
2. V. J. Abreu, "Wind Measurements from an Orbital Platform Using a Lidar System with Incoherent Detection: An Analysis," *Appl. Opt.*, **18**, 2992-7.
3. A. Garnier, "A Doppler Rayleigh Lidar for Measuring Winds in the Middle Atmosphere," *OSA Tech. Digest, Coherent Laser Radar: Tech. and Appl. Top. Meet.*, **12**, 177-9.
4. M. L. Chanin, et al., "A Doppler Lidar for Measuring Winds in the Middle Atmosphere," *Geophys. Res. Let.*, **16**, 1273-6.
5. A. Garnier and M. L. Chanin, "Description of a Doppler Rayleigh Lidar for Measuring Winds in the Middle Atmosphere," *Appl. Phys. B*, **55**, 35-40.
6. R. M. Hardesty, et al., "Observing Atmospheric Winds with a Doppler Lidar," *Opt. & Phot. News*, 12-15.
7. C. L. Korb, et al., "Edge Technique: Theory and Application to the Lidar Measurement of Atmospheric Wind," *Appl. Opt.*, **31**, 4202-13.
8. R. T. Menzies, "Doppler Lidar Atmospheric Wind Sensors: A Comparative Performance Evaluation for Global Measurement Applications from Earth Orbit," *Appl. Opt.*, **25**, 2546-53.
9. D. Rees, et al., "Observations of Atmospheric Absorption Lines from a Stabilized Balloon Platform and Measurements of Stratospheric Winds," *J. Phys. E: Sci. Instrum.*, **15**, 191-206.
10. D. Rees and I. S. McDermid, "Doppler Lidar Atmospheric Wind Sensor: Reevaluation of a 355-nm Incoherent Doppler Lidar," *Appl. Opt.*, **29**, 4133-44.

Abshire, James B. — 502
Afzal, Robert S. — 514

Ballard, J. — 506
Blair, J. Bryan — 514

Chan, Kin Pui — 473
Charland, A. — 483
Chen, H. — 495
Chiou, Er-Woon — 491
Chu, W. P. — 491

De Backer, Hugo — 487
De Muer, Dirk — 487
DeSlover, Daniel — 510, 517

Godoy, Carolina — 476
Gross, M. R. — 479
Grund, Christian J. — 473

Martinez, Ronald J. — 498
McCormick, M. P. — 491
McGee, T. J. — 479
McKenzie, R. L. — 479
Morris, P. E. — 506
Morrow, W. H. — 483

Nicholls, R. W. — 483

Post, Madison J. — 473

Rall, Jonathan A. R. — 502
Rosen, J. M. — 479

Sander, Robert K. — 498
Seville-Jones, Dyan N. — 498
She, C. Y. — 495
Singh, U. N. — 479
Slaughter, Dennis — 510, 517
Spinhirne, James D. — 514
Stix, John — 483
Swart, Daan P. J. — 487

Taylor, F. W. — 506
Tiee, Joe J. — 498
Tulloch, William — 510, 517

Vazquez, Gabriel J. — 476
Visser, Eric P. — 487

White, William — 510, 517

Yu, J. R. — 495

TECHNICAL PROGRAM COMMITTEE

Allan Carswell, General Cochair
York University, Canada

William Mankin, General Cochair
National Center for Atmospheric Research

Stuart McDermid, Program Cochair
Jet Propulsion Laboratory

William Smith, Program Cochair
University of Wisconsin, Madison

Alain Chedin
Ecole Polytechnique, France

Shepard A. Clough
Atmospheric Environmental Research, Inc.

Herbert Fisher
Meteorological Institut Munchen, Germany

Raymond M. Hoff
Atmospheric Environment Service, Canada

Horst Jager
Fraunhofer Institute, Germany

Thomas J. McGee
NASA Goddard Space Flight Center

John Meriwether
Phillips Laboratory

Clive Rodgers
Oxford University, England

Yasuhiro Sasano
National Institute for Environmental Studies, Japan

D. P. J. Swart
RIVM, Holland (The Netherlands)

Ed Westwater
NOAA/Environmental Research Laboratories